Topics in Current Chemistry Collections

Xuefeng Guo *Editor*

Molecular-Scale Electronics

Current Status and Perspectives

Springer

Topics in Current Chemistry Collections

Aims and Scope

The series *Topics in Current Chemistry Collections* presents critical reviews from the journal *Topics in Current Chemistry* organized in topical volumes. The scope of coverage is all areas of chemical science including the interfaces with related disciplines such as biology, medicine and materials science.

The goal of each thematic volume is to give the non-specialist reader, whether in academia or industry, a comprehensive insight into an area where new research is emerging which is of interest to a larger scientific audience.

Each review within the volume critically surveys one aspect of that topic and places it within the context of the volume as a whole. The most significant developments of the last 5 to 10 years are presented using selected examples to illustrate the principles discussed. The coverage is not intended to be an exhaustive summary of the field or include large quantities of data, but should rather be conceptual, concentrating on the methodological thinking that will allow the non-specialist reader to understand the information presented.

Contributions also offer an outlook on potential future developments in the field.

More information about this series at http://www.springer.com/series/14181

Xuefeng Guo
Editor

Molecular-Scale Electronics

Current Status and Perspectives

With contributions from

Jie Bai • Huanli Dong • Xuefeng Guo • Wenjing Hong
Duan Hu • Gui-Chao Hu • Wenping Hu • Rongjin Li • Xiaohui Li
Zihao Liu • Takuji Ogawa • Shizhao Ren • Jia Shi • Hyunwook Song
Yang Song • Takashi Tamaki • Zhibing Tan • Chuan-Kui Wang
Kun Wang • Ling Wang • Lu Wang • Yu Wang • Dong Xiang
Zongyuan Xiao • Zhen Xie • Bingqian Xu • Yang Yang
Guang-Ping Zhang • Lei Zhang • Xiaotao Zhang • Weigang Zhu

Springer

Editor
Xuefeng Guo
Peking University
Beijing, China

Partly previously published in Top Curr Chem (Z) Volume 374 (2016); Top Curr Chem (Z) Volume 375 (2017); Topics in Current Chemistry Volume 376 (2018).

ISSN 2367-4067
Topics in Current Chemistry Collections
ISBN 978-3-030-03304-0

Library of Congress Control Number: 2018961136

This Springer imprint is published by the registered company Springer Nature Switzerland AG
The registered company address is: Gewerbestrasse 11, 6330 Cham, Switzerland

Contents

Preface

What does the future hold for electronic devices? To what extent can their dimensions be reduced in the future? The urgent need for miniaturizing silicon-based microelectronics, which is extremely challenging, has inspired intensive research in the field of molecular electronics for a few decades. The development of efficient methodologies to integrate individual or small collections of molecules into electrical nanocircuits is currently a research focus because it can not only overcome the increasing difficulties and fundamental limitations of device miniaturization, but can also enable us to understand the intrinsic properties of materials at the atomic- and/or molecular-length scale. However, the question of how to anchor individual molecules to two electrodes continuously confused researchers throughout the world. This has been achieved thanks to the development of advanced scanning probe microscopic techniques and computational models, which have allowed reliable investigation and simulation of the conductance of single molecules sandwiched between electrodes.

This collection embraces a broad range of topics in the field of molecular-scale electronics from basic concepts and experimental investigations to theoretical simulations and further applications. It gathers together leading specialists from different disciplines, providing a deep overview of the current state of knowledge, including recent advances, open questions, and comprehensive lists of references. Although there are countless approaches of device fabrications and measurement technologies, there are selected techniques upon which the most important studies are based. The practical demonstration of these techniques is the hallmark of this collection; these examples can serve as a *passe-partout* pertinent to understanding device physics and underlying working mechanisms to many device-related research that could not be covered in this collection. In this sense, I hope that they are of good value to a wide spectrum of readers or researchers from other research fields as well.

K. Wang and B. Xu discuss various aspects of single-molecule junction electronics, with an emphasis on the single-molecule break junction technique, from the initial vision of molecular electronics, the development of experimental techniques in creating single-molecule junctions and determining single-molecule conductance, to the characterization of functional current-voltage features and investigation of physical properties beyond charge transport, such as quantum interference, heat transport, optoelectronics and spintronics. D. Xiang *et al.* provide a systematic overview of four test-beds for single-molecule junctions, with a focus on the development of state-of-the-art mechanically controlled break junctions, where three-terminal gated approaches are discussed. W. Hong *et al.* review the charge transport characterization of supramolecular junctions through a variety of non−covalent interactions and the recent progress in the formation of highly conductive molecular junctions via chemical reactions. T. Tamaki and T. Ogawa highlight molecular design for non-linear and non-symmetric single-molecule electronic properties, such as rectification, negative differential resistance, and switching, which are important components for future single-molecule information processing. C.-K. Wang *et al.* cover the theoretical and experimental progresses of molecular diodes based on either charge or spin as well as the detailed analysis of rectification mechanisms. X. Guo *et al.* summarize the strategies developed for creating single-molecule electrical switches and the mechanism of their switching effects, which is crucial for the development of molecular electronics. H. Song reviews recent progresses in constructing and characterizing state-of-the-art molecular transistors, in which the transport current is electrostatically or electrochemically modulated by direct orbital gating. Finally, W. Hu *et al.* show the engineering concept of how to utilize organic cocrystals to constitute multifunctional molecular optoelectronics, opening a complementary door for molecular electronics.

We are pleased that, exactly as planned, this collection turned out to be very well integrated, where each contribution focuses on a particular topic while still mutually supporting each other. This collection offers a good starting point for students and scientists who want to improve their understanding in the magic field of molecular electronics.

We must acknowledge many prominent researchers that have contributed to this work, some of them with articles, others with highly insightful comments, which are invaluable to the success of this text. I personally would like to express my deep thanks to the editorial staff of *Topics in Current Chemistry* and the editorial board for choosing me to help organize this collection. We do hope that the readers will enjoy the informative and enlightening journey.

Xuefeng Guo

Beijing National Laboratory for Molecular Sciences, State Key Laboratory for Structural Chemistry of Unstable and Stable Species, College of Chemistry and Molecular Engineering, Peking University, Beijing 100871, China.

Email: guoxf@pku.edu.cn

Top Curr Chem (Z) (2017) 375:17
DOI 10.1007/s41061-017-0105-z

REVIEW

Modulation and Control of Charge Transport Through Single-Molecule Junctions

Kun Wang[1] · **Bingqian Xu**[2]

Received: 12 October 2016 / Accepted: 7 January 2017 / Published online: 24 January 2017

Abstract The ability to modulate and control charge transport though single-molecule junction devices is crucial to achieving the ultimate goal of molecular electronics: constructing real-world-applicable electronic components from single molecules. This review aims to highlight the progress made in single-molecule electronics, emphasizing the development of molecular junction electronics in recent years. Among many techniques that attempt to wire a molecule to metallic electrodes, the single-molecule break junction (SMBJ) technique is one of the most reliable and tunable experimental platforms for achieving metal–molecule–metal configurations. It also provides great freedom to tune charge transport through the junction. Soon after the SMBJ technique was introduced, it was extensively used to measure the conductances of individual molecules; however, different conductances were obtained for the same molecule, and it proved difficult to interpret this wide distribution of experimental data. This phenomenon was later found to be mainly due to a lack of precise experimental control and advanced data analysis methods. In recent years, researchers have directed considerable effort into advancing the SMBJ technique by gaining a deeper physical understanding of charge transport through single molecules and thus enhancing its potential applicability in functional molecular-scale electronic devices, such as molecular diodes and molecular transistors. In parallel with that research, novel data analysis methods and approaches

Chapter 1 was originally published as Wang, K. & Xu, B. Top Curr Chem (Z) (2017) 375: 17. DOI 10.1007/s41061-017-0105-z.

✉ Bingqian Xu
bxu@engr.uga.edu

[1] Department of Physics and Astronomy and NanoSEC, University of Georgia, 220 Riverbend Road, Athens, GA 30602, USA

[2] College of Engineering and NanoSEC, University of Georgia, 220 Riverbend Road, Athens, GA 30602, USA

that enable the discovery of hidden yet important features in the data are being developed. This review discusses various aspects of molecular junction electronics, from the initial goal of molecular electronics, the development of experimental techniques for creating single-molecule junctions and determining single-molecule conductance, to the characterization of functional current–voltage features and the investigation of physical properties other than charge transport. In addition, the development of advanced data analysis methods is considered, as they are critical to gaining detailed physical insight into the underlying transport mechanisms.

Keywords Molecular electronics · Single-molecule break junction · Mechanical modulation · Molecule–electrode interfaces · Rectification · Negative differential conductance · Gating effect

1 Introduction and Background

Building electronic devices out of single molecules or collections of molecules has long been one of the loftiest goals of nanotechnology, and one of its greatest challenges. Since the early 1970s, wiring single molecules to two metallic electrodes has been proposed as both the ultimate aim of the downscaling of active electronic components such as diodes and transistors and an important path to overcoming the limit suggested by Moore's prediction [1–4]. Molecular circuits built in this manner could raise device density by a factor of up to $\sim 10^4$ compared to the current device level of silicon-based microelectronic devices [5]. Equally importantly, a nanometer-long single-molecule device would have an overwhelmingly greater level of functionality and structural flexibility than conventional semiconductor materials.

Back in 1974, Aviram and Ratner's theoretical discussion of electron transport through a single molecule acted as the catalyst for the construction of a molecular rectifier [6]. This theoretical proposal involved unidirectional electron transport between donor and acceptor levels in a single molecule (Fig. 1a). For the first time, it suggested that it was possible to create and measure a single-molecule circuit from a theoretical perspective. The original idea involved contacting a nanoscopic molecule with bulk material electrodes. Unlike the continuous and condensed energy-band dispersion of bulk materials, the energy levels in a nanoscale molecule (i.e., molecular orbitals, MOs) are quantized and discrete. These quantized energy levels are what distinguish single-molecular devices from classical p–n junctions [5]. The energy gap between the highest occupied molecular orbital (HOMO) and the lowest unoccupied molecular orbital (LUMO) is called the HOMO–LUMO gap (HLG). Thus, bridging two metallic electrodes with a single molecule causes discrete states to merge into continuous states. This unique trait is believed to lead to intriguing electrical and mechanical properties.

The excitement generated by Aviram and Ratner's initial work prompted a great deal of research in this area. However, no significant progress was achieved by experimentalists in the decade following the initial work. Wiring a molecule to electrodes or attaching the electrodes to a molecule was found to be a considerable

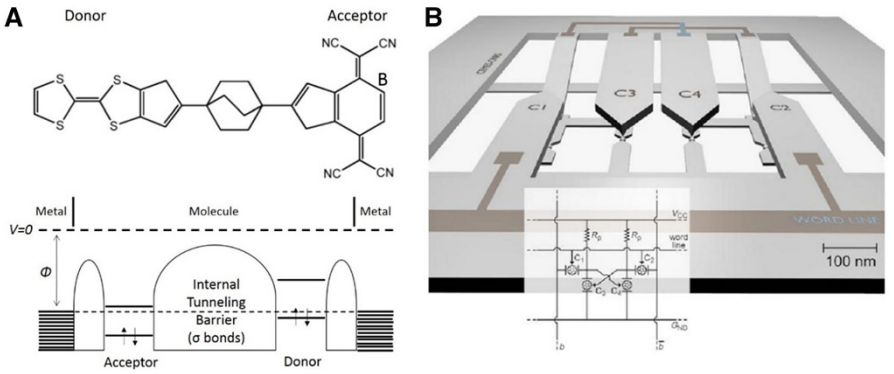

Fig. 1 **a** Molecular rectifier proposed by Aviram and Ratner in 1974. *Upper panel*: structure of the molecule with an tetracyanoquinodimethane (TCNQ) acceptor moiety and a tetrathiolfulvalene (TTF) donor moiety separated by a triple ethylene bridge. *Lower panel*: energy diagram of the molecule when in contact with anode and cathode electrodes. Reprinted with permission from [6]. Copyright (1974) Elsevier. **b** Architecture of the hybrid molecular electronic device proposed in Aviram's review paper in 2000. Reprinted with permission from [18]. Copyright (2000) Nature Publishing Group

challenge. Experimental efforts following this "bottom-up" approach employed unconventional means: the use of mercury drops as electrodes [7], the application of Lorentz force to cross metallic wires [8], and trapping molecules in a nanopore [9, 10]. However, the experimental results were chaotic and not reliable enough. Other techniques that involved sandwiching robust molecules between electrode layers proved to be too destructive for small molecules [11–13]. Reliable contact between the molecule and electrodes was very difficult to achieve, and this remained a major obstacle to progress in the development of single-molecule devices for more than a decade [14].

In the 1990s, the development of (initially) scanning tunneling microscopy (STM) and (later) atomic force microscopy (AFM) led to the most significant breakthrough in molecular electronics [15]. It was rapidly discovered that these scanning probe microscopy (SPM) techniques could be used to measure electrical properties such as conductance and *I*–*V* characteristics at the single-molecule level. The first experimental attempt to determine the conductance of a molecule was carried out by Mark Reed's group at Yale University, in collaboration with James Tour's group, then at the University of South Carolina (Fig. 2) [16]. They stretched a gold wire in a solution of sample molecules until breakage occurred, which resulted in the formation of two tips of atomic sharpness covered with molecules. These two tips were subsequently brought together by means of a piezo-controlled bendable substrate while measuring the current flow [16]. The current–voltage characteristics of benzene-1,4′-dithiol molecules were then tested. The invention of this technique, now known as a mechanically controlled break junction (MCBJ), proved to be a significant breakthrough in the field of ME, and also served as the precursor for the development of the widely used SPM break junction technique. In addition, Park et al. reported the electromigration break junction (EBJ) technique in 1999, which enabled the formation of nanoscale contacts for single molecules on

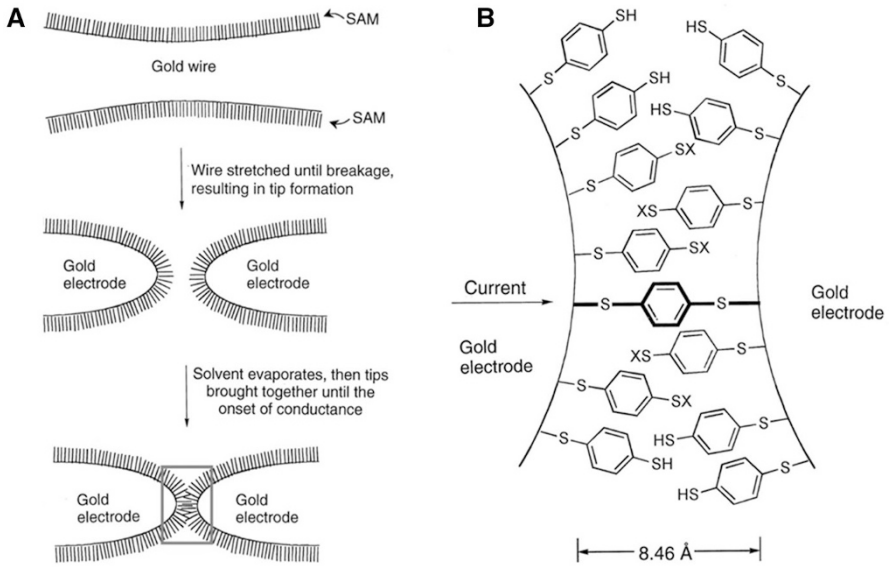

Fig. 2 Experimental work by Mark Reed et al. in 1997. **a** Schematic of the measurement process. **b** Schematic of a benzene-1,4-dithiolate SAM between proximal gold electrodes (enlarged view of the area in the *box* in **a**). Reprinted with permission from [16]. Copyright (1997) AAAS

top of an oxidized conducting substrate [17]. Review papers by Aviram [18] and Nitzan [19] in the early 2000s summarized the molecular structures proposed at that time which were promising tools for building electronic rectifiers, switches, and storage devices, and also depicted the possible architecture of hybrid molecular circuits (Fig. 1b). These works sparked worldwide interest in this subject, and represented the true beginning of molecular electronics [15]. Later in 2003, Xu and Tao provided an introduction to the STM break junction technique, which proved be another significant driving force for molecular electronics, as it provides a robust and tunable experimental platform to repeatedly create single-molecule junctions. More recently, single-molecule junction systems utilizing novel carbon-based electrode materials [20] such as carbon nanotubes [21] and graphene [22] have been shown to exhibit intriguing transport phenomena, leading to a greater understanding of molecular junction devices.

In the past two decades, remarkable progress has been made in the fabrication of metal–molecule–metal junctions using single-molecule break junction techniques, the tuning of the charge transport properties of such junctions, and our understanding the associated underlying transport mechanisms. Meanwhile, more advanced data analysis methods have emerged that allow hidden but significant details in the data to be explored, and attempts have been made to interrogate multiple properties beyond the electronic transport of single-molecule devices. In this review, we discuss the major progress made in recent years in work done to modulate charge transport through single-molecule break junction based devices, emerging methods of interpreting the relevant experimental data, and the potential

of future research and applications in molecular electronics. For more information on the techniques involved, the differences in electron transport properties between the various techniques, and characterization methods, we refer readers to reviews [23–25].

2 Single-Molecule Break Junction (SMBJ) Technique

The major barrier experimentalists encountered in the early 2000s was the large fluctuations in the datasets of conductance measurements. It was difficult to determine how many molecules were bridged across the electrodes and how many contributed to the measured results. Many discrepancies emerged not only between experimental data and simulated results but also among datasets collected from different labs [26–31]. The latter were mainly attributed to a lack of appropriate control over experimental conditions. Therefore, what was urgently required back then was a repeatable and reliable experimental platform that could at least minimize the fluctuations in experimental data, raising confidence in further investigations.

Xu and Tao's work in 2003 yielded a repeatable STM break junction (STMBJ) method [32]. This method uses a metallic STM tip as one electrode and a metallic substrate as the other electrode (Fig. 3a). Via piezoelectric control, the STM tip is brought close to the substrate, which is covered with sample molecules. The feedback loop is disengaged and the tip is pushed into contact with the substrate. It is then retracted while the tunneling current is monitored. A fresh metal–metal atomic junction is formed, and on retraction this thins down to a single atom (point contact), which is finally broken upon further withdrawal. This process results in plateaus in conductance traces at multiples of the conductance quantum G_0 ($2e^2/h$ = 77.5 μS, where e is the charge on the electron and h is Planck's constant) owing to atomic rearrangements in the junction (Fig. 4a). When the point contact breaks, if no molecule is trapped in the resulting break junction, the final step down of G_0 is

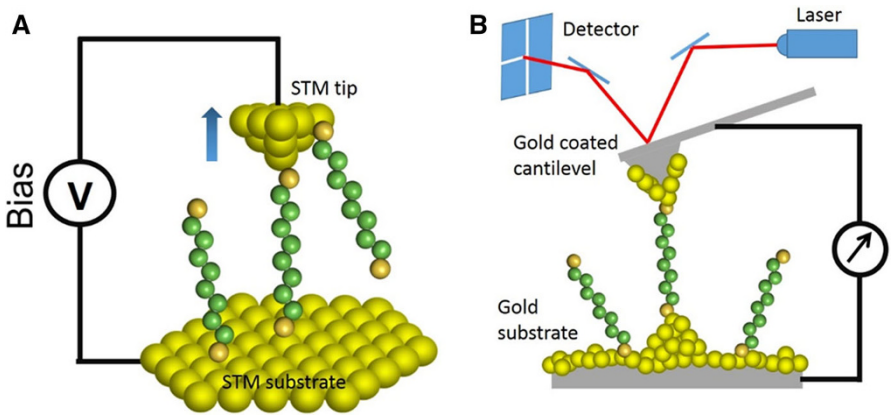

Fig. 3 Schematic representations of STMBJ (**a**) and C-AFMBJ (**b**)

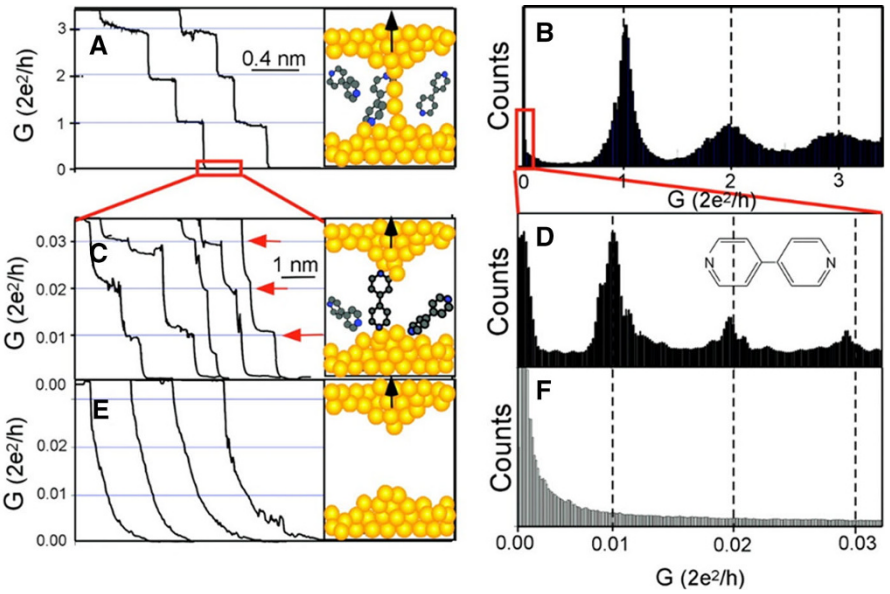

Fig. 4 STMBJ measurements conducted by Xu and Tao. **a** Conductance trace of a gold contact between a gold tip and a gold substrate with quantum steps of approximately G_0. **b** Conductance histograms constructed from thousands of the traces shown in **a**. **c** Conductance traces and junction schematic for 4,4′-bypiridine molecular junctions after the contact in **a** completely breaks. **d** Corresponding conductance histogram constructed from traces shown in **c**. **e**, **f** The conductance traces and histograms obtained when there was no molecule in solution. Reprinted with permission from [32]. Copyright (2003) AAAS

followed by a sharp exponential decay as the tip continues to retract, but if a molecule (or molecules) binds to both gold contacts, additional plateau(s) are subsequently seen in the current–distance plot at conductances $\ll G_0$, corresponding to the tunneling conductance through the molecule (Fig. 4b). Eventually, as the retraction continues, the metal–molecule–metal junction breaks down, whereupon the current rapidly falls to a very low value, consistent with tunneling through space once more. Thus, the last significant step before the conductance falls to zero is the conductance across an individual molecule. After repeating this engaging–retracting cycle thousands of times, statistical analysis of the resulting thousands of similar traces reveals peaks at the positions where plateaus appear most frequently in a conductance histogram (Fig. 4d). The first prominent peak in the histogram is believed to be the conductance when only one molecule is left in the break junction: the single-molecule conductance. This method washes out contact variations to a certain extent, and eliminated most discrepancies in early measurements. Now it is probably the most widely used method of studying electron transport in single-molecule junctions.

The conductive AFM break junction (C-AFMBJ), which is analogous to the STMBJ, uses a metal-coated AFM tip as the tip electrode and involves a laser-reflection controlled force signal detector, which enables measurements of conductance and force in parallel (Fig. 3b). Note that a C-AFMBJ works in the

same way as a STMBJ but adds one more detectable parameter—force—to the system. Other techniques employing the emerging STM technique were also developed at the same time. The I(s) (also called I(z) in the literature) technique introduced by Haiss et al. in 2003 also uses an STM tip to form molecular junctions [33]. The core difference is the junction formation method. The I(s) method avoids contact between two metal electrodes. The STM tip approaches the surface of analyte molecules and then retracts from it while the tunneling current is measured. The I(s) technique and the corresponding conductance signal are exemplified in Fig. 5a. A further development using STM employs similar ideas but focuses on the time domain and has been referred to as the I(t) method, as exemplified in Fig. 5b [34]. The STM tip is placed at a constant distance from the substrate. This distance is usually set to be less than the length of a fully extended molecule. Characteristic vibrations in current which behave like telegraphic noise signals (rightmost panel in Fig. 5b) can then be monitored. Current jumps have been attributed to the

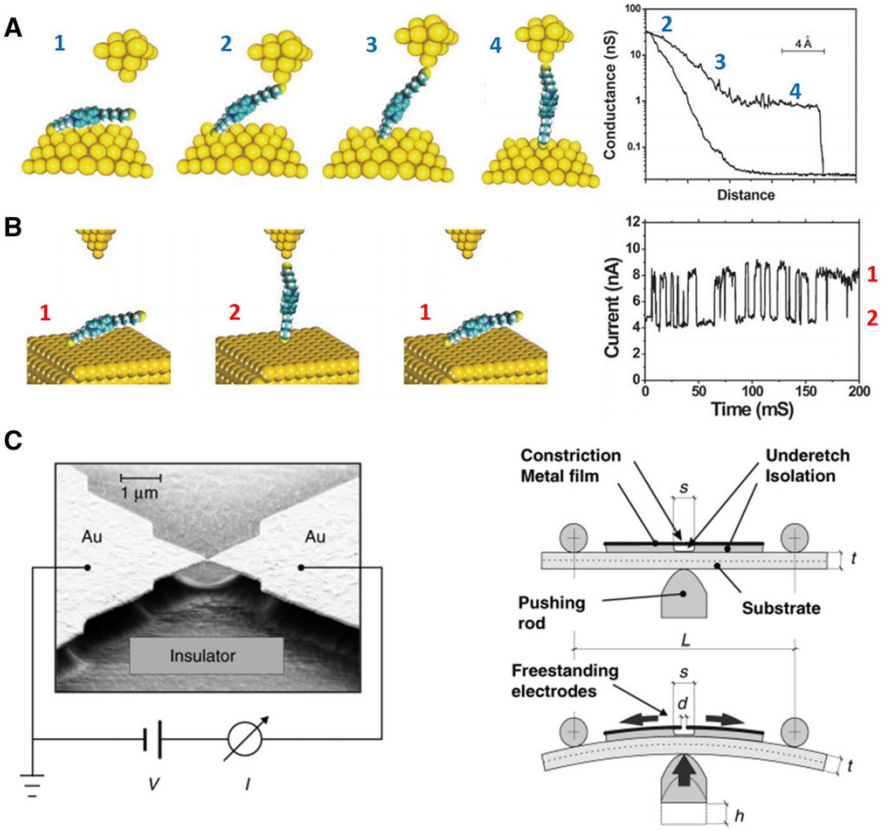

Fig. 5 Other single-molecule break junction techniques. **a** The I(s) or I(z) technique. **b** The I(t) technique. **c** The MCBJ technique. **a**, **b** are reprinted with permission from [35]. Copyright (2010) Royal Society of Chemistry. **c** is reprinted with permission from [38]. Copyright (2006) Wiley–VCH Verlag GmbH & Co. KGaA

attachment or detachment of the molecule to or from the STM tip. The conductance can be determined by calculating the peak value of the current jump and the applied bias [35]. Another method, the mechanically controlled break junction (MCBJ), uses notched metal wire fixed onto an elastic substrate [16, 36–39]. A diagram of the MCBJ is shown in Fig. 5c. The substrate is usually covered with an insulator, and the metal wire is mechanically broken by bending the substrate. A single-molecule break junction is formed when only one molecule is left in the gap between the two terminals of the broken metal wire. These methods of collecting signals by sandwiching a single molecule in a scheme of break junctions are called single-molecule break junction (SMBJ) techniques.

Using the SMBJ technique, experimentalists have obtained extensive data and observed phenomena of great interest over the past decade, such as rectification [40–42], negative differential resistance [43–45], the Kondo effect [46–48], redox switching [49–51], spin-split molecular orbitals [52–54], magnetoresistance [55], thermoelectrics [56–59], and quantum interference [60–62], which has greatly boosted the development of molecular electronics.

3 The Role of the Molecule–Electrode Interfaces

At the most basic level, control over the physical and chemical properties of a molecular junction requires an ability to create robust contacts when forming a single-molecule junction. This is a demanding task, so the role of the molecule–electrode contact interfaces was initially overlooked. To date, the influence of the molecule–electrode interfaces on the charge-transport properties of a molecular junction have proven to be rather difficult to unravel [24]. According to the Landauer–Buttiker formalism, the overall conductance of a molecular junction can be described as [63]

$$G = \frac{I}{V} = \left(\frac{2e^2}{h}\right) T_{\mathrm{L}} T_{\mathrm{mol}} T_{\mathrm{R}},$$

where I is the current through the junction, V is the applied bias, and T_{L}, T_{R}, and T_{mol} are the transmission coefficients of the left interface, the right interface, and the molecule, respectively. For nonresonant tunneling transport, when the Fermi levels of the electrodes lie in the gap between the HOMO and LUMO of the molecule, both the interfacial coupling strength and the energy level offset between the electrodes and the molecule significantly influence the conductance of the molecular junction. For resonant transport, however, the Fermi levels of the electrodes are resonant with the molecular energy levels, so the conductance depends only on the contact resistance due to the different coupling strength that determines the contact barrier height and width. For the vast majority of the molecules studied thus far, the dominant charge-transport mechanism is nonresonant tunneling. The primary reason for this is that most short molecules have a large gap between the HOMO and the LUMO, on the order of several electron volts [27].

To realize controlled charge transport in molecular junctions, both the coupling and the energy level alignment at the interfaces between the electrodes and the molecule should be precisely controlled.

(1) Alkane-based molecular junctions

Thus far, alkanes have been the most popular molecules to use in molecular junction conductance experiments [7, 64–72]. To allow them to be used in conductance experiments, the alkanes are terminated at both ends with an anchoring group capable of binding to the metallic electrodes. Alkanedithiols were the first molecular family to be systematically studied with the STM break junction approach [32]. However, shortly thereafter, other groups reported significantly different conductance values (sometimes as much as one order of magnitude different) for the same molecules [34]. Later studies were able to demonstrate that two or three different conductance values could be measured for each alkanedithiol [66, 69]. Even more conductance values were discerned using a stretch-hold-mode STMBJ [73]. These multiple conductance values occur for two reasons. First, the lowest conductance values arise when a gauche defect is present in the backbone, as shown in Fig. 6. This defect can cause a significant change in the orbital alignment with the electrodes and modify the conductance [66]. However, different medium and high conductance values have been widely attributed to changes in the contact geometry. Several theoretical and experimental studies have focused on how changes in contact configuration can affect the conductances of alkanes with thiol or other linkers, and have found that such changes can dictate the absolute conductance of the molecule [68–70, 74]. The modeled Au–thiol contact configurations mainly differed in the manner in which the sulfur anchoring groups attached to the Au clusters, so they were given different names, including "atop," "bridge," "hollow," and "gauge" [64, 68, 75, 76]. Schematics of the "atop–atop," "bridge–bridge," and "gauche" contact configurations are shown in Fig. 6b. In these cases, a change in geometry changes the coupling in the Au–linker bond, thus modifying the contact resistance without significantly changing the orbital alignment. It is clear that gold–

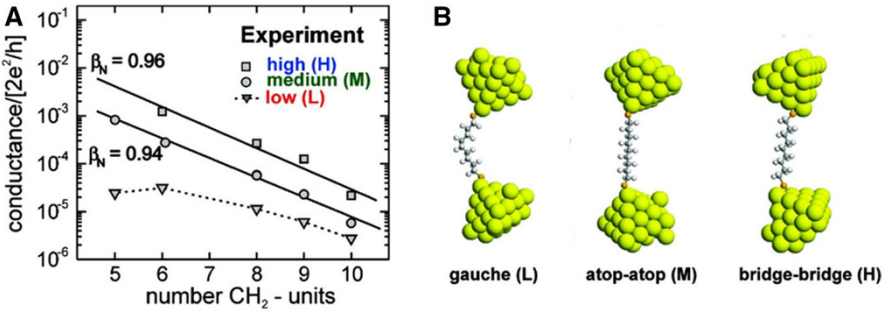

Fig. 6 **a** Chain-length dependence of the single-molecule conductance of alkanedithiol in contact with gold electrodes. Three conductance sets (high, medium, and low) were observed for each chain length. **b** Three contact configurations of the Au–C9DT–Au junction. Reprinted with permission from [66]. Copyright (2008) American Chemical Society

thiol bonds are a useful tool for studying single-molecule junctions because robust mechanical and electrical coupling can be obtained at the molecule–electrode interfaces. However, the variability observed in the conductance values implies that other metal–molecule bonds must be studied in order to improve our understanding of this phenomenon and thus progress towards the development of devices that are technologically applicable [77].

(2) Different anchoring groups

The diversity of potential anchoring groups available makes it convenient to control the interfacial characteristics of molecular junctions by selecting the anchoring groups at the molecular ends appropriately. Because of the intrinsic advantages of gold electrodes, the majority of the investigations of the effects of the anchoring group on the properties of molecular junctions have been carried out in gold electrode systems.

Due to the high covalent strength and good electronic coupling of the resulting Au–S covalent bond, thiol (–SH) has been the most widely used anchoring group for gold electrodes. However, the wide range of possible Au–S binding geometries make it a tricky choice for some molecular junction systems. Amines ($-NH_2$) were one of first anchoring groups to be studied as an alternative to thiols [78]. Amines were known to act as capping layers for Au nanoparticles, and as such were expected to provide good linkages to Au electrodes, even though there was no covalent bond. The original studies showed sufficient reproducibility to allow statistical information about the conductance to be attained, but a higher contact resistance was observed than the optimal value for Au–thiol bonds [77]. Moreover, other studies later demonstrated that multiple conductance values were possible when using amines as anchoring groups too [73, 79].

A variety of other anchoring groups have been studied, including methylsulfides (–SMe) [80], carboxylic acids (–COOH) [81], isocyanides ($-C\equiv N$) [82], selenol (–SeH) [83], diphenylphosphines (PPh_2) [84], dimethylphosphines (PMe_2) [80], and direct gold–carbon bonds (Au–C) [85, 86]. In Fig. 7, the results of several single-molecule studies of alkane chains of different lengths and with different anchoring groups are illustrated. Interestingly, all of the datasets from different groups and measurements of alkanes with different anchoring groups display similar β values, indicating that the differences in observed conductance among groups are due to differences in the contact resistance; the alignment between the molecular energy levels and the Fermi energy of the electrodes does not change significantly with the anchoring group on the alkane. This graph also suggests that the strength of binding correlates with the contact resistance of the junction. The conductance is highest for Au–thiol and Au–C bonds, while many of the electrostatic and chemisorbed species yield similar conductance values. Taken together, these studies suggest that the best possible linkers have strong covalent bonding but a restricted ability to bind in different configurations, meaning that they show a single conductance value that is as large as possible.

The effect of the anchoring group has also been studied for other molecules. For example, Wandlowski et al. recently studied the influence of the anchoring group on

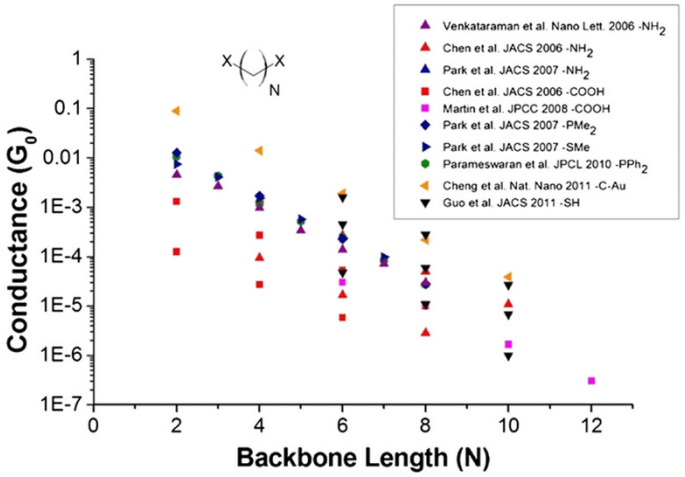

Fig. 7 Conductance values for alkane chains with various lengths and anchoring groups, as shown in the legend. Although the conductance was different with each anchoring group, the β value did not appear to change significantly with contact resistance. Reprinted from [77]. Copyright (2014) IOP Publishing

the conductance through a series of oligoyne molecular junctions (Fig. 8a) [87]. They synthesized five different anchoring structures labeled PY, NH_2, CN, SH, and BT. Interestingly, two conductance sets, high and low, were determined using both STMBJ and MCBJ for all five terminal structures. The most probable single-molecule conductances of the anchoring structures varied by more than two orders of magnitude between the high and low conductance values. The β value for the high-conductance sets ranged between 1.7 nm^{-1} (CN) and 3.2 nm^{-1} (SH) and increased in the order $\beta(CN) < \beta(NH_2) < \beta(BT) < \beta(PY) \approx \beta(SH)$.

In some cases, molecular junctions can also be formed via molecular π-orbital–metal electrode interactions [88–90]. Molecular junctions formed in this manner can yield intriguing phenomena, including higher conductance values [88] and less variability in contact geometries [90]. For instance, Yelin et al. recently reported measurements of highly transmitting molecular junctions based on oligoacenes of increasing length (Fig. 8b) [88]. In their study, the oligoacene molecules were positioned with their short axes touching the electrodes and their long axes pointing out of the junction. They found that not only were the molecular junctions highly conductive, but the conductance also reached an upper limit where it was independent of molecule length. In addition, Martin et al. reported conductance measurements obtained using C60 as the anchoring group, which hybridizes with Au electrodes through its π orbital [90]. The conductance histogram of C60-anchored molecular junctions showed a small spread in conductance values compared to a thiol-anchored molecular junction, indicating less variability in contact binding geometries. These recent studies have pointed to a new route to the construction of single-molecule junction devices by engineering the molecular π-orbital–metal electrode interactions.

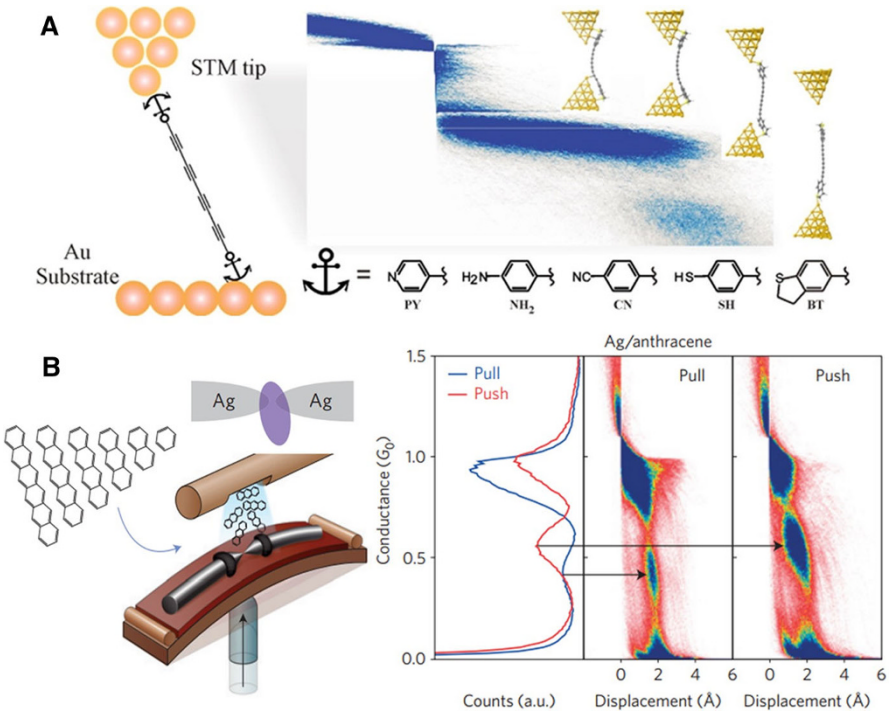

Fig. 8 **a** Schematics of functionalized oligoyene molecular junctions with different anchoring moieties (PY, NH_2, CN, SH, and BT). Reprinted from [87]. Copyright (2013) American Chemical Society. **b** *Left*: schematic of the MCBJ setup and the structures of the studied series of oligoacene molecules; *right*: pull (*blue*) and push (*red*) conductance histograms and conductance–displacement density plots constructed from pull and push conductance traces, respectively. Reprinted from [88]. Copyright (2016) Nature Publishing Group

One important goal of anchoring group selection is to enhance the strength of the coupling between the molecules and the electrodes and reduce the contact resistance to facilitate the measurement of intrinsic charge transport in molecular junctions. To realize this goal, further research leading to a better understanding of binding chemistry and synthetic methods is needed.

(3) Different electrodes

The selection of appropriate electrode materials is the other important prerequisite to realizing good molecule–electrode contacts and regulating the interfacial characteristics of molecular junctions. Gold is the most widely used electrode material due to its high mobility, high conductivity, and good fabricability, and because self-assembly methods for molecules on gold are relatively well developed. To gain deeper insight into the influence of the electrodes, researchers have explored many other metallic materials, including Ag [91], Pd [92], and Pt [82]. Changing the electrode material affects the interfacial energy level alignment and the coupling strength between the electrodes and the molecule. For example, when Ag, Pd, Au, and

Pt—which have work functions of 4.26, 5.12, 5.10, and 5.65 eV, respectively—are used as electrodes [92], the Fermi energy of the electrodes reduces with increasing work function. Correspondingly, the energy offset between the Fermi energy of the electrodes and the HOMO of the molecule decreases.

Equally important is the change in coupling strength between the electrode and the molecule. The orbital characteristics of the atoms of the electrode have a great impact on the electronic coupling between the molecular anchoring group and the electrode (and thus the conductance of the molecular junction). Ko et al. studied the effects of the electrode material on the interfacial electronic coupling and the conductance of molecular junctions using Au, Pd, and Pt as electrodes in thiol (–SH)-terminated or isothiocyanate (–NCS)-terminated molecular junctions [93]. Because Pd and Pt are group 10 elements with significant *d*-orbital characteristics, π contributions are expected at the contact, especially for –NCS anchoring groups with strong π character, which will generate an additional channel for electron transport. This is different from Au, which is a group 11 element with strong *s*-orbital characteristics that usually contacts with molecular anchoring groups via σ bonding [24]. Using Mayer two-center bond-order calculations, the quantitative sulfur–metal bond orders of –S–Au, –S–Pt, –NCS–Au, –NCS–Pd, and –NCS–Pt were found to be 0.837, 1.280, 0.393, 0.660, and 0.739, respectively. Further analysis of the anchoring group–metal bond orders revealed that the relative contribution of π character with respect to σ character in the cases of –NCS–Pd and –NCS–Pt was 1/3 and 1/2, respectively.

More recently, Adak et al. studied the impact of the electrode band structure on a series of pyridine-based molecules using Ag and Au electrodes [91]. They found that the commonly observed binary conductance states for Au-pyridine–Au molecular junctions disappeared when the electrode material was changed from Au to Ag, and the Ag-based molecular junctions usually had lower conductance than Au-based molecular junctions (Fig. 9b). Further density functional theory based calculations suggested that the coupling of the dominant transport orbital to the metal is stronger for Au-based junctions than for Ag-based junctions (Fig. 9d). This difference was attributed to relativistic effects, which result in an enhanced density of *d* states at the Fermi energy for Au compared with Ag (Fig. 9c).

Although metallic materials, especially gold, have been widely used as the electrodes in molecular junctions, the high atomic mobility of gold and the low chemical stability of metals with low work functions may lead to the destruction of molecular junctions upon oxidation or electromigration [24]. In order to realize more stable and controllable contacts for molecular electronics, researchers have developed other novel electrodes using different techniques, including carbon-based materials (graphene and carbon nanotube), silicon, and conductive polymers. We refer readers to [23, 24] for further details.

4 SPM Modulation of Single-Molecule Junction Electronics

Although the SMBJ technique has enabled the reproducible formation of metal–molecule–metal junction architectures, one dilemma that long puzzled researchers was that different values of conductance were obtained for the same

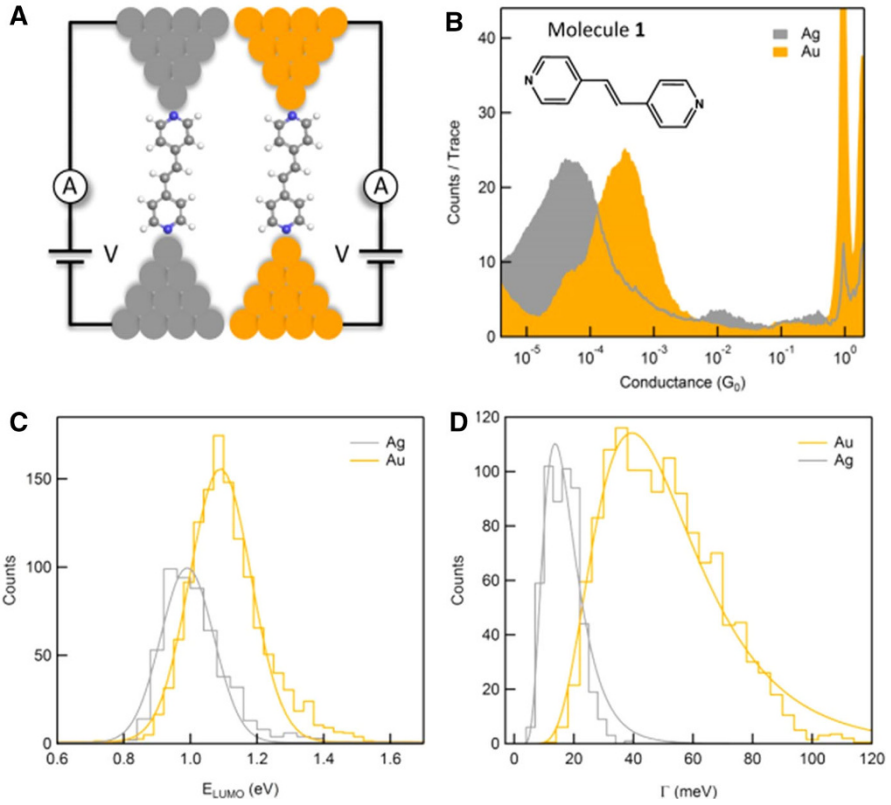

Fig. 9 **a** Schematic of molecular junctions formed using the STMBJ technique. **b** Logarithmically binned conductance histograms for measurements of Ag and Au junctions formed with molecule **1**. **c**, **d** Histograms of the energy difference between the LUMO and the metal Fermi level (E_{LUMO}) and the molecular orbital coupling (Γ) for Ag and Au junctions with molecule **1**, respectively. Reprinted from [91]. Copyright (2015) American Chemical Society

molecule in single-molecule conductance measurements. For instance, using STMBJ, Xu et al. measured a conductance of 2.5×10^{-4} G_0 for octanedithiol (C8DT) [32], while Haiss et al. reported a value of around 1.2×10^{-5} G_0 for the same molecule [34]. This order of magnitude difference in conductance values for the same molecule was surprising given that both groups used rather similar methods to perform their measurements, and this conundrum stimulated experimentalists to probe the nature of the SMBJ system, which had recently been developed.

To resolve this issue and gain deeper insight into the SMBJ system, innovations have been made that advance the measurement techniques used and modulate the measurement process using existing methods. In this section, these recently developed experimental modulations and controls for the SPMBJ system will be discussed, along with some representative findings.

4.1 Tip Movement Modulation

The power of the scanning probe microscopy (STM/AFM) experimental setup comes from the flexibility it offers the experimentalist: (1) the piezoelectric transducer (PZT) provides precise displacement of the SPM tip, allowing the gap between the tip and substrate to be adjusted (Fig. 10) [73, 94, 95], and (2) the SPM allows a bias to be applied and modulated between the tip and substrate. Both of these variables can be controlled by a computer program and a feedback mechanism.

(1) Continuous-stretching mode

In conventional SPMBJ measurements, a constant tip retraction speed is usually applied during all measurements, and the PZT signal appears to be a straight line (blue line in Fig. 11a). We denote this measurement procedure "continuous-stretching mode" SPMBJ. Though widely adopted, continuous-stretching mode SPMBJ measurements often yield conductance peaks with rather broad distributions and low intensities, which may wash out details that are important for understanding the SMBJ systems of interest. In addition, junctions are short-lived when continuous-stretching mode SPMBJ is applied.

(2) Stretch-holding mode

The peak shape of the conductance histogram is predominantly determined by the stability of the molecular junction conformation. Thus, an ability to stabilize the molecular conformation while it is measured is required. In Zhou et al.'s report, this issue was resolved by changing the tip retraction mode from continuous stretching to stretch holding [73]. The change to stretch holding involves stair-stepping the retraction process so that the system pauses or holds momentarily, allowing for the junction to settle into a quasi-relaxed state. As shown in Fig. 11b, the conductance step becomes much more distinct and well defined, and the junction has a much

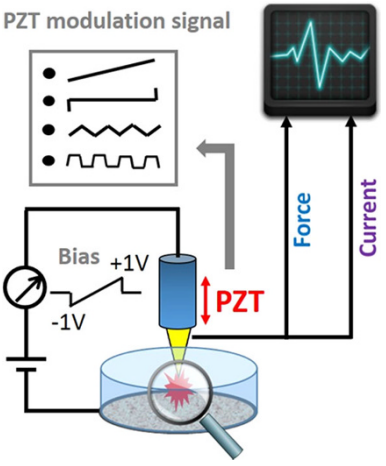

Fig. 10 SPM modulation system. Note that different PZT modulation modes are shown in the *gray box*

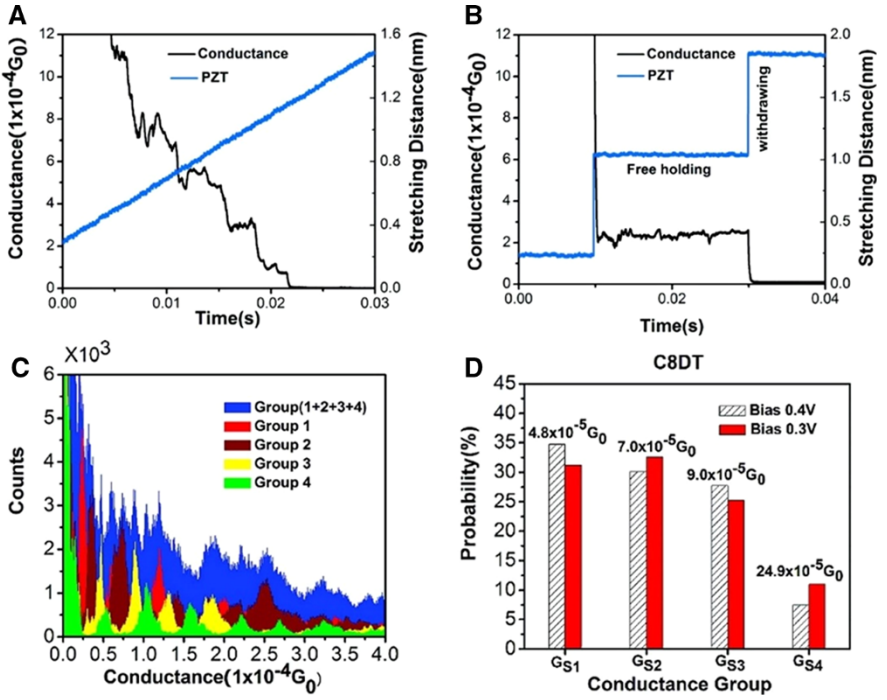

Fig. 11 **a** Typical PZT movement signal (*blue solid line*) and conductance traces (*black solid line*) in the continuous-stretching mode. **b** Typical PZT movement signal (*blue solid line*) and conductance trace (*black solid line*) in the stretch-holding mode. **c** Conductance histograms of the Au–octanediamine–Au junction with stretch-hold modulation applied. **d** Four conductance sets extracted from conductance histograms for the Au–C8DT–Au junction with stretch-hold modulation applied. Reprinted with permission from [73]. Copyright (2009) American Chemical Society

longer lifetime. This modification to tip retraction was proven to eliminate—or at least minimize—variations in experimental conditions, such as fluctuations in the junction conformation. The conductance histograms of C8DT molecules obtained using this stretch-holding mode SPMBJ revealed much finer peaks and extra conductance sets (Fig. 11c). The conductance sets at around 7.0×10^{-5} G_0 and 9.0×10^{-5} G_0 were between the previously reported medium (1.2×10^{-5} G_0) and high (2.5×10^{-4} G_0) conductance values for the Au–C8DT–Au molecular junction (Fig. 11d). Thus, the change to stretch holding for the tip retraction process resulted in the discovery of those less-populated conductance sets of the molecular junction. As introduced earlier, the possibility of various Au–S bonding configurations is proposed to be responsible for the significant differences between the experimentally observed conductance values for a particular molecule [66, 70]. Therefore, the discovery of the less-populated conductance sets not only points to the coexistence of other preferred contact conformations but also suggests that the contact conformation is highly sensitive to the measurement procedure used. Recently, using this method, Wang et al. successfully monitored the conformational transition of a DNA molecule from its B to its Z form in aqueous solution [96]. Their study

took advantage of the comparable contributions of free-held DNA molecular plateaus to the resulting histogram peak, and they constructed a DNA conformational transition trend line based only on STMBJ conductance measurements.

Equally important is that the free-held junction serves as the perfect platform for additional mechanical modulations of junction separation, which enables the discovery of more detailed information on single-molecule junction systems.

(3) Nonlinear ramp modulation

On a free-held junction achieved by setting up a constant tip–substrate separation, the SPM tip can also be modulated to cycle through multiple nonlinear ramp modes, such as "triangle," "trapezoidal," and "wave" displacements [94, 95, 97]. This can be achieved by applying an AC signal with a certain shape and frequency to the SPM PZT movement (Fig. 12a) [94]. Such modulations can influence the orientations of specific molecule–electrode contact geometries by regularly compressing and elongating the molecular junction. The C-AFMBJ allows force to be measured simultaneously with conductance, and when this sawtooth modulation is applied to C-AFMBJ, the effects of contact configurations can be explored in a clearer manner. Using this method, researchers have discovered and investigated useful features at much higher resolution in single-molecule junctions.

A "triangle" mechanical manipulation of PZT movement was carried out on the alkane molecules C8DT and C8DA to isolate the contact parts and investigate the relationship between force and conductance in detail. Individual experimental conductance traces revealed intriguing features (Fig. 12b, c) [94]. For both C8DT and C8DA, the force showed perfect correspondence with the (simultaneously measured) conductance. Interestingly, some conductance traces of C8DT showed conductance switching between different conductance sets reported in previous studies without any obvious change in force (Fig. 12b) [66, 73, 76]. This phenomenon was attributed to switching among different Au atom adsorption sites induced by the mechanical modulation. For C8DA, conductance traces presented a

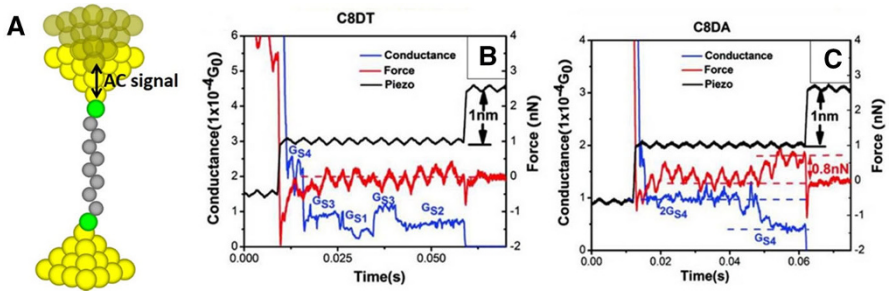

Fig. 12 **a** Schematic illustration of nonlinear ramp modulation achieved by applying an AC signal to an SPM tip. **b** Examples of stretch-hold mode force and conductance traces obtained under sawtooth modulation for the Au–C8DT–Au junction, showing obvious changes in conductance among different conductance sets. **c** Examples of stretch-hold mode force and conductance traces obtained under sawtooth modulation for the Au–C8DA–Au junction, showing changes in conductance with changes in force. **b**, **c** were reprinted with permission from [94]. Copyright (2010) American Chemical Society

conductance switch accompanied by a force change close to the Au–NH_2 binding force (Fig. 12c), strongly suggesting that the conductance variations were due to a combination of switching between different adsorption sites and the dissociation of the molecule from the Au electrode with bond breaking. Using the same modulation, Wang et al. found that the contact barrier of Au–C8DT–Au followed a unique trend as the junction separation increased: a linear increase followed by a plateau in barrier height, in contrast with that of the Au–C8DA–Au junction, which presented a near-rectangular barrier [71]. These subtle details of alkane molecular junctions unraveled by mechanical modulations of the tip–substrate separation offered significant clues regarding the reason for the different conductance sets of alkane molecular junctions, how these sets contribute to the differences in conductance, and how one set transits to another. Similarly, by applying a wave-like modulation, Quek et al. demonstrated that Au–4,4′-bipyridine–Au single-molecule junctions can be reversibly switched between two conductance states through repeated junction elongation and compression [98]. First-principles calculations suggested that the different measured conductance states arose due to distinct contact geometries at the flexible but stable nitrogen–gold bond: conductance is low when the N–Au bond is perpendicular to the conducting π-system and high otherwise. To get a more straightforward picture of the contact geometry and binding configuration of a single-molecule junction, Hihath et al. skilfully applied a small-amplitude, high-frequency, sinusoidal mechanical signal to a series of alkane-based single-molecule devices during junction formation and breakdown in a recent study (Fig. 13) [97]. Correlating the conductance and subtle change in junction length with intermolecular strain, they successfully predicted that the most likely contact configuration for the measured Au–alkanedithiol–Au molecular junctions was one in which the Au atom was in a top configuration on one side and a bridge configuration on the other. Alternatively, alkanediamines tend to bind to a Au atom in the hollow configuration.

The aforementioned mechanical modulations of SPM tip movement should lead to further advances in our understanding of the binding configurations of molecular junction devices, provide additional information about the origin of the different conductance values obtained for single-molecule devices, and yield significant insights into the wide dispersion seen in conductance histograms. Thus, the results afforded by these methods pave the way to a comprehensive understanding of and full control over the binding configurations in single-molecule devices at room temperature—a prerequisite for the design of functional molecular electronic devices.

4.2 SPM Surface Modification

A problem with SPMBJ methods is that, even though molecules are adsorbed onto the substrate and form a well-defined molecule–substrate bottom contact, the tip–molecule contact is typically less well defined [99]. When the tip attempts to contact the molecular layer, the number of sandwiched molecules cannot be determined with any certainty due the relatively large size of the tip. Fortunately, novel strategies have recently been developed to reduce the number of molecules

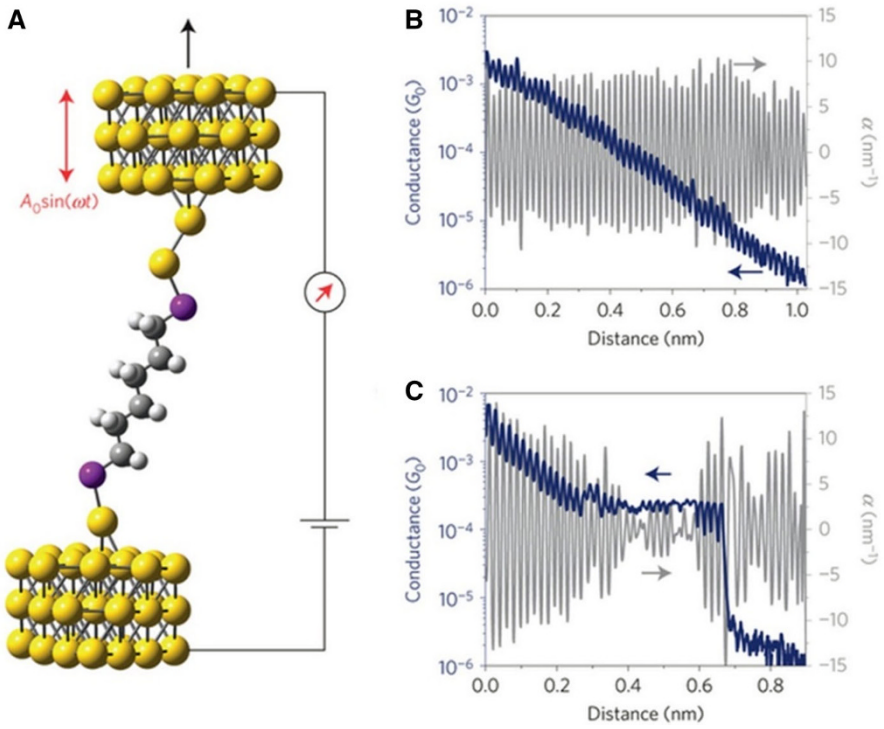

Fig. 13 Mechanically modulated STM break-junction experiments by Hihath et al. **a** Schematic of the experimental setup, showing a C6-DT molecule bound to two Au electrodes as a small sinusoidal mechanical modulation is applied while withdrawing the tip electrode. **b** Example of a current versus distance trace obtained during tip withdrawal (*blue trace*), showing no steps in the current. **c** Representative conductance versus distance (*blue*) and α versus distance (*gray*) curves measured during electrode separation for a C6-DT junction. Reprinted with permission from [97]. Copyright (2015) Nature Publishing Group

sandwiched and create well-defined (strong) top contacts, as demonstrated in Fig. 14 [23]. These strategies can be largely classified into tip modification and substrate modification strategies.

EC-STM break junction. Based on the STM break junction, an electrochemical strategy developed by Zhou et al. established a chemically well-defined metallic contact through a jump-to-contact mechanism between the tip and the substrate, as indicated in Fig. 14a [100]. The gold tip is fixed above the substrate, and the tip is electrochemically deposited in situ with a foreign metal of interest until a bridge between the tip and the substrate is formed. Different metals, such as Cu, Pd, and Fe, have been used to form a thin nanowire to bridge the tip and the substrate [100, 101]. When the tip retracts from the substrate, the elongation of the bridged nanowires generates two atomic-scale sharp electrodes, making the formation of single-molecule junctions feasible. The strategy presented in their study allows the generation of well-defined metal–molecule–metal junctions utilizing a variety of metals.

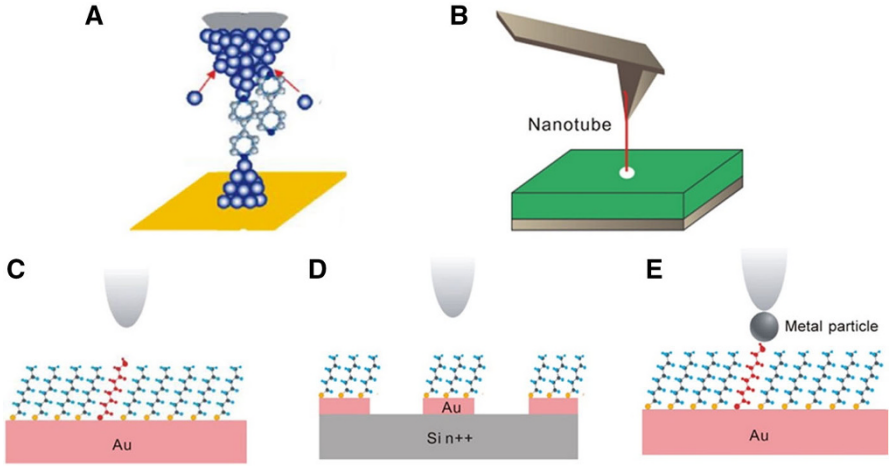

Fig. 14 SPM surface modification strategies. **a** Electrochemical jump-to-contact scanning tunneling microscopy break junction (EC-STM). Reprinted with permission from [100]. Copyright (2013) IOP Publishing. **b** Attaching nanotubes to a metal-coated AFM tip. Reprinted with permission from [102]. Copyright (2009) Nature Publishing Group. **c** Inserting target molecules into an ordered array of reference molecules. Reprinted with permission from [103]. Copyright (1996) AAAS. **d** Substrate-modified SPM junction. Reprinted with permission from [104]. Copyright (2012) Wiley–VCH Verlag GmbH & Co. KGaA. **e** Nanoparticle-based SPM junction. Reprinted with permission from [106]. Copyright (2001) AAAS. This figure was reprinted with permission from [23]. Copyright (2016) American Chemical Society

Nanotube-tip-based SPM break junction. Carbon nanotubes (CNTs) have demonstrated considerable potential for use as SPM tips [102]. The main features of CNTs are their nanoscale diameters, high aspect ratios, and remarkable mechanical and electrical properties. It is important to note that, for simplicity, the nanotubes need to be metallic if this method is to be used to electrically probe molecules. With appropriate modification of the end of the nanotube, it should be feasible to form nanotube–molecule–metal junctions and characterize the properties of those junctions, as shown in Fig. 14b.

Molecule layer-modified SPM junction. Another way to effectively address the individual molecules in an SPMBJ system is to embed target molecules into a matrix of other (often less conductive) molecules, as shown in Fig. 14c. Bumm et al. presented an approach to studying the current using highly conducting molecular wire candidates inserted into a poorly conducting alkanethiol monolayer [103]. In this approach, the target molecules were taller (higher) than the surrounding poorly conducting molecules, thus ensuring that only the target molecules were contacted. This strategy provides a way to study single-molecule electrical properties when the relevant in situ break junction technology is unavailable.

Substrate-modified SPM junction. Clement et al. reported a new approach that allows the conductance of up to a million junctions to be measured within a single C-AFM image [104]. In this approach, a large array of single-crystal Au nanodots was first fabricated on a highly doped silicon substrate, as illustrated in Fig. 14d. A molecular layer then was formed at the nanodot surface. Finally, a conducting AFM

tip was driven to contact the molecules, and a metal–molecule–metal–silicon junction was subsequently formed. By controlling the size (diameter) of the nanodots, the number of adsorbed molecules can be restricted to less than one hundred [105].

Nanoparticle-based SPM junction. Nanoparticles are smaller than a traditional SPM tip and can easily be visualized using SPM technology, thus suggesting a potential application for molecular break junctions. Cui et al. presented an approach using a C-AFM tip to contact alkanedithiol-capped gold nanoparticles embedded in a matrix of alkanethiol molecules [106]. The octanethiol monolayer acted as a molecular insulator, isolating the dithiol molecules from one another. The thiol groups at the top of the film were attached to the nanoparticles by incubating the monolayer with a gold nanoparticle solution. A gold-coated AFM tip was then used to locate and contact individual particles bonded to the monolayer, as indicated in Fig. 14e. In addition to measuring the molecular conductivity, this approach avoids the effects of variations in the contact force and other problems encountered with nonbonded contacts. One drawback of this strategy is that, because the Au nanoparticles are typically coated with an organic surfactant layer, the tip and the nanoparticle may form an additional tunneling junction (a Coulomb island) [107], so electron transport between the tip and the substrate via the nanoparticle may exhibit Coulomb blockade effects [107].

5 Data Characterization Approaches for Single-Molecule Junction Electronics

As it is usually unclear how many molecules form the junction for any given experiment, and because the exact nature of the metal–molecule bonding is not usually known, many conductance measurements are performed and the results are analyzed statistically to determine the most probable conductance of a single molecule. To extract as much information as possible from the collected data, numerous statistical methods of treating the seemingly chaotic experimental data have been developed, as described below.

(1) One-dimensional (1D) and two-dimensional (2D) histograms

As first reported by Xu and Tao [32], the single-molecule conductance can be determined using a conventional one-dimensional (1D) conductance histogram constructed from many individual conductance traces. Typical conductance traces and a 1D histogram are shown in Fig. 15a and b, respectively. Such a 1D histogram exhibits a peak, the center value of which is the most probable conductance of the molecule. The histogram is generated by directly determining the height of each current jump in the current–distance scans and then plotting these values in a histogram of counts against current (or conductance) jump value. This generates one conductance value per jump-containing current–distance scan. However, a 1D conductance histogram involves only one significant parameter: conductance, meaning that it cannot reveal other detailed features hidden in the

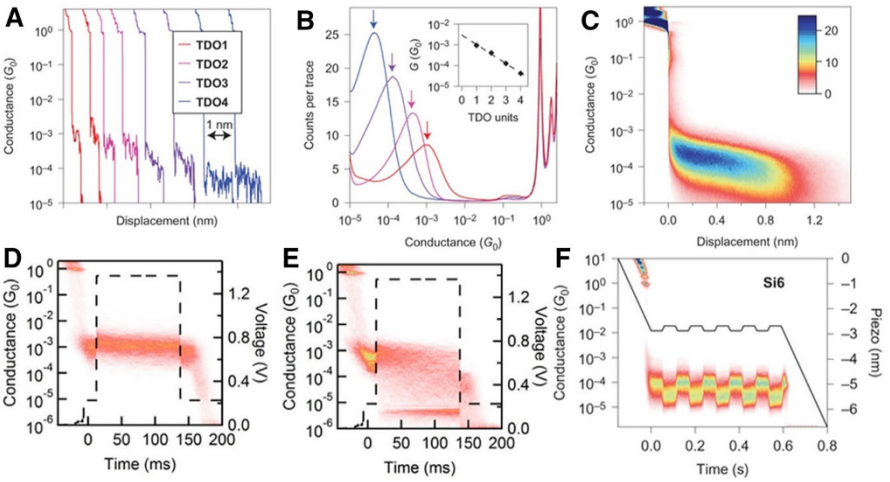

Fig. 15 **a** Sample conductance versus displacement traces for the TDO*n* series. **b** 1D log-binned conductance histograms, each composed of 20,000 traces, for TDO1–TDO4 measured at a bias of 10 mV in 1-octylbenzene. *Arrows* indicate peak conductance. **c** 2D conductance–distance histogram for TDO3 created by aligning all the traces at the point where the conductance crosses 0.5 G0 and then overlaying them. The *color bar* indicates the number of counts per 1000 traces. **d**, **e** Two-dimensional histograms created from traces obtained for a single-molecule junction formed with 1,6-hexanedithiol that sustained (**d**) or ruptured (**e**) when a bias voltage was applied (as indicated by the *dashed line*). The *flat feature* below 10^{-5} G_0 in **e** originates from measurements of broken junctions at 1.4 V. **f** 2D histograms of compression–elongation cycles for the Au–Si6–Au junction. **a**–**c** were reprinted from [109]. Copyright (2015) Nature Publishing Group. **d**, **e** were reprinted from [111]. Copyright (2015) American Chemical Society. **f** was reprinted from [110]. Copyright (2015) Nature Publishing Group

current–distance traces (i.e., the junction length and the correlation between two traces). Thus, to provide a straightforward visualization of the evolution of the junction's characteristics, two-dimensional (2D) conductance histograms are now widely used [108–110]. Such a 2D histogram is created by superimposing hundreds of conductance traces that are shifted to the same starting point, and then illustrating the data points with an additional color-coded binned coordinate. Using this method, the average junction length prior to junction rupture is clearly presented, as shown in Fig. 15c. Other than junction length information, many other interesting features have been observed in 2D histograms of molecular junctions. For example, Li et al. recently studied the stability and rupture of molecular junctions under high voltage bias [111]. A clear molecular plateau region can be seen in the 2D histogram derived from traces obtained for a single-molecule junction formed with 1,6-hexanedithiol that sustained (Fig. 15d). Meanwhile, the 2D histogram constructed from traces obtained for a single-molecule junction formed with 1,6-hexanedithiol that ruptured showed a sudden drop in conductance when a bias of 1.4 V was applied, indicating a breakdown of the molecular junction under high bias (Fig. 15e). In addition, conductance switching between two conductance states was clearly observed using the 2D histogram method (Fig. 15f) [110].

(2) Two-dimensional (2D) correlation analysis

The generation of defined peaks in "all-conductance" histograms relies on the presence of a relatively flat current-plateau region before the junction is cleaved. However, two types of information that are readily extracted using histogram methods are (1) current–distance curves with jump events, which are closely related to the mechanical nature of the molecular junction, and (2) molecular plateaus that present regular conductance fluctuations under nonlinear ramp mechanical modulations. These fluctuations in conductance are often trivial in terms of timescale and therefore only add to the background or noise in the 1D conductance histogram. To extricate the important information hidden in the fluctuating molecular plateaus, more advanced data treatment methods are required.

In order to unravel the relationship between specific signals in individual conductance traces, such as the relationship between two conductance values, Makk et al. developed a conductance 2D auto-correlation histogram (C-2DACH) utilizing time series analysis [112]. Figure 16 shows the C-2DACH for Au–4,4′-bipyridine–Au junctions. A clear blue negatively or anticorrelated region where high and low conductance sets of the junction cross is apparent (Fig. 16c). A careful check of the histograms constructed from traces (Fig. 16d) with a long plateau at either high or low conductance indicated that the observed blue region is an anticorrelation in the

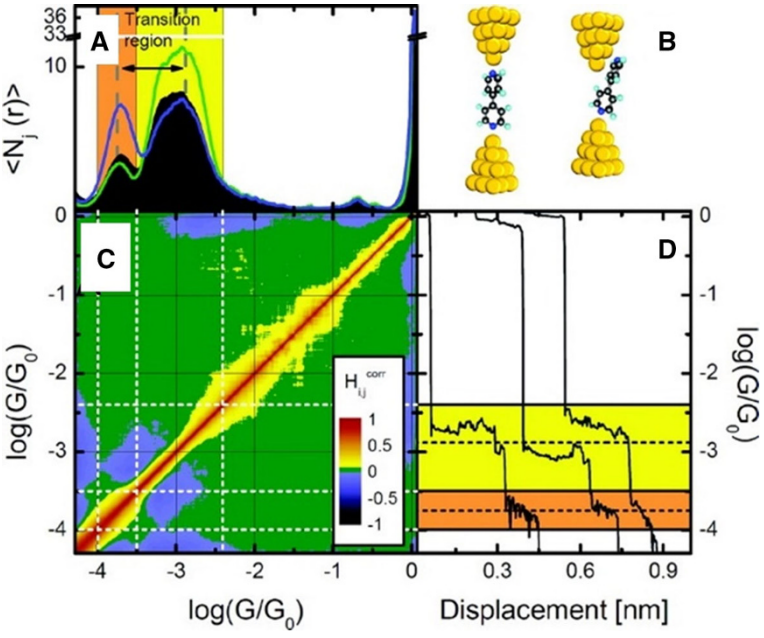

Fig. 16 Conductance autocorrelation analysis of Au–4,4′-bipyridine–Au junctions. **a** Conductance histogram using equidistant bins on a log scale. **b** Two contact binding configurations. **c** 2DACH of Au–4,4′-bipyridine–Au junctions. **d** Sample conductance traces. Reprinted with permission from [112]. Copyright (2012) American Chemical Society

length of the plateau instead of an anticorrelation in the existence of two junction configurations. To explore further, Hamill et al. recently expanded the autocorrelation to a cross-correlation by adding another variable—force—to the calculations [113]. This enabled correlation analysis of simultaneously measured force and conductance signals using the C-AFMBJ technique. Applying this newly developed force–conductance 2D cross-correlation histogram (FC-2DCCH) method to modulated Au–C8DT–Au junctions, Wang et al. mapped the correlation of force and conductance at the single-molecule level for the first time, and uncovered useful details that had never been observed before (Fig. 17) [72]. In their study, four regions of strong correlation consistently appeared in the FC-2DCCHs when modulations with different amplitudes were applied, in sharp contrast to the results obtained with no modulation (Fig. 17c). These regions reflect the conductance and force changes during transitions in the two molecule–electrode contact configurations. As the modulation amplitude was increased, intermediate transition states of the contact configurations were discerned and further confirmed by comparing individual traces.

(3) Data analysis of the *I–V* characteristics of molecular junctions

The SMBJ technique enables the measurement of not only the conductance but also the current–voltage (*I–V*) characteristics of single molecules. *I–V* curves are easily obtained by applying a bias sweep to a stabilized junction. Probably the most important information researchers wish to acquire from the measured *I–V* curves of molecular junctions is the energy gap between the Fermi level of the electrode and the frontier molecular orbital of the molecule. Data analysis methods for deriving this important information from the measured *I–V* characteristics are also well developed. An *I–V* curve can be fitted with the Landauer formula using a Levenberg–Marquardt least-squares fitting algorithm [114, 115]. This fitting process

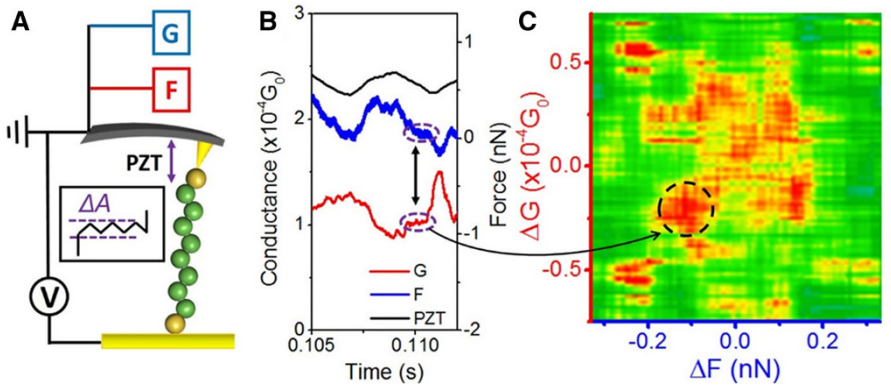

Fig. 17 Force–conductance cross-correlation analysis of the Au–octanedithiol–Au junction. **a** Schematic of a modulated Au–octanedithiol–Au molecular junction. **b** Zoomed-in views of the PZT modulation (*black*), force (*blue*), and conductance (*red*) signals. **c** FC-2DCCH of the Au–octanedithiol–Au junction under a "triangle" modulation of 1.2 Å. Reprinted from [72]. Copyright (2014) American Chemical Society

results in three parameters: the energy gap ε and the degrees of coupling to each electrode, Γ_R and Γ_L. For asymmetric *I–V* curves, the asymmetry in the coupling strength at the two contact interfaces can be interpreted by comparing the fitting parameters Γ_R and Γ_L. Symmetric *I–V* curves can also be fitted using the Simmons model, which can be used to extract additional parameters, notably the tunneling barrier height Φ and the barrier decay constant β [67, 116]. Recent developments of the Simmons model allow the rectification ratio curves derived from asymmetric experimental *I–V* curves to be fitted, yielding the decay constant $\Delta\beta$ under reverse bias [117, 118]. These analytical methods of fitting experimental data to theoretical models are powerful tools for studying the electron transport properties of molecular junctions.

Beebe et al. proposed another method for interpreting *I–V* characteristics that is based on the mechanism for field emission and has recently become widely used: transition voltage spectroscopy (TVS) (Fig. 18) [119]. In TVS, an *I–V* curve can be converted into a Fowler–Nordheim (F–N) plot, which describes the relationship of $\ln(I/V^2)$ to $1/V$ [120]. Using this TVS method, an inflection point (V_{trans}) can be obtained which is proportional to the effective barrier height (Φ) and corresponds to the energy offset between the E_F of the electrode and the closest frontier molecular orbital, either the HOMO or the LUMO [121]. The V_{trans} obtained from the F–N plot signifies the transition voltage at which a trapezoid-shaped tunneling barrier becomes a triangle-shaped barrier or direct tunneling converts to field emission. Figure 18a shows an example of an F–N plot and a schematic for the change in the tunneling barrier (inset). Asymmetric *I–V* curves usually yield the transition voltage V_{trans} at different bias values under opposite bias polarities, indicating that a trapezoid-shaped tunneling barrier converts to a triangle-shaped tunneling barrier at a smaller bias under forward bias than it does under the reverse bias. In real experiments, an F–N plot may not always produce a minimum; such a plot implies

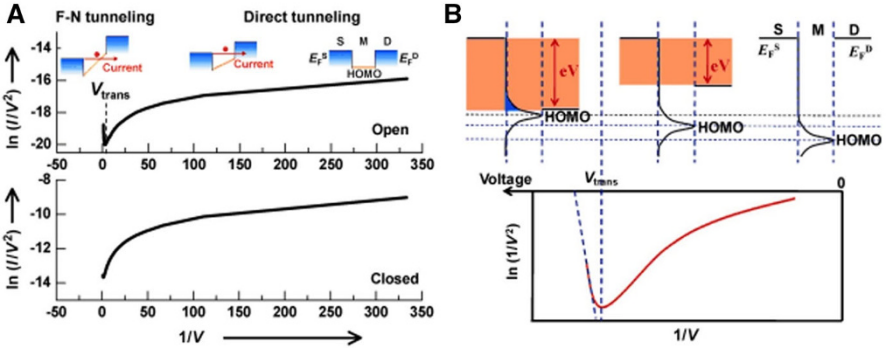

Fig. 18 **a** F–N plots of the *I–V* characteristics for a molecular junction in the open state (*top*) and closed state (*bottom*). The *insets* show the conventional barrier model in order to qualitatively explain the inflection of the F–N curve. E_F^S and E_F^D are the Fermi energies of the source and drain electrodes, respectively, and V_{trans} is the voltage at which the inflection occurs. Note that the figures are drawn for HOMO-mediated electron tunneling. **b** The resonant tunneling model used to qualitatively explain the inflection of the F–N curves. Reprinted from [120]. Copyright (2013) Wiley–VCH Verlag GmbH & Co. KGaA

that the transition voltage for the measured molecular junction was not reached within the bias range applied in the experiments.

Because the asymmetry of the molecular junction has a significant effect on the inflection behavior of the F–N plot, TVS has been used to investigate the asymmetries and the energy-level alignments of several asymmetric molecular junctions. Intuitively, asymmetric voltage drops on both sides of the metal–molecule interfaces will lead to different barrier heights for carrier tunneling. Correspondingly, the observation of different polarity-dependent values of V_{trans} confirms the presence of asymmetric interfacial contacts in the molecular junction [119]. This polarity dependence of V_{trans} was also confirmed by Bâldea et al., who calculated the ambipolar TVS using asymmetric molecule–electrode couplings [122]. Furthermore, based on extensive ab initio calculations using an analytical model of a Lorentzian-shaped transmission function, Chen et al. [123] found that asymmetric coupling at the two molecule–electrode interfaces had a significant effect on the ratio between V_{trans} and the energy offset of the nearest molecular orbital (ε_0) to E_F. The ratio $|\varepsilon_0 - E_F|/V_{trans}$ increased from 0.86 for a symmetric junction to 2.0 for a completely asymmetric junction. In experimental investigations of the effects of asymmetric coupling in molecular junctions using TVS, Wang et al. [124] observed a similar tendency: increasing the degree of asymmetric coupling decreased both the energy offset ($|\varepsilon_0 - E_F|$) and V_{trans}.

6 Progress Towards Functional Devices Utilizing Molecular Junctions

Although the initial goal of using molecular electronics to build molecular computers has still not been achieved, researchers have devoted tremendous effort to this end over the two past decades. One important step in this context is to search for molecular candidates that demonstrate functional current–voltage (I–V) properties, such as a rectification effect, negative differential conductance (NDC), and a current-switching effect [6]. It is equally important to gain a comprehensive understanding of the underlying transport mechanisms. In this section, we will discuss recent advances in single-molecule electronics with a view to creating functional I–V characteristics out of molecular junctions.

(1) Rectification: towards diodes

The diode or rectifier, which facilitates the flow of current in one (forward) bias direction and suppresses current flow in the opposite (reverse) direction, is an important two-terminal electronic component. This asymmetric I–V behavior can be experimentally achieved by simply breaking the symmetry of the molecular junction conformation. To date, rectification has been obtained with either asymmetric molecules [18, 42] or inconsistent molecule–electrode interfaces [118, 125]. However, rectification has usually been exhibited by small organic molecules containing electron donor and acceptor groups separated by an insulating group [6, 18, 126–128]. Examples of such donor–insulator–acceptor molecules are shown in Fig. 19a. In these molecules, charge transfer takes place from one electrode to the

acceptor, to the donor, and finally to the second electrode at forward bias. However, at reverse bias, the charge must migrate through the junction in the opposite direction, which requires much greater potential to align the energy levels of the donor and acceptor with those of the electrodes. Hence, the molecule produces much more current under forward bias than under reverse bias, which is the signature of rectification. For example, Hihath et al. utilized the STMBJ technique to probe the rectification exhibited by asymmetric diblock dipyrimidinyldiphenyl molecules (Fig. 19b) [129]. They demonstrated that the bias-dependent asymmetry in the electronic coupling was important for both elastic and inelastic processes in the diblock diode molecule.

Asymmetric molecule–electrode interfaces are created using two strategies: asymmetric anchoring groups and asymmetric electrodes. In such cases, the asymmetry occurs at the contacts. The frontier molecular orbital couples with one electrode more strongly than it couples with the other electrode, which weakens the ability to transport charge when it is directed from the electrode through the weakly coupled molecule–electrode interface under reverse bias. For instance, Wang et al. recently studied anchoring-group-induced rectification in a benzene-based

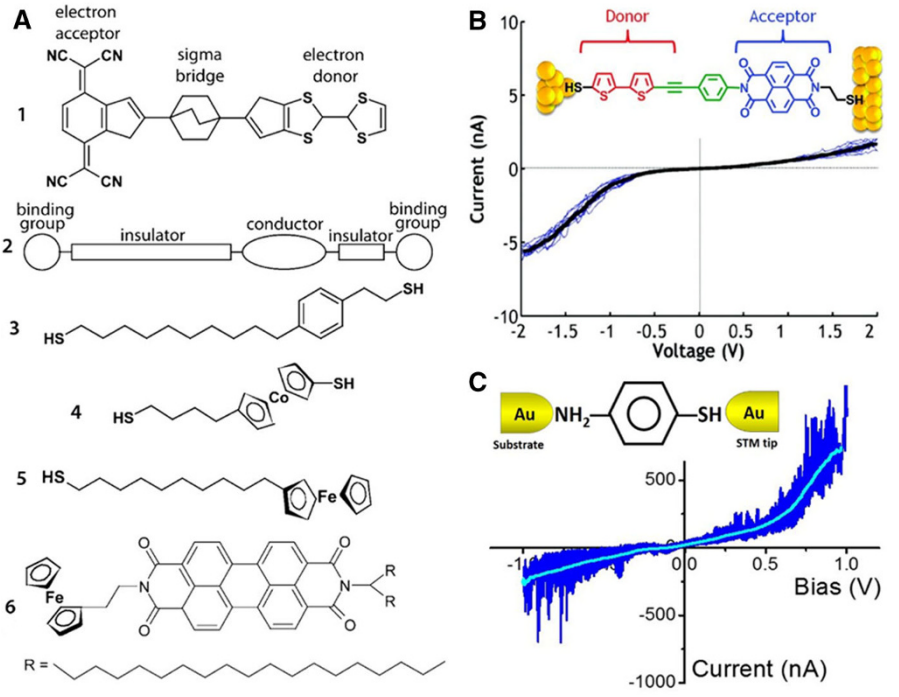

Fig. 19 **a** Examples of donor–insulator–acceptor molecules. **b** *I–V* curves (raw data in *blue* and average curve in *black*) of inverse rectification at a donor–acceptor-type molecular junction. **c** Rectifying *I–V* curves (raw data in *blue* and average curve in *cyan*) for a molecular junction with asymmetric anchoring groups. **a** was reprinted from [125]. Copyright (2010) American Chemical Society. **b** was reprinted from [129]. Copyright (2011) American Chemical Society. **c** was reprinted from [118]. Copyright (2014) American Institute of Physics

molecular junction [118]. As shown in Fig. 19c, gold was used as the electrode material and benzene as the molecular core, and the only asymmetry at their molecular junction stemmed from the anchoring groups. By fitting the rectification ratio using a modified Simmons model, the rectifying *I*–*V* behavior was found to be due to asymmetry in the potential drops across the asymmetric anchoring group–electrode interfaces.

Multiple theoretical models have been developed to understand the mechanisms that cause the rectification behavior displayed by various molecular junctions. The groups of Williams et al. and Baranger et al. proposed that molecular junctions with a single conducting molecular orbital (either the HOMO or the LUMO) that is slightly shifted from the Fermi levels of the electrodes and is asymmetrically coupled to one of the electrodes (i.e., in closer spatial proximity to one electrode than the other) can rectify [125–127]. Figure 20a and b provide schematics showing the energy levels of the molecular rectifier junctions proposed by Wiliams et al. and Baranger et al., respectively. These molecular rectifiers have a HOMO or LUMO level that is energetically positioned just above the Fermi levels of the electrodes (a small difference in energy between the Fermi levels of the electrodes and the conducting molecular orbital ensures a low switch-on bias of the molecular rectifier). The conductive molecular orbital follows the potential of the nearer electrode, and thus participates in charge transport more easily at one bias polarity. Zhao et al. recently proposed a model for molecular rectifiers with asymmetric molecule–electrode contacts. In this model, the stronger coupling at one molecular–electrode interface is viewed as being due to a closer affinity between the conducting molecular orbital and the Fermi level of the electrode (Fig. 20c) [130]. In this model, the conducting molecular orbital (HOMO or LUMO) tends to shift with the Fermi level of the strongly coupled electrode as a whole when a bias is applied. The conducting molecular orbital can lean towards the Fermi level of the strongly coupled electrode, and is dragged into the conduction window under forward bias. Under reverse bias, the conducting orbital is outside the conduction window, so little current is generated.

However, these theoretical results suggest that molecular rectifiers in the proposed models based on one conducting molecular orbital or a double barrier cannot achieve rectification ratios (RRs) exceeding $\sim$22 [125, 131]. Calculations for different types of molecular rectifiers, including the donor–insulator–acceptor model, show that molecular rectifiers in the tunneling regime cannot have RRs greater than $\sim$20 [132]. In many single-molecule junction experiments, the RR is usually below 10 [118, 129]. The upper limits for RRs of molecular diodes are far smaller than the values achieved with commercial semiconductor diodes (RR = 10^6–10^8).

To achieve higher RRs, novel molecular junction systems have been developed. For example, Cappozi et al. recently introduced a general method of creating molecular junction rectification by controlling the junction's electrostatic environment [41]. By using symmetric single-molecule junctions with two electrodes of the same metal but breaking symmetry by exposing very different electrode areas to an ionic solution (Fig. 21a), they achieved RRs in excess of 200 using a symmetric oligomer of thiophene-1,1-dioxide (TDO_n) (Fig. 21b). The asymmetrically exposed

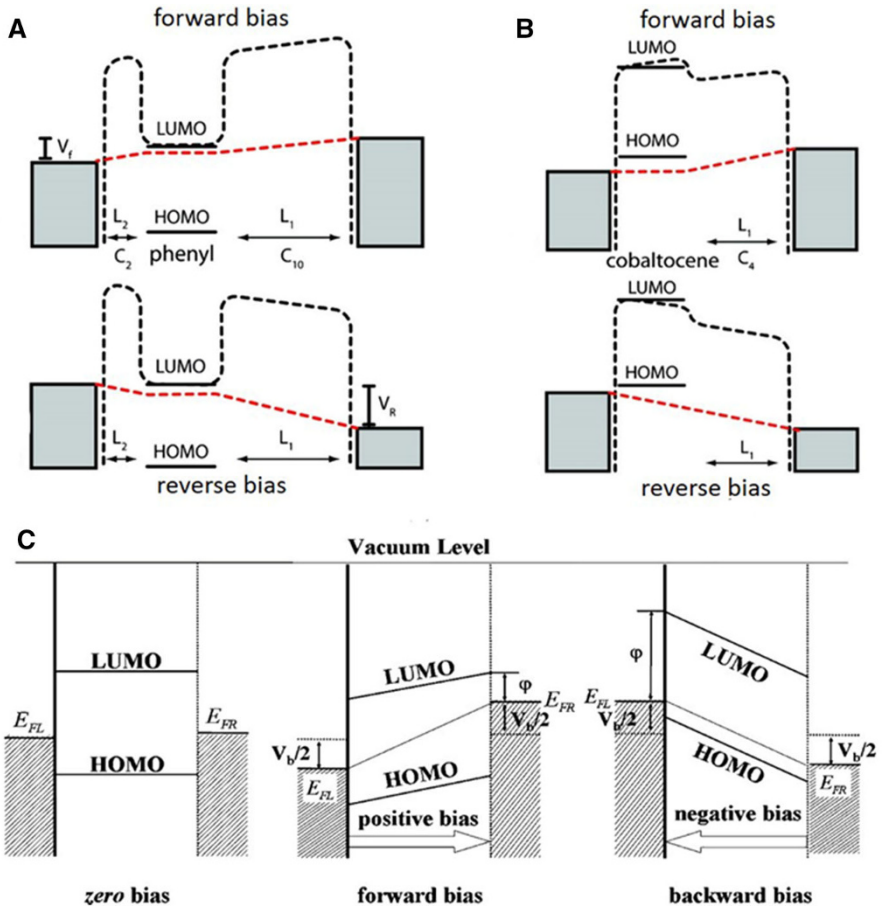

Fig. 20 Rectification mechanisms proposed by Williams (**a**), Baranger (**b**), and Zhao (**c**). **a**, **b** were reprinted with permission from [125]. Copyright (2010) American Chemical Society. **c** was reprinted with permission from [130]. Copyright (2010) American Chemical Society

electrode areas were found to be key when soaked in a polar solvent such as propylene carbonate (PC). Due to the presence of ions in the environment, an electric double layer forms at each electrode/solution interface to screen out any applied bias. The disparate areas of the electrodes result in a denser layer of charge at the electrode with the smaller tip. This causes the molecular orbitals to be pinned to the chemical potential of the substrate, resulting in a dependence of the current on the polarity of the applied bias (Fig. 21c). More recently, Guo et al. developed a molecular rectifier based on a DNA molecule for the first time [40]. In their study, a small molecule (coralyne) was intercalated into a custom-designed DNA duplex, and the resulting molecular junction composed of the DNA–coralyne complex exhibited current rectification with an RR of $\sim$15 under a voltage of 1.1 V (Fig. 21d, e), which is behavior counterintuitive to the seemingly symmetrical molecular structure of the junction. A nonequilibrium model based on Green's

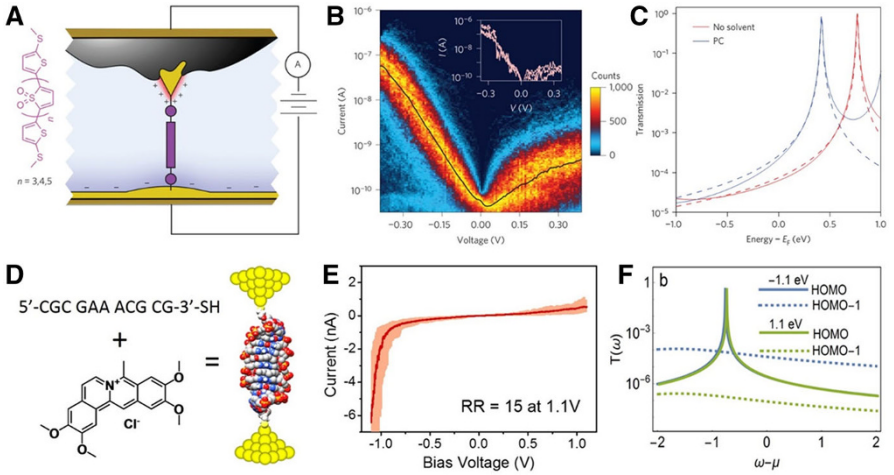

Fig. 21 **a** Molecular structure (alkyl side chains) of TDO_n and schematic of the molecular junction created using asymmetric area electrodes. **b** Two-dimensional absolute current versus voltage histogram for TDO_5 in propylene carbonate (PC). *Inset*: examples of exceptionally rectifying junctions (three selected traces). **c** DFT $+\Sigma$ calculated transmission functions for TDO_4 in a junction with no solvent molecules (*red*) and with PC on both electrodes (*blue*). *Dashed lines* indicate Lorentzian fits to these transmission functions. **d** Molecular structure and schematic of a DNA–coralyne molecular junction. **e** *I*–*V* characteristic of the DNA–coralyne molecular rectifier. Note that the rectification ratio (RR) reached 15 under a voltage of 1.1 V. **d** Contributions of HOMO (*solid lines*) and HOMO-1 (*dashed lines*) to the transmission function $T(\omega)$ as a function of ω for different values of the bias voltage V (= −1.1 and 1.1 eV). **a**–**c** were reprinted from [41]. Copyright (2015) Nature Publishing Group. **d**–**f** were reprinted from [40]. Copyright (2016) Nature Publishing Group

function revealed that coralyne-induced spatial asymmetry in the electron state distribution caused the observed rectification. This inherent asymmetry leads to changes in the coupling of the molecular HOMO-1 level to the electrodes when an external voltage is applied, resulting in an asymmetric change in transmission (Fig. 21f). This finding, that coralyne intercalation manipulates the HOMO-1 transmission function by increasing its coupling strength without perturbing the HOMO, is a feature unique to DNA–coralyne complex molecular junctions. Note that this rectification mechanism differs from any other models proposed to account for molecular junction systems that possess asymmetric molecular cores dominated by a single orbital asymmetrically coupled to the electrodes.

(2) Negative differential conductance (NDC): towards oscillators

The functional current–voltage (*I*–*V*) behavior associated with the negative differential conductance (NDC) effect of molecular junction systems has been extensively studied not only due to its counterintuitive nature but also because of its wide array of potential future applications [9, 133–139]. NDC essentially refers to nonmonotonic current–voltage; it is a rare property of certain electrical components in which an increase in the voltage across the device terminals results in a decrease in the electric current passing through the device. It is commonly used in electronic oscillators and amplifiers. At the macroscopic level, the NDC effect is the principal

feature of the *I*–*V* characteristics of resonant tunneling diodes, the bulk semiconductor devices pioneered by Esaki and his coworkers [140, 141]. Molecular junctions with semiconductor materials as their electrodes—i.e., metal–molecule–semiconductor systems—were developed to mimic the mechanism of Esaki's resonant diode and thus generate NDC phenomena [142–148]. This approach exploits the presence of a band edge of a heavily doped semiconductor material that strongly modifies the electron injection rate, leading to NDC when the molecular level shifts into the gap at the band edge [148].

Experimental attempts to produce NDC using molecular junctions comprising metallic leads have also attracted great interest, and over the last decade this effect has been observed in a large variety of molecules, including organic and metallo-organic molecules and even DNA junctions [138, 149–153]. NDC is characterized by two important factors that can vary substantially between experiments. The first is the NDC voltage—the voltage at which the current reaches a maximum. The second is the so-called peak-to-valley ratio (PVR), which is the ratio between the maximal (peak) and minimal (valley) currents. Practically speaking, the NDC voltage should be as low as possible to minimize device power consumption, while the PVR should be as large as possible. In this section, we will mainly discuss recent advances in NDC effect generation and in our understanding of the underlying mechanisms based on single-molecule break junction systems. For a review of the use of other methods to produce the NDC effect, we refer readers to [154].

6.1 Measuring NDC with the STMBJ and C-AFMBJ Techniques

Using the STMBJ technique, Tao et al. observed that the molecule OPE-NO_2 exhibited NDC when sandwiched between Au electrodes at room temperature (Fig. 22a) [45]. Although the NDC peaks occur at both positive and negative bias voltages of around ± 2 V, their PVRs are markedly different. Typically, the PVR on the high-current side of the junction is significantly larger than that on the low-current side. Since the asymmetric *I*–*V* curves are correlated with the asymmetric location of the nitro moiety, the NDC effect was attributed by Tao et al. to the electroactive nitro moiety. It was also observed that the NDC peaks usually either decrease or diminish in the reverse voltage sweep, indicating the possible involvement of an irreversible redox process. Interestingly, the magnitude of the PVR measured via the STMBJ technique is comparable to that measured using STM but is much larger than the value obtained using a nanopore technique [154]. More importantly, the NDC measured using STMBJ can be unequivocally attributed to the contribution of a single-molecule junction with covalent bonds at both molecule–electrode interfaces, as determined by a statistical analysis of a large number of repeated measurements. The NDC effect of OPE-NO_2 molecules is therefore tremendously enhanced when the STMBJ technique is used, a finding that is likely due to the enhanced contact coupling at each molecule–electrode interface, which in turn gives rise to the NDC. This finding also highlights the crucial role of the molecule–electrode contact interfaces in the electron-transport properties of molecular junctions.

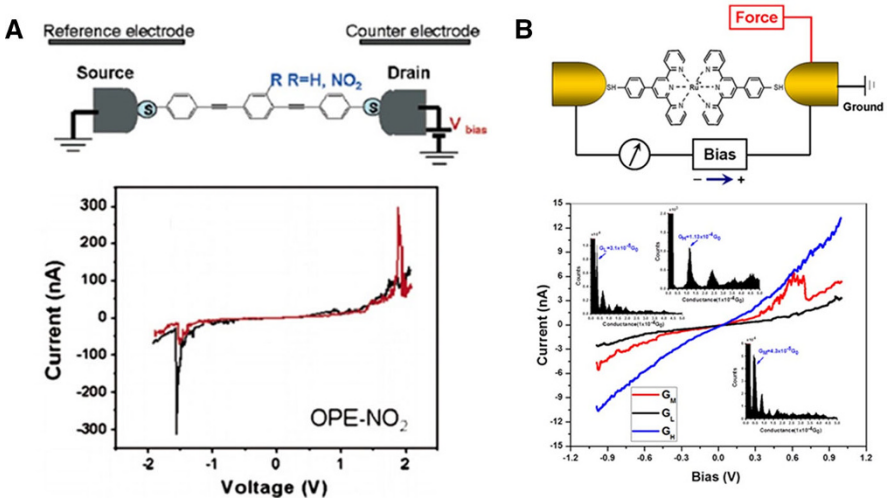

Fig. 22 **a** *Upper panel*: schematic of a single Au–molecule–Au junction; *lower panel*: *I–V* curves for the Au–(OPE-NO_2)–Au junction. **b** *Upper panel*: schematic of the Ru(tpy-SH)2 molecular junction; *lower panel*: static conductance histograms for three groups under a bias voltage of 0.3 V and *I–V* curves for junctions that lack the Ru ion center (*black*) and for junctions with the Ru ion center of three sets. **a** was reprinted with permission from [45]. Copyright (2005) American Chemical Society. **b** was reprinted with permission from [43]. Copyright (2013) Royal Society of Chemistry

Recently, Zhou et al. used the C-AFMBJ technique to study the room-temperature NDC effect of a molecular junction with a thiol-terminated Ru(II) bis-terpyridine (Ru(tpy-SH)2) molecule sandwiched between gold electrodes (Fig. 22b) [43]. They found that (i) NDC behavior is intrinsic to the Ru(tpy-SH)2 molecule; (ii) for the Ru(tpy-SH)2 molecule, NDC only occurs for a specific contact configuration (GM), not for the other two contact configurations (GL and GH); and (iii) the observed NDC for the specific contact conformation (conductance of GM) is also the result of bias-induced coupling changes, such that the greatest change in force happens at the bias where NDC is observed. The changes in force agree with the measurements of the electrode interfaces of single-molecule junctions performed with controllable mechanical modulations [94, 155, 156], indicating that the force changes are likely caused by molecule–electrode coupling changes induced by the bias. It is also possible that the conformational relaxation of molecular junctions is caused by the bias-induced twisting of molecular structures, or by bias charging on the redox-active center, as in the polaron model [157–159]. However, the underlying mechanisms for the conformational changes observed in their system under specific bias conditions require further systematic study (via theoretical calculations).

6.2 Measuring NDC with the MCBJ Technique

NDC can be achieved with the MCBJ technique as well. Recent experimental measurements of a DNA duplex (10-nm-long oligomer) have shown that it presents

an NDC effect both in a vacuum and in aqueous solution [152]. Occurring at a relatively high active voltage (2–3.6 V) with a PVR value of around 3 in solution, the NDC behavior of the DNA was attributed to the formation of a polaron, which reorganizes the conducting material at the molecular orbital level (see, e.g., [160]). Additionally, the bias voltages for the NDC peaks were observed to shift lower when the junction was exposed to vacuum conditions, a finding that was explained by the increased polaron level in the absence of polarization effects originating from the water and the ions in solution. Polaron models were also used to explain the NDC behavior of molecules with redox-active centers in which electrons can be trapped [152, 157, 161].

The observed relatively high active voltage and/or low PVR are key drawbacks to overcome. Recently, Perrin et al. reported a low bias voltage and a large NDC for a molecule consisting of two conjugated arms connected by a nonconjugated segment under high vacuum and at low temperature (6 K) (Fig. 23) [44]. In their study, the PVR was found to be as large as 15, an unusually high value for a single-molecule device. The mechanism of this NDC is thought to be the intrinsic molecular orbital alignment of the molecule. The low-temperature and high-vacuum conditions may be the main reasons for the high PVR, as they greatly diminish the influence of thermal motion and the effects of water and ions in solution, facilitating

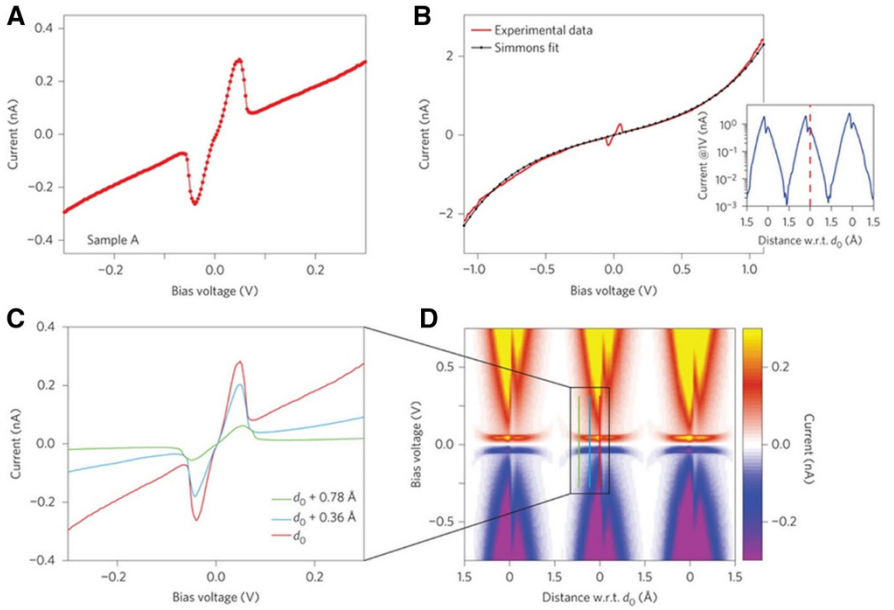

Fig. 23 **a**, **b** Typical *I–V* characteristics for the low bias (**a**) and the full bias (**b**) ranges. The *black line* is a fit using the Simmons model, with an electrode spacing of 11.0 Å. **c** Low-bias *I–V* characteristics with increasing electrode separation. **d** Map of *I–V* characteristics recorded from left to right while repeatedly increasing and reducing the electrode spacing. The spacing is relative to d_0, the electrode separation at which the NDC feature is most pronounced. The *I–V* traces shown in **c** were recorded at the positions marked by the *colored lines* in **d**. Reprinted with permission from [44]. Copyright (2014) Nature Publishing Group

accurate experimental measurements. However, these conditions could not be applied if the molecular NDC device were to be used in the real world. To mimic the routine use of current by a commercial electronic device at room temperature, it is important to explore the low-bias NDC features of the single-molecule junction under normal conditions (room temperature and normal atmospheric pressure).

Although the mechanisms of some NDC behaviors are not fully understood, single-molecule measurements have revealed some of the defining characteristics of NDC, such as low bias and large PVR, which shed light on the nature of molecular NDC. Experimentalists are now confronted with a technical bottleneck as they seek to develop low-bias, room-temperature NDC behavior with a more satisfactory PVR value. Meeting this challenge will require both the synthesis of more appropriate candidate molecules and the ability to maintain greater control over molecular junction systems.

(3) Gating: towards transistors

Building a single-molecule field-effect transistor (FET) is considered to be a critical step forward in molecular electronics. To achieve this goal, molecular junction systems must incorporate a gating electrode that shifts the energy levels of the molecule. In such devices, the energies of the molecular orbitals with respect to the Fermi level of the electrode can be directly tuned by adjusting the gate voltage. This section will discuss recent progress in gating the two terminal molecular junctions by various means, such as adding a real third electrode, electrochemical approaches, and some other proposed methods.

6.3 A Third (Gate) Electrode

A longstanding challenge in the development of a single-molecule FET is the creation of a true three-terminal device—namely, to add an actual gating electrode to the two-terminal metal–molecule–metal junction device. This requires (1) a reliable method of bridging a single molecule to the source and drain electrodes and (2) the positioning of the gate electrode a few nanometers from the molecule to achieve the required gate field. The most impressive feature of the MCBJ technique is the high mechanical stability of the system, because the electrodes are rigidly fixed to the same substrate at a short distance. This also makes MCBJ a favorable platform for building three-terminal single-molecule devices, since it allows the substrate to act as a bottom-gate electrode and enables a real gating electrode to be placed a few nanometers from the molecule [162, 163].

In 2009, Song et al. reported their experimental observations of a single-molecule FET created by utilizing the substrate as a bottom-gate electrode, based on an MCBJ setup (Fig. 24a) [162]. The molecules C8DT and BDT were tested by changing the magnitude of the gating voltage V_G. They observed a controllable gate-voltage dependence of the transition voltage V_{trans}, as obtained from the molecular junction I–V curves (Fig. 24b). For example, for the molecule C8DT (Fig. 24c), the transport at point A showed typical direct tunneling across the trapezoidal barrier at given values of V and $eV_{G,eff}$. When the applied bias was increased further to point B, a

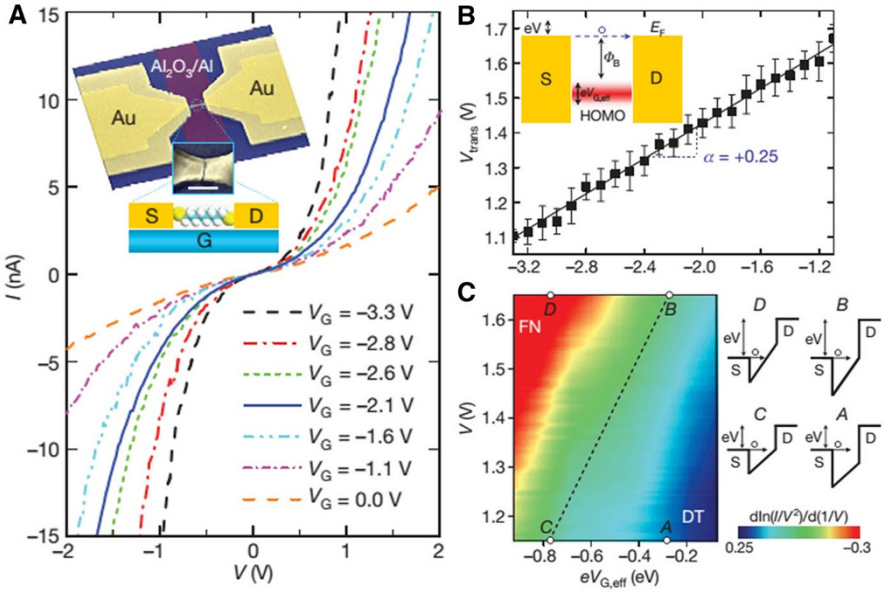

Fig. 24 Gate-controlled charge-transport characteristics of a Au–C8DT–Au junction. **a** Representative $I(V)$ curves measured at 4.2 K for different values of V_G. *Inset*: the structure of the device and a schematic. *S* source, *D* drain, *G* gate. *Scale bar* 100 nm. **b** Linear scaling of V_{trans} in terms of V_G. The *error bars* denote the standard deviations of individual measurements for several devices and the *solid line* represents a linear fit. *Inset*: schematic of the energy band for HOMO-mediated hole tunnelling, where $V_{G,eff}$ describes the actual amount of molecular orbital shift produced by gating. **c** Two-dimensional color map of $d\ln(I/V^2)/d(1/V)$ (from Fowler–Nordheim plots). Energy-band diagrams corresponding to four different regions (points A–D) are also shown. *FN* Fowler–Nordheim tunneling; *DT* direct tunneling. Reprinted with permission from [162]. Copyright (2009) Nature Publishing Group

transition from a trapezoidal to a triangular barrier shape occurred. This indicates the onset of Fowler–Nordheim tunneling. At point C, V_{trans} is at a lower bias than at point B, which can be attributed to a decrease in the $|E_F - E_{HOMO}|$ offset arising from a more negative V_G. Finally, at point D, the barrier is completely triangular and the charge transport is dominated by Fowler–Nordheim tunneling. In a three-terminal device, a negative/positive gate voltage will raise/lower the orbital energies in the molecules relative to E_F. These results demonstrate the relative movement of the molecular orbitals with respect to E_F due to gating.

Motivated by the bottom-gate design, Lee et al. recently introduced a side-gate electrode into a molecular junction system in a noncontact configuration (Fig. 25) [163]. In their work, a nanoscale side-gate electrode was defined by e-beam lithography (Fig. 25b). The *I–V* curves of a BDT molecule were measured by sweeping the gate voltage V_G while fixing the source–drain voltage. They found that the tunnel current passing through the molecular junction was weakly dependent on the gate voltage for bias voltages within ±3 V. However, the current and corresponding conductance value increased rapidly as the gate voltage became more negative (Fig. 25c). This gate effect is attributed to the special geometry of the electrodes. In contrast to the molecular junction, no gate-effect current was observed

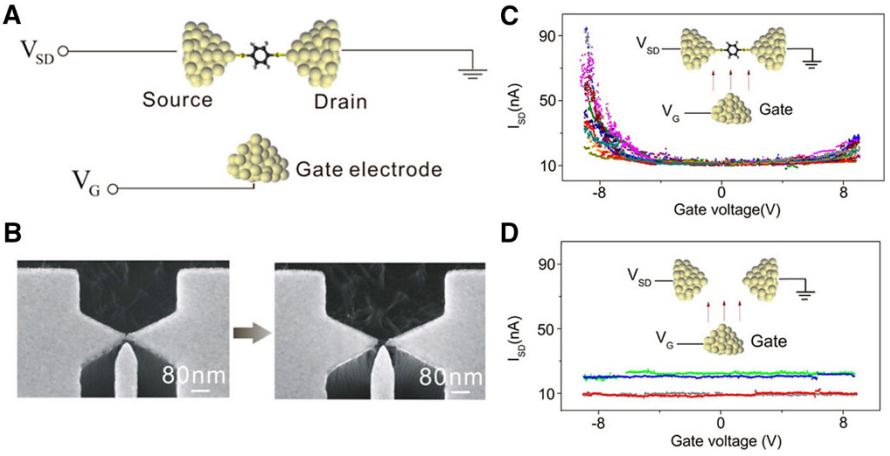

Fig. 25 **a** Schematic of a molecular transistor junction. An external electric field generated by a side-gate electrode is applied to the single-molecule junction formed by the MCBJ. **b** Top view of a scanning electron microscopy (SEM) image of a microfabricated MCBJ chip consisting of a freestanding metal bridge with a gate electrode (*left SEM image*). The push rod exerts a force that bends the substrate and breaks the metal bridge at the smallest constriction, resulting in two separate electrodes (*right SEM image*). **c**, **d** The source–drain current I_{SD} versus gate voltage V_G curves for the Au–BDT–Au molecular and molecule-free three-terminal junctions, respectively. Reprinted with permission from [163]. Copyright (2013) American Chemical Society

when the molecules were absent (i.e., a "molecule-free" junction), even when the gap size was varied (Fig. 25d). This dramatic modulation of molecular conductance by gating is considered to be due to changes in the molecular electronic structure caused by applying the electrical field to the molecular junction from the side gate, as confirmed by ab initio calculations.

6.4 Electrochemical Gating

Instead of adding an actual gating electrode, molecular junction gating can also be achieved through electrochemical approaches [164–167]. One attractive alternative is electrolyte gating, which leads to large gate efficiencies [165]. This approach can be realized using the STMBJ, C-AFMBJ, and MCBJ techniques (Fig. 26). The electrochemical gate approach allows the Fermi level of the junction electrodes to be tuned and the redox state of the molecular functional unit to be changed at room temperature under well-controlled conditions. An electrified solid–liquid interface also has the advantage that two potential differences can be controlled simultaneously: the bias voltage between the two working electrodes (source and drain) and the potential drop between each working electrode and the reference electrode [166]. The electrolyte ensures strong coupling to the applied external potential and high mobility of charge carriers (ions).

Redox-active molecules can be considered to be a unique family of switches. They are reduced or oxidized upon the application of an electrochemical gate field, thus facilitating in situ electrochemical gate-controlled charge transport. Recently,

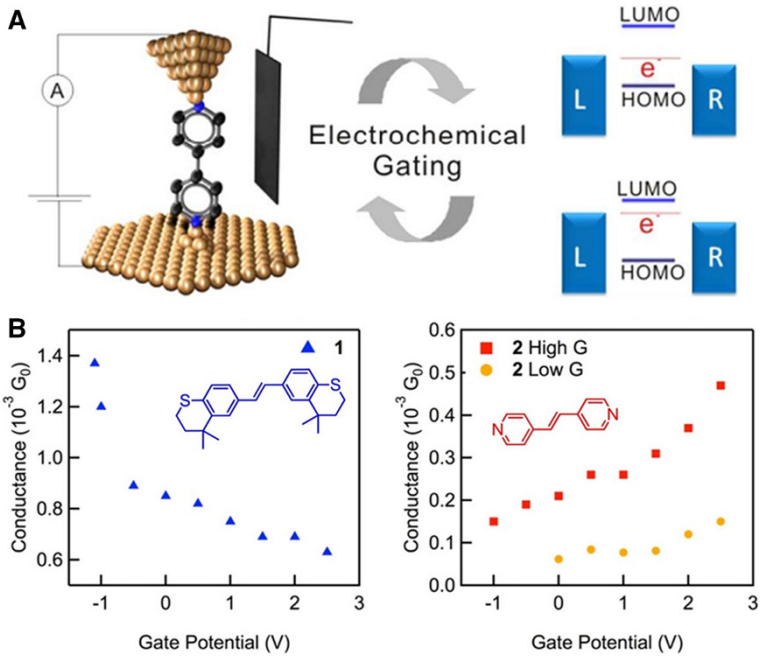

Fig. 26 **a** STMBJ and C-AFMBJ setup for the electrochemical gate effect of applied potential. Reprinted from [164]. Copyright (2014) Royal Society of Chemistry. **b** Peak conductance values versus applied gate potential for molecules **1** (*left*) and **2** (*right*), respectively. The structures of both molecules are shown in the *inset*. Reprinted from [165]. Copyright (2014) American Chemical Society

some attempts were made to study the switching behaviors of different families of redox-active molecules [167, 168]. However, achieving a high ratio between the junction conductance in the ON state and that in the OFF state remains a challenging task. Li et al. attempted to improve the electrochemical switching behavior of redox-active benzodifuran-based molecules (BDF) by selecting optimal anchoring groups [49]. Using a carbodithioate (–CS2) anchoring group instead of thiolate resulted in a dramatically increased molecular junction conductance and switching efficiency. The ON/OFF ratio for carbodithioate-BDF was claimed to be 8. A conductance ratio of almost 10 was experimentally observed for the anthraquinone/hydroanthraquinone (AQ/H2AQ) redox couple [169]. That work further demonstrated that the potential windows of the ON and OFF states can be tuned by adjusting the pH value of the electrolyte solution.

Besides redox-active molecules, Capozzi et al. reported tunable charge transport in a single-molecule junction via electrolytic gating based on a non-redox-active molecular system [165]. They demonstrated that, for the molecule 1,2-bis(4,4-dimethylthiochroman-6-yl)ethylene conducting through the HOMO, the conductance of a single-molecule junction decreased with increasing gate potential. The opposite trend was observed for the molecular system 1,2-bis(4-pyridyl)ethylene, which conducts through the LUMO (Fig. 26b). Theoretical simulation suggests that increasing the gate potential drives the LUMO in the molecular orbitals closer to the

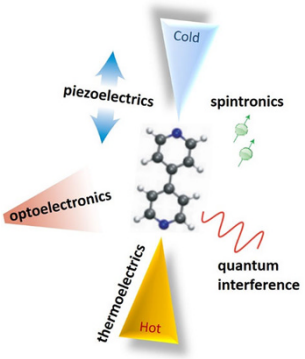

Fig. 27 Probing multiple properties of single-molecule junctions

Fermi level of the electrode and pushes the HOMO further away, resulting in enhanced charge transport for the LUMO-conducting single-molecule junction.

The electrochemical gating approach offers a highly promising platform for the construction and investigation of electrochemically controllable switches or field effect transistors (FETs) based on both redox-active and redox-inactive molecular systems.

7 Summary and Outlook

One answer to the often-posed question of "when will we see molecular electronics in the real world?" is "as soon as molecular devices can do something not currently possible with silicon" [5]. The experimental and theoretical results obtained over the past two decades for molecular junctions allow us to conclude that electron transport through molecules 1–20 nm in size has characteristics that are distinct from those of electron transport in traditional semiconductors. In this review, we have discussed recent advances in the modulation and control of charge transport through single-molecule junctions, highlighting the success of single-molecule break-junction-based techniques and how research into them has brought us closer to our ultimate aim: to build, control, and use functional molecular devices.

Although the initial goal of molecular electronics is yet to be achieved, molecular junction systems have become playgrounds for many fundamental studies that aim to improve our understanding of the physical nature of metal–molecule–metal junctions. As the field of molecular electronics has grown, physical properties beyond molecular conductance have come into view. Aside from electron transport, recent studies have begun to explore the rich physics of molecular junctions through measurements of piezoelectricity [170, 171], optical effects [172, 173], thermoelectricity [56, 57], spintronics [52, 174], and quantum interference [60, 61]—concepts for which there are no analogs in conventional electronics [25]. Various properties of a single-molecule junction that can be probed are illustrated in Fig. 27. A few experimental and theoretical works have suggested that the behavior of molecular junctions can be finely tuned by manipulating the effects of light emission, heat flow, electron spin, and quantum interference. Therefore, there is

reason to believe that investigations of these properties of single-molecule junctions will lead to a deeper understanding of charge transport through molecular junctions, the device fabrication process, and the roadmap for developing practical molecular electronics.

Acknowledgements The authors thank the U.S. National Science Foundation for funding this work (ECCS 0823849, ECCS 1231967, ECCS 1609788).

References

1. Feynman RP (1960) Eng Sci 23:22
2. Vonhippel A (1956) Science 123:315
3. Moore GE (1965) Electronics 38:114
4. Waldrop MM (2016) Nature 530:144
5. McCreery RL, Yan H, Bergren AJ (1065) Phys Chem Chem Phys 2013:15
6. Aviram A, Ratner MA (1974) Chem Phys Lett 29:277
7. Slowinski K, Chamberlain RV, Miller CJ, Majda M (1997) J Am Chem Soc 119:11910
8. Gregory S (1990) Phys Rev Lett 64:689
9. Chen J, Reed MA, Rawlett AM, Tour JM (1999) Science 286:1550
10. Zhou C, Deshpande MR, Reed MA, Jones L, Tour JM (1997) Appl Phys Lett 71:611
11. Fischer CM, Burghard M, Roth S, Vonklitzing K (1995) Appl Phys Lett 66:3331
12. McCreery RL, Bergren AJ (2009) Adv Mater 21:4303
13. Zhong ZH, Wang DL, Cui Y, Bockrath MW, Lieber CM (2003) Science 302:1377
14. Hamill J, Wang K, Xu B (2014) Rep Electrochem 4:1
15. Ratner M (2013) Nat Nanotechnol 8:378
16. Reed MA, Zhou C, Muller CJ, Burgin TP, Tour JM (1997) Science 278:252
17. Park H, Lim AKL, Alivisatos AP, Park J, McEuen PL (1999) Appl Phys Lett 75:301
18. Joachim C, Gimzewski JK, Aviram A (2000) Nature 408:541
19. Nitzan A (2001) Annu Rev Phys Chem 52:681
20. Jia C, Ma B, Xin N, Guo X (2015) Acc Chem Res 48:2565
21. Guo X, Small JP, Klare JE, Wang Y, Purewal MS, Tam IW, Hong BH, Caldwell R, Huang L, Brien S, Yan J, Breslow R, Wind SJ, Hone J, Kim P, Nuckolls C (2006) Science 311:356
22. Jia C, Migliore A, Xin N, Huang S, Wang J, Yang Q, Wang S, Chen H, Wang D, Feng B, Liu Z, Zhang G, Qu D-H, Tian H, Ratner MA, Xu HQ, Nitzan A, Guo X (2016) Science 352:1443
23. Xiang D, Wang X, Jia C, Lee T, Guo X (2016) Chem Rev 116:4318
24. Jia C, Guo X (2013) Chem Soc Rev 42:5642
25. Aradhya SV, Venkataraman L (2013) Nat Nanotechnol 8:399
26. Salomon A, Cahen D, Lindsay S, Tomfohr J, Engelkes VB, Frisbie CD (1881) Adv Mater 2003:15
27. Lindsay SM, Ratner MA (2007) Adv Mater 19:23
28. Dunlap DD, Garcia R, Schabtach E, Bustamante C (1993) Proc Natl Acad Sci USA 90:7652
29. Porath D, Bezryadin A, de Vries S, Dekker C (2000) Nature 403:635
30. Fink HW, Schonenberger C (1999) Nature 398:407
31. Kasumov AY, Kociak M, Gueron S, Reulet B, Volkov VT, Klinov DV, Bouchiat H (2001) Science 291:280
32. Xu BQ, Tao NJ (2003) Science 301:1221
33. Haiss W, van Zalinge H, Higgins SJ, Bethell D, Hobenreich H, Schiffrin DJ, Nichols RJ (2003) J Am Chem Soc 125:15294
34. Haiss W, Nichols RJ, van Zalinge H, Higgins SJ, Bethell D, Schiffrin DJ (2004) Phys Chem Chem Phys 6:4330
35. Nichols RJ, Haiss W, Higgins SJ, Leary E, Martin S, Bethell D (2010) Phys Chem Chem Phys 12:2801
36. Muller CJ, Vanruitenbeek JM, Dejongh LJ (1992) Physica C 191:485
37. Agrait N, Yeyati AL, van Ruitenbeek JM (2003) Phys Rep 377:81
38. Lörtscher E, Ciszek JW, Tour J, Riel H (2006) Small 2:973
39. Xiang D, Jeong H, Lee T, Mayer D (2013) Adv Mater 25:4845

40. Guo C, Wang K, Zerah-Harush E, Hamill J, Wang B, Dubi Y, Xu B (2016) Nat Chem 8:484
41. Capozzi B, Xia J, Adak O, Dell EJ, Liu Z-F, Taylor JC, Neaton JB, Campos LM, Venkataraman L (2015) Nat Nanotechnol 10:522
42. Diez-Perez I, Hihath J, Lee Y, Yu L, Adamska L, Kozhushner MA, Oleynik II, Tao N (2009) Nat Chem 1:635
43. Zhou J, Samanta S, Guo C, Locklin J, Xu B (2013) Nanoscale 5:5715
44. Perrin ML, Frisenda R, Koole M, Seldenthuis JS, GilJose AC, Valkenier H, Hummelen JC, Renaud N, Grozema FC, Thijssen JM, Dulić D, van der ZantHerre SJ (2014) Nat Nanotechnol 9:830
45. Xiao X, Nagahara LA, Rawlett AM, Tao N (2005) J Am Chem Soc 127:9235
46. Scott GD, Natelson D, Kirchner S, Muñoz E (2013) Phys Rev B 87:241104
47. Frisenda R, Gaudenzi R, Franco C, Mas-Torrent M, Rovira C, Veciana J, Alcon I, Bromley ST, Burzurí E, van der Zant HSJ (2015) Nano Lett 15:3109
48. Rakhmilevitch D, Korytár R, Bagrets A, Evers F, Tal O (2014) Phys Rev Lett 113:236603
49. Li Z, Li H, Chen S, Froehlich T, Yi C, Schönenberger C, Calame M, Decurtins S, Liu S-X, Borguet E (2014) J Am Chem Soc 136:8867
50. Baghernejad M, Zhao X, Baruël Ørnsø K, Füeg M, Moreno-García P, Rudnev AV, Kaliginedi V, Vesztergom S, Huang C, Hong W, Broekmann P, Wandlowski T, Thygesen KS, Bryce MR (2014) J Am Chem Soc 136:17922
51. Osorio HM, Catarelli S, Cea P, Gluyas JBG, Hartl F, Higgins SJ, Leary E, Low PJ, Martín S, Nichols RJ, Tory J, Ulstrup J, Vezzoli A, Milan DC, Zeng Q (2015) J Am Chem Soc 137:14319
52. Schwöbel J, Fu Y, Brede J, Dilullo A, Hoffmann G, Klyatskaya S, Ruben M, Wiesendanger R (2012) Nat Commun 3:953
53. Xie Z, Markus TZ, Cohen SR, Vager Z, Gutierrez R, Naaman R (2011) Nano Lett 11:4652
54. Mondal PC, Fontanesi C, Waldeck DH, Naaman R (2016) Acc Chem Res 49:2560. doi:10.1021/acs.accounts.6b00446
55. Schmaus S, Bagrets A, Nahas Y, Yamada TK, Bork A, Bowen M, Beaurepaire E, Evers F, Wulfhekel W (2011) Nat Nanotechnol 6:185
56. Chang WB, Mai C-K, Kotiuga M, Neaton JB, Bazan GC, Segalman RA (2014) Chem Mater 26:7229
57. Kim Y, Jeong W, Kim K, Lee W, Reddy P (2014) Nat Nanotechnol 9:881
58. Evangeli C, Matt M, Rincón-García L, Pauly F, Nielaba P, Rubio-Bollinger G, Cuevas JC, Agraït N (1006) Nano Lett 2015:15
59. Li Y, Xiang L, Palma JL, Asai Y, Tao N (2016) Nat Commun 7:11294
60. Vazquez H, Skouta R, Schneebeli S, Kamenetska M, Breslow R, Venkataraman L, Hybertsen MS (2012) Nat Nanotechnol 7:663
61. Vezzoli A, Grace I, Brooke C, Wang K, Lambert CJ, Xu B, Nichols RJ, Higgins SJ (2015) Nanoscale 7:18949
62. Nichols RJ, Higgins SJ (2012) Nat Nanotech 7:281
63. Akkerman HB, de Boer B (2008) J Phys Condens Matter 20:013001
64. Tachibana M, Yoshizawa K, Ogawa A, Fujimoto H, Hoffmann R (2002) J Phys Chem B 106:12727
65. Engelkes VB, Beebe JM, Frisbie CD (2004) J Am Chem Soc 126:14287
66. Li X, He J, Hihath J, Xu B, Lindsay SM, Tao N (2006) J Am Chem Soc 128:2135
67. Akkerman HB, Naber RCG, Jongbloed B, van Hal PA, Blom PWM, de Leeuw DM, de Boer B (2007) Proc Natl Acad Sci USA 104:11161
68. Kaun C-C, Seideman T (2008) Phys Rev B 77:033414
69. Li C, Pobelov I, Wandlowski T, Bagrets A, Arnold A, Evers F (2008) J Am Chem Soc 130:318
70. Paulsson M, Krag C, Frederiksen T, Brandbyge M (2009) Nano Lett 9:117
71. Wang K, Xu B (2016) Phys Chem Chem Phys 18:9569
72. Wang K, Hamill JM, Zhou J, Xu B (2014) J Am Chem Soc 136:17406
73. Zhou J, Chen F, Xu B (2009) J Am Chem Soc 131:10439
74. Dhungana KB, Mandal S, Pati R (2012) J Phys Chem C 116:17268
75. Demir F, Kirczenow G (2012) J Chem Phys 136:014703
76. Guo S, Hihath J, Diez-Perez I, Tao N (2011) J Am Chem Soc 133:19189
77. Joshua H, Nongjian T (2014) Semicond Sci Technol 29:054007
78. Quek SY, Venkataraman L, Choi HJ, Louie SG, Hybertsen MS, Neaton JB (2007) Nano Lett 7:3477
79. Zhou J, Guo C, Xu B (2012) J Phys Condens Matter 24(16):164209
80. Park YS, Whalley AC, Kamenetska M, Steigerwald ML, Hybertsen MS, Nuckolls C, Venkataraman L (2007) J Am Chem Soc 129:15768

81. Chen F, Li X, Hihath J, Huang Z, Tao N (2006) J Am Chem Soc 128:15874
82. Kiguchi M, Miura S, Hara K, Sawamura M, Murakoshi K (2007) Appl Phys Lett 91:053110
83. Patrone L, Palacin S, Bourgoin JP, Lagoute J, Zambelli T, Gauthier S (2002) Chem Phys 281:325
84. Parameswaran R, Widawsky JR, Vázquez H, Park YS, Boardman BM, Nuckolls C, Steigerwald ML, Hybertsen MS, Venkataraman L (2010) J Phys Chem Lett 1:2114
85. Hines T, Díez-Pérez I, Nakamura H, Shimazaki T, Asai Y, Tao N (2013) J Am Chem Soc 135:3319
86. Hong W, Li H, Liu S-X, Fu Y, Li J, Kaliginedi V, Decurtins S, Wandlowski T (2012) J Am Chem Soc 134:19425
87. Moreno-García P, Gulcur M, Manrique DZ, Pope T, Hong W, Kaliginedi V, Huang C, Batsanov AS, Bryce MR, Lambert C, Wandlowski T (2013) J Am Chem Soc 135:12228
88. Yelin T, Korytar R, Sukenik N, Vardimon R, Kumar B, Nuckolls C, Evers F, Tal O (2016) Nat Mater 15:444
89. Xiang L, Hines T, Palma JL, Lu X, Mujica V, Ratner MA, Zhou G, Tao N (2016) J Am Chem Soc 138:679
90. Martin CA, Ding D, Sørensen JK, Bjørnholm T, van Ruitenbeek JM, van der Zant HSJ (2008) J Am Chem Soc 130:13198
91. Adak O, Korytár R, Joe AY, Evers F, Venkataraman L (2015) Nano Lett 15:3716
92. Beebe JM, Kim B, Frisbie CD, Kushmerick JG (2008) ACS Nano 2:827
93. Ko C-H, Huang M-J, Fu M-D, Chen C-H (2010) J Am Chem Soc 132:756
94. Zhou J, Chen G, Xu B (2010) J Phys Chem C 114:8587
95. Xu B (2007) Small 3:2061
96. Wang K, Hamill JM, Wang B, Guo C, Jiang S, Huang Z, Xu B (2014) Chem Sci 5:3425
97. Rascón-Ramos H, Artés JM, Li Y, Hihath J (2015) Nat Mater 14:517
98. Quek SY, Kamenetska M, Steigerwald ML, Choi HJ, Louie SG, Hybertsen MS, Neaton JB, Venkataraman L (2009) Nat Nanotechnol 4:230
99. Chen F, Hihath J, Huang Z, Li X, Tao NJ (2007) Annu Rev Phys Chem 58:535
100. Zhou X, Peng Z, Sun Y, Wang L, Niu Z, Zhou X (2013) Nanotechnology 24:465204
101. Zhou X-S, Wei Y-M, Liu L, Chen Z-B, Tang J, Mao B-W (2008) J Am Chem Soc 130:13228
102. Wilson NR, Macpherson JV (2009) Nat Nanotechnol 4:483
103. Bumm LA, Arnold JJ, Cygan MT, Dunbar TD, Burgin TP, Jones L, Allara DL, Tour JM, Weiss PS (1996) Science 271:1705
104. Clément N, Patriarche G, Smaali K, Vaurette F, Nishiguchi K, Troadec D, Fujiwara A, Vuillaume D (2011) Small 7:2607
105. Smaali K, Clément N, Patriarche G, Vuillaume D (2012) ACS Nano 6:4639
106. Cui XD, Primak A, Zarate X, Tomfohr J, Sankey OF, Moore AL, Moore TA, Gust D, Harris G, Lindsay SM (2001) Science 294:571
107. Tour JM, Reinerth WA, Jones L, Burgin TP, Zhou C-W, Muller CJ, Deshpande MR, Reed MA (1998) Ann NY Acad Sci 852:197
108. Moreno-García P, La Rosa A, Kolivoška V, Bermejo D, Hong W, Yoshida K, Baghernejad M, Filippone S, Broekmann P, Wandlowski T, Martín N (2015) J Am Chem Soc 137:2318
109. Dell EJ, Capozzi B, Xia J, Venkataraman L, Campos LM (2015) Nat Chem 7:209
110. Su TA, Li H, Steigerwald ML, Venkataraman L, Nuckolls C (2015) Nat Chem 7:215
111. Li H, Su TA, Zhang V, Steigerwald ML, Nuckolls C, Venkataraman L (2015) J Am Chem Soc 137:5028
112. Makk P, Tomaszewski D, Martinek J, Balogh Z, Csonka S, Wawrzyniak M, Frei M, Venkataraman L, Halbritter A (2012) ACS Nano 6:3411
113. Hamill JM, Wang K, Xu B (2014) Nanoscale 6:5657
114. Büttiker M, Imry Y, Landauer R, Pinhas S (1985) Phys Rev B 31:6207
115. Briechle BM, Kim Y, Ehrenreich P, Erbe A, Sysoiev D, Huhn T, Groth U, Scheer E (2012) Beilstein J Nanotechnol 3:798
116. Simmons JG (1963) J Appl Phys 34:1793
117. Cui B, Xu Y, Ji G, Wang H, Zhao W, Zhai Y, Li D, Liu D (2014) Org Electron 15:484
118. Wang K, Zhou J, Hamill JM, Xu B (2014) J Chem Phys 141:054712
119. Beebe JM, Kim B, Gadzuk JW, Frisbie CD, Kushmerick JG (2006) Phys Rev Lett 97:026801
120. Jia C, Wang J, Yao C, Cao Y, Zhong Y, Liu Z, Liu Z, Guo X (2013) Angew Chem Int Ed 52:8666
121. Xie Z, Bâldea I, Smith CE, Wu Y, Frisbie CD (2015) ACS Nano 9:8022
122. Bâldea I (2012) Phys Rev B 85:035442
123. Chen J, Markussen T, Thygesen KS (2010) Phys Rev B 82:121412

124. Wang G, Kim Y, Na S-I, Kahng YH, Ku J, Park S, Jang YH, Kim D-Y, Lee T (2011) J Phys Chem C 115:17979
125. Nijhuis CA, Reus WF, Whitesides GM (2010) J Am Chem Soc 132:18386
126. Kornilovitch PE, Bratkovsky AM, Williams RS (2002) Phys Rev B 66:165436
127. Liu R, Ke SH, Yang WT, Baranger HU (2006) J Chem Phys 124:024718
128. Yee SK, Sun J, Darancet P, Tilley TD, Majumdar A, Neaton JB, Segalman RA (2011) ACS Nano 5:9256
129. Hihath J, Bruot C, Nakamura H, Asai Y, Diez-Perez I, Lee Y, Yu L, Tao N (2011) ACS Nano 5:8331
130. Zhao J, Yu C, Wang N, Liu H (2010) J Phys Chem C 114:4135
131. Armstrong N, Hoft RC, McDonagh A, Cortie MB, Ford MJ (2007) Nano Lett 7:3018
132. Stadler R, Geskin V, Cornil J (2008) J Phys Condens Matter 20:374105
133. Chen J, Wang W, Reed MA, Rawlett AM, Price DW, Tour JM (2000) Appl Phys Lett 77:1224
134. Fan F-RF, Yang J, Cai L, Price DW, Dirk SM, Kosynkin DV, Yao Y, Rawlett AM, Tour JM, Bard AJ (2002) J Am Chem Soc 124:5550
135. Kratochvilova I, Kocirik M, Zambova A, Mbindyo J, Mallouk TE, Mayer TS (2002) J Mater Chem 12:2927
136. Rawlett AM, Hopson TJ, Nagahara LA, Tsui RK, Ramachandran GK, Lindsay SM (2002) Appl Phys Lett 81:3043
137. Xue Y, Datta S, Hong S, Reifenberger R, Henderson JI, Kubiak CP (1999) Phys Rev B 59:R7852
138. Ying H, Zhou W-X, Chen K-Q, Zhou G (2014) Comput Mater Sci 82:33
139. Mentovich ED, Belgorodsky B, Kalifa I, Richter S (2010) Adv Mater 22:2182
140. Chang LL, Esaki L, Tsu R (1974) Appl Phys Lett 24:593
141. Esaki L (1958) Phys Rev 109:603
142. Guisinger NP, Basu R, Greene ME, Baluch AS, Hersam MC (2004) Nanotechnology 15:S452
143. Guisinger NP, Greene ME, Basu R, Baluch AS, Hersam MC (2003) Nano Lett 4:55
144. Hallbäck A-S, Poelsema B, Zandvliet HJW (2007) Appl Surf Sci 253:4066
145. Lu ZH, Khangura RS, Dharma-wardana MWC, Zgierski MZ, Ritchie D (2004) Appl Phys Lett 85:323
146. Pitters JL, Wolkow RA (2006) Nano Lett 6:390
147. Rakshit T, Liang GC, Ghosh AW, Hersam MC, Datta S (2005) Phys Rev B 72:125305
148. Rakshit T, Liang G-C, Ghosh AW, Datta S (1803) Nano Lett 2004:4
149. Le JD, He Y, Hoye TR, Mead CC, Kiehl RA (2003) Appl Phys Lett 83:5518
150. Migliore A, Nitzan A (2011) ACS Nano 5:6669
151. Bürkle M, Viljas JK, Vonlanthen D, Mishchenko A, Schön G, Mayor M, Wandlowski T, Pauly F (2012) Phys Rev B 85:075417
152. Kang N, Erbe A, Scheer E (2010) Appl Phys Lett 96:023701
153. Mentovich ED, Kalifa I, Tsukernik A, Caster A, Rosenberg-Shraga N, Marom H, Gozin M, Richter S (2008) Small 4:55
154. Bingqian X, Yonatan D (2015) J Phys Condens Matter 27:263202
155. Zhou JF, Guo CL, Xu BQ (2012) J Phys Condens Matter 24:164029
156. Zhou JF, Xu BQ (2011) Appl Phys Lett 99:042104
157. Galperin M, Ratner MA, Nitzan A (2004) Nano Lett 5:125
158. Yeganeh S, Galperin M, Ratner MA (2007) J Am Chem Soc 129:13313
159. Zazunov A, Feinberg D, Martin T (2006) Phys Rev B 73:115405
160. Galperin M, Ratner M, Nitzan A (2005) Nano Lett 5:125
161. Han JE (2010) Phys Rev B 81:113106
162. Song H, Kim Y, Jang YH, Jeong H, Reed MA, Lee T (1039) Nature 2009:462
163. Xiang D, Jeong H, Kim D, Lee T, Cheng Y, Wang Q, Mayer D (2013) Nano Lett 13:2809
164. Baghernejad M, Manrique DZ, Li C, Pope T, Zhumaev U, Pobelov I, Moreno-Garcia P, Kaliginedi V, Huang C, Hong W, Lambert C, Wandlowski T (2014) Chem Commun 50:15975
165. Capozzi B, Chen Q, Darancet P, Kotiuga M, Buzzeo M, Neaton JB, Nuckolls C, Venkataraman L (2014) Nano Lett 14:1400
166. Huang C, Rudnev AV, Hong W, Wandlowski T (2015) Chem Soc Rev 44:889
167. Li C, Stepanenko V, Lin M-J, Hong W, Würthner F, Wandlowski T (2013) Phys Status Solidi B 250:2458
168. Kay NJ, Higgins SJ, Jeppesen JO, Leary E, Lycoops J, Ulstrup J, Nichols RJ (2012) J Am Chem Soc 134:16817

169. Darwish N, Díez-Pérez I, Da Silva P, Tao N, Gooding JJ, Paddon-Row MN (2012) Angew Chem Int Ed 51:3203
170. Bruot C, Hihath J, Tao N (2012) Nat Nanotechnol 7:35
171. Bruot C, Palma JL, Xiang L, Mujica V, Ratner MA, Tao N (2015) Nat Commun 6:8032
172. Galperin M, Nitzan A (2012) Phys Chem Chem Phys 14:9421
173. Battacharyya S, Kibel A, Kodis G, Liddell PA, Gervaldo M, Gust D, Lindsay S (2011) Nano Lett 11:2709
174. Aragonès AC, Aravena D, Cerdá JI, Acís-Castillo Z, Li H, Real JA, Sanz F, Hihath J, Ruiz E, Díez-Pérez I (2016) Nano Lett 16:218

Top Curr Chem (Z) (2017) 375:61
DOI 10.1007/s41061-017-0149-0

REVIEW

Advance of Mechanically Controllable Break Junction for Molecular Electronics

Lu Wang[1] · Ling Wang[1] · Lei Zhang[1] · Dong Xiang[1]

Received: 6 November 2016 / Accepted: 16 May 2017 / Published online: 24 May 2017

Abstract Molecular electronics stands for the ultimate size of functional elements, keeping up with an unstoppable trend over the past few decades. As a vital component of molecular electronics, single molecular junctions have attracted significant attention from research groups all over the world. Due to its pronounced superiority, the mechanically controllable break junctions (MCBJ) technique has been widely applied to characterize the dynamic performance of single molecular junctions. This review presents a system analysis for single-molecule junctions and offers an overview of four test-beds for single-molecule junctions, thus offering more insight into the mechanisms of electron transport. We mainly focus on the development of state-of-the-art mechanically controlled break junctions. The three-terminal gated MCBJ approaches are introduced to manipulate the electron transport of molecules, and MCBJs are combined with characterization techniques. Additionally, applications of MCBJs and remarkable properties of single molecules are addressed. Finally, the challenges and perspective for the mechanically controllable break junctions technique are provided.

Keywords Molecular electronics · Single-molecule junctions · Mechanically controllable break junctions · Single-molecule study · Molecular devices

Chapter 2 was originally published as Wang, L., Wang, L., Zhang, L. & Xiang, D. Top Curr Chem (Z) (2017) 375: 61. DOI 10.1007/s41061-017-0149-0.

Lu Wang and Ling Wang contributed equally to this paper.

✉ Dong Xiang
xiangdongde@126.com

[1] Key Laboratory of Optical Information Science and Technology, Institute of Modern Optics, College of Electronic Information and Optical Engineering, Nankai University, Tianjin 300071, China

1 Introduction and Background

In the wake of the rapid development of the information society, the further miniaturization and functionalization of electronic devices appears to be an unstoppable trend. Simultaneously, it is difficult that the feature size of silicon-based electronic devices breaks through the intrinsic limitation of several tens of nanometers [1]. As a logical consequence, molecular electronics is a subject of interest, which probably stands for the ultimate size of functional elements. Moreover, molecular devices have a broad prospect for development due to their significant features, such as high efficiency, miniaturization, etc. In 1974, Aviram and Ratner first proposed the idea that single molecules would be promising active circuit components in the future [2, 3]. Indeed, molecules possess a number of incomparable advantages, such as low cost, smaller size, structural variety, stability, recognition, and self-assembly properties [4].

Over the past few years, a large number of research groups over the world have focused on molecular electronics [5–7]. The studies of molecular electronics have been focusing on how to control and measure the charge transport through single molecule–electrode/many molecules–electrode junctions [8]. Molecular junctions can generally be classified into two types, ensemble molecular junctions and single molecular junctions. The former is based on many molecules sandwiched between two electrodes, which is in close proximity to real devices [9]. Nevertheless, the latter is the most appropriate candidate for few or single molecules trapped in two nanoelectrodes for electron transport. Corresponding techniques have been rapidly developed to fabricate single molecular junctions, which mainly include mechanically controlled break junctions [10], scanning probe microscopy break junctions [11], electromigration breakdown junctions [12], electrochemical deposition junctions [13], and so on. In comparison, mechanically controlled break junctions (MCBJs) have been widely applied to characterize the dynamic performance of single molecular junctions due to their mechanical stability for single atoms or molecules and the finely adjustable gap size between two nanoelectrodes [14].

Not long after the beginning of investigations into molecular electronics, the MCBJ technique was first proposed by Moreland and Ekin in 1985; it was used to break a Nb-Sn filament mounted on a flexible glass beam [15]. In 1992, Muller et al. made significant progress in the technology for mechanically controlled break junctions and observed quantum effects on the conductance of a gold wire, which jumped as integral multiples of $2e^2/h$ [16]. Later, in 1997, Reed et al. applied the MCBJ to single molecular junctions, where an organic molecule, benzene-1,4-dithiol, was self-assembled onto two gold electrode ends and the relevant charge transport properties were measured [17]. Recently, the MCBJ approach has attracted significant attention in the study of electronic properties of materials [18–20]. For instance, different metals (Au [21], Ag [22], Cu [23], Pt [24], Pd [25], etc.), carbons (carbon nanotube [26], graphene [27], etc.) and other materials are applied as working electrodes in single molecular junctions, with various molecules used to explore the physical properties, such as switching, rectification, and memory.

This review presents an in-depth study that focuses on system analysis and four test-beds for single-molecule junctions, thus offering more insight into the electron transport mechanisms. In this review, we mainly present the development of state-of the-art of mechanically controlled break junctions. Three-terminal gated MCBJ approaches are introduced to manipulate the electron transport of molecule, and combinations of MCBJ with other techniques are introduced. Additionally, several pronounced physical properties and typical applications of MCBJ are addressed. Finally, the challenges and perspective for the mechanically controllable break junctions technique are provided.

2 System Analysis for Single-Molecule Junctions

As is well known, conductance measurements have been widely applied to describe the charge-transport mechanism of single molecular junctions. It is worth investigating the factors that significantly affect the conductance value. Based on this prospective, the system analysis of total molecular junctions has been achieved by dividing the system into three segments: the anchoring groups (also called link groups, which link single molecules to electrodes), molecular backbone (everything except the anchoring groups in a molecule) and electrode materials. In this section, we systematically discuss the aforementioned three segments. In addition, practical and potential anchoring groups have been primarily generalized and compared in various aspects, such as the contact resistance, formation probability, and stability. Finally and importantly, electrode materials as the highlighting factors for micro-fabrication and the molecular interaction have been presented.

2.1 Anchoring Groups

Anchoring groups, which are interfaces between molecules and microscopic electrodes, are of vital importance in the formation of stable single molecular junctions, i.e., a strong molecule–electrode coupling. There are three regimes: a weak coupling regime ($\Gamma \ll U$), a strong coupling ($\Gamma \gg U$) regimes; and an intermediate coupling regime, where U is the addition energy and Γ is defined as the broadening of the energy level in the molecules [28]. Different anchoring groups generally have different coupling strengths and the coupling strength governs the transition from coherent to incoherent transport. Besides, the anchoring groups determine the junction conductance by controlling not only the strength of the coupling to the metal but also the position of the relevant molecular energy levels [29]. Therefore, a number of potential anchoring groups have been frequently proposed and investigated over the years, such as thiol (–SH) [30], amine ($–NH_2$) [31], carboxy acid (–COOH) [32], pyridyl (–PY) [33], cyano (–CN) [33], isocyano (–NC), nitro ($–NO_2$), dimethyl phosphine ($–PMe_2$), methyl sulfides (–SMe) [34], and C_{60} [35]. Research groups select well-defined groups to form donor–acceptor bonds with electrodes according to their contact resistance, forming possibility and stability, which largely determine the conductance value.

Among these anchoring groups, thiol (–SH) groups are the earliest and most commonly used groups to connect gold electrodes with target molecules. Thiol can bond covalently to gold electrodes, and the generated Au–S bond is even stronger than the gold–gold bond. Due to this peculiarity, gold atoms from electrodes can be hauled down to produce atop, hollow, bridge structures during the process of constant stretching, which results in substantial changes in the conductance [36]. Tsutsui et al. performed a quantitative comparison of thermodynamic stability for the Au–S and Au–NH_2 bonds [31]. They showed that Au–thiol bonds are much more stable than Au–amine linkages by exhibiting a twofold higher natural lifetime for the Au–aminobenzenethiol–Au single-molecule junctions compared to the Au–benzenediamine–Au counterpart. Meanwhile, the nature life time of Au–thiol links in the self-break regime was five orders of magnitude longer than that of Au–amine contacts [31]. Tao et al. systematically studied three single molecules of alkanes terminated with dithiol, diamine, and dicarboxylic-acid [32]. They reported that the contact resistances are in the order: Au–S > Au–NH_2 > Au–COOH, which is attributed to different electronic coupling efficiencies provided by the different anchoring groups between the alkane and the electrodes. They simultaneously measured the average stretch length to obtain information on the binding strength, which varies in the order of Au–S > Au–NH_2 > Au–COOH [32]. For thiol (–SH) and carboxy acid (–COOH), the hydrogen in the two linkers plays a critical role in the binding mechanism [37]. Hong et al. reported that the junction formation probability and stability follows this order: pyridyl (–PY) > thiol (–SH) > amine (–NH_2) > cyano (–CN) [33].

Li et al. explored the effect of anchoring groups on the single-molecule charge transport through porphyrins [38]. The results showed that the anchoring effect follows the sequence of pyridyl (–PY) > amine (–NH_2) > sulfonate (–SO_3^-)>-nitrile (–CN) > carboxylic acid (–COOH) in terms of the enhancement of the molecular conductance. In addition, they found that sulfonate (–SO_3^-) is a potential group for constructing a single molecular junction. Park and Venkataraman et al. compared a series of alkanes terminated with amines (NH_2), dimethyl phosphines (PMe_2), and methyl sulfides (SMe), where the stability, stretch length, and conductance values have the following order: PMe_2 > SMe > NH_2, while the contact resistance sequence is reversed [34, 39]. Specifically, the strongest affinity for π-back-donation in the phosphines (PMe_2) corresponds to the largest conductance.

In addition to the aforementioned conventional and underlying anchoring groups, there are several groups and small molecules that result in higher conductance. MCBJ devices can be operated throughout a wide temperature range by far from room temperature to liquid helium temperature. Kiguchi et al. investigated a series of molecules bridged between various electrodes [22, 40]. For Pt, they first obtained a stable and high conductance of Pt–benzene via Pt–C bonds [24], with a series of molecular junctions of Pt/H_2, Pt/H_2O, Pt/CO, Pt/CO_2, Pt/C_2H_2, and Pt/C_6H_2 that show a main conductance of nearly $1G_0$ [41]. Recently, some authors have reported that the conductance (approximately $0.9G_0$) of two molecular junctions for Pt/ethylene and Pt/acetylene is comparable to that of a metal atomic wire, which is attributed to the effective hybridization between the metal orbitals and the π

molecular orbital [42]. Moreover, the ethylene and acetylene molecules bond separately to Pt electrodes via di–σ bonds and di–σ and π bonds. Contacting benzene and C_{60} directly with Au without anchoring groups results in high conductance values ($0.1G_0$) due to direct binding between the metals and π-conjugated molecules without anchoring groups [35]. Furthermore, electronically and structurally well-defined highly conductive single molecular junctions for naphthalene/Au and anthracene/Au were also fabricated by using the direct π-binding technique [43].

Another method to realize high conductance and stability is to form a covalent Au–C σ–Bond, which exhibits a high conductance. Cheng et al. proposed that gold atoms at the electrodes displace the trimethyltin tin linkers, leading to the formation of direct Au–C bonded single-molecule junctions (Fig. 1a) [44]. The highly conducting characteristic occurs because the Au-C bonds on the terminal methylene units are well coupled to the conjugated π system, while previous similar molecular junctions, such as Au-benzene, are formed in a different manner, in which a C atom of the benzene molecule jumps directly to the Au electrode [46]. As shown in Fig. 1b, Hong et al. then investigated the connection of TMS-terminated oligo(phenylene ethynylene)s (OPEs) to gold electrodes to create covalent Au–C anchoring sites by cleaving off trimethylsilyl (TMS) groups on two sides [45]. Gold atoms at the electrode displace the $SnMe_3$ linkers, leading to the formation of Au–C bonded single-molecule junctions. In this case, the conductance is ~100 times larger than analogous alkanes with most other bonding groups. This novel feasible method of forming Au–C σ–bonds offers a means for establishing metal–organic contacts with strong electronic coupling.

Hence, it can be concluded that an ideal anchoring group should possess three essential features: stable binding, high junction formation probability, and high conductance [47]. Moreover, different charge-transport mechanisms are affected by

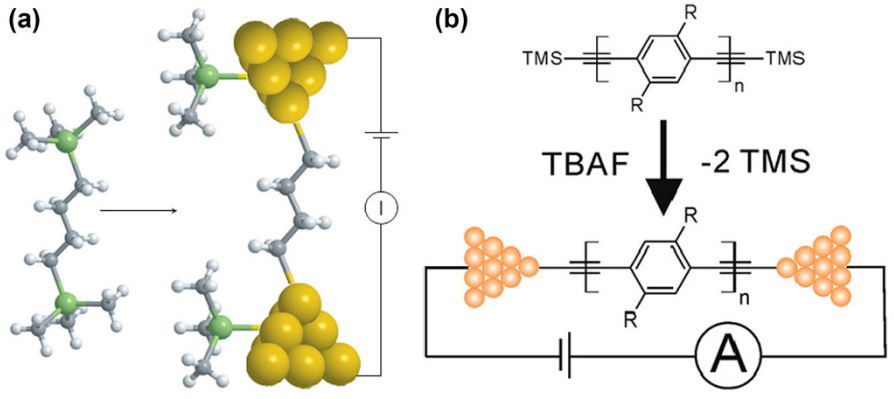

Fig. 1 Two typical examples of Au–C bond. **a** Junction formation and conductance measurements with 1,4-bis(trimethylstannyl)butane molecules between gold electrodes. (H atoms, *white*; C atoms, *grey*; Sn, *green*). Reproduced with permission from Ref. [44]. Copyright 2011, Rights Managed by Nature Publishing Group. **b** Schematics of the Au–C junction formation. TMS and TBAF are trimethylsilyl and tetrabutylammonium fluoride respectively. Reproduced with permission from Ref. [45]. Copyright 2013, American Chemical Society

different anchoring groups. The electrons of the molecular junction systems are transported through the closest frontier molecular orbitals [the highest occupied molecular orbital (HOMO) or lowest unoccupied molecular orbital (LUMO)] of the molecule and the Fermi energy level (E_F) of metal electrode. The energy gap between molecular frontier orbital and Fermi level of electrode can be investigated by transition voltage spectra (TVS), which in some cases also can be used to prove the molecular presence in the junction.

2.2 Molecular Backbone

The molecular backbone, the molecular part besides the anchoring groups, is generally wire-like, which plays an important role in electron-transport mechanisms [48]. The studies of the molecular backbone involve the realization of single-molecule functional devices, such as rectifiers, diodes, switches, etc.

Wire-like backbones exhibit diverse electron-transport mechanisms because of their varying lengths. These mechanisms mainly include non-resonant tunneling and charge hopping. In general, electron transport in short molecule is achieved by non-resonant tunneling and this transport mechanism is coherent tunneling. When molecular length increases to a certain value, charge hopping will replace non-resonant. With non-resonant tunneling dominating, small molecules exhibit the dependence of length, while large molecules dominated by charge hopping show a weakly length-dependent and temperature-variant behavior [51]. Several types of molecules with variable lengths, such as *p*-phenylene ethylene (OPE), *p*-phenylene vinylene (OPV), oligophenylene-imine (OPI), and oligofluoreneimine (ONI), have been investigated. The electron-transport mechanism transforms from tunneling to hopping as the molecular length increases. Herein, an example of *p*-phenylene ethylene (OPE) is illustrated. By employing seven OPE molecular wires with varied lengths, Lu et al. demonstrated that a clear transition of the length dependence of the molecular resistance occurred between OPE3 and OPE4 at approximately 2.75 nm [49]. As shown in Fig. 2, there is an exponential decay in the single-molecule conductance as the molecular length increases, and subsequently, the conductance value of larger molecules tends to decline, but the range of the reduction is lower, which indicates that the dominant charge-transport mechanism in OPE1–OPE3 was different from that in the longer OPE molecules. Parallel cases can be found in Refs. [52, 53]. Based on previous study, several relevant studies have been reported. Sedghi et al. proposed that the transport in porphyrin molecules as long as 5–10 nm is convincingly described by a theory based on phase-coherent electron tunneling using the Fermi energy (E_F) as a single adjustable parameter, which is different from the traditional incoherent thermally assisted hopping mechanism [54]. Xiang et al. studied the charge transport in DNA duplexes and revealed a partial coherent and partial hopping regime for charge transport. Moreover, several reports shed more light on the charge-transport mechanisms [55].

In addition, quantum interference (QI) between de Broglie waves, which is strongly dependent on the structure of the molecular backbone, also plays a significant role in electron-transport mechanisms. QI can be divided into constructive interference and destructive interference. Recently, Manrique et al. investigated

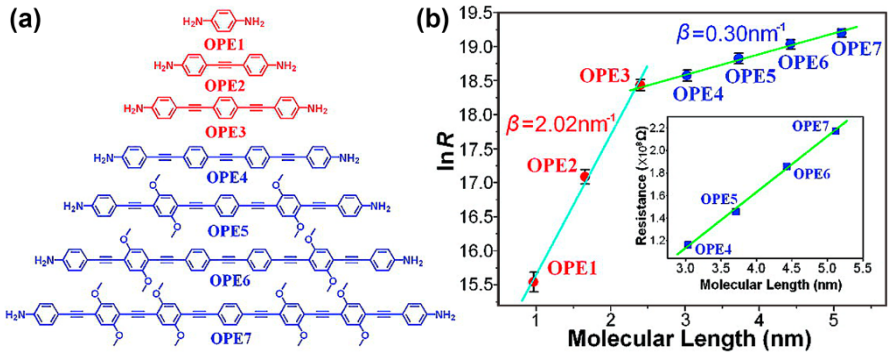

Fig. 2 An example of transition from coherent tunneling to incoherent hopping. **a** Structures of seven amine-terminated OPE molecular wires studied in this work. **b** Semilog plot of single molecular resistance versus molecular length for all of the Au–molecular wire–Au junctions. The *lines* are linear fits according to the equation: $R = R_0 \exp(\beta l)$, where R is the junction resistance, R_0 is the contact resistance, β is the exponential prefactor, and l is the molecular length. The *inset* is a linear plot of resistance against length, demonstrating the linear scaling of resistance with length for longer OPE molecules. Reproduced with permission from Ref. [49]. Copyright 2009, American Chemical Society

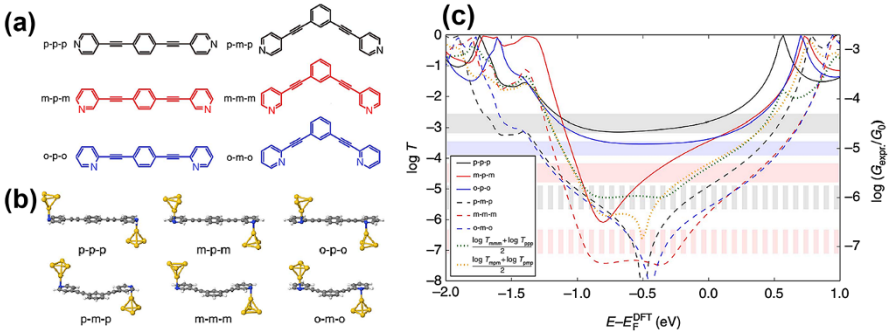

Fig. 3 A quantum circuit rule for interference effects in single-molecule electrical junctions. **a** Six molecular structures, based on the presence of a *para* or *meta* central phenyl ring. **b** Idealized junction geometries for all six molecules with the gold tip attached perpendicular to the pyridine ring. **c** Transmission curves with and without metal-ring coupling. *Dashed lines* are without metal-ring coupling, the continuous curves are with metal-ring coupling. Reproduced with permission from Ref. [56]. Copyright 2015, Nature Publishing Group

a quantum circuit rule including quantum interference effects in the conductive properties of oligo (phenyleneethynylene) (OPE)-type molecules with three aromatic rings [56]. They proposed six molecular structures with and without metal-ring coupling (shown in Fig. 3a, b). The results showed that significant changes in the molecular conductance are caused by the variations in the connectivity of the central ring rather than the terminal rings. As shown in Fig. 3c, a further study of transmission curves with and without the metal-ring coupling revealed a destructive QI behavior, where the conductance value for meta coupling is much less than that for *para* and *ortho* coupling. Detailed information is provided in Ref [56]. These two opposite interference states, the constructive and destructive

states, can be used to enhance the ON/OFF ratio, which results in a potential functional switching device with a single-molecule junction.

2.3 Electrode Material

As a vital component of a single molecular junction, electrode materials exert a significant effect on efficient charge transport. Thus, various research groups have considered different electrode materials, such as metallic electrodes and carbon-based electrodes.

Gold, a noble metal, is by far the most common metal used as a microscopic electrode, with the Au–S bond formed as the most common combination. As previously mentioned, the widespread use of gold connected with molecules is attributed to the high junction formation probability, chemical stability, and electrical conductivity. There are mature fabrication and measurement techniques for single-molecule junctions based on gold electrodes (Fig. 4a, b). To achieve a stable molecular device structure, which allows one to vary the inter-electrode distance at the sub-Angstrom scale, Molen et al. combined the two techniques of MCBJs and 2D Au nanoparticle–molecule networks to form a nanoparticle–molecule–nanoparticle junction [63]. However, some other metals can be used as electrodes, including Ag, Cu, Pt, and Pb, of which the conductance of Pt and Pb are more than 1 G_0 due to the presence of more than one conductance channel with transmission coefficients smaller than 1 [64, 65]. This does not, however, mean that metal materials are perfect candidates as electrodes due to the atomic dislocation and poor stability of metal–single molecule–metal junctions. Nonmetallic contacts,

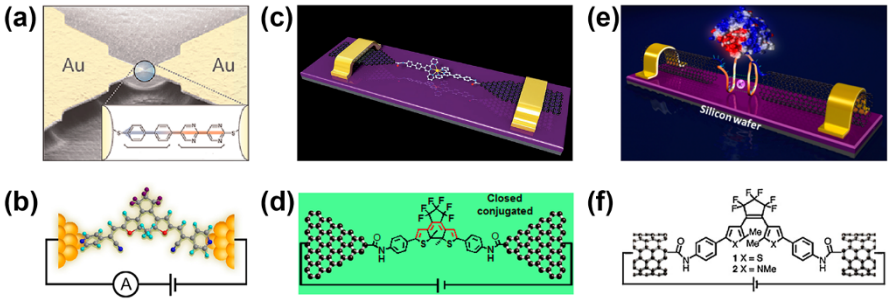

Fig. 4 Molecular junctions with different materials. **a** Microfabricated gold electrodes embedded by the dipyrimidinyl diphenyl diode (SB) molecule with donor and acceptor moieties using the MCBJ technique. Reproduced with permission from Ref. [57]. Copyright 2012, American Chemical Society. **b** An Au–4Py–Au junction connected to a circuit. Reproduced with permission from Ref. [58]. Copyright 2012, American Chemical Society. **c** A single-molecule device based on graphene point contacts. Reproduced with permission from Ref. [59]. Copyright 2012, Wiley–VCH Verlag GmbH & Co. KGaA, Weinheim. **d** A graphene-diarylethene (closed conjugated DAE)-graphene junction connected to a circuit. Reproduced with permission from Ref. [60]. Copyright 2015, American Chemical Society. **e** Single-walled carbon nanotube (SWCNT)-DNA junctions fabricated by covalently connecting cut SWCNTs with a DNA aptamer. Reproduced with permission from Ref. [61]. Copyright 2011, Wiley–VCH Verlag GmbH & Co. KGaA, Weinheim. **f** Diarylethene molecular bridges between the ends of an individual SWCNT electrode connected to a circuit. Reproduced with permission from Ref. [62]. Copyright 2009, Elsevier B.V

as an emerging field, have attracted increasing attention in recent studies. As a result, there are low-dimensional carbon nanostructures with excellent electrical conductivity, including single-walled carbon nanotubes (SWCNTs) and graphene (shown in Fig. 4c, e), used to form carbon electrode–molecule junctions, and both nanostructures are sp^2-hybridized, which facilitates the incorporation of the target molecules into the tiny electrode couple. Cao et al. used graphene as an electrode to produce a point contact by dash-line lithography, and molecular devices were covalently created by absorbing amine-terminated molecules into the electrodes [59]. Liu et al. investigated the coupling of individual DNA aptamers with SWCNTs at point contacts to form single-molecule devices, in which DNA with a single-stranded nucleic acid ligand facilitates the formation of strong and selective binding [61], and recently, All-carbon molecular tunnel junctions have demonstrated extraordinary stability under extreme bias and thermal changes [66]. DNA-assisted SWCNTs have been used, where DNA-assisted dispersion ensures that the two ends of the SWCNTs can be easily functionalized directly [67]. Employing metallic SWCNTs as nanoelectrodes, Zhu et al. have successfully fabricated single molecular junctions based on a series of oligophenyls [67]. Stable zigzag graphene nanoribbons (ZGNRs) can be connected with molecules (biphenyl molecules [68], benzene [69]; and so on) to form molecular junctions for the study of magneto-resistance. Three-terminal devices that allow single molecules to be both gated and imaged at the atomic scale have been achieved with graphene as electrode [70]. Besides, plasmon excitation is a candidate for investigation of carbon electrodes [71]. Thus, carbon materials as nanoscale electrodes represent a promising direction. The disadvantage of carbon electrodes is that the yield of the single molecular junction is relatively low due to the fixed gap between electrodes. The MCBJ method can finely and reversibly adjust the nanogap between carbon electrodes to match the size of any molecules, which would result in a high probability of the occurrence of single-molecule devices. Thus, the MCBJ method may provide an option to improve the yield of carbon-based molecular devices.

In addition to metals and carbon-based materials, the silicon electrode, as a mature practical material, is also regarded as an object to realize nanojunctions due to its high conductance and the ability to tune its Fermi level by doping. For example, Ashwell et al. reported a fabrication method of vertical nanogap structures featuring two highly doped silicon microelectrodes, with the molecules bridging into nanogaps via Si–C linkages conducted by in situ synthesis of conjugated wires [72].

3 Mechanically Controllable Break Junctions

3.1 Introduction of Mechanically Controllable Break Junctions

The MCBJ technique, as a handy tool to precisely control the single molecular junction, has been extensively applied in recent years [77]. The schematic of the latest overall MCBJ setup is shown in Fig. 6a. Viewed from the bottom up, we observe three sections: a pushing rod for forming nanogap, a flexible substrate

(silicon, spring steel; or phosphor bronze) integrated with the nanostructures, and two lateral supports that exert a force to the bendable substrate [1]. A pushing rod maintains contact with the central part of the flexible substrate, on which a microfabricated metallic wire is mounted between the two lateral supports. In general, this entire apparatus is driven by a mechanical actuator (a stepping motor or piezoelement), and the combination of both has recently been utilized more frequently to enable a fine control of the elongation [78].

3.1.1 Principle

In this three-point adjustable bending mechanism as shown in Fig. 5a, the pushing rod that drives an upward force causes progressive bending of the substrate, which results in continuous stretching of the metal wire. As the metal wire is being elongated, the cross section at the central section is scaled down until its fracture, and then, two metal electrodes at the atomic level with clean surfaces are simultaneously generated. In contrast, as the substrate is relaxed, the inevitable contraction of the metal wire ultimately causes the two electrodes to return to an original wire. The nanogap between two facing electrodes can be accurately regulated during the bending and relaxing process (shown in Fig. 5b). There is an applied bias voltage within the scope of 80–330 mV to promote the insertion of molecules into the gap. After the molecular junctions are formed, it is important to study the charge-transport properties of the single molecular junctions connected with a microscopic circuit [79].

The prerequisite for a high coupling efficiency between the electrodes and molecules is to set the gap size slightly larger than the length of the molecules and to precisely control the size. This requires an incredibly low attenuation factor between the gap size, Δd, and the displacement of the pushing rod, Δh. The attenuation factor is given by $r = \Delta d/\Delta h = 6ts/L^2$, where t is the thickness of the flexible substrate, s is the length of the suspended bridge, and L is the distance between the two lateral

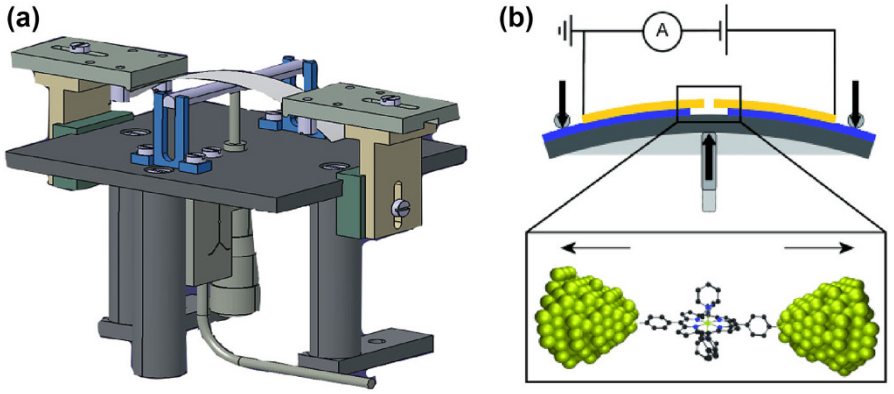

Fig. 5 Schematic of the MCBJ setup. **a** Side-view schematic of a real MCBJ setup. Reproduced with permission from Ref. [4]. Copyright 2013, American Chemical Society. **b** Mechanism of the MCBJ setup. Reproduced with permission from Ref. [80]. Copyright 2011, Perrin et al.; licensee Beilstein-Institut

supports [81]. Generally, the value of factor $r = 5 \times 10^{-6}$ can be achieved, which indicates that many displacements of the pushing rod can merely create little gap changes, and the gap size can be adjusted with picometer precision [82].

3.1.2 Advantages

Over the years, the constant attention on the MCBJ technique is ascribed to its advantages over other test-beds for single-molecule junctions. First, the clean face-to-face electrodes generated by MCBJ weakens the influence of contaminants [83], and the cyclic process for repeatedly breaking and linking the junctions facilitates the collection of more experimental data to decrease data discretization in dynamic configurations [84]. Second, the MCBJ setup is extremely stable in the whole temperature range, and disruptive factors (such as external vibration, thermal drifts, and the discontinuous motion of the pushing rod) can be almost entirely ignored. As a result of the extremely low attenuation ($\sim 5 \times 10^{-6}$) and micro-level control of the pushing rod, the accuracy of mechanical adjustment can approach a picometer scale. Meanwhile, with sophisticated micro-fabrication, the investigation of single molecular junctions can be more easily conducted. Third, the MCBJ technique can be conveniently combined with other systems, such as inelastic electron tunneling spectroscopy, surface-enhanced Raman scattering, and electrochemical deposition.

Along with the aforementioned significant advantages of the MCBJ technique, a few disadvantages exist in imaging of the junction configuration. In the process of forming single molecular junctions, we cannot use MCBJ technique to obtain the evolution of the tip atoms, which is also a challenge for STM and AFM another drawback of MCBJ technique is that it is non-convenient to add a gate electrode in a solid state compared to electromigration technique. Moreover, the sites where the molecules are inserted remain unknown, which confines the exploration of the underlying influence factor of the conductance. The integration of MCBJ and other techniques will overcome these issues. Nevertheless, MCBJ has played a major role in the research of charge transport properties for single molecules.

3.1.3 MCBJ Chip Fabrication

In recent years, progress in micro/nanofabrication technologies has enhanced the accuracy grade of MCBJ chips, which even reaches several nanometers [85]. There have mainly been three stages in the evolution of MCBJ chips over more than 30 years; in turn, these are the following: hand-operated mechanical notching, chemical deposition, and E-beam lithography.

The original MCBJ chips contained a simple metal wire, in which the minimum diameter is merely 100 μm, and the center section is notched by a sharp knife to form a groove for fracture [15]. Subsequently, the notched metal wire is glued symmetrically on a flexible substrate with two drops of conductive adhesive and the location of notched wire is shown in Fig. 6a. It can be clearly observed that two electrodes are too thick and rough to be connected with a molecule, which definitely prevents the measurement of the conductance of a single-molecule junction. Moreover, the manual process is error-prone and uncontrollable. Another type of the

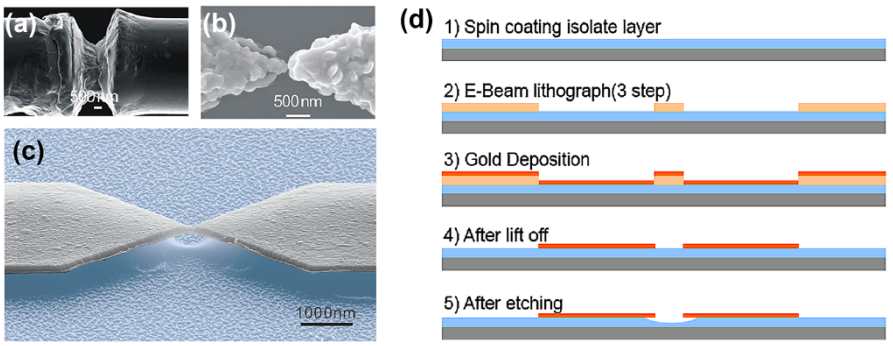

Fig. 6 Three typical kinds of MCBJ chips and specific manufacturing process of EBL MCBJ. **a** Mechanically cut gold wire as electrodes. **b** Electrochemically deposition-based electrodes. Reproduced with permission from Ref. [75]. Copyright 2010, Wiley–VCH. **c** Representative scanning electron microscope image of EBL-defined electrodes on flexible substrates. Reproduced with permission from Ref. [86]. Copyright 2013, Nature Publishing Group. **d** Chip microfabrication process. Reproduced with permission from Ref. [87]. Copyright 2012, American Institute of Physics

chips prepared for the MCBJ setup are manufactured with electrochemical deposition on the basis of optical lithography in ambient condition, called EC-MCBJ (shown in Fig. 6b). The specific procedures are as follows: first, a counter electrode fixed on a substrate with a larger gap can be achieved with optical lithography, and then, electrochemical deposition can be implemented to with fill the gap metal particles, creating two tip-like electrodes. The gap size can be adjusted with the MCBJ method. A more detailed description for electrochemical deposition is presented in the articles by Yi et al. [76] and Tian et al. [88–90]. This technique combines the characteristics of the stable structure from MCBJ with the merit of the steerable electrode shape from electrochemical deposition. At the same time, issues of contamination and a relatively low accuracy are unavoidable. Besides, MCBJ chips can be fabricated with gradually mature E-beam lithography and reactive ion etching, which are sophisticated and advanced techniques (shown in Fig. 7c). The entire process operated on a substrate can be summarized in five steps: (1) an isolated layer is spin-coated on a flexible substrate; (2) a standard E-beam lithography is carried out to construct an electrode pattern as a mask, which includes three different steps: spinning the photoresist, writing the pattern and development; (3) a metal layer is deposited on the mask; (4) the exposed photoresist is lifted off; and (5) counter free-standing nanoelectrodes are obtained by using reactive ion etching on the subjacent isolated layer [87].

3.1.4 Other Configurations of Mechanically Controllable Break Junctions

Low-dimensional structures, such as atomic and molecular junctions, are promising thermoelectric materials with quantum confinement effects. Tsutsui et al. introduced a novel device to simultaneously evaluate the conductance and thermopower of atomic and molecular junctions [92]. As shown in Fig. 7a, a microheater consisting of Pt coils with a 300-nm line-space is fabricated using the original structure of

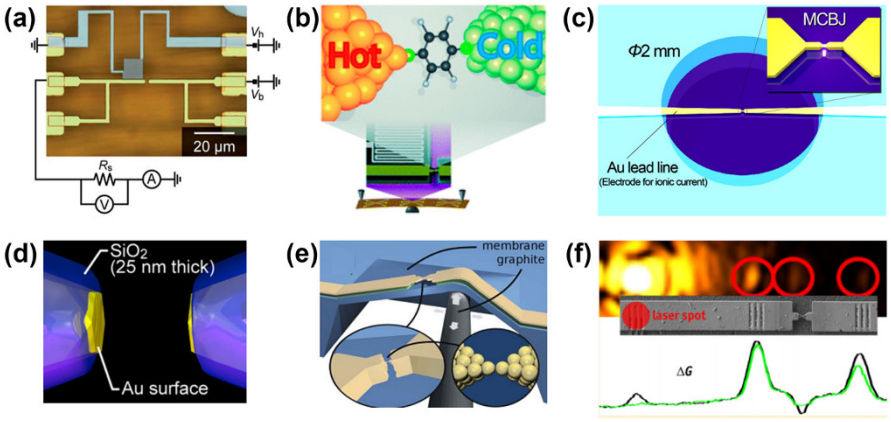

Fig. 7 Modifications of a basic MCBJ configuration. **a** Optical microscopic image of a microheater-embedded MCBJ consisting of a Pt coil (*grey*) and a free-standing Au junction (*yellow*) on a polyimide-coated phosphor bronze substrate. **b** Schematic of a microheater-embedded mechanically controllable break junction with hot and cold electrodes at room temperatures. Reproduced with permission from Ref. [92]. Copyright 2014, The Royal Society of Chemistry. **c** Schematic illustration of MCBJ electrodes symmetrically placed in a liquid container with a diameter of 2 mm. Reproduced with permission from Ref. [94]. Copyright 2014, American Chemical Society. **d** The formed Au electrodes are covered with SiO_2 except the fresh breakage surface with an area of approximately 80 × 80 nm. Reproduced with permission from Ref. [91]. Copyright 2014, AIP Publishing LLC. **e** The chips with the membranes are then clamped onto a stretching mechanism consisting of a sample holder, which carries the chip and a fine tip controlled by a uniaxial piezostage. Reproduced with permission from Ref. [95]. Copyright 2008, American Institute of Physics. **f** A sample showing three gatings on the left and the right side of the constriction (*top*) and light-induced conductance change (*bottom*). Reproduced with permission from Ref. [96]. Copyright 2014, American Chemical Society

microchips. Thus, the device can generate a temperature gradient where an electrode close to the Pt coil is hot due to Joule heating from a variable voltage V_h and the other electrode away from the Pt coil is cold, and simultaneously, the local junction configurations can be adjusted by the MCBJ setup (shown in Fig. 7b) [92]. Negative thermopower in the Au atomic chain is observed at a low V_h, which mirrors the quantum nature. However, there is positive thermopower at an increased V_h, which is ascribed to the disordered Au nanocontacts that result from excessive local heating. Meanwhile, a sensitivity of the thermoelectricity on the atomic contact configurations or the BDT molecular junction is observed. The microheater-embedded MCBJ, as an improvement on the MCBJ, is a direct and powerful approach to probe low-dimensional thermoelectric structures using thermopower measurements [93].

In previous sections, the basic mechanically controllable break junction was introduced in detail. However, it is difficult to investigate some additional phenomena, such as thermoelectricity, therefore, the basic MCBJ needs to be modified. To tackle the current noise-jamming problem in electrolyte solutions, as this noise probably affects electrical signals through the junctions, Doi et al. modified the basic MCBJ to determine the mechanisms responsible for the background current [94]. Figure 7c shows a scanning electron microscopy (SEM)

image of an MCBJ with a nanogap formed by the self-breaking method, and the nanogap is symmetrically immersed in a cylindrical structure with a diameter of 2 mm. Subsequently, NaCl aqueous solutions with various concentrations fill the cylindrical structure, with an external electrical field applied to control ionic transport. The results reveal that the current noise increases as the ionic concentration increased. By solving the time-dependent Nernst–Planck and Poisson equations, it is observed that the applied field and length of the nanogap produce a significant effect on the ionic response. The experimental and theoretical results are conducive to the exploration of the background current and lay a good foundation for follow-up studies. To suppress the effects of electronic noise and ionic current in an electrolyte solution, Taniguchi et al. proposed a SiO_2-coated MCBJ method where the electrodes in MCBJ are entirely enclosed with a thin SiO_2 layer [91]. As shown in Fig. 9d, two SiO_2 layers, respectively, that are under and on top of the electrodes are deposited by a chemical vapor deposition based on the E-beam lithography technique.

Besides, the contact between pushrod and chips generally is straight shape, Sheer et al. achieved a single-atom contact by fabricating silicon membrane substrate and fine tip (shown in Fig. 9e). With this method, it allows controlling more than one junction on the same chip; detailed explanation can be seen in Ref. [95]. Recently, Sheer et al. further integrated line gratings into the metallic leads that increase the surface plasmon polarizations (SPP) excitation efficiency (shown in Fig. 9f) [96]. They found a clear distance and polarization dependence of the conductance enhancement, demonstrating the direct impact of SPPs to the conductance change by both thermal expansion and photo-assisted transport. These innovative structures and results have a huge impact on the design of opto-nanoelectronic devices whose conductance is controllable by the excitation of surface plasmon polaritons [96]. Due to the increased attention on single molecular junctions, there will be more modifications of MCBJ devices in the near future.

3.1.5 Conductance Measurement with MCBJ

The measurement of single molecular junctions is critical for exploring charge transport at the molecular level, which is an exciting but challenging endeavor. Compared with the traditional scanning tunneling microscopic technique (STM), the MCBJ approach experienced a late start, and the corresponding measuring method still has room for improvement. Nevertheless, Reed et al. obtained the conductance of a molecule connected with electrodes by MCBJ [17], which marked the arrival of the measuring era for single molecular junctions. In the experiment, benzene-1,4-dithiol immersed in tetrahydrofuran (THF) solution was embedded in counter electrodes, which are two terminals of breakage metal wire, at room temperature, subsequently forming a self-assembled monolayer (SAM) on the electrode surface. This approach presented an extremely stable gold–sulfur–aryl–sulfur–gold configuration. As observed in Fig. 8a, there was a highly reproducible apparent gap at approximately 0.7 V (current–voltage curve), with two steps concurrently observed in both bias directions (conductance–voltage curve); this indicates that the number of active molecules was restricted to as low as one active molecule. This study not

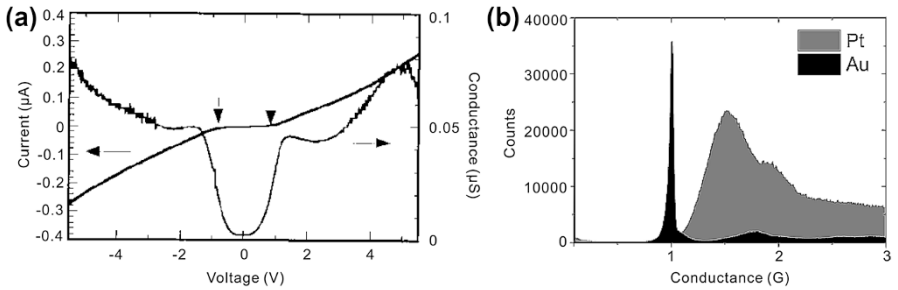

Fig. 8 One-dimension conductance measurement. **a** Typical I(V) characteristics, which illustrate a gap of 0.7 V; and the first derivative G(V). Reproduced with permission from Ref. [17]. Copyright 1997, AAAS. **b** Histograms of conductance values for Au and Pt collected from 20,000 individual breaking traces. Reproduced with permission from Ref. [64]. Copyright 2015 Sabater et al.; licensee Beilstein-Institut

only provides a quantitative conductance measurement of molecules ranging from several to individual molecules in molecular junctions but also paves a way for investigating the electrical characteristic of a single atomic chain. Based on this method, the one-dimension conductance measurement has been further developed, and simultaneously, the two-dimension conductance histogram, due to its comprehensive information, has been used extensively.

A number of research groups have studied the forming probability of single-atomic chains of the late transition metals and noble metals (Ni, Pd, Pt, Cu, Ag, Au), among which Au and Pt exhibit the strongest tendency to form chains [97]. Ruitenbeek et al. investigated both metals and obtained the corresponding conductance histogram (shown in Fig. 8b) [64]. Clean metallic Au contacts are characterized by a high sharp peak at 1 G_0, while Pt has a much broader peak at 1.5 G_0, in which G_0 (corresponding to a resistance of approximately 12.9 KΩ) is the conductance quantum that is given by $G_0 = 2e^2/h$, where h is the Planck's constant and e is the electron charge. Based on the analysis of the conductance channels and transmission properties, it is obvious that Au has one conductance channel with nearly perfect transmission, while Pt possesses more than one channel but with transmissions smaller than 1 G_0.

The one-dimensional conductance measurement plays an important role in describing the junction configuration in the opening and closing processes. Wu et al. discussed the G–z curves in OPE-dithiol molecules solution and its pure solvent [30]. As shown in Fig. 9a, there are a series of steps at several G_0 values, with the last step at approximately $G = G_0$, which corresponds to a single atomic chain. Electron tunneling started to appear below approximately $10^{-3}G_0$. When OPE-dithiol molecules were introduced, an additional stable plateau was found at $G \approx 10^{-4}G_0$, which indicated the formation of a gold-single molecule-gold system such as the inserted structure (shown in Fig. 9b). It is easy to observe that the conductance values decrease gradually as the stretch length increases. Recently, Zant et al. discovered a conductance increase with an increasing electrode separation for Fe^{II}-complex molecular junctions [98]. More important studies are required to obtain more uniform and consistent results.

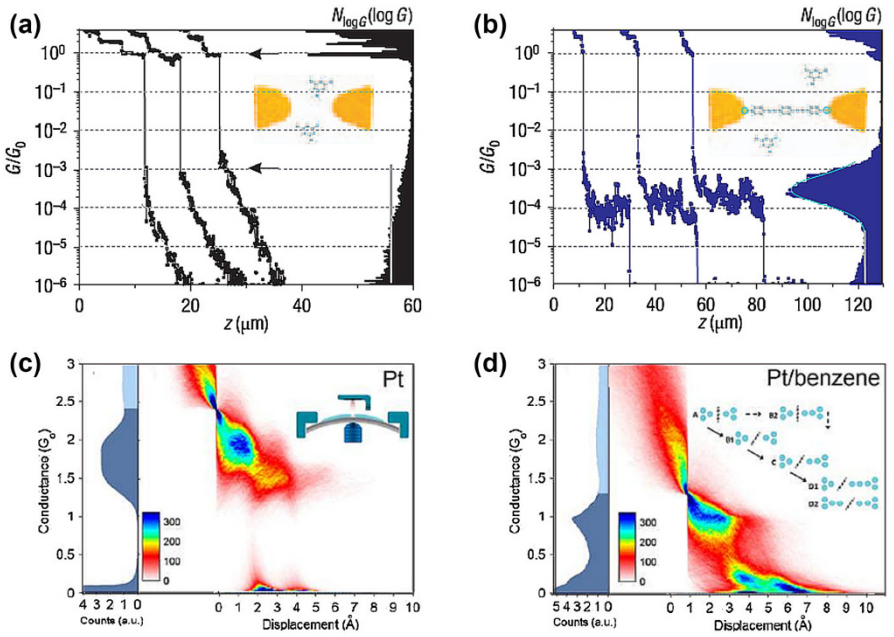

Fig. 9 Molecular conductance measurement with MCBJ. **a** Three typical single $G(z)$ curves measured in pure solvent (*black curves*). **b** Three typical single $G(z)$ curves measured in the same solvent but with added OPE–dithiol molecules (*blue curves*). Reproduced with permission from Ref. [30]. Copyright 2008, Nature Publishing Group. **c** Conductance histogram and 2D histograms of the number of counts at each conductance—displacement combination. *Insets* mechanically controllable break junction apparatus. **d** Conductance histogram and 2D histograms of the number of counts at each conductance—displacement combination. *Insets* artist's impression of the evolution of the Pt/benzene hybrid junction during stretching. Reproduced with permission from Ref. [14]. Copyright 2013, American Chemical Society

The construction of two-dimensional trace histograms builds on the assumption that the time-dependent (or distance-dependent) conductance evolution near and after the rupture of the last gold bond is characteristic of the respective metal–molecule bond with time (or distance) as X-axis and conductance as Y-axis [99]. The traces are shifted along the X-axis to make the break pint of the last atomic contact coincide. The 2-D trace histograms are plotted as intensity graphs of which deep color represents a high probability of corresponding values. Furthermore, the two-dimensional conductance-displacement histograms provide access to the dynamic structure of the junctions during elongation processes. The histograms are constructed by setting a specific conductance value as a first data point, assigning it as a relative distance of $z = 0$ for each trace, and then overlapping all of the individual traces in 2D space [22]. As shown in Fig. 9c, d, zero displacement is set to a fixed conductance value (2.4 G0 for Pt, 1.3 G0 for Pt/benzene) selected at the top edge of the peak in the conductance histogram. In general, elongation of electrodes results in a breakage or pulling an atom from the electrodes, and Fig. 9c clearly shows the breakage situation. After implanting benzene into the gap between two Pt electrodes, the conductance decrease is attributed to a transition from a perpendicular orientation to a tilted orientation of the benzene molecule in the

junction (shown in Fig. 9d, A and *B*1, respectively) [14]. Details of the experiment and analysis are discussed in Ref. [12]. However, the combination of 1D and 2D histograms can ensure that unmistakable structural evolution information is obtained, and thus, it is clear why a growing number of research groups regard both as regular comparison graphs for an effective study [100].

3.2 Gated Mechanically Controllable Break Junctions

Since the introduction of the mechanically controllable break junction (MCBJ) technique in 1985, it has produced enormous and far-reaching functions of metal atomic wires and single-molecule two-terminal devices for molecular electronics. A number of scientists gradually explored two-terminal molecular junctions towards functional devices and gained a series of achievements, such as rectifiers, switches, etc. For further research, field-effect transistor (FET) architectures have been demonstrated as feasible candidates, which require three-terminal molecular chips as the source, drain, and gate electrodes [101]. Until now, three-terminal structures based on MCBJ two-terminal chips have primarily been focused on junctions containing a side gate, back gate, and so on. In this section, these two types of gatings will be explained in detail.

3.2.1 Side-Gated Mechanically Controllable Break Junctions

Side-gated MCBJ, as a method of fabricating three-terminal single molecular devices, was designed by Xiang et al. [102] on the basis of the conventional back-gated MCBJ and the formation of a side gate after electromigration [73]. In addition to defining two-terminal chips on a spring steel substrate, there is an additional step in which a nanoscale side-gate electrode that is several nanometers from the bridge is fabricated by e-beam lithography before a suspended metal bridge is generated, with the thin bridge constricted to 30 nm [102]. The fabricated chip is then placed on a three-point adjustable bending mechanism, and the push rod exerts an upward force to break the metal bridge, which generates a nanogap, as shown in Fig. 10a. In this experiment, a measurement of the gate-controlled current was conducted on a gold-1,4-benzenedithiol (BDT)-gold single molecular junction. As shown in Fig. 10b, the current flowing through source and drain electrodes is maintained at an almost constant value as a small gate voltage is applied. However, the current increases exponentially as the gate voltage negatively increased [102]. The obvious advantage of the side-gated structure is the non-breakage of the side gate electrode in comparison to the sandwich-gated MCBJ, and simultaneously, the molecular energy levels can be shifted with the gate electrode. However, the gate efficiency of the device is extremely influenced by the space between the gate electrode and molecular junction [1]. At the same time, the electric potential from the gate can possibly suffer from the shielding by the two metal electrodes, which results in only the molecules close to gate electrode being perfectly controlled by the side-gate electrode [1].

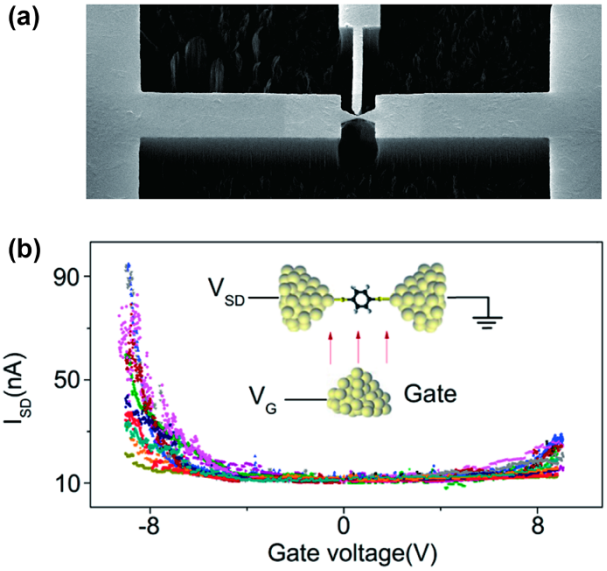

Fig. 10 Side-gated mechanically controllable break junctions. **a** Top view of a scanning electron microscopy (SEM) image of a microfabricated MCBJ chip consisting of a freestanding metal bridge with a gate electrode. **b** The current was modulated by the gate voltage in 12 different molecular junctions. The *inset* schematics illustrate the three-terminal junction with BDT bridged between the source and drain electrodes. Reproduced with permission from Ref. [102]. Copyright 2013, American Chemical Society

3.2.2 Back-Gated and Sandwich-Gated Mechanically Controllable Break Junctions

In addition to side-gated MCBJs, there are several other realizations of gated mechanically controllable break junctions including back-gated MCBJs, sandwich-type gated MCBJs, and others. Back-gated molecular structures, as the first observed gated molecular devices, have a wide range of applications. In 2005, Champagne et al. first used a heavily doped Si substrate as the gate electrode [103]. They employed traditional lithographic techniques to minimize the molecule gate spacing or to limit the thickness of the SiO_2 dielectric layer to as small as 40 nm to enable useful gating. Similarly, Martin et al. utilized high-resolution e-beam lithography to pattern the dielectric polyimide coated on a phosphor bronze substrate, and then, the gold layer was evaporated above polyimide [104]. Compared with the silicon gate electrode, the phosphor bronze shows the characteristic of excellent flexibility to sustain a large curvature bend. Based on the phosphor bronze substrate, Ballmann et al. developed bottom-gated MCBJs, which employed a high-κ insulator (κ dielectric permittivity) to systematically improve the gate coupling [105].

Martin and Perrin et al. successively studied a sandwich-type gated MCBJ shown in Fig. 11a (false color scanning electron microscope (SEM) image of a three-terminal MCBJ device and a two-terminal MCBJ) [106, 107]. The obvious feature is that the gate is suspended, and this method is similar to electromigration. They combined a previous microfabrication technique with an oxidized aluminum gate

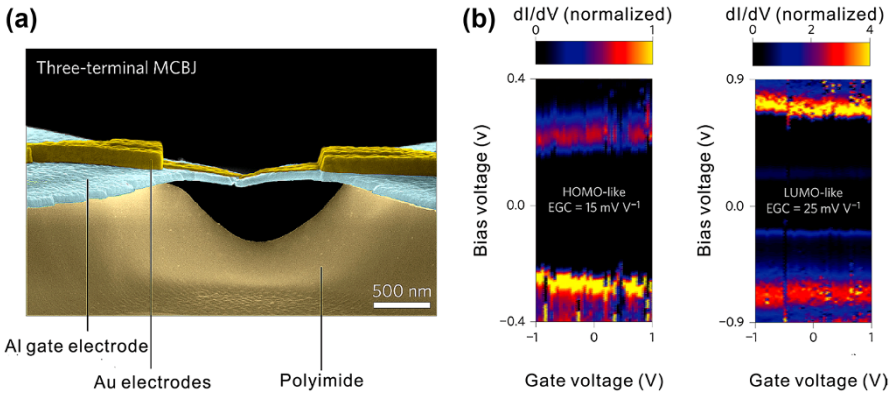

Fig. 11 Sandwich-type gated mechanically controllable break junctions. **a** False color scanning electron microscope (SEM) image of a three-terminal MCBJ device and a two-terminal MCBJ. The gate is made of aluminum and covered with a plasma-enhanced native aluminum oxide layer. The gold electrodes are deposited on top of the gate dielectric. **b** Gate diagrams recorded for different junction configurations and during different breaking events. Color-coded d*I*/d*V* curves plotted versus gate and bias voltage. The dependence of the resonance shift on the gate voltage allows us to attribute resonances in the left to an occupied level (HOMO-like, located at ~0.3 eV for zero gate voltage) and those in the right to an unoccupied level (LUMO-like, located at ~0.75 eV for zero gate voltage). Reproduced with permission from Ref. [107]. Copyright 2013, Nature Publishing Group

under a high-power oxygen plasma in a reactive ion etcher. Eventually, they isotropically dry-etched to remove part of the polyimide layer, which produced partially suspended Au/Al_2O_3/Al structures. This method is able to mechanically break the gold wire [8]. Perrin et al. found that the HOMO-like and LUMO-like level positions depend on the gate voltage with an electrostatic gate coupling of ~15 and ~25 mV V^{-1}, respectively (shown in Fig. 11b), and simultaneously, the molecular orbital levels can be controllably raised or lowered with the electrostatic gate [107]. They concluded that the movement of the molecular levels is the result of interactions between electrons and image charges by changing the gate voltage and electrode gap, respectively, which is also used by other groups. Research details of gated MCBJ and the modulation of molecular orbital levels are discussed in Refs. [106, 107].

Above all, these gated MCBJs can not only mechanically control the space between source and drain but also electrostatically control the gate, which provides a platform for studying characteristics of coulomb blockade, the Kondo effect, etc. [103, 104, 106, 107]. Compared with electromigration, this technique represents higher yields of molecular junctions and a precise control of the distance between a pair of electrodes with picometer precision [106]. The evolution of these gated MCBJs has resulted in an improvement of gate electrode materials ranging from silicon [103], phosphor bronze [104], to aluminum [108] (flexibility: aluminum > phosphor bronze > silicon). However, it is somewhat unavoidable that a relatively large curvature bending of the substrate for an appropriate gap size can result in the fracture of the gate dielectric layer.

In summary, the gated mechanically controllable break junction has experienced significant development in the past 10 years. In the meantime, gated MCBJs play an excellent role in the study of electron-transport properties and molecular-level transistors for single molecular junctions. Furthermore, more attention should be paid to improving gated MCBJs to enable the study of other physical properties, such as thermoelectricity [109].

3.3 Characterization Techniques for Single-Molecule Junctions

3.3.1 Inelastic Electron Tunneling Spectroscopy

Inelastic electron tunneling spectroscopy (IETS) is a promising spectroscopic technique, which has shown excellent resolution (at the single molecule level) and sensitivity in the in situ investigation of molecular junctions [110, 111]. It was discovered by Jaklevic and Lambe in 1966 [112]. At present, it is becoming a powerful tool for the investigation of molecular electronics and surface and interfacial phenomena. It can be used for investigating the low excited states in a wide variety of experimental systems in the energy range of several electron volts. IETS is a very useful approach when combined with MCBJ for investigating the relationship between the charge transport properties of the molecular junctions and the molecular conformation or orientation [111]. The combination has excellent reproducibility and superior stability; therefore, it allows for repeated measurements within a few hours and can provide highly reliable conductance values [113]. The principle of IETS is not complicated, as shown in Fig. 12a, b; it displays the energy band diagram of the tunneling junction and the related I(V), dI/dV, and $\mathrm{d}^2I/\mathrm{d}V^2$ [114]. Under a low applied voltage, the tunneling through the barrier is elastic, while the inelastic tunneling caused by the interaction between the excited states of the adsorbed molecules and the electron creates the additional transmission channel; moreover, there is a change of hω in the energy. Each peak in the curve of $\mathrm{d}^2I/\mathrm{d}V^2$ vs. V corresponds to an additional channel, and the molecular vibrational mode spectra are provided.

An example of experimental IETS spectra of Au-oligo(phenylene ethynylene)-dithiol (OPE3)-Au junctions based on a highly stable MCBJ system at liquid helium temperature (4.2 K) in vacuum varied with the electrode displacement is illustrated in Fig. 12c. The IETS spectra vary at different displacements of the electrodes, as clearly observed obviously; in the top panel, the second and fourth conductance states are nearly similar, but their IETS spectra are relatively different, and this is more obvious in Fig. 12d. Therefore, molecule junctions can have relatively different IETS although they have similar conductance states, and the displacement between the electrodes also affects the IETS. Moreover, their investigations also revealed that the IETS spectra vary with the configurations of molecule junctions. This has provided us a new way to obtain special properties of the molecule junction from multiple perspectives. The IETS information confirmed that the I–V properties or conductance states clearly come from the molecular junction.

IETS is a supplement to Raman and IR especially in many highly symmetrical molecules, and it can produce some of the features that are forbidden in other

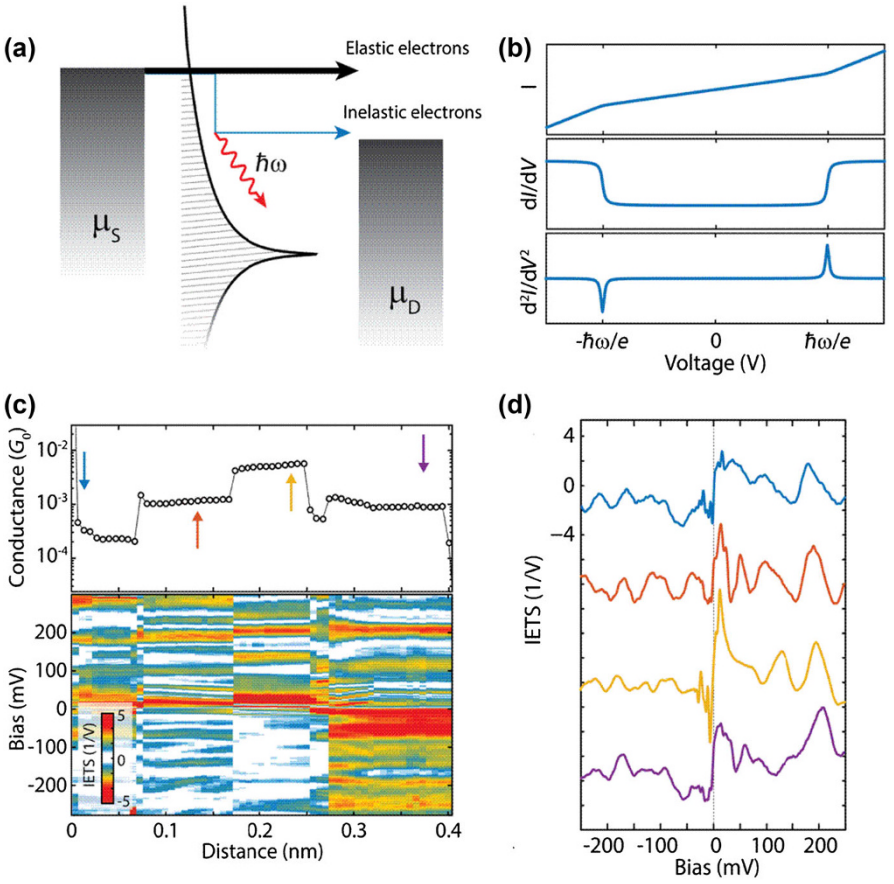

Fig. 12 Principle of IETS and the IETS of the OPE3 molecule combined with MCBJ. **a** Schematic of the IETS in a single-molecule junction. **b** IETS shows up as a kink in the I–V (*upper panel*), a step in the d*I*/d*V* (*middle panel*), and a peak in d^2I/dV^2 (*bottom panel*) curve. **c** Low bias conductance trace recorded during the stretching of OPE3 molecular junction (*top*), and color-map of IETS signal during stretching (*bottom*). **d** Extracted IETS master curves at the positions indicated by the *arrows* in **c**. Reprinted with permission from Ref. [115]. Copyright 2015 Frisenda et al.; licensee Beilstein-Institut

vibrational spectra [116]. Though it is becoming a common technique for molecular investigations, it faces a challenge as one cannot obtain accurate geometric parameters due to the complexity of the inherent spectrum caused by coupling of local vibrations [117].

3.3.2 Surface-Enhanced Raman Spectroscopy

Surface-enhanced Raman scattering (SERS) is considered a type of label-free and high-sensitivity analytical technique, in either theoretical research or experimental research, and it is widely used in many fields, such as material analysis, environmental monitoring and surveillance, single-molecule detection, and

biomedical imaging [118, 119]. SERS is an intrinsic phenomenon based on the nanostructure because the intensity of the Raman scattered light depends on the size, shape, and particle spacing on the nanoscale [120]. The first observation of SERS was on a roughly electrochemical silver electrode in 1974 by Fleischmann et al. [121]. The combination of SERS and MCBJ was used by Tian et al. to determine the SERS intensity of molecules between two nano-electrodes on a Si chip as the gap size decreased [122]. Ward et al. and Konishi et al. reported the conductance measurements and the SERS spectra of single-molecule junctions [123, 124].

Figure 13 shows the SERS spectra of a single 4,4′-bipyridine molecule junction in three different modes and the intensity of the Raman signals. This experiment was performed combined with the MCBJ technique for 4,4′-bipyridine molecule solution at room temperature. In Fig. 13a, there are three modes including the totally symmetrical mode (red), and the non-totally symmetric b_1 (blue), and b_2 (green) modes. The intensities of the non-totally symmetric b_1 and b_2 modes are higher than that of the totally symmetrical mode, and combined with Fig. 13b, it suggests that the produced SERS spectra are dependent on the formation of single molecule junctions [125].

SERS has a greater potential application due to its high sensitivity, superior flexibility, and more. The signal enhancement of SERS mainly comes from two mechanisms: an electromagnetic mechanism, which is due to localized surface plasmon resonance [126], and a chemical mechanism, which results from charge transport [127]. The local electromagnetic mechanism is the main contributor; besides, the Herzberg-Teller type transition also plays an important role [128, 129]. Though SERS has ultrahigh sensitivity, it still has challenges: a lack of applicability to substrates of any composition, a lack of applicability to substrates of any surface morphology, [120] and low reproducibility of the SERS signal [130].

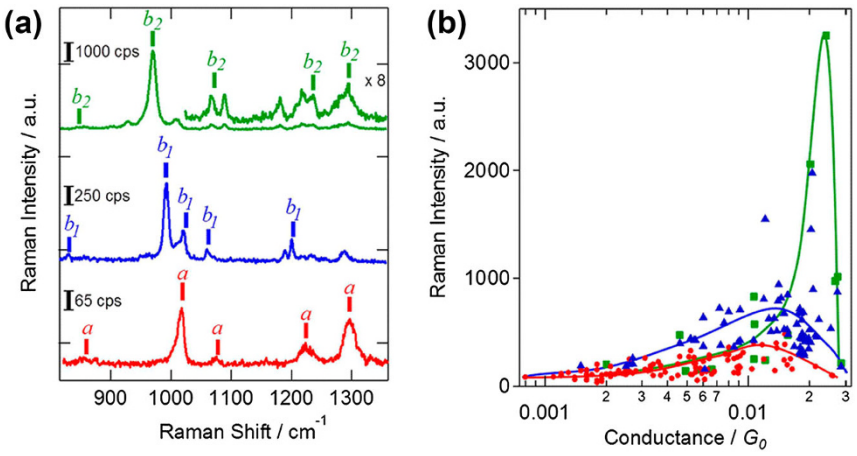

Fig. 13 Surface-enhanced Raman spectroscopy combined with mechanically controllable break junctions. **a** SERS spectra of a single 4,4′-bipyridine molecule junction in three different modes. In total, symmetrical mode (*red*), and non-totally symmetric b_1 (*blue*), and b_2 modes (*green*). **b** Intensity of SERS of a (*red*), b_1 (*blue*), and b_2 (*green*) modes. Reprinted with permission from Ref. [124]. Copyright 2013, American Chemical Society

3.3.3 Noise Spectroscopy

Noise is an obstacle to the identification of some important signatures of a single molecule, but noise analysis can also provide valuable information, which cannot be obtained by current–voltage measurement in single-molecule science. In particular, noise spectroscopy has proven to be a powerful method for investigating the properties of devices and materials, as well as the metal–molecule contacts, which is a research area that lacks exploration [131]. It is important to understand the fluctuation of the conductance value and the characteristics of the noise in the study of molecular devices [1]. A random telegraph noise was observed under high bias voltages in monomolecular junctions, and it is due to an electron trapping process [132]. The telegraph-like current fluctuations were mainly ascribed to the thermal activation of the formation and disconnection of the band between the molecule and electrodes; this is due to the dynamic reconfiguration of the molecule, which is induced by the current [131]. In a molecule-free device, a $1/f$ noise and thermal noise were observed. A Lorentzian-shaped noise was observed in the investigation of 1,4-benzenediamine (BDA) molecules when relatively small voltages (approximately 20 mV) were applied in the mechanically controllable break junction devices [87]. The $1/f$ noise in different materials can be attributed to different fluctuation processes [87]. The Lorentzian-shaped noise was related to the telegraph-like current fluctuations, and this is a universal phenomenon.

The noise spectroscopy for a BDT molecule in the gap was combined with the MCBJ device to create a more stable molecule junction and investigate the noise characteristics. As illustrated in Fig. 14a, a $1/f$ noise and thermal noise can be obtained in the gap junction without the molecule, and the $1/f^2$ noise arose when a molecule was applied to the gap and attached with two electrodes. The measurement of the noise characteristics was performed over a wide range of frequencies (10^0–10^5 Hz) [82]. From Fig. 14b, it can be concluded that the $1/f^2$ noise is a common

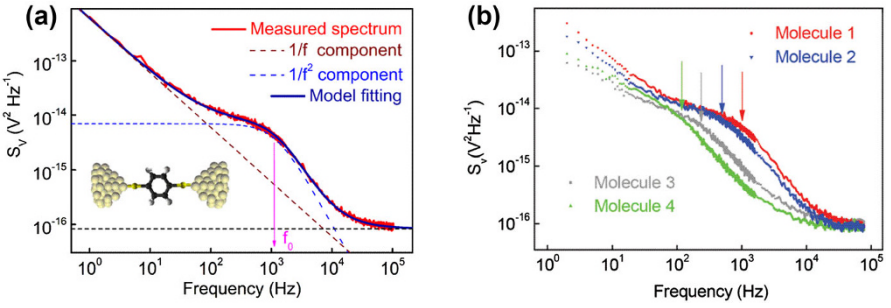

Fig. 14 Noise spectroscopy feature of the BDT molecule junction. **a** The voltage noise power spectral density of a molecule-containing junction with a BDT molecule bridging the electrodes in a lock-in state. The measured noise spectrum and model are, respectively, represented by the *red* and *blue solid lines*. The *dashed line* represents the $1/f$, $1/f^2$ and thermal noise. Reprinted with permission from Ref. [131]. Copyright 2015, American Institute of Physics. **b** The voltage power spectral density for four different molecules. These molecules have same kind of binding group ($-NH_2$), but vary in length. The backbone of molecule 1 to 4 have 1, 2, 3, 4 phenyl rings, respectively. Reprinted with permission from Ref. [82]. Copyright 2014, The Royal Society of Chemistry

feature in the noise measurement of different molecules. All the features of the noise measurement observed in Fig. 14 can be explained with a general Landau model by considering the relationship between the charge transfer in the single molecule and the structure reconfiguration in the coupling of the molecule with the electrodes.

In addition, the shot noise can be used to evaluate both the Fano factor and the transmitting channels. This is caused by the discrete property of the charge [4]. Scheer et al. measured the shot noise of single-molecule Au—1,4-benzenedithiol–Au junctions with an MCBJ device at 4.2 K and revealed the number of transport channels [77]. Generally, the noise measurement and analysis on the current flow in a single molecule junction can provide more information about the process of electron tunneling and the characteristics of the coupling between molecules and electrodes.

3.3.4 Transition Voltage Spectroscopy

Before the introduction for transition voltage spectroscopy (TVS), we make a comparison about two approximate models (the Simmons model and the single-level model). In the Simmons model, the molecule with a particular length connected between two electrodes can be seen as a potential barrier, which transforms in the order of rectangle, trapezoidal, and triangle barrier with an increased bias voltage [133]. The main deficiency of the Simmons model is that the nature of a molecule cannot be taken into account when assuming a molecule as a tunneling barrier. In the single-level model, it assumed that current is carried just by one molecular orbital closest to the Fermi level, and the transport is described by a transmission function $T(E)$ that depends explicitly on energy (E). This transmission function peaks around the molecular levels and the I(V) relationship can be calculated from the Landauer formula [133]. When bias voltage increases to make the Fermi level align with the closest molecular level, nonresonant tunneling transforms into resonant tunneling. There are two parameters for single-level model which include level alignment and coupling strength between electrodes and molecules. The first parameter (level alignment) has been mentioned above. The other one (coupling strength) determines the joint strength between the molecule and the electrode (see Sect. 2.1). Both of these two parameters combine to determine the conductance of single-molecule junctions [134].

It is important to precisely evaluate the energy level alignment in molecular electronics for a better understanding of the charge-transport mechanism [135]. In recent years, transition voltage spectroscopy (TVS) has become an excellent tool in experimental molecular electronics. Initially, Beebe et al. first reported the introduction of TVS in terms of the Simmons model [133]. They found that current–voltage measurements of metal–molecule–metal junctions exhibit an inflection point on a plot of $\ln(1/V^2)$ vs. $1/V$, i.e., a minimum voltage in Fowler–Nordheim (FN) representation, and this inflection voltage is called the transition voltage. They found that the transition voltage scales down linearly with the energy offset between Fermi level of electrode and the molecular orbital. Hence, TVS is proposed as a simple and powerful spectroscopic tool to study the positions of molecular levels even if the bias voltage is moderate and resonance is not yet

reached. However, the interpretations of TVS and the employed model are still under debate [133, 136, 137]. Huisman et al. found that the Simmons model employed far is inconsistent with experimental data, while a coherent molecular transport model (single-level model) does justify TVS as a spectroscopic tool [136].

Xiang et al. have measured gap size-dependent transition from direct tunneling to field emission in single-molecule junctions with MCBJ technique. As shown in Fig. 15a, the inflection point shifts to lower biases as the gap size decreases, revealing that field emission transport is enhanced in single-molecule junctions as the gap size between two nanoelectrodes is reduced [138], and the correlation between the number of molecules in the junction and transition voltage was not found (shown as Fig. 15b). These results showed that the distance change between the electrodes and associated alternations of the molecular electronic structure rather than inter-molecular tunneling result in the enhancement of field emission for alkanedithiols. Liao et al. studied the gate-modulation mechanism in Au–BDT–Au junctions with the TVS technique [139]. In addition, they showed the relation between the gate voltage and transition voltage with a 2D contour map. Combined with the appearance and analysis for the experiment, it was confirmed that the closest molecular orbital or the dominating conduction orbital, which controls the charge transport in an Au-BDT-Au molecule junction, is the HOMO level. Above all, TVS is not only a valuable investigative tool but also a useful means of checking the presence of molecules in junctions in the future.

3.3.5 Thermoelectricity

The thermoelectric effect was used to study the direct heat transfer in electric power in the 19th century [140]. The thermoelectric effect enables direct conversion of thermal energy into electricity, which means that a temperature gradient in a

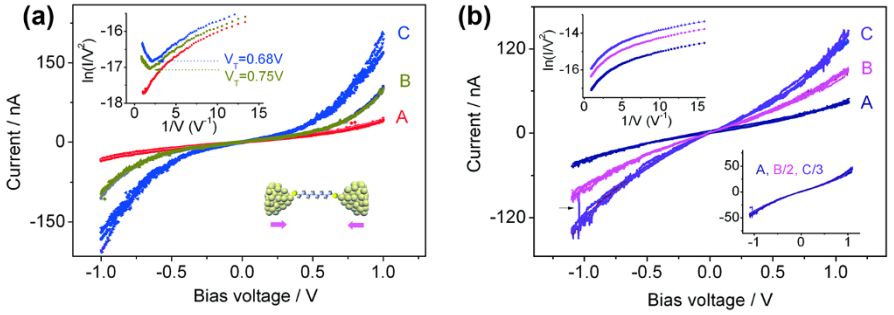

Fig. 15 Gap size-dependent transitions. **a** I/V curves of single-molecule (1,8-octanedithiol) junctions with three different gap sizes. Curves *B* and *C* were recorded after the gap size was decreased by approximately 0.2 and 0.4 nm based on curves A. The *insert* shows corresponding $\ln(I/V^2)$ versus 1/V characteristics. **b** I/V curves of the molecular junction with varied number of trapped molecules at a fixed gap size. The measured I/V responses fall mainly into three sets of curves. The sets represent multiples ($B = 2$, $C = 3$) of the fundamental characteristics ($A = 1$). The *arrow* indicates the change of number of trapped molecules in the junction. *Top insert* no field emission was observed independent of the number of entrapped molecules. *Bottom insert* verifies that the I/V curves are multiples of each other. Reprinted with permission from Ref. [138]. Copyright 2011, The Royal Society of Chemistry

material induces diffusion of majority charge carriers from the hot to the cold region and builds electric voltage there [141]. The thermoelectric experimental measurement on molecular junctions, such as the measurement of S, was first reported by Ludoph and Ruitenbeek [142]. Thermopower is one of the most important characteristics of the thermoelectric transport. Thermopower can provide information on the electronic structures of molecular junctions by measuring the voltage drop or induced current of the molecular junctions caused by the temperature difference [143]. Additionally, it can be used to detect the thermoelectric transport features through quantum dots or molecules. For example, Paulsson and Datta [144] suggested that the nature of charge carriers (either holes or electrons) involved in the transport can be determined from the sign of the thermoelectric potential and the Fermi level position with respect to the HOMO and LUMO of the molecules.

Generally, the thermopower is also called the Seebeck coefficient, S in the case of zero bias, the Seebeck coefficient is related to the transmission coefficient on the Fermi level of the electrodes, and the S for molecular junctions can be expressed as follows: [144]

$$S = -\frac{\pi^2 k_B^2 T}{3e}\frac{\partial \ln \Gamma(E)}{\partial \mathrm{E}}\Big|_{\mathrm{E}=E_F}$$

where $\Gamma(E)$ is the transmission coefficient, k_B is the Boltzmann constant, E_F is the Fermi level, and T is the average absolute temperature of the junctions. Moreover, S is sensitive to minor changes in the transmission coefficient. Therefore, as mentioned above, a positive S comes from hole transport through the HOMO, while a negative S represents electron transport through the LUMO [145]. Taniguchi et al. [141] investigated the thermoelectricity in atom-sized junctions with MCBJ setup to fabricated atom-sized junction, they measured the electrical conductance and thermoelectric power of gold nanocontacts simultaneously down to the single atom size. As Fig. 16 illustrates, they used the lifetime of single atom contacts as atomic thermometer, the average lifetime τ_{ave} acquired from $1G_0$ plateau lengths decayed exponentially with dc voltage V_h, and energy barrier height was used for recalculating effective temperature T_c from average lifetime τ_{ave}, the thermopower S_c of Au single-atom chain is deduced from ΔV_c. They found junction conductance-dependent thermoelectric voltage oscillations and observed that quantum confinement effects only appeared in statistics because the thermoelectricity was sensitive to the geometry in the atom-sized junctions.

Paulsson et al. provided a theoretical estimate of the thermoelectric current and voltage over a phenyl dithiol molecule [144]. They showed that the thermoelectric voltage is (1) insensitive to the detailed coupling to the contacts, (2) large enough to be measured, and (3) should give valuable information, which is not readily accessible through other experiments, on the location of the Fermi energy relative to the molecular levels [144]. Through the numerous thermoelectric experiments, molecular junctions can be a promising candidate for energy harvesting. For a practical molecular thermoelectricity device, it is essential to develop molecular wires with high thermoelectric conversion efficiency.

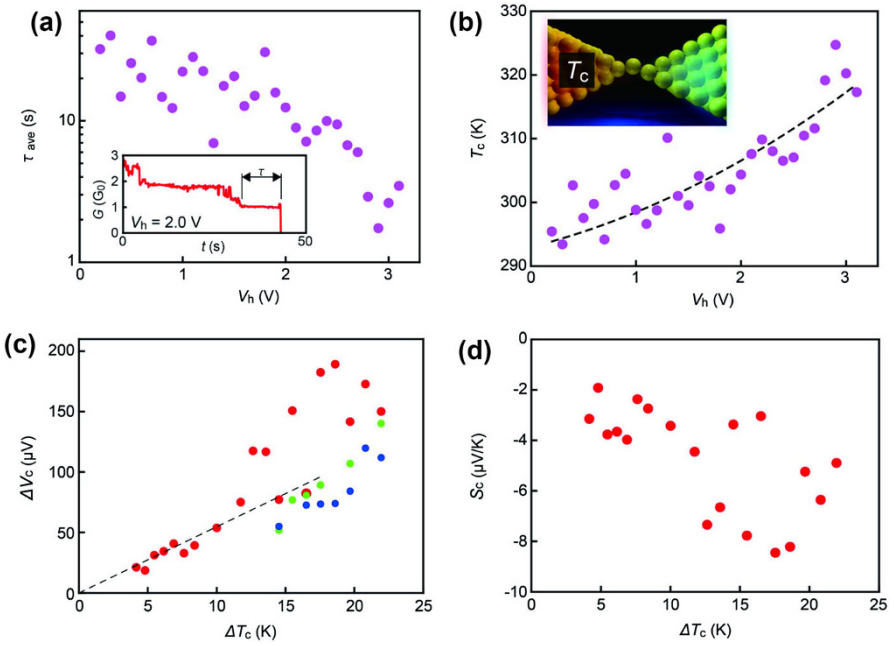

Fig. 16 Thermopower of Au single-atom contacts. **a** The average holding time τ of single-atom contacts (*inset*) decayed exponentially with V_h. **b** The effective temperature T_c at the hot side of single-atom chains obtained from **a**. *Broken line* is a quadratic fit to the plot. **c** Thermovoltage of single atom contacts ΔV_c obtained from the peak at $G_{m,1}$ (*red*), $G_{m,2}$ (*green*), and $G_{m,3}$ (*blue*) plotted against the local temperature gradient ΔT_c. The *dotted line* is a linear fit at $\Delta T_c < 15$ K. **d** Thermopower S_c of single-atom contacts. Reproduced with permission from Ref. [141]. Copyright 2013, Macmillan Publishers Limited

3.4 Applications of MCBJs and Remarkable Properties of Single Molecules

3.4.1 Rectification

As one of the most fundamental phenomenon for single-molecule junctions, rectification has become increasingly mature, and functional diodes have been developed [108, 146, 147]. The main principle of rectification is the dependence of the asymmetric current response to the external voltage [4], with extreme responses corresponding to the diode effect. Molecular rectification was first theoretically proposed by Aviram and Ratner [2], and it consists of a π donor system and a π acceptor, with both connected to a σ insulator bridge (the Aviram–Ratner model). The molecular LUMO and HOMO levels are slightly higher or lower than the Fermi level of two electrodes at zero bias voltage, while the energy gap between the LUMO and HOMO tends to be smaller or larger at certain voltages or at reverse voltage, which results in significant current differences under both conditions. Afterwards, Kornilovitch, Bratkovsky, and Williams also presented a resonant tunneling mechanism, but this contained one conducting molecular level that was asymmetrically distributed between Fermi levels of two sides [148], which caused asymmetric tunneling barriers that resulted in rectification (the KBW model). Datta

and Paulsson et al. observed an asymmetric current–voltage characteristic with intrinsic symmetric system [149], which is attributed to unequal coupling and charging effects (the Datta–Paulsson model). The electron-transport process of the first model is divided into three steps, that from the metal electrode to the donor, then to the acceptor, and finally to the other electrode; the other two models have only two steps. Meanwhile, the main discrepancy in the latter two models is that the asymmetric energy level is shifted by the electric field and through the charging energy, respectively [57].

In addition, Lortscher et al. then investigated rectification with single diblock molecules where the donor and acceptor are covalently linked without the σ bridge compared with the Aviram-Ratner model [57]. Due to the electronic overlap of the two moieties, the whole transport process contains two steps instead of three for zero, forward and reverse voltages, as shown in Fig. 17a. Remarkably, the I–V curves at various temperatures showed a pronounced nonsymmetric current, with the largest rectification ratio of up to 11 [57] (Fig. 17b). Another method to realize a high rectification ratio is by applying a gate electrode to a single-molecule junction [108, 150]. Perrin et al. utilized an optimized asymmetric molecule (DPE-2F) to conduct this research. The electron transport mechanism is shown in Fig. 17c, with the level alignment and misalignment controlled by the gate electrode at forward

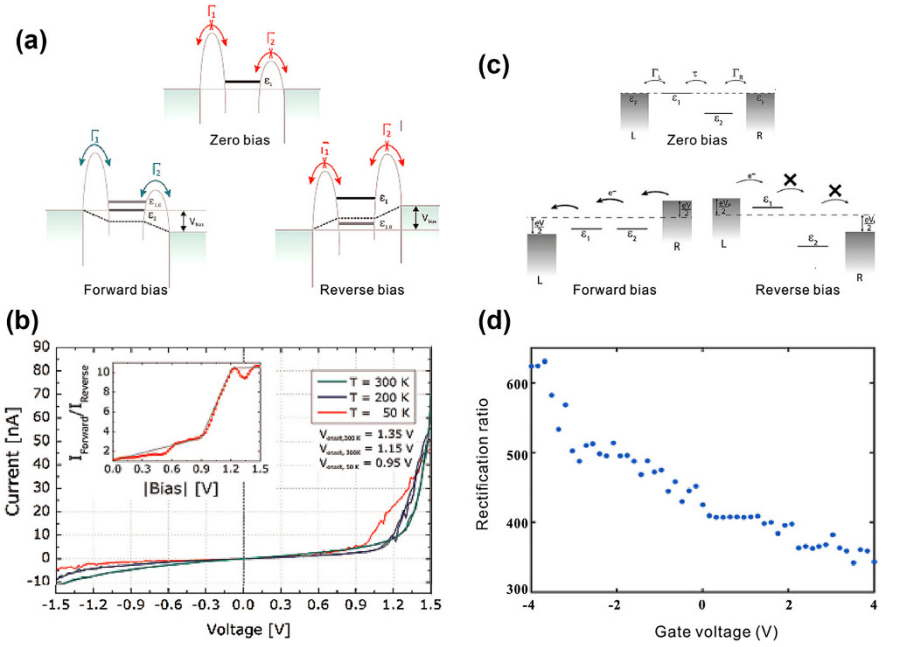

Fig. 17 Rectification behaviors. **a** Rectification mechanism for diblock dipyrimidinyl diphenyl (SB) molecule. **b** I–V traces for the Au–SB diode–Au junction recorded at temperatures ranging from 300 to 50 K. The *inset* shows the rectification ratio as a function of bias for 50 K. Reproduced with permission from Ref. [57]. Copyright 2012, American Chemical Society. **c** Rectification mechanism for DPE-2F molecule. **d** Schematic diagram of the rectification ratio as a function of gate voltage. Reproduced with permission from Ref. [108]. Copyright 2016, The Royal Society of Chemistry

and reverse bias voltages [108]. As observed in Fig. 17d, the rectification ratio (RR) depends strongly on the size and direction of the gate voltage, and the largest ratio can even reach above 600. Therefore, the rectification mechanism based on the orbital structure can be determined in the molecule. Molecular-level architecture with a small energy gap between the HOMO and LUMO can improve the RR value [74]. In summary, the influence factors of rectification are not confined to intrinsic molecular structures and energy levels, and factors such as the interface between electrodes and single molecules should be considered. Based on rectification effect, functional diodes have been realized. Molecular diodes are important in the nanoscale electronics field because they provide the basis for more complex device structures and promote the development of molecular electronics [151]. The first single-molecule diode was fabricated with the MCBJ technique based on lithography by Weber et al. [146]. Besides, various methods and experiments have been investigated in the design of molecular diodes. Though molecular diodes have been studied for more than four decades and various issues hinder the commercial applications, it is an inevitable trend to accomplish the commercialization of molecular diodes.

3.4.2 The NDR Effect

The negative differential resistance (NDR) effect can be found in single-molecule junctions except in semiconductors, which means that the current flowing in molecules decreases as the bias voltage between the source and drain increases. It has been determined that most NDR behaviors are ascribed to the matching-mismatching of molecular energy levels with those of their adjacent leads and that the relatively narrow and sharp peaks in the I–V curves are due to the abnormal electron density of states in the weak binding of the junction system [152]. The NDR effect has been investigated in DNA and other molecular junctions by the MCBJ technique in previous years [18, 153]. At low temperatures, the NDR effect was observed when voltages that access the first molecular orbitals in resonance were applied [153]. Kang et al. drew a conclusion from the DNA molecular junctions that the peaks of NDR occurred at a lower voltage and the amplitude simultaneously decreased under high vacuum conditions [18]. Meanwhile, they demonstrated that this type of NDR behavior was caused by a change in the polaron mode due to the coupling of the molecular level. In particular, Perrin et al. successfully observed a pronounced NDR effect for a target molecule in which two conjugated systems linked by a non-conjugated moiety generated two coupled sites [154]. Then, the energy of two sites can be separated when a voltage is applied to the molecular junction, which restrains the resonant transport in the system and thus results in a reduction of the current (the NDR effect). It is also conspicuous that the NDR feature can be by mechanically controlling the space of the electrodes, which reveals the negative correlation as the peak amplitude grows larger as the space becomes slightly smaller (shown in Fig. 18a, b) [154]. At the same time, Zu et al. theoretically designed isolated molecular nanowires made of thiophene oligomers and one-dimensional gold, and an unexpected NDR behavior was shown [155]. Li et al. reported that the modification of the bridging group in a single cross-

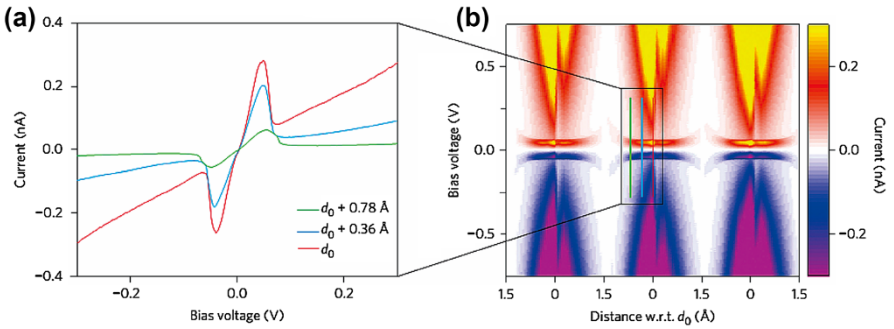

Fig. 18 The behaviors of negative differential resistance (NDR) effect. **a** Low-bias I–V characteristics for increasing electrode separation. **b** Map of I–V characteristics recorded from left to right while repeatedly increasing and reducing the electrode spacing. The spacing is relative to d_0, the electrode separation at which the NDR feature is most pronounced. The I–V traces shown in **a** are recorded at the positions marked by the *colored lines* in **b**. Reproduced with permission from Ref. [154]. Copyright 2014, Nature Publishing Group

conjugated molecular junction can produce a robust NDR behavior due to the enhancement of the communication between two π systems [156]. More efforts will be made to experimentally realize the designs and to achieve a more significant NDR effect.

3.4.3 Coulomb Blockade and Kondo Effect

The research scale for single-molecule junctions is the nanoscale or an even smaller scale, which gives rise to remarkable quantum transport phenomenon, such as Coulomb blockade, the Kondo effect, etc. A brief description of the two quantum phenomenon will be introduced in this section. The Coulomb blockade effect is drastically determined by the strength of coupling between molecules and the two electrodes. Coulomb blockade emerges in the relatively weak coupling mechanism because the energy of an electron in the molecules is too small to tunnel into the molecular island, and there is mutual repulsion between electrons in and outside the molecules, which results in the single-electron transport regime. However, Coulomb blockade is absent in a comparatively strong coupling mechanism due to the broadening of the frontier molecular orbital levels.

The Coulomb blockade effect can be eliminated by adding a gate electrode to a two-terminal junction to resonantly modulate the molecular energy levels with the Fermi levels of the source and drain [157]. Based on Coulomb blockade, there are some potential real devices that can be developed, such as single-electron transistors (SETs), single-electron memory, and so on. As a result, the study of the Coulomb blockade effect is capable of promoting the understanding of the electron transport mechanism in molecular junctions.

The Kondo effect, also called the Kondo resonance in the conductance, plays a significant part in electron transport. Found in metals, including in magnetic impurities, the Kondo effect manifests as a type of abnormal minimum in the resistance as a consequence of an exchange coupling between the spins of localized

magnetic impurity systems and delocalized conduction electrons [152]. In single-molecule junction configurations, the localized spin of the molecule can be screened by the conducting electron spin in the electrodes in the exchange coupling process [158], resulting in a conductance peak at a low bias voltage (the Kondo resonance in the conductance). With the MCBJ technique, Wagner et al. reported a switch between the pseudo-singlet state and the pseudo-triplet state, which was respectively assigned to the absence and occurrence of a Kondo-like anomaly [159]. Recently, Frisenda et al. investigated the Kondo effect in a neutral and stable all-organic radical single molecule break junction in two-terminal and three-terminal solid-state electronic devices [160]. They found that the Kondo anomaly is robust regardless of mechanical and electrostatic changes. In summary, Coulomb blockade and the Kondo effect both arise from the electron–electron interactions in single-molecule quantum dots. Thus, the integrated studies for both effects offer an effective method to further explore quantum transport properties in single molecular devices.

3.4.4 Single-molecule Field-effect Transistors

Normally, a field-effect transistor (FET) is a semiconductor device that controls the output circuit current by controlling the electric field effect of the input circuit. However, single-molecule FETs incorporating individual molecules are unique tools for examining the fundamental physics and chemistry of electronic transport in molecular systems at the single nanometer scale. For single-molecule FETs, source and drain are acted with two terminals of electrodes, between which electric current is regulated by using a voltage applied on the gate electrode [8]. In general, the length of molecules used for single-molecule transistors are typically more than 1 nm. Smaller molecules have a high level splitting, so that their charge state cannot be changed with the gate electrode [50]. Field effect transistors are divided into two categories: junction field effect transistor (JFET) and metal–oxide semiconductor (MOS-FET), while silicon MOS-FETs are the most frequently used building blocks in today's integrated circuit chips [161]. The development of electronics is now facing a bottleneck, which is due to the scaling of the feature size of FET. Therefore, many researchers are seeking methods to resolve this issue, and the single molecule as conduction channels attracts much interest due to their inherent advantage of an extremely small size [162, 163]. Single-molecule FETs are considered as the highest-potential devices with an architecture at the sub-7-nm scale [164], and they has been explored actively over the past decades.

In general, single-molecule FET can be considered to be three-terminal molecular junctions, which are fabricated with source, drain, and gate electrodes. As shown in Fig. 19a, benzenedithiol molecules were bridged between electrode nanogap formed using the electromigration break junction method, and a back gate device configuration with conventional Al_2O_3/Al electrode was used to investigate the electrostatic modulation of current flowing through the molecule [74]. In this example of single-molecule FET, the gate electrode modulated the single-molecule conductance via the electrostatic tuning of the molecular orbital levels (Fig. 19b). However, the gate electrode needs to be placed as close to the molecule as possible to overcome the screen effect. Xiang et al. has fabricated a side-gated three-terminal

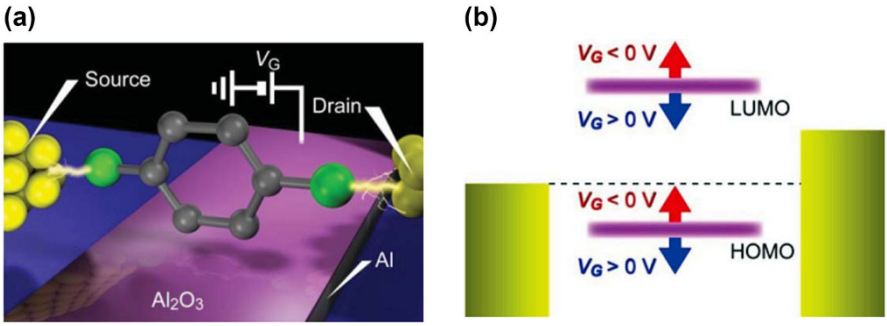

Fig. 19 Single-molecule FETs. **a** Schematic view of the single-molecule FET. The Al/Al_2O_3 bottom gate electrode was used for modulating the source-drain current flowing through an individual benzenedithiol molecule. **b** The HOMO and the LUMO are fixed at the positions relative to the Fermi level (*dotted line*) with the source-gate voltage V_G. The orbital energy levels can be shifted upward (downward) by the negative (positive) V_G. Reprinted with permission from Ref. [74]. Copyright 2012 by the authors; licensee MDPI, Basel, Switzerland

junction by MCBJ, which has achieved a tiny distance of several nanometers between gate electrode and molecule [102]. Another method to decrease space of the molecule and gate is to reduce the thickness of the electrode by changing the material of source and drain electrodes into graphene, which benefits the control of gate electrode to molecular orbitals. Besides, a challenge to fabricate single-molecule FET is the low device yield, a feasible scheme to resolve this issue is by combining the MCBJ technique with three-terminal junctions due to MCBJ's mechanical controllability for nanogap between source and drain electrodes.

3.4.5 Single-molecule Switches

A single molecule converted with different states can be used as a switch [165]. Molecular switches are basic devices in the field of molecule electronics and application examples of a functional molecule. The construction of molecular switches is a crucial step in the application of molecular electronics, and many studies have been conducted over the past decades. The conductance of molecular switches changes when some external stimuli (light [166], electric field [167], temperature, magnetic field, etc.) are applied to the molecule or electrodes. By changing the charge states, spin states, dipole orientations, and molecular configuration, the properties of the molecules can be switched [168]. Molecular switches can also be connected to the electrodes based on break junction techniques (MCBJs, STM-BJs, electromigration break junctions, etc.) through chemical connections. In this section, we mainly introduce some external stimuli induced switches (light-induced switching, field-induced switching, etc.) in detail, and the remaining are precisely described in [1, 168].

Light-induced switching Photochromic systems play a significant role in the fabrication of molecular device prototypes, and the reversible light-induced discoloration reaction lamp can switch the conductance of molecule junctions. In general, light-induced switching means that molecular structures change with light

stimuli, and molecular structures vary from *cis*-isomerization to *trans*-isomerization or conversely. *Cis* and *trans* isomerization are just a pair of molecules that have the same formula but whose functional groups are rotated into a different orientation in three-dimensional space. *Cis* means that functional groups are on one side of the carbon chain while the *trans* are on the opposite side of the carbon chain [169]. A photochromic molecule can be fabricated into photochromic switches due to its different properties under visible light and UV light; here, the center ring of 1,2-diarylethene photochromic molecules will repeat the process of opening and closing under light illumination [74]. Azobenzenes are the frequently used photochromic molecules as a result of their special photoisomerization property. However, only changes in the length occur by the transformation of states between *trans* and *cis* isomerization, while diarylethene (DAE) can change its electrical properties by transforming the states between a conjugated closing form and non-conjugated opening form. Erbe et al. used DAE molecules between Au electrodes to show the controlling process of conductive states by dominant light irradiation [166]. Sendler et al. reported the controlled in situ switching of diarylethene molecules (switchable molecular wire) from their nonconductive to conductive state in contact to gold nanoelectrodes via controlled light irradiation [166] (shown in Fig. 20a). Before irradiation, there are no defined conductance plateaus due to a lack of fully conjugated molecular states (shown in Fig. 20b). After irradiation, they observed definite plateaus in the conductance range identified as molecular conductance for

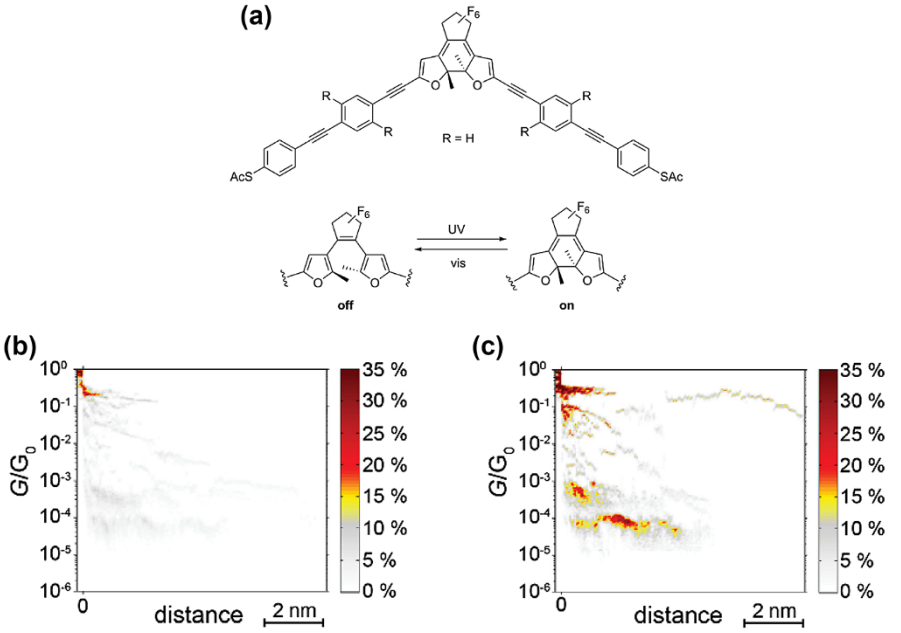

Fig. 20 Light-induced switching. **a** Investigated photochromic switch SMW (switchable molecular wire) with the different side-groups H. Irradiation with UV (visible) light induces a switching from the off (on)-state to the on(off)-state form for both molecules. Histograms of (**b**) and (**c**) in situ switched off and on. Reprinted with permission from Ref. [166]. Copyright 2015, WILEY–VCH Verlag GmbH & Co. KgaA

the switchable molecular wires assembled in the on state, which indicates a successful switching to the on state (shown in Fig. 20c). These findings are an important step toward the development of real molecular electronics devices.

Electric field-induced switching The electric field can also dominate the single-molecule switching, as it has the potential of applying a wide range in switching the molecular fluorescence. The electric field can change the potential energy and finally decrease the switching barrier [168]. This is because of the existence of an intrinsic electric dipole moment after the electric field is added, and the electric field can lead to the *trans–cis* isomerization of the molecule. Most of the related studies take the electric field into consideration. Numerous studies indicated that the main contributor to the single-molecule fluorescence switch is the electron transport between different areas in the single molecule. Electric field and other external conditions can also be used for controlling molecules to realize similar functions besides light.

It is obvious that molecular switches can have various driving mechanisms due to their original essential characteristic. A common problem that comes with molecular switches on the surface is the stability of the switches in external environments, but this can be overcome by using the thiol-terminated conjugated molecule, which has a stable Au–S bond [168]. In addition, the coupling condition of the molecule and electrodes is another issue, which involves many factors, such as the structure of the molecule and anchoring groups. First-principle calculations will provide information about the mechanism of molecular switching and enable a detailed comparison between experiment and theory to obtain accurate explanations of the mechanism. However, molecular switches have been investigated for decades, but they need to be studied to overcome the problems that hinder further development. After all, the research into single-molecule switches plays a significant role in the field of integration of molecular electronics and will promote the long-term development of molecular electronics.

4 Summary and Outlook

In this review, we systematically summarized the recent development of mechanically controlled break junctions (MCBJs) for single-molecule systems. With advanced microfabrication technology, MCBJ chips are finely produced and connected with individual molecules, in which the accuracy can reach sub-nanometer levels that are constantly improved on by the exploitation of new technology. Meanwhile, some modifications for MCBJ have been achieved to satisfy specific research needs, such as thermoelectricity. In the view of present processes for molecular electronics, scientists and groups are leaving no stone unturned in the search for a higher level of conductance values, in which junction systems (anchoring groups, backbones, and electrode materials) play a key role. Thus, it is essential to deeply understand the electron transport mechanisms of molecular junctions, especially the interface between molecules and the two metal leads. Moreover, gated MCBJ techniques can be used to mechanically and electrolytically align the energy levels of different types of molecules with the

Fermi levels of electrodes and to thus realize three-terminal structures for transistors.

The purpose of this review is to explain the MCBJ method and elucidate promising development directions to as large an extent as possible. At present, significant progress in single-molecule electronics is due in large part to the MCBJ technique, which depends on its unique superiority, such as mechanical stability, precise controllability, and the presence of fewer contaminations. It is undeniable that intrinsic properties of a molecular junction cannot be well characterized solely with the MCBJ method. The combination of MCBJ with other analytical techniques (for example, TVS, IETS, noise spectroscopy, thermoelectricity, etc.) seems to be an irresistible trend, which can be used to obtain energy level information and contact configurations. Another effective approach is gated MCBJs, where the electrochemical-gated MCBJs that change the conductance by switching the redox reaction and adjusting the Fermi level appear to be an excellent direction based on previous back- and side-gating techniques.

Overall, molecular electronics is still in the nascent stage, even though it has achieved significant and ongoing progress [170]. The first and foremost challenge is the bond between electrodes and molecules, which involves the selection of different molecules and electrode materials. We know that one main issue in these single molecular devices is that the conductance has remained extremely low compared to traditional devices, leading to a lower cut-off frequency of the molecular device (it could be approximated, in a simple dipole configuration, by $G/(2\pi C)$, with G and C the device dynamic conductance and capacitance) [171]. The design and synthesis of target molecules is an important topic for energy level matching with electrodes and even for featured functional devices. Au–C and C–C bonds represent relatively stable and well-defined electron transport systems. As a result, in addition to metallic electrodes, carbon-based materials (graphene and carbon nanotubes) can be integrated with the MCBJ technique, with the advantages of gap tunability and high conductance. This new electrode material can enable the realization of real logical and memory molecular elements, in which the development process is limited by the issue of device-to-device variation in the tiny structures. The encapsulation of entire molecular junctions with peculiar functions (rectification, switching, etc.) is a potential solution to overcome the variation and instability. Among these functional devices, switching is currently undergoing the most rapid evolution that approaches actual applications, and scientists and groups are expected to shed more light on reversible and stable switches. Based on the premise of single-molecule simulation, the results can be obtained more efficiently by the simultaneous methods of experiment and theory that enable rapid progress. According to the current trends, molecular electronics will become more prosperous and would potentially find its place in the commercial market.

Acknowledgements We are grateful for financial support from the National Natural Science Foundation of China (21303171, 61571242), Tianjin Municipal Science and Technology Commission (No. 14JCQNJC03000), and the Fundamental Research Funds for the Central Universities of China.

References

1. Xiang D, Wang X, Jia C, Lee T, Guo X (2016) Molecular-scale electronics: from concept to function. Chem Rev 116:4318–4440
2. Aviram A, Ratner M (1974) Molecular rectifiers. Chem Phys Lett 29:277–283
3. Liu Y, Offenhäusser A, Mayer D (2010) An electrochemically transduced XOR logic gate at the molecular level. Angew Chem Int Ed Engl 49:2595–2598
4. Xiang D, Jeong H, Lee T, Mayer D (2013) Mechanically controllable break junctions for molecular electronics. Adv Mater 25:4845–4867
5. Liu SP, Weisbrod SH, Tang Z, Marx A, Scheer E, Erbe A (2010) Direct measurement of electrical transport through G-quadruplex DNA with mechanically controllable break junction electrodes. Angew Chem Int Ed Engl 49:3313–3316
6. Prins F, Monrabal-Capilla M, Osorio EA, Coronado E, van der Zant HS (2011) Room-temperature electrical addressing of a bistable spin-crossover molecular system. Adv Mater 23:1545–1549
7. Song H, Kim Y, Jang YH, Jeong H, Reed MA, Lee T (2009) Observation of molecular orbital gating. Nature 462:1039–1043
8. Perrin ML, Burzurí E, van der Zant HS (2015) Single-molecule transistors. Chem Soc Rev 44:902–919
9. Sun L, Diaz-Fernandez YA, Gschneidtner TA, Westerlund F, Lara-Avila S, Moth-Poulsen K (2014) Single-molecule electronics: from chemical design to functional devices. Chem Soc Rev 43:7378–7411
10. Xiang D, Pyatkov F, Schröper F, Offenhäusser A, Zhang Y, Mayer D (2011) Molecular junctions bridged by metal ion complexes. Chemistry 17:13166–13169
11. Xu B, Tao NJ (2003) Measurement of single-molecule resistance by repeated formation of molecular junctions. Science 301:1221–1223
12. Thurmer DJ, Bof Bufon CC, Deneke C, Schmidt OG (2010) Nanomembrane-based mesoscopic superconducting hybrid junctions. Nano Lett 10:3704–3709
13. Hoven CV, Wang H, Elbing M, Garner L, Winkelhaus D, Bazan GC (2010) Chemically fixed *p*-n heterojunctions for polymer electronics by means of covalent B-F bond formation. Nat Mater 9:249–252
14. Yelin T, Vardimon R, Kuritz N, Korytár R, Bagrets A, Evers F, Kronik L, Tal O (2013) Atomically wired molecular junctions: connecting a single organic molecule by chains of metal atoms. Nano Lett 13:1956–1961
15. Moreland J, Ekin JW (1985) Electron tunneling experiments using Nb-Sn "break" junctions. J Appl Phys 58:3888–3895
16. Muller CJ, van Ruitenbeek JM, de Jongh LJ (1992) Conductance and supercurrent discontinuities in atomic-scale metallic constrictions of variable width. Phys Rev Lett 69:140–143
17. Reed MA (1997) Conductance of a molecular junction. Science 278:252–254
18. Kang N, Erbe A, Scheer E (2010) Observation of negative differential resistance in DNA molecular junctions. Appl Phys Lett 96:023701
19. Karimi MA, Bahoosh SG, Valášek M, Bürkle M, Mayor M, Pauly F, Scheer E (2016) Identification of the current path for a conductive molecular wire on a tripodal platform. Nanoscale 8:10582–10590
20. Hayakawa R, Karimi MA, Wolf J, Huhn T, Zöllner MS, Herrmann C, Scheer E (2016) Large magnetoresistance in single-radical molecular junctions. Nano Lett 16:4960–4967
21. Kim Y, Pietsch T, Erbe A, Belzig W, Scheer E (2011) Benzenedithiol: a broad-range single-channel molecular conductor. Nano Lett 11:3734–3738
22. Li Y, Kaneko S, Fujii S, Kiguchi M (2015) Symmetry of single hydrogen molecular junction with Au, Ag, and Cu electrodes. J Phys Chem C 119:19143–19148
23. Fujii S, Kaneko S, Chenyang L, Kiguchi M (2015) Single naphthalene and anthracene molecular junctions using Ag and Cu electrodes in ultra high vacuum. Appl Surf Sci 354:362–366
24. Kiguchi M, Tal O, Wohlthat S, Pauly F, Krieger M, Djukic D, Cuevas JC, van Ruitenbeek JM (2008) Highly conductive molecular junctions based on direct binding of benzene to platinum electrodes. Phys Rev Lett 101:046801
25. Ko CH, Huang MJ, Fu MD, Chen CH (2010) Superior contact for single-molecule conductance: electronic coupling of thiolate and isothiocyanate on Pt, Pd, and Au. J Am Chem Soc 132:756–764

26. Hong L, Tanaka H, Ogawa T (2013) Rectification direction inversion in a phosphododecamolybdic acid/single-walled carbon nanotube junction. J Mater Chem C 1:1137–1143
27. Wu B, Geng D, Guo Y, Huang L, Xue Y, Zheng J, Chen J, Yu G, Liu Y, Jiang L, Hu W (2011) Equiangular hexagon-shape-controlled synthesis of graphene on copper surface. Adv Mater 23:3522–3525
28. Jia C, Guo X (2013) Molecule-electrode interfaces in molecular electronic devices. Chem Soc Rev 42:5642–5660
29. Zotti LA, Kirchner T, Cuevas JC, Pauly F, Huhn T, Scheer E, Erbe A (2010) Revealing the role of anchoring groups in the electrical conduction through single-molecule junctions. Small 6:1529–1535
30. Wu S, González MT, Huber R, Grunder S, Mayor M, Schönenberger C, Calame M (2008) Molecular junctions based on aromatic coupling. Nat Nanotechnol 3:569–574
31. Tsutsui M, Taniguchi M, Kawai T (2009) Quantitative evaluation of metal-molecule contact stability at the single-molecule level. J Am Chem Soc 131:10552–10556
32. Chen F, Li X, Hihath J, Huang Z, Tao N (2006) Effect of anchoring groups on single-molecule conductance: comparative study of thiol-, amine-, and carboxylic-acid-terminated molecules. J Am Chem Soc 128:15874–15881
33. Hong W, Manrique DZ, Moreno-García P, Gulcur M, Mishchenko A, Lambert CJ, Bryce MR, Wandlowski T (2012) Single molecular conductance of tolanes: experimental and theoretical study on the junction evolution dependent on the anchoring group. J Am Chem Soc 134:2292–2304
34. Park YS, Whalley AC, Kamenetska M, Steigerwald ML, Hybertsen MS, Nuckolls C, Venkataraman L (2007) Contact chemistry and single-molecule conductance: a comparison of phosphines, methyl sulfides, and amines. J Am Chem Soc 129:15768–15769
35. Kiguchi M, Murakoshi K (2009) Highly conductive single molecular junctions by direct binding of pi-conjugated molecule to metal electrodes. Thin Solid Films 518:466–469
36. Frei M, Aradhya SV, Hybertsen MS, Venkataraman L (2012) Linker dependent bond rupture force measurements in single-molecule junctions. J Am Chem Soc 134:4003–4006
37. Ahn S, Aradhya SV, Klausen RS, Capozzi B, Roy X, Steigerwald ML, Nuckolls C, Venkataraman L (2012) Electronic transport and mechanical stability of carboxyl linked single-molecule junctions. Phys Chem Chem Phys 14:13841–13845
38. Li ZH, Smeu M, Ratner MA, Borguet E (2013) Effect of anchoring groups on single molecule charge transport through porphyrins. J Phys Chem C 117:14890–14898
39. Park YS, Widawsky JR, Kamenetska M, Steigerwald ML, Hybertsen MS, Nuckolls C, Venkataraman L (2009) Frustrated rotations in single-molecule junctions. J Am Chem Soc 131:10820–10821
40. Nakazumi T, Kaneko S, Kiguchi M (2014) Electron transport properties of Au, Ag, and Cu atomic contacts in a hydrogen environment. J Phys Chem C 118:7489–7493
41. Tal O, Kiguchi M, Thijssen WHA, Djukic D, Untiedt C, Smit RHM, van Ruitenbeek JM (2009) Molecular signature of highly conductive metal–molecule–metal junctions. Phys Rev B 80:085427
42. Nakazumi T, Kaneko S, Matsushita R, Kiguchi M (2012) Electric conductance of single ethylene and acetylene molecules bridging between Pt electrodes. J Phys Chem C 116:18250–18255
43. Liu CY, Kaneko S, Komoto Y, Fujii S, Kiguchi M (2015) Highly conductive single naphthalene and anthracene molecular junction with well-defined conductance. Appl Phys Lett 106:103103
44. Cheng ZL, Skouta R, Vazquez H, Widawsky JR, Schneebeli S, Chen W, Hybertsen MS, Breslow R, Venkataraman L (2011) In situ formation of highly conducting covalent Au–C contacts for single-molecule junctions. Nat Nanotechnol 6:353–357
45. Hong W, Li H, Liu SX, Fu Y, Li J, Kaliginedi V, Decurtins S, Wandlowski T (2012) Trimethylsilyl-terminated oligo(phenylene ethynylene)s: an approach to single-molecule junctions with covalent Au–C sigma-bonds. J Am Chem Soc 134:19425–19431
46. Chen W, Widawsky JR, Vázquez H, Schneebeli ST, Hybertsen MS, Breslow R, Venkataraman L (2011) Highly conducting pi-conjugated molecular junctions covalently bonded to gold electrodes. J Am Chem Soc 133:17160–17163
47. Kaliginedi V, Rudnev AV, Moreno-García P, Baghernejad M, Huang C, Hong W, Wandlowski T (2014) Promising anchoring groups for single-molecule conductance measurements. Phys Chem Chem Phys 16:23529–23539
48. Zhang R, Li B, Yang J (2015) A first-principles study on electron donor and acceptor molecules adsorbed on phosphorene. J Phys Chem C 119:2871–2878

49. Lu Q, Liu K, Zhang H, Du Z, Wang X, Wang F (2009) From tunneling to hopping: a comprehensive investigation of charge transport mechanism in molecular junctions based on oligo(*p*-phenylene ethynylene)s. ACS Nano 3:3861–3868
50. Chen F, Tao NJ (2009) Electron transport in single molecules: from benzene to graphene. Accounts Chem Res 42:573
51. Hines T, Diez-Perez I, Hihath J, Liu H, Wang ZS, Zhao J, Zhou G, Müllen K, Tao N (2010) Transition from tunneling to hopping in single molecular junctions by measuring length and temperature dependence. J Am Chem Soc 132:11658–11664
52. Choi SH, Risko C, Delgado MC, Kim B, Brédas JL, Frisbie CD (2010) Transition from tunneling to hopping transport in long, conjugated oligo-imine wires connected to metals. J Am Chem Soc 132:4358–4368
53. Taherinia D, Smith CE, Ghosh S, Odoh SO, Balhorn L, Gagliardi L, Cramer CJ, Frisbie CD (2016) Charge transport in 4 nm molecular wires with interrupted conjugation: combined experimental and computational evidence for thermally assisted polaron tunneling. ACS Nano 10:4372–4383
54. Sedghi G, García-Suárez VM, Esdaile LJ, Anderson HL, Lambert CJ, Martin S, Bethell D, Higgins SJ, Elliott M, Bennett N, Macdonald JE, Nichols RJ (2011) Long-range electron tunnelling in oligo-porphyrin molecular wires. Nat Nanotechnol 6:517–523
55. Xiang L, Palma JL, Bruot C, Mujica V, Ratner MA, Tao N (2015) Intermediate tunnelling-hopping regime in DNA charge transport. Nat Chem 7:221–226
56. Manrique DZ, Huang C, Baghernejad M, Zhao X, Al-Owaedi OA, Sadeghi H, Kaliginedi V, Hong W, Gulcur M, Wandlowski T, Bryce MR, Lambert CJ (2015) A quantum circuit rule for interference effects in single-molecule electrical junctions. Nat Commun 6:6389
57. Lörtscher E, Gotsmann B, Lee Y, Yu L, Rettner C, Riel H (2012) Transport properties of a single-molecule diode. ACS Nano 6:4931–4939
58. Kim Y, Hellmuth TJ, Sysoiev D, Pauly F, Pietsch T, Wolf J, Erbe A, Huhn T, Groth U, Steiner UE, Scheer E (2012) Charge transport characteristics of diarylethene photoswitching single-molecule junctions. Nano Lett 12:3736–3742
59. Cao Y, Dong S, Liu S, He L, Gan L, Yu X, Steigerwald ML, Wu X, Liu Z, Guo X (2012) Building high-throughput molecular junctions using indented graphene point contacts. Angew Chem Int Ed Engl 51:12228–12232
60. Jia C, Ma B, Xin N, Guo X (2015) Carbon electrode-molecule junctions: a reliable platform for molecular electronics. Acc Chem Res 48:2565–2575
61. Liu S, Zhang X, Luo W, Wang Z, Guo X, Steigerwald ML, Fang X (2011) Single-molecule detection of proteins using aptamer-functionalized molecular electronic devices. Angew Chem Int Ed Engl 50:2496–2502
62. Liu S, Shen Q, Cao Y, Gan L, Wang ZX, Steigerwald ML, Guo XF (2010) Chemical functionalization of single-walled carbon nanotube field-effect transistors as switches and sensors. Coordin Chem Rev 254:1101–1116
63. Guédon CM, Zonneveld J, Valkenier H, Hummelen JC, van der Molen SJ (2011) Controlling the interparticle distance in a 2D molecule-nanoparticle network. Nanotechnology 22:125205
64. Sabater C, Untiedt C, van Ruitenbeek JM (2015) Evidence for non-conservative current-induced forces in the breaking of Au and Pt atomic chains. Beilstein J Nanotechnol 6:2338–2344
65. Agrait N, Yeyati AL, van Ruitenbeek JM (2003) Quantum properties of atomic-sized conductors. Phys Rep 377:81–279
66. Yan H, Bergren AJ, McCreery RL (2011) All-carbon molecular tunnel junctions. J Am Chem Soc 133:19168–19177
67. Zhu J, McMorrow J, Crespo-Otero R, Ao G, Zheng M, Gillin WP, Palma M (2016) Solution-processable carbon nanoelectrodes for single-molecule investigations. J Am Chem Soc 138:2905–2908
68. Wang B, Li J, Yu Y, Wei Y, Wang J, Guo H (2016) Giant tunnel magneto-resistance in graphene based molecular tunneling junction. Nanoscale 8:3432–3438
69. Fan ZQ, Xie F, Jiang XW, Wei ZM, Li SS (2016) Giant decreasing of spin current in a single molecular junction with twisted zigzag graphene nanoribbon electrodes. Carbon 110:200–206
70. Wickenburg S, Lu J, Lischner J, Tsai HZ, Omrani AA, Riss A, Karrasch C, Bradley A, Jung HS, Khajeh R, Wong D, Watanabe K, Taniguchi T, Zettl A, Neto AHC, Louie SG, Crommie MF (2016) Tuning charge and correlation effects for a single molecule on a graphene device. Nat Commun 7:13553

71. Yu R, García de Abajo FJ (2016) Electrical detection of single graphene plasmons. ACS Nano 10:8045–8053
72. Ashwell GJ, Phillips LJ, Robinson BJ, Urasinska-Wojcik B, Lambert CJ, Grace IM, Bryce MR, Jitchati R, Tavasli M, Cox TI, Sage IC, Tuffin RP, Ray S (2010) Molecular bridging of silicon nanogaps. ACS Nano 4:7401–7406
73. Mangin A, Anthore A, Della Rocca ML, Boulat E, Lafarge P (2009) Transport through metallic nanogaps in an in-plane three-terminal geometry. J Appl Phys 105:014313
74. Tsutsui M, Taniguchi M (2012) Single molecule electronics and devices. Sensors (Basel) 12:7259–7298
75. Yi ZW, Banzet M, Offenhäusser A, Mayer D (2010) Fabrication of nanogaps with modified morphology by potential-controlled gold deposition. Phys Status Solidi-R 4:73–75
76. Yi Z, Trellenkamp S, Offenhäusser A, Mayer D (2010) Molecular junctions based on intermolecular electrostatic coupling. Chem Commun (Camb) 46:8014–8016
77. Karimi MA, Bahoosh SG, Herz M, Hayakawa R, Pauly F, Scheer E (2016) Shot noise of 1,4-Benzenedithiol single-molecule junctions. Nano Lett 16:1803–1807
78. Alwan M, Candoni N, Dumas P, Klein HR (2013) Statistical evidence of strain induced breaking of metallic point contacts. Eur Phys J B 86:1–5
79. Ienaga K, Nakashima N, Inagaki Y, Tsujii H, Kimura T, Kawae T (2012) Study of ferromagnetic transition in Pd nanometer-scale constrictions using a mechanically controllable break junction technique. Appl Phys Lett 101:123114
80. Perrin ML, Martin CA, Prins F, Shaikh AJ, Eelkema R, van Esch JH, van Ruitenbeek JM, van der Zant HS, Dulić D (2011) Charge transport in a zinc-porphyrin single-molecule junction. Beilstein J Nanotechnol 2:714–719
81. Ruben M, Landa A, Lörtscher E, Riel H, Mayor M, Gorls H, Weber HB, Arnold A, Evers F (2008) Charge transport through a cardan-joint molecule. Small 4:2229–2235
82. Xiang D, Lee T, Kim Y, Mei T, Wang Q (2014) Origin of discrete current fluctuations in a single molecule junction. Nanoscale 6:13396–13401
83. Frisenda R, Parlato L, Barra M, van der Zant HS, Cassinese A (2015) Single-molecule break junctions based on a perylene-diimide cyano-functionalized (PDI8-CN2) derivative. Nanoscale Res Lett 10:1011
84. Huang C, Rudnev AV, Hong W, Wandlowski T (2015) Break junction under electrochemical gating: testbed for single-molecule electronics. Chem Soc Rev 44:889–901
85. Nedelcu M, Saifullah MSM, Hasko DG, Jang A, Anderson D, Huck WTS, Jones GAC, Welland ME, Kang DJ, Steiner U (2010) Fabrication of sub-10 nm metallic lines of low line-width roughness by hydrogen reduction of patterned metal-organic materials. Adv Funct Mater 20:2317–2323
86. Schirm C, Matt M, Pauly F, Cuevas JC, Nielaba P, Scheer E (2013) A current-driven single-atom memory. Nat Nanotechnol 8:645–648
87. Sydoruk VA, Xiang D, Vitusevich SA, Petrychuk MV, Vladyka A, Zhang Y, Offenhäusser A, Kochelap VA, Belyaev AE, Mayer D (2012) Noise and transport characterization of single molecular break junctions with individual molecule. J Appl Phys 112:014908
88. Yang Y, Chen ZB, Liu JY, Lu M, Yang DZ, Yang FZ, Tian ZQ (2011) An electrochemically assisted mechanically controllable break junction approach for single molecule junction conductance measurements. Nano Research 4:1199–1207
89. Wen HM, Yang Y, Zhou XS, Liu JY, Zhang DB, Chen ZB, Wang JY, Chen ZN, Tian ZQ (2013) Electrical conductance study on 1,3-butadiyne-linked dinuclear ruthenium(II) complexes within single molecule break junctions. Chem Sci 4:2471–2477
90. Yang Y, Liu J, Feng S, Wen H, Tian J, Zheng J, Schöllhorn B, Amatore C, Chen Z, Tian Z (2015) Unexpected current–voltage characteristics of mechanically modulated atomic contacts with the presence of molecular junctions in an electrochemically assisted–MCBJ. Nano Research 9:560–570
91. Arima A, Tsutsui M, Morikawa T, Yokota K, Taniguchi M (2014) Fabrications of insulator-protected nanometer-sized electrode gaps. J Appl Phys 115:114310
92. Morikawa T, Arima A, Tsutsui M, Taniguchi M (2014) Thermoelectric voltage measurements of atomic and molecular wires using microheater-embedded mechanically-controllable break junctions. Nanoscale 6:8235–8241
93. Tsutsui M, Morikawa T, He Y, Arima A, Taniguchi M (2015) High thermopower of mechanically stretched single-molecule junctions. Sci Rep 5:11519

94. Doi K, Tsutsui M, Ohshiro T, Chien CC, Zwolak M, Taniguchi M, Kawai T, Kawano S, Di Ventra M (2014) Nonequilibrium ionic response of biased mechanically controllable break junction (MCBJ) electrodes. J Phys Chem C Nanomater Interfaces 118:3758–3765
95. Waitz R, Schecker O, Scheer E (2008) Nanofabricated adjustable multicontact devices on membranes. Rev Sci Instrum 79:093901
96. Benner D, Boneberg J, Nurnberger P, Waitz R, Leiderer P, Scheer E (2014) Lateral and temporal dependence of the transport through an atomic gold contact under light irradiation: signature of propagating surface plasmon polaritons. Nano Lett 14:5218–5223
97. Bahn SR, Jacobsen KW (2001) Chain formation of metal atoms. Phys Rev Lett 87:266101
98. Frisenda R, Harzmann GD, Celis Gil JA, Thijssen JM, Mayor M, van der Zant HS (2016) Stretching-induced conductance increase in a spin-crossover molecule. Nano Lett 16:4733–4737
99. Martin CA, Ding D, Sorensen JK, Bjornholm T, van Ruitenbeek JM, van der Zant HSJ (2008) Fullerene-based anchoring groups for molecular electronics. J Am Chem Soc 130:13198–13199
100. Moreno-García P, Gulcur M, Manrique DZ, Pope T, Hong W, Kaliginedi V, Huang C, Batsanov AS, Bryce MR, Lambert C, Wandlowski T (2013) Single-molecule conductance of functionalized oligoynes: length dependence and junction evolution. J Am Chem Soc 135:12228–12240
101. Tao NJ (2006) Electron transport in molecular junctions. Nat Nanotechnol 1:173–181
102. Xiang D, Jeong H, Kim D, Lee T, Cheng Y, Wang Q, Mayer D (2013) Three-terminal single-molecule junctions formed by mechanically controllable break junctions with side gating. Nano Lett 13:2809–2813
103. Champagne AR, Pasupathy AN, Ralph DC (2005) Mechanically adjustable and electrically gated single-molecule transistors. Nano Lett 5:305–308
104. Martin CA, Smit RH, van der Zant HS, van Ruitenbeek JM (2009) A nanoelectromechanical single-atom switch. Nano Lett 9:2940–2945
105. Ballmann S, Weber HB (2012) An electrostatic gate for mechanically controlled single-molecule junctions. New J Phys 14:123028
106. Martin CA, van Ruitenbeek JM, van der Zant HS (2010) Sandwich-type gated mechanical break junctions. Nanotechnology 21:265201
107. Perrin ML, Verzijl CJ, Martin CA, Shaikh AJ, Eelkema R, van Esch JH, van Ruitenbeek JM, Thijssen JM, van der Zant HS, Dulić D (2013) Large tunable image-charge effects in single-molecule junctions. Nat Nanotechnol 8:282–287
108. Perrin ML, Galán E, Eelkema R, Thijssen JM, Grozema F, van der Zant HSJ (2016) A gate-tunable single-molecule diode. Nanoscale 8:8919–8923
109. Kim Y, Jeong W, Kim K, Lee W, Reddy P (2014) Electrostatic control of thermoelectricity in molecular junctions. Nat Nanotechnol 9:881–885
110. Galperin M, Ratner MA, Nitzan A, Troisi A (2008) Nuclear coupling and polarization in molecular transport junctions: beyond tunneling to function. Science 319:1056–1060
111. Song H, Lee T, Reed M (2014) Inelastic electron tunneling spectroscopy of molecular transport junctions. J Korean Phys Soc 64:1539–1544
112. Jaklevic RC, Lambe J (1966) Molecular vibration spectra by electron tunneling. Phys Rev Lett 17:1139–1140
113. Ségerie A, Liégeois V, Champagne B (2015) Inelastic electron tunneling of C60 on gold surfaces from first-principles calculations. J Phys Chem C 119:803–818
114. Reed MA (2008) Inelastic electron tunneling spectroscopy. Mater Today 11:46–50
115. Frisenda R, Perrin ML, van der Zant HS (2015) Probing the local environment of a single OPE3 molecule using inelastic tunneling electron spectroscopy. Beilstein J Nanotechnol 6:2477–2484
116. Lykkebo J, Gagliardi A, Pecchia A, Solomon GC (2013) Strong overtones modes in inelastic electron tunneling spectroscopy with cross-conjugated molecules: a prediction from theory. ACS Nano 7:9183–9194
117. Deng MS, Ye G, Cai SH, Sun GY, Jiang J (2015) Probing flexible conformations in molecular junctions by inelastic electron tunneling spectroscopy. AIP Adv 5:017144
118. Schlücker S (2014) Surface-enhanced Raman spectroscopy: concepts and chemical applications. Angew Chem Int Ed Engl 53:4756–4795
119. Wang X, Wang C, Cheng L, Lee ST, Liu Z (2012) Noble metal coated single-walled carbon nanotubes for applications in surface enhanced Raman scattering imaging and photothermal therapy. J Am Chem Soc 134:7414–7422

120. Li JF, Tian XD, Li SB, Anema JR, Yang ZL, Ding Y, Wu YF, Zeng YM, Chen QZ, Ren B, Wang ZL, Tian ZQ (2013) Surface analysis using shell-isolated nanoparticle-enhanced Raman spectroscopy. Nat Protoc 8:52–65
121. Fleischmann M, Hendra PJ, McQuillan AJ (1974) Raman spectra of pyridine adsorbed at a silver electrode. Chem Phys Lett 26:163–166
122. Tian JH, Liu B, Li X, Yang ZL, Ren B, Wu ST, Tao N, Tian ZQ (2006) Study of molecular junctions with a combined surface-enhanced Raman and mechanically controllable break junction method. J Am Chem Soc 128:14748–14749
123. Ward DR, Halas NJ, Ciszek JW, Tour JM, Wu Y, Nordlander P, Natelson D (2008) Simultaneous measurements of electronic conduction and Raman response in molecular junctions. Nano Lett 8:919–924
124. Konishi T, Kiguchi M, Takase M, Nagasawa F, Nabika H, Ikeda K, Uosaki K, Ueno K, Misawa H, Murakoshi K (2013) Single molecule dynamics at a mechanically controllable break junction in solution at room temperature. J Am Chem Soc 135:1009–1014
125. Matsushita R, Kiguchi M (2015) Surface enhanced Raman scattering of a single molecular junction. Phys Chem Chem Phys 17:21254–21260
126. Yamamoto YS, Ozaki Y, Itoh T (2014) Recent progress and frontiers in the electromagnetic mechanism of surface-enhanced Raman scattering. J Photoch Photobio C 21:81–104
127. Huang YF, Wu DY, Zhu HP, Zhao LB, Liu GK, Ren B, Tian ZQ (2012) Surface-enhanced Raman spectroscopic study of *p*-aminothiophenol. Phys Chem Chem Phys 14:8485–8497
128. Lombardi JR, Birke RL (2009) A unified view of surface-enhanced Raman scattering. Acc Chem Res 42:734–742
129. Urumese A, Jenjeti RN, Sampath S, Jagirdar BR (2016) Colloidal europium nanoparticles via a solvated metal atom dispersion approach and their surface enhanced Raman scattering studies. J Colloid Interface Sci 476:177–183
130. Cialla D, März A, Böhme R, Theil F, Weber K, Schmitt M, Popp J (2012) Surface-enhanced Raman spectroscopy (SERS): progress and trends. Anal Bioanal Chem 403:27–54
131. Xiang D, Sydoruk V, Vitusevich S, Petrychuk MV, Offenhäusser A, Kochelap VA, Belyaev AE, Mayer D (2015) Noise characterization of metal-single molecule contacts. Appl Phys Lett 106:063702
132. Kim Y, Song H, Kim D, Lee T, Jeong H (2010) Noise characteristics of charge tunneling via localized states in metal–molecule–metal junctions. ACS Nano 4:4426–4430
133. Beebe JM, Kim B, Gadzuk JW, Frisbie CD, Kushmerick JG (2006) Transition from direct tunneling to field emission in metal-molecule-metal junctions. Phys Rev Lett 97:026801
134. Rodríguez JCCSE (2010) Molecular electronics: an introduction to theory and experiment. World Scientific, Hardcover
135. Nose D, Dote K, Sato T, Yamamoto M, Ishii H, Noguchi Y (2015) Effects of interface electronic structures on transition voltage spectroscopy of alkanethiol molecular junctions. J Phys Chem C 119:12765–12771
136. Huisman EH, Guedon CM, van Wees BJ, van der Molen SJ (2009) Interpretation of transition voltage spectroscopy. Nano Lett 9:3909–3913
137. Trouwborst ML, Martin CA, Smit RH, Guedon CM, Baart TA, van der Molen SJ, van Ruitenbeek JM (2011) Transition voltage spectroscopy and the nature of vacuum tunneling. Nano Lett 11:614–617
138. Xiang D, Zhang Y, Pyatkov F, Offenhäusser A, Mayer D (2011) Gap size dependent transition from direct tunneling to field emission in single molecule junctions. Chem Commun 47:4760–4762
139. Xiang A, Li H, Chen S, Liu SX, Decurtins S, Bai M, Hou S, Liao J (2015) Electronic transport in benzodifuran single-molecule transistors. Nanoscale 7:7665–7673
140. Pennelli G (2014) Review of nanostructured devices for thermoelectric applications. Beilstein J Nanotechnol 5:1268–1284
141. Tsutsui M, Morikawa T, Arima A, Taniguchi M (2013) Thermoelectricity in atom-sized junctions at room temperatures. Sci Rep 3:3326
142. Ludoph B, van Ruitenbeek JM (1999) Thermopower of atomic-size metallic contacts. Phys Rev B 59:12290
143. Zimbovskaya NA (2016) Seebeck effect in molecular junctions. J Phys: Condens Matter 28:183002
144. Paulsson M, Datta S (2003) Thermoelectric effect in molecular electronics. Phys Rev B 67:241403
145. Aradhya SV, Venkataraman L (2013) Single-molecule junctions beyond electronic transport. Nature Nanotech 8:399–410

146. Elbing M, Ochs R, Koentopp M, Fischer M, von Hänisch C, Weigend F, Evers F, Weber HB, Mayor M (2005) A single-molecule diode. Proc Natl Acad Sci USA 102:8815–8820
147. Yuan L, Nerngchamnong N, Cao L, Hamoudi H, del Barco E, Roemer M, Sriramula RK, Thompson D, Nijhuis CA (2015) Controlling the direction of rectification in a molecular diode. Nat Commun 6:6324
148. Kornilovitch PE, Bratkovsky AM, Williams RS (2002) Current rectification by molecules with asymmetric tunneling barriers. Phys Rev B 66:165436
149. Zahid F, Ghosh AW, Paulsson M, Polizzi E, Datta S (2004) Charging-induced asymmetry in molecular conductors. Phys Rev B 70:35–40
150. Damle P, Rakshit T, Paulsson M, Datta S (2002) Current-voltage characteristics of molecular conductors: two versus three terminal. Ieee T Nanotechnol 1:145–153
151. Batra A, Meisner JS, Darancet P, Chen Q, Steigerwald ML, Nuckolls C, Venkataraman L (2014) Molecular diodes enabled by quantum interference. Faraday Discuss 174:79–89
152. Zimbovskaya NA, Pederson MR (2011) Electron transport through molecular junctions. Phys Rep 509:1–87
153. Lörtscher E, Riel H (2010) Molecular electronics—resonant transport through single molecules. Chimia 64:376–382
154. Perrin ML, Frisenda R, Koole M, Seldenthuis JS, Gil JA, Valkenier H, Hummelen JC, Renaud N, Grozema FC, Thijssen JM, Dulić D, van der Zant HS (2014) Large negative differential conductance in single-molecule break junctions. Nat Nanotechnol 9:830–834
155. Zu FX, Liu ZL, Yao KL, Fu HH, Gao GY, Yao W (2013) Large negative differential resistance and rectifying behaviors in isolated thiophene nanowire devices. J Chem Phys 138:154707
156. Li XF, Qiu Q, Luo Y (2014) Tuning electron transport through a single molecular junction by bridge modification. J Appl Phys 116:013701
157. Moth-Poulsen K, Bjørnholm T (2009) Molecular electronics with single molecules in solid-state devices. Nat Nanotechnol 4:551–556
158. Rakhmilevitch D, Korytár R, Bagrets A, Evers F, Tal O (2014) Electron-vibration interaction in the presence of a switchable Kondo resonance realized in a molecular junction. Phys Rev Lett 113:236603
159. Wagner S, Kisslinger F, Ballmann S, Schramm F, Chandrasekar R, Bodenstein T, Fuhr O, Secker D, Fink K, Ruben M, Weber HB (2013) Switching of a coupled spin pair in a single-molecule junction. Nat Nanotechnol 8:575–579
160. Frisenda R, Gaudenzi R, Franco C, Mas-Torrent M, Rovira C, Veciana J, Alcon I, Bromley ST, Burzurí E, van der Zant HS (2015) Kondo effect in a neutral and stable all organic radical single molecule break junction. Nano Lett 15:3109–3114
161. Li H, Wang L, Liu QH, Zheng JX, Mei WN, Gao ZX, Shi JJ, Lu J (2012) High performance silicene nanoribbon field effect transistors with current saturation. Eur Phys J B 85:274
162. Riel H, Wernersson L, Hong M, del Alamo J (2014) III–V compound semiconductor transistors—from planar to nanowire structures. MRS Bull 39:668–677
163. Fan D, Kang N, Ghalamestani SG, Dick KA, Xu HQ (2016) Schottky barrier and contact resistance of InSb nanowire field-effect transistors. Nanotechnology 27:275204
164. Guerfi Y, Larrieu G (2016) Vertical silicon nanowire field effect transistors with nanoscale gate-all-around. Nanoscale Res Lett 11:210
165. Pathem BK, Claridge SA, Zheng YB, Weiss PS (2013) Molecular switches and motors on surfaces. Annu Rev Phys Chem 64:605–630
166. Sendler T, Luka-Guth K, Wieser M, Lokamani Wolf J, Helm M, Gemming S, Kerbusch J, Scheer E, Huhn T, Erbe A (2015) Light-induced switching of tunable single-molecule junctions. Adv Sci 2:1500017
167. Wu R, Chen R, Qin C, Gao Y, Qiao Z, Zhang G, Xiao L, Jia S (2015) An electric field induced reversible single-molecule fluorescence switch. Chem Commun (Camb) 51:7368–7371
168. Zhang JL, Zhong JQ, Lin JD, Hu WP, Wu K, Xu GQ, Wee AT, Chen W (2015) Towards single molecule switches. Chem Soc Rev 44:2998–3022
169. Craig NC, Chen A, Suh KH, Klee S, Mellau GC, Winnewisser BP, Winnewisser M (1997) Contribution to the study of the gauche effect. The complete structure of the anti rotamer of 1,2-Difluoroethane. J Am Chem Soc 119:4789–4790
170. van der Molen SJ, Naaman R, Scheer E, Neaton JB, Nitzan A, Natelson D, Tao NJ, van der Zant H, Mayor M, Ruben M, Reed M, Calame M (2013) Visions for a molecular future. Nat Nanotechnol 8:385–389
171. Trasobares J, Vuillaume D, Theron D, Clement N (2016) A 17 GHz molecular rectifier. Nat Commun 7:12850

Top Curr Chem (Z) (2017) 375:42
DOI 10.1007/s41061-017-0123-x

REVIEW

Supramolecular Systems and Chemical Reactions in Single-Molecule Break Junctions

Xiaohui Li[1] · Duan Hu[1] · Zhibing Tan[1] · Jie Bai[1] · Zongyuan Xiao[1] · Yang Yang[1] · Jia Shi[1] · Wenjing Hong[1]

Received: 9 November 2016 / Accepted: 18 February 2017 / Published online: 23 March 2017

Abstract The major challenges of molecular electronics are the understanding and manipulation of the electron transport through the single-molecule junction. With the single-molecule break junction techniques, including scanning tunneling microscope break junction technique and mechanically controllable break junction technique, the charge transport through various single-molecule and supramolecular junctions has been studied during the dynamic fabrication and continuous characterization of molecular junctions. This review starts from the charge transport characterization of supramolecular junctions through a variety of noncovalent interactions, such as hydrogen bond, π–π interaction, and electrostatic force. We further review the recent progress in constructing highly conductive molecular junctions via chemical reactions, the response of molecular junctions to external stimuli, as well as the application of break junction techniques in controlling and monitoring chemical reactions in situ. We suggest that beyond the measurement of single molecular conductance, the single-molecule break junction techniques provide a promising access to study molecular assembly and chemical reactions at the single-molecule scale.

Chapter 3 was originally published as Li, X., Hu, D., Tan, Z., Bai, J., Xiao, Z., Yang, Y., Shi, J. & Hong, W. Top Curr Chem (Z) (2017) 375: 42. DOI 10.1007/s41061-017-0123-x.

✉ Yang Yang
yangyang@xmu.edu.cn

✉ Jia Shi
jshi@xmu.edu.cn

✉ Wenjing Hong
whong@xmu.edu.cn

[1] State Key Laboratory of Physical Chemistry of Solid Surfaces, College of Chemistry and Chemical Engineering, Pen-Tung Sah Institute of Micro-Nano Science and Technology, Collaborative Innovation Center of Chemistry for Energy Materials, Xiamen University, Xiamen 361005, China

Keywords Break junction · Molecular assembly · Supramolecular interaction · Chemical reaction

1 Introduction

Measurements of charge transport through single-molecule junctions are fundamental prerequisites in studying the chemistry and physics at the single-molecule scale. Among the techniques developed for this purpose, single-molecule break junction techniques including scanning tunneling microscope break junction (STMBJ) technique and mechanically controllable break junction (MCBJ) technique are widely used to characterize the conductance of single-molecule junctions [1–4]. Substantial progress has been made over the past decades, such as the dependence of conductance on anchoring groups [5–8], molecular length [9, 10], electrochemical gating [11–14], quantum interference effect [15–19], contacts geometries [10, 20, 21], and the evolution of molecular conformation [22–25]. Beyond the measurements of junctions bridged by a single molecule, some recent reports revealed that single-molecule break junction techniques can be applied to the charge transport studies of supramolecular systems [19, 26–28]. Investigating of charge transport through molecular junctions bridged via self-assembly is essential for the understanding of the intrinsic properties through noncovalent supramolecular interactions at the single-molecule scale.

Charge transport measurements also provide a unique access to monitor and tune the chemical reaction process at the single-molecule scale. Some recent investigations revealed that the charge transport process can be utilized to investigate reactions at the interface of electrode–molecule and molecule–molecule in situ [29–31], which may offer new platforms for the further understanding of the role of charge transport in the catalysis process and provide diverse driving forces to control chemical reactions.

This review specifically focuses on the supramolecular interaction and the in situ characterization of chemical reaction by single-molecule break junction techniques. We review the recent progress of the conductance measurements of supramolecular junctions bridged through noncovalent interactions using break junction techniques. We further summarize the construction of highly conductive molecular junctions by chemical reactions, and the latest works of promoting single-molecule chemical reactions by oriented electric field using STMBJ technique.

2 Supramolecular Interactions in Single Molecular Junctions

Since supramolecular interaction has gained extensive attention in many branches of chemistry, exploring the charge transport through noncovalently bonded supramolecular interaction is of great significance for the construction of molecular devices [32]. With the technical progress of break junction, molecular electronics has gone far beyond the electrical characterization of single-molecule systems, and

offers the opportunity to more complicated supramolecular junctions that constructed by noncovalent interactions.

2.1 Hydrogen Bond

As one of the most widely investigated supramolecular interactions, hydrogen bond has attracted much interest in single-molecule electronics. Early in 2013, employing a STM-based $I(t)$ technique [33], Nishino et al. characterized the electron transport through a series of carboxylic dimers, which are combined by a hydrogen bond [34, 35]. Compared to alkanes that have a similar molecular length, the H-bonded carboxylic dimer exhibits a better conductive capability for short cases. However, as the molecular length increases, the H-bonded dimers become less conductive than their alkane counterparts. Namely, there is a crossover in the plot of conductance versus molecular length (Fig. 1b). According to theoretical calculations of projected density of states (PDOS), the enhanced conductivity of the H-bonded dimers was attributed to the higher density of states of the H-bonded part. Recently, Hou's group and Mujica's group published comprehensive theoretical studies on electron transport through hydrogen bonds. To explain the interesting crossover and the large decay constant, possible mechanisms from the perspective of the coupling efficiency between carboxyl and sulfur atom, as well as the role of resonance, were demonstrated [36, 37].

To investigate the electron transport through multiple hydrogen bonds, we recently designed and synthesized a series of pyrimidine-dione (UPy) derivatives [28]. Using the STMBJ technique, the measured conductance of a molecular dimer terminated with thiols was characterized to be 7.9×10^{-4} G_0, which is comparable to our previous report of conjugated oligo(phenylene ethynylene) junctions [29], while the conductances of molecular dimers terminated with pyridyl and amino group were more than one order of magnitude lower, owing to the weak N–Au bond. Compared to the measurements of simple single-molecular junction, the formation probability for supramolecular systems is relatively low. For molecule terminated with thiol, the formation probability is 14.7%, which decreased to 5.2

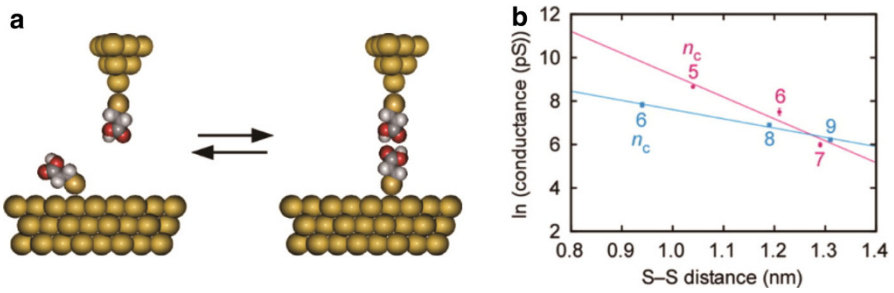

Fig. 1 **a** Schematic of measurements of electron transport through H-bonded carboxylic alkanethiol dimer. **b** Natural logarithm of conductance versus S–S distance for H-bonded C_nCOOH dimer (*pink circles*) and alkanedithiolate systems (*blue circles*), where n_c represents the number of carbon atoms in the molecular junctions. Reproduced with permission from Nishino et al. [34]. Copyright 2013, American Chemical Society

and 2.6% for molecule terminated with pyridyl and amino groups, respectively. This work indicated that the molecular junction fabricated upon weak supramolecular interactions could also be highly conductive, which opened up a novel strategy for the construction of the molecular electronic devices through molecular assembly.

Hydrogen bonds are ubiquitous in biological systems, for therein they preserve the double-stranded structure of DNA. In molecular electronics, the unique characteristics of DNA such as identifiability and self-assembly, make it a promising material for circuit elements [38, 39]. For this purpose, understanding the charge transport properties of hydrogen bond in DNA is an essential issue. Chang et al. exploited the hydrogen bond interaction in nucleoside-base pairs by combining STM and conductive probe atomic force microscopy (CP-AFM) techniques [40]. The electro-mechanical model is able to detect the atomic forces and tunneling current simultaneously, thus allowing counting hydrogen bonds in DNA base pairs.

Besides the base pairs, the break junction methods had also been extended to the measurement of more complicated double-stranded DNA (dsDNA). Here, we will mainly focus on the topic of mutation detection in dsDNA using electric-based methods. Using the STMBJ technique, Hihath et al. reported that the mismatch or methylation of base pairs can change the conductance of dsDNA significantly, even up to an order of magnitude. Different with the general STMBJ method, Nishino et al. developed a new method to achieve mutation detection using a functionalized molecular tip [41, 42]. The STM tip and substrate were functionalized by target single-stranded DNA (ssDNA). The gap between the STM tip and substrate was bridged by the in situ hybridization of ssDNA during conductance measurement (Fig. 2a). Specifically, this method can be successfully used for mutation detection in mixed samples. As shown in Fig. 2b, current histogram showed two well-defined peaks, when the substrate was modified by both pure complementary and methylated ssDNA. Conductance measurements in those works indicate that DNA methylation caused decrease in conductance compared to the original one, although methylation of bases can further increase the stability of dsDNA, due to the methylation-induced increase in polarizability [43, 44]. It should be noted that stronger bond strength does not necessarily means better electron transport since it is determined by the alignment of the Fermi level of the electrodes and the frontier molecular orbitals of the molecules.

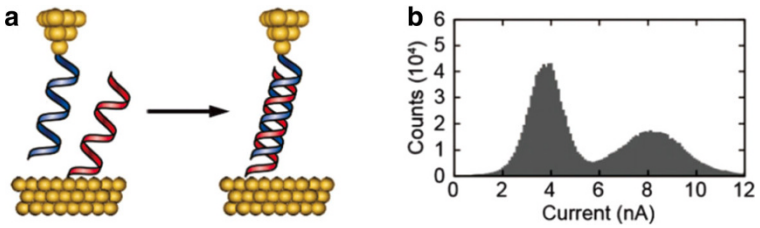

Fig. 2 **a** Schematic of STM tip and gold substrate modified by target single-stranded DNA. Reproduced with permission from Nishino et al. [41]. Copyright 2013, Royal Society of Chemistry. **b** Results of conductance measurements of mixed sample using a DNA tip. Reproduced with permission from Phuc et al. [42]. Copyright 2014, Royal Society of Chemistry

2.2 π–π Stacking Interactions

π–π stacking interactions between aromatic units play a significant role in molecular recognition and supramolecular assembly. For instance, it can stabilize the double stranded structure of DNA and the tertiary structure of protein. Therefore, understanding the electron transport through π–π stacking is a prerequisite for fabricating biomolecule-based devices. In a pioneering work, Wu et al. reported that π–π stacking interaction is strong enough for the formation of molecular junction [45]. Using MCBJ technique, they studied a series of oligo-phenylene ethynylene (OPE) derivatives (Fig. 3). For molecules **1** and **2** (Fig. 3) that were terminated with two anchoring groups, distinct peaks were observed in the corresponding histograms as expected. Interestingly, in terms of molecules **3** and **4**, though there is but one valid anchoring group in each of them, pronounced peaks at 6.6×10^{-4} G_0 and 5.9×10^{-4} G_0 appeared in their conductance histograms respectively. Considering the single anchoring group and the lower conductance, they speculated that the formation of the molecular junctions is ascribed to the π–π stacking interaction between two adjacent molecules.

To further investigate the π–π stacking interaction, Martín et al. designed a series of molecules featured with different steric hindrance and anchoring groups, as given in Fig. 3 [46]. Compared to molecules **5** and **7**, there are steric hindrance caused by bulky *tert-butyl* substituents in the case of molecules **6** and **8**. For molecules **5** and **7**, an additional peak appeared due to the formation of molecular junctions by π–π stacking. In contrast, the conductance peak disappeared for molecules **6** and **8**. Li et al. characterized asymmetric perylene tetracarboxylic bisimides (PBI) with the anchoring group at only one end. It was found that these molecules can form π–π stacking dimers. Moreover, the conductances of π–π stacked molecular junctions kept constant under the electrochemical modulation [47]. Employing the electrochemically assisted mechanically controllable break junction (EC-MCBJ) technique [48, 49], Zheng et al. reported a conductance of 5.1×10^{-6} G_0 for molecule **1** by *I–V* curve measurements [50], as shown in Fig. 4, which is much lower than previous reports [45, 51]. Considering the difference between *I–V* curve measurement and conductance histogram construction in practical experiment operations, they attributed the lower conductance value to a OPE-dithiol dimer that established by the π–π stacking interaction between two adjacent molecules [50]. González et al. explored the dependence of the formation of π–π stacked molecular junction on environmental condition, demonstrating that it would benefit from the presence of polar molecules [52].

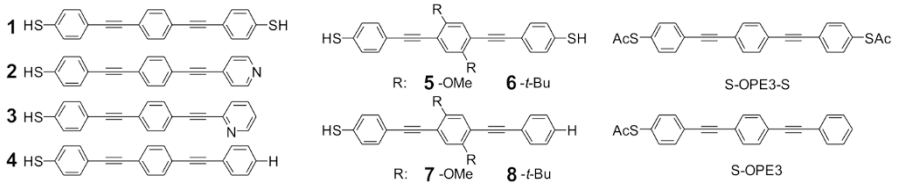

Fig. 3 The corresponding molecular structures discussed

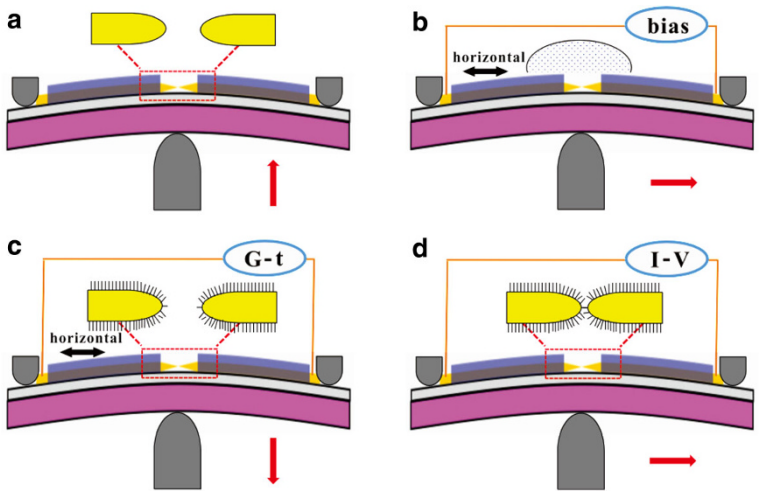

Fig. 4 Schematic of the EC-MCBJ operation process: **a** the electrodes pair was opened to fabricate a nanogap larger than the probe molecule; **b** added the solution and applied bias; **c** the *G–t* curve was monitored during the closing process; **d** the measurement was turned to *I–V* mode once the plateau emerged in *G–t* curve. Inserted *red arrows*: schematics of stepping motor movement. Reproduced with permission from Zheng et al. [51]. Copyright 2016 Elsevier Ltd.

Using MCBJ technique, Frisenda et al. studied the quantum interference effect on charge transport through π–π stacked dimer under accurate control of the distance between the electrodes at sub-angstrom level [19]. According to theoretical calculations, both the electronic coupling between the HOMOs of the two molecules

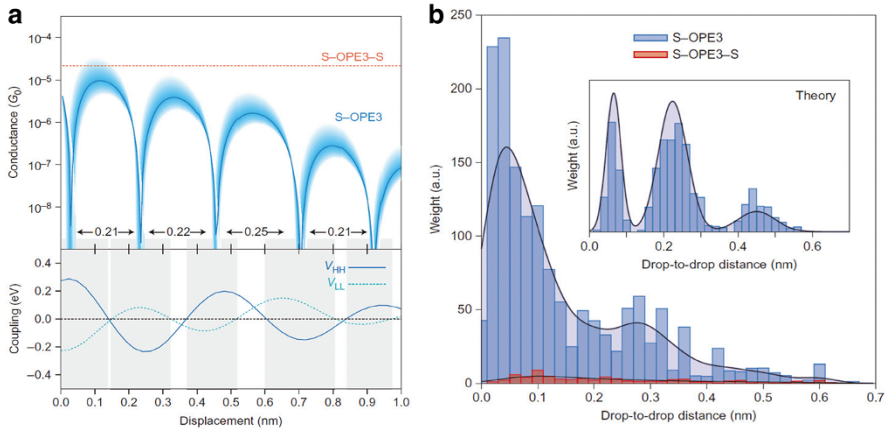

Fig. 5 **a** Theoretical simulation results of molecules of S-OPE3-S and S-OPE3. The *top panel* shows the theoretical conductance of molecule S-OPE3-S (the *red dashed line*) and molecular dimer of S-OPE3 (*blue curve*); the *bottom panel* shows the evolution of electronic coupling between the HOMOs of two stacked S-OPE3 molecules versus relative displacement, as well as that of the LUMOs. **b** Histograms of the drop-to-drop distance of experimental study and theoretical study (*inset*). Reproduced with permission from Frisenda et al. [19]. Copyright 2016, Springer Nature

and the electronic coupling between their LUMOs are dependent on the stacking geometry of the two molecules, as shown in the bottom panel of Fig. 5a. As a result, the conductance of π–π stacked molecule S-OPE3 will show quasiperiodic change during the separation of the π–π stacked molecular dimer, as shown in the top panel of Fig. 5a.

To achieve more precise and stable mechanical control over the electrodes during separation process, Frisenda et al. adopted well-defined metallic electrodes which were patterned by lithography. Statistical analysis of full data sets from conductance measurements indicates that the molecular dimer features two peaks at 1×10^{-5} G_0 and 2×10^{-7} G_0, suggesting at least two favorable stacking geometries. Further statistical analysis of the drop-to-drop distance demonstrates that the distance between two peaks is about 0.22 nm, which is comparable with theoretical prediction (Fig. 5b). Those statistical analyses together indicate that the conductance drops in molecular dimer is not an accidental event but resulting from the destructive quantum interference effects along the breaking process of π–π stacked dimers.

When the π–π stacked systems (stacked guests) were sealed in self-assembled cages [53], the inclusion complexes show unique electrical characteristics. Using STMBJ technique, Kiguchi et al. investigated a series of such complexes including discrete conventional aromatics guests and gold-ion cluster guests (Fig. 6a) [54–56]. No distinguishable signature was obtained when empty cages were used during the conductance measurements. In contrary, for the inclusion complexes, electrical characterization demonstrated that the complexes were highly conductive. Statistical analysis of stretching distance of Au ion cluster in Fig. 6b indicated that the panel ligands at the ends of the cage serve as anchoring groups and the temperature dependence measurement showed that charge transport through single Au ion cluster was dominated by tunneling mechanism [55]. Furthermore, inclusion complexes containing two identical aromatics (homocomplex) and different aromatics (heterocomplex) were investigated using STMBJ technique (Fig. 7). The insertion of two identical aromatics induced high conductivity up to 5×10^{-3} G_0, while the conductance histogram of heterocomplex exhibited two distinct conductance peaks at 3×10^{-3} G_0 and 1×10^{-4} G_0. The two obvious conductance peaks were attributed to different order of the two different aromatics relative to

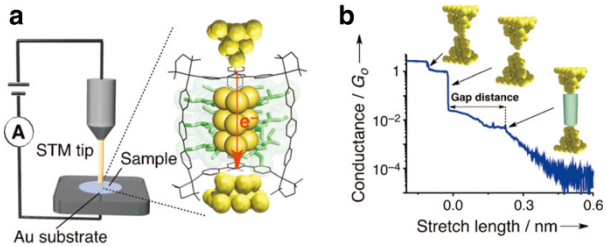

Fig. 6 **a** Schematic of the conductance measurements of Au ion cluster using STMBJ technique. **b** Statistical analysis of stretching distance of Au ion cluster and cartoons of molecular junction evolution during the junction stretching. Reproduced with permission from Kiguchi et al. [55]. Copyright 2013, WILEY–VCH Verlag GmbH & Co. KGaA, Weinheim

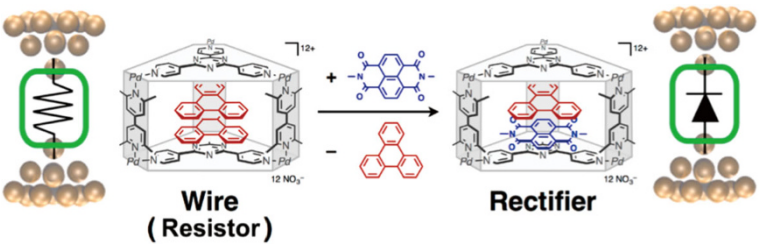

Fig. 7 Schematic illustration of chemical structures and molecular junctions of homocomplex (*left*) and heterocomplex (*right*). Reproduced with permission from Fujii et al. [56]. Copyright 2015, American Chemical Society

electron transport direction at a fixed bias voltage. Statistical analysis of the *I*–*V* curves provided experimental direct evidence for the rectification properties of heterocomplex junctions.

2.3 Host–Guest Interactions

Host–guest complexation has attracted considerable attentions due to their wide application, including biological systems, pharmaceuticals, and chemical sensors. Typically, the formation of a host–guest system requires both appropriate geometrical fitting and noncovalent interaction. The latter includes but is not restricted to hydrogen bonding, cation–π interaction, π–π stacking interaction, van der Waals force, and hydrophobic interaction.

The microscopic structure of a molecular junction, i.e., contact geometry, local environment and molecular conformation, will change the single-molecule conductance greatly. Thus, though π-conjugated molecules are promising building blocks for molecular devices, it is difficult to characterize them precisely because of their volatility. As a common host in the host–guest complexations, cyclodextrins (CDs) are typically composed of 6, 7, or 8 glucose monomers, which constitute the toroidal structure with a hydrophobic internal cavity and a hydrophilic outer surface. The dual structure is an ideal host to restrict the structural change of guest molecules. Inspired by this, Kiguchi et al. investigated the charge transport properties of the π-conjugated molecular junction covered with permethylated α-cyclodextrin (PM α-CD) using STMBJ technique [57]. The conductance histograms showed that the conductance fluctuation of the covered π-conjugated molecular junction was smaller than that of the initial π-conjugated molecular junction, indicating that the introduction of CDs host was efficient for restricting the intramolecular structural fluctuation and intermolecular interactions. Theoretical calculations revealed that the rotational barrier of π-conjugated molecule covered by PM α-CD was higher. Further, the intermolecular interactions between π-conjugated molecules and neighboring molecules were negligible owing to the long intermolecular distance introduced by the hindrance of CDs according to X-ray diffraction characterizations. Therefore, covering a single π-conjugated molecule with a host molecule like CDs is a promising technique to control single-molecule devices precisely.

Recently, Zhang et al. explored the electrical properties of a series of viologens and their host–guest complexes threaded through Cucurbit[8]uril (CB[8]), as depicted in Fig. 8a [27]. Spectroscopic characterization for viologen-CB[8] complexes demonstrated that the stoichiometric ratio between host and guest was 1:1. As shown in Fig. 8a, the viologen-based molecules $\mathbf{1}^{2+}$ and $\mathbf{3}^{2+}$ threaded through CB[8] in a symmetrical manner. However, the structure of $\mathbf{2}^{2+}$ was asymmetric with respect to the host cavity. The conductance histograms showed that the CB[8]-viologen host–guest complexes were more conductive than those of corresponding viologen-based molecules (Fig. 8b). The conductance of $\mathbf{1}^{2+}$ increased by 3.4-fold upon threading into the CB[8] host, while 2.0-fold for $\mathbf{2}^{2+}$ and 2.7-fold for $\mathbf{3}^{2+}$, respectively. The difference in increase of the conductance was attributed to the different symmetry of their structures as mentioned above. Interestingly, UV–Vis spectra and electrochemical results displayed the similar optical band gap as well as the redox potential of viologen molecules and corresponding CB[8] complexes, demonstrating the negligible differences in alignment between the molecular energy levels and the Fermi levels of the electrodes. They speculated that the outer-sphere reorganization energy plays a crucial part according to the Marcus-type model. The discrepancy of local microenvironment within the complex cavity leads to the variation of the medium dielectric properties, thus resulting in the reduction in outer sphere reorganization energy and the increase in the conductance of viologen-CB[8] complexes.

2.4 Charge-Transfer Interactions

Molecular charge-transfer complex, generated from the assembling of the molecules via donor–acceptor interactions, had become a hot topic owing to the versatile

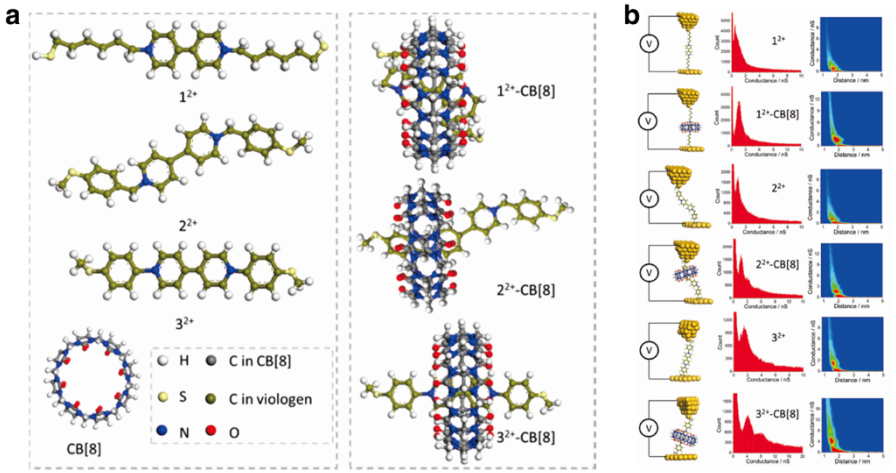

Fig. 8 **a** Structures of viologens and viologen-CB[8] complexes. **b** Schematics of molecular junctions and the corresponding conductance histograms. Reproduced with permission from Zhang et al. [27]. Copyright 2016, American Chemical Society

electronic functionality. Since its discovery in 1973, tetrathiafulvalene-tetracyanoquinodimethane (TTF-TCNQ) charge-transfer complex with high conductivity has been an attractive candidate in the field of molecular electronics [58, 59]. Recently, Garcia et al. investigated the charge transport of a π-extended TTF (exTTF: 9,10-bis(1,3-dithiol-2-ylidene)-9,10-dihydroanthracene) and its charge-transfer complex with F4TCNQ (2,3,5,6-tetrafluoro-7,7,8,8-tetracyanoquinodimethane) [60]. When exTTF was measured individually, no well-defined plateau was observed in the conductance histograms. According to the theoretical calculation, the conductance value of exTTF was below the measurement sensitivity. In contrast, two pronounced conductance plateaus were observed for exTTF-F_4TCNQ complex. The higher conductance was comparable to that of F_4TCNQ, and the lower conductance was assigned to the exTTF-F_4TCNQ complex.

Thiophene-based materials have been widely studied in organic electronics and photonics. Employing the STMBJ technique, Vezzoli et al. found the conductances of molecular junctions bridged by dialkylterthiophene or dialkylbenzene increase significantly upon the formation of a charge-transfer complex with tetracyanoethylene (TCNE) [61]. Such substantial enhancement in conductances can be attributed to the generation of Fano resonance near the Fermi level of the metal electrodes. The above-mentioned research demonstrated that the formation of charge-transfer complex had significant effect on junction conductance, which provides an access to modulate the charge transport through molecular junctions at the single-molecule scale.

Fullerenes and porphyrins are able to form supramolecular complex through donor–acceptor interactions. Nishino et al. investigated the electronic properties of a single fullerene-porphyrin complex by STM technique [62]. The STM tip was covered by fullerene derivatives, and highly oriented pyrolytic graphite (HOPG) was modified with porphyrin derivatives to serve as substrate (Fig. 9a). As shown in Fig. 9b, the asymmetry in *I–V* characteristics showed that single fullerene-porphyrin complex exhibited obvious rectifying behavior. Combined with the STM images, they found that the electron tunneling enhanced by the charge-transfer interaction was localized at the pyrrole moieties.

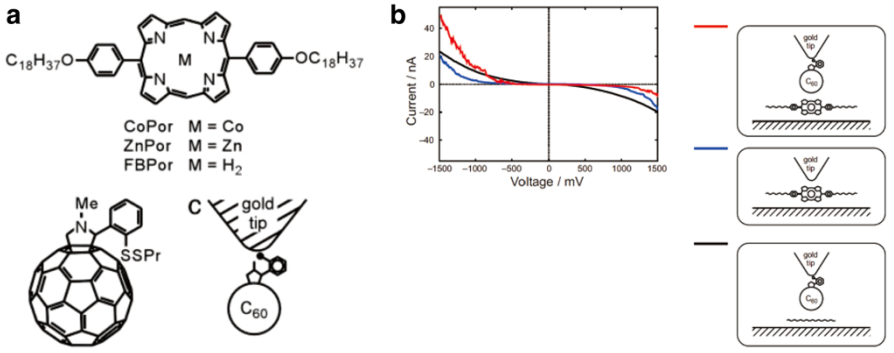

Fig. 9 **a** Chemical structures of molecules and schematic of fullerene modified STM tip. **b** The *I–V* curves measured under different conditions. Reproduced with permission from Nishino et al. [62]. Copyright 2005, National Academy of Sciences

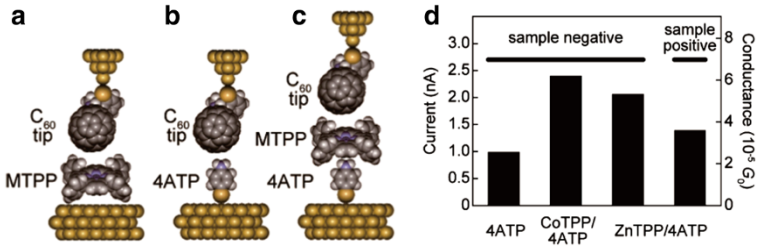

Fig. 10 **a–c** Schematics of three molecular junctions using the fullerene-modified tips to form porphyrin-fullerene complexes. **d** Current and conductance histograms of the molecular junctions depicted in **b** and **c**. Reproduced with permission from Bui et al. [26]. Copyright 2013, American Chemical Society

Porphyrin derivatives can be physically adsorbed on HOPG through π–π stacking interaction. When using gold substrate, however, the electronic coupling between gold substrate and porphyrin derivatives is insufficient. As a result, no discernible signal was obtained when metallotetraphenylporphyrin (MTPP, M: Co or Zn) was directly adsorbed on gold substrate using the fullerene-modified tip, as depicted in Fig. 10a [26]. Instead of introducing anchoring groups into porphyrin derivatives, an alternative protocol was developed, as-called ligation-mediated coupling [63]. As shown in Fig. 10c, the MTPP was pre-immobilized by axial coordination to 4-aminothiophenol (4-ATP), which is bonded to gold substrate through thiol group. Then the assembly was further incorporated with the fullerene modified on the tip to form the more conductive molecular junction. The conductance of the longer MTPP-ligated junction (Fig. 10b) was higher than that of the nonligated junction (Fig. 10c). This abnormal phenomenon can be interpreted by the stronger interaction of MTPP-fullerene complexes compared to the unfavorable electronic interaction between fullerene and 4-ATP. Then, the rectifying property was assessed under opposite bias voltage. As shown in Fig. 10d, the current of ZnTPP/4ATP junction decreased dramatically compared to that under sample negative bias voltage.

3 Chemical Reactions in Single Molecular Junctions

Chemical reactions provide plethoric approaches to synthesize functional substances and to generate forms of energy from raw materials. To date, one of the main challenges in molecular electronics lies in the controllable measurements of electron transport during chemical reaction process. In turn, electron transport measurement offers unique platform to study chemical reactions at the single-molecule scale.

3.1 Response to External Stimuli

As mentioned above, the conductance of molecular junction is sensitive to microscopic structure and local environment around it, providing the basis for utilizing molecular junction as a sensor for the external stimuli. As bio-recognition

molecules are promising blocks in fabricating nanodevice, peptide and DNA based biosensors have received considerable attentions in recent years. Xiao et al. investigated the pH dependent behavior of three simple peptides using STMBJ technique at the single-molecule level [64]. The conductances of these peptide junctions decreased with the increase of pH, which was ascribed to the changes of tunneling barrier caused by protonation and deprotonation of amine and carboxyl groups. Scullion et al. reported the conductance change of a peptide molecular junction with a more complex structure, containing $H(EL)_5C$ (H: histidine, E: forglutamic acid, L: leucine, C: cysteine), during the variation of pH [65]. At low pH (2.0), the peptide with a compact α-helical conformation exhibited a higher conductance up to 2.2×10^{-5} G_0, while the conductance decreased below the detection limit (6.5×10^{-7} G_0) when the pH increased to 6.9. The decrease was caused by the deprotonation of glutamic acid residues at high pH, which leads to more relaxing conformation and extended molecular length. Apart from pH, conformational change of the peptides can also be modulated by metal ions, which can be incorporated with peptides to form the metal-peptide complexes. Xiao et al. found that the conductance of peptide junctions would change dramatically after binding with different metal ions (Cu^{2+}, Ni^{2+}, Na^{+}, K^{+} and Zn^{2+}). They claimed that the changing degree of the conductance was dominated by the sequence, molecular length of peptides and the nature of metal ions.

3.2 The Formation of Disulfide Bridge

Nishino et al. studied the electron transport properties of disulfide bond that formed in situ by the coupling of two alkanedithiols [66]. During conductance measurements, the distance between the molecular tip and the substrate were kept constant by the feedback loop of the STM. The disulfide-containing molecular junctions were found to be less conductive compared to their all-carbon counterparts within the investigated range. Based on theoretical calculation, the decreased conductance originated from weaker coupling between disulfide-containing molecules and gold electrodes. Wang et al. extended the exploration of disulfide bridge to conjugated molecules [67]. The conductance of the dimeric 1,4-benzenedithiol (BDT) junction wired through disulfide bridge was 6.14×10^{-6} G_0, almost three orders lower than those of molecular junctions that connected through acetylenic bond instead of disulfide bridge [10]. Statistical analysis of stretching curves revealed that the length of molecular junctions was 1.35 nm, which agrees well with the result of DFT calculation. Within the framework of this model, the dihedral angle of disulfide bridge tended to take a perpendicular conformation, which was unfavorable for the conjugation of BDT dimer.

3.3 The Formation of Highly Conductive Au–C Contact

Enhancing the coupling between electrode and molecule is of great significance in constructing molecular electronics. Typically, molecules were attached to the electrodes through conventional anchoring groups, including thiols (SH), methyl sulphide (SMe), amines (NH_2), cyano (CN), and pyridyl (Py). However, these

anchoring groups hinder the sufficient electronic coupling between the target molecules and electrodes because they are intervening ones. To minimize the anchoring groups effect, molecules should be directly and covalently bonded to electrodes. Venkataraman et al. demonstrated a method to form covalent Au–C bond using trimethyltin ($SnMe_3$-) terminated alkanes and conjugated molecules (methylene-terminated oligophenyls) [68, 69]. The terminated $SnMe_3$ groups cleaved off in situ to form covalent Au–C bond at the molecule-electrode interface. The conductances of these covalent Au–C bonded molecular junctions are typically two orders of magnitude higher than the analogous molecules that were terminated with amines [70]. However, when the sp^2 benzene carbon was covalently coupled to gold electrodes, the conductance (3×10^{-2} G_0) is comparable to other benzene derivatives terminated with conventional anchoring groups [71]. In contrary, the conductance of molecular junction bridged by *p*-xylylene through Au–Csp^3 bond would reach up to 9×10^{-1} G_0 [69]. A rationale for this discrepancy is, the π system is not well coupled to the gold electrodes and the sp^2 linked σ system is poorly conductive. While, for the *p*-xylylene one, the highly conductive Au–Csp^3 bonds enhance the coupling between the π system of *p*-xylylene and the electrodes greatly due to the direct introduction of methylene to benzene ring.

Trialkylsilyl is a versatile protecting group in organic chemistry because the deprotection of it can be easily achieved with the treatment of tetrabutylammonium fluoride (TBAF) [72]. Inspired by this, we developed an alternative strategy to establish highly conductive and directional Au–C contacts using trimethylsilyl or trialkylsily-terminated derivatives [29, 30, 73]. A series of trimethylsilyl-terminated OPEs were synthesized to create Au–C contacts with the presence of TBAF (Fig. 11a) [29]. The formation of alkynyl-Au bond was confirmed by STM imaging and gap-mode Raman spectroscopy under similar conditions with conductance measurements. The most probable conductances of OPE derivatives are about one order of magnitude higher than the thiol-terminated analogues (Fig. 11c). However, oligomerization was observed during the long-term conductance measurements of OPE1 (Fig. 11b). Further, trialkylsilyl-terminated derivatives were extended to a cruciform conjugated molecule (Fig. 12) [30], which terminated with pyridyl and triisopropylsilyl-protected groups at the end of the two linear arms. Upon desilylation with TBAF, the conductance increased more than one order of magnitude, induced by the complete conversion from coordinative Au-pyridyl bond to covalent Au–C bond. Theoretical study revealed that charge transport through Au-pyridyl bonded configuration was predominantly by the LUMO and the HOMO of Au–C bonded configuration. More importantly, this study offers a promising and facile approach to modulate conductance by in situ selective anchoring. The conductance of molecular junctions with identical hearts will be also affected by different connectivities. Lambert et al. demonstrated theoretically that a simple mid-gap ratio rule (MRR) could be used to predict conductance ratio of graphene-like molecules with the same aromatic core but different connectivities to electrodes, which was verified experimentally using the pyrene-derivatives coupling to gold electrodes through Au–C bond [73, 74].

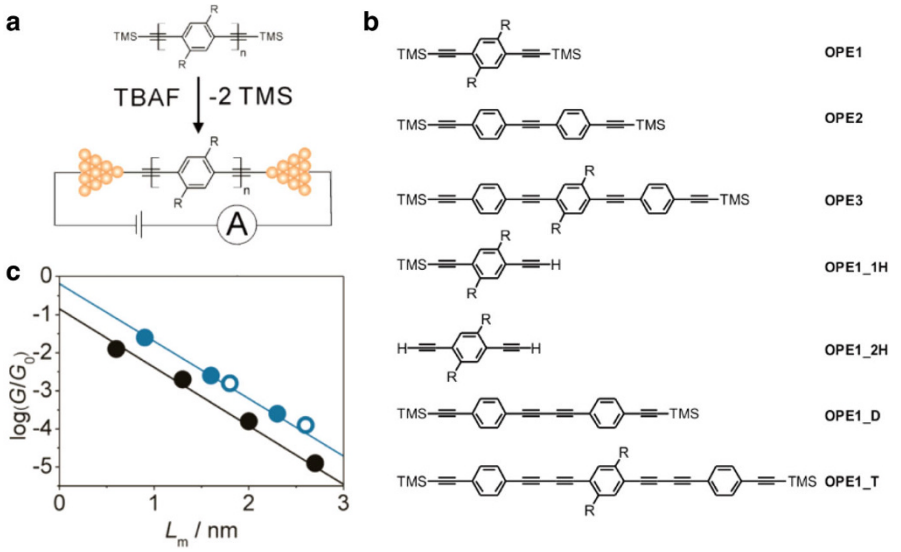

Fig. 11 **a** Schematic of in situ formation of covalent Au–C bond. **b** Chemical structure of molecules. **c** Dependence of OPEs (*filled blue circles*) and dithiol analogous (*black circles*) on molecular length. The most probable conductances of OPE1_D and OPE1_T were represented by the *open blue circles*. Reproduced with permission from Hong et al. [29]. Copyright 2012, American Chemical Society

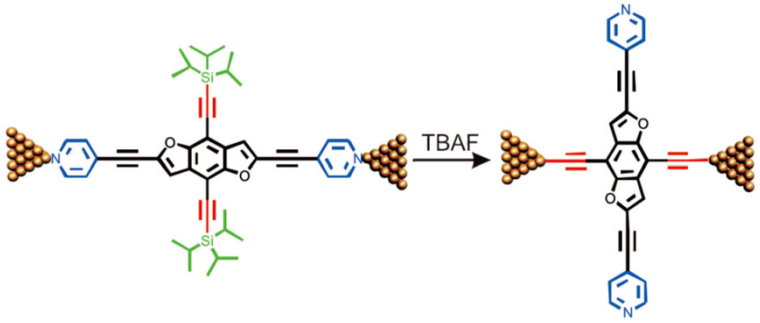

Fig. 12 Schematic of molecular conductance along different charge transport pathways. Reproduced with permission from Huang et al. [30]. Copyright 2015, WILEY–VCH Verlag GmbH & Co. KGaA, Weinheim

3.4 The Diels–Alder Reaction

Early in 2010, Meir et al. predicted theoretically that the appropriately oriented external electric field (EEF) will accelerate a classic pericyclic reaction, the Diels–Alder reaction by aligning the direction of EEF along the "reaction axis" [75]. Recently, Aragonès et al. confirmed experimentally that the EEF is able to control the Diels–Alder reactivity using STMBJ technique [31]. To orient the reactants, furan was attached to the STM tip, while the gold substrate was modified with rigid dienophile, norbornylogous (NB) bridges, as depicted in Fig. 13a. From the

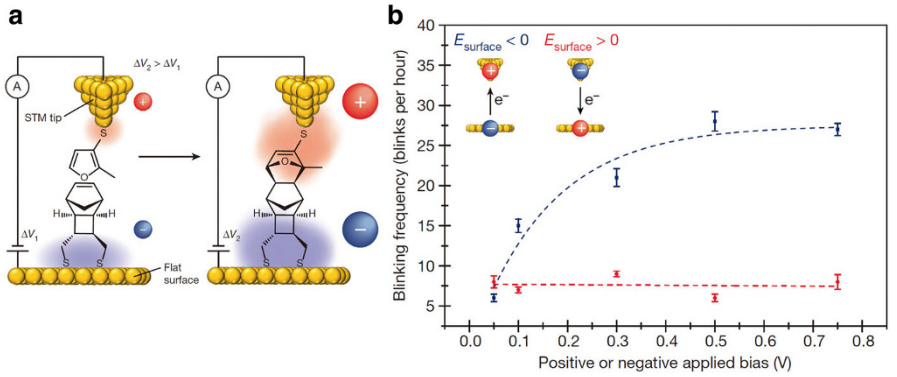

Fig. 13 **a** Schematic of the formation of molecular junction through the Diels–Alder reaction using blinking technique. **b** Blinking frequency at positive biases (*red*) and negative biases (*blue*). Reproduced with permission from Aragones et al. [31]. Copyright 2016 Springer Nature

technical point of view, STM technique provides an ideal platform to generate directional electric field within a nanogap and detect the formation of molecular junctions through the Diels–Alder reaction using blinking technique [76]. Theoretically, the barrier height will decrease by stabilizing one of the dominant resonance contributors of the transition state at negatively biased EEF. Experimental results showed that the reaction rate was increased by up to fivefold at negative biases when the strength of the field increased. While at positive biases, the reaction rate remained constant within the applied biases window. The trends of experimental results were in accordance with theoretical calculations, which suggested the key role of EEF in the in situ chemical reaction.

4 Outlook

In this review, we highlight some recent developments in the characterization of charge transport through supramolecular systems and chemical reactions at the single-molecule scale. Owing to the continuous progress, the well-established single-molecule break junction techniques have been proved to be a promising tool for the study of molecular interactions and chemical reactions at the single-molecule scale. To further reveal the role of charge transport in the molecular assembly/chemical reaction at the single-molecule scale, novel experimental techniques are required. For instance, the incorporation of in situ spectroscopic techniques and external stimuli into single-molecule break junction techniques, such as light, electrical field and heat, as well as the high time-resolved characterization technique, which is essential for the measurements of transient processes.

Acknowledgements This work was supported by National Natural Science Foundation of China (Nos. 21673195, 21503179, 61573295, 21403181), Natural Science Foundation of Fujian Province (No. 2016J05162), Young Thousand Talent Project of China, and the Fundamental Research Funds for the Central Universities (Xiamen University: Nos. 20720170035, 20720160092).

References

1. Xiang D, Jeong H, Lee T, Mayer D (2013) Mechanically controllable break junctions for molecular electronics. Adv Mater 25:4845–4867
2. Chen F, Hihath J, Huang ZF, Li XL, Tao NJ (2007) Measurement of single-molecule conductance. Annu Rev Phys Chem 58:535–564
3. Huang CC, Rudnev AV, Hong WJ, Wandlowski T (2015) Break junction under electrochemical gating: Testbed for single-molecule electronics. Chem Soc Rev 44:889–901
4. Xiang D, Wang XL, Jia CC, Lee T, Guo XF (2016) Molecular-scale electronics: From concept to function. Chem Rev 116:4318–4440
5. Chen F, Li XL, Hihath J, Huang ZF, Tao NJ (2006) Effect of anchoring groups on single-molecule conductance: Comparative study of thiol-, amine-, and carboxylic-acid-terminated molecules. J Am Chem Soc 128:15874–15881
6. Park YS, Whalley AC, Kamenetska M, Steigerwald ML, Hybertsen MS, Nuckolls C, Venkataraman L (2007) Contact chemistry and single-molecule conductance: A comparison of phosphines, methyl sulfides, and amines. J Am Chem Soc 129:15768–15769
7. Hong WJ, Manrique DZ, Moreno-Garcia P, Gulcur M, Mishchenko A, Lambert CJ, Bryce MR, Wandlowski T (2012) Single molecular conductance of tolanes: Experimental and theoretical study on the junction evolution dependent on the anchoring group. J Am Chem Soc 134:2292–2304
8. Kaliginedi V, Rudnev AV, Moreno-Garcia P, Baghernejad M, Huang CC, Hong WJ, Wandlowski T (2014) Promising anchoring groups for single-molecule conductance measurements. Phys Chem Chem Phys 16:23529–23539
9. Capozzi B, Dell EJ, Berkelbach TC, Reichman DR, Venkataraman L, Campos LM (2014) Length-dependent conductance of oligothiophenes. J Am Chem Soc 136:10486–10492
10. Moreno-Garcia P, Gulcur M, Manrique DZ, Pope T, Hong WJ, Kaliginedi V, Huang CC, Batsanov AS, Bryce MR, Lambert C, Wandlowski T (2013) Single-molecule conductance of functionalized oligoynes: Length dependence and junction evolution. J Am Chem Soc 135:12228–12240
11. Prins F, Barreiro A, Ruitenberg JW, Seldenthuis JS, Aliaga-Alcalde N, Vandersypen LMK, van der Zant HSJ (2011) Room-temperature gating of molecular junctions using few-layer graphene nanogap electrodes. Nano Lett 11:4607–4611
12. Diez-Perez I, Li ZH, Guo SY, Madden C, Huang HL, Che YK, Yang XM, Zang L, Tao NJ (2012) Ambipolar transport in an electrochemically gated single-molecule field-effect transistor. ACS Nano 6:7044–7052
13. Li Y, Baghernejad M, Qusiy A-G, Manrique DZ, Zhang G, Hamill J, Fu Y, Broekmann P, Hong WJ, Wandlowski T, Zhang D, Lambert C (2015) Three-state single-molecule naphthalenediimide switch: Integration of a pendant redox unit for conductance tuning. Angew Chem Int Ed 54:13586–13589
14. Osorio HM, Catarelli S, Cea P, Gluyas JB, Hartl F, Higgins SJ, Leary E, Low PJ, Martin S, Nichols RJ, Tory J, Ulstrup J, Vezzoli A, Milan DC, Zeng Q (2015) Electrochemical single-molecule transistors with optimized gate coupling. J Am Chem Soc 137:14319–14328
15. Arroyo CR, Tarkuc S, Frisenda R, Seldenthuis JS, Woerde CH, Eelkema R, Grozema FC, van der Zant HS (2013) Signatures of quantum interference effects on charge transport through a single benzene ring. Angew Chem Int Ed 52:3152–3155
16. Markussen T, Schiotz J, Thygesen KS (2010) Electrochemical control of quantum interference in anthraquinone-based molecular switches. J Chem Phys 132:224104
17. Markussen T, Stadler R, Thygesen KS (2010) The relation between structure and quantum interference in single-molecule junctions. Nano Lett 10:4260–4265
18. Manrique DZ, Huang CC, Baghernejad M, Zhao XT, Al-Owaedi OA, Sadeghi H, Kaliginedi V, Hong WJ, Gulcur M, Wandlowski T, Bryce MR, Lambert CJ (2015) A quantum circuit rule for interference effects in single-molecule electrical junctions. Nat Commun 6:6389
19. Frisenda R, Janssen VAEC, Grozema FC, van der Zant HSJ, Renaud N (2016) Mechanically controlled quantum interference in individual π-stacked dimers. Nat Chem. doi:10.1038/NCHEM.2588
20. Li XL, He J, Hihath J, Xu BQ, Lindsay SM, Tao NJ (2006) Conductance of single alkanedithiols: Conduction mechanism and effect of molecule-electrode contacts. J Am Chem Soc 128:2135–2141
21. Sergueev N, Tsetseris L, Varga K, Pantelides S (2010) Configuration and conductance evolution of benzene-dithiol molecular junctions under elongation. Phys Rev B 82:073106
22. Venkataraman L, Klare JE, Nuckolls C, Hybertsen MS, Steigerwald ML (2006) Dependence of single-molecule junction conductance on molecular conformation. Nature 442:904–907

23. Finch CM, Sirichantaropass S, Bailey SW, Grace IM, García-Suárez VM, Lambert CJ (2008) Conformation dependence of molecular conductance: Chemistry versus geometry. J Phys Condens Matter 20:022203
24. Mishchenko A, Vonlanthen D, Meded V, Burkle M, Li C, Pobelov IV, Bagrets A, Viljas JK, Pauly F, Evers F, Mayor M, Wandlowski T (2010) Influence of conformation on conductance of biphenyl-dithiol single-molecule contacts. Nano Lett 10:156–163
25. Li H, Garner MH, Shangguan Z, Zheng Q, Su TA, Neupane M, Li P, Velian A, Steigerwald ML, Xiao S, Nuckolls C, Solomon GC, Venkataraman L (2016) Conformations of cyclopentasilane stereoisomers control molecular junction conductance. Chem Sci 7:5657–5662
26. Bui PT, Nishino T, Yamamoto Y, Shiigi H (2013) Quantitative exploration of electron transfer in a single noncovalent supramolecular assembly. J Am Chem Soc 135:5238–5241
27. Zhang W, Gan S, Vezzoli A, Davidson RJ, Milan DC, Luzyanin KV, Higgins SJ, Nichols RJ, Beeby A, Low PJ, Li B, Niu L (2016) Single-molecule conductance of viologen-cucurbit[8]uril host-guest complexes. ACS Nano 10:5212–5220
28. Wang L, Gong ZL, Li SY, Hong WJ, Zhong YW, Wang D, Wan LJ (2016) Molecular conductance through a quadruple-hydrogen-bond-bridged supramolecular junction. Angew Chem Int Ed 55:12393–12397
29. Hong WJ, Li H, Liu SX, Fu Y, Li J, Kaliginedi V, Decurtins S, Wandlowski T (2012) Trimethylsilyl-terminated oligo(phenylene ethynylene)s: An approach to single-molecule junctions with covalent Au–C σ-bonds. J Am Chem Soc 134:19425–19431
30. Huang CC, Chen SJ, Baruel Ornso K, Reber D, Baghernejad M, Fu YC, Wandlowski T, Decurtins S, Hong WJ, Thygesen KS, Liu SX (2015) Controlling electrical conductance through a pi-conjugated cruciform molecule by selective anchoring to gold electrodes. Angew Chem Int Ed 54:14304–14307
31. Aragones AC, Haworth NL, Darwish N, Ciampi S, Bloomfield NJ, Wallace GG, Diez-Perez I, Coote ML (2016) Electrostatic catalysis of a Diels-Alder reaction. Nature 531:88–91
32. Cordier P, Tournilhac F, Soulie-Ziakovic C, Leibler L (2008) Self-healing and thermoreversible rubber from supramolecular assembly. Nature 451:977–980
33. Haiss W, Nichols RJ, van Zalinge H, Higgins SJ, Bethell D, Schiffrin DJ (2004) Measurement of single-molecule conductivity using the spontaneous formation of molecular wires. Phys Chem Chem Phys 6:4330–4337
34. Nishino T, Hayashi N, Bui PT (2013) Direct measurement of electron transfer through a hydrogen bond between single molecules. J Am Chem Soc 135:4592–4595
35. Bui PT, Nishino T (2014) Electron transfer through coordination bond interaction between single molecules: Conductance switching by a metal ion. Phys Chem Chem Phys 16:5490–5494
36. Wimmer M, Palma JL, Tarakeshwar P, Mujica V (2016) Single-molecule conductance through hydrogen bonds: The role of resonances. J Phys Chem Lett 7:2977–2980
37. Li Y, Tu XC, Wang ML, Wang H, Sanvito S, Hou S (2014) Microscopic mechanism of electron transfer through the hydrogen bonds between carboxylated alkanethiol molecules connected to gold electrodes. J Chem Phys 141:174702
38. Livshits GI, Stern A, Rotem D, Borovok N, Eidelshtein G, Migliore A, Penzo E, Wind SJ, Di Felice R, Skourtis SS, Cuevas JC, Gurevich L, Kotlyar AB, Porath D (2014) Long-range charge transport in single G-quadruplex DNA molecules. Nat Nanotech 9:1040–1046
39. Timper J, Gutsmiedl K, Wirges C, Broda J, Noyong M, Mayer J, Carell T, Simon U (2012) Surface "click" reaction of DNA followed by directed metalization for the construction of contactable conducting nanostructures. Angew Chem Int Ed 51:7586–7588
40. Chang S, He J, Kibel A, Lee M, Sankey O, Zhang PM, Lindsay S (2009) Tunnelling readout of hydrogen-bonding-based recognition. Nat Nanotechnol 4:297–301
41. Nishino T, Bui PT (2013) Direct electrical single-molecule detection of DNA through electron transfer induced by hybridization. Chem Commun 49:3437
42. Phuc Tan B, Nishino T, Shiigi H, Nagaoka T (2015) One-by-one single-molecule detection of mutated nucleobases by monitoring tunneling current using a DNA tip. Chem Commun 51:1666–1669
43. Sowers LC, Shaw BR, Sedwick WD (1987) Base stacking and molecular polarizability-effect of a methyl-group in the 5-position of pyrimidines. Biochem Biophys Res Commun 148:790–794
44. Wang SH, Kool ET (1995) Origins of the large differences in stability of DNA and RNA helice-C-5 methyl and 2′-hydroxyl effects. Biochem 34:4125–4132
45. Wu S, Gonzalez MT, Huber R, Grunder S, Mayor M, Schoenenberger C, Calame M (2008) Molecular junctions based on aromatic coupling. Nat Nanotechnol 3:569–574

46. Martin S, Grace I, Bryce MR, Wang C, Jitchati R, Batsanov AS, Higgins SJ, Lambert CJ, Nichols RJ (2010) Identifying diversity in nanoscale electrical break junctions. J Am Chem Soc 132:9157–9164
47. Li C, Stepanenko V, Lin M-J, Hong WJ, Würthner F, Wandlowski T (2013) Charge transport through perylene bisimide molecular junctions: An electrochemical approach. Phys Status Solidi B 250:2458–2467
48. Yang Y, Liu JY, Feng S, Wen HM, Tian JH, Zheng JT, Schollhorn B, Amatore C, Chen ZN, Tian ZQ (2016) Unexpected current-voltage characteristics of mechanically modulated atomic contacts with the presence of molecular junctions in an electrochemically assisted-MCBJ. Nano Res 9:560–570
49. Yang Y, Chen ZB, Liu JY, Lu M, Yang DZ, Yang FZ, Tian ZQ (2011) An electrochemically assisted mechanically controllable break junction approach for single-molecule junction conductance measurements. Nano Res 4:1199–1207
50. Zheng JT, Yan RW, Tian JH, Liu JY, Pei L, Wu DY, Dai K, Yang Y, Jin S, Hong W, Tian ZQ (2016) Electrochemically assisted mechanically controllable break junction studies on the stacking configurations of oligo(phenylene ethynylene)s molecular junctions. Electrochim Acta 200:268–275
51. Kaliginedi V, Moreno-Garcia P, Valkenier H, Hong WJ, Garcia-Suarez VM, Buiter P, Otten JL, Hummelen JC, Lambert CJ, Wandlowski T (2012) Correlations between molecular structure and single-junction conductance: A case study with oligo(phenylene-ethynylene)-type wires. J Am Chem Soc 134:5262–5275
52. González MT, Leary E, Rl García, Verma P, Herranz MAN, Rubio-Bollinger G, Martín N, Agraït NS (2011) Break-junction experiments on acetyl-protected conjugated dithiols under different environmental conditions. J Phys Chem C 115:17973–17978
53. Yamauchi Y, Yoshizawa M, Akita M, Fujita M (2010) Engineering double to quintuple stacks of a polarized aromatic in confined cavities. J Am Chem Soc 132:960–966
54. Kiguchi M, Takahashi T, Takahashi Y, Yamauchi Y, Murase T, Fujita M, Tada T, Watanabe S (2011) Electron transport through single molecules comprising aromatic stacks enclosed in self-assembled cages. Angew Chem Int Ed 50:5708–5711
55. Kiguchi M, Inatomi J, Takahashi Y, Tanaka R, Osuga T, Murase T, Fujita M, Tada T, Watanabe S (2013) Highly conductive [3 × n] gold-ion clusters enclosed within self-assembled cages. Angew Chem Int Ed Engl 52:6202–6205
56. Fujii S, Tada T, Komoto Y, Osuga T, Murase T, Fujita M, Kiguchi M (2015) Rectifying electron-transport properties through stacks of aromatic molecules inserted into a self-assembled cage. J Am Chem Soc 137:5939–5947
57. Kiguchi M, Nakashima S, Tada T, Watanabe S, Tsuda S, Tsuji Y, Terao J (2012) Single-molecule conductance of pi-conjugated rotaxane: New method for measuring stipulated electric conductance of pi-conjugated molecular wire using STM break junction. Small 8:726–730
58. Anderson PW, Lee PA, Saitoh M (1973) Remarks on giant conductivity in TTF-TCNQ. Solid State Commun 13:595–598
59. Alves H, Molinari AS, Xie H, Morpurgo AF (2008) Metallic conduction at organic charge-transfer interfaces. Nat Mater 7:574–580
60. Garcia R, Angeles Herranz M, Leary E, Gonzalez MT, Rubio Bollinger G, Buerkle M, Zotti LA, Asai Y, Pauly F, Carlos Cuevas J, Agrait N, Martin N (2015) Single-molecule conductance of a chemically modified, Pi-extended tetrathiafulvalene and its charge-transfer complex with F(4)TCNQ. Beilstein J Org Chem 11:1068–1078
61. Vezzoli A, Grace I, Brooke C, Wang K, Lambert CJ, Xu B, Nichols RJ, Higgins SJ (2015) Gating of single-molecule junction conductance by charge transfer complex formation. Nanoscale 7:18949–18955
62. Nishino T, Ito T, Umezawa Y (2005) A fullerene molecular tip can detect localized and rectified electron tunneling within a single fullerene-porphyrin pair. PNAS 102:5659–5662
63. Arima V, Blyth RIR, Della Sala F, Del Sole R, Matino F, Mele G, Vasapollo G, Cingolani R, Rinaldi R (2004) Long-range order induced by cobalt porphyrin adsorption on aminothiophenol-functionalized Au(111): The influence of the induced dipole. Mater Sci Eng C 24:569–573
64. Xiao XY, Xu BQ, Tao NJ (2004) Conductance titration of single-peptide molecules. J Am Chem Soc 126:5370–5371
65. Scullion L, Doneux T, Bouffier L, Fernig DG, Higgins SJ, Bethell D, Nichols RJ (2011) Large conductance changes in peptide single-molecule junctions controlled by pH. J Phys Chem C 115:8361–8368
66. Nishino T (2010) Charge transport induced by formation of a single covalent bond. ChemPhysChem 11:3405–3407

67. Wang L, Li SY, Yuan JH, Gu JY, Wang D, Wan LJ (2014) Electron transport characteristics of the dimeric 1,4-benzenedithiol junction. Chemistry Asian J 9:2077–2082
68. Cheng ZL, Skouta R, Vazquez H, Widawsky JR, Schneebeli S, Chen W, Hybertsen MS, Breslow R, Venkataraman L (2011) In situ formation of highly conducting covalent Au–C contacts for single-molecule junctions. Nat Nanotechnol 6:353–357
69. Chen W, Widawsky JR, Vázquez H, Schneebeli ST, Hybertsen MS, Breslow R, Venkataraman L (2011) Highly conducting pi-conjugated molecular junctions covalently bonded to gold electrodes. J Am Chem Soc 133:17160–17163
70. Hybertsen MS, Venkataraman L, Klare JE, Whalley AC, Steigerwald ML, Nuckolls C (2008) Amine-linked single-molecule circuits: Systematic trends across molecular families. J Phys Condens Mat 20:374115
71. Venkataraman L, Klare JE, Tam IW, Nuckolls C, Hybertsen MS, Steigerwald ML (2006) Single-molecule circuits with well-defined molecular conductance. Nano Lett 6(3):458–462
72. Gawronski J, Wascinska N, Gajewy J (2008) Recent progress in Lewis base activation and control of stereoselectivity in the additions of trimethylsilyl nucleophiles. Chem Rev 108:5227–5252
73. Sangtarash S, Huang CC, Sadeghi H, Sorohhov G, Hauser J, Wandlowski T, Hong WJ, Decurtins S, Liu SX, Lambert CJ (2015) Searching the hearts of graphene-like molecules for simplicity, sensitivity, and logic. J Am Chem Soc 137:11425–11431
74. Geng Y, Sangtarash S, Huang CC, Sadeghi H, Fu YC, Hong WJ, Wandlowski T, Decurtins S, Lambert CJ, Liu SX (2015) Magic ratios for connectivity-driven electrical conductance of graphene-like molecules. J Am Chem Soc 137:4469–4476
75. Meir R, Chen H, Lai WZ, Shaik S (2010) Oriented electric fields accelerate Diels-Alder reactions and control the endo/exo selectivity. ChemPhysChem 11:301–310
76. Haiss W, Wang CS, Grace I, Batsanov AS, Schiffrin DJ, Higgins SJ, Bryce MR, Lambert CJ, Nichols RJ (2006) Precision control of single-molecule electrical junctions. Nat Mater 5:995–1002

Top Curr Chem (Z) (2017) 375:79
DOI 10.1007/s41061-017-0167-y

REVIEW

Nonlinear and Nonsymmetric Single-Molecule Electronic Properties Towards Molecular Information Processing

Takashi Tamaki[1] · **Takuji Ogawa**[1]

Received: 13 February 2017 / Accepted: 23 August 2017 / Published online: 5 September 2017

Abstract This review highlights molecular design for nonlinear and nonsymmetric single-molecule electronic properties such as rectification, negative differential resistance, and switching, which are important components of future single-molecule information processing devices. Perspectives on integrated "molecular circuits" are also provided. Nonlinear and nonsymmetric single-molecule electronics can be designed by utilizing (1) asymmetric molecular cores, (2) asymmetric anchoring groups, (3) an asymmetric junction environment, and (4) asymmetric electrode materials. This review mainly focuses on the design of molecular cores.

Keywords Single-molecular electronics · Molecular diode · Negative differential resistance · Molecular switch · Molecular curcuit

1 Introduction

The top-down approach to the miniaturization of silicon-based electronic circuits is facing physical limitations. These limitations were first predicted in the 1970s, based on theoretical considerations. In 1974, Aviram and Ratner (AR) proposed an alternative—a bottom-up approach involving the use of organic molecules to form electronic devices [1]. Since then, single-molecule devices have been studied extensively [2, 3]. For instance, in the past few years, the charge-transport properties

Chapter 4 was originally published as Tamaki, T. & Ogawa, T. Top Curr Chem (Z) (2017) 375: 79. DOI 10.1007/s41061-017-0167-y.

✉ Takuji Ogawa
ogawa@chem.sci.osaka-u.ac.jp

[1] Department of Chemistry, Graduate School of Science, Osaka University, 1-1 Machikaneyama-cho, Toyonaka, Osaka 560-0043, Japan

of metal-(single molecule)-metal junctions have been explored, mainly using the mechanically controllable break junction (MCBJ) technique [4, 5], the scanning tunneling microscopy break junction (STM-BJ) technique [6], conductive atomic force microscopy (cAFM) [7], electron migration measurements [8], nanogap electrodes [9], and scanning tunneling spectroscopy (STS) in the case of mixed self-assembled monolayers (SAMs) [10].

From the viewpoint of an organic chemist, a molecular structure can be designed and synthesized as needed. As discussed below, the relationship between the molecular structure of a material and its electrical properties has gradually been elucidated. Therefore, it is now possible to improve the electrical performance of a material by optimizing its structure. Furthermore, single-molecule devices can be integrated and "molecular circuits," which are extremely small electronic devices, can be realized as alternatives to silicon-based devices.

In this review, we summarize the molecular structures and underlying mechanisms of single-molecule devices that show rectification, negative differential resistance (NDR), and switching behavior, which have generally been investigated using break junction methods. In addition, we describe future perspectives on the use of integrated molecular circuits to perform information processing with molecular electronics.

2 Rectification

A rectifier is an electrical device in which the current flows in only one direction, and it usually consists of a p-n junction of p- and n-type semiconductors. As mentioned above, AR proposed a single-molecule diode that consisted of donor (D) and acceptor (A) moieties linked by a σ-insulator, i.e., a D-σ-A-type molecule, thus mimicking the semiconductor p-n junction [1]. Since then, several single-molecule rectifiers consisting of D and A moieties have been studied (see Scheme 1).

Four general approaches to realizing rectification characteristics have been proposed. The first is to design a molecular backbone, the second is to use asymmetric anchoring groups [11–13], the third is to control the junction environment [14], and the fourth is to use different metals as the electrodes [15]. Herein, we only summarize the first approach, as our aim is to primarily focus on the relationship between the structure of a molecule and its rectification characteristics.

2.1 D-σ-A-Type Molecules

The first molecule proposed by AR had a quinone moiety as the acceptor, an ethyl linker as the σ-bond insulator, and methoxy-substituted benzene as the donor (Diode-1). The second molecule they proposed had a tetracyanoquinodimethane (TCNQ) moiety as the acceptor, bicyclo[2.2.2]octane as a more rigid insulator, and thiofulvalene (TTF) as the donor (Diode-2). The rectification mechanism of this type of single-molecule rectifier can be divided into three steps (Fig. 1). (1) When

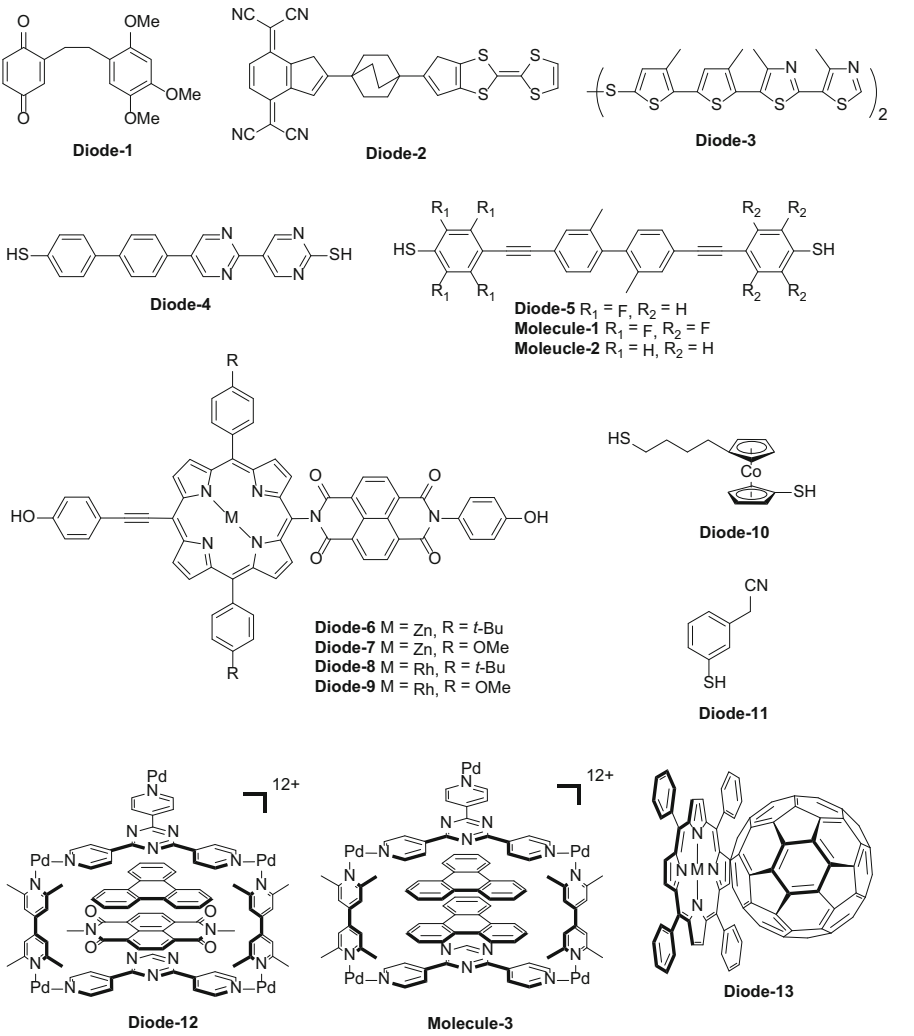

Scheme 1 Molecular structures of single-molecule diodes

the lowest unoccupied molecular orbital (LUMO) of the acceptor moiety and the Fermi level of the anode align under a forward bias voltage (V_F), electrons can move from the electrode to the acceptor. (2) The electrons in the highest occupied molecular orbital (HOMO) of the donor moiety are transferred to the anode. (3) When the now-occupied level of the acceptor and the holes remaining in the ionized donor have similar energies, electron tunneling occurs. In contrast, under a reverse bias voltage (V_B), the first step of the rectification process is the internal tunneling of electrons from the HOMO of the donor to the LUMO of the acceptor. After this initial step, tunneling occurs between the electrodes. The nonreversibility of the internal tunneling phenomenon is responsible for the rectification properties of the D-σ-A-type molecule.

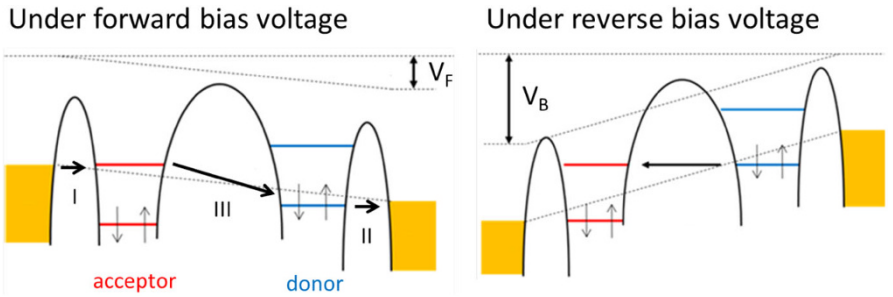

Fig. 1 Schematics of rectification mechanisms under forward and reverse biases (V_F and V_B, respectively). Reprinted from *Chemical Physics Letters* [1], copyright 1974, with permission from Elsevier

A D-σ-A-type diode was proposed by Perrin et al. in 2015 as a "single-molecule resonant tunneling diode," wherein phenyl-ethynyl-phenyl and fluorophenyl-ethynyl-phenyl linked by a $–CH_2CH_2–$ chain exhibited orbital resonance when using an asymmetric two-site model, as analyzed by the nonequilibrium Green's function (NEGF) method in combination with density functional theory (DFT) calculations [16]. The molecule was synthesized by Galan et al. [17]. However, electronic measurements have not yet been performed at the single-molecule device level.

Another theoretical D-σ-A-type molecular rectifier was proposed by Ding et al. in 2015 [18]. They performed a systematic computational search of the molecular frameworks that would allow for intrinsic rectification using 52 molecules and found that *N*-phenylbenzamide is a promising framework, exhibiting both suitable conductance and rectification properties. Thirty additional derivatives and conformers of *N*-phenylbenzamide were screened to demonstrate that electron-donating substituent groups enhance rectification by raising the energy of the channel such that it is closer to the Fermi level.

However, even though several D-σ-A-type rectifiers have been suggested theoretically, there are no reports of the experimental confirmation of the rectification phenomenon.

2.2 D-A Directly Connected Molecules

In 2002, Yu's group proposed a molecular design for a single-molecule rectifier (Diode-3) that was different from those suggested by AR. In the former, the donor and acceptor groups are connected directly, i.e., without an insulator in-between [19]. The designed diblock molecule consised of an electron-donating bithiophene block and an electron-accepting bithiazole block. A SAM of this diblock molecule showed rectification behavior during scanning tunneling spectroscopy (STS) measurements.

Diez-Perez et al. discussed the mechanistic details of rectification by a D-A directly connected molecule using a dipyrimidinyl-diphenyl diblock (Diode-4) by (1) controlling the orientation of the molecular diode and (2) using the STM-BJ technique, in which an alternating current (AC) distance-modulated signal was used [20]. The molecular orientation was controlled by the following method: (1) the two thiol-anchoring groups were protected with different groups (trimethylsilylethyl and cyanoethyl); (2) the cyanoethyl group was deprotected with sodium ethoxide; (3) a SAM was prepared on a gold substrate by immersing the substrate into the solution; and (4) another trimethylsilylethyl group was deprotected with tetrabutylammonium fluoride. In this SAM, the thiol group was exposed topside. Therefore, a molecular bridge could be formed by bringing a STM tip close to the substrate. The single-molecule bridge was formed by the conventional break junction technique based on the AC-modulated tip–substrate distance. The symmetric tetraphenyl molecule did not exhibit rectification, as shown in Fig. 2a and c. On the contrary, the dipyrimidinyl-diphenyl diblock behaved as a single-molecule rectifier (Fig. 2b, d). The rectification mechanism underlying this molecular design involves the following steps: (1) an electron is transferred from the electron-rich diphenyl block to the anode, resulting in the formation of a hole in the molecule; (2) the generated hole is transferred to the cathode under an electric field; and (3) this hole, when injected into the cathode, recombines with an electron. The lack of symmetry in the *I–V* characteristics is caused by the lack of symmetry of the hole wavefunction as a function of the applied electric field. The probabilities of hole transfer from the anode to the molecule ($\gamma_{\text{anode}} \propto |\psi_{\text{h}}(r_{\text{a}})|^2$, where ψ_{h} is the hole wavefunction and r_{a} is the anode spatial coordinate) were obtained from DFT calculations. As a result, the transfer probability was higher at a positive bias voltage ($\gamma_{\text{anode}}^{V>0}$) than at a negative bias voltage ($\gamma_{\text{anode}}^{V<0}$). The calculated *I–V* curve was also nonsymmetric and indicative of rectification.

Lörtscher et al. performed measurements of the same diblock molecule (Diode-4) using the MCBJ method to show that it exhibits rectification behavior [21]. They discussed the rectification mechanism and proposed a combined model (Fig. 3d) in which the dipyrimidinyl-diphenyl diblock molecule is affected by an asymmetric electronic field and charging.

Using computational studies, the bias-dependent transmission spectra for this diblock molecule were analyzed to reveal that the transmissions in the bias window were different under positive and negative bias voltages [22–24].

Also using computational studies, Yuan et al. revealed that the D-A-type thiophene dimer acts as a rectifier [25]. Thiophene is connected at the α-position and the α- and β-hydrogens of each thiophene are substituted by an amino (electron-donating) group and/or a nitro (electron-withdrawing) group. Through NEGF-DFT calculations, rectification behavior was observed in the *I–V* characteristics.

2.3 D-Perpendicular-A-Type Molecules

Elbing et al. designed a weakly coupled D-A system [26]. The molecule consisted of phenyl-ethynyl-phenyl (an electron-donating part, D) and fluorophenyl-ethynyl-

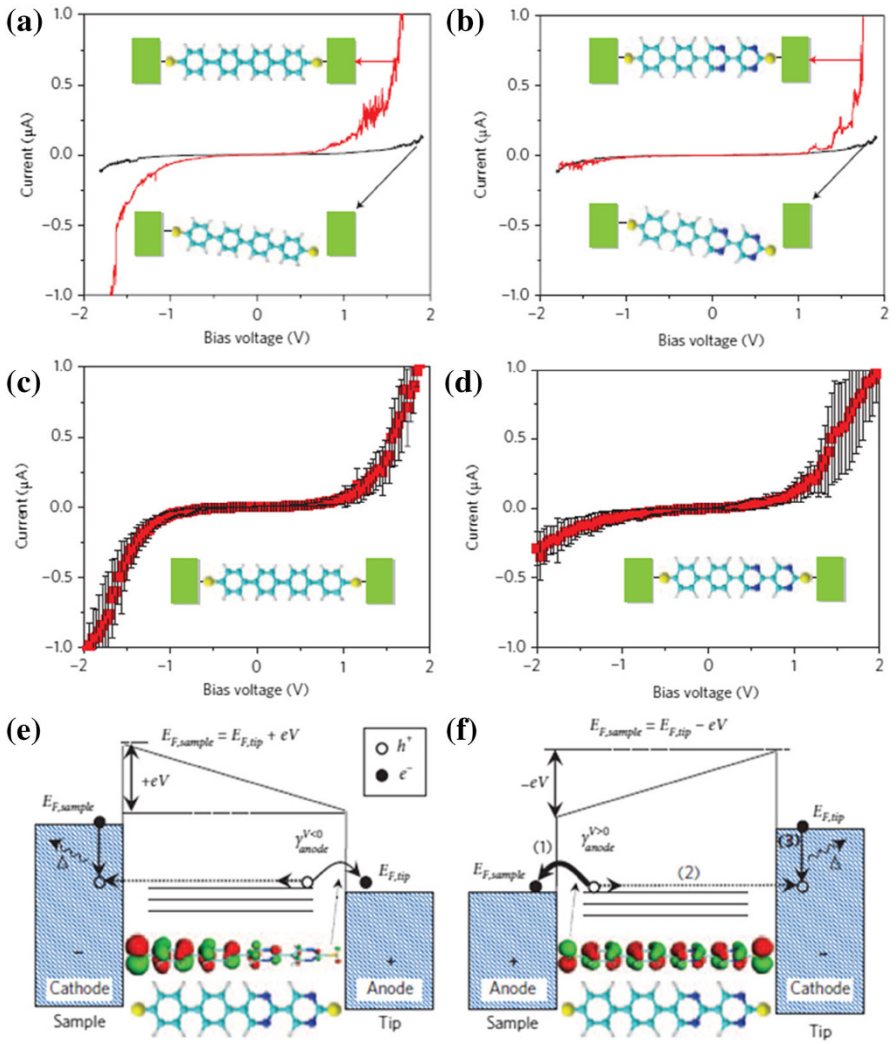

Fig. 2 a–f Current–voltage (*I–V*) curves for **a**, **c** a symmetric tetraphenyl molecule and **b**, **d** a diblock diode, and representations of the rectification mechanisms of diblock diodes with **e** negatively and **f** positively biased tips [20]. Adapted with the permission of Macmillan Publishers Ltd.: *Nature Chemistry*, copyright 2009

phenyl (an electron-accepting part, A) π-systems, which are fused by a biphenylic C–C bond (Fig. 4a). The steric repulsion of the two methyl groups *ortho* to the biphenylic C–C link results in a torsion angle of 75° in the crystal (87° from DFT calculations [27]) to separate both π-systems. The *I–V* characteristics were measured using the MCBJ technique (Fig. 4b, c). Rectification behavior was observed only in the case of Diode-5, with control experiments not showing rectification with Molecule-1 and -2. The same result was obtained through NEGF-DFT calculations [27]. Further, it was revealed that the asymmetric evolutions and

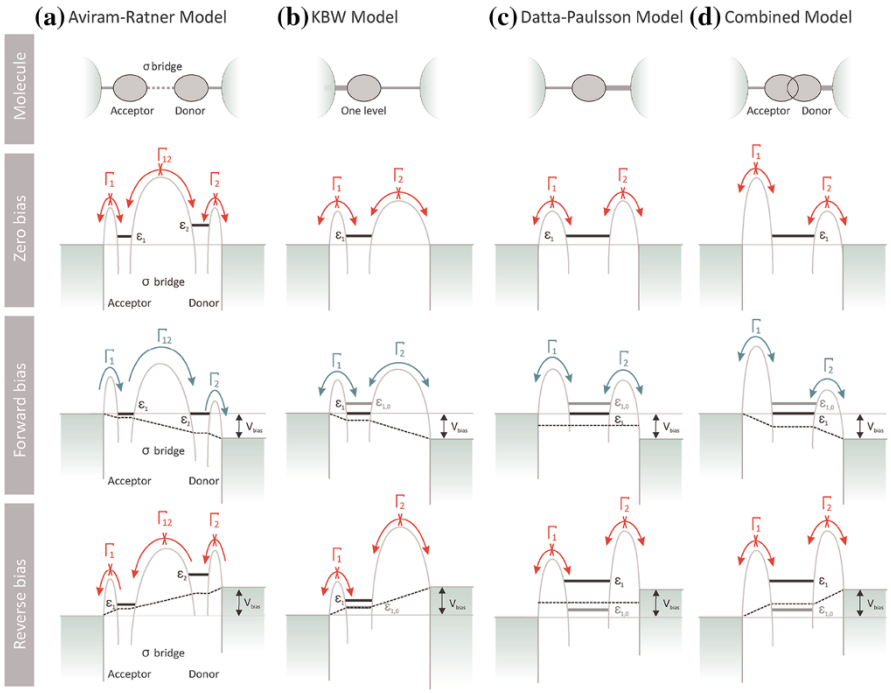

Fig. 3 Comparison of models for a single-molecule diode. (*a*) The AR-type diode mentioned above. (*b*) The Kornilovitch, Bratkovsky, and Williams (KBW) model. In this model, the asymmetric tunneling barrier is responsible for rectification. (*c*) The Datta–Paulsson (DP) model, in which the charging of the energy levels was considered. (*d*) Combined model based on the KBW and DP models. Adapted with permission from *ACS Nano*, copyright 2012 [21]

the alignment of the molecular projected self-consistent Hamiltonian (MPSH) states [25, 28, 29] of the molecular diode under the applied bias are required to generate the observed rectification behavior.

Handayani et al. designed D-perpendicular-A-type molecules in which the naphthalene (acceptor) moiety is connected to a porphyrin (donor) unit at the *meso* position (Diode-6, -7, -8, and -9), as shown in Fig. 5 [30]. The molecules have hydroxyl-anchoring groups at both ends to connect with gold electrodes or carbon nanotube (CNT) electrodes. While rectification was not observed experimentally in this molecule, it shows promise as a single-molecule rectifier.

2.4 Non-D-A-Type Molecules

Liu et al. used computational studies to demonstrate the plausibility of fabricating excellent molecular diodes using asymmetric metallocenes (Diode-10), wherein the distances between the two anchoring thiol groups and the metallocenes differ (Fig. 6) [31]. In the proposed molecular design, it is expected that there will be an asymmetric potential drop along the molecule. A resonant level that provides a link between the left and right electrodes is considered, with the level being more

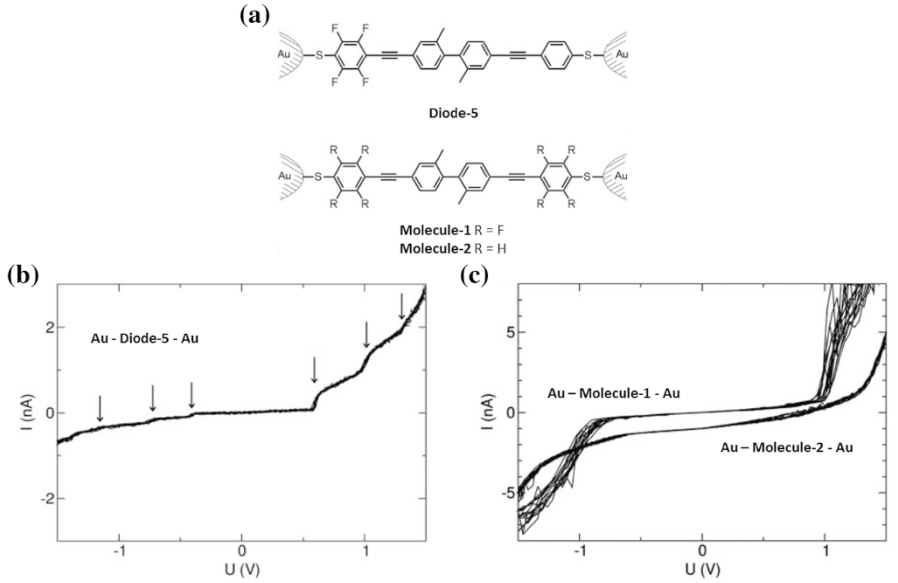

Fig. 4 **a** Schematics of a single-molecule bridge with an asymmetric diode (Diode-5) and symmetric molecules (Molecule-1 and -2) designed and synthesized by Elbing et al. **b**, **c** *I–V* characteristics for molecules Diode-5, Molecule-1, and Molecule-2 as determined using the MCBJ technique. Copyright 2005 National Academy of Science [26]

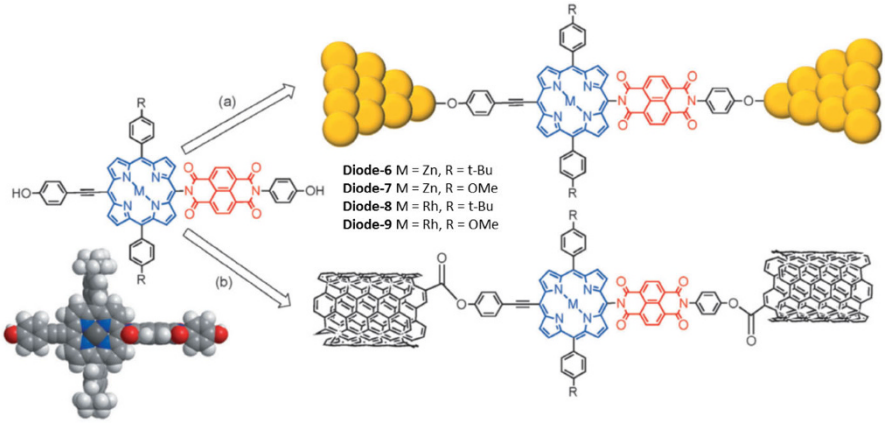

Fig. 5 Chemical structure of a porphyrin-naphthalenediimide molecule and schematics of Au-molecule-Au and CNT-molecule-CNT junctions. Adapted with the permission of Wiley, copyright 2014 [30]

strongly coupled to the right electrode than to the left one. Without a loss in generality, the authors assume that the energy of the level is slightly higher than the equilibrium chemical potential. Further, it is assumed that the level is more strongly coupled to the right electrode than to the left. When a bias voltage is applied, the resonant level will track the chemical potential of the right electrode, while most of

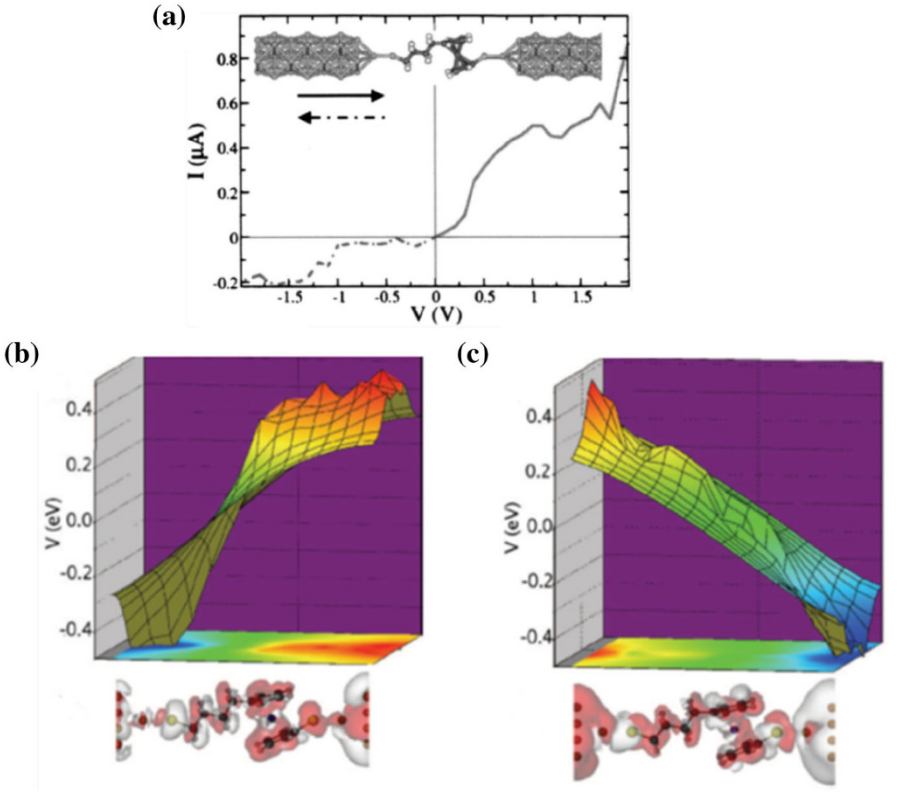

Fig. 6 **a** Chemical structure of the studied cobaltocene derivative Diode-10. **b** Calculated *I–V* characteristic of Diode-10. *Inset* shows the system studied. **c**, **d** Voltage profile and change in charge distribution upon application of biases of −1 and +1 eV. *Red* and *light-gray colors* denote positive and negative differences in charge, respectively. Reprinted with the permission of AIP Publishing [31]

the voltage drop will occur between the left electrode and the resonant level. Thus, a forward bias results in a flow of current from the left to the right. In contrast, under a reverse bias, the resonant level will have higher energy than the two chemical potentials, resulting in a poor current flow. Because of this mechanism, it should be possible to achieve rectification. The potential drop in the molecules can be highly nonuniform based on the characteristics of the different chemical bonds. The designed molecule Diode-10 has a low-conductivity covalent σ-bonded part and a high-conductivity conjugated π part, such that the potential will drop mainly at the σ-bonded part. By introducing a thiol anchoring group at the conjugated π-part, the rectification mechanism mentioned above can be realized. Moreover, the authors propose four factors for improving the effectiveness of the rectification phenomenon. (1) The degree of asymmetry. A significant difference in the voltage drops of the right and left electrodes leads to good rectification. (2) The difference in the energies of the Fermi level and the conducting molecular states. A small energy difference allows for operation at a low bias voltage. (3) The sharpness of the

resonance peak in the density of states (DOS). A sharp resonance peak reduces the leakage current under reverse bias. (4) The number of molecular conducting states. When the conducting states are symmetrical in the bias window, the forward and reverse voltage thresholds will be the same. The reason the authors use the metallocene moiety is that organometallic molecules have smaller HOMO–LUMO gaps than organic molecules do, so factor (2) above is optimized. The calculated *I–V* characteristics of Diode-10 are shown in Fig. 6b; it can be seen that the device exhibits rectification behavior. The potential profile under a reverse negative bias (Fig. 6c) shows, as expected, insignificant variation from the right electrode to the cobaltocene moiety; this is followed by a sharp drop over the alkane chain. On the other hand, the potential drops more uniformly under a positive bias.

SAMs of molecules bearing the ferrocene moiety and an alkane chain [32] and a single-molecule bridge consisting of a similar molecule [33–35] have been found to show rectification. However, they contained an asymmetric anchoring group. Further, different metal electrodes were used.

Guo et al. reported a DNA-based molecular rectifier that was constructed by the site-specific intercalation of coralyne into a custom-designed 11-base-pair DNA duplex [36]. NEGF calculations performed using a coherent tight-bonding model based on DFT suggested that the rectification behavior was primarily attributable to the coralyne-induced local spatial asymmetry of the distribution of electron states along the DNA chain.

Troisi et al. explored voltage-controlled intramolecular stereochemical modification via computational studies [37, 38]. They analyzed the conformational motions driven by the electric field. When the molecule has a freely rotatable and strong dipole moiety, such as a C–F or C–CN bond, partial rotation of the molecule may be induced and the conformation can be changed by applying forward and reverse biases. In fact, the most stable structures under positive and negative biases were different, with the dipole following the electric field. They theoretically calculated the *I–V* characteristics for 2-(3-mercaptophenyl)acetonitrile (Diode-11) using the most stable structures at each voltage and observed rectification behavior.

2.5 D-A π-Stacked-Type Molecule

Fujii et al. measured the *I–V* characteristics of a heterogeneous π-stacking complex (Diode-12) using the STM-BJ method. They found that rectification could be realized (Fig. 7b) [39]. The heterogeneous complex was composed of triphenylene (electron donor) and naphthalenediimide (electron acceptor) inserted in a cage molecule, as shown in Fig. 7a, with the molecules forming a junction; current could tunnel along the vertical direction to the π-plane. No rectification was observed through the homogeneous complex (Molecule-3) when only triphenylene was present in the cage. However, the results of NEGF-DFT calculations indicated rectification (Fig. 7c). While the transmission in the case of the homogeneous complex was independent of the bias voltage, the transmission peak of the LUMO approached the Fermi level under positive bias and moved to a higher energy under negative bias; this is why a larger current was obtained under positive bias. The origin of the shift in the LUMO level could be determined by examining the local

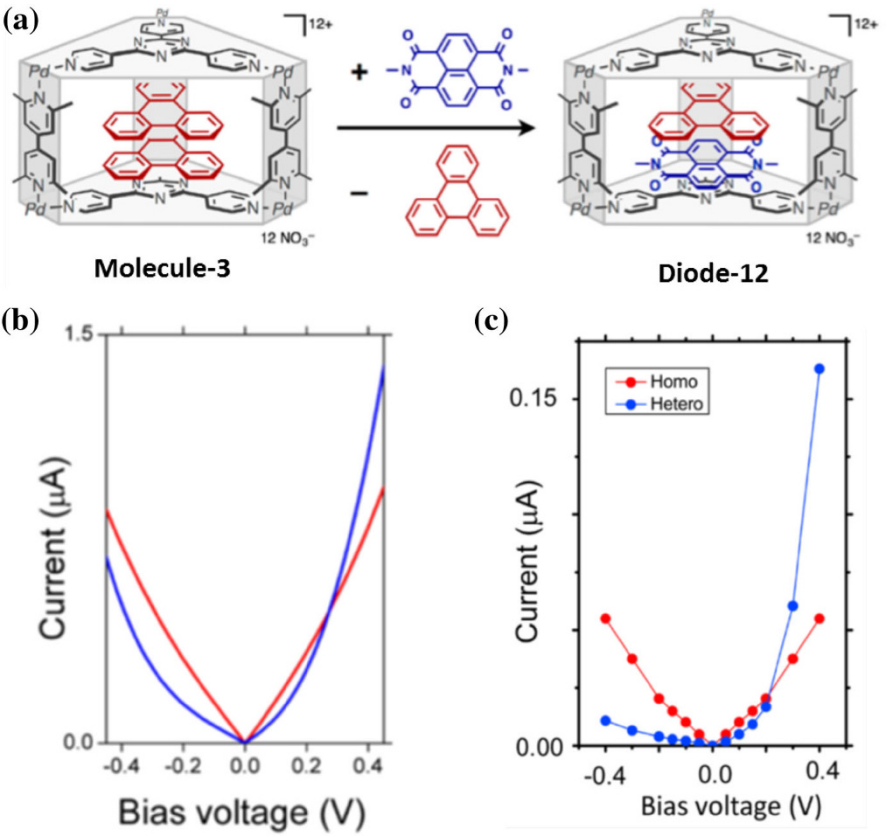

Fig. 7 **a** Chemical structures of homogeneous and heterogeneous complexes. **b**, **c** *I–V* characteristics for homogeneous (*red line*) and heterogeneous (*blue line*) complexes as determined through **b** measurements and **c** calculations. Adapted with the permission of the American Chemical Society, copyright 2015 [39]

DOS. The local DOS corresponding to the LUMO peak showed strong hybridization with one electrode. This asymmetric contribution of the transmission LUMO channel resulted in bias-voltage-dependent transport.

Based on computational studies, Fomine's group reported that various pairs of charge-transfer complexes (Diode-13) exhibit rectification behavior [40–42]. The *I–V* characteristics of the complexes of a free base or a metal porphyrin (donor) with fullerene [60] (acceptor) were calculated. The results indicated that the complex of zinc porphyrin with fullerene [60] exhibited the highest rectification ratio.

2.6 Summary

Though there have been several computational reports on the design of molecular rectifiers, the number of experimental studies wherein rectification has been observed remains limited. The single-molecule rectifiers confirmed experimentally are D-A directly-connected-type molecules such as the Diode-4 molecule [20],

D-perpendicular-A-type molecules such as Diode-5, which are fused by a biphenylic C–C bond [26], or D-A π-stacked-type molecules such as Diode-12 [39]; all of these have D and A moieties. In other words, a molecule with D and A moieties that are not conjugated to each other would be a suitable candidate for a single-molecule rectifier. However, to the best of our knowledge, there is no experimental report of D-σ-A-type molecules, which were originally proposed by AR. One of the reasons for this is a technical one: owing to the presence of a σ component in the molecule, the single-molecule electronic resistance increases, making the observed current smaller than what can be measured at the appropriate bias voltages.

As mentioned above, there have been several attempts to confirm whether rectification was realized. However, it remains difficult to design a high-performance single-molecule rectifier that exhibits a high rectification ratio and a low threshold voltage. One can modify molecular structures by adding various substituents to the D or A moieties. This would allow the dependence of the rectification properties on the molecular structure to be explored. Furthermore, in addition to D-A systems, organic chemists should explore other novel molecular systems too.

3 Negative Differential Resistance (NDR)

The NDR, which is a widely exploited feature in electronic semiconductor devices, is characterized by a decrease in the current when the voltage is increased. NDR behavior should be readily realizable in single-molecule devices because the electrical state of the molecule can be changed by varying the applied voltage, owing to the redox reaction that occurs. Here, we summarize three models: charging, conformation changing, and level matching.

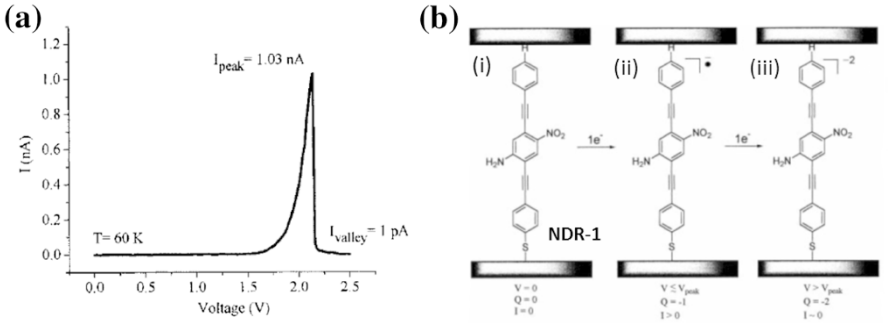

Fig. 8 **a** *I–V* characteristics of a Au-NDR-1-Au device at 60 K. **b** Potential mechanism responsible for NDR behavior. As voltage is applied, the molecules (*i*) undergo one-electron reduction to form radical anion (*ii*), which results in a conductive state. Further increasing the voltage causes another one-electron reduction, leading to the formation of insulating dianion state (*iii*). Reprinted with the permission of the AAAS, copyright 1999 [43]

3.1 Charging Model

The first instance of NDR in an organic molecule was reported by Chen et al. in 1999 in the case of a SAM of molecule NDR-1 between Au electrodes (Fig. 8a) [43]. The proposed mechanism for the NDR is a two-step reduction process that modifies charge transport through the molecule (Fig. 8b). As the applied voltage is increased, the molecule undergoes a one-electron reduction to form the radical anion, resulting in high conductivity through the molecule. A further increase in the voltage causes a second electron reduction, leading to the formation of the dianion state and the subsequent blocking of the current. The width of the current peak ($\sim$0.7 V) correlates well with the difference in the one-electron and two-electron peak reduction potentials ($\Delta E_p = 0.63$ V for the molecule with no thiol group [44]). NDR behavior was not observed in the control molecule, which did not have any amino or nitro groups.

A series of similar oligo(phenylene ethynylene) molecules were studied in terms of their electrochemical potentials, molecular orbitals [45], and *I–V* characteristics using the cAFM technique [46], the scanning probe microscopy (SPM) technique [47–49], DFT calculations [50, 51], and theoretical calculations based on a polaron model [52] in order to elucidate the underlying mechanism.

3.2 Conformation Change Model

Zhou et al. measured the *I–V* characteristics of a thiol-terminated Ru bis-terpyridine (NDR-2) molecule using the STM-BJ technique (Fig. 9a) and were able to observe low-bias NDR characteristics [53]. During the single-molecule measurements, three single-molecule conductance values (G_L, G_M, and G_H) were obtained from the three different bridge conformations (top–top, hollow–top, and hollow–hollow) [54, 55]. NDR behavior was only observed in the hollow-top conformation (Fig. 9b), which indicated that the NDR is not only intrinsic to the molecule but also contact-conformation dependent. They monitored the changes in the force during the bias sweep (Fig. 9c). The greatest change in the force occurred at the bias at which the NDR was observed. On the basis of a statistical analysis of 50 *I–V* curves, it was determined that the NDR peak always accompanies a force peak (Fig. 9d). The peaks showing the changes in the average force were located at a bias of 0.601 ± 0.171 V, with the change in the force being 0.319 ± 0.098 nN. The changes in the force were likely caused by changes in the molecule–electrode coupling induced by the bias. It is also possible that the conformational relaxation of the molecular junctions was caused by the bias-induced twisting of the molecular structures or the bias charging of a redox-active center, as in the polaron model [52]. This suggests that the coupling between the molecular core of NDR-2 and the contacts results in the NDR behavior.

3.3 Level Matching Model

Pati et al. investigated the transport properties of Fe bis-terpyridine between gold electrodes using NEGF-DFT calculations [56]. The calculated *I–V* characteristics

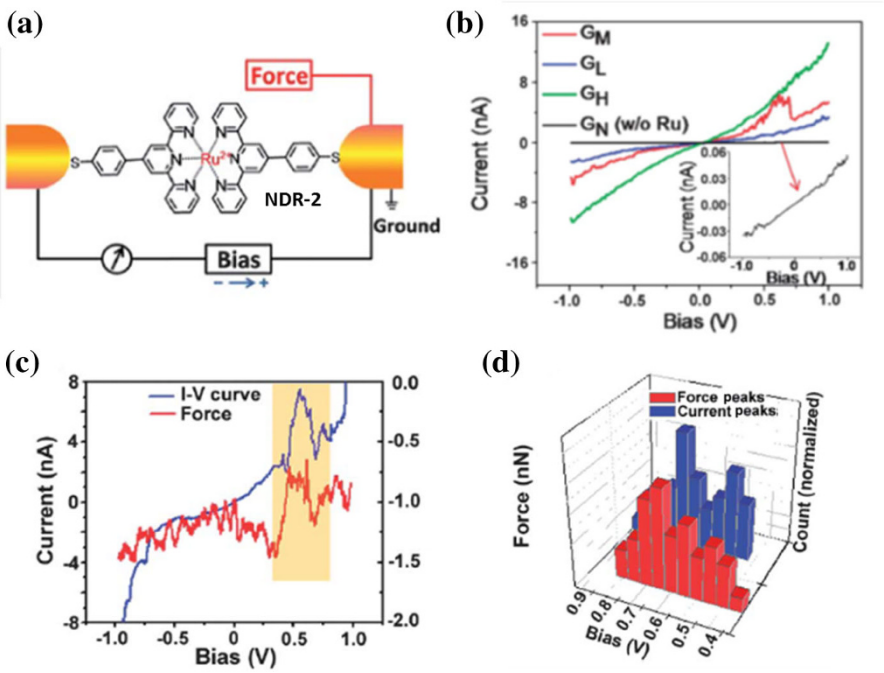

Fig. 9 **a** Schematic image of a single-molecule junction between electrodes as obtained by the STM-BJ method. **b** *I–V* characteristics of thiol-terminated Ru bis-terpyridine molecule in each bridge conformation. **c** Representative monitored *I–V* curves (*blue*) and force changes (*red*). *Shaded area* shows NDR and force peaks. **d** Histograms of NDR peak position (*blue*) and force peak position (*red*) corresponding to 50 curves each, as shown in **c**. Reproduced with the permission of The Royal Society of Chemistry [53]

were indicative of NDR behavior. To elucidate the origins of the NDR, they calculated the transmissions of a molecular junction as a function of the bias voltage. They found that the bias-dependent transition in the broken-symmetry phase of the molecular wavefunction leads to a nonlinear change in the coupling between the molecule and the lead, which results in the observed NDR.

Perrin et al. observed an intrinsic and pronounced NDR effect in a single thiolated-arylethynylene molecule with a 9,10-dihydroanthracene core (NDR-3 in Scheme 2) using the MCBJ technique at 6 K (Fig. 10a). In contrast, a fully conjugated molecule with an anthracene core (Molecule-4 in Scheme 2) did not show NDR (Fig. 10b). They conducted NEFG-DFT calculations to obtain insights into the origin of the NDR. They transformed the HOMO and HOMO-1 into an equivalent set of localized molecular orbitals (LMOs) by addition and subtraction, and found that one LMO was located on the left half of the molecule and the other on the right half, as shown in Fig. 10c. Thus, this molecular junction system was described using a two-site model. The mechanism responsible for the NDR is as follows. At zero bias, the two states are in resonance with each other and the conductance is high (Fig. 10d). When a bias voltage is applied, the energies of the two states shift in the opposite directions (Fig. 10e). Under a large enough bias

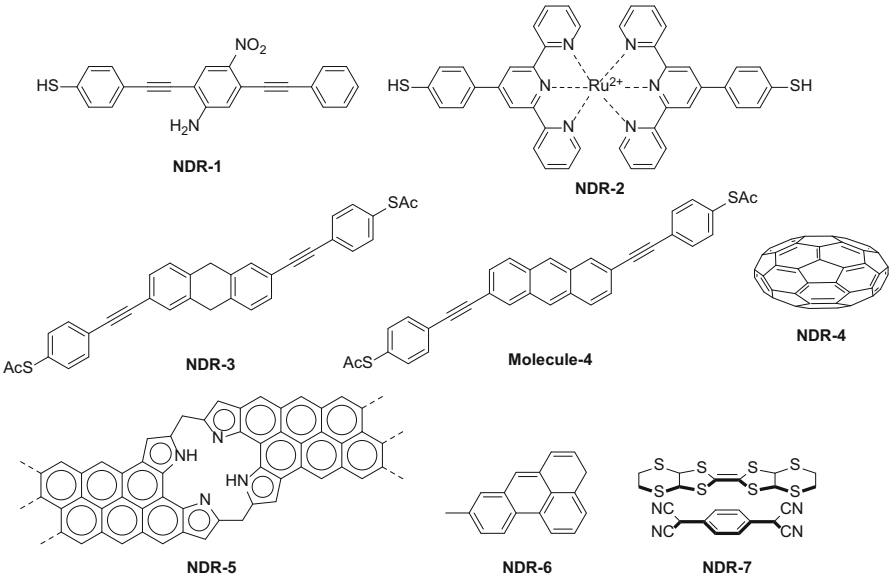

Scheme 2 Molecular structures of single-molecule NDR devices

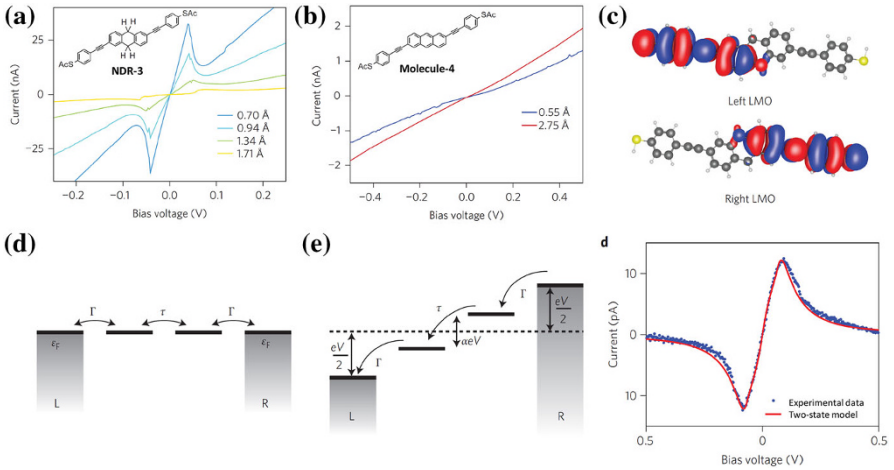

Fig. 10 **a**, **b** *I–V* characteristics recorded during one breaking event on **a** AH and **b** AC with different electrode–electrode distances. **c** Left and right LMOs obtained by calculating the sum of and the difference between HOMO and HOMO-1. **d**, **e** Energy diagrams of molecular junction **d** without and **e** with an applied bias voltage. ε_F is the Fermi energy of the gold electrodes, Γ is the tunneling coupling of each site to the neighboring electrode, and τ is the coupling parameter between two states. **f** Background-corrected *I–V* characteristics recorded for the AH molecule (*blue dots*) and fitting curve (*red solid line*) obtained using the two-state model. Adapted with the permission of Macmillan Publishers Ltd.: *Nature Nanotechnology*, copyright 2014 [57]

voltage, the current is suppressed to a high degree. The current through the two-state system was determined based on NEGF-DFT calculations; the results are shown in Fig. 10f. That there was excellent agreement between the results supports the use of this two-state model to describe transport through the NDR-3 molecule. In contrast, similar calculations for Molecule-4 did not show the NDR effect.

Based on computational studies, the following molecules were proposed for use as single-molecule NDR devices: squashed fullerene (NDR-4) [58], a porphyrin-based molecule embedded between graphene-nanoribbon electrodes (NDR-5) [59], a pyrene-based molecule with asymmetric contact geometries (NDR-6) [60], a dimer composed of bis-ethylenedithiotetrathiafulvalene (BEDT-TTF) and tetracyanoquinodimethane (TCNQ) with a donor–acceptor interaction (NDR-7) [61], and molecular junctions wherein a thiolated organic molecule bridges a pair of transition metals [62]. However, some of these devices may be technically difficult to achieve.

3.4 Summary

Contrary to our expectations, there are not many reports of NDR in single-molecule devices. The probable reasons for this are that the voltage required for the redox reactions is too high for metal-molecule-metal junctions to endure. To overcome this limitation, one can reduce the redox potential by changing the molecular structure.

From the viewpoint of an organic chemist, the charging model is the most acceptable one for optimizing the molecular structure. The electrical properties of the molecule can be modified by changing the substituents in the molecule.

4 Switching

Switches are widely used devices that exhibit ON and OFF states in response to an external stimulus: touching, pushing, sliding, heating, light or radio wave irradiation, among others. In the same manner, single-molecule switches are single-molecule devices that are sensitive to such external stimuli and exhibit high (ON) and low (OFF) conductance states. In this review, we focus on four types of external stimuli: optical, electrical, chemical, and mechanical.

4.1 Optical Stimulus

The first experimentally realized single-molecule photoswitch was based on diarylethene derivatives (Switch-1 in Scheme 3) [63, 64]. Diarylethene is a well-known photochromic moiety in which the photochromic reaction occurs reversibly between the open form with a hexatriene structure and the closed form with a cyclohexadiene structure under irradiation with light of specific wavelengths (Fig. 11a). The closed form has a completely π-conjugated electronic system that works as a current path, resulting in a higher conductivity than that of the open form. Dulic et al. measured conduction through a Au-(Switch-1)-Au junction using

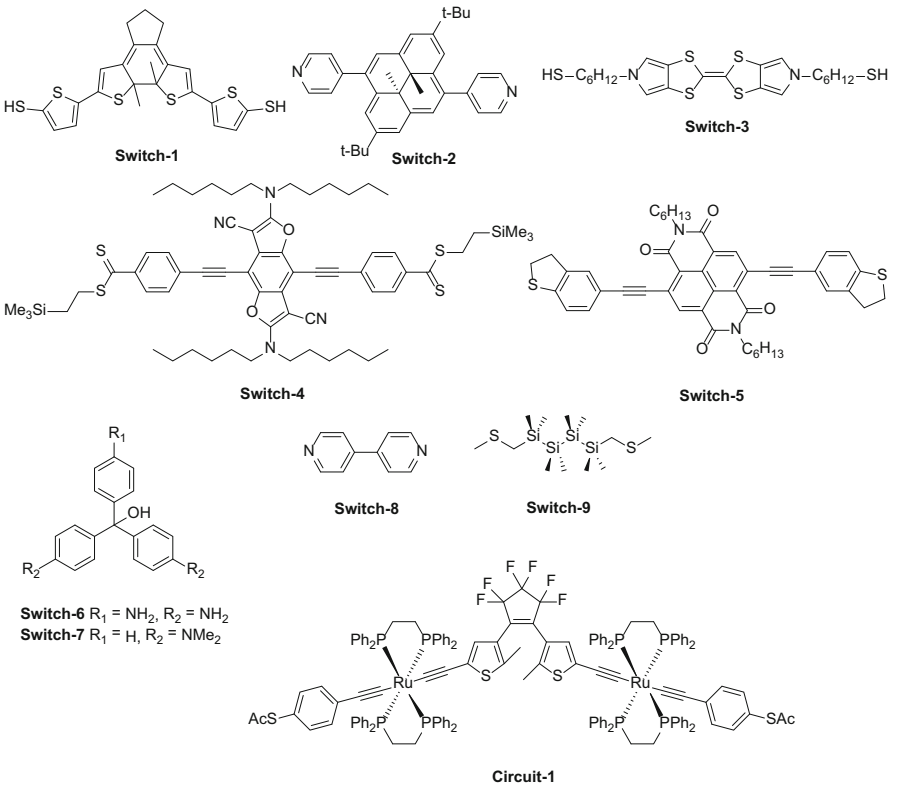

Scheme 3 Molecular structures of single-molecule switches and a circuit

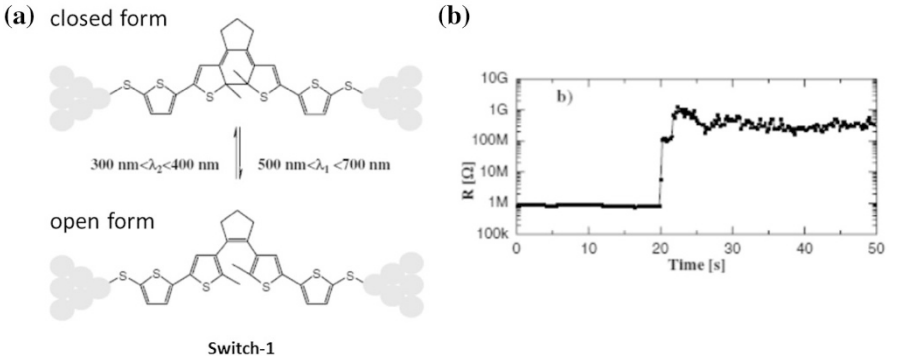

Fig. 11 **a** Chemical structure of dithienylethene in closed and open forms. **b** Resistance vs. time curve for the Au-dithienylethene-Au junction. At $t = 0$, a lamp was turned on ($\lambda = 546$ nm). Reprinted with the permission of the American Physical Society, copyright 2003 [65]

the MCBJ technique [65]. Although they succeeded in observing a decrease in the conductance of approximately three orders of magnitude owing to isomerization from the closed form to the open one, the reverse process did not take place. They performed control experiments with a Au-air-Au junction and a Au-trithiophene-Au junction under irradiation but did not observe any jumps in the conductance (Fig. 11b). Thus, it was confirmed that the change in the conductance was attributable to the isomerization of the diarylethene moiety. Similar experiments on photochromic switching using dithienylethene derivatives with different anchoring groups were performed by two other groups with the STM-BJ technique [66, 67]. Kim et al. measured the *I–V* characteristics of four different difurylethene molecules in both open and closed forms using the MCBJ technique [68]. They observed that the conductance switching ratio is dependent on the type of anchoring group used. Computational studies were conducted on the Au-diarylethene-Au junction [69, 70]. Reversible photoswitching behavior was only observed in the graphene-diarylethene-graphene junction when many molecular junctions were used in the device [9].

A reversible single-molecule photoswitch was realized by Roldan et al. [71]. They used the molecule Switch-2, which has dimethyldihydropyrene (DHP)/cyclophanediene (CPD) isomeric structures, as shown in Fig. 12a. DHP is a polycyclic π-conjugated (highly conductive) unit that optically transforms into a less π-conjugated (less conductive) CPD isomer. CPD reversibly reverted both photochemically and thermally to DHP. MCBJ measurements were performed, and fully reversible photoswitching behavior was observed (Fig. 12b).

4.2 Electrochemical Stimulus

SMC switching through electrochemical gating has been reported using a bipyridinium ion [72], oligo(phenylenediamine) derivatives [73], and perylene diimide derivatives. Kay et al. observed "OFF-ON-OFF-ON-OFF" conductance switching behavior in the case of the molecule Switch-3 using the STM-BJ technique in an ionic liquid [74]. The molecule Switch-3 can take monocationic

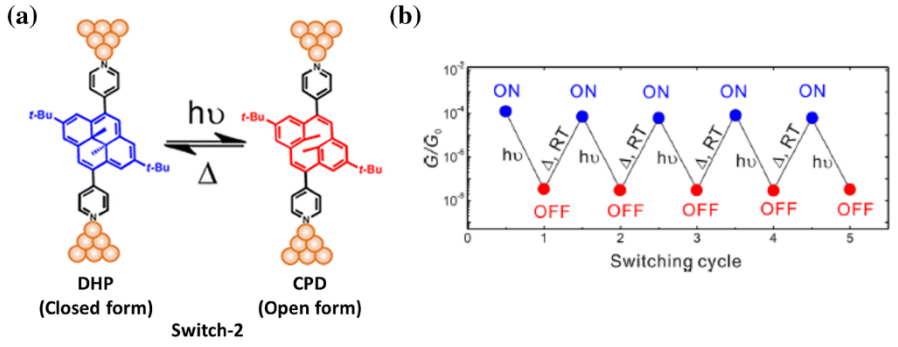

Fig. 12 **a** Isomerization of the DHP/CPD system. **b** Fully reversible cycles of photothermally triggered SMC switching between DHP (ON state) and CPD (OFF state). Adapted with the permission of the American Chemical Society, copyright 2013 [71]

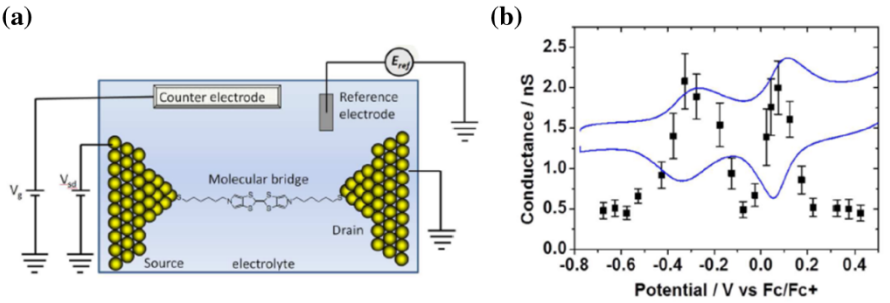

Fig. 13 Cyclic voltammogram (*blue line*) and plot of SMC against sample electrochemical potential for Switch-3. Adapted with the permission of the American Chemical Society, copyright 2012 [74]

(Switch-$3^{\bullet+}$) and dicationic (Switch-3^{2+}) forms. The SMC of Switch-3 was measured by scanning the electrochemical potential, as shown in Fig. 13 (black marks). The conductance curve showed two peaks corresponding to the redox transitions of the molecule.

Li et al. observed the electrochemical switching of the SMC in the molecule Switch-4, which has redox-active benzodifuran as the core, using the STM-BJ and MCBJ techniques [75]. A unique result was observed: the ON/OFF ratio was three times higher when carbodithioate ($–CS_2^-$) was used as the anchoring group instead of thiolate ($–S^-$). This is because the single-molecule resistance with the $–CS_2^-$ anchoring group was lower than that with the $–S^-$ group, so that the effect of the change of resistance of the core part was larger in the case of the former anchoring group.

Li et al. studied charge transport through core-substituted naphthalenediimide (Switch-5) using the STM-BJ technique [76]. Switch-5 has three redox states: neutral, radical anion, and dianion species. These species demonstrated electrochemical gating in an ionic liquid, with reversible conductance switching behavior observed between the three species. The authors performed NEGF-DFT calculations related to the charge double layer in the molecular junction formed by the ions in the supporting electrolyte. The results agreed qualitatively with those obtained experimentally.

4.3 Chemical Stimulus

Li et al. realized SMC switching by changing the pH of the solution while using Switch-6 and -7 in acidic and basic solutions, as shown in Fig. 14 [77]. Under acidic conditions (pH 5.5) Switch-6 and -7 are in the conjugated form, while they lose the conjugation under basic conditions (pH 13.6) due to the introduction of an OH group at the central carbon atom (Fig. 14a). The SMC values under acidic conditions were two orders of magnitude higher than those under basic conditions; this was true for both Switch-6 and -7. Sequential switching was demonstrated by modulating the pH, and a reversible change in conductance was observed (Fig. 14b, c). A control experiment with octanedithiol showed no dependence on pH. NEGF-

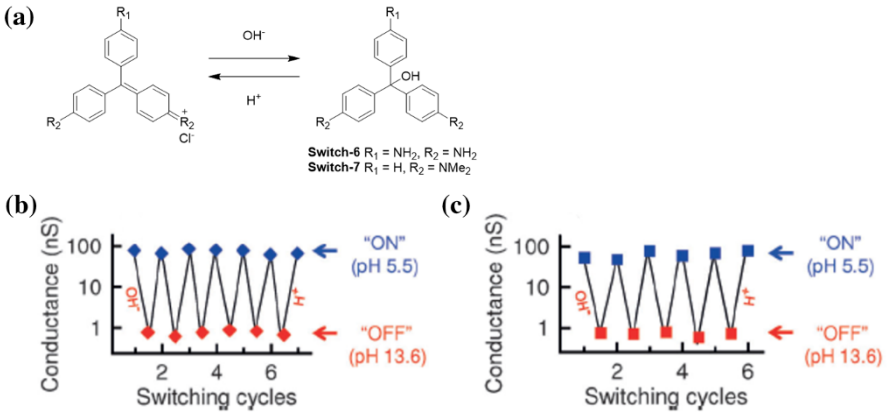

Fig. 14 **a** Molecular structures of Switch-6 and -7 at different pH values. Sequential cycles of pH-induced conductance switching of **b** Switch-6 and **c** Switch-7 are shown. Adapted with the permission of Wiley, copyright 2014 [77]

DFT calculations predicted that the transmission through either Switch-6 or -7 at pH 5.5 was more than two orders of magnitude higher than that at pH 13.6; this was in agreement with the experimentally measured conductance values.

4.4 Mechanical Stimulus

Quek et al. demonstrated a mechanically driven single-molecule switch using the STM-BJ method [78]. They found that the 4,4′-bipyridine derivative (Switch-8) exhibited two different SMC values (high and low G) in the conductance histograms (Fig. 15a). Further, the switching of the SMC could be realized by mechanically manipulating the Au–Au distance (Fig. 15b). The transmissions in 55 relaxed junctions were calculated in order to determine the dependencies of the conductance on the vertical distance between the Au electrodes, the angle α between the nitrogen–gold bond and the π-system, and the minimum carbon–gold distance. The mechanism of switching was found to be the following: (1) an initially broken Au contact has a Au–Au separation that is too small to accommodate a bipyridine molecule in a vertical geometry (Fig. 15c); (2) a molecular junction is formed in the high-G configuration; (3) as the junction is elongated, the high-G geometry tends to snap to a low-G one; (4) in contrast, as the junction is compressed, the junction switches to the tilted (high-G) geometry.

Similar switching behavior based on the mechanical modulation of Au–Au distances was observed in the case of permethyloligosilanes (Switch-9) by Su et al. using STM-BJ measurements [79]. In contrast, the 1,8-bis(methylthio)octane molecular bridge showed constant conductance. By comparing an entire series of oligosilanes, it was concluded that the switching behavior did not arise from a change in the internal Si–Si–Si–Si dihedral geometry but from the change in the dihedral geometry of the two terminals (Me–S–CH_2–$SiMe_2$–). It is likely that the

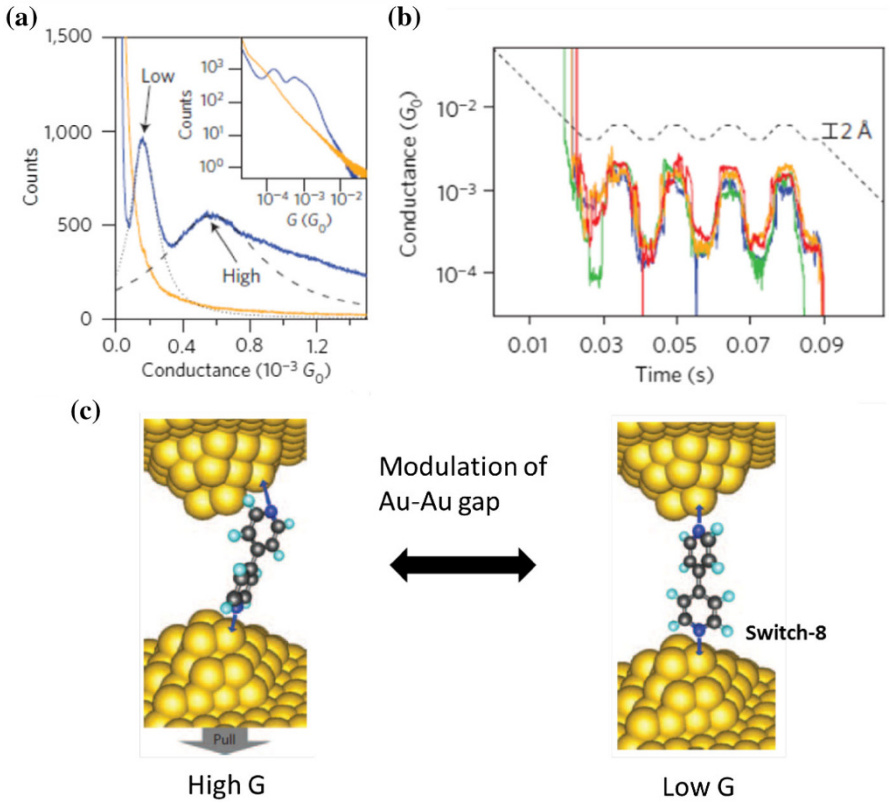

Fig. 15 **a** Conductance histogram of Switch-8 (*blue line*). Also shown is a histogram of conductance measured in solvent alone (*yellow*). *Black dashed lines* represent Lorentzian fits of the two peaks. *Inset* is the same histogram shown on a log–log scale. **b** Sample bipyridine switching conductance traces (*colored solid lines*). These traces were recorded while applying nonlinear ramps (*dashed black line*) with a STM tip. **c** Schematics illustrating high-G and low-G configurations, which exhibited mechanically induced switching in the case of junctions. Adapted with the permission of Macmillan Publishers Ltd.: *Nature Nanotechnology*, copyright 2009 [78]

terminal dihedral angles are particularly sensitive to changes in the Au–Au distance because the sulfur lone pairs are easily affected by the Au atoms. This hypothesis was confirmed by DFT analysis. The total potential energies of the A–A, O–A, and O–O conformers (Fig. 16a) were calculated for various Au–Au distances (Fig. 16b), and the most favorable conformers for each Au–Au distance were estimated. Tunneling-coupling calculations were performed on the lowest-energy geometries optimized without any dihedral constraints; the results were indicative of the switching mechanism of the SMC (Fig. 16c). The O–O conformer is favorable for longer Au–Au distances and the junction shows high conductance; on the other hand, the O–A or A–A conformer is favorable for shorter Au–Au distances and the junction shows low conductance. A similar DFT analysis was conducted for the 1,6-bis(methylthio)hexane junction. The results showed that there is no change in the

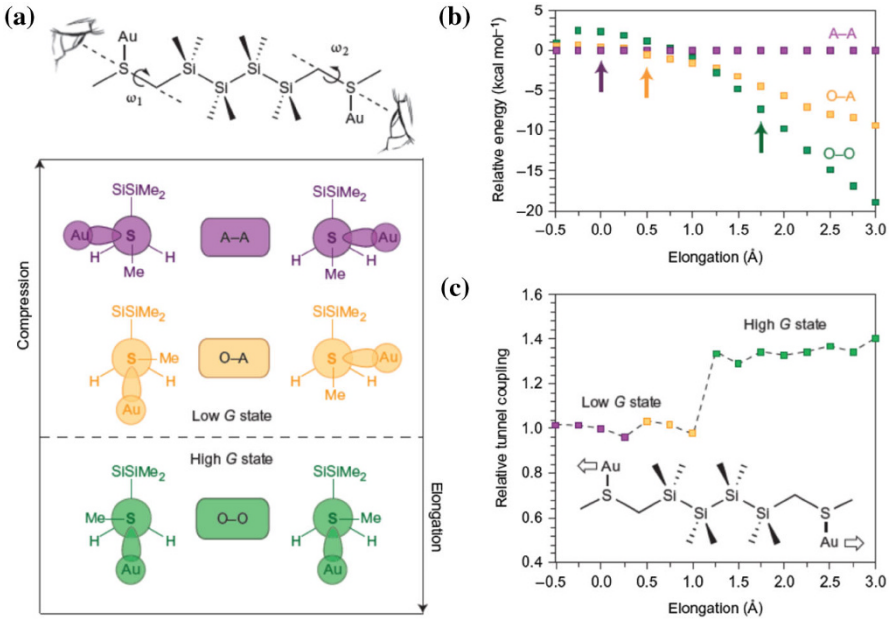

Fig. 16 **a** Newman projections for A–A (*purple*), O–A (*yellow*), and O–O (*green*) dihedral configurations from perspective of the sulfur-methylene σ-bond in the Au-oligosilane-Au junction. **b** Relative energies of A–A, O–A, and O–O conformers in the Au-oligosilane-Au junction as determined by subtracting the total energy of the A–A conformer at each Au–Au distance. *Colored arrows* denote specific Au–Au distances at which each configuration experiences its lowest total energy. **c** Tunneling coupling as a function of Au–Au distance plotted relative to tunnel coupling at the elongation = 0 point for the Au-oligosilane-Au junction. Tunneling-coupling calculations were performed for the lowest-energy geometries, which were optimized without a dihedral constraint. Adapted with the permission of Macmillan Publishers Ltd.: *Nature Chemistry*, copyright 2015 [79]

conduction at any of the Au–Au distances because of the poor conjugation of the C–C σ-bond. Thus, strong σ-conjugation in the oligosilane backbone is important.

4.5 Summary

As shown above, various single-molecule switches have been investigated. However, only a few single-molecular switches, namely Switch-8 and -9, exhibit switching behavior while maintaining the metal-molecule-metal junction. Although these switches are reversible and allow for the junction to be maintained, the STM-BJ technique was used. Further, the number of switching cycles was limited because of the low junction stability. Thus, observations of the switching behavior using the MCBJ method, wherein a more stable molecular junction can be formed, are desired.

As for the relationship between the molecular structures and the switching properties, as expected, no clear interpretation could be made because we primarily focused on the switching behavior and did not perform any chemical modifications.

However, by optimizing the molecular structures, one can ensure better performance, such as a high ON/OFF ratio and stable ON and OFF states.

5 Integration of Single-Molecule Electronic Devices

Logic gates are important components in information processing, and there have been several attempts to realize them using organic compounds, including using photoluminescent molecules [80], DNA molecules [81, 82], ion transistors [83], bacteria [84], enzymes [85], and SAM devices [86].

Meng et al. succeeded in fabricating single-molecule resettable logic gates using the molecule Circuit-1 [87]. They synthesized a dithienylethene photochromic unit bearing redox-active ruthenium complexes at both ends (Fig. 17a), and realized multifunctional switching properties through light irradiation and/or electrochemical gating. The charge-transport properties of this molecular device were measured between gold nanoelectrodes fabricated by on-wire lithography; the device acted as an OR logic gate in response to optical and electrochemical stimuli (Fig. 17a–c). The two distinct states corresponding to the device's conductivity could be clearly observed after different cycles. Reversible photo- and electron-triggered resistive switching could be induced for several cycles and the bi-state system could be maintained, suggesting that such a device is potentially applicable in resettable electronic logic gates. A multi-addressable molecular device composed of two dithienylethenes and three ruthenium complexes was also synthesized and tested; it was found that the device could function as an AND-OR logic gate.

How can single-molecule devices be integrated in the desired sequences? One efficient method is through the sequential coupling of reactions. In this manner, different units can be connected in a stepwise fashion based on cycles of (1) a cross-coupling reaction involving units with deactivated functional groups and (2) the activation of the functional group [88–90]. For example, as shown in Scheme 4 [90], a porphyrin unit with a triflate group and a porphyrin unit with a hydroxyl group and a boronic ester were first connected via a cross-coupling reaction. Next, the hydroxyl group in the obtained dimer was activated by triflation; this was followed by the cross-coupling reaction with the dimer, porphyrin unit bearing a hydroxyl group, and boronic ester, affording a trimer. With this molecular design, each porphyrin unit was connected via a phenylene linker, with the energy levels of the units being independent, as demonstrated by the results of optical and electrochemical measurements and DFT calculations. In fact, STS measurements were performed on an isolated zinc porphyrin trimer on a Au(111) surface (Fig. 18a). It was observed that the LUMO energy of each zinc porphyrin unit was slightly different (Fig. 18d) [91].

Any type of molecular core can be used as the unit in this strategy, meaning that the various functional molecular structures mentioned in the previous sections can be integrated in a programmed order. This should result in the desired logic gates and "molecular circuits".

Can charge transport through integrated molecular circuits be evaluated? The functionalities of such circuits would depend on those of the components. In 2008,

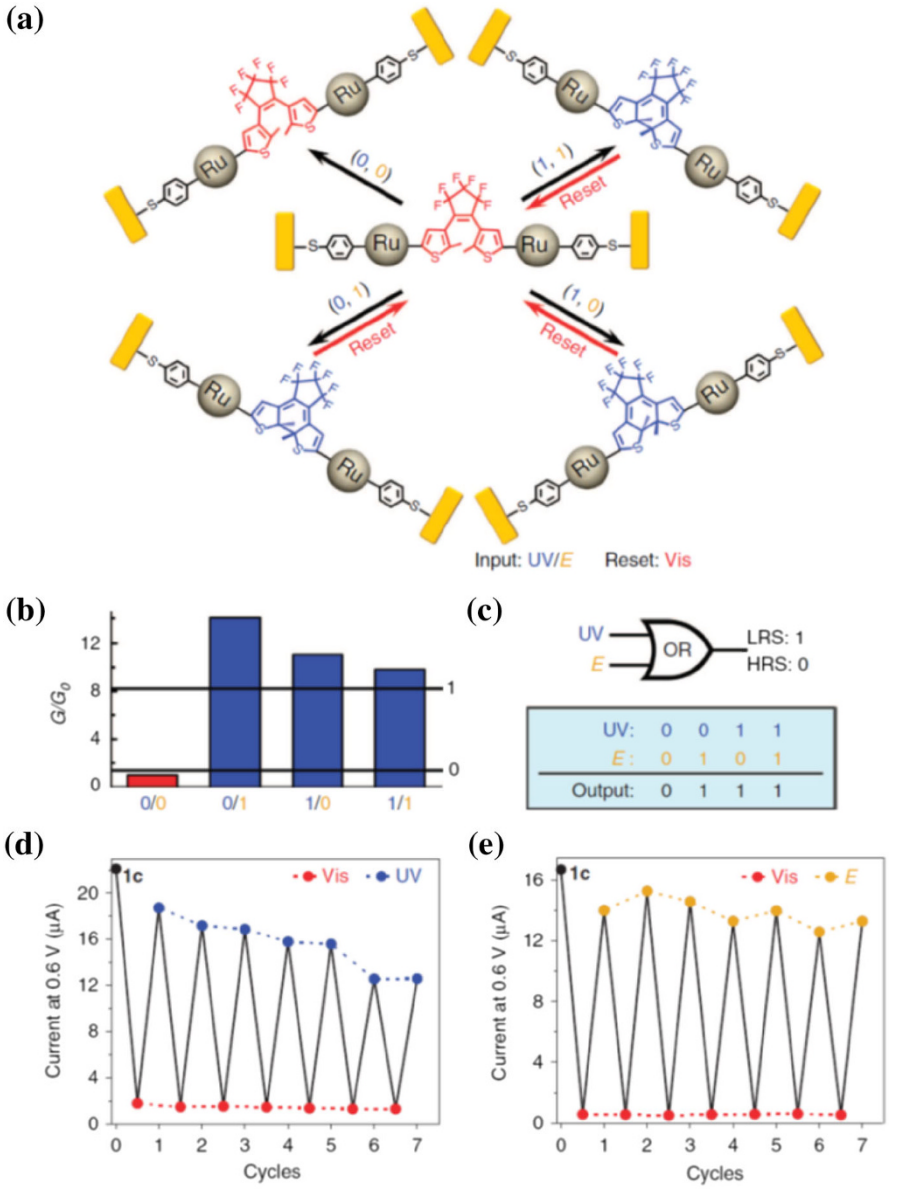

Fig. 17 **a** Scheme of a logic gate based on a target molecule with one dithienylethene and two ruthenium complex moieties: isomerization within nanogap devices under different inputs (UV irradiation and electrolysis). Resetting is triggered by visible-light irradiation (700 nm, 2 h). **b** Change in conductance with different input combinations. **c** Symbol and truth table for OR logic gate. **d**, **e** Endurance performance: current response of the molecule under alternating visible-light irradiation (700 nm, 2 h) and **d** UV irradiation (365 nm, 30 min) or **e** electrochemical stimuli (oxidation at 450 mV and reduction at −50 mV, 10 min). Current values were recorded at 0.6 V bias in vacuum. Adapted with the permission of Macmillan Publishers Ltd.: *Nature Communications*, copyright 2014

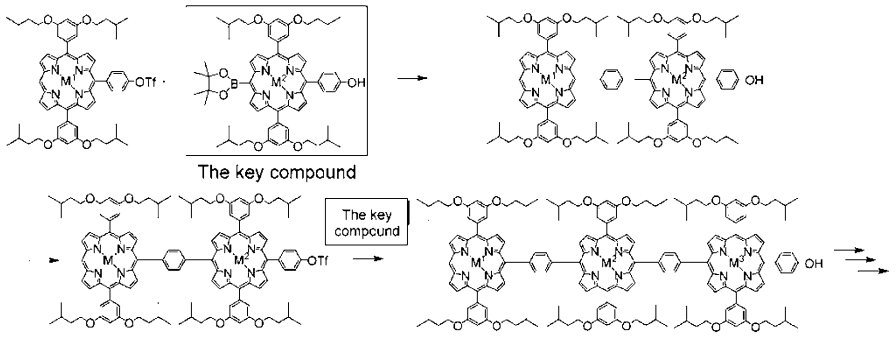

Scheme 4 Scheme for synthesizing porphyrin oligomers via consecutive coupling reactions. Reprinted with the permission of the American Chemical Society, copyright 2014 [90]

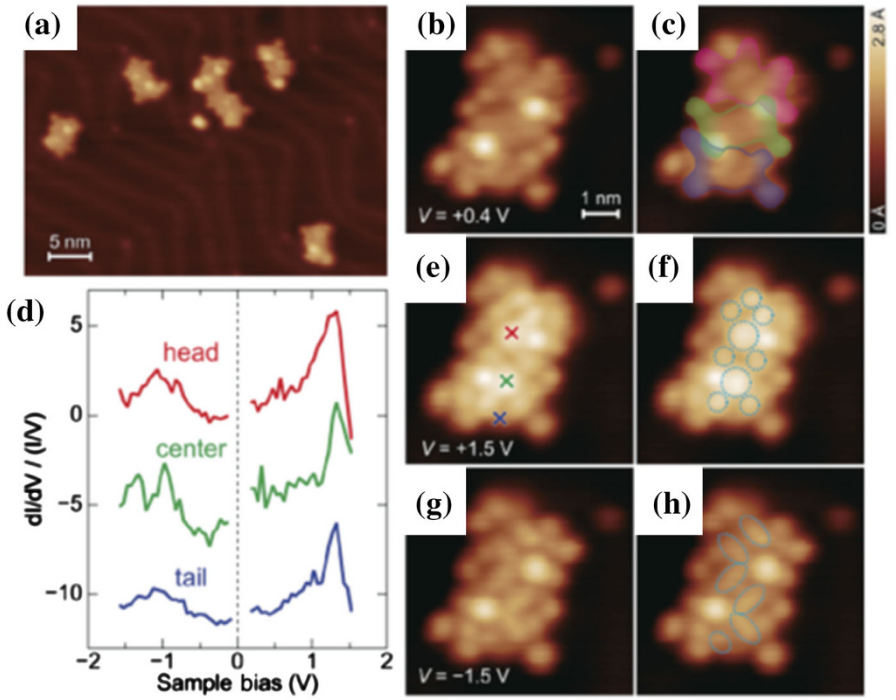

Fig. 18 **a** Typical STM images of a zinc porphyrin trimer on Au(111) ($V = +0.4$ V and $I = 50$ pA). **b**, **c**, **e**–**h** High-magnification images of the trimer acquired using $V =$ (**b**, **c**) +0.4, (**e**, **f**) +1.5, and (**g**, **h**) −1.5 V at $I = 50$ pA. **d** Normalized dI/dV curves of the trimer. *Red*, *green*, and *blue curves* were recorded at the positions in **e** marked by crosses in the corresponding colors. Reproduced with the permission of The Royal Society of Chemistry [91]

de Leeuw's group reported that electrical resistance through an integrated organic layer consisting of two different molecules could be described based on multiple transmission probabilities for each component of the junction [92]. In the case of charge transport through single-molecule devices, Chen's group reportedin 2014

that the SMC can be described as $G = G_0 T_L T_m T_R$, where G_0 is the conductance quantum ($2e^2/h = 77.5$ μS) and T_L, T_R, and T_m represent the transmissions at the contacts between the two electrodes and the molecular core, respectively [93]. In the tunneling regime, T_m is expressed as $e^{-\beta L}$ for homogeneous oligomers such as normal alkanes [94], oligophenylenes [95], oligothiophenes [96], and porphyrin oligomers [6, 97, 98], where β is the decay constant for the transmission and L is the molecular length. This is the case for a series circuit. A method for estimating the conductance of molecular wires bonded in parallel was proposed by Magoga and Jaochim [99]. When the molecule forms two parallel paths and the transmissions through the paths are T_1 and T_2, the transmission, T, through the entire molecule can be expressed as $T = T_1 + T_2 + 2(T_1 \times T_2)^{1/2}$ [100]. The electrical conductance of a single-molecule circuit with parallel paths was measured using the break junction technique. It was found that the equation given above is not applicable in the case of actual single-molecule devices because of quantum interference [101].

6 Conclusions and Perspectives

Since Aviram and Ratner first proposed single-molecule electronics, various functional single-molecule devices have been realized. In the case of rectifiers, donor–acceptor systems have primarily been used, with rectification behavior being observed in the *I–V* characteristics. However, the mechanism of rectification has not been elucidated completely. In the case of NDR, even though several candidate molecules have been proposed theoretically, only a few actual observations of NDR characteristics have been reported. This is because it is difficult to synthesize these devices and to perform measurements on them. Finally, in the case of switches, various stimuli such as irradiating light, electrochemical gating, and chemical and physical stimuli have been used to realize switching behavior. However, only a few molecular switches have been synthesized in which the molecular junction was maintained. New molecular switches that can be used in integrated molecular circuits are desired. In order to develop molecular circuits, techniques for integrating molecules must be designed and a framework for predicting the functions of such circuits as well as a platform for using them must be developed.

In addition to the functional single-molecule devices introduced in this review, many other molecular devices have been investigated using various methods. Thus, the underlying mechanism for charge transport through metal-molecule-metal junctions is now understood. Furthermore, the relationship between molecular structures and their electrical properties has been gradually uncovered. Thus, it should be possible to design better single-molecule devices based on these guidelines. It seems that primarily physicists are interested in single-molecule devices and that only relatively basic molecules have been studied. For the realization of next-generation single-molecule electronics, new functional devices must be studied and their performances should be improved. Further, they should be integrated to realize molecular circuits based on developments in different fields. Indeed, collaborations between Breslow's, Venkataraman's, and Hybertsen's groups, whose fields are chemical synthesis, single-molecule measurements, and

theoretical transport calculations, respectively, have yielded significant insights in this regard [101].

References

1. Aviram A, Ratner MA (1974) Chem Phys Lett 29:277–283
2. Su TA, Neupane M, Steigerwald ML, Venkataraman L, Nuckolls C (2016) Nat Rev Mater 1:16002
3. Xiang D, Wang X, Jia C, Lee T, Guo X (2016) Chem Rev (Washington, DC, USA) 116:4318–4440
4. Moreland J, Ekin JW (1985) J Appl Phys 58:3888–3895
5. Reed MA, Zhou C, Muller CJ, Burgin TP, Tour JM (1997) Science 278:252–254
6. Xu B, Tao NJ (2003) Science 301:1221–1223
7. Wold DJ, Frisbie CD (2000) J Am Chem Soc 122:2970–2971
8. Park H, Lim AKL, Alivisatos AP, Park J, Mceuen PL (1999) Appl Phys Lett 75:301–303
9. Li T, Hu W, Zhu D (2010) Adv Mater (Weinheim, Ger) 22:286–300
10. Cui XD, Primak A, Zarate X, Tomfohr J, Sankey OF, Moore AL, Moore TA, Gust D, Harris G, Lindsay SM (2001) Science 294:571–574
11. Batra A, Darancet P, Chen Q, Meisner JS, Widawsky JR, Neaton JB, Nuckolls C, Venkataraman L (2013) Nano Lett 13:6233–6237
12. Derosa PA, Guda S, Seminario JM (2003) J Am Chem Soc 125:14240–14241
13. Wang K, Zhou J, Hamill JM, Xu B (2014) J Chem Phys 141:054712
14. Capozzi B, Xia J, Adak O, Dell EJ, Liu Z-F, Taylor JC, Neaton JB, Campos LM, Venkataraman L (2015) Nat Nanotechnol 10:522–527
15. Kim T, Liu Z-F, Lee C, Neaton JB, Venkataraman L (2014) Proc Natl Acad Sci USA 111:10928–10932
16. Perrin ML, Galan E, Eelkema R, Grozema F, Thijssen JM, Van Der Zant HSJ (2015) J Phys Chem C 119:5697–5702
17. Galan E, Perrin ML, Lutz M, Van Der Zant HSJ, Grozema FC, Eelkema R (2016) Org Biomol Chem 14:2439–2443
18. Ding W, Koepf M, Koenigsmann C, Batra A, Venkataraman L, Negre CFA, Brudvig GW, Crabtree RH, Schmuttenmaer CA, Batista VS (2015) J Chem Theory Comput 11:5888–5896
19. Ng M-K, Lee D-C, Yu L (2002) J Am Chem Soc 124:11862–11863
20. Diez-Perez I, Hihath J, Lee Y, Yu LP, Adamska L, Kozhushner MA, Oleynik II, Tao J (2009) J Nat Chem 1:635–641
21. Lörtscher E, Gotsmann B, Lee Y, Yu L, Rettner C, Riel H (2012) ACS Nano 6:4931–4939
22. Cui B, Fang CF, Zhai YX, Yin S, Gao K, Liu DS (2011) Appl Phys Lett 98:133101
23. Mahmoud A, Lugli P (2012) J Appl Phys 112:113720
24. Zhang G-P, Xie Z, Song Y, Hu G-C, Wang C-K (2014) Chem Phys Lett 591:296–300
25. Yuan S, Dai C, Weng J, Mei Q, Ling Q, Wang L, Huang W (2011) J Phys Chem A 115:4535–4546
26. Elbing M, Ochs R, Koentopp M, Fischer M, Von Hänisch C, Weigend F, Evers F, Weber HB, Mayor M (2005) Proc Natl Acad Sci USA 102:8815–8820
27. Li Y, Yao J, Liu C, Yang C (2008) J Mol Struc-THEOCHEM 867:59–63
28. Stokbro K, Taylor J, Brandbyge M, Mozos JL, Ordejón P (2003) Comp Mater Sci 27:151–160
29. Yuan S, Wang S, Mei Q, Ling Q, Wang L, Huang W (2011) J Phys Chem A 115:9033–9042
30. Handayani M, Gohda S, Tanaka D, Ogawa T (2014) Chem Euro J 20:7655–7664
31. Liu R, Ke S-H, Yang W, Baranger HU (2006) J Chem Phys 124:024718
32. Nijhuis CA, Reus WF, Whitesides GM (2009) J Am Chem Soc 131:17814–17827
33. Cui B, Xu Y, Ji G, Wang H, Zhao W, Zhai Y, Li D, Liu D (2014) Org Electron 15:484–490
34. Nijhuis CA, Reus WF, Whitesides GM (2010) J Am Chem Soc 132:18386–18401
35. Jeong H, Kim D, Wang G, Park S, Lee H, Cho K, Hwang W-T, Yoon M-H, Jang YH, Song H, Xiang D, Lee T (2014) Adv Funct Mater 24:2472–2480
36. Guo C, Wang K, Zerah-Harush E, Hamill J, Wang B, Dubi Y, Xu B (2016) Nat Chem 8:484–490
37. Troisi A, Ratner MA (2004) Nano Lett 4:591–595
38. Troisi A, Ratner MA (2002) J Am Chem Soc 124:14528–14529

39. Fujii S, Tada T, Komoto Y, Osuga T, Murase T, Fujita M, Kiguchi M (2015) J Am Chem Soc 137:5939–5947
40. García M, Guadarrama P, Ramos E, Fomine S (2011) Synth Met 161:2390–2396
41. Fomine S (2013) J Mol Model 19:65–71
42. Montiel F, Fomina L, Fomine S (2015) J Mol Model 21:1–8
43. Chen J, Reed MA, Rawlett AM, Tour JM (1999) Science 286:1550–1552
44. Chen J, Wang W, Reed MA, Rawlett AM, Price DW, Tour JM (2000) Appl Phys Lett 77:1224–1226
45. Fan F-RF, Lai RY, Cornil J, Karzazi Y, Brédas J-L, Cai L, Cheng L, Yao Y, Price DW, Dirk SM, Tour JM, Bard AJ (2004) J Am Chem Soc 126:2568–2573
46. Rawlett AM, Hopson TJ, Nagahara LA, Tsui RK, Ramachandran GK, Lindsay SM (2002) Appl Phys Lett 81:3043–3045
47. Fan F-RF, Yang J, Dirk SM, Price DW, Kosynkin D, Tour JM, Bard AJ (2001) J Am Chem Soc 123:2454–2455
48. Fan F-RF, Yang J, Cai L, Price DW, Dirk SM, Kosynkin DV, Yao Y, Rawlett AM, Tour JM, Bard AJ (2002) J Am Chem Soc 124:5550–5560
49. Fan F-RF, Yao Y, Cai L, Cheng L, Tour JM, Bard AJ (2004) J Am Chem Soc 126:4035–4042
50. Taylor J, Brandbyge M, Stokbro K (2003) Phys Rev B 68:121101
51. Ren Y, Chen K-Q, Wan Q, Pan A, Hu WP (2010) Phys Lett A 374:3857–3862
52. Yeganeh S, Galperin M, Ratner MA (2007) J Am Chem Soc 129:13313–13320
53. Zhou J, Samanta S, Guo C, Locklin J, Xu B (2013) Nanoscale 5:5715–5719
54. Dhungana KB, Mandal S, Pati R (2012) J Phys Chem C 116:17268–17273
55. Komoto Y, Fujii S, Nakamura H, Tada T, Nishino T, Kiguchi M (2016) Sci Rep 6:26606
56. Pati R, Mcclain M, Bandyopadhyay A (2008) Phys Rev Lett 100:246801
57. Perrin ML, Frisenda R, Koole M, Seldenthuis JS, Giljose AC, Valkenier H, Hummelen JC, Renaud N, Grozema FC, Thijssen JM, Dulić D, Van Der Zantherre SJ (2014) Nat Nanotechnol 9:830–834
58. Fan Z-Q, Chen K-Q, Wan Q, Zou BS, Duan W, Shuai Z (2008) Appl Phys Lett 92:263304
59. Nozaki D, Lokamani A, Santana-Bonilla A, Dianat R Gutierrez, Cuniberti G (2015) J Phys Chem Lett 6:3950–3955
60. Xia C-J, Liu D-S, Liu H-C, Zhai X-J (2011) Physica E 43:1518–1521
61. Geng H, Hu Y, Shuai Z, Xia K, Gao H, Chen K (2007) J Phys Chem C 111:19098–19102
62. Dalgleish H, Kirczenow G (2006) Nano Lett 6:1274–1278
63. Irie M, Fukaminato T, Matsuda K, Kobatake S (2014) Chem Rev (Washington, DC, USA) 114:12174–12277
64. Matsuda K, Irie M (2004) J Photoch Photobio C 5:169–182
65. Dulić D, Van Der Molen S, Kudernac T, Jonkman H, De Jong J, Bowden T, Van Esch J, Feringa B, Van Wees B (2003) Phys Rev Lett 91:207402
66. Jin H, Fan C, Paul AL, Joakim A, Stephen DS, Devens G, Thomas AM, Ana LM, Jun L, Otto FS, Stuart ML (2005) Nanotechnology 16:695
67. Tam ES, Parks JJ, Shum WW, Zhong Y-W, Santiago-Berríos MEB, Zheng X, Yang W, Chan GKL, Abruña HD, Ralph DC (2011) ACS Nano 5:5115–5123
68. Kim Y, Hellmuth TJ, Sysoiev D, Pauly F, Pietsch T, Wolf J, Erbe A, Huhn T, Groth U, Steiner UE, Scheer E (2012) Nano Lett 12:3736–3742
69. Tsuji Y, Staykov A, Yoshizawa K (2009) J Phys Chem C 113:21477–21483
70. Jia C, Wang J, Yao C, Cao Y, Zhong Y, Liu Z, Liu Z, Guo X (2013) Angew Chem Int Edit 52:8666–8670
71. Roldan D, Kaliginedi V, Cobo S, Kolivoska V, Bucher C, Hong W, Royal G, Wandlowski T (2013) J Am Chem Soc 135:5974–5977
72. Haiss W, Van Zalinge H, Higgins SJ, Bethell D, Höbenreich H, Schiffrin DJ, Nichols RJ (2003) J Am Chem Soc 125:15294–15295
73. Chen F, He J, Nuckolls C, Roberts T, Klare JE, Lindsay S (2005) Nano Lett 5:503–506
74. Kay NJ, Higgins SJ, Jeppesen JO, Leary E, Lycoops J, Ulstrup J, Nichols RJ (2012) J Am Chem Soc 134:16817–16826
75. Li Z, Li H, Chen S, Froehlich T, Yi C, Schönenberger C, Calame M, Decurtins S, Liu S-X, Borguet E (2014) J Am Chem Soc 136:8867–8870
76. Li Y, Baghernejad M, Qusiy A-G, Zsolt Manrique D, Zhang G, Hamill J, Fu Y, Broekmann P, Hong W, Wandlowski T, Zhang D, Lambert C (2015) Angew Chem Int Edit 54:13586–13589

77. Li Z, Smeu M, Afsari S, Xing Y, Ratner MA, Borguet E (2014) Angew Chem Int Edit 53:1098–1102
78. Quek SY, Kamenetska M, Steigerwald ML, Choi HJ, Louie SG, Hybertsen MS, Neaton JB, Venkataraman L (2009) Nat Nanotechnol 4:230–234
79. Su TA, Li H, Steigerwald ML, Venkataraman L, Nuckolls C (2015) Nat Chem 7:215–220
80. De Silva AP, Uchiyama S (2007) Nat Nanotechnol 2:399–410
81. Okamoto A, Tanaka K, Saito I (2004) J Am Chem Soc 126:9458–9463
82. Wang D, Fu Y, Yan J, Zhao B, Dai B, Chao J, Liu H, He D, Zhang Y, Fan C, Song S (2014) Anal Chem 86:1932–1936
83. Tybrandt K, Forchheimer R, Berggren M (2012) Nat Commun 3:871
84. Wang B, Kitney RI, Joly N, Buck M (2011) Nat Commun 2:508
85. Katz E, Privman V (2010) Chem Soc Rev 39:1835–1857
86. Collier CP, Wong EW, Belohradský M, Raymo FM, Stoddart JF, Kuekes PJ, Williams RS, Heath JR (1999) Science 285:391–394
87. Meng F, Hervault Y-M, Shao Q, Hu B, Norel L, Rigaut S, Chen X (2014) Nat Commun 5:3023
88. Ernst JT, Kutzki O, Debnath AK, Jiang S, Lu H, Hamilton AD (2002) Angew Chem Int Edit 41:278–281
89. Noguchi H, Hojo K, Suginome M (2007) J Am Chem Soc 129:758–759
90. Tamaki T, Nosaka T, Ogawa T (2014) J Org Chem 79:11029–11038
91. Shiotari A, Ozaki Y, Naruse S, Okuyama H, Hatta S, Aruga T, Tamaki T, Ogawa T (2015) RSC Adv 5:79152–79156
92. Van Hal PA, Smits ECP, Geuns TCT, Akkerman HB, De Brito BC, Perissinotto S, Lanzani G, Kronemeijer AJ, Geskin V, Cornil J, Blom PWM, De Boer B, De Leeuw DM (2008) Nat Nanotechnol 3:749–754
93. Huang M-J, Hsu L-Y, Fu M-D, Chuang S-T, Tien F-W, Chen C-H (2014) J Am Chem Soc 136:1832–1841
94. Li C, Pobelov I, Wandlowski T, Bagrets A, Arnold A, Evers F (2008) J Am Chem Soc 130:318–326
95. Venkataraman L, Klare JE, Nuckolls C, Hybertsen MS, Steigerwald ML (2006) Nature 442:904–907
96. Yamada R, Kumazawa H, Noutoshi T, Tanaka S, Tada H (2008) Nano Lett 8:1237–1240
97. Sedghi G, Garcia-Suarez VM, Esdaile LJ, Anderson HL, Lambert CJ, Martin S, Bethell D, Higgins SJ, Elliott M, Bennett N, Macdonald JE, Nichols RJ (2011) Nat Nanotechnol 6:517–523
98. Sedghi G, Esdaile LJ, Anderson HL, Martin S, Bethell D, Higgins SJ, Nichols RJ (2012) Adv Mater (Weinheim, Ger) 24:653–657
99. Magoga M, Joachim C (1999) Phys Rev B 59:16011–16021
100. Joachim C, Gimzewski JK, Aviram A (2000) Nature 408:541–548
101. Vazquez H, Skouta R, Schneebeli S, Kamenetska M, Breslow R, Venkataramanl, Hybertsen MS (2012) Nat Nanotechnol 7:663–667

Top Curr Chem (Z) (2017) 375:85
https://doi.org/10.1007/s41061-017-0170-3

REVIEW

Towards Rectifying Performance at the Molecular Scale

Guang-Ping Zhang[1] · Zhen Xie[1] · Yang Song[2] · Gui-Chao Hu[1] · Chuan-Kui Wang[1]

Received: 19 July 2017 / Accepted: 22 September 2017 / Published online: 24 October 2017

Abstract Molecular diode, proposed by Mark Ratner and Arieh Aviram in 1974, is the first single-molecule device investigated in molecular electronics. As a fundamental device in an electric circuit, molecular diode has attracted an enduring and extensive focus during the past decades. In this review, the theoretical and experimental progresses of both charge-based and spin-based molecular diodes are summarized. For the charge-based molecular diodes, the rectifying properties originated from asymmetric molecules including D–σ–A, D–π–A, D–A, and σ–π type compounds, asymmetric electrodes, asymmetric nanoribbons, and their combination are analyzed. Correspondingly, the rectification mechanisms are discussed in detail. Furthermore, a series of strategies for modulating rectification performance is figured out. Discussion on concept of molecular spin diode is also involved based on a magnetic co-oligomer. At the same time, the intrinsic mechanism as well as the modulation of the spin-current rectification performance is introduced. Finally, several crucial issues that need to be addressed in the future are given.

Keywords Molecular electronics · Molecular rectification · Charge-current rectification · Spin-current rectification

Chapter 5 was originally published as Zhang, G-P., Xie, Z., Song, Y., Hu, G-C. & Wang, C-K. Top Curr Chem (Z) (2017) 375: 85. https://doi.org/10.1007/s41061-017-0170-3.

✉ Gui-Chao Hu
hgc@sdnu.edu.cn

✉ Chuan-Kui Wang
ckwang@sdnu.edu.cn

[1] Shandong Province Key Laboratory of Medical Physics and Image Processing Technology, School of Physics and Electronics & Institute of Materials and Clean Energy, Shandong Normal University, Jinan 250358, China

[2] School of Physics and Technology, University of Jinan, Jinan 250022, China

1 Introduction

Building functional devices using single molecules is considered as a fantastic alternative solution for the size-miniaturization of silicon-based electric components, which evolves to be a promising field known as molecular electronics [1–3]. Among all the molecular functional devices, molecular diode, as a basic element in logic circuit, has attracted the most attention [4–11]. Molecular diode, as its name suggests, is a device with functionality of current rectifying at the molecular scale, which allows current to flow in one direction while blocking it from flowing in the opposite direction. This concept was first proposed by Aviram and Ratner [12]. After that, a lot of work and research have been devoted to designing molecular diodes with high stability and excellent performance both experimentally [13–30] and theoretically [31–46].

In order that a molecular device functions as a current rectifier, it must be physically asymmetric [3]. Following this principle, various molecular diodes have been designed with either asymmetric molecules [15–17, 19–30, 47–49] or asymmetric interfaces between molecule and electrodes [13, 14, 31, 50]. At present, the former has shared the majority since it is very difficult to preciously control the molecule–electrode interface at the atomic detail [51]. In recent years, extensive studies have been carried out on two-dimensional materials [52–57], such as graphene, which also provide good candidates for designing molecular diodes with remarkable performance due to their novel electric properties.

On the other hand, the exploration of electronic spin, another degree of freedom of electrons, offers a new way to design extremely fascinating properties for functional molecular devices due to the merits of weak spin–orbit and hyperfine interactions in organic molecules [58–61]. Molecular spin diode [62–65], which rectifies the spin current of a molecular device, plays an important role in the molecular spintronics with combining the advantages of spintronics and molecular electronics. The utilization of new functional molecules, such as organic magnets [66–68], highlights the design of molecular spin diodes based on an asymmetric magnetic co-oligomer structure [64, 69–73].

For practical application, it is of crucial importance to gain a high rectification ratio in molecular diodes, and to modulate the performance of rectification. Therefore, in this review the mechanisms of rectification in molecular diodes and the efficient ways to modulate their rectifying performance are specifically focused on.

2 Charge-based molecular diodes and their rectifying mechanisms

2.1 D-bridge-A type molecular diodes

D-bridge-A type molecules, where an electron donor (D) and acceptor (A) are connected by a bridge segment, have intrinsic asymmetries in the molecule itself. Therefore, they can in principle be used to construct molecular diodes. The D-bridge-A type molecules can be divided into two kinds according to whether the bridge is saturated (σ) or conjugated (π), namely, D–σ–A type and D–π–A type.

2.1.1 D-σ-A type molecular diodes

The first prototype molecular diode was proposed by Aviram and Ratner (AR) [12], which was based on a D–σ–A molecule (denoted as TTF–σ–TCNQ) shown in Fig. 1a. The AR model of molecular diode works as follows [11]. Due to the difference in electron affinity for the donor and acceptor segments, the lowest unoccupied molecular orbital (LUMO) and the highest occupied molecular orbital (HOMO) of the donor moiety LUMO(D) and HOMO(D) are energetically higher than the counterparts of the acceptor LUMO(A) and HOMO(A), respectively. When the molecule is sandwiched between two metal electrodes, the HOMO(D)/LUMO(A) is slightly below/above the Fermi energy (E_F) of the left/right electrode as depicted in Fig. 1b. As soon as a positive bias voltage is applied, as shown in Fig. 1c, the E_F of the anode/cathode electrode will easily align with HOMO(D)/LUMO(A), and then electron transfer from HOMO(D) to anode electrode and from cathode electrode to LUMO(A) will occur, which makes the molecule a zwitterion with both the acceptor and donor segments charged. Since LUMO(A) is higher than HOMO(D), the electron can tunnel from the acceptor segment to donor moiety with the help of external electric field bringing the molecule back to the ground state.

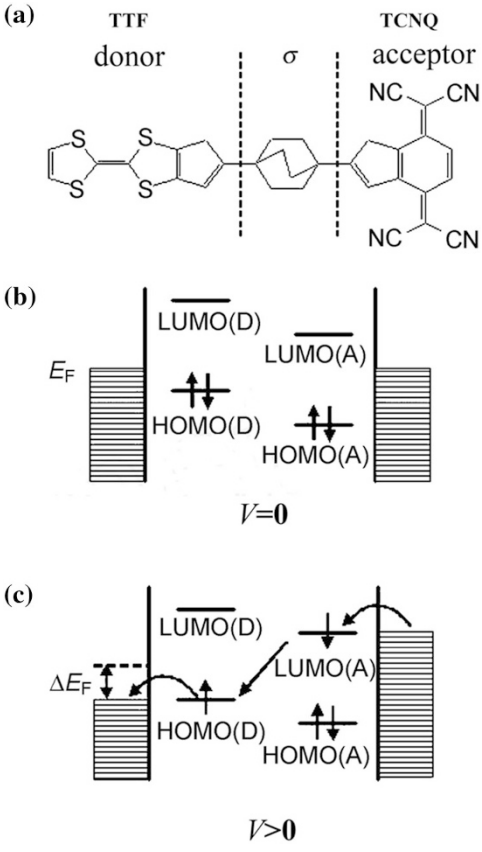

Fig. 1 **a** The prototype D–σ–A rectifying molecule TTF–σ–TCNQ proposed by Aviram and Ratner. The energy level diagrams of the AR model under, **b** zero bias voltage, and **c** a positive bias voltage. The E_F is the Fermi energy of electrodes, and LUMO(D), HOMO(D), LUMO(A), and HOMO(A) are the lowest unoccupied molecular orbital and the highest occupied molecular orbital for donor and acceptor segments, respectively. Reproduced with permission from Ref. [11]. Copyright 2009 China Academic Journal Electronic Publishing House

However, it needs a much larger bias voltage to take the E_F of the left electrode above LUMO(D) and the E_F of the right electrode below HOMO(A) to generate a conducting current. Therefore, a rectifying effect can be expected, and the current prefers to flow in the direction from the donor moiety to the acceptor segment.

Inspired by the theoretical proposal by Aviram and Ratner, a lot of effort has been devoted to verifying the rectifying effect in this molecular system [6, 74–76], which can date back to 1983 [74]. However, the suggested D–σ–A molecule of TTF–σ–TCNQ was never synthesized in experiment. Meanwhile, the studies on demonstrating the rectifying characteristics of other D–σ–A molecules have also been plagued due to the lack of advanced experimental techniques to prepare and measure rectification of a molecular monolayer [32, 77]. Although it has been proven that Langmuir–Blodgett (LB) monolayers of D–σ–A molecules do rectify [18, 19, 24, 26, 78–80], there are different rectifying mechanisms other than that for AR model. For example, Metzger et al. [78] observed a clear current rectification in LB monolayers of dimethyanilinoazafullerene sandwiched between gold electrodes as shown in Fig. 2. The current flows more easily from the acceptor fragment to donor segment, which is completely opposite to that for the AR model. Meanwhile, Hou et al. [26] also obtained a rectifying effect in the current–voltage (I–V) curve for a very similar system with the forward current flowing in the same direction to

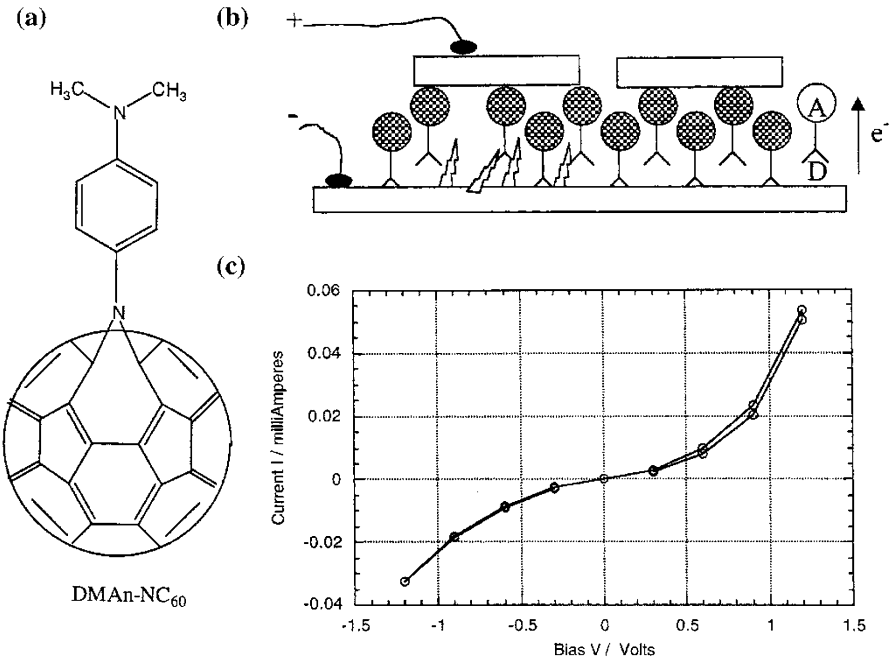

Fig. 2 **a** DMAn-NC_{60}, dimethylanilinoaza[C_{60}]fullerene, where dimethylaniline ring is the electron donor and C_{60} is the electron acceptor connected by a saturated nitrogen atom. **b** Schematic of the DMAn-NC_{60} monolayer on gold substrate. The current prefers to flow in the direction from acceptor to donor. **c** Measured I–V curve, which shows an asymmetric feature arising from the organic monolayer. Reproduced with permission from Ref. [78]. Copyright 2003 American Chemical Society

that for AR model (Fig. 3). Even so, detailed analysis revealed that the rectification was attributed to the molecules and asymmetric geometry in the molecular junctions. In addition, Ho et al. [80] figured out that the preferred current flow direction of an analogue of the AR prototype molecular rectifier, TTF–σ-(trinitrofluorene), depended on the electrode materials used in the experiment. This indicates that the mechanisms for rectification in real molecular rectifiers are very complicated depending on a number of factors.

2.1.2 D–π–A type molecular diodes

As the researchers were impeded during fabricating and measuring D–σ–A type molecular rectifiers, D–π–A type molecules were reported experimentally to have pronounced rectification effects [15–17, 20, 36, 81–83]. In 1990, Ashwell et al. found that when an electron donor and acceptor are connected by a conjugated bridge, it could also realize rectification [17]. The structure of the molecule is schematically shown in Fig. 4a, where the electron donor quinolinium and the electron acceptor phenyldicyanomethanide are bridged by a π –CH=C(CN)– segment. There is also a long hydrophobic hexadecyl tail in the molecule connecting to the donor segment. The mechanism for the rectification in $C_{16}H_{33}$–Q3CNQ was conjectured to follow the AR model. However, asymmetric molecule–electrode contacts were produced due to different electrode materials of Mg and Pt used in the experiment, which might cause a Schottky barrier. To eliminate the Schottky barrier effect that could not be ruled out from being the origin of the observed rectification, ω-tricosenoic acid was used to space the molecule from the metal electrode providing unequivocally evidence that the rectification was indeed from the $C_{16}H_{33}$–Q3CNQ molecule [20].

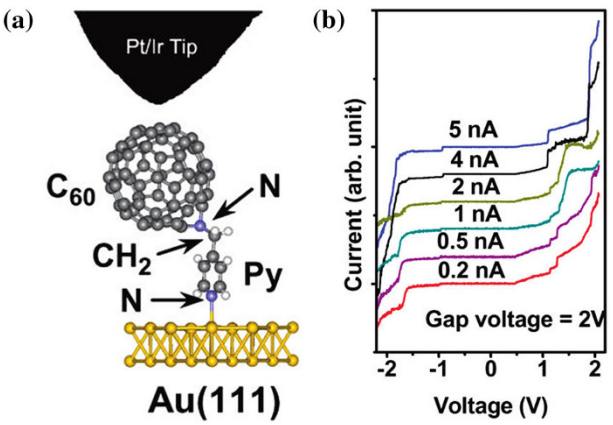

Fig. 3 **a** A *N*-3-γ-pyridyl aza [60] fulleroid (C_{60}NPy) sandwiched between the Au(111) bottom electrode and Pt/Ir tip, where pyridyl moiety is the electron donor and C_{60} is the electron acceptor. **b** Measured *I*–*V* curves with different set-point current. The bias voltage was applied to the gold substrate electrode. Reproduced with permission from Ref. [26]. Copyright 2006 American Chemical Society

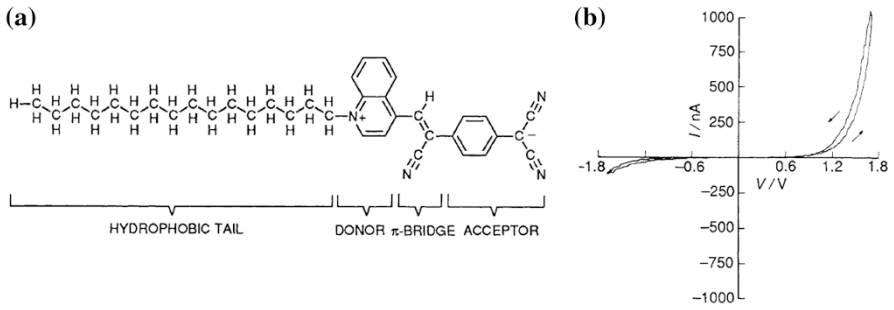

Fig. 4 **a** Molecular structure of $C_{16}H_{33}$–Q3CNQ. **b** *I–V* plot for Mg|$C_{16}H_{33}$–Q3CNQ LB film|Pt junctions. Reproduced with permission from Ref. [17]. Copyright 1990 Royal Society of Chemistry

2.2 D–A type molecular diodes

In 2002, Yu et al. investigated the rectification properties of a structure simple rectifying molecule by inserting the individual active molecule into the self-assembled monolayer (SAM) of alkanethiolates. The active rectifying molecule was a conjugated diblock co-oligomer [21, 22], in which the electron-rich thiophene segment (D) and electron-poor thiazole fragment (A) were directly coupled together, and it resembled traditional *p–n* junctions in structure. The diblock co-oligomer was assembled into the monolayer of alkanethiolates on gold substrate with the thiophene block preferentially bound to the bottom substrate. Therefore, the diblock co-oligomer molecule was widely separated in space allowing the measurement of electric properties of an individual target. A pronounced rectification was demonstrated by using a Pt/Ir scanning tunneling microscopy (STM) tip held at a constant position above the target molecule. Further investigation was then followed to prove that the rectification originated from the diblock co-oligomer itself and was not from the asymmetric molecule–electrode contacts [23]. For this purpose, the top Pt/Ir STM tip was replaced by a gold nanoparticle so that the thiophene–thiazole diblock co-oligomer was chemically bonded to two gold electrodes through S–Au bonds. The rectification properties persisted and an opposite rectifying direction was observed as soon as the orientation of the diblock co-oligomer was reversed (Fig. 5), which firmly attributed the rectification to intrinsic asymmetry in the diblock co-oligomer. However, the direction of easy current flow was from the electron-rich thiophene block to the electron-deficient thiazole block, which was the same with that of AR model but entirely opposite to that of a macro *p–n* junction. Based on a model calculation, Hu et al. proposed an bias-induced orbital hybridization mechanism for the rectification in the D–A diodes [38]. It was theoretically demonstrated that the positive bias tended to delocalize the molecular orbitals through the hybridization while the negative bias enhanced the mismatch of energy levels and had no effect on the hybridization. Therefore, the tunneling orbital under a positive bias was a delocalized one while it was a localized one under a negative bias, which resulted in the rectification.

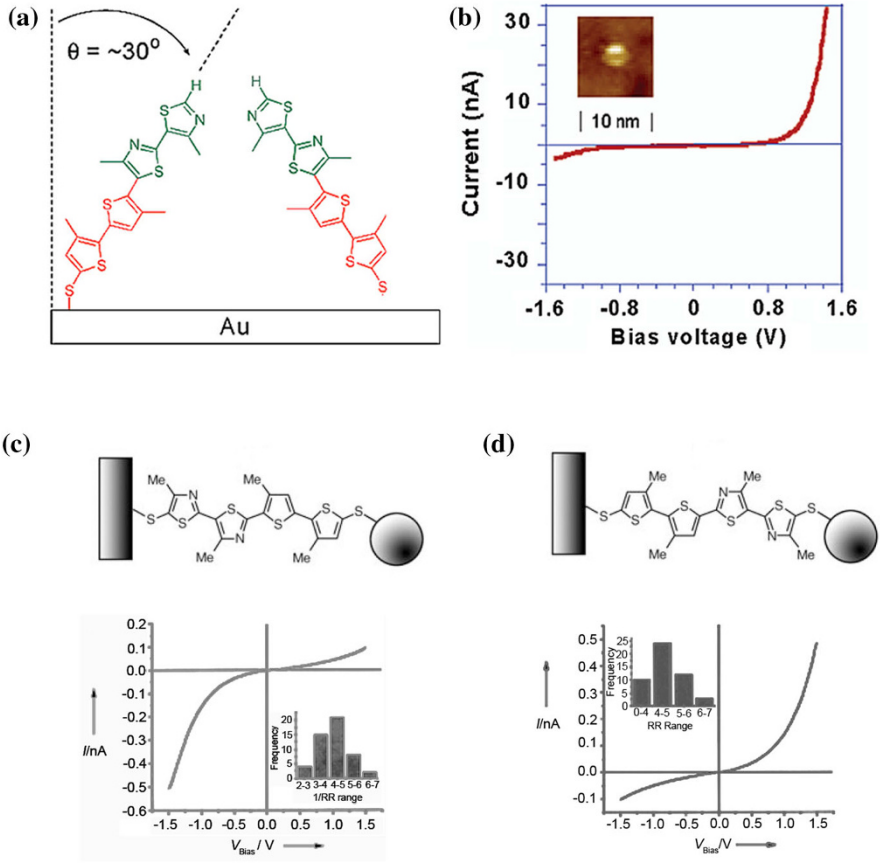

Fig. 5 **a** Schematic illustration of the orientation of conjugated diblock molecules covalently attached to a gold surface through the terminal thiolate group. **b** The *I–V* characteristic of the isolated diblock co-oligomer molecule inserted into pre-assembled monolayers of decanethiolates on Au/mica (setpoint conditions: + 1000 mV and 2 pA). The *inset* is constant-current STM image of the mixed monolayers on Au/mica. **c**, **d** Schematics of a conjugated diblock co-oligomer molecule covalently attached to a gold surface and a gold nano-particle through the terminal thiolate groups at both sides with different orientations and the corresponding *I–V* curves (*lower panels*). Reproduced with permission from Ref. [21]. 2002 American Chemical Society. Reproduced with permission from Ref. [23]. Copyright 2004 Wiley–VCH

Afterwards, another diblock co-oligomer with a more simple structure, namely dipyrimidinyl–diphenyl co-oligomer, as shown in Fig. 6a, was experimentally synthesized [25]. It was revealed that, oppositely to the thiophene–thiazole co-oligomer, the current preferred to flow from the electron acceptor dipyrimidinyl moiety to the electron donor diphenyl block in dipyrimidinyl–diphenyl co-oligomer diode [27]. The rectification in dipyrimidinyl–diphenyl co-oligomer was interpreted in terms of localization of the wavefunction of the hole ground state at one end of the diblock under the applied electric field [37], as shown in Fig. 6c, d, where the right electrode (STM tip) was kept grounded and the left electrode (substrate) was

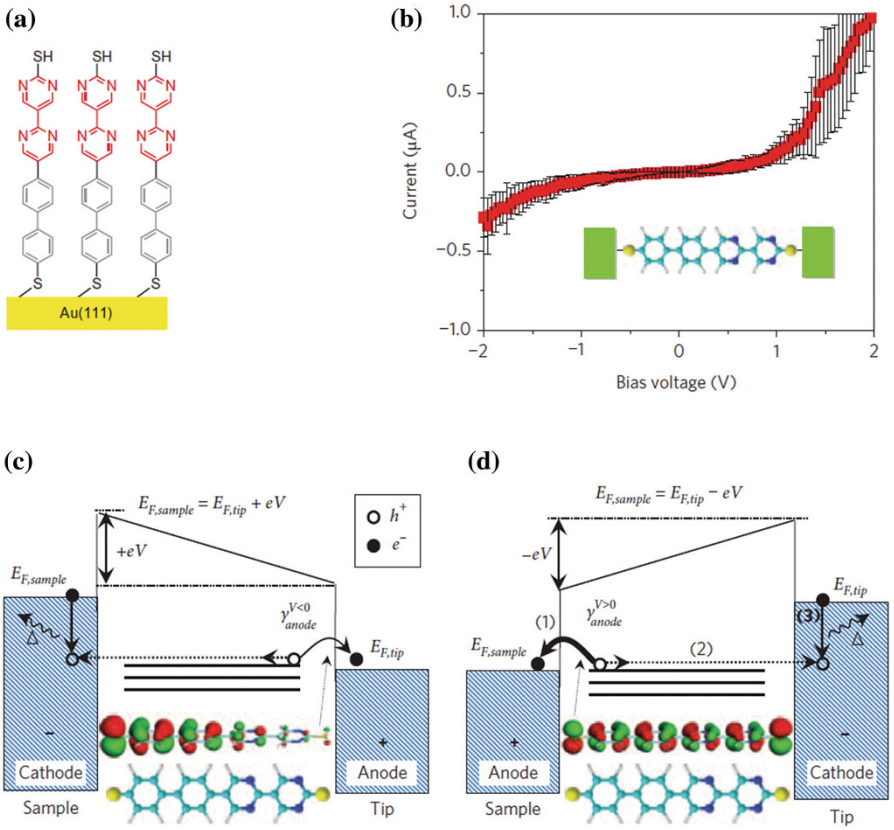

Fig. 6 **a** Diagram of the synthesized dipyrimidinyl–diphenyl co-oligomer adsorbed on the gold substrate. **b** *I–V* curve of the dipyrimidinyl–diphenyl co-oligomer diode. **c**, **d** Conduction mechanism for the dipyrimidinyl–diphenyl molecular junction under negative and positive bias voltages, respectively. Reproduced with permission from Ref. [27]. Copyright 2009 Macmillan Publishers Limited

biased either positively or negatively. The conduction process is as follows: (1) an electron transfers from the electron-rich diphenyl block to the anode, which generates a hole in the molecule, (2) the generated hole transfers under an electric field to the cathode, and (3) the injected hole in the cathode recombines with an electron of higher energy (releasing heat at the electrode). The hole wavefunction at $V = -1$ V mainly localizes at the biphenyl end of the molecule and it turns to be delocalized over the whole molecule at $V = 1$ V. Therefore, the probability γ_{anode} ($\gamma_{\text{anode}} \propto |\Psi_{\text{hole}}(r)|^2$) of the hole transfer from the anode to the molecule is larger under positive bias than that at negative bias, i.e., $\gamma_{\text{anode}}^{V>0} > \gamma_{\text{anode}}^{V<0}$. Consequently, the nonsymmetrical behavior of the hole wavefunction as a function of the applied electric field causes an asymmetry in the *I–V* characteristics. Furthermore, the rectification of dipyrimidinyl–diphenyl co-oligomer at different temperatures was investigated by using the mechanically controllable break-junction technique, and a

temperature-independent rectification in the temperature range between 300 and 50 K was revealed [84].

2.3 σ–π type molecular diodes

To improve the yields of working molecular devices in experiment, a new technique for fabricating junctions was put forward by Nijhuis and Whitesides et al. [85], where the SAMs of the target molecules were chemically adsorbed on a ultraflat surface of template-stripped silver (Ag^{TS}) substrate and a eutectic alloy of gallium and indium EGaIn with a skin of gallium oxide Ga_2O_3 (noted as Ga_2O_3/EGaIn) was then covered on the top acting as the top electrode. This technique is sufficiently convenient to experimentally provide high yields of usable junctions and large amounts of measurement data necessary for meaningful statistical analysis. By using this technique, a new kind of molecular diodes has been systematically investigated [86–97]. This molecular diode consists of an electron-rich ferrocenyl (Fc) group headed *n*-alkanethiolate (noted as SC_nFc) and it is chemically adsorbed on the Ag^{TS} bottom electrode with S–Ag bond while there is a van der Waals interaction between the ferrocenyl head group and Ga_2O_3/EGaIn top electrode (here we call this kind of rectifier σ–π type molecular diode). It was shown that the rectification ratio could reach up to as high as 1×10^2 with a log-standard deviation of 3.0 [86]. Indeed, this kind of σ–π molecular rectifier was alluded to in a much earlier work, where the electron acceptor TCNQ was connected to a saturated alkyl chain chemically adsorbed on Ag substrate through the thiol ending group and was covered by a SAM of alkanethiolates on the top [98].

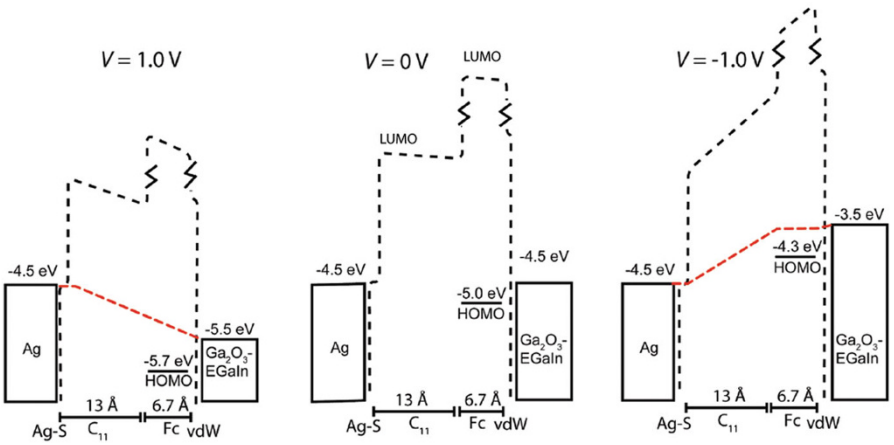

Fig. 7 Schematic representation of the energy level diagrams (with respect to vacuum) of the Ag^{TS}–$SC_{11}Fc$//Ga_2O_3/EGaIn junctions at 1.0 V (*left*), 0 V (*middle*), and − 1.0 V (*right*). The Ga_2O_3/EGaIn top electrode is biased and the Ag^{TS} bottom electrode is grounded. The *black dashed lines* indicate the LUMO barrier widths and heights while the *red dashed lines* indicate the potential drops across the junctions when a bias is applied. Reproduced with permission from Ref. [88]. Copyright 2010 American Chemical Society

Nijhuis et al. proposed an electron transport model to interpret the high rectification in $SC_{11}Fc$ rectifiers [88]. As shown in Fig. 7, the HOMO level of the ferrocenyl head group couples more strongly to the Ga_2O_3/EGaIn top electrode than to the Ag bottom electrode, since it is in close proximity to the former and separated from the latter by the undecane backbone. Therefore, it follows the E_F of Ga_2O_3/EGaIn top electrode under bias voltage. At zero bias voltage, it lies under the E_F of the electrodes, while the LUMOs for the ferrocenyl head group and alkyl chain are far above the E_F (Fig. 7, middle column). When a positive bias voltage, such as 1.0 V, is applied (here the top Ga_2O_3/EGaIn electrode is biased), the HOMO of the ferrocenyl head group is lowered accompanying the E_F of top Ga_2O_3/EGaIn electrode and it is still below E_F of both electrodes (Fig. 7, left column). In this case, the charge cannot flow through the HOMO and instead it must tunnel through not only the undecane backbone but also the ferrocenyl moiety. However, at a negative bias voltage, the E_F of the Ga_2O_3/EGaIn electrode increases, and consequently the HOMO level rises up into the bias window between the E_F of the two electrodes (Fig. 7, right column) participating in the charge transport. In this case, the charge transport is tunneling through the hendecane, which is much shorter than the whole molecule length. Therefore, the rectification in $SC_{11}Fc$ was attributed to the non-uniform potential drops arising from the asymmetrically positioned and electronically coupled of accessible molecular orbital to one electrode in the junction.

More interestingly, solid-state devices have been fabricated experimentally by Lee et al. based on rigid or even flexible substrates using the distinctive ferrocenyl headed alkanethiolates [99, 100]. Also, they found an unusual temperature dependence of the leakage current at large bias voltages and temperatures higher than 220 K, namely the current density decreases as the temperature increases, which was ascribed to redox-induced conformational changes of the SC_nFc molecules.

2.4 Molecular diodes from asymmetric molecule–electrode interfaces

All of the above-mentioned molecular rectifiers have intrinsic structural asymmetries in the molecules themselves. Therein, asymmetric electronic structures under positive and negative bias voltages are the origin of rectification. Besides that, evident rectification may also be observed when there are asymmetries at the two interfaces between the molecule and electrodes in the molecular devices. One kind of the interfacial asymmetries arises from the different surface morphologies of metal electrodes at the molecule–electrode contacts. This kind of interfacial asymmetry is mostly due to the techniques used to form the molecular devices, such as LB monolayer technique [101, 102], electromigration breakdowns [103], electrical chemical depositions [104], and surface diffusion-mediated depositions [105], and it is really a very big challenge to control the details of the molecule–electrode interface in experiments. While the molecule–electrode contacts may significantly influence the character or the performance of molecular devices, a more advanced technique, namely mechanically controllable break-junction technique, which can establish stable molecule–electrode contacts has been consequently developed [106–109]. This technique greatly improves the stability and

repeatability of the molecule–electrode contacts and therefore largely boosts the research in molecular electronics. Meanwhile, the mechanically controllable break-junction technique also helps to reduce the influence of the first kind of interfacial asymmetry on the performance of molecular diodes. On the other hand, there is also another interfacial asymmetry, which originates from different molecule–electrode bonding by different anchoring groups or different electrode materials. This kind of interfacial asymmetry can be used to produce a noticeable rectifying effect even for symmetric molecules. For example, SAMs of C_6H_5–C≡C–C_6H_4–C≡C–C_6H_4SH molecules have been observed to rectify between Au(111) or Ag(111) electrodes [14]. The rectification was rationalized by the simple triangular barrier model (Fig. 8). When the symmetric molecule adsorbs on the left metal substrate, the sulfur atom will take electrons from the substrate and donates them to the conjugated backbone of the adsorbate. This reduces the barrier Φ_1 from the metal substrate to the molecular conducting level. Meanwhile, the molecule connects to the tip electrode through the phenyl group in the form of van der Waals contact with a larger barrier Φ_2. At a moderate positive bias voltage, the tunneling electron needs to overcome the barrier Φ_1. However, it needs to overcome a much larger barrier Φ_2 under the negative bias. This is why an obvious rectifying effect was observed in the experiment.

On the other hand, Chen et al. experimentally fabricated heterometallic devices based upon on-wire lithography (OWL) method, which were made of Au and Pt metal nanorods separated by a nanometer-sized gap [110]. A symmetric molecule of thiol-terminated oligo(phenylene ethynylene) (OPE) was assembled into the heterometallic nanogaps to form molecular junctions (Fig. 9). Diode behavior was obtained for the *I*–*V* measurements, which was rationalized by the different coupling strengths between S–Au and S–Pt [111].

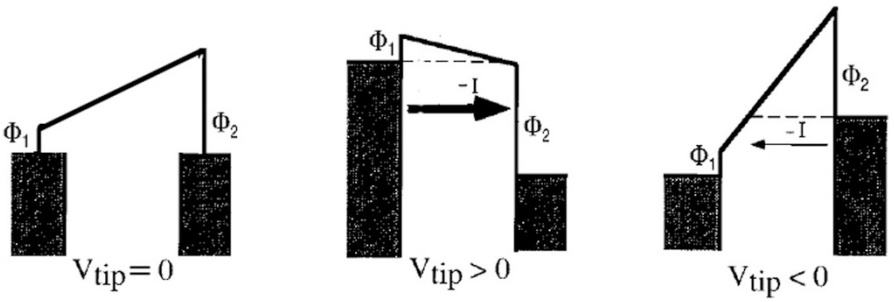

Fig. 8 Schematic of the barriers when the SAMs of C_6H_5–C≡C–C_6H_4–C≡C–C_6H_4SH molecules are between Ag and Au electrodes. With no bias applied, the chemical potential is constant. The sulfur adsorbed on the metal acts as a donor to the molecule reducing the barrier Φ_1 from the metal substrate to the molecular conducting level, while the tip to molecule barrier is Φ_2. The bias voltage is applied on the tip. Reproduced with permission from Ref. [14]. Copyright 1997 American Institute of Physics

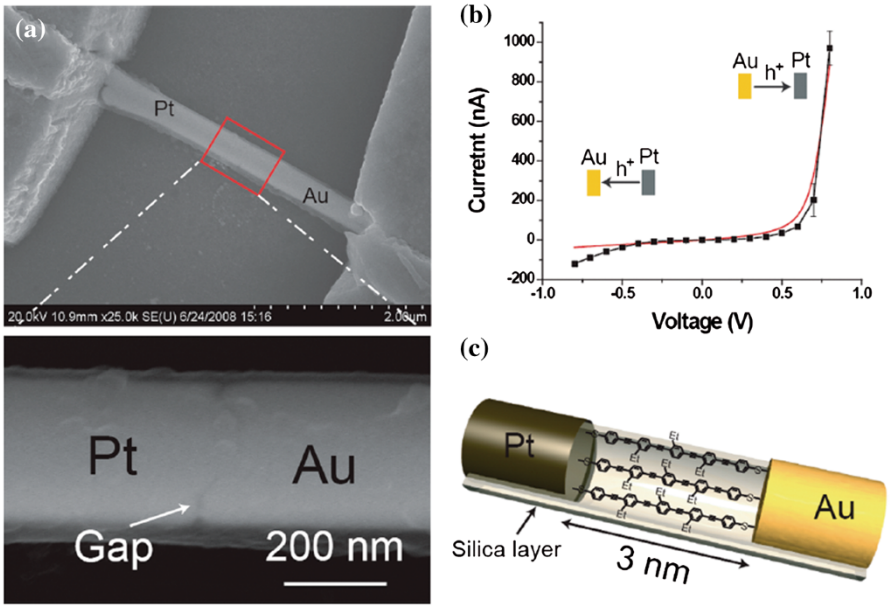

Fig. 9 **a** SEM image of an OWL-fabricated device with a ~ 3-nm Au–Pt heterometallic nanogap. **b** Representative *I–V* response for a ~ 3-nm OWL-fabricated heterometallic nanogap device modified with OPE. **c** A sketch of the device depicting the OPE molecules spanning the ~ 3-nm gap. Reproduced with permission from Ref. [110]. Copyright 2009 American Chemical Society

2.5 Molecular diodes based on low-dimensional materials

With the development of materials science, the building components of molecular devices have stepped far beyond organic molecules and traditional bulk noble metals. In recent years, various kinds of new materials with low-dimensional features, such as graphene, silicene, germanene, stanene, borophene, MoS_2, WS_2, and carbon nanotube, have been successfully synthesized in experiments [52–57], and they have demonstrated a lot of extraordinary electronic and structural properties that bulk materials do not have. Enlightened by this, researchers have been trying to replace the bulk noble metal materials with these lower-dimensional materials to accelerate the miniaturization of electronic devices. For this purpose, understanding the electron transport properties of these novel low-dimensional materials is an essential issue.

Since the single atomic layered material graphene was experimentally obtained in 2004 [52], it has gained extensive interest because of its unique properties [112, 113], such as exceptionally high electric [114] and thermal conductivity [115], extraordinary mechanical strength [116], and quantum Hall effect [117]. It is worth noting that the electronic properties of graphene can be tuned by tailoring its geometric structure. If graphene is trimmed into graphene nanoribbons (GNRs), the electronic structures will be extremely sensitive to the edge patterns and ribbon widths. Namely, the zigzag edged graphene nanoribbons (zGNRs) are shown to be

zero-gap materials, whereas the armchair edged graphene nanoribbons (aGNRs) have finite energy gaps, which shrink with the ribbon width following a $3N + 1$ rule [118–122]. More importantly, by using GNRs as electrodes, the mismatch of energy level alignment at the molecule–electrode interfaces encountered in metal–molecule–metal junctions will be considerably reduced since the molecules and electrodes are the same material (carbon atoms). All these properties indicate a great potential application of GNRs in nano electronics. For example, Li et al. explored the rectifying behaviors of a D–π–A molecular diodes sandwiched between two GNR electrodes [123]. They found that the rectification directions of the molecular diodes were highly related to the edge pattern of GNRs, i.e., the diodes with metallic zGNR electrodes had a forward rectification, which was consistent with that suggested by Aviram and Ratner [12], while the rectification was completely reversed when the electrodes were replaced by the semiconducting aGNRs. More interestingly, the rectification performance was largely improved with an increase of the band-gap for aGNR electrodes and could reach as large as 4002, which suggested a novel effective pathway to greatly raise rectifying behaviors of a donor–acceptor molecule.

Considering the difference in band structures and conductivities for GNRs with different edge patterns, combination of zGNR and aGNR as electrodes can be used to construct heterojunctions that may potentially have rectifying behaviors [124]. As

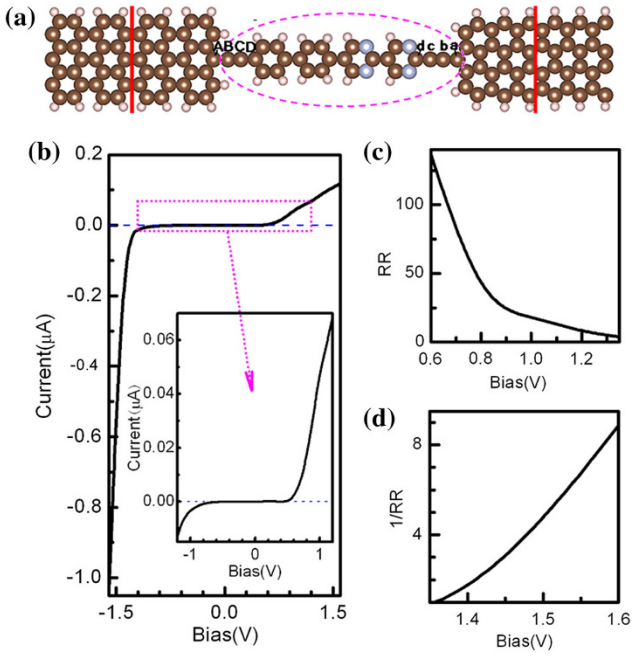

Fig. 10 **a** The schematic of a molecular diode, where a dipyrimidinyl–diphenyl molecule is sandwiched between two zGNR and aGNR electrodes. **b–d** The *I–V* curves and the rectification ratio curves of the molecular junction. Reproduced with permission from Ref. [124]. Copyright 2013 American Chemical Society

shown in Fig. 10a, a dipyrimidinyl–diphenyl molecule was sandwiched between zGNR and aGNR electrodes, and it was quite interesting to find that the rectifying direction of the molecular junction turned to be bias voltage dependent, i.e., this molecular device displayed an obvious forward rectifying behavior at low bias voltage, while the rectifying direction was reversed as the bias voltage became larger. It was revealed that the asymmetric shift of perturbed molecular energy levels and the asymmetric spatial distribution of frontier molecular orbitals upon the reversal of bias voltage as well as the band structures of the electrodes gave rise to the rectifying behaviors.

As known, the band structures of GNRs are sensitive to their geometric structures. Therefore, besides tailoring the edge patterns, other decoration methods have also been employed to modulate the electronic structures of GNRs and the electron transport properties of molecular devices that are designed based on them. One of the important and efficient ways to tuning the electronic properties and expanding the applications of GNRs is doping with foreign atoms, such as B and N [125–133]. In this way, Song et al. proposed molecular diodes with very high rectification ratios constructed by sandwiching an azulene-like dipole molecule between a pristine zGNR electrode and an aGNR electrode that was doped by a series of foreign atoms [134]. The excellent rectifying performance was well understood by the symmetry analyses of Bloch wave functions of the corresponding subbands around E_F. It is known to all that only when the energy subbands of occupied states of one electrode are overlapped with the subbands of unoccupied states of the other electrode is it possible for the electrons to tunnel through the molecular junction from one electrode to the other. The second prerequisite for a current flowing across the molecular junction is that the tunneling electron must preserve its symmetry in the wavefunctions across the whole molecular junction if there are symmetries in the geometric structure. Moreover, it was found that the molecular devices with III main group dopants in the aGNR electrode exhibited a better rectifying performance than the respective devices with V main group dopants. Specifically, the boron (aluminum) dopants in the aGNR electrode promoted a better rectifying performance for the molecular junctions than the respective nitrogen (phosphorus) dopants, and also it was figured out that the rectifying performance closely depended on the concentration of dopants (Fig. 11).

Besides doping, adsorbing molecules on the GNRs can also significantly change the rectifying performance of molecular heterojunctions. In 2016, azulene-like molecular junctions using B-doped aGNRs as electrodes were designed by Xie et al. for potential sensors of toxic gas molecules, such as CO, NO, or NO_2 [135]. The adsorption of these gas molecules on the B-doped site on aGNRs could selectively change the *I–V* characteristics of the molecular junctions depending on the specific adsorbate. In addition, Cao et al. designed molecular diodes with prominent rectification effects by asymmetrically hydrogenating the edges of zGNRs at the left and right side of the molecular junctions [136] (Fig. 12). It was found that the dihydrogenation of the edge in zGNR could block the electron transfer, resulting in a decrease in the conductivity compared to the cases of monohydrogenation and the pristine one. The asymmetric distributions of frontier wavefunctions under the

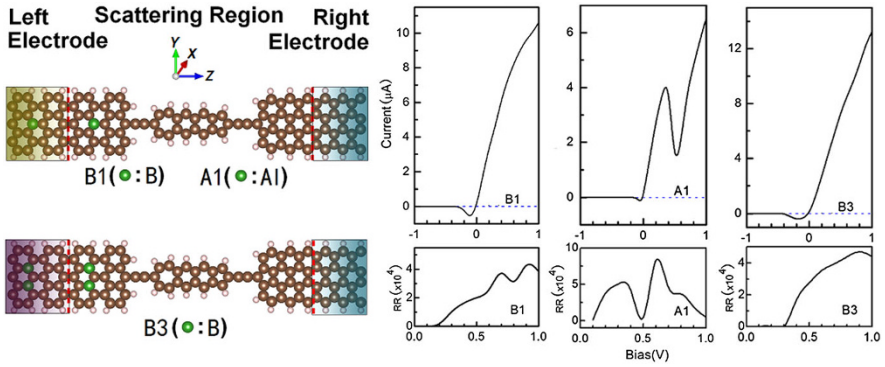

Fig. 11 Schematic of GNRs-based molecular diodes, and corresponding *I–V* curves and rectification ratios. Reproduced with permission from Ref. [134]. Copyright 2014 American Chemical Society

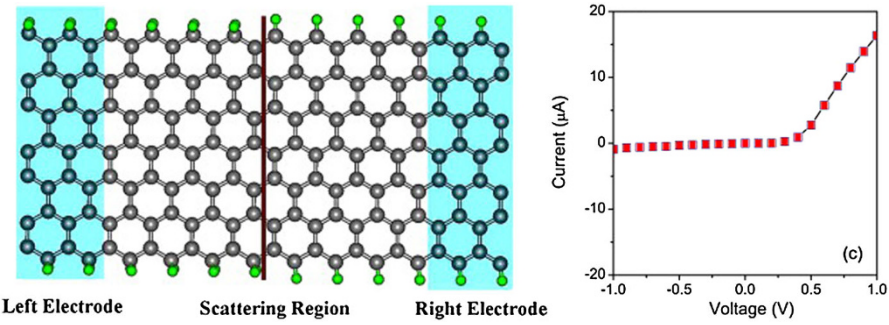

Fig. 12 The zGNR heterojunction with asymmetric edge hydrogenations, and the corresponding *I–V* curve. Reproduced with permission from Ref. [136]. Copyright 2013 Published by Elsevier B.V

positive and reversal bias voltages caused by dehydrogenation were revealed to be the main reason for the rectification.

Carbon nanotubes (CNT), often visualized as seamlessly rolled-up graphene ribbons, are another kind of commonly used one-dimensional material, which also play an important role in building nanodevices [137–141]. Similar to the case of GNRs, the transport properties of single-walled carbon nanotubes (SWCNTs) can also be tuned by doping foreign atoms [142, 143], adsorbing gas molecules [144, 145], introducing defects [143, 146], and so on. Until now, there have been a variety of molecular diodes proposed and designed by using CNTs as the fundamental element. For example, Cheng et al. investigated the effects of nitrogen–vacancy complex on electronic transport properties of spiral chirality (4, 2) SWCNT-based molecular device [143]. They theoretically demonstrated that salient rectifying performance could be obtained and largely tuned by introducing the complex defects with carbon vacancy and nitrogen dopant (Fig. 13).

Meanwhile, amounts of nanodevices based on other low-dimensional materials such as silicene, germanene, borophene, boron-nitride nanoribbon (BNNR), MoS_2 and WS_2, have been proposed in the past few years [147–152]. For instance, Cheng

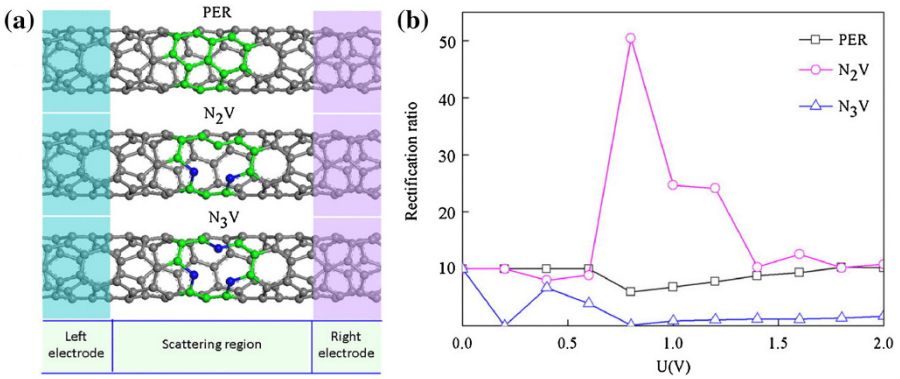

Fig. 13 **a** Schematic structures of (4, 2) SWCNT junctions with defects of different carbon vacancies and nitrogen dopants, and **b** the corresponding bias-dependent rectification ratios. Reproduced with permission from Ref. [143]. Copyright 2013 AIP Publishing LLC

et al. investigated the transport properties of a series of armchair silicene nanoribbons (aSiNRs) in which two phosphorus atoms substitute two adjacent silicon atoms in the same sublattice [147]. When the doping sites of phosphorus atoms were changed from the edge to the center of aSiNRs, the characteristics of the phosphorus-doped 7-aSiNRs converted from semiconducting to metallic. It was also demonstrated that the device based on edge-doped 7-aSiNR manifested an obvious rectifying performance. Furthermore, Song et al. studied the rectifying properties of hydrogenated zigzag edged SiNRs and germanene nanoribbons (zGeNRs) [153]. When one of the electrodes was hydrogenated from silicene (germanene) to silicane (germanane), striking rectifying behavior with giant rectification ratios could be witnessed. In recent years, researchers have proven that different kinds of 2D materials in a similar lattice constant can be spliced together to construct heterojunctions [154–157]. Inspired by this, Sun et al. investigated the electron transport property of a MoS_2/WS_2 heterojunction, which showed a striking rectification behavior [148]. Interestingly, it was also revealed that the rectification direction could be inverted by means of adsorbing NH_3 molecules due to the modification of the substrate electronic structure and the charge transfer from the adsorbate to the heterojunction (Fig. 14).

Since any asymmetries in geometric structure of nanodevices may induce rectification behaviors, explicit structural asymmetries have been brought into the scattering region of 2D materials-based nanodiodes [158–160]. Zhang et al. investigated the electron transport properties of a zigzag edged trigonal graphene nanoflake (zTGNF) that was connected to two gold electrodes via atomic carbon chains, and high-performance rectifying behaviors were found. More intriguingly, as shown in Fig. 15a, the rectification direction could be easily modulated by altering the odevity of the number of carbon atoms in the atomic carbon chains [159]. Ji et al. further calculated the transport properties of zTGNF between GNR electrodes, and high-performance rectification was obtained [160]. Considering that the anchoring groups between center molecule and electrodes are of great

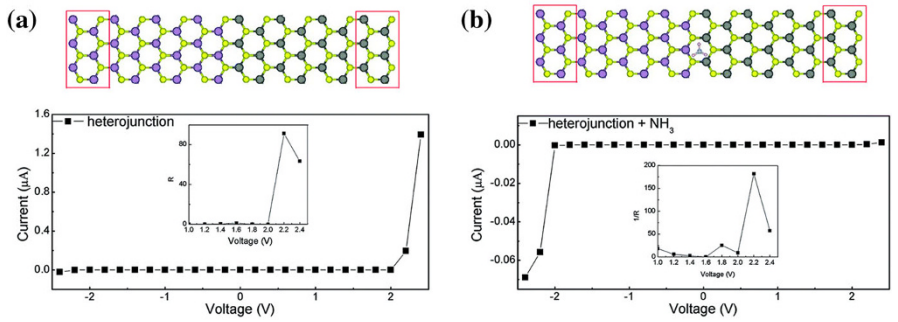

Fig. 14 Schematic structures of MoS_2/WS_2 heterojunctions **a** without and **b** with NH_3 adsorption and the corresponding *I–V* curves. The *insets* are the bias-dependent rectification ratios. Reproduced with permission from Ref. [148]. Copyright 2016 The Royal Society of Chemistry

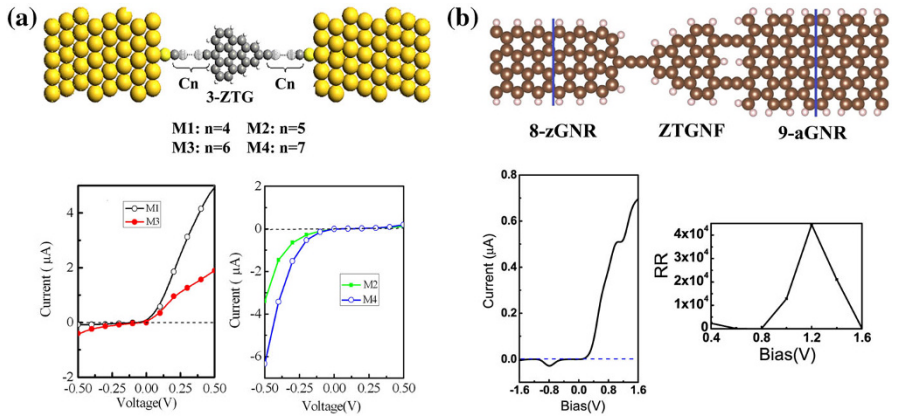

Fig. 15 **a** Geometrical structure of nanojunctions comprised of C*n*/3-ZTG/C*n* ($n = 4, 5, 6, 7$) and corresponding *I–V* curves. **b** The schematic structure of molecular junction with zTGNF and corresponding *I–V* curve and rectification ratio. Reproduced with permission from Ref. [159]. Reproduced with permission from Ref. [160]. Copyright 2016 Elsevier B.V

significance in regulating rectification performance, different numbers of carbon atomic chains (CACs) were adopted as the anchoring groups to connect the zTGNF to GNR electrodes. The rectifying behavior could be optimized by changing the number of CACs, and giant rectification ratio was presented when zTCNF was connect to the GRN electrode by one and two CACs at the left and right side, respectively, as shown in Fig. 15b.

3 Modulations of rectifying performance

Understanding the mechanisms of functional molecular devices is one of the main focuses of research in the field of molecular electronics. Based on this achievement, on the other hand, it is desirable to control the performance of molecular devices.

For this aim, researchers have developed various kinds of methods to control or tune the performance of rectification in molecular diodes both experimentally and theoretically. In the following content, we will devote to review the work contributing to modulating the rectification performance of molecular diodes.

In 2005, Yu et al. found that the rectification direction could be controlled by the pH value of surround solvent [25]. When the dipyrimidinyl–diphenyl co-oligomer molecular diode was immersed in perchloric acid, the rectifying direction was observed to be reversed. At the same time, the change of rectifying direction was reversible. That is, when the solvent was neutralized by sodium ethoxide, the rectifying direction was recovered (Fig. 16). It was speculated that the inversion of the rectifying direction in perchloric acid was from the protonation of nitrogen atoms in dipyrimidinyl block. This inference was theoretically verified by Zhang et al. using density functional theory in combination with non-equilibrium Green's function method [40]. They found that the rectifying direction was highly dependent on the configuration of protonation (Fig. 17). The protonation of the outer pyrimidinyl was favorable for enhancing the conductivity and rectifying performance, while the protonation of the inner pyrimidinyl played a key role for inverting the rectifying direction. This provides a feasible way to modulate the rectification of molecular diodes by tuning the PH value of surrounding solvent.

Contacts between molecule and electrodes in molecular junctions play a crucial role in determining the corresponding electric properties. Therefore, one can control the rectifying performance of molecular diodes by elaborately designing the organic-metal interface. It was experimentally reported that the rectifying direction of the dipyrimidinyl–diphenyl co-oligomer diode could be reversed by substituting an isocyanide group for the thiol group at the diphenyl side [161]. This interesting phenomenon was subsequently well understood from a theoretical point of view [41]. It was figured out that the strong electron-withdrawing isocyanide and

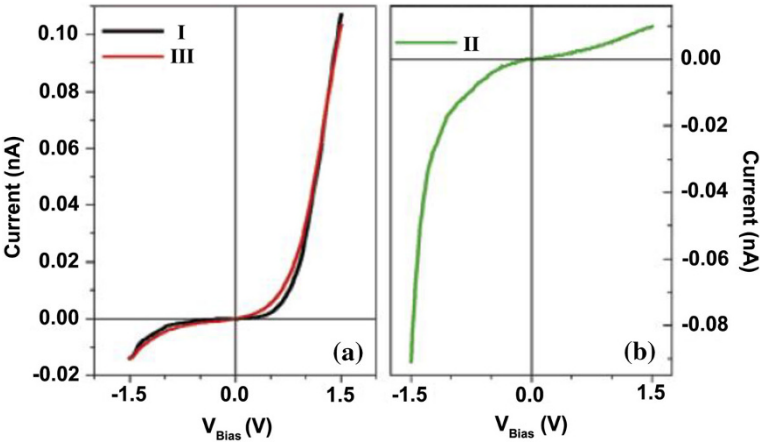

Fig. 16 Averaged *I–V* curves measured for **a** deprotonated dipyrimidinyl–diphenyl co-oligomer (I sample before protonation, III sample after protonation–deprotonation), and **b** assembly protonated by $HClO_4$. Reproduced with permission from Ref. [25]. Copyright 2005 American Chemical Society

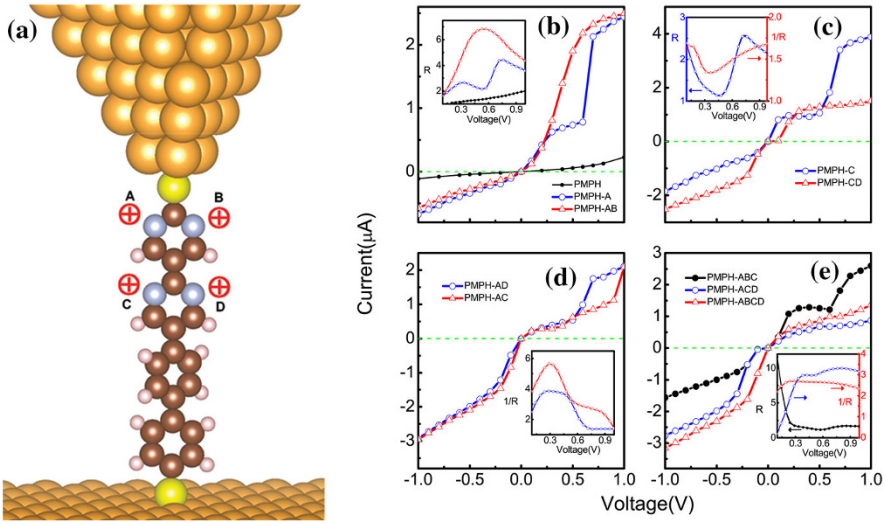

Fig. 17 **a** Schematic of the possible protonation locations in dipyrimidinyl–diphenyl molecular junction. **b–e** The calculated *I–V* curves for each protonation configuration. The *insets* are bias-dependent rectification ratios. Reproduced with permission from Ref. [40]. Copyright 2012 American Chemical Society

electron-donating thiol group lead to the frontier molecular orbitals highly localized on either pyrimidinyl moiety or diphenyl block so that these frontier molecular orbitals had monotonic evolutions under positive and negative bias voltages. However, when the isocyanide group and thiol group were exchanged, namely, the isocyanide group was at the pyrimidinyl side while the thiol group at the diphenyl side, the synergistic effect of the ending groups and the molecule backbone contributed to a largely enhanced rectification ratio (Fig. 18).

As revealed by Hu et al., there are two competitive mechanisms dominating the rectification in pyrimidinyl-phenyl co-oligomers [43, 44, 162, 163]. That is, asymmetric energy shift of LUMO and asymmetric spatial distribution of corresponding wavefunction under positive and negative bias voltages. The current of pyrimidinyl-phenyl molecular junctions was found mainly contributed by the LUMO. However, the LUMO approaches the E_F under positive bias voltages while it departs from the E_F under negative bias voltages. Meanwhile, the positive bias voltage aggravates the spatial localization of LUMO on the pyrimidinyl block while the LUMO tends to spatially delocalize on both segments under negative bias voltages. Therefore, the former leads to the current flowing preferably from pyrimidinyl block to phenyl moiety, but the latter results in a rectification in the opposite direction. It is found that the offset between the LUMO and E_F under zero bias voltage is the key parameter to determine which mechanism is the dominative one. That is to say, one can control the rectifying direction of pyrimidinyl-phenyl co-oligomers by modulating the location of LUMO relative to the E_F. Both first-principles calculations and Su–Schrieffer–Heeger (SSH) modeling suggest that varying the molecular length of pyrimidinyl-phenyl diblock co-oligomers can be an

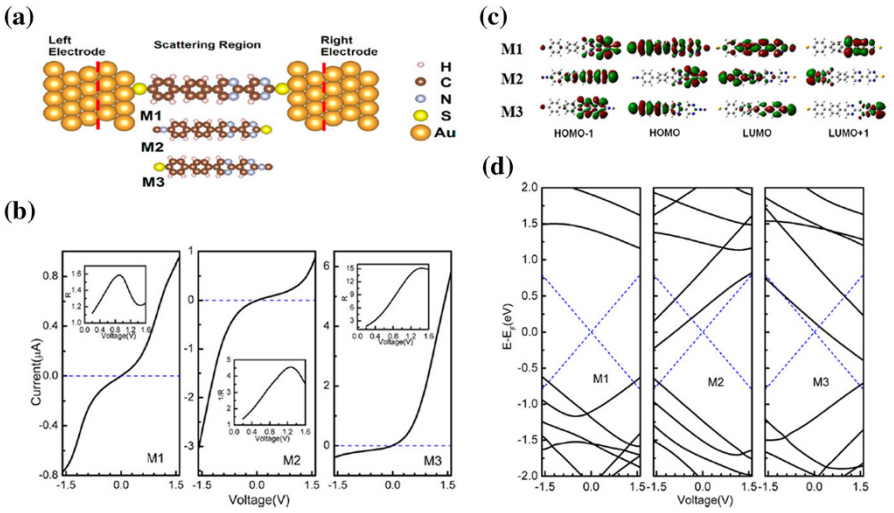

Fig. 18 **a** Schematic structures of three molecular junctions: M1 corresponds to the molecule connected to electrodes via two thiol groups; M2 is the junction where the left thiol group is replaced by an isocyanide group while the isocyanide group appears in the right terminal for M3. **b** *I–V* curves for molecular junctions M1, M2, and M3 as shown in **a**. The insets are the bias-dependent rectification ratios. **c** Spatial distributions of the frontier molecular orbitals for M1, M2, and M3 at zero bias voltage. **d** Evolution of MPSH eigenvalues under bias voltages for M1, M2, and M3. The dashed lines indicate the bias window. Reproduced with permission from Ref. [41]. Copyright 2012 American Chemical Society

efficient way to control the rectifying direction of diblock co-oligomers since the HOMO–LUMO gap can be efficiently tuned by changing the molecular length (see Fig. 19) [44, 162].

Moreover, it was found that stretching or contracting the molecular junction by an external force could also induce the energy change of molecular levels, especially LUMO, with respect to the E_F, and hence could be used as a method to trigger the switch of rectifying direction in pyrimidinyl-phenyl co-oligomers (Fig. 20) [163]. This was explained by variations in the coupling strength between molecule and electrodes arising from stretching or contracting the molecular junction. As was shown experimentally by Tao et al., the decrease in coupling strength between molecule and electrodes could cause a shift up in molecular energy levels with respect to the E_F [164]. So, LUMO will move away from the E_F when the molecular junction is stretched and move towards the E_F when the molecular junction is compressed. By this, the rectifying direction of pyrimidinyl-phenyl co-oligomers can be controlled through externally stretching or contracting of the molecular junction. And the numerical calculations further suggest that the inversion of rectifying direction is molecular length dependent. When the molecular length is too short, taking 2PM2PH for an example, the HOMO–LUMO gap is so large and hence the LUMO is far enough away from the E_F that it is difficult to change the rectifying direction by stretching and contracting of the molecular junction.

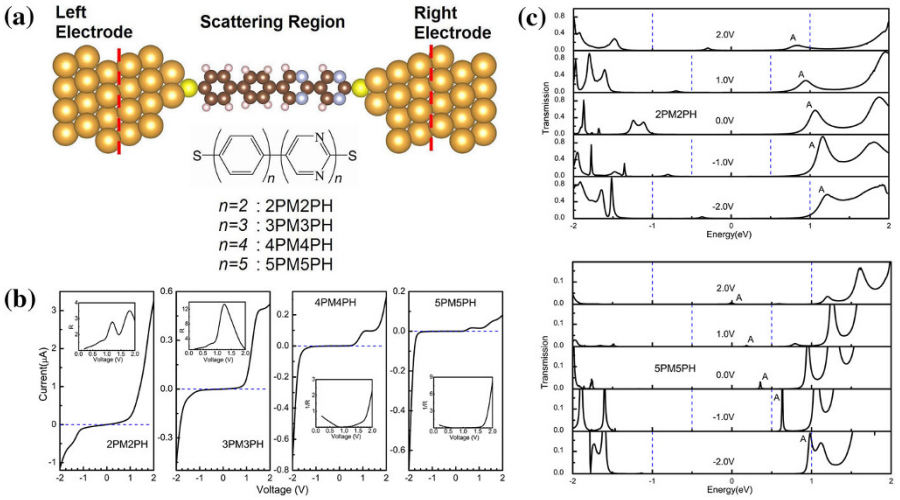

Fig. 19 **a** Modeling structure of the calculated pyrimidinyl-phenyl diblock cooligomer molecular junctions. Molecules with different lengths ($n = 2, 3, 4, 5$) are denoted as 2PM2PH, 3PM3PH, 4PM4PH, and 5PM5PH, respectively. **b** *I–V* curves of the four molecular junctions. The insets are the rectification ratio or inverted rectification ratio. **c** The bias-dependent electronic transmission spectra for 2PM2PH and 5PM5PH. The dashed blue lines indicate the bias window. Reproduced with permission from Ref. [44]. Copyright 2013 Elsevier B.V

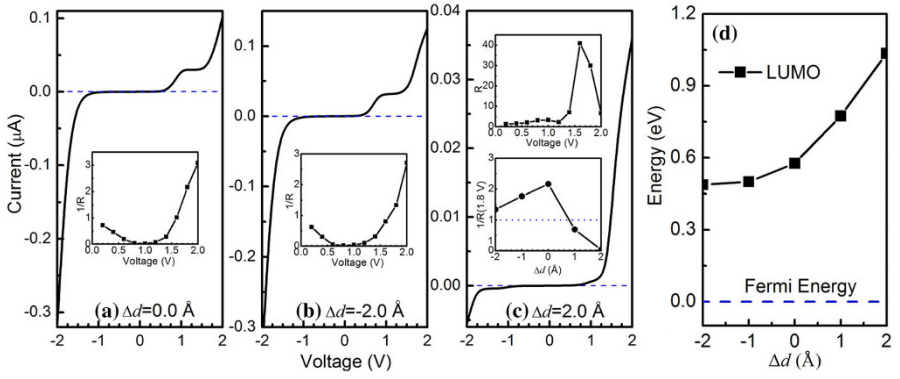

Fig. 20 **a–c** *I–V* curves for 4PM4PH with $\triangle d = 0$ and $\pm$ 2.0 Å, where $\triangle d$ represents the change of the distance between two electrodes based on the equilibrium one. The *insets* are the bias-dependent rectification ratio. **d** The energy evolution of LUMO versus $\triangle d$ at zero bias. Reproduced with permission from Ref. [163]. Copyright 2013 AIP Publishing LLC

In addition, varying the portion of electron-donating or electron-withdrawing moieties in the diblock co-oligomer with a specific length also plays an effective role in tuning the alignments of frontier molecular orbitals with respect to the E_F [43]. For molecular rectifiers based on pyrimidinyl-phenyl co-oligomers, it was found that the 1:1 proportion of the two moieties favored the largest rectification ratio for a short pyrimidinyl-phenyl co-oligomer, however, the optimal proportion

for the largest rectification ratio was not 1:1 any longer when the pyrimidinyl-phenyl co-oligomer became longer. More interestingly, a proportion-dependent variation of the rectifying direction was observed for the longer pyrimidinyl-phenyl co-oligomer (Fig. 21).

As mentioned above, the rectification of σ–π type molecular diodes is dominated by the frontier occupied molecular orbitals, which asymmetrically localize on the electron-rich moiety. In 2015, Yuan et al. experimentally realized the control of the rectifying direction in ferrocenyl–alkanethiolates by adjusting the location of ferrocenyl group in the alkyl backbones (Fig. 22) [28]. Moreover, the validity of this method was further verified in bipyridyl-alkanethiolates by a theoretical work where the ferrocenyl group was replaced by the bipyridyl group [46]. More interestingly, it was revealed that the rectification ratios of ferrocenyl–alkanethiolates could be largely modulated by the odd–even number of repetitive methylene units in the alkyl chain [29, 45, 165]. However, the odd–even modulation on the rectification ratios was completely reversed by replacing the electrodes from gold to silver due to the different bond angles of Au–S–C and Ag–S–C (Fig. 23). These studies provide powerful and efficient pathways to control the rectifying performance in σ–π type molecular diodes.

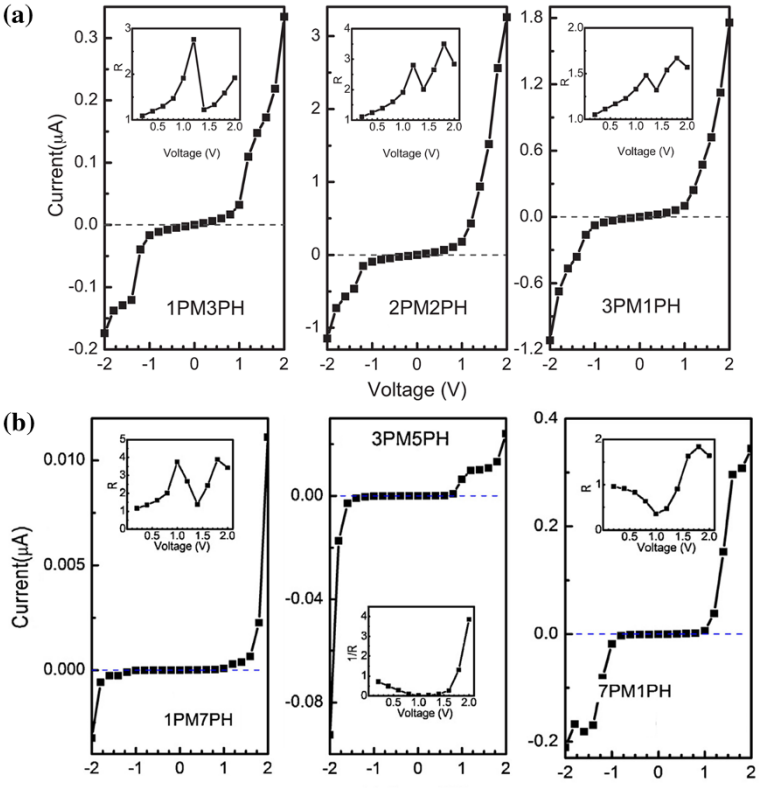

Fig. 21 *I–V* curves for pyrimidinyl-phenyl co-oligomer diodes with a **a** shorter molecular length and **b** a longer molecular length. Reproduced with permission from Ref. [43]. Copyright 2014 Elsevier B.V

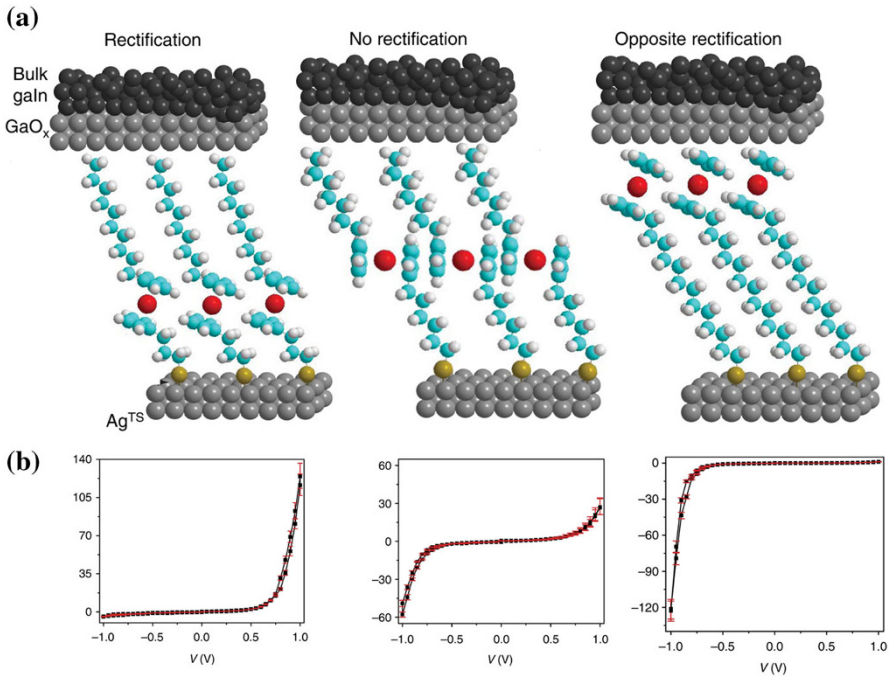

Fig. 22 **a** Schematic structures for ferrocenyl–alkanethiolate molecular junctions with ferrocenyl group at different locations in alkanethiolate backbones. **b** Corresponding *I-V* curves for molecular junctions in **a**. Reproduced with permission from Ref. [28]. Copyright 2015 Macmillan Publishers Limited

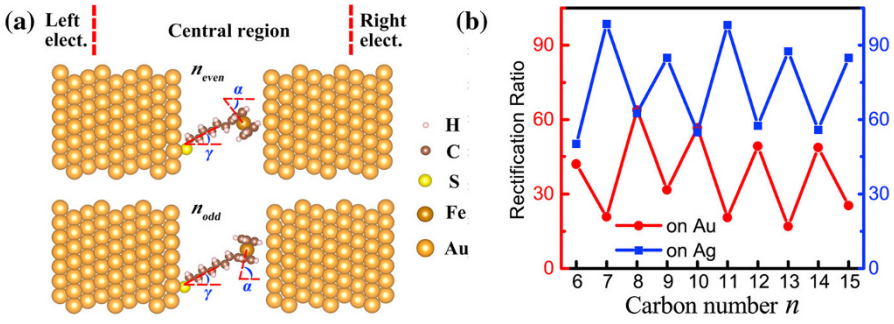

Fig. 23 **a** Schematic structures for ferrocenyl–alkanethiolate between gold electrodes with odd or even number of methylene units in the alkyl chain. **b** Rectification ratios of ferrocenyl–alkanethiolate diodes as a function of the number of methylene units in the alkyl chain on gold or silver substrate electrodes. Reproduced with permission from Ref. [45]. Copyright 2017 Elsevier B.V

4 Spin-based molecular diodes

4.1 Spin diodes and mechanisms

As discussed above, for normal charge-current rectifying devices, the magnitude of current under positive and reversal negative bias voltages is not symmetric, namely, $I_c(V) \neq -I_c(-V)$. Similarly, for a spin diode, the magnitude of spin current, defined as $I_s = \frac{\hbar}{2e}(I_\uparrow - I_\downarrow)$, is also asymmetric under positive and reversal negative bias voltages, i.e., $I_s(V) \neq -I_s(-V)$ [64]. To characterize the efficiency of a spin-current rectification, spin-current rectification ratio is accordingly defined as $\mathrm{SRR} = -I_s(V)/I_s(-V)$. It is noted that the spin-current rectification is a little more complex to describe because the spin current contains both magnitude and orientation of spin polarization. As a result, the value of SRR can be negative, which indicates the reversal of polarization for the spin current. The spin-current rectification may appear in two forms or their combination. One is that the spin polarization of the spin current is unchanged but the magnitude of spin current is asymmetric with the reversal of bias voltage. The other one is that only the spin polarization of the spin current is inversed when the bias is reversed. Therefore, there are four possible types of I–V relations for a molecular spin device: (1) $I_c(V) = -I_c(-V)$ and $I_s(V) = -I_s(-V)$ mean both charge current and spin current are symmetric with the reversal of bias voltage; (2) only the charge current is rectified, which shows $I_c(V) \neq -I_c(-V)$ and $I_s(V) = -I_s(-V)$; (3) only the spin current is rectified with $I_c(V) = -I_c(-V)$ and $I_s(V) \neq -I_s(-V)$; and lastly (4) both charge current and spin current are rectified with $I_c(V) \neq -I_c(-V)$ and $I_s(V) \neq -I_s(-V)$. The second case has been discussed above. The following discussion will focus on the last two cases.

Molecular spin diode requires a structural asymmetry in spin degree of freedom. It was theoretically demonstrated that a molecular spin diode may be realized based on a magnetic co-oligomer [64]. The proposed molecular spin diode comprises a segment of ferromagnetic oligomer poly(1,4-bis-(2,2,6,6-tetramethyl-4-oxy-4-piperidyl-1-oxyl))-butadiin) (poly-BIPO) [166] with N_1 sites and a segment of nonmagnetic polyacetylene oligomer with N_2 sites, which is sandwiched between two metal electrodes (Fig. 24). By changing the E_F of electrodes, the two kinds of spin-current rectification are realized with or without concomitant charge-current rectification. For the case of only spin-current rectification, it requires that the conducting charge channel is symmetric while the conducting spin channel is asymmetric under a positive and negative bias voltage, which is fulfilled by setting the $E_F = 0$. In this case, as shown in Fig. 24b, the spin-down HOMO (spin-up HOMO) and spin-up LUMO (spin-down LUMO) are symmetrically located about the E_F. The intensities of transmission peaks contributed by them are equal under zero bias voltage. However, they have completely opposite energy shift trends under positive and negative bias. That leads to a symmetric magnitude of current but an opposite spin polarization of the spin current when the bias is reversed. For the case of both the charge current and spin current are rectified, it needs asymmetries in both the charge and spin channels, which is realized by setting a nonzero E_F, for

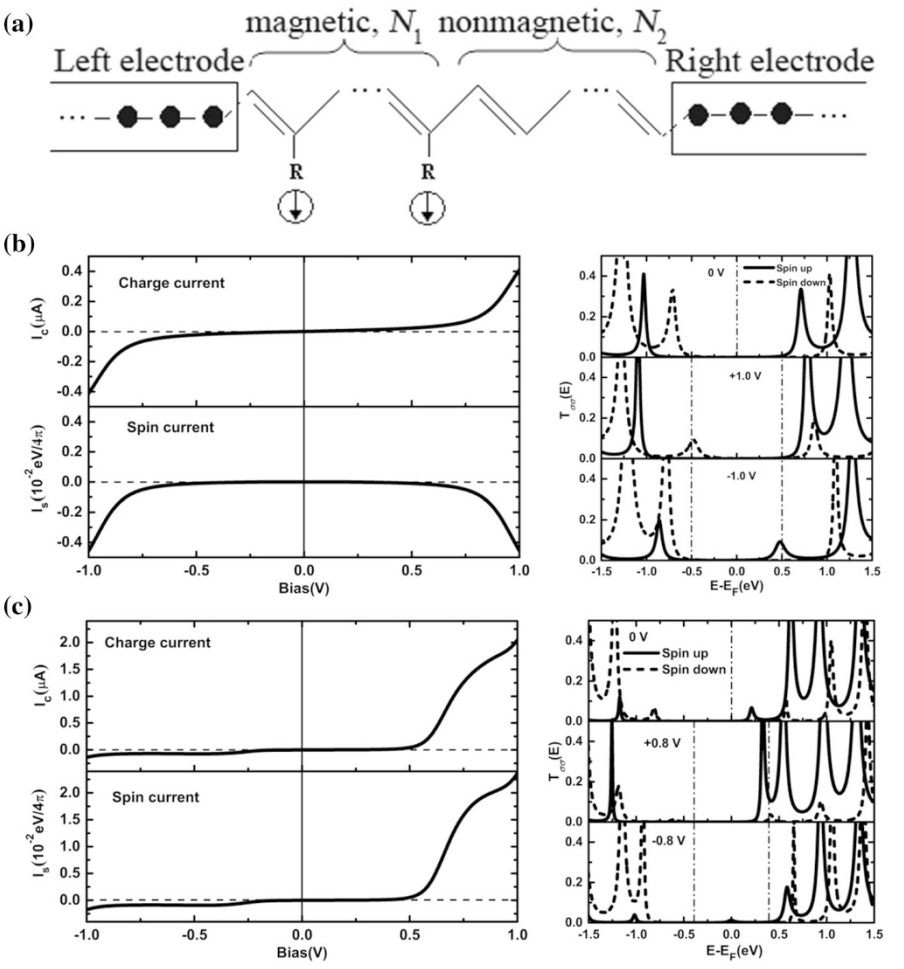

Fig. 24 **a** Schematic of a metal/magnetic-nonmagnetic co-oligomer/metal spin diode. Charge current, spin current, and the spin-resolved transmission spectra for **b** $N_1 = N_2 = 10$, $E_F = 0$, and **c** $N_1 = N_2 = 16$, $E_F = 0.3$ eV. Reproduced with permission from Ref. [64]. Copyright 2008 American Institute of Physics

example, $E_F = 0.3$ eV. In this case, the transport is dominated by the spin-up LUMO, but the transmission height is asymmetric under positive and negative bias voltages. This leads to a rectification for both the charge current and spin current.

4.2 Modulations of spin-current rectification performance

Some methods mentioned above used to modulate the charge-current rectification have been proved to be also efficient to modulate the spin-current rectification. For example, the variation of the molecular length of the magnetic co-oligomer has been verified to largely tune the spin-current rectification ratio as well as the rectifying

direction [70]. As shown in Fig. 25, for a co-oligomer with shorter molecular length, the spin-current rectification ratio is weakened sharply while the charge-current rectification ratio changes little as the molecular length increases. However, for a co-oligomer with longer molecular length, both the spin-current and charge-current rectification ratios increase quickly with the molecular length. More interestingly, the rectifying directions of both spin-current and charge-current rectification are inverted at a critical molecular length. The mechanism of length-dependent inversion of rectification in this spin diode is similar as that in the D–A charge current diode, that is, the exchange of two dominant mechanisms between asymmetric shift of molecular levels and asymmetric spatial localization of wavefunctions for the conducting orbitals. A feature analysis about this was given in Ref. [71], where a method by applying a gate voltage on the device was also proposed to manipulate the rectification direction.

In addition, by adjusting the proportion between the magnetic and nonmagnetic moiety in the co-oligomer diode, the rectification ratios of charge current and spin current were shown to be largely modulated [69]. As shown in Fig. 25c, the numerical calculation suggested that equal length for the two components favored the largest rectification ratios. It was also found that the coupling strength between the organic co-oligomer and electrodes played a crucial role in determining the rectifying performance of both spin current and charge current [72]. As shown in Fig. 26, in the case of spin-independent interfacial coupling, the rectification ratios

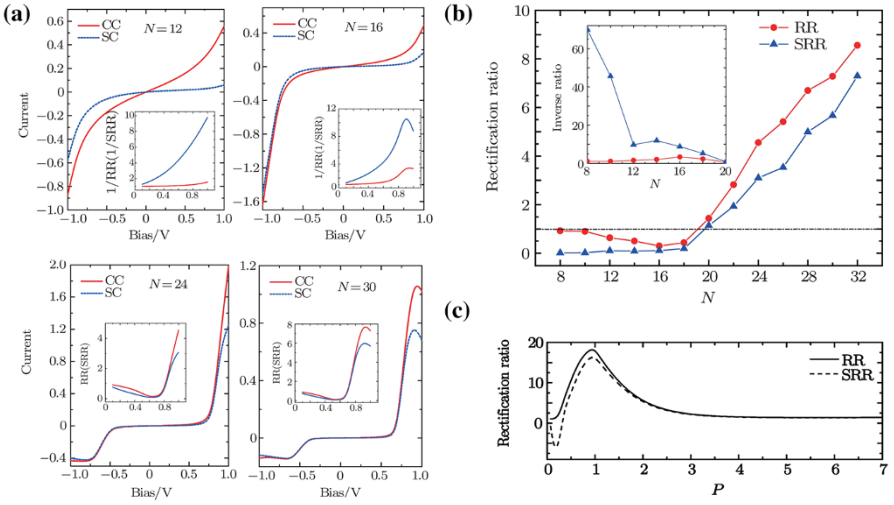

Fig. 25 **a** Calculated charge-current (CC) and spin-current (SC) as a function of bias voltage with $N = 12$, 16, 24, 30 ($N_1 = N_2 = N/2$). *Solid red lines* correspond to charge current in units of μA, and *dashed blue lines* indicate spin current in units of $\frac{\hbar}{2e}$. The *inserts* are bias-dependent rectification ratios. **b** Dependence of charge-current and spin-current rectification ratios on the molecular length N at $|V| = 1.0$ V. The insert is the inverted rectification ratio at short molecular length. **c** Dependence of rectification ratio on the proportion, which is defined as $P = N_1/N_2$ with $N = N_1 + N_2 = 30$. Reproduced with permission from Ref. [69]. Copyright 2011 Chinese Physical Society and IOP Publishing Ltd. Reproduced with permission from Ref. [70]. Copyright 2016 Chinese Physical Society and IOP Publishing Ltd

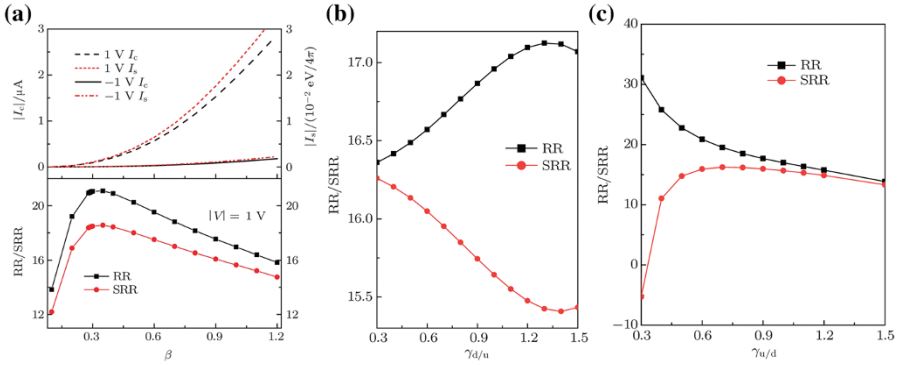

Fig. 26 **a** Dependence of charge current, spin current, charge-current rectification ratio (*RR*) and spin-current rectification ratio (*SRR*) on the spin-independent interfacial coupling parameter β at $|V| = 1.0$ V. Dependence of *RR* and *SRR* on the spin-dependent interfacial coupling parameter ratio for **b** $\gamma_{d/u} = \beta^{down}/\beta^{up}$(with $\beta^{up} = 1.0$), and **c** $\gamma_{u/d} = \beta^{up}/\beta^{down}$(with $\beta^{down} = 1.0$) at $|V| = 1.0$ V, where β^{up} and β^{down} are spin up and spin down interfacial coupling parameters, respectively. Reproduced with permission from Ref. [72]. Copyright 2015 Chinese Physical Society and IOP Publishing Ltd

of both spin current and charge current were effectively controlled by tuning the coupling strength at the molecule–electrode interface. However, in the case of spin-resolved interfacial coupling, the spin-up interfacial coupling, of which the spin orientation was opposite to the radical spin of the magnetic moiety, was more effective on modulating the rectification. Specifically, a weak spin-up coupling is advantageous to realize a large charge-current rectification, while a strong one is good for improving the spin-current rectification.

The spin state of the magnetic molecule was found to be another interesting way to modulate the rectifying performance [73]. The author claimed that, by exciting the radical spins from the ferromagnetic ground state one by one, both the eigenlevels and the wavefunctions of the frontier orbitals were modulated. As a result, the charge current and spin current would depend on the number of excited spins. As shown in Fig. 27, although the RR and SRR are suppressed at most spin-excited states, an abnormal increase of RR and SRR can still be obtained, e.g., $N_s = 1$ or $N_s = 3$, where N_s is the number of excited radical spins.

5 Summary and outlook

In this review, we summarize the progress of molecular diodes in the past decades, including charge-current diodes and spin-current diodes. Here, the molecular diodes with rectification originated from the asymmetric molecules are mainly focused on. The mechanisms of rectification and the methods to efficiently modulate the rectifying performance are reviewed in detail.

Overall, the molecular diode is still in its nascent stage, although there has been a significant achievement in the past 40 years since it was first proposed. Of course, most of the present challenges faced in the branch of molecular diodes are also

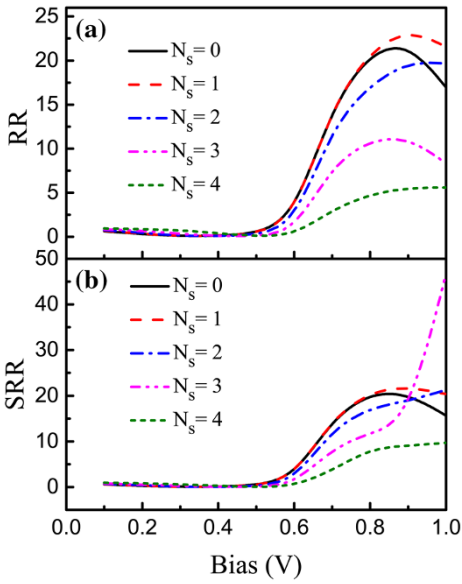

Fig. 27 Bias-dependence of **a** charge-current rectification ratio (*RR*) and **b** spin-current rectification ratio (*SRR*) for different spin-excited states. Reproduced with permission from Ref. [73]. Copyright 2014 Chinese Physical Society and IOP Publishing Ltd

formidable tasks to conquer in the field of molecular electronics. Understanding the movement of electrons through a single-molecule device and then controlling this process are of fundamental importance to the application of molecular devices [167, 168]. To achieve this goal, reliable molecular devices with long-term stability need to be fabricated. This work is very challenging because a number of factors including the used techniques, the chemical and physical properties of the active molecules, and especially the nature of interfaces between the molecule and electrodes, have contributions [169]. Therefore, the first and foremost challenge is to experimentally find efficient ways to reduce the variability of molecular devices, which needs to manipulate the molecule–electrode interfaces with atomic accuracy [170]. In this term, more advanced and new techniques are highly needed to be further developed. Grafting a single molecule into a nano-sized gap to form a stable molecular device is a nontrivial task, but to preciously align the discrete molecular energy levels with the continuous states of the electrodes and to control the interfacial coupling strength are even more difficult ones. So, the second formidable challenge is to control the energy level alignments at the molecule–electrode interfaces and the interfacial coupling strength, which have been proven to significantly influence the rectifying performance of molecular diodes [171]. At present, the rectification ratios of already-designed molecular diodes are still very low compared to those of commercial silicon-based diodes, which are generally between 10^5 and 10^8. For practical application, it is very imperative to acquire molecular diodes with superior rectification ratios by exploring new rectifying mechanisms or new building materials. In addition, the external environment is another unavoidable factor that should be seriously considered, which may affect the performance and lifetime of molecular devices since it is inevitable for them to work in ambient conditions for the sake of cheapness and wide usage. Also, efficient

integration strategies for compatibly bridging the molecular world with conventional electronics need to be elaborately developed [172, 173].

On the other hand, from a theoretical point of view, many theories and approaches have been developed all along with the progress of molecular electronics. In particular, the development of ab initio based methods makes it possible to study the electrical properties of molecular devices in a much more reliable way. The calculations from density functional theory based methods provide a detailed information about the conductance of molecular devices and possible structures of the molecule–electrode interfaces. These theoretical methods can now be able to successfully describe the general experimental trends [174]. However, it is still a challenge to provide quantitative predictions that can be directly compared with the experiments, which might be due to the insufficient description of the electronic correlations in the many-electron systems. Moreover, most theoretical approaches avoid considering the excitations of the active molecule by the passing electrons in the molecular device especially at high biases, which may lead to structural changes that can dramatically affect the transport properties. In this sense, further development of current methods or introducing more advanced theories are greatly in demand. Undoubtedly, the pace of molecular diodes or molecular devices going into the real world depends on the truly multidisciplinary collaboration of theory, synthetic chemistry, device fabrication, material engineering, physics, biology, and so on. Still, we have enough reason to believe that the field of molecular electronics has a promising future for bridging traditional electronics to the world of diverse organic molecules.

Acknowledgements Support from the National Natural Science Foundation of China (Grant Nos. 11374195, and 11604122), the Natural Science Foundation of Shandong Province (Grant No. ZR2014AM017), and the Taishan Scholar Project of Shandong Province are gratefully acknowledged.

References

1. Metzger RM, Mattern DL (2011) Unimolecular electronic devices. Top Curr Chem 313:39
2. Metzger RM (2015) Unimolecular electronics. Chem Rev 115:5056
3. Xiang D, Wang X, Jia C, Lee T, Guo X (2016) Molecular-scale electronics: from concept to function. Chem Rev 116:4318
4. Metzger RM (1999) The unimolecular rectifier: unimolecular electronic devices are coming. J Mater Chem 9:2027
5. Metzger RM (1999) Electrical rectification by a molecule: the advent of unimolecular electronic devices. Acc Chem Res 32:950
6. Metzger RM (2003) Unimolecular electrical rectifiers. Chem Rev 103:3803
7. Metzger RM (2009) Unimolecular electronics and rectifiers. Synth Met 159:2277
8. Metzger RM (2001) Rectification by a single molecule. Synth Met 124:107
9. Lo W-Y, Zhang N, Cai Z, Li L, Yu L (2016) Beyond molecular wires: design molecular electronic functions based on dipolar effect. Acc Chem Res 49:1852
10. Iwane M, Fujii S, Kiguchi M (2017) Molecular diode studies based on a highly sensitive molecular measurement technique. Sensors 17:956
11. Liu H, Zhao J (2009) Experimental and theoretical study of molecular rectification. Prog Chem 21:1154
12. Aviram A, Ratner MA (1974) Molecular rectifiers. Chem Phys Lett 29:277

13. Kushmerick JG, Holt DB, Yang JC, Naciri J, Moore MH, Shashidhar R (2002) Metal-molecule contacts and charge transport across monomolecular layers: measurement and theory. Phys Rev Lett 89:086802
14. Dhirani A, Lin P-H, Guyot-Sionnest P, Zehner RW, Sita LR (1997) Self-assembled molecular rectifiers. J Chem Phys 106:5249
15. Metzger RM et al (1997) Unimolecular electrical rectification in hexadecylquinolinium tricyanoquinodimethanide. J Am Chem Soc 119:10455
16. Chen B, Metzger RM (1999) Rectification between 370 and 105 K in hexadecylquinolinium tricyanoquinodimethanide. J Phys Chem B 103:4447
17. Ashwell GJ, Sambles JR, Martin AS, Parker WG, Szablewski M (1990) Rectifying characteristics of Mg|($C_{16}H_{33}$–Q3CNQ LB film)||Pt structures. J Chem Soc Chem Commun 19:1374
18. Geddes NJ, Sambles JR, Jarvis DJ, Parker WG, Sandman DJ (1990) Fabrication and investigation of asymmetric current–voltage characteristics of a metal/langmuir–blodgett monolayer/metal structure. Appl Phys Lett 56:1916
19. Geddes NJ, Sambles JR, Jarvis DJ, Parker WG, Sandman DJ (1992) The electrical properties of metal-sandwiched Langmuir–Blodgett multilayers and monolayers of a redox-active organic molecular compound. J Appl Phys 71:756
20. Martin AS, Sambles JR, Ashwell GJ (1993) Molecular rectifier. Phys Rev Lett 70:218
21. Ng M-K, Lee D-C, Yu L (2002) Molecular diodes based on conjugated diblock co-oligomers. J Am Chem Soc 124:11862
22. Ng M-K, Yu L (2002) Synthesis of amphiphilic conjugated diblock oligomers as molecular diodes. Angew Chem Int Ed 41:3598
23. Jiang P, Morales GM, You W, Yu L (2004) Synthesis of diode molecules and their sequential assembly to control electron transport. Angew Chem Int Ed 43:4471
24. Honciuc A, Jaiswal A, Gong A, Ashworth K, Spangler CW, Peterson IR, Dalton LR, Metzger RM (2005) Current rectification in a Langmuir–Schaefer monolayer of fullerene-bis-[4-diphenylamino-4″-(*N*-ethyl-N-2‴-ethyl) amino-1,4-diphenyl-1,3-butadiene] malonate between Au electrodes. J Phys Chem B 109:857
25. Morales GM, Jiang P, Yuan S, Lee Y, Sanchez A, You W, Yu L (2005) Inversion of the rectifying effect in diblock molecular diodes by protonation. J Am Chem Soc 127:10456
26. Wang B, Zhou Y, Ding X, Wang K, Wang X, Yang J, Hou JG (2006) Conduction mechanism of Aviram–Ratner rectifiers with single pyridine-σ-C_{60} oligomers. J Phys Chem B 110:24505
27. Díez-Pérez I, Hihath J, Lee Y, Yu L, Adamska L, Kozhushner MA, Oleynik II, Tao N (2009) Rectification and stability of a single molecular diode with controlled orientation. Nat Chem 1:635
28. Yuan L, Nerngchamnong N, Cao L, Hamoudi H, Del Barco E, Roemer M, Sriramula RK, Thompson D, Nijhuis CA (2015) Controlling the direction of rectification in a molecular diode. Nat Commun 6:6324
29. Nerngchamnong N, Yuan L, Qi D-C, Li J, Thompson D, Nijhuis CA (2013) The role of van der Waals forces in the performance of molecular diodes. Nat Nanotechnol 8:113
30. Zhang N, Lo W-Y, Cai Z, Li L, Yu L (2017) Molecular rectification tuned by through-space gating effect. Nano Lett 17:308
31. Stokbro K, Taylor J, Brandbyge M (2003) Do Aviram–Ratner diodes rectify? J Am Chem Soc 125:3674
32. Mujica V, Ratner MA, Nitzan A (2002) Molecular rectification: why is it so rare? Chem Phys 281:147
33. Taylor J, Brandbyge M, Stokbro K (2002) Theory of rectification in tour wires: the role of electrode coupling. Phys Rev Lett 89:138301
34. Troisi A, Ratner MA (2002) Molecular rectification through electric field induced conformational changes. J Am Chem Soc 124:14528
35. Gasyna ZL, Morales GM, Sanchez A, Yu L (2006) Asymmetric current–voltage characteristics of molecular junctions containing bipolar molecules. Chem Phys Lett 417:401
36. Krzeminski C, Delerue C, Allan G, Vuillaume D, Metzger RM (2001) Theory of electrical rectification in a molecular monolayer. Phys Rev B 64:085405
37. Oleynik II, Kozhushner MA, Posvyanskii VS, Yu L (2006) Rectification mechanism in diblock oligomer molecular diodes. Phys Rev Lett 96:096803
38. Hu GC, Wei JH, Xie SJ (2007) Bias-induced orbital hybridization in diblock co-oligomer diodes. Appl Phys Lett 91:142115

39. Huang J, Li Q, Li Z, Yang J (2009) Rectifying effect in polar conjugated molecular junctions: a first-principles study. J Nanosci Nanotechnol 9:774
40. Zhang G-P, Hu G-C, Li Z-L, Wang C-K (2012) Theoretical studies on protonation-induced inversion of the rectifying direction in dipyrimidinyl–diphenyl diblock molecular junctions. J Phys Chem C 116:3773
41. Zhang G-P, Hu G-C, Song Y, Li Z-L, Wang C-K (2012) Modulation of rectification in diblock co-oligomer diodes by adjusting anchoring groups for both symmetric and asymmetric electrodes. J Phys Chem C 116:22009
42. Nakamura H, Asai Y, Hihath J, Bruot C, Tao N (2011) Switch of conducting orbital by bias-induced electronic contact asymmetry in a bipyrimidinyl-biphenyl diblock molecule: mechanism to achieve a *pn* directional molecular diode. J Phys Chem C 115:19931
43. Hu G, Zhang G, Li Y, Ren J, Wang C (2014) Proportion effect in diblock co-oligomer molecular diodes. Chem Phys Lett 614:207
44. Zhang G-P, Xie Z, Song Y, Hu G-C, Wang C-K (2014) Molecular-length induced inversion of rectification in diblock pyrimidinyl-phenyl molecular junctions. Chem Phys Lett 591:296
45. Wang S, Wei M-Z, Hu G-C, Wang C-K, Zhang G-P (2017) Mechanisms of the odd–even effect and its reversal in rectifying performance of ferrocenyl-*n*-alkanethiolate molecular diodes. Org Electron 49:76
46. Zhang G-P, Wang S, Wei M-Z, Hu G-C, Wang C-K (2017) Tuning the direction of rectification by adjusting the location of the bipyridyl group in alkanethiolate molecular diodes. J Phys Chem C 121:7643
47. Liu H, Li P, Zhao J, Yin X, Zhang H (2008) Theoretical investigation on molecular rectification on the basis of asymmetric substitution and proton transfer reaction. J Chem Phys 129:224704
48. Hihath J, Bruot C, Nakamura H, Asai Y, Díez-Pérez I, Lee Y, Yu L, Tao N (2011) Inelastic transport and low-bias rectification in a single-molecule diode. ACS Nano 5:8331
49. Yoon HJ, Liao K-C, Lockett MR, Kwok SW, Baghbanzadeh M, Whitesides GM (2014) Rectification in tunneling junctions: 2,2′-bipyridyl-terminated *n*-alkanethiolates. J Am Chem Soc 136:17155
50. Zhao J, Yu C, Wang N, Liu H (2010) Molecular rectification based on asymmetrical molecule-electrode contact. J Phys Chem C 114:4135
51. Xue Y, Ratner MA (2003) Microscopic study of electrical transport through individual molecules with metallic contacts. II. Effect of the interface structure. Phys Rev B 68:115407
52. Novoselov KS, Geim AK, Morozov SV, Jiang D, Zhang Y, Dubonos SV, Grigorieva IV, Firsov AA (2004) Electric field effect in atomically thin carbon films. Science 306:666
53. Koski KJ, Cui Y (2013) The new skinny in two-dimensional nanomaterials. ACS Nano 7:3739
54. Feng B et al (2016) Experimental realization of two-dimensional boron sheets. Nat Chem 8:563
55. Dávila ME, Xian L, Cahangirov S, Rubio A, Lay GL (2014) Germanene: a novel two-dimensional germanium allotrope akin to graphene and silicene. New J Phys 16:095002
56. Zhu F, Chen W, Xu Y, Gao C, Guan D, Liu C, Qian D, Zhang S, J-f Jia (2015) Epitaxial growth of two-dimensional stanene. Nat Mater 14:1020
57. Coleman JN et al (2011) Two-dimensional nanosheets produced by liquid exfoliation of layered materials. Science 331:568
58. Sanvito S, Rocha AR (2006) Molecular-spintronics: the art of driving spin through molecules. J Comput Theor Nanosci 3:624
59. Sanvito S (2011) Molecular spintronics. Chem Soc Rev 40:3336
60. Dediu VA, Hueso LE, Bergenti I, Taliani C (2009) Spin routes in organic semiconductors. Nat Mater 8:707
61. Wolf SA, Awschalom DD, Buhrman RA, Daughton JM, Von Molnar S, Roukes ML, Chtchelkanova AY, Treger DM (2001) Spintronics: a spin-based electronics vision for the future. Science 294:1488
62. Dalgleish H, Kirczenow G (2006) Spin-current rectification in molecular wires. Phys Rev B 73:235436
63. Braunecker B, Feldman DE, Li F (2007) Spin current and rectification in one-dimensional electronic systems. Phys Rev B 76:085119
64. Hu G, He K, Xie S, Saxena A (2008) Spin-current rectification in an organic magnetic/nonmagnetic device. J Chem Phys 129:234708
65. Zeng M, Shen L, Zhou M, Zhang C, Feng Y (2011) Graphene-based bipolar spin diode and spin transistor: rectification and amplification of spin-polarized current. Phys Rev B 83:115427

66. Miller JS (2002) Organic magnets-a history. Adv Mater 14:1105
67. Jain R, Kabir K, Gilroy JB, Mitchell KAR, Wong K, Hicks RG (2007) High-temperature metal-organic magnets. Nature 445:291
68. Veciana J, Iwamura H (2000) Organic magnets. MRS Bull 25:41
69. Hu G-C, Wang H, Ren J-F (2011) Effect of proportion on rectification in organic co-oligomer spin rectifiers. Chin Phys B 20:077306
70. Hu G-C, Zhang Z, Li Y, Ren J-F, Wang C-K (2016) Length dependence of rectification in organic co-oligomer spin rectifiers. Chin Phys B 25:057308
71. Hu GC, Zhang Z, Zhang GP, Ren JF, Wang CK (2016) Inversion of spin-current rectification in magnetic co-oligomer diodes. Org Electron 37:485
72. Hu G-C, Zuo M-Y, Li Y, Zhang Z, Ren J-F, Wang C-K (2015) Effect of interfacial coupling on rectification in organic spin rectifiers. Chin Phys B 24:077308
73. Zuo M-Y, Hu G-C, Li Y, Ren J-F, Wang C-K (2014) Spin-excited states and rectification in an organic spin rectifier. Chin Phys B 23:087306
74. Metzger R, Panetta C (1983) Progress in cohesive energies, and in building organic un imolecular rectifiers. J Phys Colloq 44:1605
75. Metzger R, Panetta C, Miura Y, Torres E (1987) Progress towards organic single-monolayer rectifiers. Synth Met 18:797
76. Metzger RM, Panetta CA (1988) Rectification in Langmuir–Blodgett monolayers of organic D–σ–A molecules. J Chim Phys 85:1125
77. Metzger RM, Panetta CA (1989) Possible rectification in Langmuir–Blodgett monolayers of organic D–σ–A molecules. Synth Met 28:807
78. Metzger RM et al (2003) Electrical rectification in a Langmuir–Blodgett monolayer of dimethyanilinoazafullerene sandwiched between gold electrodes. J Phys Chem B 107:1021
79. Shumate WJ, Mattern DL, Jaiswal A, Dixon DA, White TR, Burgess J, Honciuc A, Metzger RM (2006) Spectroscopy and rectification of three donor–sigma–acceptor compounds, consisting of a one-electron donor (pyrene or ferrocene), a one-electron acceptor (perylenebisimide), and a C_{19} swallowtail. J Phys Chem B 110:11146
80. Ho G, Heath JR, Kondratenko M, Perepichka DF, Arseneault K, Pézolet M, Bryce MR (2005) The first studies of a tetrathiafulvalene–σ–acceptor molecular rectifier. Chem Eur J 11:2914
81. Metzger RM, Xu T, Peterson IR (2001) Electrical rectification by a monolayer of hexadecylquinolinium tricyanoquinodimethanide measured between macroscopic gold electrodes. J Phys Chem B 105:7280
82. Ashwell GJ, Tyrrell WD, Whittam AJ (2003) Molecular Rectification: self-assembled monolayers of a donor–(π-bridge)–acceptor chromophore connected via a truncated Au–S–$(CH_2)_3$ bridge. J Mater Chem 13:2855
83. Jaiswal A, Amaresh RR, Lakshmikantham M, Honciuc A, Cava MP, Metzger RM (2003) Electrical rectification in a monolayer of zwitterions assembled by either physisorption or chemisorption. Langmuir 19:9043
84. Lörtscher E, Gotsmann B, Lee Y, Yu L, Rettner C, Riel H (2012) Transport properties of a single-molecule diode. ACS Nano 6:4931
85. Chiechi RC, Weiss EA, Dickey MD, Whitesides GM (2008) Eutectic gallium–indium (EGaIn): a moldable liquid metal for electrical characterization of self-assembled monolayers. Angew Chem Int Ed 47:142
86. Nijhuis CA, Reus WF, Whitesides GM (2009) Molecular rectification in Metal–SAM–Metal oxide–metal junctions. J Am Chem Soc 131:17814
87. Nijhuis CA, Reus WF, Barber JR, Dickey MD, Whitesides GM (2010) Charge transport and rectification in arrays of SAM-based tunneling junctions. Nano Lett 10:3611
88. Nijhuis CA, Reus WF, Whitesides GM (2010) Mechanism of rectification in tunneling junctions based on molecules with asymmetric potential drops. J Am Chem Soc 132:18386
89. Nijhuis CA, Reus WF, Siegel AC, Whitesides GM (2011) A molecular half-wave rectifier. J Am Chem Soc 133:15397
90. Reus WF, Thuo MM, Shapiro ND, Nijhuis CA, Whitesides GM (2012) The SAM, not the electrodes, dominates charge transport in metal-monolayer//Ga_2O_3/gallium–indium eutectic junctions. ACS Nano 6:4806
91. Mentovich ED, Rosenberg-Shraga N, Kalifa I, Gozin M, Mujica V, Hansen T, Richter S (2013) Gated-Controlled rectification of a self-assembled monolayer-based transistor. J Phys Chem C 117:8468

92. Jiang L, Yuan L, Cao L, Nijhuis CA (2014) Controlling leakage currents: the role of the binding group and purity of the precursors for self-assembled monolayers in the performance of molecular diodes. J Am Chem Soc 136:1982
93. Yuan L, Jiang L, Thompson D, Nijhuis CA (2014) On the remarkable role of surface topography of the bottom electrodes in blocking leakage currents in molecular diodes. J Am Chem Soc 136:6554
94. Yuan L, Breuer R, Jiang L, Schmittel M, Nijhuis CA (2015) A molecular diode with a statistically robust rectification ratio of three orders of magnitude. Nano Lett 15:5506
95. Nerngchamnong N, Thompson D, Cao L, Yuan L, Jiang L, Roemer M, Nijhuis CA (2015) Nonideal electrochemical behavior of ferrocenyl–alkanethiolate SAMs maps the microenvironment of the redox unit. J Phys Chem C 119:21978
96. Thompson D, Nijhuis CA (2016) Even the odd numbers help: failure modes of SAM-based tunnel junctions probed via odd-even effects revealed in synchrotrons and supercomputers. Acc Chem Res 49:2061
97. Song P, Yuan L, Roemer M, Jiang L, Nijhuis CA (2016) Supramolecular vs electronic structure: the effect of the tilt angle of the active group in the performance of a molecular diode. J Am Chem Soc 138:5769
98. Chabinyc ML et al (2002) Molecular rectification in a metal–insulator–metal junction based on self-assembled monolayers. J Am Chem Soc 124:11730
99. Jeong H et al (2014) Redox-induced asymmetric electrical characteristics of ferrocene–alkanethiolate molecular devices on rigid and flexible substrates. Adv Funct Mater 24:2472
100. Jeong H, Jang Y, Kim D, Hwang W-T, Kim J-W, Lee T (2016) An in-depth study of redox-induced conformational changes in charge transport characteristics of a ferrocene–alkanethiolate molecular electronic junction: temperature-dependent transition voltage spectroscopy analysis. J Phys Chem C 120:3564
101. Mantooth BA, Weiss PS (2003) Fabrication, assembly, and characterization of molecular electronic components. Proc IEEE 91:1785
102. Wang W, Lee T, Reed MA (2005) Electron tunnelling in self-assembled monolayers. Rep Prog Phys 68:523
103. Park J, Pasupathy AN, Goldsmith JI, Chang C (2002) Coulomb blockade and the Kondo effect in single-atom transistors. Nature 417:722
104. Xiang J, Liu B, Wu ST, Ren B, Yang FZ, Mao BW, Chow YL, Tian ZQ (2005) A controllable electrochemical fabrication of metallic electrodes with a nanometer/angstrom-sized gap using an electric double layer as feedback. Angew Chem Int Ed 44:1265
105. Bonifas AP, McCreery RL (2010) "Soft" Au, Pt and Cu contacts for molecular junctions through surface-diffusion-mediated deposition. Nat Nanotechnol 5:612
106. Reed MA, Zhou C, Muller C, Burgin T, Tour J (1997) Conductance of a molecular junction. Science 278:252
107. Xiang D, Jeong H, Lee T, Mayer D (2013) Mechanically controllable break junctions for molecular electronics. Adv Mater 25:4845
108. Xiang D, Jeong H, Kim D, Lee T, Cheng Y, Wang Q, Mayer D (2013) Three-terminal single-molecule junctions formed by mechanically controllable break junctions with side gating. Nano Lett 13:2809
109. Wang L, Wang L, Zhang L, Xiang D (2017) Advance of mechanically controllable break junction for molecular electronics. Top Curr Chem 375:61
110. Chen X, Yeganeh S, Qin L, Li S, Xue C, Braunschweig AB, Schatz GC, Ratner MA, Mirkin CA (2009) Chemical fabrication of heterometallic nanogaps for molecular transport junctions. Nano Lett 9:3974
111. Fu X-X, Zhang R-Q, Zhang G-P, Li Z-L (2014) Rectifying properties of oligo(phenylene ethynylene) heterometallic molecular junctions: molecular length and side group effects. Sci Rep 4:6357
112. Allen MJ, Tung VC, Kaner RB (2009) Honeycomb carbon: a review of graphene. Chem Rev 110:132
113. Novoselov KS, Fal VI, Colombo L, Gellert PR, Schwab MG, Kim K (2012) A roadmap for graphene. Nature 490:192
114. Novoselov KS, Geim AK, Morozov SV, Jiang D, Katsnelson MI, Grigorieva IV, Dubonos SV, Firsov AA (2005) Two-dimensional gas of massless dirac fermions in graphene. Nature 438:197
115. Balandin AA (2011) Thermal properties of graphene and nanostructured carbon materials. Nat Mater 10:569

116. Lee C, Wei X, Kysar JW, Hone J (2008) Measurement of the elastic properties and intrinsic strength of monolayer graphene. Science 321:385
117. Zhang Y, Tan Y-W, Stormer HL, Kim P (2005) Experimental observation of the Quantum Hall Effect and Berry's phase in graphene. Nature 438:201
118. Zhang GP, Fang XW, Yao YX, Wang CZ, Ding ZJ, Ho KM (2011) Electronic structure and transport of a carbon chain between graphene nanoribbon leads. J Phys Condens Matter 23:025302
119. Son Y-W, Cohen ML, Louie SG (2006) Energy gaps in graphene nanoribbons. Phys Rev Lett 97:216803
120. Nakada K, Fujita M, Dresselhaus G, Dresselhaus MS (1996) Edge state in graphene ribbons: nanometer size effect and edge shape dependence. Phys Rev B 54:17954
121. Brey L, Fertig HA (2006) Electronic states of graphene nanoribbons studied with the dirac equation. Phys Rev B 73:235411
122. Martin I, Blanter YM (2009) Transport in disordered graphene nanoribbons. Phys Rev B 79:235132
123. Li J, Zhang ZH, Kwong G, Tian W, Fan ZQ, Deng XQ (2013) A new exploration on the substantial improvement of rectifying behaviors for a donor–acceptor molecular diode by graphene electrodes. Carbon 61:284
124. Song Y, Xie Z, Zhang G-P, Ma Y, Wang C-K (2013) Bias dependence of rectifying direction in a diblock co-oligomer molecule with asymmetric graphene nanoribbon electrodes. J Phys Chem C 117:20951
125. Ervasti MM, Fan Z, Uppstu A, Krasheninnikov AV, Harju A (2015) Silicon and silicon–nitrogen impurities in graphene: structure, energetics, and effects on electronic transport. Phys Rev B 92:235412
126. Zhou Y-C, Zhang H-L, Deng W-Q (2013) A 3n rule for the electronic properties of doped graphene. Nanotechnology 24:225705
127. Zheng Y, Jiao Y, Ge L, Jaroniec M, Qiao SZ (2013) Two-step boron and nitrogen doping in graphene for enhanced synergistic catalysis. Angew Chem Int Ed 52:3110
128. Zhao P, Liu DS, Li SJ, Chen G (2013) Modulation of rectification and negative differential resistance in graphene nanoribbon by nitrogen doping. Phys Lett A 377:1134
129. Yao W, Yao KL, Gao GY, Fu HH, Zhu SC (2013) Boron-doping controlled peculiar transport properties of graphene nanoribbon *p–n* junctions. Solid State Commun 153:46
130. Liang J, Jiao Y, Jaroniec M, Qiao SZ (2012) Sulfur and nitrogen dual-doped mesoporous graphene electrocatalyst for oxygen reduction with synergistically enhanced performance. Angew Chem Int Ed 51:11496
131. Zeng J, Chen K-Q, He J, Fan Z-Q, Zhang X-J (2011) Nitrogen doping-induced rectifying behavior with large rectifying ratio in graphene nanoribbons device. J Appl Phys 109:124502
132. Yu SS, Zheng WT, Wen QB, Jiang Q (2008) First principle calculations of the electronic properties of nitrogen-doped carbon nanoribbons with zigzag edges. Carbon 46:537
133. Zhang DH, Yao KL, Gao GY (2011) The peculiar transport properties in *pn* junctions of doped graphene nanoribbons. J Appl Phys 110:013718
134. Song Y, Xie Z, Ma Y, Li Z-L, Wang C-K (2014) Giant rectification ratios of azulene-like dipole molecular junctions induced by chemical doping in armchair-edged graphene nanoribbon electrodes. J Phys Chem C 118:18713
135. Xie Z, Zuo X, Zhang G-P, Li Z-L, Wang C-K (2016) Detecting CO, NO and NO_2 gases by boron-doped graphene nanoribbon molecular devices. Chem Phys Lett 657:18
136. Cao C, Chen L-N, Long M-Q, Xu H (2013) Rectifying performance in zigzag graphene nanoribbon heterojunctions with different edge hydrogenations. Phys Lett A 377:1905
137. Khoo KH, Neaton JB, Son YW, Cohen ML, Louie SG (2008) Negative differential resistance in carbon atomic wire-carbon nanotube junctions. Nano Lett 8:2900
138. Yuzvinsky TD, Mickelson W, Aloni S, Begtrup GE, Kis A, Zettl A (2006) Shrinking a carbon nanotube. Nano Lett 6:2718
139. Cumings J, Zettl A (2004) Localization and nonlinear resistance in telescopically extended nanotubes. Phys Rev Lett 93:086801
140. Cook BG, French WR, Varga K (2012) Electron transport properties of carbon nanotube-graphene contacts. Appl Phys Lett 101:153501
141. Yan Q, Zhou G, Hao S, Wu J, Duan W (2006) Mechanism of nanoelectronic switch based on telescoping carbon nanotubes. Appl Phys Lett 88:173107
142. Czerw R et al (2001) Identification of electron donor states in N-doped carbon nanotubes. Nano Lett 1:457

143. Cheng C, Hu H, Wei Y, Zhang Z, Wang X, Zhao J, Peng P (2013) Rectifying behaviors introduced by nitrogen–vacancy complex in spiral chirality single walled carbon nanotube device. J Appl Phys 114:083711
144. Zanolli Z, Leghrib R, Felten A, Pireaux J-J, Llobet E, Charlier J-C (2011) Gas sensing with Au-decorated carbon nanotubes. ACS Nano 5:4592
145. He J, Chen K-Q (2012) Humidity effects on the electronic transport properties in carbon based nanoscale device. Phys Lett A 376:869
146. Wu J, Hagelberg F, Dinadayalane TC, Leszczynska D, Leszczynski J (2011) Do stone-wales defects alter the magnetic and transport properties of single-walled carbon nanotubes? J Phys Chem C 115:22232
147. Cheng C, Hu H, Zhang Z, Zhang H (2016) Perfect rectifying behavior induced by AA–P_2 dopants in armchair silicene nanoribbon devices. RSC Adv 6:7042
148. Sun J, Lin N, Ren H, Tang C, Yang L, Zhao X (2016) Gas adsorption on MoS_2/WS_2 in-plane heterojunctions and the I–V response: a first principles study. RSC Adv 6:17494
149. Yu Z, Hu ML, Zhang CX, He CY, Sun LZ, Zhong J (2011) Transport properties of hybrid zigzag graphene and boron nitride nanoribbons. J Phys Chem C 115:10836
150. Song Y-L, Zhang J-M, Lu D-B, Xu K-W (2013) Structural and electronic properties of a single C chain doped zigzag silicene nanoribbon. Phys E 53:173
151. Ni Z, Liu Q, Tang K, Zheng J, Zhou J, Qin R, Gao Z, Yu D, Lu J (2012) Tunable bandgap in silicene and germanene. Nano Lett 12:113
152. Wang QH, Kalantar-Zadeh K, Kis A, Coleman JN, Strano MS (2012) Electronics and optoelectronics of two-dimensional transition metal dichalcogenides. Nat Nanotechnol 7:699
153. Song Y, Su Y, Zhang G-P, Wang C-K, Chen G (2017) Hydrogenation-induced giant rectifying behaviors in silicene and germanene heterojunctions. Comput Mater Sci 129:37
154. Liu L et al (2014) Heteroepitaxial growth of two-dimensional hexagonal boron nitride templated by graphene edges. Science 343:163
155. Jung J, Qiao Z, Niu Q, MacDonald AH (2012) Transport properties of graphene nanoroads in boron nitride sheets. Nano Lett 12:2936
156. Modarresi M, Roknabadi MR, Shahtahmasbi N (2011) Transport properties of an armchair boron–nitride nanoribbon embedded between two graphene electrodes. Phys E 43:1751
157. Bernardi M, Palummo M, Grossman JC (2012) Optoelectronic properties in monolayers of hybridized graphene and hexagonal boron nitride. Phys Rev Lett 108:226805
158. Qiu M, Liew KM (2011) Transport properties of a single layer armchair h-BNC heterostructure. J Appl Phys 110:064319
159. Zhang Z, Zhang J, Kwong G, Li J, Fan Z, Deng X, Tang G (2013) All-Carbon sp–sp^2 hybrid structures: geometrical properties, current rectification, and current amplification. Sci Rep 3:2575
160. Ji X-L, Xie Z, Zuo X, Zhang G-P, Li Z-L, Wang C-K (2016) Giant rectification in graphene nanoflake molecular devices with asymmetric graphene nanoribbon electrodes. Phys Lett A 380:3198
161. Lee Y, Carsten B, Yu L (2009) Understanding the anchoring group effect of molecular diodes on rectification. Langmuir 25:1495
162. Hu GC, Zhang GP, Ren JF, Wang CK, Xie SJ (2011) Length-dependent inversion of rectification in diblock co-oligomer diodes. Appl Phys Lett 99:082105
163. Zhang G-P, Hu G-C, Song Y, Xie Z, Wang C-K (2013) Stretch or contraction induced inversion of rectification in diblock molecular junctions. J Chem Phys 139:094702
164. Bruot C, Hihath J, Tao N (2012) Mechanically controlled molecular orbital alignment in single molecule junctions. Nat Nanotechnol 7:35
165. Yuan L, Thompson D, Cao L, Nerngchangnong N, Nijhuis CA (2015) One carbon matters: the origin and reversal of odd–even effects in molecular diodes with self-assembled monolayers of ferrocenyl–alkanethiolates. J Phys Chem C 119:17910
166. Korshak YV, Medvedeva TV, Ovchinnikov AA, Spector VN (1987) Organic polymer ferromagnet. Nature 326:370
167. Moth-Poulsen K, Bjørnholm T (2009) molecular electronics with single molecules in solid-state devices. Nat Nanotechnol 4:551
168. Ratner M (2013) A brief history of molecular electronics. Nat Nanotechnol 8:378
169. Guo X (2014) Molecular electronics: challenges and opportunities. AIMS Mater Sci 1:11
170. Lörtscher E (2013) Wiring molecules into circuits. Nat Nanotechnol 8:381

171. Jia C, Guo X (2013) Molecule-electrode interfaces in molecular electronic devices. Chem Soc Rev 42:5642
172. Yu X, Lovrinčić R, Kraynis O, Man G, Ely T, Zohar A, Toledano T, Cahen D, Vilan A (2014) Fabrication of reproducible, integration-compatible hybrid molecular/Si electronics. Small 10:5151
173. Aragonès AC, Darwish N, Ciampi S, Sanz F, Gooding JJ, Díez-Pérez I (2017) Single-molecule electrical contacts on silicon electrodes under ambient conditions. Nat Commun 8:15056
174. Hybertsen MS, Venkataraman L, Klare JE, Whalley AC, Steigerwald ML, Nuckolls C (2008) Amine-linked single-molecule circuits: systematic trends across molecular families. J Phys Condens Matter 20:374115

Top Curr Chem (Z) (2017) 375:56
DOI 10.1007/s41061-017-0144-5

REVIEW

Switching Effects in Molecular Electronic Devices

Zihao Liu[1] · Shizhao Ren[1] · Xuefeng Guo[1]

Received: 9 November 2016 / Accepted: 25 April 2017 / Published online: 10 May 2017

Abstract The creation of molecular electronic switches by using smart molecules is of great importance to the field of molecular electronics. This requires a fundamental understanding of the intrinsic electron transport mechanisms, which depend on several factors including the charge transport pathway, the molecule–electrode coupling strength, the energy of the molecular frontier orbitals, and the electron spin state. On the basis of significant progresses achieved in both experiments and theory over the past decade, in this review article we focus on new insights into the design and fabrication of different molecular switches and the corresponding switching effects, which is crucial to the development of molecular electronics. We summarize the strategies developed for single-molecule device fabrication and the mechanism of these switching effects. These analyses should be valuable for deeply understanding the switching effects in molecular electronic devices.

Keywords Molecular electronics · Device fabrication · Switching effects

Chapter 6 was originally published as Liu, Z., Ren, S. & Guo, X. Top Curr Chem (Z) (2017) 375: 56. DOI 10.1007/s41061-017-0144-5.

Zihao Liu and Shizhao Ren contributed equally to this work.

✉ Xuefeng Guo
guoxf@pku.edu.cn

[1] Beijing National Laboratory for Molecular Sciences, State Key Laboratory for Structural Chemistry of Unstable and Stable Species, College of Chemistry and Molecular Engineering, Peking University, Beijing 100871, People's Republic of China

1 Introduction

With the aspiration of miniaturization of silicon-based integrated circuit, using single molecules to build functional devices seems to be a promising alternative solution for this issue. To this end, molecular switches, rectifiers, and transistors have been extensively studied in the past decades [1]. Among these devices, molecular switches have attracted great attention because switches are basic components of most electronic devices with broad applications in information storage, logic data manipulation, and signal processing.

In electrical engineering, a switch is an electrical component that can break an electrical circuit, interrupting the current or diverting it from one conductor to another. The mechanism of a macro-size switch may be operated directly by a human operator to control a circuit, may be operated by a moving object such as a door-operated switch, or may be operated by some sensing element for pressure, temperature, or flow. In contrast, the fabrication of molecular switches is entirely different. Firstly, a molecular material with reliable switching should be properly designed. The switching molecule should have reversible bistable states that might possess different electron conductance. An anchoring group is needed for integrating the functional molecule into an electrical circuit. For potential applications in the field of logic gates and memory storage, the on/off ratio of the switch should be large enough to be distinguished. These electrical switches based on single molecules have obvious advantages such as size (several nanometers), speed (potential switching times $\sim$100 ps), and stability. Secondly, the technique capable of linking a single molecule into the circuit should be developed [2].

A wide variety of triggers, including physical ones, such as light [3–17], mechanical stimulation [18], bias voltage [19], and temperature, and chemical ones, such as electrochemical gate [20], pH [21], and chemical reactant [22], have been used to tune the molecular electron transport property. Accordingly, on the basis of the switching mechanisms, the devices can typically be divided into two types: conformation-induced and charging/redox switches [2]. In the first case, a molecular isomerization will happen, which is caused by chemical bond formation and cleavage. In the second case, the molecule takes up (or gives up) an electron, leading to a charge state alteration. In some conditions, the molecular behavior cannot be observed directly. Theoretical computation is always used to explain the mechanism of the experimental results and guide the design of molecular switches.

In this review, we start with the introduction of the fabrication of single-molecule junctions. Then we overview the principles used for building a single-molecule switch. Finally, we review another kind of switch based on molecular monolayers. This research field is a quickly growing one. Having limited reference and space, we will only be able to cover some major contributions and highlight some important points. Readers who feel interested can read several superior review articles covering the different aspects of molecular switches [1, 2 23].

2 Single-Molecule Device Fabrication

One of the biggest challenges in molecular electronics is to develop reliable strategies for building robust molecular junctions at the molecular level. In this regard, discrete methods have been developed and can be classified into two main methods: one is based on metal electrodes and the other is based on carbon electrodes. Metal electrode fabrication strategies include scanning tunneling microscopy break junction (STM-BJ), mechanically controllable break junction (MCBJ), electro-migration break junction, electrochemical deposition junction, surface-diffusion-mediate deposition junction. Carbon electrodes are usually fabricated by carbon nanotubes and graphene. There is a particular review elsewhere [1]. Here, we briefly introduce the frequently used methods for building single-molecule electronic switches including STM-BJ, MCBJ, and carbon electrode fabrication.

2.1 Molecular Junction Based on Metal Electrodes

2.1.1 Scanning Tunneling Microscopy Break Junction (STM-BJ)

Scanning tunneling microscopy (STM) has played an important role and been wildly used in the field of molecular electronics. Molecules are linked between a metal tip and a conductance substrate by forming covalent bonds between the molecules and the electrodes. Typically, the molecules have an opportunity to bridge both the tip and the substrate when pulling the tip close enough to the substrate. During pulling away the tip from the substrate, the number of bridged molecule can be changed. Finally, the metal–molecular–metal junction is broken. As a STM-BJ is highly reproducible, tens of thousands of molecular conductance curves can be obtained in a test. Through statistical analysis, the random error of a single test can be reduced (Fig. 1).

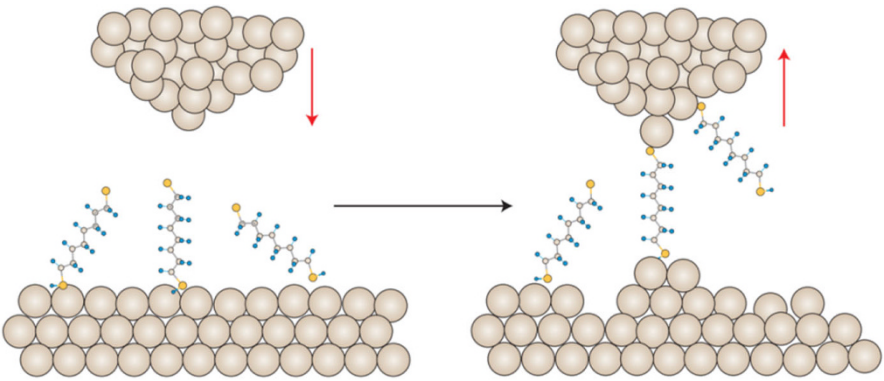

Fig. 1 STM break junction technique used to form single Au-molecule–Au junctions. When the Au tip moves into the Au substrates, which are covered with target molecules, molecule junctions are formed. As the Au tip is lifted, the molecular bridges then lose contact with either the tip or the Au substrate. Reproduced with permission from Ref. [24]. Copyright 2005 Nature Publishing Group

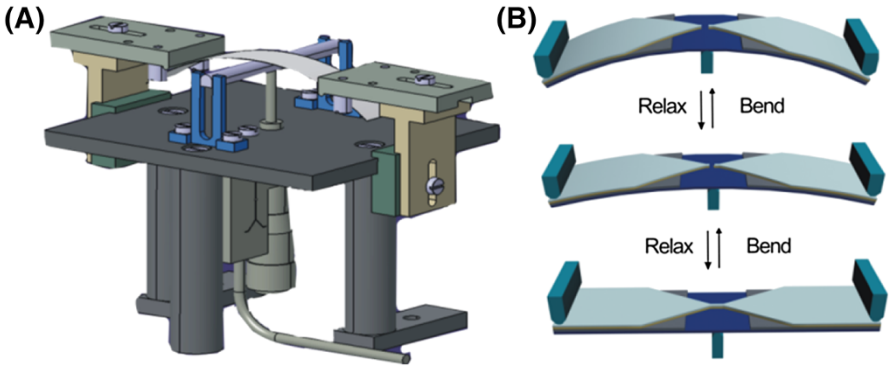

Fig. 2 **a** A schematic of the MCBJ setup. **b** The working principle of the MCBJ setup. A suspended metal bridge with a constriction is microfabricated onto the substrate. When the push rod adds a bending force on the substrate, the movement in the Z direction causes an elongation of the constriction until a break occurs in the metal bridge, resulting in the formation of two separated nanoscale electrodes. Reproduced with permission from Ref. [25]. Copyright 2013 Wiley-VCH

2.1.2 Mechanically Controllable Break Junction (MCBJ)

Mechanically controllable break junction represents a fundamental technique for investigating molecular electronic junctions, especially for the study of the electronic properties of single molecules [25]. The MCBJ technique offers a continuously tunable gap size between two tip-shaped electrodes with the impressive mechanical stability for building a single-molecule device. An MCBJ setup typically consists of three parts: a flexible substrate containing a macrofabricated metal wire or patterned nanostructure, a push rod to break the nanostructure, and a counter support to bend the substrate. A vertical movement of the push rod, which can be accurately controlled by a piezoelectric actuator or motor, can exert a force on the bending beam. As the beam is bent, the metal iron start to elongate and this leads to the reduction of the cross section at the notch and finally leads to a break of the metal wire (Fig. 2).

The MCBJ technique has several advantages. (1) The MCBJ setup can be easily integrated with other systems such as high vacuum system or Raman spectrometer. (2) A fresh break cross section of the gold bridge is mechanically crated by the MCBJ experiment without additional chemical treatments. The pollutant is depressed in the fresh electrodes. (3) The disturbing effect from the push rod can be strongly reduced on the junction. Because of mechanical configuration of the three-point bend apparatus, the vertical motion of the push rod (ΔX) causes only a highly reduced horizontal displacement (ΔZ) of the electrodes ($\Delta Z/\Delta X > 10{,}000$). (4) Benefited from lithographic techniques, the electrode can be scaled down to molecular dimension, which is suitable for single-molecule measurements. Furthermore, the bridged molecular number can be preciously changed by controlling the gap size.

2.2 Carbon-Based Molecular Junction

Since their discovery of carbon nanotubes in 1991 [26] and graphene in 2004 [27], carbon materials, which mean the allotropes of carbon, have been drawing more and more attention because of their unique features. On the other hand, with the development of nanoscale devices, the scale of electrical devices has been decreased to the nanoscale, resulting in numerous problems in silicon-based devices [28]. One possible way to overcome these difficulties is to find other suitable materials to replace silicon. Carbon materials are the most promising one. Single-walled carbon nanotubes (SWCNTs) [29–33] and graphene [34] are typical ones.

SWCNTs and graphene are made of carbon atoms, which are hybridized with other three atoms, forming a network of sp^2-hybridized carbon atoms. Carbon is the most basis element in creatures, making SWCNTs and graphene compatible to bio/organic molecules [35, 36]. Compared with metal electrodes, SWCNTs and graphene have a more clear and robust connection with molecules [37], making the experimental results more reproducible [38]. In combination with the ability of mass producing SWCNTs and graphene, all these features make them excellent electrodes for single-molecule devices [1, 39].

There are two key elements in fabricating a single-molecule device with carbon electrodes [1, 37, 38]. The first one is the formation of nanoscale gaps, which must be suitable for unique molecules with the controllable size and the defined edge structure. A proper gap size affords a high yield of device fabrication, and the clear structure offers the experimental data with a small variation. As for SWCNTs [1], the mostly used approaches for gap formation are focused-ion-beam etching, electrical breakdown, and lithography-defined oxidative cutting. Electrical burning [40] and dash-line lithography [34] are the most used ways for gap formation on graphene. The other key element is the way to link molecules. Different connection methods result in different interfaces between molecules and electrodes, which affect the conducting ability effectively. One approach is to bond the electrodes and molecules covalently through chemical reactions. The other one is physical absorption such as π–π stacking, using aromatic rings as the anchoring groups.

2.2.1 SWCNTs

SWCNTs were discovered earlier than graphene, having a more detailed study in single-molecule devices [36]. SWCNT is a one-dimensional nanowire with the configuration-dependent conductance [37], which makes the contribution to the electrical versatility. Every atom of SWCNTs is exposed to an external environment, making them highly sensitive to external stimuli. It is easy to be decorated with functional groups, which can be covalently bonded with molecules in a robust way. The low-dimensional nature can produce nanoscale gaps that are comparable with the molecule's size. These advantages make SWCNTs extraordinary electrodes in single-molecule devices.

In 2006, Guo et al. [41] constructed a covalently bonded single-molecule device based on SWCNT electrodes. They used a lithography-defined oxidative cutting method to form gaps with carboxyl ends. Firstly, SWCNT was spanned with PMMA, then electron beam lithography (EBL) was used to form a window

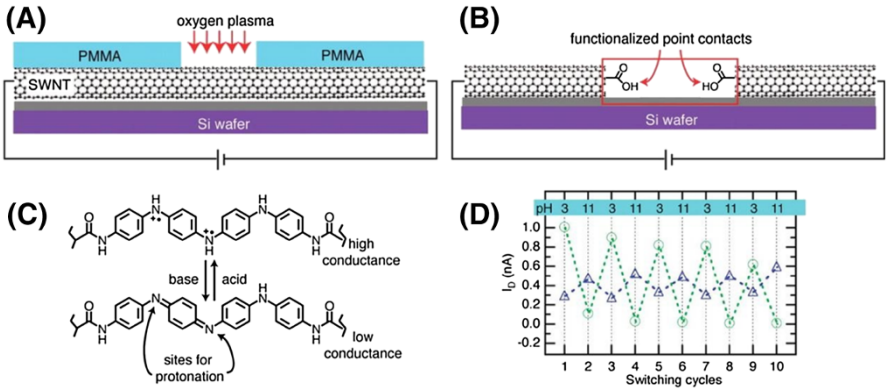

Fig. 3 **a** Etching SWCNTs with oxygen plasma induced through a window of PMMA formed by e-beam lithography. **b** Two SWCNT electrodes with carboxylic acids on the end. **c** Oligoanilines show low/high conductance with the protonation and deprotonations process. **d** *Green circles* show the pH dependence of oligoanilines. The *blue triangles* show a slight change of conductance in control groups. Reproduced with permission from Ref. [41]. Copyright 2006 AAAS

precursor of less than 10 nm in PMMA (Fig. 3a), followed by using reactive ion etching (RIE) to etch away the exposed SWCNTs, thus forming a gap between SWCNTs with carboxyl groups on both ends (Fig. 3b). Functional molecules with amino terminals can covalently bond with SWCNT electrodes through amination reactions. The diameter of SWCNTs limits the number of molecules connected in the gap, making it a real single-molecule device. More importantly, covalent bonds offer the devices great robustness and reliability, ensuring that the device can undergo extreme conditions. They had several molecules with different functions bonded with carbon electrodes. Among them, oligoanilines (Fig. 3c) showed low/high conductance corresponding to the inherent protonation and deprotonations processes. The high/low conductance of molecules resulted in the on/off states of the devices, which can be proven by the fluctuation of currents through the devices. When the devices were immersed in solution with different pH in turn, correspondingly the current showed an alternate switch (Fig. 3d), thus affording an ultrasensitive pH sensor. Moreover, with the diversity of the molecular structures, the devices can be fabricated with other desired functionalities.

As the electrodes of single-molecule devices, SWCNTs exhibit good compatibility with numerous functional molecules to form single-molecule devices, which enable the detection of conductance data and monitoring of the interaction of bio-matter [35, 42, 43], such as the kinetics of DNA and protein activities. SWCNT is an outstanding material in molecular electronics. However, the inherent variability of SWCNTs [34, 38] and the sensitivity to the gate voltage [37] blocks the way to wider applications.

2.2.2 Graphene

In comparison with SWCNTs, graphene shows a homogeneous quality, and this two-dimensional material has the ability to be fabricated in high throughout without the gate dependence as well, making graphene a star material of electrodes [34, 37, 38].

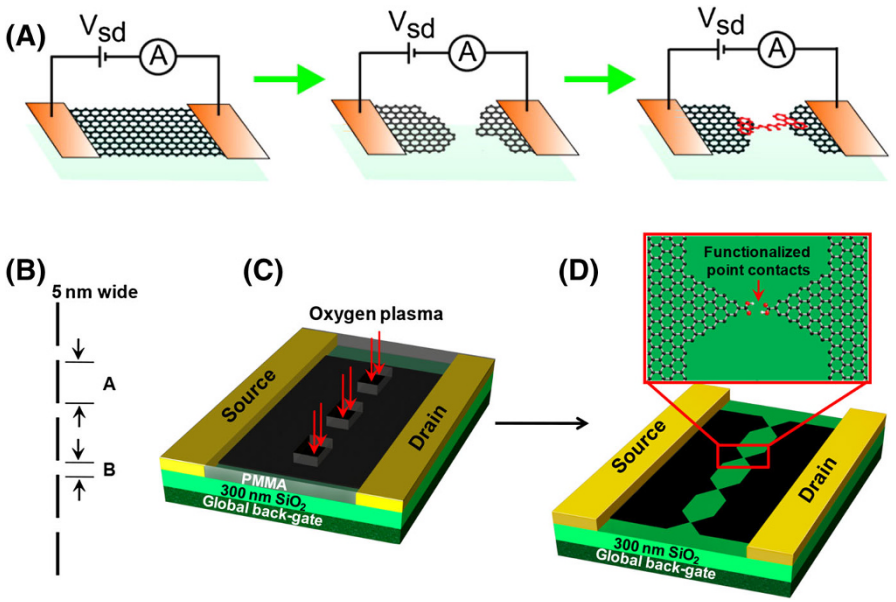

Fig. 4 **a** Depositing molecules inside a few-layer graphene nanogap, formed by feedback-controlled electro-burning. DLL method to form graphene point contacts arrays with gaps ≤10 nm. **b** A *dashed line* of 5-nm width; **c** using oxygen plasma to etch away graphene through the PMMA window; **d** point contacts arrays with gaps ≤10 nm with carboxylic acid-terminated. Reproduced with permission from Ref. [40]. Copyright 2011 American Chemical Society. Reproduced with permission from Ref. [34]. Copyright 2012 Wiley-VCH

In 2011, Prins [40] used a feedback-controlled electro-burning to form 1–2 nm gaps in graphene (Fig. 4a), then an anthracene terminated molecule was used to bridge graphene electrodes via π–π stacking. It showed a good gate controlled I–V characters in room temperature, exhibiting a simple gate-depended switching effect of single-molecule devices based on graphene electrodes. However, the electro-burning process cannot be well controlled, and the number of molecules attached is not clear, making the devices unstable.

In order to overcome these problems, Cao et al. [34] developed a new method called "dash-line lithography" (DLL) to form graphene point contacts arrays with gaps of ≤10 nm. A DesignCAD file of a dash line (Fig. 4b) in a width of 5 nm was designed to open windows in PMMA. Then they used oxygen plasma to etch away the exposed graphene through the PMMA window (Fig. 4c). By applying gradual etching and undercutting of PMMA, graphene point contacts arrays were formed, with carboxylic acid on the ends (Fig. 4d). These carboxylic acid-terminated point contacts can covalently bond with molecules decorated with amines via amide linkages.

This covalent bond is robust enough to undergo chemical reactions, such as the coordination reaction. The molecules with a tridentate-aromatic pocket can coordinate with Co^{2+} ions (Fig. 5a). When the molecule-bonded devices were immersed in Co^{2+} solution, the devices behaved a high conductance state. Once

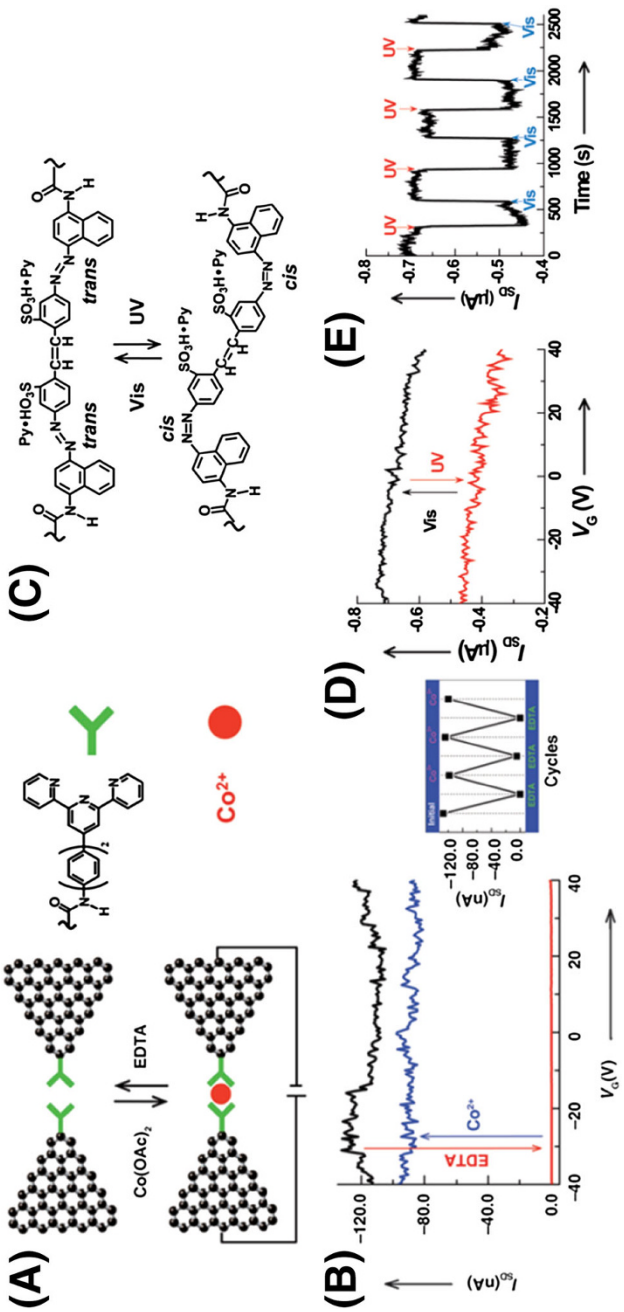

Fig. 5 **a** Schematic representation of the reversible coordination reaction. **b** Conductance cycles of the devices with alternate treatments of EDTA and Co^{2+} solutions. **c** Schematic representation of the azobenzene molecule in response to Vis and UV light. **d**, **e** Electrical characteristics of the graphene-azobenzene device. Reproduced with permission from Ref. [34]. Copyright 2012 Wiley-VCH. Reproduced with permission from Ref. [44]. Copyright 2013 Wiley-VCH

ethylene diamine tetra acetic acid (EDTA) was introduced to wash off the ions, the devices showed an off state with no current flow through. Figure 5b shows the conductance cycles of the devices, with a good stability, indicating the reproducibility and reliability of their devices. In their further investigation [44], by using the same DLL method, they built graphene-azobenzene devices, which can switch on and off in response to the irradiation of visible and UV light. Figure 5e shows the reversible photoswitching current. Compared with the pyrrole-based molecules covalently bonded with SWCNTs [45], these devices achieved a reversible photoswitching property. However, the devices cannot stay in an on state for a long time; once it was kept in darkness for 60 h, the current had a decrease. In addition to the photoswitching ability, these devices were sensitive to pH, owing to the two sulfonic acid groups. The conductance showed a switching cycle when alternatively immersed in the solution in low and high pH. These methods of creating functional molecular devices are useful for developing new devices with diverse functions and promoting the application of single-molecule devices.

In addition to different functional molecules, graphene-based electrodes can also be covalently connected with bio-matters. For the purpose of detecting metal ions, Gao et al. built graphene-enzyme devices [46]. The DNAzyme is sensitive to Cu^{2+}, which can split the substrate strand, producing an open circuit. These devices can detect Cu^{2+} ions even at the fM level. It may be further developed for real-time detection of various chemical and biological reactions. However, the device stability remains a challenge for biological connections. In future developments, the gap size and the electrode geometry will be the main challenges. Developing reliable methods with precise control of the electrode shape and gap size is a compelling obligation.

3 Single-Molecule Switches

The design and synthesis of switchable molecules are undoubtedly one of the great triumphs in the field of molecular electronics. Functional cores are usually modified with two anchoring groups for covalently binding to the electrodes and forming robust molecular junctions. Current methods for tuning electron transport are shown as follows: changing the electron transport pathway by triggering molecular conformation transitions (light-, mechanically, and chemically induced transitions) and tuning the molecular energy level. In detail, there are three ways of tuning the molecular energy level: (1) continuous excitation of molecular vibrations by electron carriers may induce switching (current-induced switching by inelastic scattering); (2) acting a sufficiently high electric field on a molecule may induce switching (field-induced switching); (3) heating of the molecular system may result in (non-selective) switching.

3.1 Conformation-Induced Switch

The conformational change between two or more stable states is a conspicuous switching pattern, which does not produce additional reactants or redundant products. Two principles should be considered: (1) conformational switches with molecules exhibiting different stable isomers, and (2) conformational switches with

molecular reorientation. The changes can be reversibly triggered by light, bias voltage, mechanical force, etc.

Light provides a noninvasive, easily addressable and cheap way for controlling the switches. Photochromic molecules, such as azobenzene [12], diarylethene (DAE) [5, 10], sipropyran [47], dihydroazulene (DHA)/vinylheptafulvene (VHF) [11], and dimethyldihydropyrene (DHP)/cyclophanediene (CPD) [6, 9] derivatives, have been widely investigated in single-molecule devices and in solution. However, molecular properties in solvent and in the solid state are significantly different. The resonance effect between molecules and electrodes plays an important role. For example, in general, by exposing a DAE derivative to UV light, the devices represent a photoswitching behavior from the insulating state (off state) to the high conductance state (on state), which is due to the ring closure generating a conjugated pathway for electron transfer through the molecule. Dulic et al. built a one-way optoelectronic switch between gold electrodes using the MCBJ method [14]. They achieved DAE switching from the high-conductance state to the low-conductance (ring-opening process) state under visible light (546 nm). However, they failed to achieve the opposite process under UV illumination (313 nm). They explained that the presence of the gold quenched the excited state of the molecules in the open form. Different from gold electrodes, the lithography-defined oxidative cutting method was used to fabricate a single-molecule device with carbon electrodes [45]. This work used thiophene-based and pyrrole-based molecules as the functional cores (Fig. 6a). Thiophene-based molecules had a photocyclization as UV light was applied, resulting in an increase of current (Fig. 6b). The device could maintain a high-level conductance even without UV light, but it was unable to photochemically switch back. The pyrrole-based device had the ability to switch on under irradiation of UV light and thermally switch back in a dark condition overnight (Fig. 6c). Both molecules acted differently in comparison with their behaviors in solution. This may result from carbon electrodes, which might affect the energy structure of molecules when they are covalently bonded. This work gives a primary model of photoswitchable single-molecule devices, but the respond time and reversible switch remains obvious obstacles. Another work from Jia et al. [48] demonstrated the similar phenomenon. They covalently bonded DAE derivatives with graphene point contacts constructed by the DLL method. These DAE-graphene devices could switch from the off state to the on state. Taking both barrier and resonant tunneling models into consideration, the spectroscopic analyses proved the molecule–electrode coupling strength. This work also demonstrated a way that the investigation of new molecular structures can modulate the relationship between the charge transport mechanism and the electronic structure of molecular junctions. To reduce the strong conjunction between the photochromic core and the electrode, there are two feasible ways: (1) impairing the bonding strength by substituting the anchoring group with a weak bonding one; (2) modifying the linker group between the anchor and the functional core with unconjugated alkyl groups.

Broman et al. replaced sulfhydryl groups with MeS groups and realized reversible switching between DHA and VHF [11]. The bonding strength and the electron-transport mechanism can be experimentally tested. The stability diagram (Fig. 7) represents a set of characteristic Coulomb blockade diamonds, which

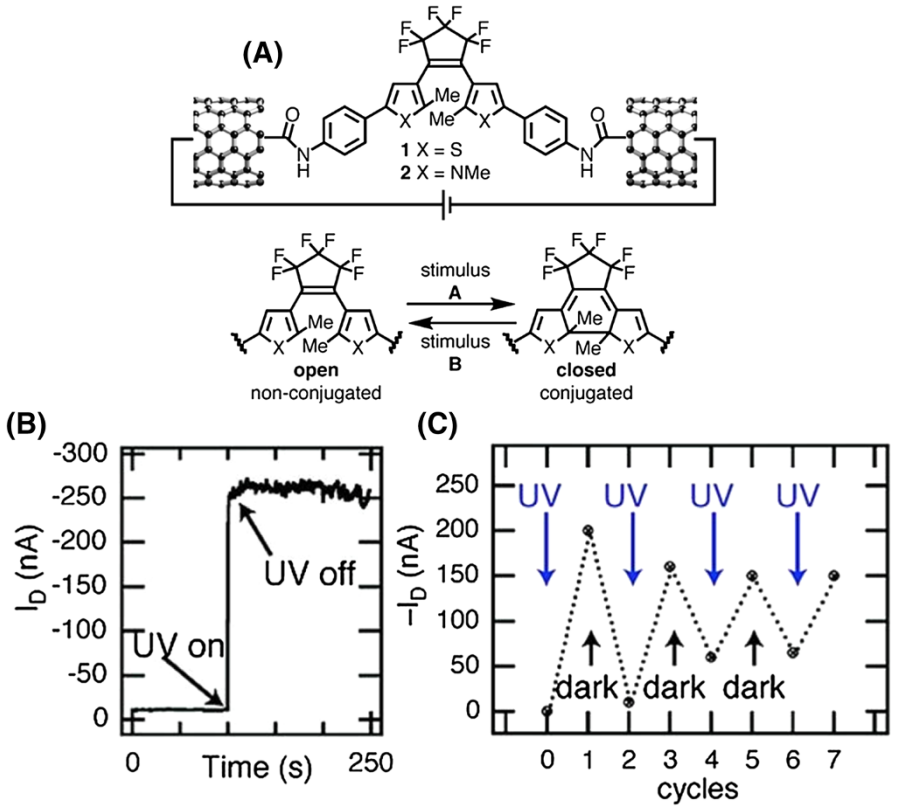

Fig. 6 **a** Schematic representation of single-molecular devices and the switching mechanism of functional cores. **b** Current changes as the stimuli are introduced. **c** Switching circles as the device is exposed to UV light and left in dark for 12 h. Reproduced with permission from Ref. [45]. Copyright 2007 American Chemical Society

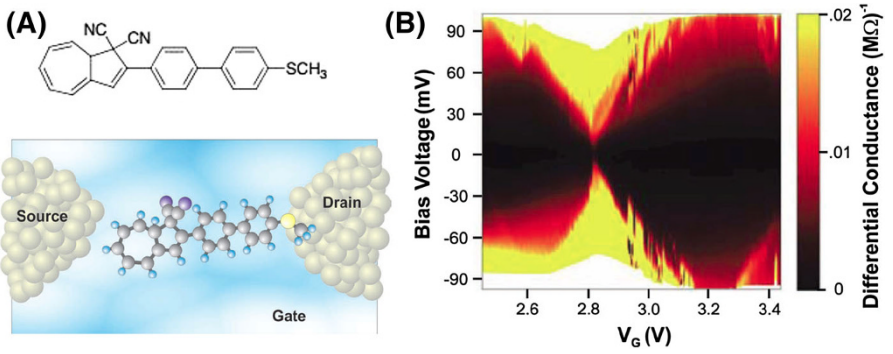

Fig. 7 **a** Schematic representation of the sample geometry of the molecule anchored via the SMe group to one electrode in the silver nanogap. **b** Stability diagram for single-molecule junctions taken right after the molecule was caught in the nanogap. Reproduced with permission from Ref. [11]. Copyright 2012 Wiley-VCH

implies that the molecule is weakly coupled to electrodes and the transport through the molecule goes by sequential tunneling. However, weakly bonding leads to unsteady devices. An intrinsic contradiction of optimizing the device stability and molecular–electrode conjunction is inevitable.

In the most recent work, the strong conjunction problem has been solved by Guo's group [49]. By adding three non-conjugated CH_2 groups between the dithienylethene core and anchoring group NH_2 (Fig. 8a), a reversible light-induced single-molecule switch was achieved in graphene-based single-molecule junctions. They achieved building reliable switching devices with remarkable properties in the levels of accuracy (on/off ratio of $\sim$100), stability (over a year), and reproducibility (46 devices with more than 100 cycles for photoswitching). This work demonstrated the importance of molecular engineering in modulating the molecule–electrode

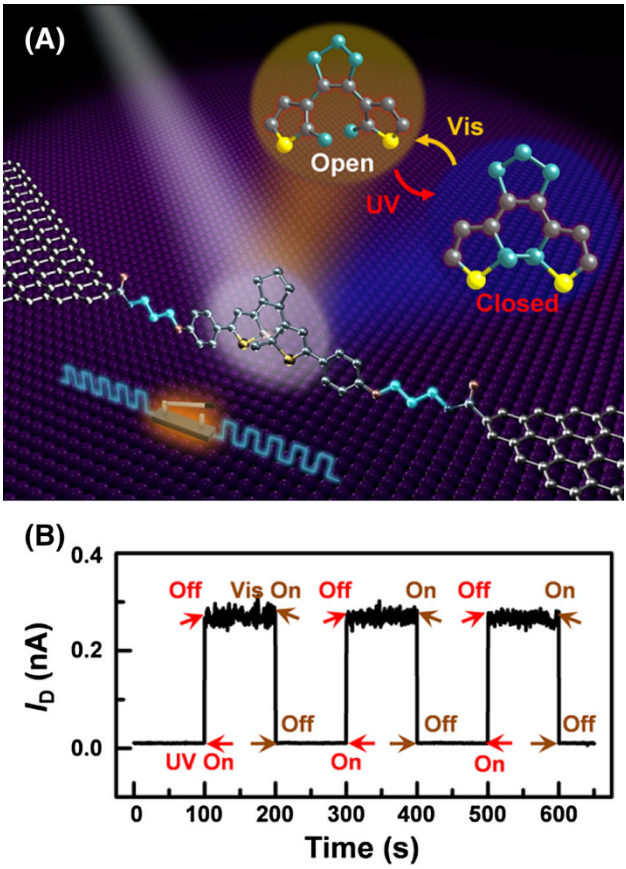

Fig. 8 **a** Schematic of a graphene based molecular junction that highlights the expansion of the molecular bridge by methylene groups. **b** Real-time measurements of the current through a diarylethene molecule that reversibly switches between the closed and open forms, upon exposure to ultraviolet (UV) and visible (Vis) radiation, respectively. $V_D = 100$ mV and $V_G = 0$ V. Reproduced with permission from Ref. [49]. Copyright 2016 AAAS

coupling strengths, and also proved that molecules with desired functionalities could be the key element for future molecular electronics.

Besides light illumination, mechanical force offers a novel tuning method that can trigger chemically inert molecules to present a switching behavior. This is due to the internal configuration change of the molecule or the interface conformation change between the electrode and the molecule. The mechanical force systems are usually fabricated by STM-BJ or MCBJ. The force can be controlled through the metal electrode distance in succession. Quek et al. [50] demonstrated reversible binary switching by mechanical control of the metal–molecule contact geometry in a 4,4′-bipyridine single-molecule junction. The conductance change was due to the distinct contact at the flexible but stable Au–N bond by first-principle calculation. The low conductance was derived from perpendicular between N-bond and conducting π-system. The on/off ratio of this device was approximately 10. In another attempt, oligosilanes showed reversible switching during mechanical tuning through stereoelectronic effect. The $(SiMe_2)_n$ $(n = 1–10)$ oligosilanes, whose backbone have strong σ conjugation, are connected to the metal electrodes by methylthiomethyl linkers using STM-BJ [51]. Different from Quek's work [50], elongating the molecular junction led to a decrease of conductance and compressing the electrode led to an increase in conductance. As calculated by the DFT theory, the molecule had three terminal (C–S–C–Si) dihedral angles, which couple the electrode-linker orbital into the σ framework acting as a gate led to two conductive states (Fig. 9).

When a molecule has more than two anchoring groups, elongating the molecule not only causes the breaking of molecular junctions but also leads to the change of the anchoring points, which will change the electron transport pathway. Kiguchi et al. designed a covered quaterthiophene (QT) that has two thiophene ring anchors

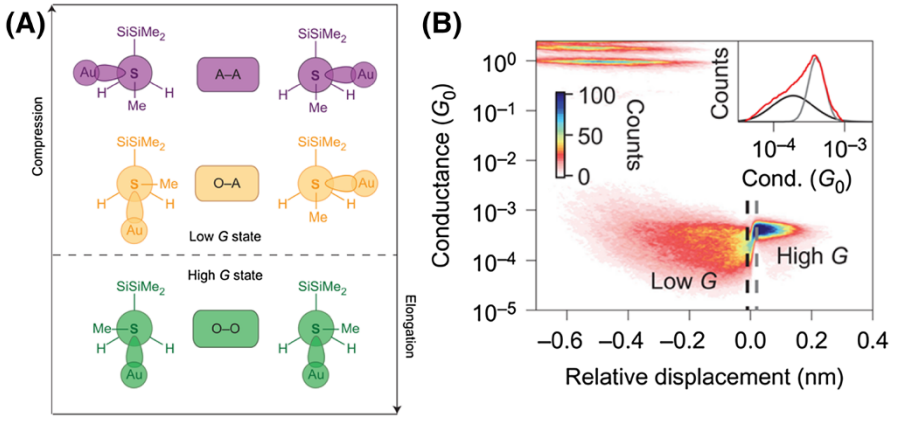

Fig. 9 **a** DFT calculations describing the mechanism for switching as the oligosilanes are elongated in the junction. *A* Newman projections for the *A–A* (*purple*), *O–A* (*yellow*), and *O–O* (*green*) dihedral configurations from the perspective of the sulfur–methylene σ bond in the Au–Si4–Au system. Junction elongation strains the molecule into the higher conducting *O–O* conformer. **b** Statistics of conductance curve measured in the Au–Si4–Au system, which demonstrates the conductance switching. Reproduced with permission from Ref. [51]. Copyright 2015 Nature Publishing Group

on each side and connected to the molecule using STM-BJ (Fig. 10) [52]. The single-molecule junction showed three distinct conductance states with values of 0.05 G_0 (high), 0.005 G_0 (medium), and 0.0005 G_0 (low). Each conductance state corresponds to a pair of anchoring groups with distinct molecular lengths.

Chemical stimuli such as acid and base, metal ions, and chemical reactants can change the molecular conductance by tuning the conformation or setting off chemical reactions. Li et al. built a proton-triggered switch based on a molecular transistor with a novel edge–on gate [54]. The pyridinoparacyclophane (PPC) moiety was linked in the circuit using the STM-BJ method. The "on" and "off" switch could be reversibly set off by deprotonation and protonation of the pyridine ring. Further experiments focused on investigating the conductance of PCC with different substitutions of pyridine. The *para*-position of pyridine was functionalized with $–NO_2$, –Cl, –H, $–OCH_3$, and $–N(CH_3)_2$ (Fig. 11a). The conductance value of these protonated molecules remained consistent, which indicates the independence of the substituents on the pyridine ring. The switch mechanism was ascribed to the change in charge tunneling channels form HOMO in neutral molecules to LUMO in protonated ones.

Chemical reactants have an important effect on the device conductance, which in turn can show the reaction behavior of chemical reactants, offering a new way to understanding the mechanism of these chemical and biological activities. Different from the former studies, which bonded molecules in nanogaps between SWCNTs, Sorgenfrei et al. used an electrochemical oxidation to from point defects in carbon nanotube, then the probe DNA was covalently bonded there via an amide linkage [55]. This device could offer more rapid conductance change and higher yield because of the real-time monitoring while the point defects grew. By using an AFM tip to apply the gate voltage and combining the electrical data with spatial map, a scanning gate microscopy (SGM) was obtained to observe the defects. When the

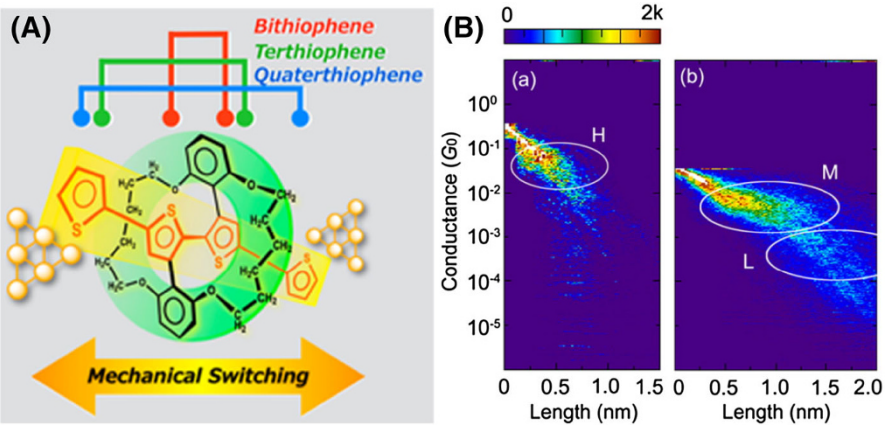

Fig. 10 **a** Schematic of mechanically induced quaterthiophene molecular junctions. **b** 2D conductance histograms constructed for *H*, and *M* and *L* conductance regimes, respectively; *white circles* are eye-guides to highlight *H*-, *M*-, and *L*-conductance states. Reproduced with permission from Ref. [53]. Copyright 2014 American Chemical Society

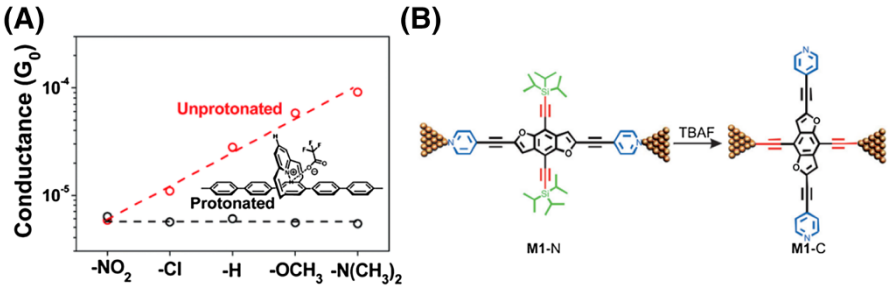

Fig. 11 **a** Conductance of protonated and unprotonated molecular junctions with different side groups. **b** Setting a course for molecular conductance along different pathways based on M1-N and M1-C. Reproduced with permission from Ref. [54]. Copyright 2016 The Royal Society of Chemistry. Reproduced with permission from Ref. [22]. Copyright 2015 Wiley-VCH

probe DNA was connected with target DNA, there was a conductance decrease (Fig. 12b), representing the off state of the device. On the contrary, when there was no target DNA, the device showed a high conductance, representing the on state (Fig. 12a). After the DNA combination, there were more detailed changes in the current, because of the conformational change of DNA. This study developed a single-molecule device with high sensitivity and high time resolution, showing the potential in kinetics monitoring of DNA and protein activities.

In 2012, Choi et al. attached a single lysozyme with SWCNT on the side wall via π–π stacking (Fig. 12c). Lysozyme is big enough to be identified by AFM (Fig. 12d), guaranteeing the single-molecule level [56]. Treating the device with peptidoglycan substrate made an increase of current (Fig. 12e), and the device showed a two-level random telegraph signal as a symbol of the single-molecule event. This device is stable with a temporal resolution into the single-microsecond regime, providing the basis of electrical monitoring of molecular dynamics.

Using the EBL to make SWCNT point contacts, Liu et al. [57] covalently bonded SWCNT electrodes with DNA, which were decorated with amine at the both ends. The DNA contained hydroxypyridone nucleobases (H) in the opposite position of DNA, as a flat bidentate ligand to form a stable metal-mediated base pair. The conductance of DNA increased with the number of H. Since the introduction of metal ions, which reinforce the π–π stacking of base-pairs in DNA, the conductance was improved. Because of the coordination of Cu^{2+} ions in DNA, they used a heated EDTA buffer to wash off Cu^{2+} ions, forming a metal-free DNA. This treatment resulted in a decrease in current, corresponding to the off state. Subsequently, after immersed in Cu^{2+} solution, the device gave out an increase in conductance. Alternately treating the device with EDTA and Cu^{2+} led to an on/off current switching circle. Similar conductance switching phenomenon was also found for other metal ions. This work indicated the potential of single metallo-DNA devices, which can act as reversible sensors of metal ions.

Huang et al. achieved irreversible control of the electrical conductance through changing the molecular orientation by selective gold electrode anchoring [22]. They rationally designed and synthesized a cruciform conjugated molecule with a benzo

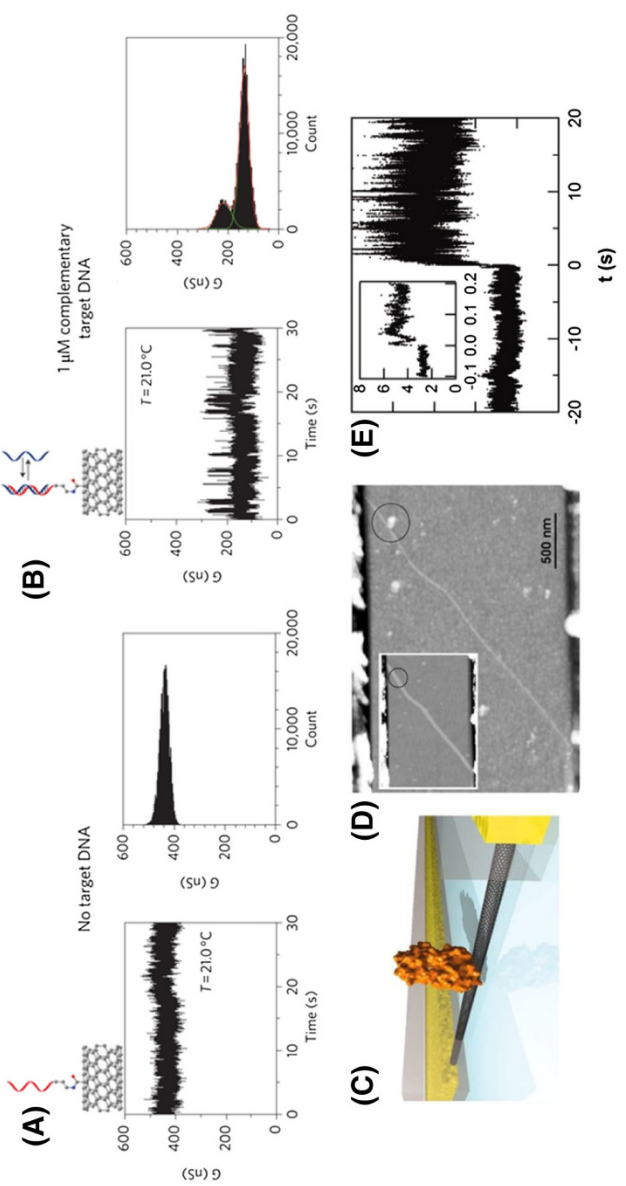

Fig. 12 **a**, **b** Conductance of the device without/with complementary DNA and the corresponding conductance-based histograms. **c** Schematic representation of lysozyme located on the SWCNTs. **d** AFM topography of a SWCNT device before and after treatment with lysozyme. **e** Addition of peptidoglycan substrate made an increase of current. Reproduced with permission from Ref. [55]. Copyright 2011 Nature Publishing Group. Reproduced with permission from Ref. [56]. Copyright 2012 AAAS

(1, 2-b: 4, 5-b′) difuran core M1 (Fig. 11b). By adding tetrabutylammonium fluoride (TBAF), the protection group TIPS (TIPS = tri-isopropylsilyl) was cleaved in situ. A complete conversion from nitrogen atom-anchoring junctions to carbon atom-anchoring junctions was achieved and this led to more than an order of magnitude increase of the conductance. The conductance changing was attributed to the change between two electronic transport pathways.

3.2 Electrochemical Switch

Charging generally leads to notable changes in the molecular conductivity and can therefore be used as a switching mechanism. Molecular charging may occur via virtual occupation of an ionization level or by resonant tunneling to a molecular orbital, followed by geometric reorganization that stabilizes the charge state. Alternatively, it may result from external gating, which changes the energetic position of the molecular energy levels with respect to the Fermi level of the contacts, thus leading to charging.

There are two approaches for building a gate-controlled device. First, a third electrode can be added in a two terminal junctions. However, building a three-terminal electrode at the molecular level is a great challenge. In addition, an important limitation of solid-state three-terminal single-molecule devices is their low gate coupling ξ [58], being defined as the ratio between the molecular orbital energy shift ($E_{HOMO/LUMO}$) and the actual applied gate voltage (V_G). An alternative solution for this approach is to build a planar device, where an electrode gate is separated from the source-drain connects by a slight insulation film such as SiO_2 [24]. The second way is to import an electrochemical gate. In this approach, the

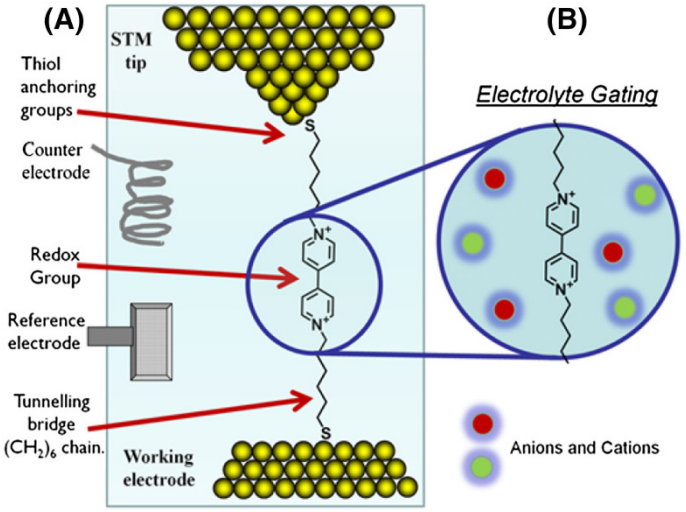

Fig. 13 Schematic diagram of the four-electrode cell (**a**) and the electrochemical double layer under a gate voltage (**b**). Reproduced with permission from Ref. [59]. Copyright 2015 American Chemical Society

molecular junction is immersed in an electrolyte, as shown in Fig. 13 [59]. The functional molecule was linked between the two metal electrodes, which can be viewed as the drain and source electrodes. The counter and reference electrode combination provided the gate electrode in this four-electrode bipotentiostat setup, with independent electrochemical potential control of the source and drain. Since the electrochemical electrode modulates the molecular bridge through the formation of an electronic double layer, it is presented as a more efficient alternative to control charge transport in a single-molecule electrical contact.

Molecules "wired" between single-molecule electrochemical junctions include redox active organic molecules, such as viologens [20], pyrrolo-tetrathiafulvalene (pTTF) [60], oligoanilines [61], oligothiophenes [62], unsubstituted and substituted oligo(phenylene ethynylenes) (OPEs) [63, 64], ferrocene [65], anthraquinone [66, 67], perylene tetracarboxylic bisimide (PBI) [68, 69], benzodifuran [70], pyrrolidine-substituted perylenetetracarboxylic diimide (PTCDI) [71], redox-active proteins [72], and transition metal complex [73]. Some nonredox active molecules can also be adjusted by electrolyte gating, for example bispyridylethylene [74].

The intrinsic principle of electrochemical gating is to tune the energy level of the molecule. If the electrochemical potential is outside the HOMO–LUMO gap of the molecule, this apparently leads to charging of the molecule. If the molecule traps an electron (the LUMO level becomes available), this is a reduction process. Vice versa, if an electron is donated (or a hole is taken up, as the HOMO level becomes available), then the process is called oxidation [58]. An attempt for building an electrochemical control was achieved by Bahernejad et al. using an anthraquinone (AQ) center [52]. Two isomeric AQ-based derivatives, AQ-1,5 and AQ-1,4, were linked to molecular junctions by the STM-BJ technique (Fig. 14a–c). By varying the electrode potential over a range of ~ 1 V, the conductance had a changing with over an order of magnitude. At the redox potential, changing in redox state leads to reversible conductance switching. This was accompanied by changes in conjugation pattern from linear (reduced state) to cross-conjugated (oxidized state). These observations were supported by DFT-based transport calculations.

Gating effect is a crucial parameter for an electrochemical gating. Li et al. correlated the molecule/electrode contact resistance to the electrochemical gating effect [70]. They studied a benzodifuran core-based single-molecule redox switch in $HClO_4$ electrolyte using both STM-BJ and MCBJ methods. An anchoring group effect had also been tested (Fig. 14d–f). The on/off ratio rose from 2.5 to 8 when using CS_2^- group to replace thiol group. These results showed that we could improve the gating effect by reducing the resistance between electrodes and molecules.

By changing aqueous electrolyte into ionic liquid, Osorio et al. quantitatively investigated the gating difference between aqueous electrolyte and ionic liquid. They constructed a single-molecule electrochemical gating of a viologen molecular bridge in 1-butyl-3-methylimidazolium triflate (BMIM-OTf) [59]. A hard gating with gate-coupling efficiency $\xi = 1$ was found in ionic liquid, while a soft gate with $\xi < 0.2$ was found in aqueous solution. Since the gating coupling is controlled by electrostatic interactions between the double layer gate and the redox bridge, its efficiency might be expected to depend on both of these components and vary

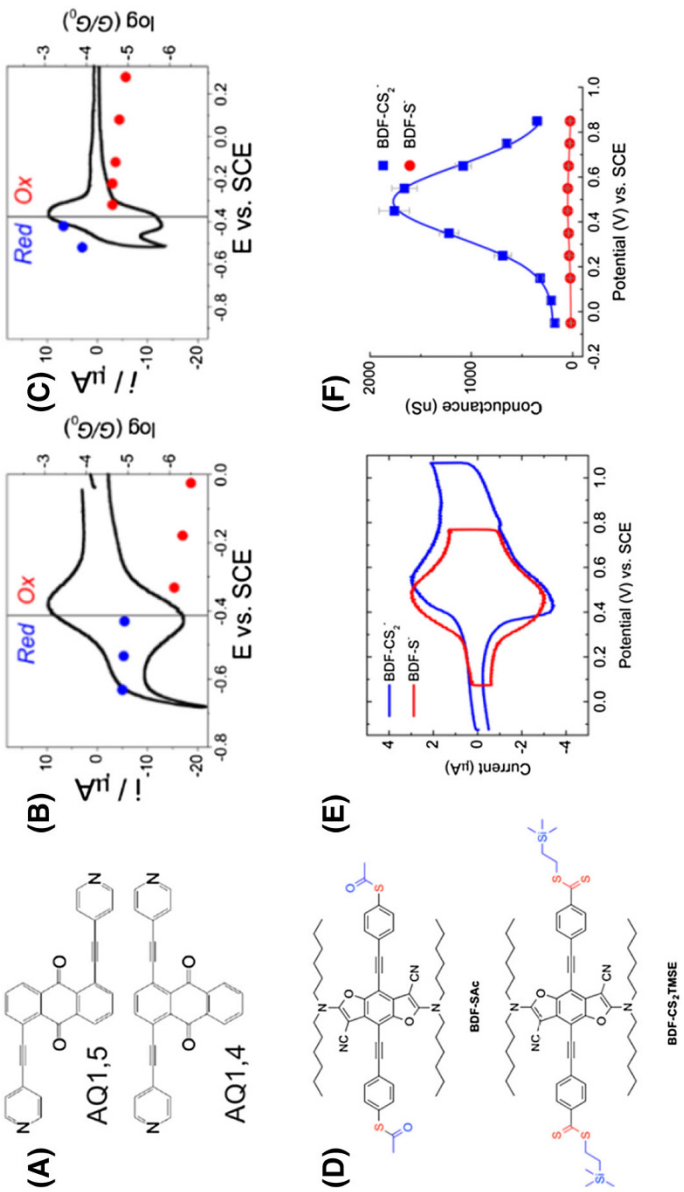

Fig. 14 **a** Molecular structure of AQ-1,5 and AQ-1.4. Experimental molecular conductance as a function of the applied gating potential vs. SCE for AQ-1,5 (**b**) and AQ-1.4 (**c**). **d** Molecular structure of two benzodifuran derivatives. **e** Cyclic voltammograms of BDF-S-(*red*) and BDF-CS2-(*blue*) on Au(111) electrodes in 0.1 M HClO4. Scan rate: 0.5 V s^{-1}. **f** Single-molecule conductance of BDF-S-(*red circles*) and BDF-CS2-(*blue squares*) as a function of gating (substrate electrode) potential determined from STM-BJ experiments. Reproduced with permission from Ref. [52, 70]. Copyright 2014 American Chemical Society

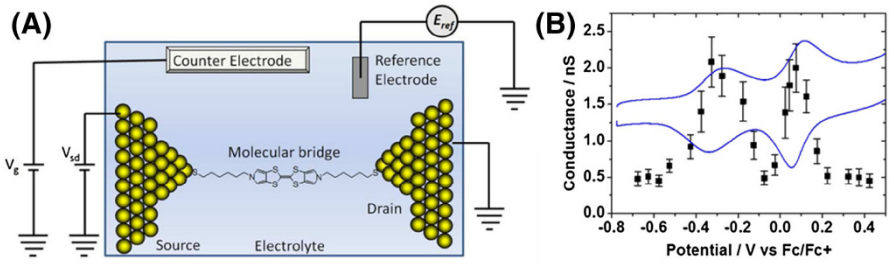

Fig. 15 **a** An electrochemical molecular break junction with electrolyte gating. **b** Plot of conductance of pTTF against the sample electrochemical potential (with $V_{bias} = +0.6$ V, *black point*) and a cyclic voltammogram (*blue line*) of a pTTF monolayer. Reproduced with permission from Ref. [59]. Copyright 2012 American Chemical Society

between redox systems. A similar trend can be seen in the data for a redox active pyrrolo-tetrathiafulvalene bridge, with a gate coupling of $\xi = 0.8$–1 in ionic liquid in comparison with a lower value ($\xi = 0.5$) in aqueous solution. Kay et al. investigated redox-active pTTF moieties in room-temperature ionic liquid (RTIL) [60]. Compared with aqueous solution, RTIL is more stable, which enables the study of molecular conductance over a much wider electrochemical potential range. pTTF first switch to its monocationic state ($pTTF^{+\cdot}$) and then to its dicationic state ($pTTF^{2+\cdot}$) (Fig. 15).

The charge-transport mechanism can be described as a two-step Kuznstzov–Ulstrup Model (Fig. 16). In this model, charge is transported ("hops") through either the reduced or oxidized state of the molecule. First, the redox center reorganizes through environmental and internal fluctuations in order to let the relevant molecular orbitals approach the Fermi level of one electrode. Charge is then transferred onto the redox center through a Franck–Condon-type transition. It is accompanied by partial vibrational relaxation and subsequent charge transfer to the other electrode in the adiabatic limit. In this partially relaxed state, many electrons or holes can transfer across, benefiting to the enhancement in the junction current seen close to the reversible potential. In contrast, in the weak-coupling (diabatic) limit, complete vibrational relaxation occurs before the electron/hole transfers to the second electrode, and current enhancement is minimal.

Besides electrolyte environment, a local microenvironment also has a large impact on the molecular conductance. In a recently work, Zhang et al. used Cucurbit(8) uril to host the viologen (bipyridinum), forming a 1:1 supramolecular complex [20]. The experimental result showed that the conductance of viologen derivatives increased upon encapsulation within the hydrophobic CB(8) cavity. This can be explained by reduced outer sphere reorganization energy within the framework of Marcus-type model for electron transfer.

The electrochemical gating method provides an effective method for tuning the energy level of a single molecule and further results in the redox reaction and corresponding switching effect. Great efforts have been made in tuning different kinds of functional molecules and optimizing the device performance. Miniaturization of this four-electrode system and finding applications will be the next step in this field.

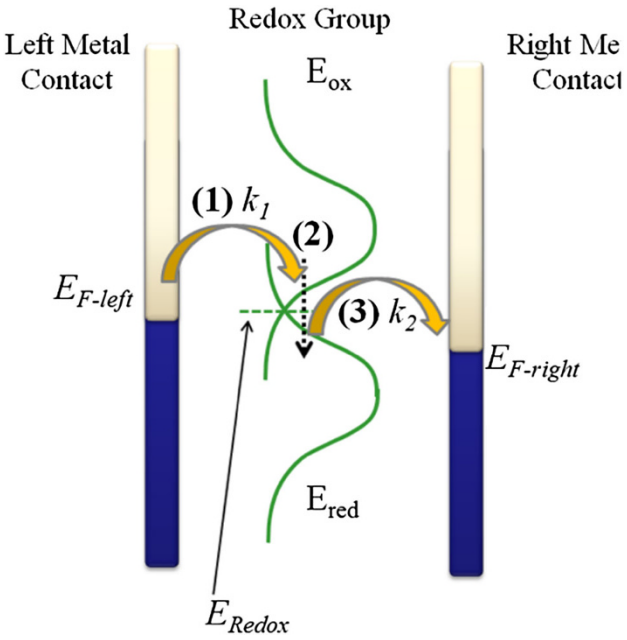

Fig. 16 KU model. The first step of charge transfer occurs when the HOMO is close to the Fermi level of the "left-hand" gold electrode, and involves hole tunneling to the HOMO of the molecular bridge (or electron tunneling from the HOMO). The oxidized and vibrational group relaxes toward the Fermi level of the "right-hand" gold electrode. Reproduced with permission from Ref. [59]. Copyright 2012 American Chemical Society

3.3 Electron Spin Tuning-Based Switch

Spintronics utilizes the spin degree of freedom of electrons to transfer and manipulate information, thus offering low-power and high-speed electronic devices. Electron spin tuning can be operated in two ways: one is to contact organic molecules between two ferromatic electrodes, called the spintronic progress, and the other is to use a molecule with a tunable spin state that can be triggered by the spin crossover effect. Transporting spin electrons through organic molecules takes advantage of the weak spin–orbit and hyperfine interactions in the organic compound. This leads to the possibility of preserving spin coherence over time and distance much longer than in conventional metals. For unpaired spins, the Kondo effect has been observed at a low temperature anomaly at small voltage.

In a previous work, the idea of using organic molecules as spin valves with large magnetoresistance ratios has been proven theoretically to be feasible by using non-equilibrium transport methods and density functional theory [75]. Either *n*-octane-dithiolate or 1,4-*n*-phenyl-dithiolate was analyzed with a nickel connect. The octane molecule had a tunneling-like transport behavior and an order of magnetoresistance. For the case of transport through molecular states extending throughout the entire molecule (1,4-*n*-phenyl-dithiolate), much larger magnetoresistance can be achieved.

This can be attributed to the strong current suppression in the antiparallel configuration due to the spin-selective coupling of the molecule with the leads.

A novel single-radical molecular junction, which has a large magnetoresistance, was successfully done by Hayakawa et al. [76]. An oligo(*p*-phenyleneethynylene) (OPE) backbone, {4-({(2,5-bis(4-sulfanylphenyl(eth-1-yn-2-yl))phenyl)carbonyl}(methyl)amino)-2,2,6,6-tetramethylpiperidin-1-yl}oxidanyl (TEMPO-OPE), was placed on an Au electrode by using the MCBJ method at 4.2 K (Fig. 17). Substantially, MRs of 16–278% were observed at 4 T while MRs in non-radical OPE were only found to be 2–4%. The unpaired electron can reduce the coupling of the current-carrying molecular orbital with metal electrodes, which results in large MRs for TEMPO-OPE.

Spin crossover (SCO) phenomenon can lead to the bistability, which has been observed in some metal-containing molecules. The most investigated metal ion Fe(II) can be used as an example to illuminate the principle of electron configuration. When the iron atom is surrounded by an octahedral ligand environment, its five spin-degenerate 3d levels will be spilt into a doublet and a triplet. The filling order of these levels with the six electrons of Fe(II) depends on the ratio between the ligand field energy, E_{LF}, and the spin exchange energy, E_{EXC}. If $E_{LF} \gg E_{EXC}$, electrons are all paired up and the triplet is completely filled. This case is defined as the low-spin (LS) state, which gives a total spin $S = 0$. Inversely, if $E_{EXC} \gg E_{LF}$, the levels are filled based on Hund's rule and the spin reaches a maximum value, $S = 2$. This case is defined as the high-spin (HS) state. The E_{EXC}/E_{LF} ratio can be adjusted by external stimuli such as pressure, temperature, and mechanical force. In addition to the total spin, the LS and HS states present the difference in geometry, electronic structure, and HOMO–LUMO gap energy. According to the theoretical prediction, in general the HS state has a higher conductance than the LS state.

Frisenda et al. have studied a mechanically Fe(II) spin crossover switches by using a MCBJ technique [77]. Two trepyridines form an orthometric coordination under the relaxation condition and the electron was in a low-spin state (Fig. 18).

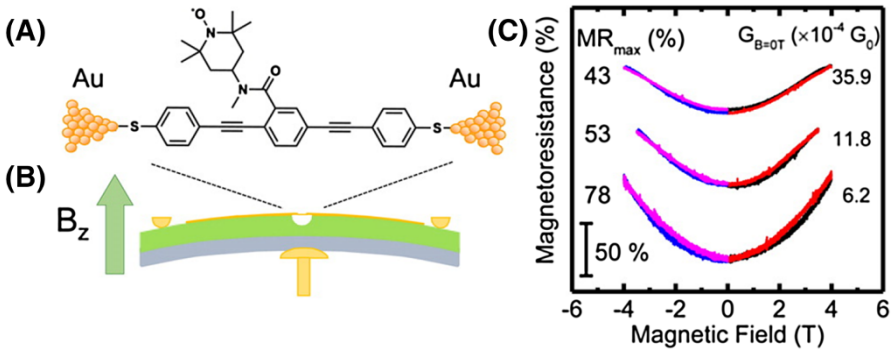

Fig. 17 Schematic illustration of single-molecule junctions for TEMPO-OPE (**a**) and pristine OPE (**b**). **c** Magnetoresistance curves from TEMPO-OPE molecular junctions. Reproduced with permission from Ref. [76]. Copyright 2016 American Chemical Society

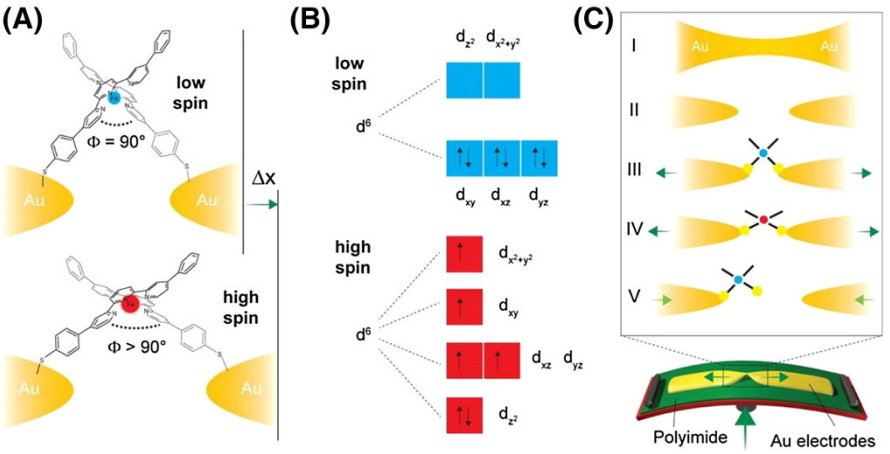

Fig. 18 **a** Sketch of a Fe(II)-based SCO molecular junction in the ideal arrangement to trigger the LS to HS switch by separating the electrodes by Δx. **b** Fe(II) 3d levels involved in the spin-crossover phenomenon. **c** Schematic illustration of a MCBJ setup (*bottom*) with the molecule placed in the junction as sketched in **a**. Reproduced with permission from Ref. [77]. Copyright 2016 American Chemical Society

When elongating the gap between two electrodes, the molecule got stretched, reaching a coordination angle larger than 90. The current had a two-orders-of-magnitude increase in this process. This can be explained by switching the LS state to the HS state.

Apart from setting up a transition metal ion in the electron transport pathway, which can directly tune the current, a magnetic coupling path can also be orthogonally oriented to the conductance channel. Wagner et al. synthesized a molecule modulated by two cobalt ion centers [78]. They found a bias-driven switching, which has been assigned to the transition from the pseudo-singlet of the ground state of a coupled spin system to a pseudo-triplet state at a higher bias voltage. Aragonès et al. built a junction by bridging individual Fe(II) SCO complexes, [Fe(tzpy)2(NCS)2], with high- and low-spin states between a gold electrode and a magnetically polarized nickel electrode [79]. The switching mechanism was based on spin-dependent transport in a single-molecule device that results in the strong interaction of a paramagnetic molecule with heavy-metal surface atoms. This switch led to a large conductance switch (>100) at room temperature.

Another nickel electrode-based single-molecule device was investigated by Brooke et al. [80]. They integrated a non-redox active molecule 4,4′-bipyridine (44BP) into two Ni electrodes by using STM-BJ and electrochemical gating. The conductance and gain of the resulting Ni–44BP–Ni electrochemical transistor was significantly higher than an analogous Au-based device. Ab initio calculations revealed that this behavior arose because charge transport was mediated by spin-polarized Ni d-electrons, which hybridize strongly with molecular orbitals to form a "spinterface".

3.4 Other Switching Mechanisms

Except for the classic mechanisms, switching phenomena such as stochastic switching and charge-state alteration have also been found in the recent work. A field (bias voltage)-induced conductance switching was found by Schwarz et al. [19]. Three organometallic compounds, which had individual metal centers (Fe, Ru, Mo) in the transport pathway, were studied. The *I–V* curves of single-molecule devices fabricated by MCBJ could be classified by two types. The first type was found for all compounds and was characterized by a small hysteresis that affected only a particular section of the voltage. The conductance gap was not altered, and the transition between the curves was continuous. The second type of curves was only observed for Mo compounds and distinct from the first type by a lower current and an abrupt switching (on/off ratio $\sim$1000) between two distinct curves, accompanied by an obvious hysteresis. The conductance gaps changed substantially (from 0.15 to 0.85 V). Theoretical results showed that bias-driven charging indicated an oxidation/reduction mechanism mediated by a weakly coupled, localized molecular orbital that is unique to the Mo compound because of its spin-polarized ground state. Raising bias voltage can also apply a force on the dipole of an asymmetric molecule that can reorient the molecule from the ground state ("off") into a metastable configuration ("on") and back [81].

In some cases, stochastic switching was observed. This phenomenon was firstly investigated in self-assembled monolayer (SAM) systems. Through a room-temperature STM system, the oligo(phenynylene ethynylene) (OPE) was found to show stochastic switching and remain the effect when the side group of OPE was changed [82]. Further experiments showed that molecules with higher degrees of confrontational freedom exhibited higher switching rates. A supposed explanation for these results was given when the authors observed stochastic switching in simple alkanedithiols embedded in alkanethiolate SAMs. The authors argued that the switching was caused by changes in the Au–S bond between the molecules and the gold substrate rather than internal molecular electronic changes. In single-molecule junction systems, a temperature-dependent stochastic switching effect has been demonstrated in a graphene–diarylethene–graphene junction (Fig. 19) [49]. This phenomenon was observed only for the closed form in the temperature range of 160–240 K. The stochastic switching was attributed to DAE conformational change, possibly driven by molecular charging, which means changing occupation of the molecular HOMO. Consequently, two mechanisms have been proposed to explain stochastic switching: (1) molecular motion due to the conformational changes; (2) bond-fluctuation due to the attachment/detachment process of the molecules tethered to the gold surface in a random manner [83].

3.5 Multiple Responses

We have discussed different kinds of molecular switches above. One goal in the field is to build a "molecular chip" by using integrated molecular switches. There are two strategies for integrating these switches into the electrical circuit. The first way is to install several molecular switches in series in the same molecular junction.

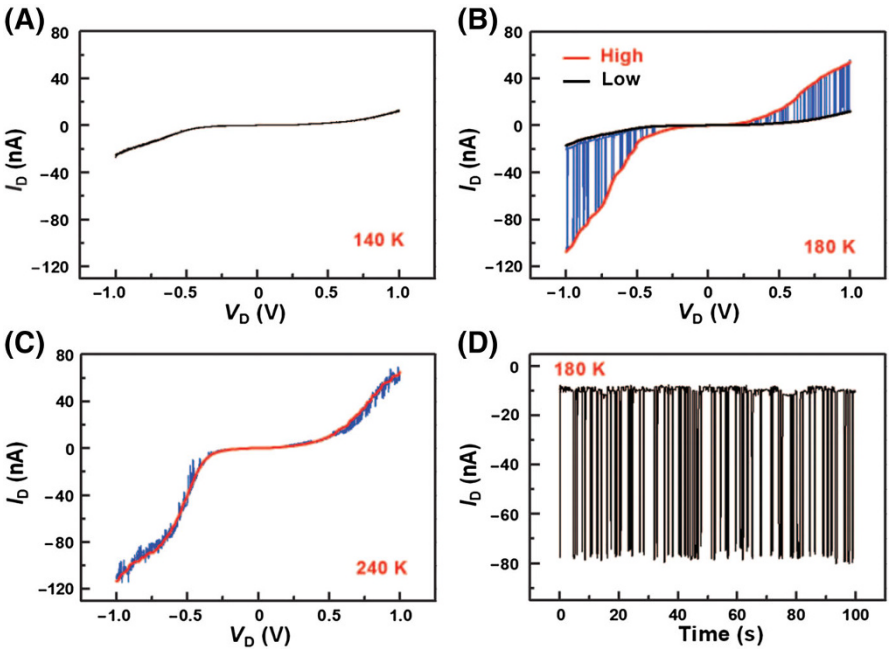

Fig. 19 Temperature-dependent stochastic switching of graphene–diarylethene–graphene junctions. **a** *I–V* characteristics of a single diarylethene junction in the closed form screened at 140 K for at least three times, which did not show stochastic switching. **b** Stochastic switching between two conductive states at 180 K. **c** *I–V* characteristics at 240 K. The stochastic conductance switching started to disappear at this temperature. **d** Real-time recording of stochastic conductance switching at 180 K, with a source-drain bias of −0.8 V and a gate voltage of 0 V. Reproduced with permission from Ref. [49]. Copyright 2016 AAAS

Another way is to integrate molecular junctions. However, the latter method needs extensive accurate control at the molecular level. The former method was studied by Meng et al. [84, 85]. The orthogonally modulated molecular transport junctions were achieved via chemically fabricated nanogaps (on-wire lithography) functionalized with DAE units bearing organometallic ruthenium fragments (Fig. 20). The stepwise control of molecular isomerization can be repeatedly and reversibly completed with use of orthogonal electrochemical and optical stimuli to realize the controllable switching of conductivity between two distinct states. An electronic logic gate can be achieved such as two-input OR and a three-input AND–OR, proving that rational chemical design can lead to multifunctional molecular devices. There are limitations in this molecular device: the molecular gap fabricated by on-wire lithography is an ensemble molecular gap which can only show ensemble average molecular characteristics. What's more, response time of the devices is in a range of 30 min resulting from ensemble properties of the devices. Another multi-responsive single-molecule switch triggered by photon and chemical stimuli was fabricated by Darwish et al. [47]. They designed the switch by using a spiropyran center, which is responsive to many kinds of stimuli such as light, solvent, metal ion, gas, acid, and base.

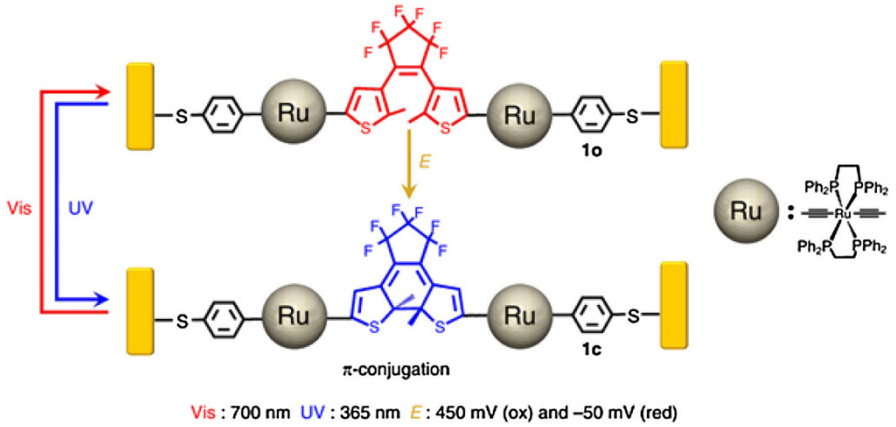

Fig. 20 Schematic of molecular isomerization under external control. Reproduced with permission from Ref. [84]. Copyright 2014 Nature Publishing Group

4 Film-Based Switches

The film formed by organic molecules can be used as a smart surface [86], which is able to respond to external stimuli. According to the types of stimulus, different molecules were designed to achieve multiple functional devices. Organic molecules with their own features, such as photochemically and electrochemically switching abilities, can be combined together, affording molecules with various functions and thus forming multifunctional films.

For example, DAE is a photo and electrochromic unit with the multi-functions. It was the most commonly used key element for building smart surfaces. In 2012 [87], the DAE unit was combined with polymerizable groups, in the presence of phenyl spacers, which ensured their functionality that electronic-redox switching can be achieved in polymer electrodes. The electro-polymerization process can be realized and remain stable in open air, having a potential in future applications of closed electronic devices. DAE films can also be applied in photoswitchable devices [88, 89]. They can absorb UV light to form a closed state and visible light to an open state. The conductance of this device showed repeated conductance switching when UV and Vis lights were alternatively introduced to illuminate the DAE film.

This phenomenon was well investigated by using STM when DAEs were inserted into a monolayer of dodecanethiol (Fig. 21a) [90]. DAE has two states (Fig. 21a), which shows a bright pot with a higher configuration. When UV and Vis light were interacted in turn, the reversible switching behavior of individual molecules was observed in STM images (Fig. 21c). The variation of height was also consistent with the experiments. This work gave us a clear image of the reversible change of DAE, offering a better understanding of DAE ensemble phenomena.

When the DAE unit was combined with a chiral unit [90], the molecular layer can show reversible colors with the irradiation of UV and Vis light, exhibiting a new way in developing functional devices. Amphiphilic photochromic DAE [91] can also be achieved by decorating the photochromic DAE unit with a cholesterol unit

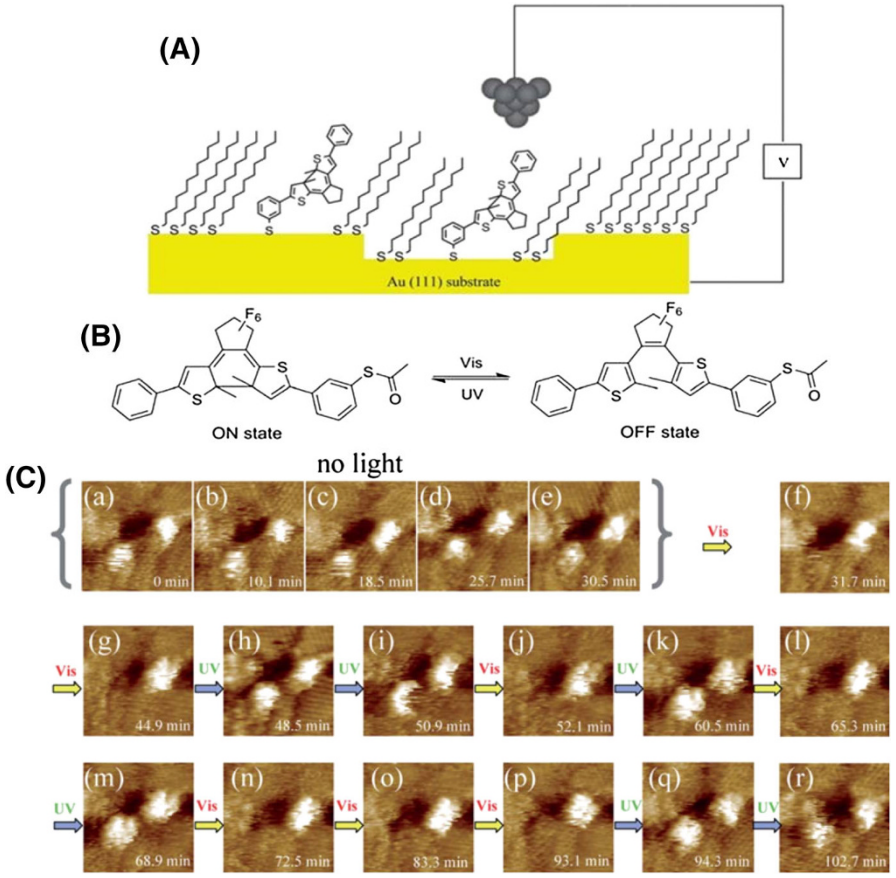

Fig. 21 **a** Individual DAE molecules were located within a self-assembled monolayer of dodecanethiol. **b** Schematic diagram of the on and off states of DAE. **c** Reversible switching behaviors of individual molecules. Reproduced with permission from Ref. [90]. Copyright 2013 Royal Society of Chemistry

(providing hydrophobic functionality) and a poly (ethylene glycol)-modified pyridinium group (providing hydrophilic functionality). This molecule reacted to UV and Vis light with configuration changes (Fig. 22a), which result in a transformation of hydrophobicity/hydrophilicity, showing different dynamic self-assembly behaviors in aqueous (Fig. 22b) and organic media (Fig. 22c). This allowed photocontrolled vesicle formation in water and self-assembly of organ-gel fibers in organic media. This research exhibited the potential use of DAE in photocontrolled chemical release systems.

The various functionalities and fundamental understanding of DAEs offer a remarkable symbol of functional molecules, fostering the rapid development of this field towards practical application. Functional molecules with a revisable switching effect can be applied between metal electrodes, which have a screening of the field effect, resulting in inefficient switching and poor on/off ratio [92]. On the contrary, the low-dimensional carbon material only screens the gate field in junction regions.

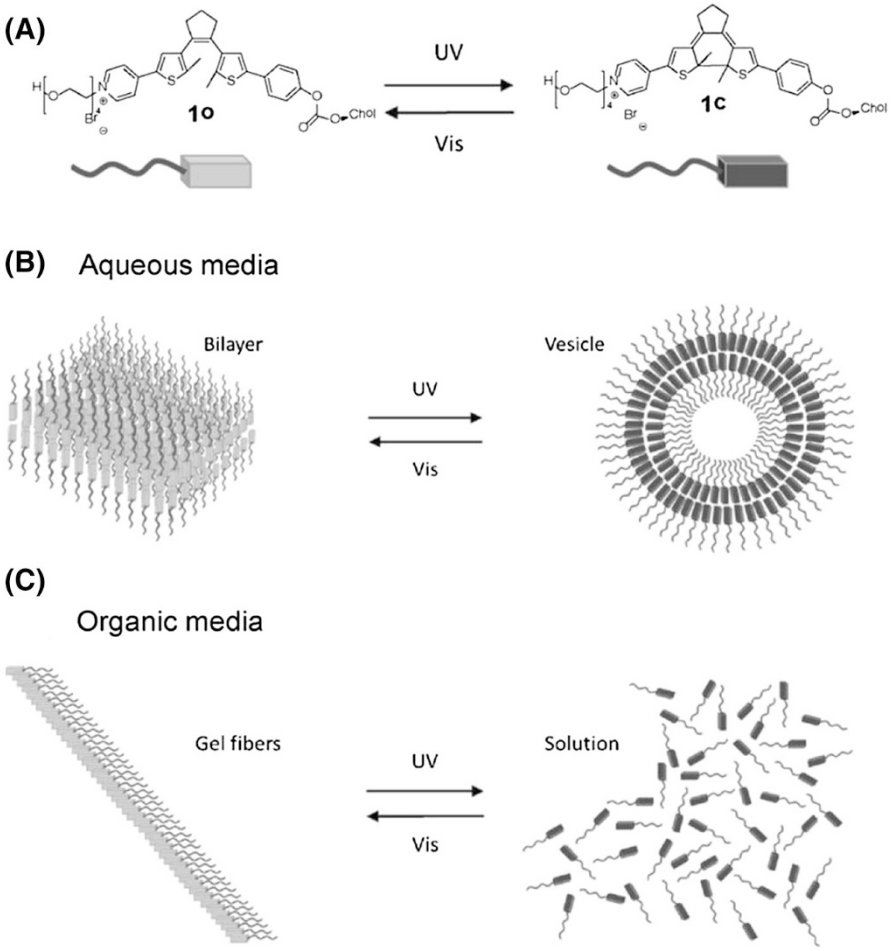

Fig. 22 **a** Open and closed forms of decorated DAE. **b**, **c** Light-induced dynamic self-assembly behaviors of decorated DAE. Reproduced with permission from Ref. [91]. Copyright 2014 Wiley-VCH

Hence, the gate regulation can be more efficient with high on/off ratio. For example, hexabenzocoronenes (HBCs) were chosen as a monomer to form monolayers in a self-assembled way between SWCNT electrodes with a current on/off ratio of $\sim 10^5$. HBC can also react to environment stimulus such as temperature and photon. The combination of top–down fabrication and bottom–up self-assembly gave a new way in constructing molecular devices, showing a new device type of environmental and chemical sensing.

By using the similar method, a water-processed copper phthalocyanine (CuPc) monolayer was used with SWCNT electrodes for high sensitive photo-detector [93] at room temperature, with responsivity greater than 10^8 A W^{-1}, detectivities greater than 7×10^{15} Jones.

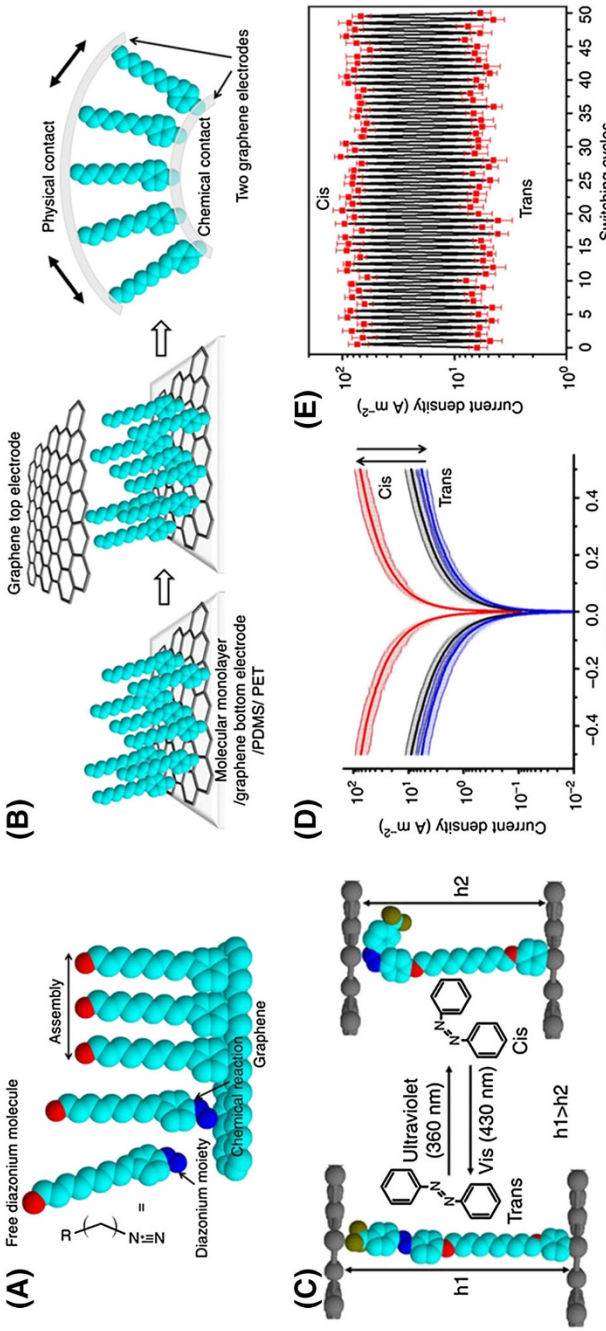

Fig. 23 **a** Self-assembled process of aryl diazonium molecules on graphene. **b** Schematic diagram of transparent and flexible devices based on graphene electrodes. **c** Molecular transmission distance (*h1*, *h2*) corresponding to molecular conformation in reaction to light irradiation. **d** Current characteristics of a device. **e** Changes in current density of the device. Reproduced with permission from Ref. [97]. Copyright 2013 Nature Publishing Group

In comparison with SWCNTs, graphene electrodes exhibit outstanding interface contact with organic molecules, and its humongous electric character offers higher stability and will not be influenced by gate regulation, making it suitable for molecular electronics. Cao et al. used graphene sheets as electrodes to measure the electrical conductance of poly (3-hexylthpene-2,5diyl) (P3HT) [94]. This device had responsivity as high as 8.3 A W^{-1} and on/off ration of 10^5. This device also showed reversible photocurrents by switching on/off light, offering a new application in developing integrated ultrasensitive devices. In 2010, CuPc LB monolayers were applied with single-layer graphene electrodes [95], with a carrier mobility of 0.04 cm^2 v^{-1} s^{-1}, an on/off ration current ratio over 10^6, and the best responsivity of about 7.1 $\times$ 10^5 A W^{-1}. This similar fabrication method [92] with graphene electrodes gives new material options in future devices.

With the development of molecular devices, the wearable device is drawing increasing attention [96]. Graphene as an intrinsically transparent, conductive, and flexible electrode meets the need of wearable devices. In 2013, Seo et al. reported a photo-switchable device with highly transparency and flexibility [97]. They used aryl diazonium compounds, which undergo a self-assembled process on graphene electrodes, and the diazonium unit was covalently connected with carbon atoms in the graphene plane (Fig. 23a). On the other side, a layer of graphene as top electrode was connected with molecular monolayers by physical contact (Fig. 23b). This vertical device combined chemical and physical contact together and maintained the good conductance as well as high flexibility. Since the molecule has UV/Vis absorption, its configuration can switch with light induction (Fig. 23c). Figure 23e shows the reversible current of this device with good stability. Unlike the traditional electrodes [94, 95, 98], this vertical structure provides a new way in flexibility devices.

5 Conclusion

The switching effect is an essential phenomenon in our daily life. Design and fabrication of switchable devices with good stability and reproducibility is of great importance to the development of the field of nano/molecular electronics. In this review, metal- and carbon-based molecular junctions were discussed. Carbon electrodes have unique characteristics, promising the potential of carbon era after silicon. On the other hand, as the essence of functionality in the material world, molecules exhibit numerous characteristics. Understanding and using these unique qualities is the goal we are pursuing. To this end, conformation transformation, electrochemical gating, and electron spin tuning are mostly used as the intrinsic mechanism for explaining the intrinsic molecular switching effect. Different triggers, such as light, mechanical force, bias voltage, gating, and chemical reactant, have been proven suitable for particular situations. Molecular film-based devices provide us the nature of the ensemble, while single-molecule devices offer a way to learn the rich information hidden in the ensemble at the single-event level. The combination of reliable electrodes with functional molecules creates new opportunities to achieve remarkable electrical characteristics. However, there are still

some challenges that need to be overcome. The stability and reproducibility of molecular devices remain challenging. An electrode with controllable configuration is the foundation of molecular devices. Hence, new methods for precise formation of molecular junctions are crucial. The contact interface between molecules and electrodes is also of great importance to modulate the transport characteristics of molecular devices. Therefore, further investigation of the contact interface should be done to solve this problem. In addition to these, as the detailed mechanism of molecular conformational changes or biomolecular interactions is not fully understood, the development of more stable and reliable molecular devices is in great need.

Acknowledgements This work was supported by the National Natural Science Funds of China (21225311, 91333102, and 21373014) and the 973 Project (2012CB921404 and 2012CB921403).

References

1. Xiang D, Wang X, Jia C, Lee T, Guo X (2016) Chem Rev 116:4318
2. van der Molen SJ, Liljeroth P (2010) J Phys Condens Matter 22:133001
3. Zhang X, Hou L, Samori P (2016) Nat Commun 7:11118
4. Taherinia D, Frisbie CD (2016) J Phys Chem C 120:6442
5. Sendler T, Luka-Guth K, Wieser M, Lokamani, Wolf J, Helm M, Gemming S, Kerbusch J, Scheer E, Huhn T, Erbe A (2015) Adv Sci 2:1500017
6. Hu W, Zhang G-P, Duan S, Fu Q, Luo Y (2015) J Phys Chem C 119:11468
7. Tsuji Y, Hoffmann R (2014) Angew Chem Int Ed 53:4093
8. Zheng YB, Pathem BK, Hohman JN, Thomas JC, Kim M, Weiss PS (2013) Adv Mater 25:302
9. Roldan D, Kaliginedi V, Cobo S, Kolivoska V, Bucher C, Hong W, Royal G, Wandlowski T (2013) J Am Chem Soc 135:5974
10. Kim Y, Hellmuth TJ, Sysoiev D, Pauly F, Pietsch T, Wolf J, Erbe A, Huhn T, Groth U, Steiner UE, Scheer E (2012) Nano Lett 12:3736
11. Broman SL, Lara-Avila S, Thisted CL, Bond AD, Kubatkin S, Danilov A, Nielsen MB (2012) Adv Funct Mater 22:4249
12. Martin S, Haiss W, Higgins SJ, Nichols RJ (2010) Nano Lett 10:2019
13. Choi BY, Kahng SJ, Kim S, Kim H, Kim HW, Song YJ, Ihm J, Kuk Y (2006) Phys Rev Lett 96:156106
14. Dulic D, van der Molen SJ, Kudernac T, Jonkman HT, de Jong JJ, Bowden TN, van Esch J, Feringa BL, van Wees BJ (2003) Phys Rev Lett 91:207402
15. Lin W, Zhao Q, Sun H, Zhang KY, Yang H, Yu Q, Zhou X, Guo S, Liu S, Huang W (2015) Adv Opt Mater 3:368
16. Sun H, Liu S, Lin W, Zhang KY, Lv W, Huang X, Huo F, Yang H, Jenkins G, Zhao Q, Huang W (2014) Nat Commun 5:3601
17. Zhang KY, Chen X, Sun G, Zhang T, Liu S, Zhao Q, Huang W (2016) Adv Mater 28:7137
18. Rascón-Ramos H, Artés JM, Li Y, Hihath J (2015) Nat Mater 14:517
19. Schwarz F, Kastlunger G, Lissel F, Egler-Lucas C, Semenov SN, Venkatesan K, Berke H, Stadler R, Lortscher E (2016) Nat Nano 11:170
20. Zhang W, Gan S, Vezzoli A, Davidson RJ, Milan DC, Luzyanin KV, Higgins SJ, Nichols RJ, Beeby A, Low PJ, Li B, Niu L (2016) ACS Nano 10:5212
21. Li Z, Smeu M, Afsari S, Xing Y, Ratner MA, Borguet E (2014) Angew Chem Int Ed 53:1098
22. Huang C, Chen S, Baruel Ornso K, Reber D, Baghernejad M, Fu Y, Wandlowski T, Decurtins S, Hong W, Thygesen KS, Liu SX (2015) Angew Chem Int Ed 54:14304
23. Zhang JL, Zhong JQ, Lin JD, Hu WP, Wu K, Xu GQ, Wee AT, Chen W (2015) Chem Soc Rev 44:2998
24. Tao NJ (2006) Nat Nano 1:173
25. Xiang D, Jeong H, Lee T, Mayer D (2013) Adv Mater 25:4845

26. Iijima S (1991) Nature 354:56
27. Novoselov KS, Geim AK, Morozov SV, Jiang D, Zhang Y, Dubonos SV, Grigorieva IV, Firsov AA (2004) Science 306:666
28. Thompson SE, Parthasarathy S (2006) Mater Today 9:20
29. Ajayan PM, Ebbesen TW (1997) Rep Prog Phys 60:1025
30. Tans SJ, Verschueren ARM, Dekker C (1998) Nature 393:49
31. Dai H (2002) Acc Chem Res 35:1035
32. Robertson J (2007) Mater Today 10:36
33. Feldman AK, Steigerwald ML, Guo X, Nuckolls C (2008) Acc Chem Res 41:1731
34. Cao Y, Dong S, Liu S, He L, Gan L, Yu X, Steigerwald ML, Wu X, Liu Z, Guo X (2012) Angew Chem Int Ed 51:12228
35. Liu S, Guo X (2012) NPG Asia Mater 4:e23
36. Guo X (2013) Adv Mater 25:3397
37. Perrin ML, Burzuri E, van der Zant HSJ (2015) Chem Soc Rev 44:902
38. Jia C, Ma B, Xin N, Guo X (2015) Acc Chem Res 48:2565
39. Sun L, Diaz-Fernandez YA, Gschneidtner TA, Westerlund F, Lara-Avila S, Moth-Poulsen K (2014) Chem Soc Rev 43:7378
40. Prins F, Barreiro A, Ruitenberg JW, Seldenthuis JS, Aliaga-Alcalde N, Vandersypen LMK, van der Zant HSJ (2011) Nano Lett 11:4607
41. Guo X, Small JP, Klare JE, Wang Y, Purewal MS, Tam IW, Hong BH, Caldwell R, Huang L, O'Brien S, Yan J, Breslow R, Wind SJ, Hone J, Kim P, Nuckolls C (2006) Science 311:356
42. Liu S, Zhang X, Luo W, Wang Z, Guo X, Steigerwald ML, Fang X (2011) Angew Chem Int Ed 50:2496
43. Wang H, Muren NB, Ordinario D, Gorodetsky AA, Barton JK, Nuckolls C (2012) Chem Sci 3:62
44. Cao Y, Dong S, Liu S, Liu Z, Guo X (2013) Angew Chem Int Ed 52:3906
45. Whalley AC, Steigerwald ML, Guo X, Nuckolls C (2007) J Am Chem Soc 129:12590
46. Gao L, Li LL, Wang X, Wu P, Cao Y, Liang B, Li X, Lin Y, Lu Y, Guo X (2015) Chem Sci 6:2469
47. Darwish N, Aragones AC, Darwish T, Ciampi S, Diez-Perez I (2014) Nano Lett 14:7064
48. Jia C, Wang J, Yao C, Cao Y, Zhong Y, Liu Z, Liu Z, Guo X (2013) Angew Chem Int Ed 52:8666
49. Jia C, Migliore A, Xin N, Huang S, Wang J, Yang Q, Wang S, Chen H, Wang D, Feng B, Liu Z, Zhang G, Qu D-H, Tian H, Ratner MA, Xu HQ, Nitzan A, Guo X (2016) Science 352:1443
50. Quek SY, Kamenetska M, Steigerwald ML, Choi HJ, Louie SG, Hybertsen MS, Neaton JB, Venkataraman L (2009) Nat Nano 4:230
51. Su TA, Li H, Steigerwald ML, Venkataraman L, Nuckolls C (2015) Nat Chem 7:215
52. Baghernejad M, Zhao X, Baruel Ornso K, Fueg M, Moreno-Garcia P, Rudnev AV, Kaliginedi V, Vesztergom S, Huang C, Hong W, Broekmann P, Wandlowski T, Thygesen KS, Bryce MR (2014) J Am Chem Soc 136:17922
53. Kiguchi M, Ohto T, Fujii S, Sugiyasu K, Nakajima S, Takeuchi M, Nakamura H (2014) J Am Chem Soc 136:7327
54. Li L, Lo WY, Cai Z, Zhang N, Yu L (2016) Chem Sci 7:3137
55. Sorgenfrei S, Chiu C-Y, Gonzalez RL, Yu Y-J, Kim P, Nuckolls C, Shepard KL (2011) Nat Nano 6:126
56. Choi Y, Moody IS, Sims PC, Hunt SR, Corso BL, Perez I, Weiss GA, Collins PG (2012) Science 335:319
57. Liu S, Clever GH, Takezawa Y, Kaneko M, Tanaka K, Guo X, Shionoya M (2011) Angew Chem Int Ed 50:8886
58. Guo S, Artés JM, Díez-Pérez I (2013) Electrochim Acta 110:741
59. Osorio HM, Catarelli S, Cea P, Gluyas JB, Hartl F, Higgins SJ, Leary E, Low PJ, Martin S, Nichols RJ, Tory J, Ulstrup J, Vezzoli A, Milan DC, Zeng Q (2015) J Am Chem Soc 137:14319
60. Kay NJ, Higgins SJ, Jeppesen JO, Leary E, Lycoops J, Ulstrup J, Nichols RJ (2012) J Am Chem Soc 134:16817
61. Chen F, He J, Nuckolls C, Roberts T, Klare JE, Lindsay S (2005) Nano Lett 5:503
62. Xu BQ, Li XL, Xiao XY, Sakaguchi H, Tao NJ (2005) Nano Lett 5:1491
63. Xiao X, Nagahara LA, Rawlett AM, Tao N (2005) J Am Chem Soc 127:9235
64. He J, Fu Q, Lindsay S, Ciszek JW, Tour JM (2006) J Am Chem Soc 128:14828
65. Xiao X, Brune D, He J, Lindsay S, Gorman CB, Tao N (2006) Chem Phys 326:138
66. Darwish N, Díez-Pérez I, Guo S, Tao N, Gooding JJ, Paddon-Row MN (2012) J Phys Chem C 116:21093

67. Darwish N, Diez-Perez I, Da Silva P, Tao N, Gooding JJ, Paddon-Row MN (2012) Angew Chem Int Ed 51:3203
68. Xu, Xiao, Yang X, Zang L, Tao (2005) J Am Chem Soc 127:2386
69. Li, Hihath J, Chen F, Masuda T, Zang L, Tao (2007) J Am Chem Soc 129:11535
70. Li Z, Li H, Chen S, Froehlich T, Yi C, Schonenberger C, Calame M, Decurtins S, Liu SX, Borguet E (2014) J Am Chem Soc 136:8867
71. Díez-Pérez I, Li Z, Guo S, Madden C, Huang H, Che Y, Yang X, Zang L, Tao N (2012) ACS Nano 6:7044
72. Pia EAD, Chi Q, Jones DD, Macdonald JE, Ulstrup J, Elliott M (2011) Nano Lett 11:176
73. Albrecht T, Guckian A, Kuznetsov AM, Vos JG, Ulstrup J (2006) J Am Chem Soc 128:17132
74. Capozzi B, Chen Q, Darancet P, Kotiuga M, Buzzeo M, Neaton JB, Nuckolls C, Venkataraman L (2014) Nano Lett 14:1400
75. Rocha AR, Garcia-suarez VM, Bailey SW, Lambert CJ, Ferrer J, Sanvito S (2005) Nat Mater 4:335
76. Hayakawa R, Karimi MA, Wolf J, Huhn T, Zollner MS, Herrmann C, Scheer E (2016) Nano Lett 16:4960
77. Frisenda R, Harzmann GD, Celis Gil JA, Thijssen JM, Mayor M, van der Zant HS (2016) Nano Lett 16:4733
78. Wagner S, Kisslinger F, Ballmann S, Schramm F, Chandrasekar R, Bodenstein T, Fuhr O, Secker D, Fink K, Ruben M, Weber HB (2013) Nat Nano 8:575
79. Aragones AC, Aravena D, Cerda JI, Acis-Castillo Z, Li H, Real JA, Sanz F, Hihath J, Ruiz E, Diez-Perez I (2016) Nano Lett 16:218
80. Brooke RJ, Jin C, Szumski DS, Nichols RJ, Mao BW, Thygesen KS, Schwarzacher W (2015) Nano Lett 15:275
81. Meded V, Bagrets A, Arnold A, Evers F (2009) Small 5:2218
82. Lewis PA, Inman CE, Yao Y, Tour JM, Hutchison JE, Weiss PS (2004) J Am Chem Soc 126:12214
83. Blum AS, Kushmerick JG, Long DP, Patterson CH, Yang JC, Henderson JC, Yao Y, Tour JM, Shashidhar R, Ratna BR (2005) Nat Mater 4:167
84. Meng F, Hervault YM, Shao Q, Hu B, Norel L, Rigaut S, Chen X (2014) Nat Commun 5:3023
85. Meng F, Hervault Y-M, Norel L, Costuas K, Van Dyck C, Geskin V, Cornil J, Hng HH, Rigaut S, Chen X (2012) Chem Sci 3:3113
86. Wesenhagen P, Areephong J, Fernandez Landaluce T, Heureux N, Katsonis N, Hjelm J, Rudolf P, Browne WR, Feringa BL (2008) Langmuir 24:6334
87. Logtenberg H, van der Velde JHM, de Mendoza P, Areephong J, Hjelm J, Feringa BL, Browne WR (2012) J Phys Chem C 116:24136
88. van der Molen SJ, Liao J, Kudernac T, Agustsson JS, Bernard L, Calame M, van Wees BJ, Feringa BL, Schönenberger C (2009) Nano Lett 9:76
89. van Leeuwen T, Pijper TC, Areephong J, Feringa BL, Browne WR, Katsonis N (2011) J Mater Chem 21:3142
90. Arramel, Pijper TC, Kudernac T, Katsonis N, van der Maas M, Feringa BL, van Wees BJ (2013) Nanoscale 5:9277
91. Van Herpt JT, Areephong J, Stuart MCA, Browne WR, Feringa BL (2014) Chem Eur J 20:1737
92. Guo X, Myers M, Xiao S, Lefenfeld M, Steiner R, Tulevski GS, Tang J, Baumert J, Leibfarth F, Yardley JT, Steigerwald ML, Kim P, Nuckolls C (2006) Proc Natl Acad Sci USA 103:11452
93. Liu S, Wei Z, Cao Y, Gan L, Wang Z, Xu W, Guo X, Zhu D (2011) Chem Sci 2:796
94. Cao Y, Liu S, Shen Q, Yan K, Li P, Xu J, Yu D, Steigerwald ML, Nuckolls C, Liu Z, Guo X (2009) Adv Funct Mater 19:2743
95. Cao Y, Wei Z, Liu S, Gan L, Guo X, Xu W, Steigerwald ML, Liu Z, Zhu D (2010) Angew Chem Int Ed 49:6319
96. Kim D, Jeong H, Lee H, Hwang WT, Wolf J, Scheer E, Huhn T, Jeong H, Lee T (2014) Adv Mater 26:3968
97. Seo S, Min M, Lee SM, Lee H (2013) Nat Commun 4:1920
98. Guo X, Xiao S, Myers M, Miao Q, Steigerwald ML, Nuckolls C (2009) Proc Natl Acad Sci USA 106:691

Topics in Current Chemistry (2018) 376:37
https://doi.org/10.1007/s41061-018-0215-2

REVIEW

Electrostatic Gate Control in Molecular Transistors

Hyunwook Song[1]

Received: 5 March 2018 / Accepted: 27 August 2018

Abstract
Molecular transistors, in which single molecules serve as active channel components in a three-terminal device geometry, constitute the building blocks of molecular scale electronic circuits. To demonstrate such devices, a gate electrode has been incorporated in several test beds of molecular electronics. The frontier orbitals' alignments of a molecular transistor can be delicately tuned by modifying the molecular orbital energy with the gate electrode. In this review, we described electrostatic gate control of solid-state molecular transistors. In particular, we focus on recent experimental accomplishments in fabrication and characterization of molecular transistors.

Keywords Molecular electronics · Molecular transistor · Charge transport · Break junction

1 Introduction

The demonstration of electronic devices using individual molecules as device components is a prospective attempt to ultimately shrink the size of device constituents and to increase integration density [1–8]. As a result, molecular devices have attracted much interest over the past decades [9–22]. A solid-state molecular transistor with electrostatic gating was reported in 2009 [13], demonstrating that the relative alignment of molecular energy levels in the transistors can be controlled with the gate electrode.

Herein, our prime concern was recent advances in the electrostatic gate control of solid-state molecular transistors. This manuscript is comprised of four parts. After the Introduction, we briefly describe device Fabrication. In the

Chapter 7 was originally published as Song, H. Topics in Current Chemistry (2018) 376: 37. https://doi.org/10.1007/s41061-018-0215-2.

✉ Hyunwook Song
hsong@khu.ac.kr

[1] Department of Applied Physics, Kyung Hee University, Yongin 446-701, South Korea

Published online: 08 September 2018

section Characterization, we emphasize the expertise of methods of characterizing molecular transistors that have developed, involving temperature-variable and length-dependent transport measurements, transition voltage spectroscopy (TVS), and inelastic electron tunneling spectroscopy (IETS). Finally, we discuss Gate-Controlled Charge Transport in Solid-State Molecular Transistors, which is necessary to achieve functional molecular transistors. The manuscript concludes with a final Conclusions section.

Molecular transistor test beds have also been employed to investigate two mesoscopic transport mechanisms in quantum dots (QDs) [10–12, 14, 23–33]: Coulomb blockades, where the current is tuned by the sequential charging of molecular ODs owing to Coulomb interaction, and the Kondo effect, where carrying charges interact with the local spin of the QDs that increases the conductance at a low bias. This review article will not cover issues of molecular QD transistors based on the subsequent single-electron tunneling process. Previous reviews refer to this subject [6, 17, 23, 26, 32].

2 Fabrication

2.1 Electromigrated Break Junctions

The fabrication of a molecular transistor is a very challenging task because traditional lithographic techniques are still not able to deliver resolution at single molecule level. Nevertheless, a diversity of delicate experimental methods has been carried out successfully. A common strategy in these techniques is the formation of a few nanometer gap electrodes (acting as a source and drain electrode) combined with gate electrodes. One of the most frequently adopted methods to form the nanometer-sized gap is the use of the electromigrated break junction (EBJ) method [11–13]. A large density current is applied to an unbroken thin and narrow metal wire predefined by electron-beam lithography. Metal atoms are then electromigrated, eventually breaking the continuous metal wire. Nanogap electrodes with distances of roughly a few nanometers can often be produced so that individual molecules can connect the gap between the source and drain electrodes. In particular, EBJs are advantageous in making a three-terminal device configuration since a gate electrode can easily form on the substrate before the electromigration procedure is accomplished (Fig. 1).

An active electromigration process has been adopted to create nanogap electrodes [23, 24]. If the resistance of the metal wires is raised during a voltage sweep by the initially set value, the applied voltage is decreased and the voltage sweep is reiterated with a renewed target resistance of the metal wire. Finally, the resistance can reach the tunneling resistance (a few kΩ). The active electromigration process is described in Fig. 2. A nanoscale constriction with a few kΩ regimes can be acquired with almost perfect repeatability. Compared to the active electromigration process, the abrupt electromigration breaking produces a large gap size or small metal clusters. Unintentional metal debris in the gap can mask intrinsic transport properties of a single molecule in the transistors. To circumvent this problem, thin metal wires are

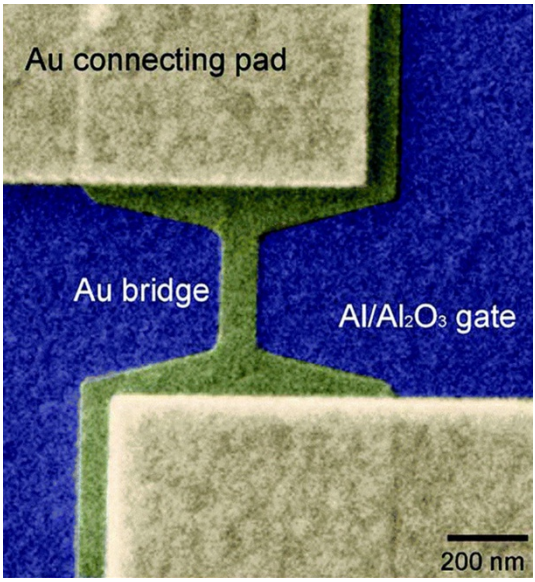

Fig. 1 Helium ion microscope image of a molecular transistor prior to the breaking process Reproduced with permission from [24]. Copyright (2010) Royal Society of Chemistry

first narrowed to a few-atom contraction at room temperature. This allows for spontaneous breaking of the wire, preventing the formation of metal debris and resulting in two separate electrodes in the nanometer range.

2.2 Mechanically Controllable Break Junctions

The mechanically controllable break junction (MCBJ) was invented by Moreland et al. [34] and Muller et al. [35]. Reed et al. [36] used the MCBJ technique for the first time in 1997 in order to examine the charge transport via individual molecules. The MCBJ technique consists of a lithographically defined and suspended bridge fixed onto the flexible substrate, which is bendable with a three-point counter support configuration. As the substrate is bent, the metal wire is elongated. The gap between two metal electrodes can be finely tuned by bending or relaxing the suspended bridge onto the flexible substrate. After trapping the molecules, including functional end groups, into the gap, the opposite electrodes can be connected, and then the charge transport properties through the component molecules are investigated. This technique allows for a powerful statistical analysis by performing repeated measurements for the molecules of interest [20, 21].

Champagne et al. [37] lithographically prepatterned a metal wire onto a heavily doped silicon substrate that acts as a bottom gate electrode. The efficiency of gate coupling was about 0.67% and was broken down near 12 V, giving rise to an energy level shift of 80 meV for a single C_{60} transistor. A similar back-gating method was employed by Martin et al. [38]. They used a patterned gold wire onto the top of phosphorous bronze wafer covered with polyimide and released it by removing the

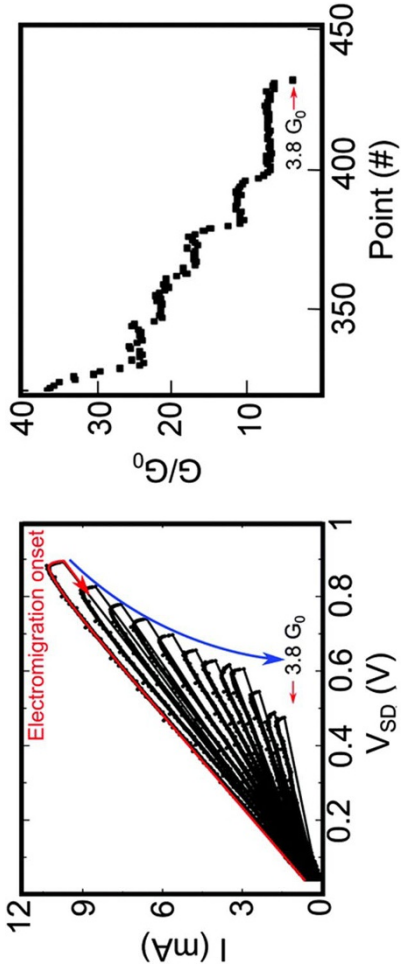

Fig. 2a,b Electromigration with an active breaking scheme. **a** *I*(*V*) data from a succession of ramps across a junction. The *blue arrow* indicates how the junction evolves as the nanoconstriction forms. **b** The same data truncated at the *red arrow* position in **a** Reproduced with permission from [24]. Copyright (2010) Royal Society of Chemistry

polyimide. Rather than using the substrate as a bottom gate electrode, they fabricated a new local gate electrode positioned under the bridge. As applying a gate voltage, the broken metal electrodes (source and drain) were pulled towards the substrate by the electric field, which was operated as a nanomechanical switch based on a single atom.

Xiang et al. [39] recently demonstrated a single molecule transistor that can shift the energy levels of the channel molecule by adding a gate electrode to an MCBJ. In this study, electron beam lithography was employed to create three-terminal electrode configurations, including a thin and narrow bridge with a contact of 30 nm and a local side-gated electrode (Fig. 3). Using this non-contact side-gate electrode, the molecular energy level could be shifted, simultaneously modulating the charge transport of individual molecules. The gate efficiency was significantly dependent on the gap size between the local gate electrode and the channel molecule.

2.3 Graphene Nanogap Electrodes

Due to the high mobility of gold atoms at room temperature, the nanogap electrodes are not stable under ambient conditions. An alternative method for the creation of a robust electrode pair with a nanometer-scale gap can be the use of graphene electrodes [40]. Prins et al. [41] used a feedback-controlled electroburning technique to make a graphene layer electrode with a nanometer-scale separation. The electroburning process is triggered by Joule heating accompanied with large current densities, which involves carbon atoms reacting with oxygen at elevated temperatures. The conductance of the graphene layer electrodes are gate-independent, such that the features of the bridged molecules will not be concealed by the graphene layer's response to the gate voltage.

Figure 4a shows a schematic of the graphene layers used for electroburning and the formation of nanogap electrodes, which was performed under ambient conditions. The feedback control scheme is similar to methods adopted for the electromigration process of metal wires [42]. A voltage ramp was applied to the graphene layers and the current was monitored simultaneously. Upon the occurrence of current reduction, the voltage was swept back to zero. Immediately afterwards, a new voltage sweep started and the procedure was repeated again, which narrows gradually down the graphene electrodes. While the electroburning process proceeded, the conductance was dropped in steps and the voltage value at which the electroburning process takes place was reduced (Fig. 4b). For graphene nanogap electrodes, the conductance did not change within the range of V_G between ± 40 V, which implies that they are suitable to electrically connect individual molecules and to investigate their three-terminal charge transport.

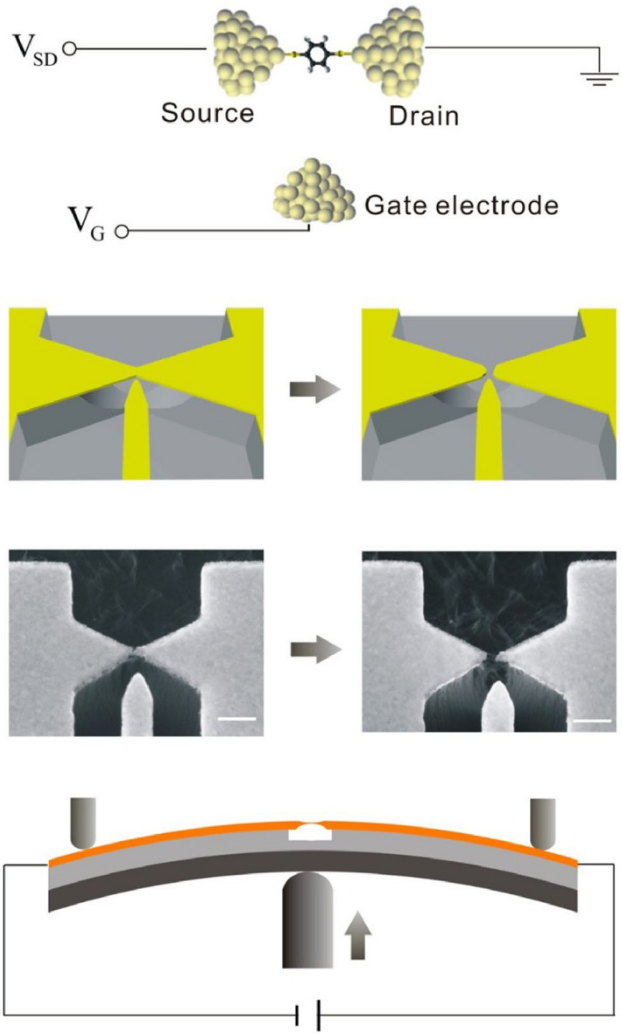

Fig. 3 Schematic illustrating a molecular transistor junction. An external electric field generated by a side-gate electrode is applied to the single-molecule junction formed by the mechanically controllable break junction (MCBJ) Reproduced with permission from [39]. Copyright (2013) American Chemical Society

3 Characterization

3.1 Temperature-Variable and Length-Dependent Charge Transport

To fully understand the transport properties of a molecular transistor, detailed microscopic analysis of the channel molecules would be necessary. A hurdle to overcome is unambiguously demonstrating that charge transport takes place only via the channel molecules. The exquisite characterization of the charge transport properties has

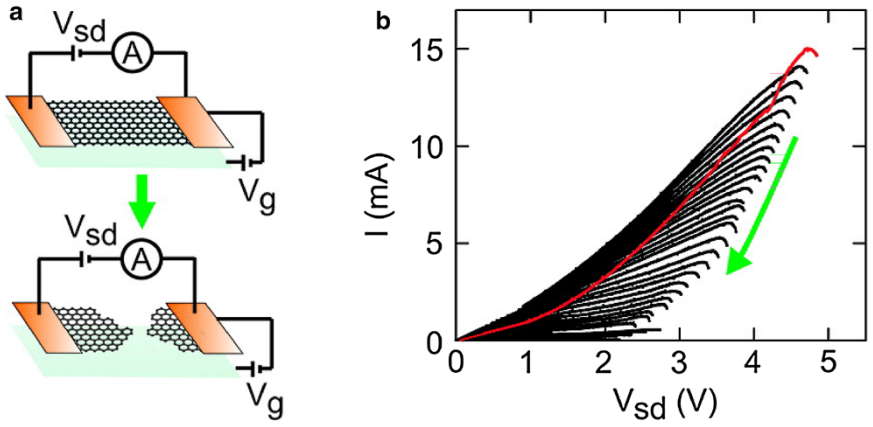

Fig. 4 **a** Schematic of the feedback-controlled electroburning process before (*top*) and after (*bottom*) the formation of nanometer sized gaps in few-layer graphite flakes. **b** $I(V)$ traces of the evolution (*green arrow*) of the feedback-controlled electroburning. The first $I(V)$ trace is displayed in *red* Reproduced with permission from [41]. Copyright (2011) American Chemical Society

attracted much attention in the field of molecular electronics, and so far a variety of experimental methods have been developed.

The current-carrying mechanism via the channel molecules in the transistor can be unveiled by evaluating the characteristic dependences of operating temperature and molecular length [43–53]. Tunneling transport is dominant for comparatively short molecules and the channel conductance (G) decays exponentially as the molecular length increases, according to $G \propto \exp(-\beta d)$ [1, 2], where d is the length of molecules (i.e., a tunneling distance) and β is the decay coefficient. This transport mechanism is also distinguished by the temperature independence of the current (I)-voltage (V) characteristics. Figure 5a shows a representative $I(V)$ curve of 1,8-octanedithiol contacting the gold nanogap electrodes created by the electromigrated break junction [53]. Such temperature independence of the $I(V)$ characteristic is a definitive feature of tunneling, and removes many other potential conduction mechanisms. In addition, the conductance of five different alkanedithiol molecules containing between 8 (DC8) and 12 (DC12) carbon atoms was measured to evaluate the influence of molecular length on conductance (Fig. 5b). The semilogarithmic plot of the conductance vs. the molecular length was found to be linear where the β value was found to be 0.88 per carbon atom from the slope of the linear fit [53]. The tunneling conduction mechanism can be anticipated rationally as the Fermi energy of the electrode is placed within the large highest occupied molecular orbital (HOMO)–lowest unoccupied molecular orbital (LUMO) gap of short molecules.

It is well known that hopping conduction occurs for charge transport through a long conjugated molecular wire. The hopping conductance is thermally activated, as described by the Arrhenius relation [1, 2]:

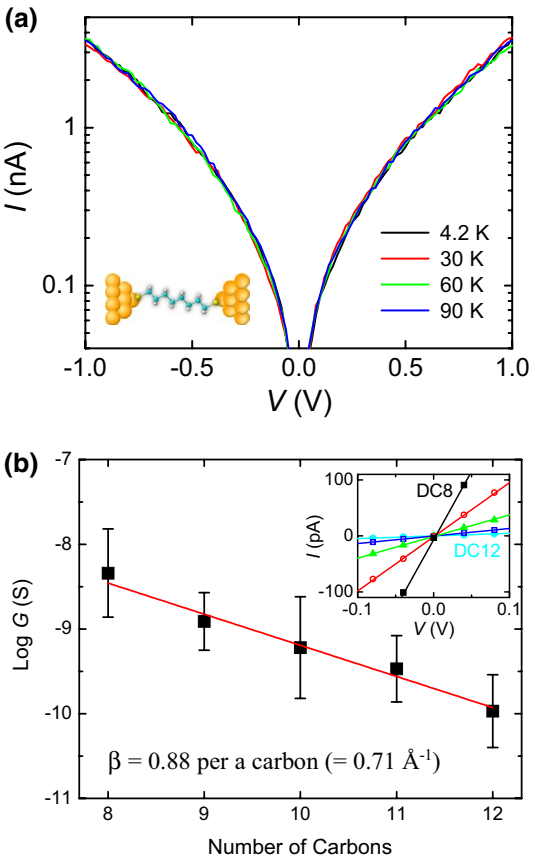

Fig. 5 **a** Semilog plot of the temperature-variable $I(V)$ characteristics of Au–1,8-octanedithiol–Au junctions at selected temperatures (4.2, 30, 60, and 90 K). **b** Semilog plot of the conductance vs. the number of carbon atoms for five different length alkanedithiol nanogap junctions. The decay coefficient (β) can be determined from the linear fit (*solid line*), yielding a β value of 0.88 per carbon atom. The inset shows length-dependent $I(V)$ curves in the low-bias linear regime, where the conductance values are obtained from linear fits of the data Reproduced with permission from [53]. Copyright (2010) American Chemical Society

$$G \propto \exp\left(\frac{-E_a}{k_B T}\right) \tag{1}$$

where T is temperature, k_B is the Boltzmann constant, and E_a is the activation energy for hopping conduction. The hopping process can be also identified by length-dependent transport, where the conductance exhibits a inversely linear scaling with the length of molecules.

Interestingly, van der Zant et al. [54] studied the temperature dependent and gated three-terminal molecular transistors using sulfur end-functionalized tercyclohexylidene molecules. In the regime of low temperatures, temperature-dependent transport was not observed, whereas at temperatures higher than 150 K, the current increased exponentially as temperature rises (Fig. 6). For the entire temperature regimes of 10–300 K, a single level transport model at various gate voltages elucidates that the temperature dependent transport results from the Fermi distribution in the electrodes [54].

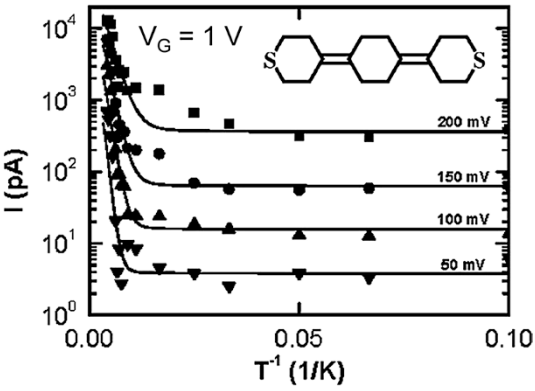

Fig. 6 Current as a function of the inverse of temperature of the sulfur end-functionalized tercyclohexylidene molecule (see the inset) for four different source-drain voltages (50, 100, 150, and 200 mV) with a gate voltage of 1.0 V Reproduced with permission from [54]. Copyright (2006) American Chemical Society

3.2 Transition Voltage Spectroscopy

Transition voltage spectroscopy (TVS) has been used to obtain an invaluable insight into the frontier orbital level alignments in molecular tunneling transistors [55–60]. This is accomplished by determining the transition voltage (V_{trans}) in which the inflection behavior of the Fowler–Nordheim (F–N) plot, $\ln(I/V^2)$ vs $1/V$ takes place. In the Simmons tunneling barrier model, the inflection points of the F–N plot decided from the measured I(V) curves have been utilized to show that the barrier tilted by the applied source-to-drain voltage changes from a trapezoidal form (for direct tunneling) to a triangular form (for F–N tunneling) [55]. Later, Araidai et al. [58] explained that the slope changes in the F–N plots do not certainly point to the conversion between the two regimes of direct tunneling and F–N tunneling. In lieu, such an inflecting aspect in the F–N plots occurs when the frontier molecular orbital level (HOMO or LUMO) comes near the edge of the bias window of the electrodes (Fig. 7), based on the transmission function calculation [58]. The ratio of V_{trans} to the HOMO energy level was found to fluctuate with the junction asymmetry (η) between 0.86 (for a symmetric junction) and 2.0 (for a completely asymmetric junction) (Fig. 8) [59]. This study implies that one needs to deliberate the junction asymmetry when using TVS as a quantitative analytic implement to explore the energy level alignment of molecular transistors. TVS provides a useful spectroscopic approach to elucidate the molecular orbital level alignments in the transistors, in that V_{trans} is a usually smaller value than the electrode voltage required to attain the resonant condition. However, the scarcity of information about the potential drop over the molecular transistors restricts delicately identifying the location of the molecular levels.

3.3 Inelastic Electron Tunneling Spectroscopy

Inelastic electron tunneling spectroscopy (IETS) has been established in the field of molecular electronics as a method to examine the molecular vibration and extract information about the molecular conformation or orientation [61–66]. IETS has become one of cardinal analytic techniques adopted to identify molecules forming the active region of a junction [63, 64], similar to Raman and infrared spectroscopy

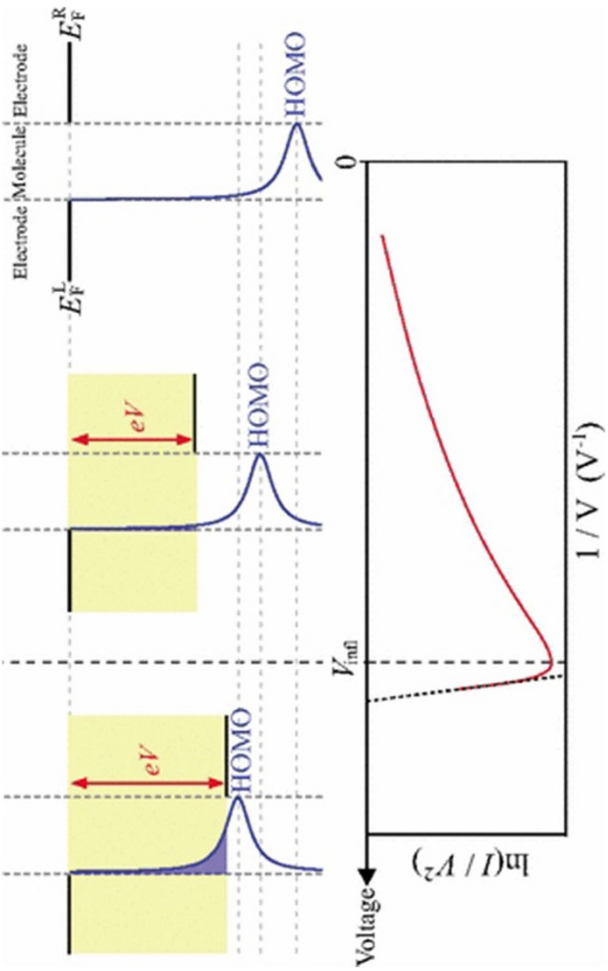

Fig. 7 Schematic of the single transport level model to qualitatively evaluate the inflection of the Fowler–Nordheim (F–N) curve Reproduced with permission from [58]. Copyright (2010) American Physical Society

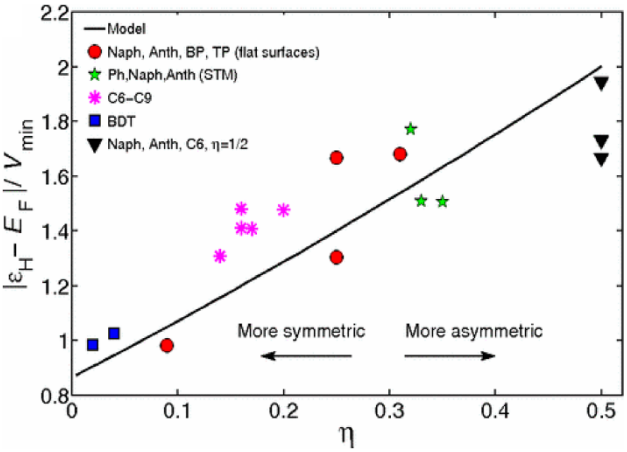

Fig. 8 Ratio between the highest occupied molecular orbital (HOMO) energy at zero bias and the minimum voltage vs. the asymmetry parameter. The *solid line* was obtained from a Lorentzian transmission function Reproduced with permission from [59]. Copyright (2010) American Physical Society

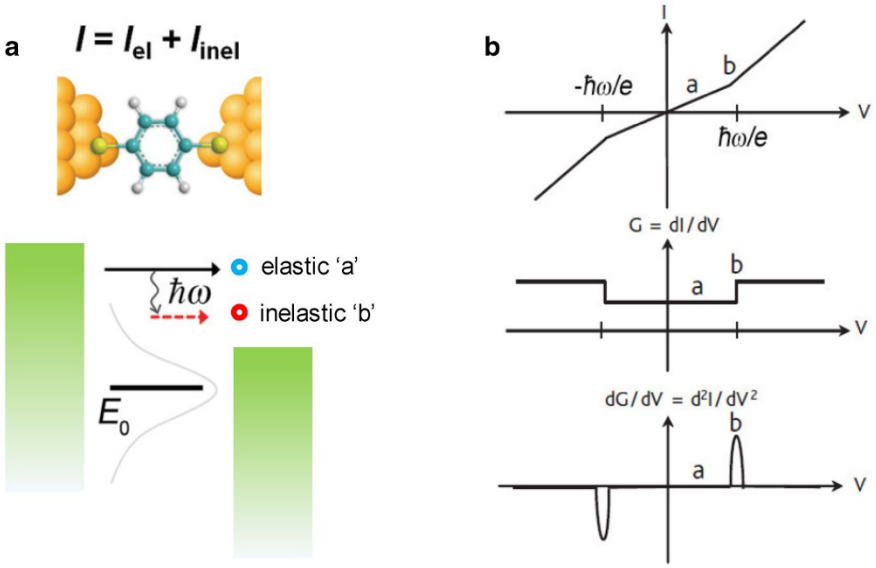

Fig. 9 **a** A schematic of a metal–molecule-metal junction and energy band diagram with a vibrational mode of frequency ω localized inside where 'a' is the elastic tunneling process and 'b' is the inelastic tunneling process along with the **b** corresponding I(V), d*I*/d*V*, and d^2I/dV^2 characteristics Reproduced with permission from [67]. Copyright (2016) Taylor and Francis Group

for macroscopic samples. The principle of IETS is based on tunneling electrons through an inelastic process with internal molecular vibrations in the transistors [61, 62]. This technique can detect the vibration modes of molecules by means of

an inelastic tunneling process. In IETS measurements, the total current is categorized into an elastic electron tunneling part and an inelastic electron tunneling part as described in Fig. 9a. When a small bias voltage is applied, an electron from an occupied state on the left electrode tunnels into an empty state on the right electrode and its energy is conserved (process a) [67]. In the elastic tunneling process, the current increases linearly with a small applied bias (less than the characteristic vibrational energy). However, if the specific mode of vibration, corresponding to a frequency of ω, is positioned in the transistor, an inelastic tunneling electron forfeits a quantum of energy ($\hbar\omega$) to excite the vibrational mode. The electron can then tunnel into another empty state as the applied voltage exceeds a molecular vibrational energy ($eV \geq \hbar\omega$) (process b). Such a process can open a new inelastic channel with an increase in a total probability of tunneling. Eventually, an overall tunneling current displays a kink in the $I(V)$ curves (shown in Fig. 9b) [67]. One can observe such kinks as a step in the differential conductance (dI/dV) plot and therefore as a peak in the second derivative d^2I/dV^2 plot. A phase-sensitive lock-in technique is typically used to directly detect the second derivative signal with a high signal-to-noise ratio [63]. The IETS can become fruitful for analyzing various features of the molecular transistors, such as molecule-electrode interfacial characteristics and electron-molecule interactions. However, the interpretation of the IETS is not always clear for molecules with a large variety of nuclei and a number of chemical bonds.

4 Gate-Controlled Charge Transport in Solid-State Molecular Transistors

A molecular transistor that is based on the electrostatic gate control of molecular orbital levels [68–71], has been a great challenge in the field since the inception of molecular electronics. Theoretical studies have indicated that the electrostatic gate modulation of an individual molecule is feasible in a manner analogous to a traditional field-effect transistor (FET) [72, 73]. Orbital modulation based on a single molecule has been demonstrated by using a two-terminal scanning tunneling microscopy in solution [74], encouraging the invention of three-terminal device implementations, in spite of concerns regarding the degree of electrostatic gate modulation that can be fulfilled in an FET configuration.

We demonstrated direct electrostatic gate control of molecular orbital levels in the form of solid-state devices with FET configurations by employing multiprobe transport techniques combined a variety of transport techniques that yield coherent characterization results of the molecular transistor [13]. We made molecular transistors by creating nanogap source and drain electrodes contacted with two prototypical molecules containing conjugated and nonconjugated backbones onto a bottom gate electrode. The nanogap electrodes were made through the EBJ technique described in a previous section. We attained the V_{trans} values by using TVS at various voltages applied to a gate electrode, and observed a linear relationship between the V_{trans} values and the gate voltages in the molecular transistors (Fig. 10). The slope of the linear fitting, $\alpha = \Delta V_{trans}/\Delta V_G$, was defined as a gate efficiency factor, where the absolute value of α indicates the degree of gating

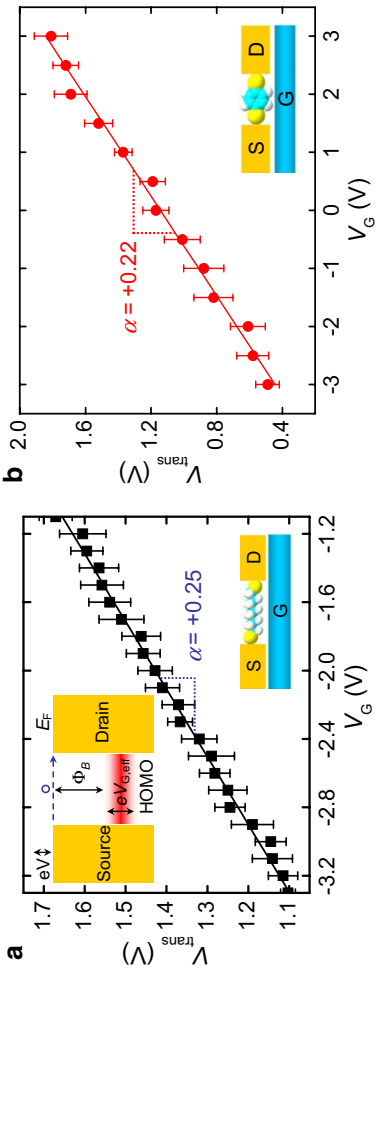

Fig. 10 **a** Linear scaling of V_{trans} in terms of V_G for 1,8-octanedithiol. *Inset* Schematic of the energy band for HOMO-mediated hole tunneling. **b** Linear scaling of V_{trans} in terms of V_G for 1,4-benzenedithiol Reproduced with permission from [13]. Copyright (2009) Nature Publishing Group

molecular orbital energy [13]. As operating in traditional FET devices, a negative (or positive) gate voltage would raise (or lower) the molecular orbital energies relative to the electrode's Fermi level (E_F). Consequently, a positive value of α implies tunneling through HOMO (i.e., p-type) and a negative value of α corresponds to tunneling through LUMO (i.e., n-type). We also investigated the interplay of tunneling charges and molecular vibrations using IETS, which confirmed the clear existence of the molecules incorporated into the transistors [63, 64]. The influence of IETS spectra on the molecular orbital gating was examined. The IETS spectra of transistors that use nonconjugated alkanedithiol were essentially not affected by the gate voltage (Fig. 11a) [13]. This finding implies that charge transport through the transistors is non-resonant because a large energy difference exists between the HOMO of alkanedithiol and the E_F. In contrast to alkanedithiol, we showed that the applied gate voltage considerably modulates the IETS spectra of transistors that use conjugated benzenedithiol (Fig. 11b) [15]. Specifically, the spectral intensities increased quietly and the shapes of the spectral peaks also changed as a negative gate voltage increased, which identified an increasing coupling between the tunneling charges and the molecular vibrations. This would be most probably because of near resonance between the HOMO of benzenedithiol and the E_F [65, 66]. The results collectively validate the concept of electrostatic gate control in molecular transistors.

Similarly, Xiang et al. [75] analyzed the gating effect of benzodifuran (BDF) molecular transistors. The AlO_x/Al beneath the molecules acts as the gate electrode to control the current via the BDF molecules (Fig. 12a). The conductance decreased simply as the gate voltage increased (Fig. 12b). By employing a single-level model [75], where a single molecular orbital level of an energy ε_0 is presumed to be in contact with the source and drain electrodes with the coupling strengths, Γ_L and Γ_R, the transport current can be estimated with the Landauer formula as follows:

$$I = \frac{2e}{h}\int_{-\infty}^{\infty} T(E,\ V)[f(E - eV/2) - f(E + eV/2)]\ \mathrm{d}E \tag{2}$$

Here, e is the elementary charge, h is Planck's constant, and $f(E)$ is the Fermi–Dirac distribution function. The transmission function, $T(E, V)$, depends on the energy, E, and voltage, V. $T(E, V)$ is estimated using a Lorentzian function. Figure 12c illustrates the dependence of ε_0 on the gate voltages, in which ε_0 increases monotonically with increasing gate voltage. The gate voltage modulates the energy gap between the molecular orbital level and the E_F. For example, the HOMO level moved away from the E_F when the gate voltage was applied from a negative to positive value. Therefore, the shift trend of the molecular orbital levels with the gating effect provides an obvious demonstration to verify the transporting frontier molecular orbital level [75]. As one considers that the positive gate voltage drops the molecular orbital levels, the charge carriers is transported via the HOMO. Furthermore, the gating efficiency of the orbital level shift for the applied gate voltage was estimated to be about 40 mV V^{-1} in the BDF transistor. However, the coupling strengths, Γ_L and Γ_R, did not depend monotonically on the applied gate voltage

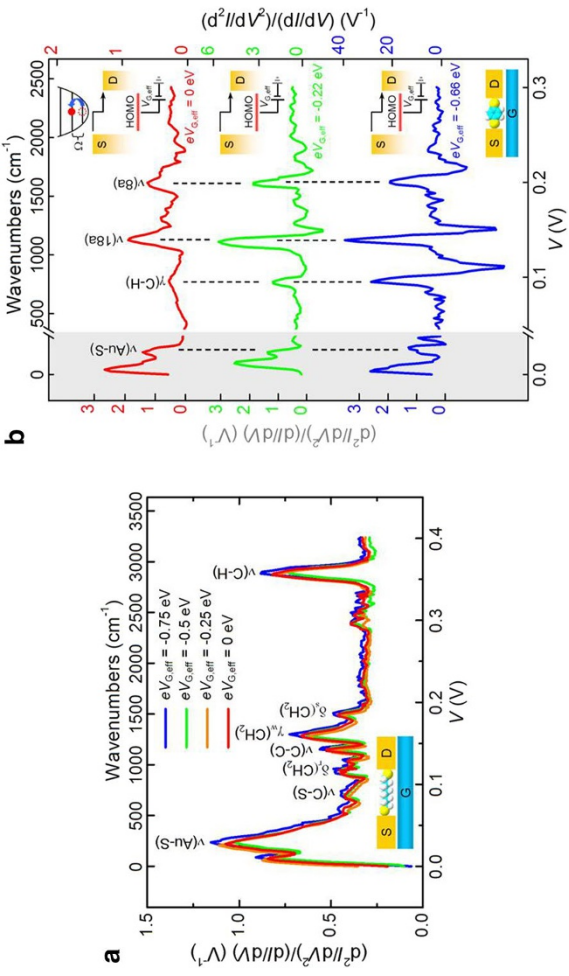

Fig. 11 **a** Inelastic electron tunneling spectroscopy (IETS) spectra for a Au–millimolar octanedithiol (ODT)–Au junction measured at 4.2 K for different gate voltages with assigned vibration modes. **b** IETS spectra for a Au–benzene-1,4-dithiol (BDT)–Au junction measured at 4.2 K for different gate voltages with assigned vibration modes. *Insets* Energy diagrams illustrating inelastic tunneling as the position of the HOMO resonance shifts as a result of gating Reproduced with permission from [13]. Copyright (2009) Nature Publishing Group

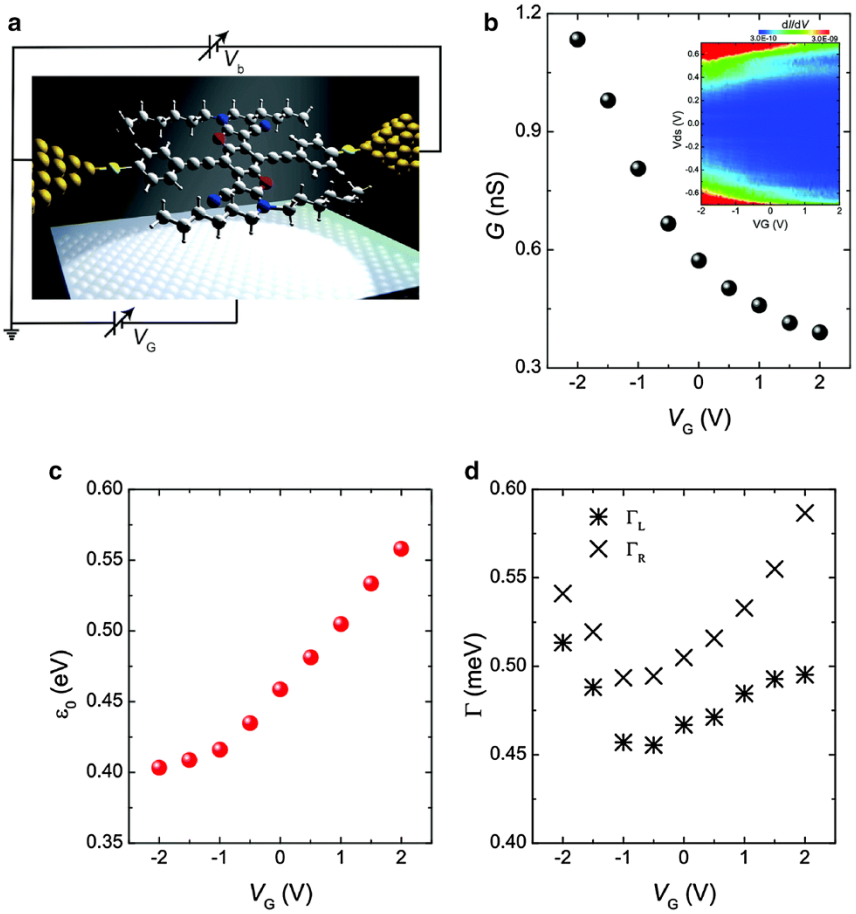

Fig. 12 **a** Schematic of the BDT transistor. A back gate electrode is located beneath the benzodifuran (BDF) molecule. **b** Low-bias conductance as a function of the gate voltage. Inset Differential conductance (stability diagram) as a function of the gate and bias voltages. The differential conductance is numerically calculated from the $I(V)$ curves. **c** ε_0 value as a function of the gate voltage. **d** Influence of the gate voltage on the nearest molecular orbital coupling strength to the left (*star*) and right (*cross*) electrodes Reproduced with permission from [75]. Copyright (2015) Royal Society of Chemistry

(Fig. 12d). The comparable values of Γ_L and Γ_R implied a nearly symmetrical coupling of the HOMO of the BDF to both the source and drain electrodes. This result explicitly indicates that the modulation of charge transport results from the shift of the molecular transport level with orbital gating.

Using graphene nanogap electrodes, Prins et al. [41] fabricated molecular transistors using curcuminoid molecules functionalized with anthracene (Fig. 13a, b). The anthracene functional groups can interact well with the π-electron system of the graphene electrodes due to their long conjugated systems, which thus presents a robust contact to the electrodes. However, the curcuminoid parts have a large π-electron density, effectively transporting charge carriers. Figure 13c shows typical changes of

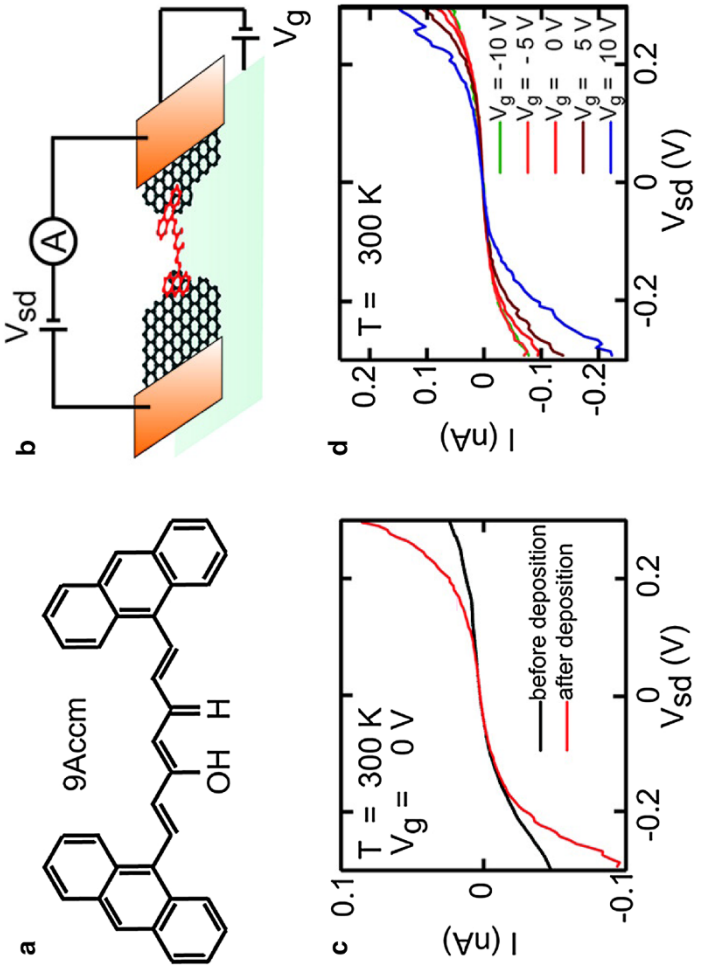

Fig. 13 **a** Chemical structure of anthracene-terminated curcuminoid wires (1,7-(di-9-anthracene)-1,6-heptadiene-3,5-dione). **b** Artist's impression of a single 9Accm molecule bridging a graphene nanogap, representing the ideal transistor configuration. **c** *I*(*V*) characteristics of the nanogapped electrodes before and after being bridged by the 9Accm molecules at 300 K. **d** Dependence of the *I*(*V*) characteristics of the nanogapped electrodes bridged by 9Accm molecules on the applied back-gate voltage measured at 300 K Reproduced with permission from [41]. Copyright (2011) American Chemical Society

the $I(V)$ characteristic after molecular depositions. The conductance of the curcuminoid transistors was clearly dependent on the gate voltages at room temperature, as displayed in Fig. 13d. This study showed the possibility of molecular transistors made from graphene nanogap electrodes operating at room temperature.

Exploiting three-terminal MCBJs, Perrin et al. [76] examined the effect of metal electrodes on controlling the molecular orbital levels in the porphyrin-based transistors, allowing electrostatic gate tuning of the energy levels. While the electrodes' gap remained fixed, they determined the current vs. both the source-to-drain bias and gate voltages, and plotted dI/dV as a two-dimensional contour map, where the resonant state related to an occupied level shifted away from the E_F as the gate voltage increased (Fig. 14). The molecular energy levels in the transistors shifted fairly to the E_F with a decrease in the electrodes' gap, mainly because of a renormalized gap resulting from interplays between image charges on the metal electrodes. These results demonstrated experimentally the collective impacts of gating the molecular orbitals both mechanically and electrostatically.

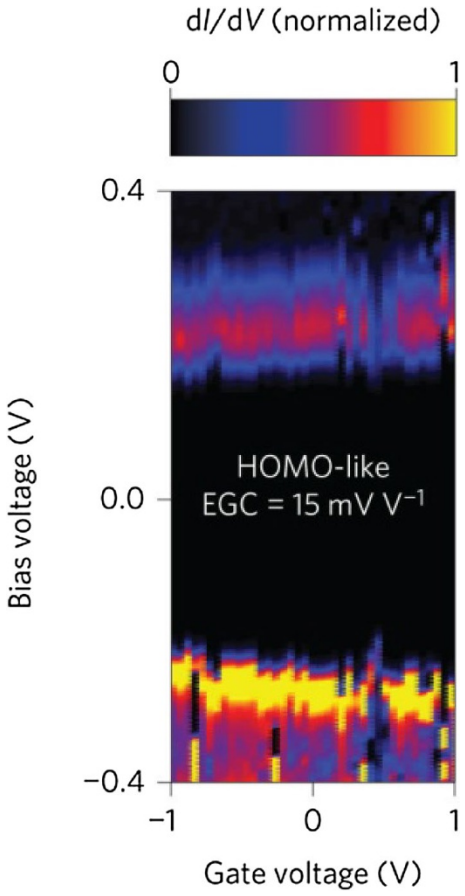

Fig. 14 Gate diagrams for different junction configurations and during different breaking events represented by color-coded dI/dV vs. gate and bias voltages Reproduced with permission from [76]. Copyright (2013) Nature Publishing Group

In recent experiments, Kim et al. [77] probed the electrostatic control of thermoelectric properties in molecular transistors. By exploiting two prototypes of biphenyl-4,4′-dithiol (BPDT) and fullerene ©$_{60}$) transistors, they observed that the Seebeck coefficient and the conductance were simultaneously tuned by the electrostatic gating (Fig. 15a). Figure 15b shows a decrease in the Seebeck coefficient of the BPDT transistors ($S_{\mathrm{Au–BPDT–Au}}$) with increasing gate voltage. The thermoelectric properties could be modulated electrostatically by 35%. Additionally, $S_{\mathrm{Au–BPDT–Au}}$ has a positive value for all the gate voltages, which indicates that the carrier transport is based on hole tunneling (p-type). It was seen that $S_{\mathrm{Au–C_{60}–Au}}$ was much greater than $S_{\mathrm{Au–BPDT–Au}}$ and could be adjusted by 300% with the gate voltages (Fig. 15c). Such a large gating efficiency originates from the resonant tunneling transport across the C_{60} transistors. Furthermore, the negative value of $S_{\mathrm{Au–C_{60}–Au}}$ implies that the transport is based on electron tunneling. These results demonstrate the correlation of the carrier transport with the thermoelectric characteristics of molecular transistors.

5 Conclusion and Outlook

Here, I discussed recent experimental advances in the electrostatic gate control of molecular transistors. The ability to control charge transport in molecular transistors is necessary for diverse potential applications of molecular electronics. As reviewed, molecular transistors have advanced considerably in recent years by introducing a variety of electrostatic gate control techniques. These findings will help in the design of future molecular electronic circuits and further miniaturization of electronic devices. The fulfillment of true molecular transistors requires reproducible nanogap electrodes, where the component single molecules are coupled electrostatically to the gating electrodes. For example, Datta et al. [73] observed that the geometry of nanogap electrodes significantly affects the molecule-gate coupling. Specifically, they demonstrated that the tapered shape nanogap electrodes yield approximately three orders of magnitude enhancement in the gate efficiency. In addition, the diminished cross-sectional area of the tapered electrodes can help a single, or a few, molecules to bridge nanogap electrodes. Further detailed analysis of the device geometry in gating molecular transistors will be necessary for the realization of ultimate molecular electronic devices. Particularly, electrochemical gating is a fascinating alternative work in that enhanced gate efficiency can be accomplished by creating a large interfacial capacitance on the nanometer regime. Several research groups have adopted this technique to modulate charge transport in molecular transistors [44, 47, 49, 51, 78].The most important task is the development of a high yield method that

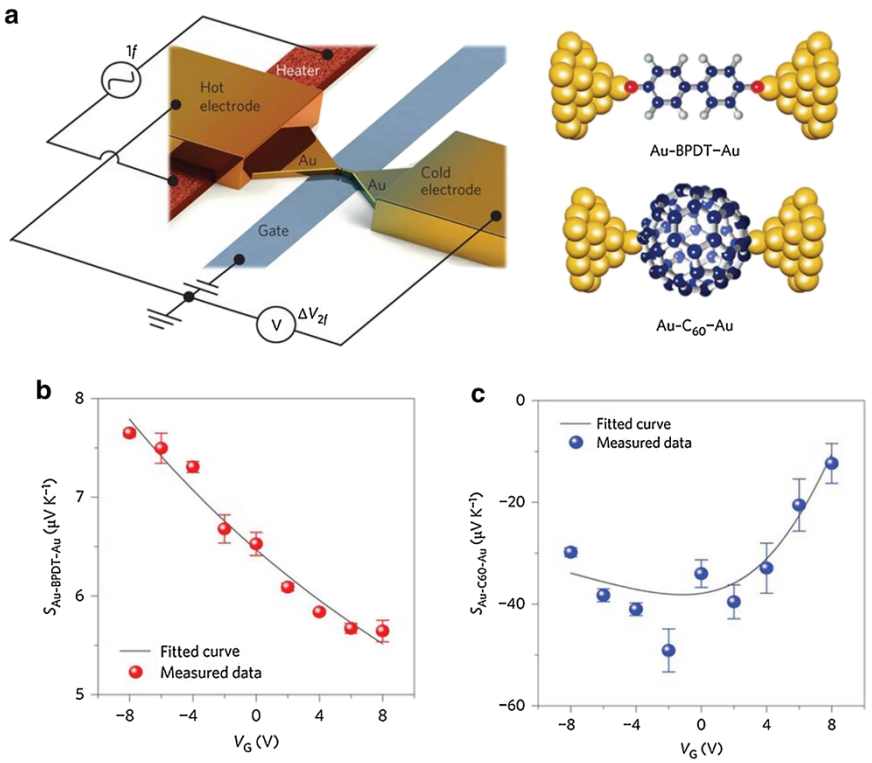

Fig. 15 **a** Schematic of the electromigrated break junctions with an integrated heater (*left*) and the molecular junctions studied in this work (*right*). **b** Seebeck coefficient of the BDT junctions as a function of V_G. **c** Seebeck coefficient of the C_{60} junctions as a function of V_G Reproduced with permission from [77]. Copyright (2014) Nature Publishing Group

fabricates 'working' transistors. New device architectures and designs are necessary to construct reliable and easily accessible molecular transistors [79–88].

Acknowledgement This work was supported by the National Research Foundation of Korea (2016R1D1A1B03935647).

References

1. Song H, Reed MA, Lee T (2011) Adv Mater 23:1583
2. Xiang D, Wang X, Jia C, Lee T, Guo X (2016) Chem Rev 116:4318
3. Tao NJ (2006) Nat Nanotechnol 1:173
4. Li T, Hu W, Zhu D (2010) Adv Mater 22:286
5. Karthäuser S (2011) J Phys Condens Mater 23:013001
6. Moth-Poulsen K, Bjørnholm T (2009) Nat Nanotechnol 4:551
7. Ebling M, Ochs R, Koentopp M, Fischer M, von Hänisch C, Weigend F, Evers F, Weber HB, Mayor M (2005) Proc Natl Acad Sci USA 102:8815
8. Aviram A, Ratner MA (1974) Chem Phys Lett 29:277

9. Metzger RM, Chen B, Hopfner U, Lakshmikantham MV, Vuillaume D, Kawai T, Wu X, Tachibana H, Hughes TV, Sakurai H, Baldwin JW, Hosch C, Cava MP, Brehmer L, Ashwell GJ (1997) J Am Chem Soc 119:10455
10. Kubatkin S, Danilov A, Hjort M, Cornil J, Brédas J-L, Stuhr-Hansen N, Hedegård P, Bjørnholm T (2003) Nature 425:698
11. Park H, Park J, Lim AKL, Anderson EH, Alivisatos AP, McEuen PL (2000) Nature 407:57
12. Park J, Pasupathy AN, Goldsmith JI, Chang C, Yaish Y, Petta JR, Rinkoski M, Sethna JP, Abruna HD, McEuen PL, Ralph DC (2002) Nature 417:722
13. Song H, Kim Y, Jang YH, Jeong H, Reed MA, Lee T (2009) Nature 462:1039
14. van der Molen SJ, Liljeroth P (2010) J Phys Condens Mater 22:133001
15. Quek SY, Kamenetska M, Steigerwald ML, Choi HJ, Louie SG, Hybertsen MS, Neaton JB, Venkataraman L (2009) Nat Nanotechnol 4:230
16. Blum AS, Kushmerick JG, Long DP, Patterson CH, Yang JC, Henderson JC, Yao Y, Tour JM, Shashidhar R, Ratna BR (2005) Nat Mater 4:167
17. Guo X, Small JP, Klare JE, Wang Y, Purewal MS, Tam IW, Hong BH, Caldwell R, Huang L, O'Brien S, Yan J, Breslow R, Wind SJ, Hone J, Kim P, Nuckolls C (2006) Science 311:356
18. Choi BY, Kahng SJ, Kim S, Kim H, Kim HW, Song YJ, Ihm J, Kuk Y (2006) Phys Rev Lett 96:156106
19. Lee J, Chang H, Kim S, Bang GS, Lee H (2009) Angew Chem 121:8653
20. Lörtscher E, Ciszek JW, Tour J, Riel H (2006) Small 2:973
21. Lörtscher E, Gotsmann B, Lee Y, Yu L, Rettner C, Riel H (2012) ACS Nano 6:4931
22. Green JE, Choi JW, Boukai A, Bunimovich Y, Johnston-Halperin E, DeIonno E, Luo Y, Sheriff BA, Xu K, Shin YS, Tseng H-R, Stoddart JF, Heath JR (2007) Nature 445:414
23. van der Zant HSJ, Kervennic Y-V, Poot M, O'Neill K, de Groot Z, Heeersche HB, Stuhr-Hansen N, Bjørnholm T, Vanmaekelbergh D, van Walree CA, Jenneskens LW (2006) Faraday Discuss 131:347
24. Perrin ML, Burzurí E, van der Zant HSJ (2015) Chem Soc Rev 44:902
25. Datta S (2005) Quantum transport: atom to transistor. Cambridge University Press, Cambridge
26. Liang W, Shores MP, Bockrath M, Long JR, Park H (2002) Nature 417:725
27. Natelson D, Yu LH, Ciszek JW, Keane ZK, Tour JM (2006) Chem Phys 324:267
28. Heersche HB, de Groot Z, Folk JA, Kouwenhoven LP, van der Zant HSJ, Houck AA, Labaziewicz J, Chuang IL (2006) Phys Rev Lett 96:017205
29. Osorio EA, O'Neill K, Wegewijs M, Stuhr-Hansen N, Paaske J, Bjørnholm T, van der Zant HSJ (2007) Nano Lett 7:3336
30. Scott GD, Keane ZK, Ciszek JW, Tour JM, Natelson D (2009) Phys Rev B 79:165413
31. Scott GD, Natelson D (2010) ACS Nano 4:3560
32. Osorio EA, Bjørnholm T, Lehn J-M, Ruben M, van der Zant HSJ (2008) J Phys Condens Mater 20:374121
33. Yu LH, Keane ZK, Ciszek JW, Cheng L, Stewart MP, Tour JM, Natelson D (2004) Phys Rev Lett 93:266802
34. Moreland J, Ekin JW (1985) J Appl Phys 58:3888
35. Muller CJ, van Ruitenbeek JM, de Jongh LJ (1992) Phys C 191:485
36. Reed MA, Zhou C, Muller CJ, Burgin TP, Tour JM (1997) Science 278:252
37. Champagne AR, Pasupathy AN, Ralph DC (2005) Nano Lett 5:305
38. Martin CA, Smit RHM, van der Zant HSJ, van Ruitenbeek JM (2009) Nano Lett 9:2940
39. Xiang D, Jeong H, Kim D, Lee T, Cheng Y, Wang Q, Mayer D (2013) Nano Lett 13:2809
40. Jia C, Ma B, Xin N, Guo X (2015) Acc Chem Res 48:2
41. Prins F, Barreiro A, Ruitenberg JW, Seldenthuis JS, Aliaga-Alcalde N, Vandersypen LMK, van der Zant HSJ (2011) Nano Lett 11:4607
42. Prins F, Hayashi T, de vos van Steenwijk BJA, Gao B, Osorio EA, Muraki K, van der Zant HSJ (2009) Appl Phys Lett 94:123108
43. Panzer MJ, Frisbie CD (2008) Adv Mater 20:3177
44. Díez-Pérez I, Li Z, Guo S, Madden C, Huang H, Che Y, Yang X, Zang L, Tao N (2012) ACS Nano 6:7044
45. Diez-Perez I, Hihath J, Lee Y, Yu L, Adamska L, Kozhushner MA, Oleynik II, Tao N (2009) Nat Chem 1:635
46. Kamenetska M, Quek SY, Whalley AC, Steigerwald ML, Choi HJ, Louie SG, Nuckolls C, Hybertsen MS, Neaton JB, Venkataraman L (2010) J Am Chem Soc 132:6817
47. Osorio HM, Catarelli S, Cea P, Gluyas JBG, Hartl F, Higgins SJ, Leary E, Low PJ, Martin S, Nichols RJ, Tory J, Ulstrup J, Vezzoli A, Milan DC, Zeng Q (2015) J Am Chem Soc 137:14319

48. Capozzi B, Chen Q, Darancet P, Kotiuga M, Buzzeo M, Neaton JB, Nuckolls C, Venkataraman L (2014) Nano Lett 14:1400
49. Li X, Xu B, Xiao X, Yang X, Zang L, Tao N (2006) Faraday Discuss 131:111
50. He J, Fu Q, Lindsay S, Ciszek JW, Tour JM (2006) J Am Chem Soc 128:14828
51. Darwish N, Díez-Pérez I, Da Silva P, Tao N, Gooding JJ, Paddon-Row MN (2012) Angew Chem Int Ed 51:3203
52. Venkataraman L, Klare JE, Tam IW, Nuckolls C, Hybertsen MS, Steigerwald ML (2006) Nano Lett 6:458
53. Song H, Kim Y, Jeong H, Reed MA, Lee T (2010) J Phys Chem C 114:20431
54. Poot M, Osorio E, O'Neill K, Thijssen JM, Vanmaekelbergh D, van Walree CA, Jenneskens LW, van der Zant HSJ (2006) Nano Lett 6:1031
55. Beebe JM, Kim B, Gadzuk JW, Frisbie CD, Kushmerick JG (2006) Phys Rev Lett 97:026801
56. Huisman EH, Guédon CM, van Wees BJ, van der Molen SJ (2009) Nano Lett 9:3909
57. Baldea I (2010) Chem Phys 377:15
58. Araidai M, Tsukada M (2010) Phys Rev B 81:235114
59. Chen J, Markussen T, Thygesen KS (2010) Phys Rev B 82:121412
60. Beebe JM, Kim B, Frisbie CD, Kushmerick JG (2008) ACS Nano 2:827
61. Jaklevic RC, Lambe J (1966) Phys Rev Lett 17:1139
62. Lambe J, Jaklevic RC (1968) Phys Rev 165:821
63. Wang W, Lee T, Kretzschmar I, Reed MA (2004) Nano Lett 4:643
64. Kushmerick JG, Lazorcik J, Patterson CH, Shashidhar R, Seferos DS, Bazan GC (2004) Nano Lett 4:639
65. Persson BNJ, Baratoff A (1987) Phys Rev Lett 59:339
66. Galperin M, Ratner MA, Nitzan A (2004) J Chem Phys 121:11965
67. Kim Y, Song H (2016) Appl Spectrosc Rev 51:603
68. Di Ventra M, Pantelides ST, Lang ND (2010) Appl Phys Lett 76:3448
69. Solomon PM, Lang ND (2008) ACS Nano 2:435
70. Damle P, Rakshit T, Paulsson M, Datta S (2002) IEEE Trans Nanotechnol 1:145
71. Lang ND, Solomon PM (2005) Nano Lett 5:921
72. Ghosh AW, Rakshit T, Datta S (2004) Nano Lett 4:565
73. Datta SS, Strachan DR, Johnson ATC (2009) Phys Rev B 79:205404
74. Piva PG, DiLabio GA, Pitters JL, Zikovsky J, Rezeq M, Dogel S, Hofer WA, Wolkow RA (2005) Nature 435:658
75. Xiang A, Li H, Chen S, Liu S-X, Decurtins S, Bai M, Hou S, Liao J (2015) Nanoscale 7:7665
76. Perrin ML, Verzijl CJO, Martin CA, Shaikh AJ, Eelkema R, van Esch JH, van Ruitenbeek JM, Thijssen JM, van der Zant HSJ, Dulić D (2013) Nat Nanotechnol 8:282
77. Kim Y, Jeong W, Kim K, Lee W, Reddy P (2014) Nat Nanotechnol 9:881
78. Capozzi B, Chen Q, Darancet P, Kotiuga M, Buzzeo M, Neaton JB, Nuckolls C, Venkataraman L (2014) Nano Lett 143:1400
79. Behnia S, Fathizadeh S, Ziaei J (2017) Phys Lett A 381:36
80. Fu B, Mosquera MA, Schatz GC, Ratner MA, Hsu LY (2018) Nano Lett 18:5015
81. Fathizadeh S, Behnia S, Ziaei J (2018) J Phys Chem B 122:2487
82. Komoto Y, Fujii S, Kiguchi M (2018) Mater Chem Front 2:214
83. Nasri A, Boubaker A, Hafsi B, Khaldi W, Kalboussi A (2017) Org Electron 48:7
84. Yamamoto M, Azuma Y, Sakamoto M, Teranishi T, Ishii H, Majima Y, Noguchi Y (2017) Sci Rep 7:1589
85. Troiani F, Godfrin C, Thiele S, Balestro F, Wernsdorfer W, Klyatskaya S, Ruben M, Affronte M (2017) Phys Rev Lett 118:257701
86. Lovat G, Choi B, Paley DW, Steigerwald ML, Venkataraman L, Roy X (2017) Nat Nanotechnol 12:1050
87. Mitchell AK, Pedersen KGL, Hedegård P, Paaske J (2017) Nat Commun 8:15210
88. Xu Q, Scuri G, Mathewson C, Kim P, Nuckolls C, Bouilly D (2017) Nano Lett 17:5335

Top Curr Chem (Z) (2016) 374:83
DOI 10.1007/s41061-016-0081-8

REVIEW

Organic Cocrystals: New Strategy for Molecular Collaborative Innovation

Yu Wang[1] · Weigang Zhu[2] · Huanli Dong[2] · Xiaotao Zhang[1] · Rongjin Li[1] · Wenping Hu[1,2]

Received: 16 July 2016 / Accepted: 31 October 2016 / Published online: 24 November 2016

Abstract Organic cocrystals that are composed of two or more components usually exhibit novel, unpredictable, and even unique properties rather than a simple combination of the properties of their components, such as white-light emission, ambipolar charge transport, nonlinear optics, and ferroelectricity. Since cocrystal engineering represents a novel strategy for synthesizing multifunctional materials, which opens the door for molecular collaborative innovation, it has aroused much attention in recent years. However, as it is also a relatively new research field, it is only in its early stages of development. In order to provide readers with an understanding of the future design of cocrystals for potential applications, a brief review of organic cocrystals is presented here, including an introduction to organic cocrystals as well as discussions of cocrystal preparation, methods and techniques of characterization, and multifunctional applications of cocrystals. Moreover, the outlook for further studies and applications of cocrystal engineering is considered.

Keywords Cocrystals · Optoelectronics · Organic materials · Crystal engineering

Chapter 8 was originally published as Wang, Y., Zhu, W., Dong, H., Zhang, X., Li, R. & Hu, W. Top Curr Chem (Z) (2016) 374: 83. DOI 10.1007/s41061-016-0081-8.

✉ Huanli Dong
dhl522@iccas.ac.cn

✉ Wenping Hu
huwp@tju.edu.cn

[1] Key Laboratory of Molecular Optoelectronic Sciences, Department of Chemistry, School of Science, Tianjin University & Collaborative Innovation Center of Chemical Science and Engineering, Tianjin 300072, People's Republic of China

[2] Laboratory of Organic Solids, Institute of Chemistry, Chinese Academy of Sciences, Zhongguancun, Beijing 100190, People's Republic of China

1 Introduction

Recently, cocrystal engineering—a novel strategy for designing multifunctional organic materials—has attracted increasing attention. In contrast to inorganic materials, organic materials show significant advantages in terms of, for example, large-scale fabrication, low cost, and flexibility [1–4]. Moreover, compared to polymers, the crystallinity of small molecules tends to be better, which not only improves physicochemical properties but also makes it easier to study the relationships between structure and properties for such materials. Also, the limitations of organic materials are an obstacle to their utilization in multifunctional materials, whereas cocrystal engineering makes it possible to create new organic materials with novel physicochemical properties. For example, semiconductors usually exhibit either electron or hole transport, and only rarely ambipolar charge transport. On the other hand, it has been reported that some cocrystals, such as C_{60}–Co porphyrin and DBTTF–TCNQ [5–7], show balanced ambipolar charge transport, since they present both donor and acceptor character. Moreover, organic cocrystals are known to possess unique advantages in various fields, including ferroelectricity and nonlinear optics [8–12].

The first cocrystal to be discovered was quinhydrone, by F. Wöhler in 1844 [13], but cocrystal engineering only began to attract considerable attention in 1973, when the cocrystal TTF–TCNQ [14] was found to be highly conducting across a large temperature range, giving it a range of potential applications in organic optoelectronics [15]. In 2004, the cocrystal (BEDT-TTF)–(TCNQ) was the first to show ambipolar charge-transport behavior at low temperature [16], opening another door to organic cocrystal electronics. Moreover, cocrystal engineering has demonstrated its utility in various areas, such as ferroelectronics [17, 18]. While most ferroelectric materials are inorganic compounds or organic polymers, organic cocrystals with noncovalent interactions can present promising ferroelectric properties near room temperature, making organic cocrystal engineering very attractive.

Given the wide spectrum of potential applications of organic cocrystals in various fields, organic cocrystal engineering provides a highly efficient and convenient way to design new materials with desirable properties [10]. However, as it is a new research area, it is still full of challenges. First, the fundamental principles of cocrystal design are still not clear, as not every combination of donor and acceptor will self-assemble into a cocrystal. Moreover, there is still a lack of understanding of the basic interaction mechanism during cocrystallization, as well as the relationships between the packing mode and the properties of the cocrystal. Also, a methodology for designing and optimizing cocrystal packing and structures so as to synthesize cocrystals with desired properties is yet to be fully elucidated [19]. Therefore, more in-depth studies are needed to facilitate the design of these multifunctional materials.

In order to address these fundamental issues in this novel field, a review of organic cocrystals is presented here. This review is organized as follows. First, a brief introduction to organic cocrystals is provided, followed by discussions of methods and techniques of preparing and characterizing them. Multifunctional

applications of organic cocrystals are then described. Finally, we attempt to predict future directions in cocrystal engineering. We hope that this review will be beneficial to future investigations aiming at multifunctional applications of organic cocrystals.

2 General Characteristics of Organic Cocrystals

2.1 The Definition of a Cocrystal

Recently, cocrystal engineering has attracted much attention, as cocrystals usually show unique properties rather than a simple combination of the properties of their constituent components. Although cocrystal engineering has long been known to possess immense potential in organic materials science, the development of this field has generally proceeded rather slowly. The first cocrystal, quinhydrone, was discovered by F. Wöhler in 1844, but the term "cocrystal," which was first proposed by Schmidt and Snipes in 1967 [20], remained controversial for a long time. Scientists in the fields of crystal science and engineering have proposed several labels for this type of crystal, such as "molecular complex," "composite crystal" [21], and "lattice compound" [22]. However, since receiving the approval of Gautam R. Desiraju [23], a senior organic cocrystal scientist, the term "cocrystal" has become widely accepted. The definition of a cocrystal has also been the source of debate. Aakeroy and Salmon thought that ionic compounds should not be classified as cocrystals [24]. In 2007, Bond proposed that a cocrystal should be either a solvate, molecular complex, lattice compound, or solid solution [25]. Stahly put forward a similar view that a cocrystal is made up of two or more components with a crystalline structure, where a component could be an atom, an ionic compound, or a molecule [26]. This debate continued until 2012, when, after discussions among cocrystal scientists, a cocrystal was defined as a crystalline solid material consisting of two or more molecules in the same crystal lattice [27].

2.2 The Driving Force for Cocrystal Formation

As mentioned above, cocrystals usually contain two components, which are called the donor and acceptor. Figure 1 shows common donors and acceptors that can cocrystallize through noncovalent interactions, including charge-transfer interactions, π–π interactions, hydrogen bonds, and halogen bonds. Noncovalent interactions not only dominate the cocrystal self-assembly process and the dynamic processes involved, but they also govern the structure and stability of the cocrystal, as well its properties. Herein, we introduce some common noncovalent interactions involved in cocrystal engineering.

Charge transfer (CT) is one of the most common interactions that occur in organic cocrystals [28]. As shown in Fig. 1, when a strong acceptor such as TCNQ forms a complex with an acceptor such as TTF [14, 15], perylene [29], or pyrene [30], the charge-transfer interaction is usually the driving force for cocrystal formation. In the strong intermolecular interactions that take place between charge-

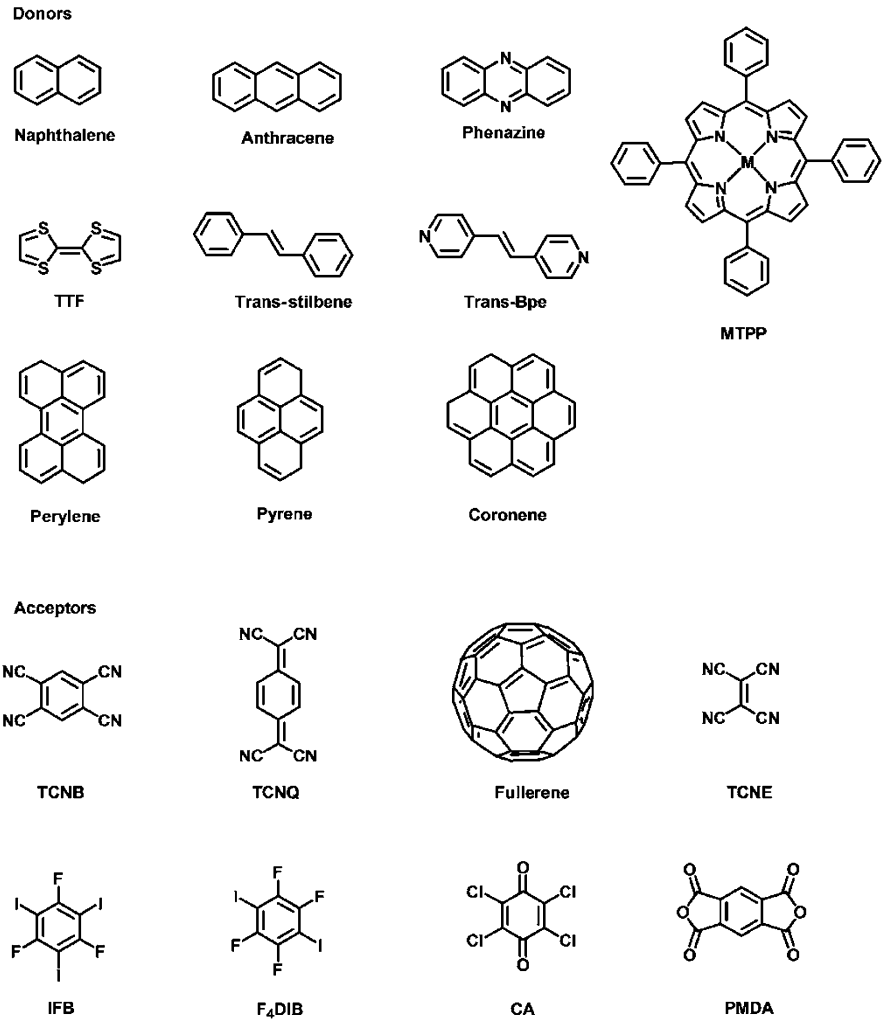

Fig. 1 Common donors and acceptors used in organic cocrystals

donating and charge-accepting materials, charge transfer occurs from the highest occupied molecular orbital (HOMO) of the donor to the lowest unoccupied molecular orbital (LUMO) of the acceptor. The strength of this interaction can be characterized by ρ, the degree of charge transfer, which depends on the ionization potential of the donor, the electron affinity of the acceptor, and the electrostatic Coulomb interactions in the complex. Charge-transfer complexes are one of the earliest reported types of cocrystals; indeed, most of the cocrystals reported so far present charge-transfer interactions. These materials have been studied for several decades, and various charge-transfer complexes have been shown to exhibit not only high room-temperature conductivity or high-temperature superconductivity but also

properties such as ambipolar transport, photoconductivity, ferroelectricity, or magnetic properties [31–35].

π stacking (π–π) interactions between π-donors, such as porphyrins and acene-based derivatives, and π-accepting ring systems, such as fullerenes, can also be the driving force for the self-assembly of various complexes in solution as well as in the solid state [36, 37]. π stacking interactions usually lead to cocrystals with optoelectronic properties; for instance, DPTTA–C_{60} [38], with its strong π–π interaction, displays high ambipolar charge-transport mobility.

Hydrogen bonds play an important role in the design of organic cocrystals, as they are stable and show good directivity, which makes it easier to predict structural consequences of these bonds. Complexes based on hydrogen bonds can form in both the solid state and in solution, and the hydrogen bonding present is closely related to the properties and functions of these cocrystals [39–42]. For instance, due to the polar and directional properties of hydrogen bonds, they have been used to design cocrystals with two-dimensional (2D) structure. Figure 2 shows a supramolecular network of PTCDI (perylene tetracarboxylic diimide) and melamine [43] based on hydrogen bonding, which was characterized by scanning tunneling microscopy (STM). The structure of a PTCDI–melamine junction is shown in Fig. 2c, demonstrating the strong and directional hydrogen bonding involved in the intermolecular interactions.

The halogen bond (XB), as shown in Fig. 3, is a noncovalent interaction between a halogen atom (XB donor) and a nucleophilic region (XB acceptor) [44, 45]. The halogen bond exhibits unique character: it is directional, strength-tunable, hydrophobic, and more effective in supramolecular self-assembly than a hydrogen bond. Figure 4 displays 2D cocrystallization based on halogen bonding [46], in which 3F3I acts as the XB donor and 3N as the XB acceptor. The presence of a binary network structure sustained by XBs was supported by the results of high-resolution STM. Moreover, cocrystals with halogen bonds also possess promising properties such as light emission, conductivity, and magnetism.

Although there are many kinds of intermolecular interactions and each interaction has its own unique character, the driving force for cocrystal formation is usually not just one type of noncovalent interaction but the simultaneous cooperation of several noncovalent interactions. Since there are close relationships between the intermolecular interactions present in a cocrystal and its structure and properties, studying these relationships may aid the design of cocrystals with particular desired properties.

2.3 Factors that Influence Cocrystal Properties

Since cocrystals usually exhibit unique properties rather than a simple combination of the properties of their components, it is important to attempt to understand the influence of various factors on cocrystal properties. The donor, the acceptor, and their arrangement in the cocrystal are the most important influences on cocrystal properties such as the crystal structure, the degree of charge transfer, and the cocrystal's optoelectronic properties [47].

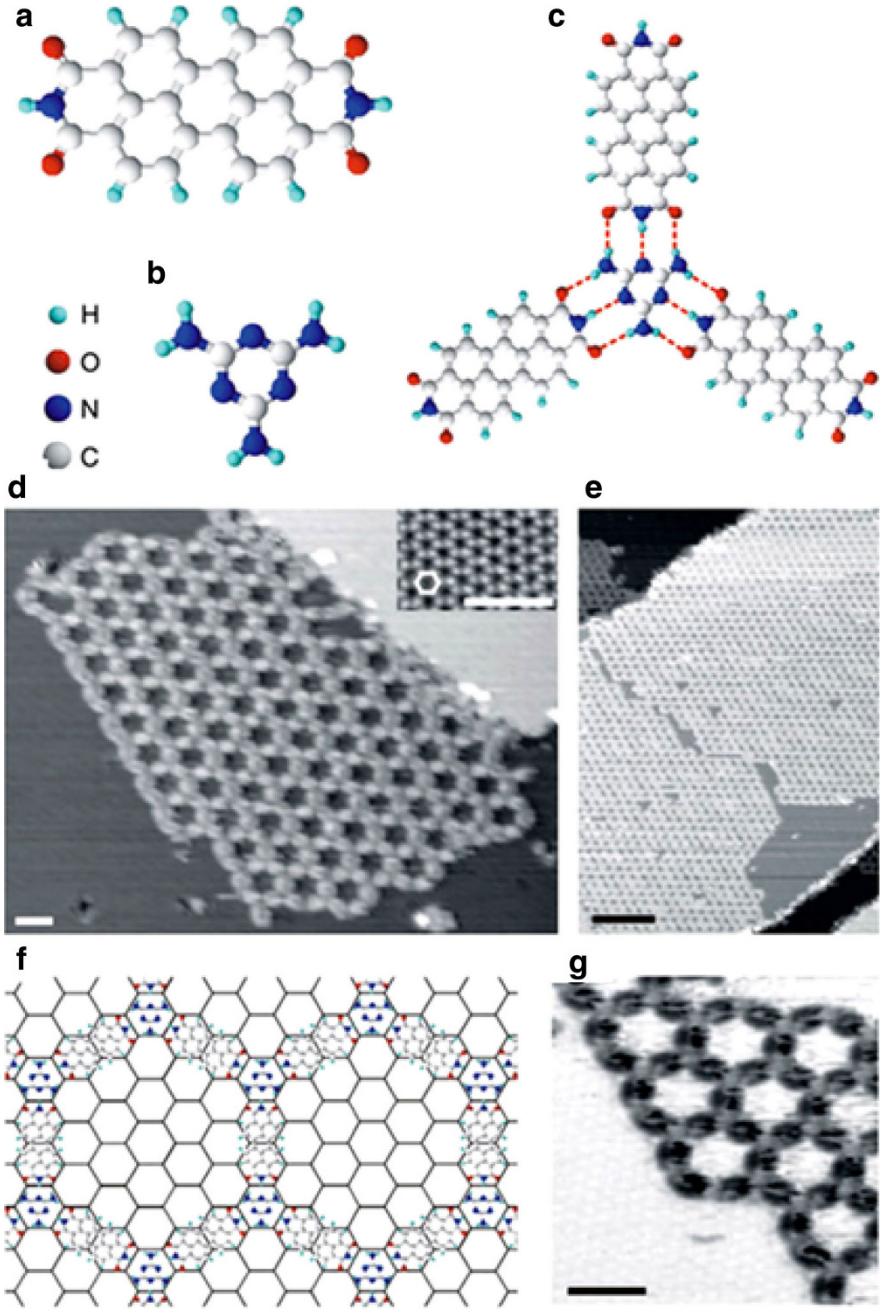

Fig. 2a–g Self-assembly of PTCDI and melamine into a supramolecular structure. Reproduced with permission from [43]

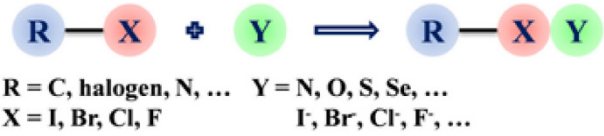

Fig. 3 Schematic of a halogen bond

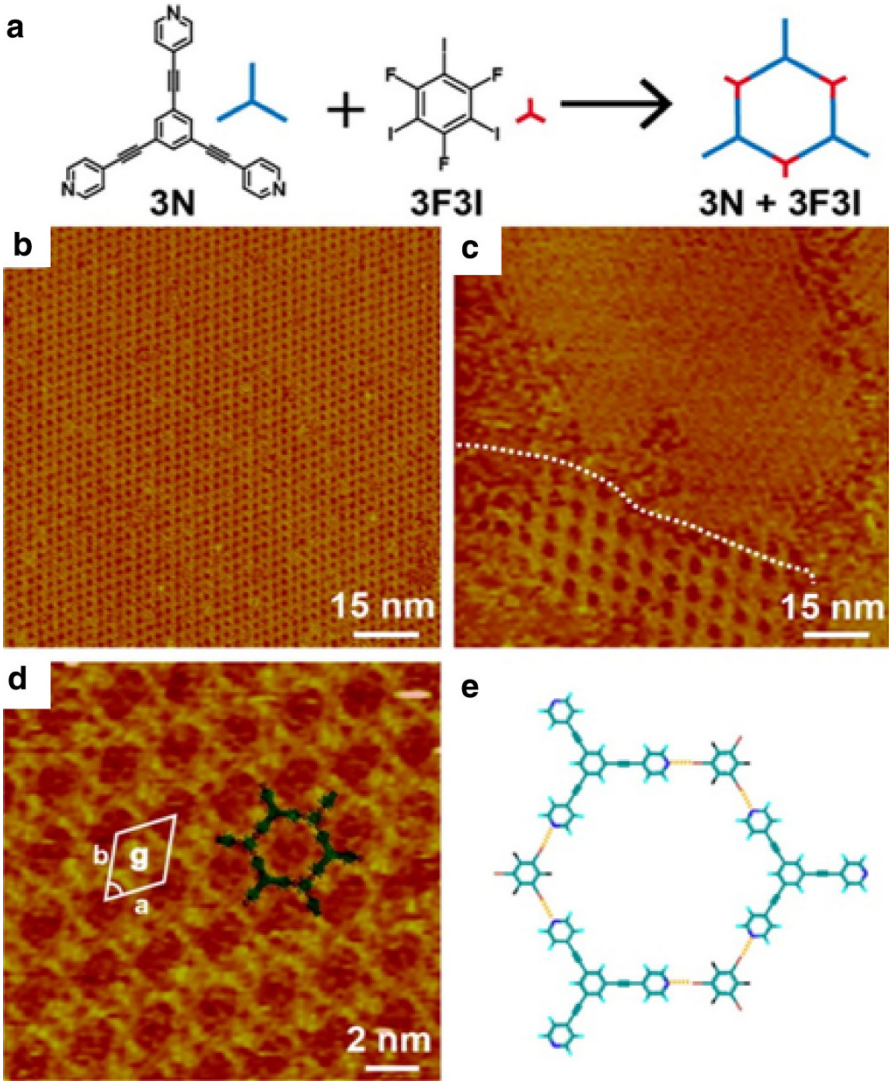

Fig. 4 **a** Self-assembly of 3N and 3F3I into a 3N–3F3I honeycomb structure. **b**, **d** STM images of the 3N–3F3I honeycomb structure. **c** STM image showing the coexistence of a close-packed 3N structure and a 3N–3F3I network. **e** Structural model of the 3N–3F3I honeycomb structure. Reproduced with permission from [46]. Copyright © 2015 American Chemical Society

Although cocrystals usually exhibit properties that are different from those of their components, they do reflect the individual properties of the donor and acceptor to some degree. For instance, the three most common acceptors used in organic cocrystals are 7,7,8,8-tetracyanoquinodimethane (TCNQ), tetracyanobenzene (TCNB), and fullerene (C_{60}) [48–52]. TCNQ is a strong acceptor that exhibits a high n-type charge-transfer mobility of 1.6 $cm^2\ V^{-1}\ s^{-1}$ [53] as well as good photoresponse behavior, with an on/off ratio of 160 [48]. TCNB is a molecule that produces bright blue fluorescence [54], and C_{60} is utilized to form complexes with various π-conjugated molecules [55, 56]. In line with these characteristics, cocrystals based on TCNQ and C_{60} usually possess good electrical properties, while TCNB is mainly used to produce cocrystals with particularly attractive optical properties [11]. Thus, when designing a cocrystal to have specific desired properties, the characteristics of both the donor and the acceptor should be considered.

Theoretically, the ratio of donor molecules to acceptor molecules in a cocrystal could be any value. For 1:1 complexes, there are two packing modes: mixed stacking, in which the donor and acceptor alternate (…DADA…), as seen in teracene–TCNQ [57], perylene–TCNQ [29], and DBTTF–TCNQ [58]; and segregated stacking, in which the donor and acceptor pack separately (DDDD…AAAA), as observed in TTF–TCNQ [14] (Fig. 5). Ratios other than 1:1 are less common in cocrystals. Producing cocrystals with such ratios requires the appropriate selection of the donor, acceptor, and preparation conditions. For example, coronene and TCNQ can form cocrystals with various molar ratios ranging from 1:1 to 3:1. In cocrystals containing unequal proportions of donor and acceptor molecules, the extra donor or acceptor molecules exist either within the stack, as in the $(coronene)_2TCNQ$ cocrystal, or within a new stack, as in $(coronene)_3TCNQ$, in which the extra coronene molecules are located perpendicular to and between stacks [59]. Different packing structures usually lead to different properties. For example, segregated-stacking systems usually display high electrical conductivity whereas mixed-stacking cocrystals are semiconductors or insulators [60].

However, the properties of a cocrystal depend not only on the packing mode but also ρ, a defining feature of charge-transfer cocrystals. ρ, which takes a value between 0 and 1, is determined by the donor's ionization potential, the acceptor's electron affinity, and the electrostatic Coulomb interactions in the complex. Its value is closely related to numerous physical properties [61, 62]. Similarly, cocrystals that are dominated by charge transfer are electrically insulating due to the

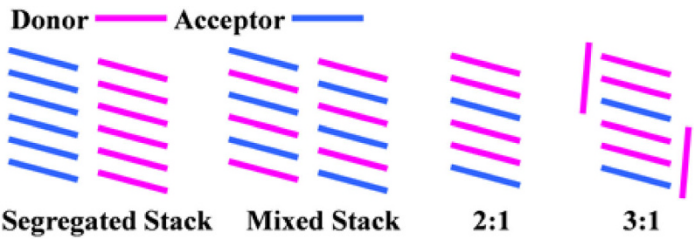

Fig. 5 Cocrystal packing structures with different donor to acceptor ratios: 1:1 (segregated stack and mixed stack), 2:1 (modeled as $(coronene)_2TCNQ$), and 3:1 (modeled as $(coronene)_3TCNQ$)

presence of strong Coulomb interactions, while cocrystals in which there is charge transfer but it does not dominate over other interactions are potentially highly conducting [61]. In fact, the degree of charge transfer is also related to the packing structure [63]. Cocrystals dominated by charge transfer display strongly ionic character, which can lead to segregated stacking, whereas cocrystals with smaller ρ values tend to be neutral, resulting in mixed stacking.

The band structure of a cocrystal, which is related to various optoelectronic properties, is closely related to the choice of donor and acceptor. Through theoretical studies, it was demonstrated that the cocrystal's HOMO is most closely correlated with the HOMO of the donor, while the acceptor's LUMO makes the largest contribution to the cocrystal's LUMO. A study of the conduction and valence bands of tetracene–TCNQ [64] showed that the charge density of the conduction band is centered on the acceptor and has a similar shape to a single TCNQ molecule, whereas the charge density of the valence band is centered on the donor molecule and has a similar shape to a single tetracene molecule. Since the electronic band structure influences both the structure and the charge-transfer properties of the cocrystal, realizing a cocrystal with particular desired properties requires an understanding and appropriate tailoring of the electronic band structure.

3 Methods and Techniques of Cocrystal Preparation and Characterization

3.1 Preparation Methods for Cocrystals

Generally, due to strong intermolecular interactions (as discussed above), cocrystals spontaneously self-assemble. Therefore, it is not necessary to use special methods to achieve cocrystallization. Overall, preparation methods can be categorized into three types: liquid-phase, vapor-phase, and solid-phase methods, among which liquid-phase methods are the most common since they are convenient, fast, and inexpensive. Liquid-phase methods include drop-casting, liquid–liquid interfacial precipitation (LLIP) [5], reprecipitation [65], solvent vapor annealing (SVA) [66], and diffusion, among others. These methods generate cocrystals in a similar manner to the growth of single-component crystals from a solution of that component, except that a donor–acceptor mixed solution is used instead. However, it is notable that such preparation techniques require that the components have similar solubilities. By contrast, vapor-phase methods are less commonly reported [7, 67], although they are essential when cocrystallizing some organics with poor solubilities. However, these methods tend to be applied to insoluble compounds with similar sublimation points, so that both co-sublimation as well as co-deposition can be performed. Solid-phase preparation methods have a long history and mainly refer to mechanochemical preparation methods, such as grinding and solvent-assisted grinding [68, 69]. As such methods do not necessarily require a solvent, they can be relatively cheap and easy to carry out, meaning that they are widely used, especially in relation to pharmaceuticals. However, it is worth noting that

mechanochemical methods tend to produce materials with amorphous phases, the properties of which may differ from those of the corresponding crystalline phases.

3.2 Basic Characterization Techniques for Cocrystals

After successfully preparing cocrystals, methods and techniques of characterizing them are required to study their features, such as their intermolecular interactions and crystal structures, which are closely related to their properties. Such characterization is necessary to get an overall understanding of the cocrystal structure as well as its properties.

The self-assembly behavior of the donor and acceptor molecules in a mixed solution reflects the intrinsic character of the resulting complex, so studying this behavior affords us a better understanding of the cocrystallization process. Since ultraviolet (UV), fluorescence (FL), and nuclear magnetic resonance (NMR) spectroscopic methods have been used to study supramolecular chemistry for many years [70], they can also be applied in studies of the self-assembly behavior of cocrystals in mixed solutions. After cocrystallization, the HOMO–LUMO gap narrows, leading to a new redshifted absorption band [71] or redshifted fluorescence. Due to the strong interaction between donor and acceptor molecules, Förster resonance energy transfer (FRET) and photoinduced charge transfer (PET) as well as fluorescence quenching [72] are possible. Also, due to changes in the molecular environment, the NMR spectrum shifts [73]. Using these spectral changes, we can deduce the donor to acceptor ratio in a complex, the association constant, and so on. If there are noncovalent interactions between the donor and acceptor molecules, these may be reflected in their spectra in mixed solution.

For instance, when studying the charge-transfer complex between C_3HAT-TIm and H_2P, the UV spectrum observed in mixed solution was found to differ from the original spectrum of one of the components in solution [74]: as shown in Fig. 6, upon the addition of C_3HAT-TIm, the original band of H_2P at 418 nm decreased

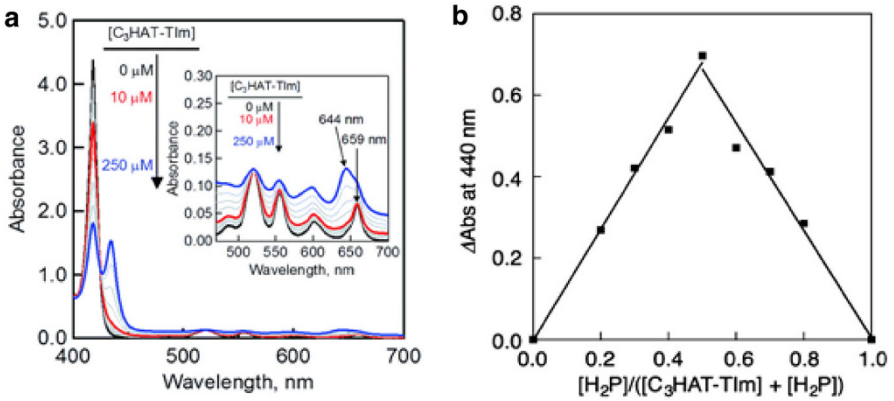

Fig. 6 **a** Changes in the absorption spectrum upon the addition of H_2P to C_3HAT-TIm. **b** The Job plot for the complexation of H_2P and C_3HAT-TIm. Reproduced with permission from [74] (published by The Royal Society of Chemistry)

and a new strong absorption peak at 440 nm appeared, indicating the formation of the typical CT complex composed of C_3HAT-TIm and H_2P. Using the absorption band at 440 nm, a Job plot was obtained which exhibited a maximum at 0.5, demonstrating that the component ratio in the CT complex is 1:1. However, it is important to note that not all complexes present a new absorption band that is distinct from those exhibited by the components of the complex. For instance, for the DPTTA–TCNQ complex [75], the absorption spectrum of the mixed solution largely corresponds to the combined spectra of DPTTA and TCNQ. This is probably due to the rather weak intermolecular interactions between these components in the ground state.

Fluorescence quenching is another common phenomenon in organic complexes. It can be subdivided into static quenching and dynamic quenching [77]. Generally, static quenching is due to the formation of a complex, while dynamic quenching is mainly attributable to the random collisions of molecules. Studies of fluorescence quenching can lend insight into the behavior of an excited complex, which in turns leads to a greater understanding of cocrystal engineering. If we consider the charge-transfer cocrystal PyTs–BuV [76], as shown in Fig. 7, increasing the amount of BuV was found to efficiently decrease the fluorescence intensity of PyTs in aqueous solution, indicating the formation of the complex. The quenching mechanism was elementary static quenching due to the formation of stable stacked complexes. This was explained by the sphere-of-action model [78], which highlighted the strong electrostatic interactions present in the PyTs–BuV system.

The properties of a complex in a mixed solution of its components cannot always be assumed to be the same as the properties of a solid cocrystal of these components, as there can be differences between the complex and cocrystal. Generally, as also seen in the solution phase, the UV and FL spectra of a cocrystal are redshifted compared to those of a single component of the cocrystal due to the narrowing of the energy gap during cocrystallization. Solid-state NMR (SSNMR) also provides an efficient way to obtain detailed structural information about organic cocrystals. There will be changes in NMR properties such as chemical shifts and relaxation times upon cocrystallization, and these changes can be utilized to prove the formation of cocrystals and observe structural features such as hydrogen bonding. For instance, in the cocrystal of palmitic acid and nicotinamide [79] shown

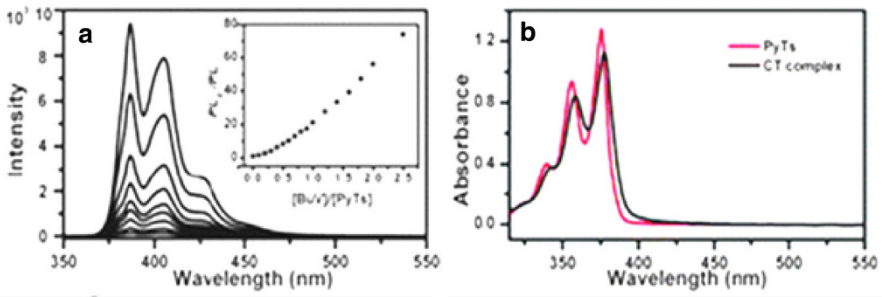

Fig. 7 **a** Fluorescence spectra of PyTs mixed with various amounts of BuV. **b** Absorption spectra of PyTs and the PyTs–BuV cocrystal. Reproduced with permission from [76]

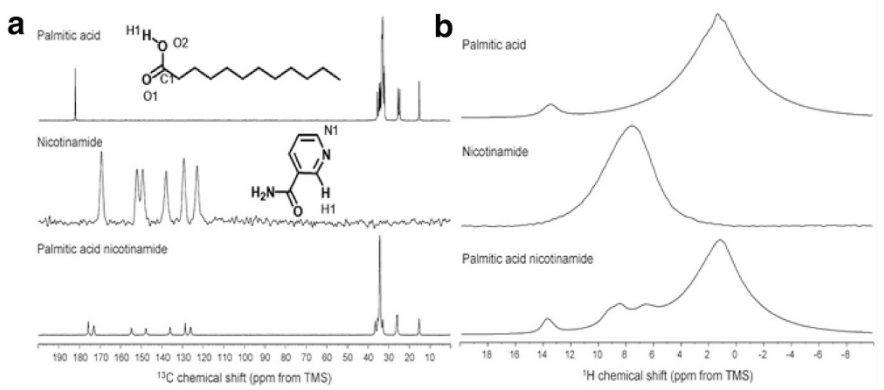

Fig. 8 **a** ^{13}C SSNMR spectra of palmitic acid, nicotinamide, and the cocrystal of these molecules. **b** ^{1}H SSNMR spectra of the same three samples under the same field. Reproduced with permission from [79]. Copyright © 2008 American Chemical Society

in Fig. 8, there is hydrogen bonding between the carboxylic acid donor (H1) and the pyridine acceptor (N1), as well as between the H1 hydrogen in nicotinamide and the carbonyl (O1) acceptor. The differences between the 1D ^{1}H and ^{13}C SSNMR spectra of the cocrystal and those of the components of the cocrystal demonstrate the formation of the cocrystal. It is clear that the ^{1}H chemical shift of H1 of nicotinamide in the cocrystal reflects substantial deshielding, while the signal from H1 of palmitic acid in the cocrystal is observed at 13.7 ppm, meaning that this H1 is only slightly deshielded. This spectral behavior indicates the presence of a hydrogen bond.

Note that not all complexes display different spectral behavior from their components (see, for example, the absorption spectra of the DPTTA–TCNQ complex and its components). Therefore, suitable characterization techniques should be chosen and analysis should be based on the results from several techniques. For instance, the application of X-ray photoelectron spectroscopy (XPS) and electron spin resonance (ESR) spectroscopy is crucial to studying charge-transfer interactions. XPS is an effective method that can be used to determine the compositions of compounds and to derive valence-state information about cocrystals. Since cocrystal formation leads to the redistribution of electron density, it is possible to estimate changes in the valence state. The Bpe–TCNB cocrystal [80], for instance, exhibits a strong charge-transfer interaction in the ground state. The XPS spectra of Bpe, TCNB, and the cocrystal of them are shown in Fig. 9. It is clear that the N 1*s* peak of the cocrystal is shifted to 400.52 eV, indicating the appearance of $BpeN^{+}$, which explains the existence of charge-transfer interactions between Bpe and TCNB.

Electron spin resonance (ESR) [82–84] spectroscopy is a sensitive method for identifying unpaired electrons and attributes when studying D–A charge-transfer interactions. An ESR signal is observed in the presence of charge transfer. The *g* factor for the ESR spectrum can be calculated as follows:

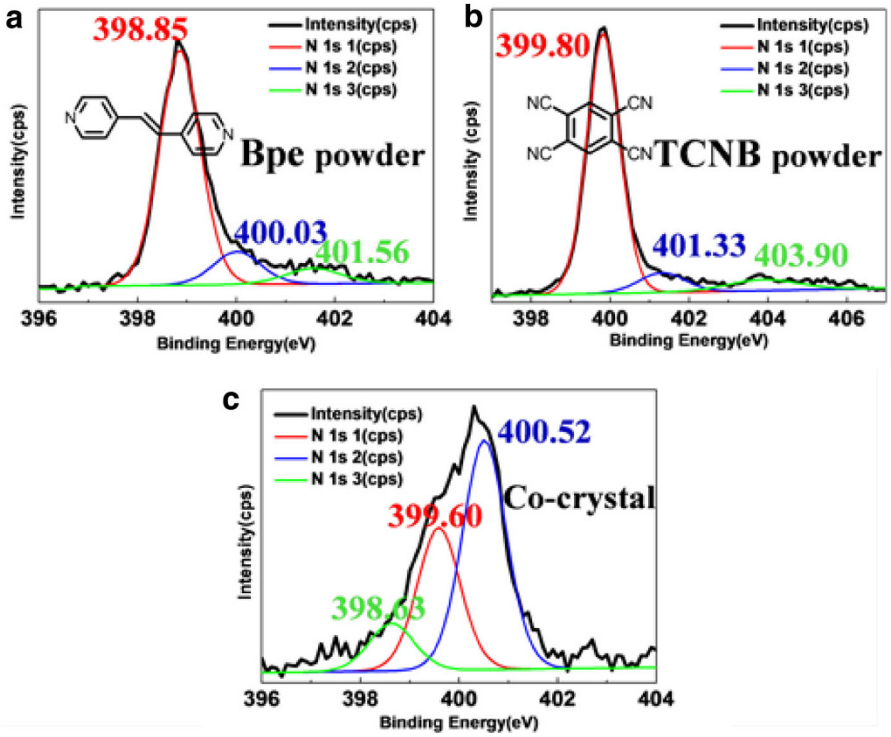

Fig. 9 XPS profiles of **a** Bpe powder, **b** TCNB powder, and **c** the Bpe–TCNB cocrystal. The binding energy was referenced to the C 1*s* line at 284.7 eV (C=C). Reproduced with permission from [80]

$$h\gamma = g\mu_B H_{center},$$

where h, γ, μ_B, and H_{center} are the Planck constant, the microwave frequency applied, the Bohr magneton, and the center-of-resonance magnetic field, respectively. The g factor depends on the electronic structure of the compound, and each molecule has its particular value; for example, the g factor of a C_{60} radical anion is generally around 1.996–1.999 at room temperature. Figure 10 shows the ESR spectrum of the cocrystal DPTTA–DTTCNQ [81], which demonstrates the existence of unpaired electrons.

The degree of charge transfer, as mentioned above, is closely related to the donor's ionization potential, the acceptor's electron affinity, and the electrostatic Coulomb interactions in the complex. In charge-transfer cocrystals, it is related to many properties, such as conductivity [61]. There are two kinds of methods for determining the degree of charge transfer: diffraction (including X-ray diffraction and neutron scattering) and spectroscopy (Raman, IR, and so on [47]).

Single-crystal X-ray diffraction is an efficient means of analyzing the structure and charge-transfer character of a cocrystal in depth. It is well known that bond-length changes during cocrystallization are a function of the degree of charge transfer in the cocrystal. Such changes are most deeply studied in TCNQ-based

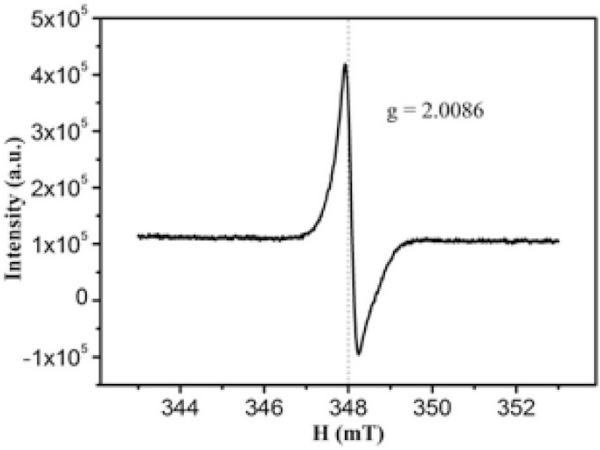

Fig. 10 Electron spin resonance spectrum for a 50-mg cocrystal of DPTTA-DTTCNQ. Reproduced with permission from [81]

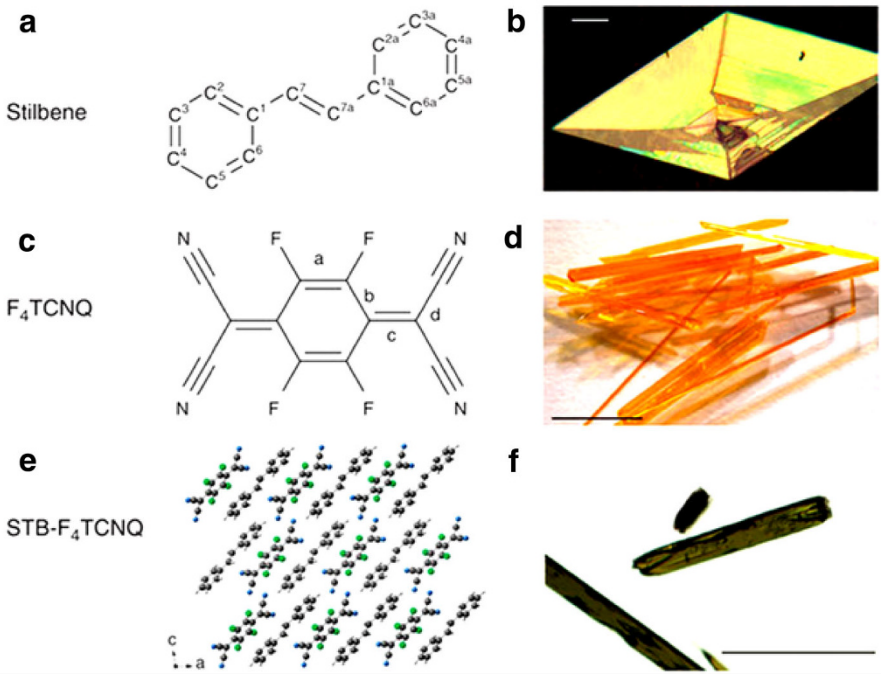

Fig. 11 **a** Chemical structure of stilbene and **b** an optical image of a stilbene crystal. **c** Chemical structure of F_4TCNQ and **d** an optical image of F_4TCNQ crystals. **e** Chemical structure of the cocrystal and **f** an optical image of the cocrystal. Reproduced with permission from [88]

cocrystals [85–87]. As reported in 2014, the degree of charge transfer in the cocrystal STB–F_4TCNQ can be calculated as

$$\rho = \frac{1}{2}\left(\left[1 - \frac{b_{CT} - c_{CT}}{b_N - c_N}\right] + \left[1 - \frac{d_{CT} - c_{CT}}{d_N - c_N}\right]\right),$$

in which b, c, and d represent the lengths of bonds b, c, and d in F_4TCNQ (see Fig. 11), the subscript "CT" refers to bonds in the acceptor when it is in the CT complex STB–F_4TCNQ, and the subscript "N" refers to bonds in neutral F_4TCNQ. In order to reduce the influence of thermal expansion, the bond lengths of the neutral and complexed F_4TCNQ were compared at the same temperature [88].

IR and Raman spectroscopy have also been widely used in studies of cocrystals. The electron densities of the donor and acceptor molecules are redistributed during complexation, and the structures of the donor and acceptor molecules are changed to different degrees, which may be reflected in their IR and Raman spectra. Generally, the IR and Raman spectra of a cocrystal are combinations of the IR or Raman spectra of their components, albeit with a few peaks shifted.

For fullerene (C_{60}), the peak at 1429 cm^{-1} in its IR spectrum is the most sensitive to changes in the molecule's environment. The shift Δv of the peak at 1429 cm^{-1} increases almost linearly with the degree of charge transfer: $\rho = 0.03\Delta v$ [50]. However, it should be pointed out that this equation can only be applied in the absence of peak splitting and absorption bands of solvents and donors. Moreover, when Δv is less than 2.5 cm^{-1}, the shift cannot be attributed to charge transfer; it may be due to the influence of the crystal field.

For TCNQ and its derivatives, the C=C and C≡N stretching peaks are sensitive to changes in charge. Since donors do not usually contribute any observable features to the C≡N stretching region of TCNQ, the degree of charge transfer can be investigated using the C≡N stretching mode. During picene–F_4TCNQ

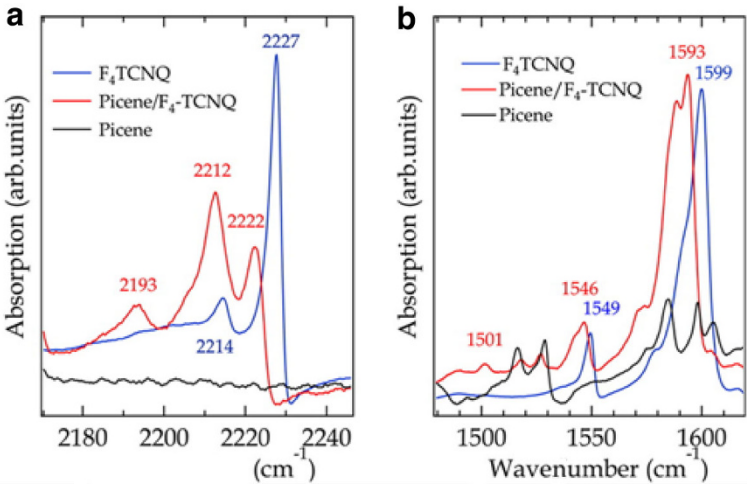

Fig. 12 IR absorption spectra of picene, F_4TCNQ, and the cocrystal picene–F_4TCNQ [67]. Copyright © 2014 American Chemical Society

crystallization [67], a new peak appears at 2193 cm^{-1}, indicating charge transfer. Moreover, there are two further bands at 2222 and 2212 cm^{-1}, in contrast to those seen at 2227 cm^{-1} and 2214 cm^{-1} in neutral F_4TCNQ, as shown in Fig. 12. Therefore, the value of ρ can be calculated as

$$\rho = \frac{2\Delta v}{v_0\left(1-\frac{v_1^2}{v_0^2}\right)}.$$

In which $\Delta v = v_0 - v_{ct}$ and the values of v_0, v_1, and v_{ct} represent the C≡N stretching peaks of F_4TCNQ, the F_4TCNQ anion ($\rho = 1$), and the cocrystal picene–F_4TCNQ, respectively. The value of ρ was finally calculated as $0.14e$.

Aside from studying intermolecular interactions, it is also essential to explore the macroscopic properties of cocrystals, such as their thermal stability. Thermogravimetric analysis (TG) and differential scanning calorimetry (DSC) measurements are used to study the thermal stability of cocrystals. For example, thermogravimetric curves of fullerene complexes can usually be divided into three temperature ranges. The first corresponds to the removal of solvent, the second to donor decomposition, and the third to the sublimation of fullerenes [50]. Aside from the thermal stability, DSC curves also provide information about cocrystal properties that depend on temperature, such as phase transitions. For instance, the cocrystal CuQ_2–TCNQ [89] has two forms and converts into another polymorph upon mechanical stimulation. Therefore, DSC measurements were performed to study the phase transition process. As shown in Fig. 13, upon heating, form II turns into form I, while cooling did not lead to the formation of form II, indicating that the process is monotropic and form II is less thermodynamically favored.

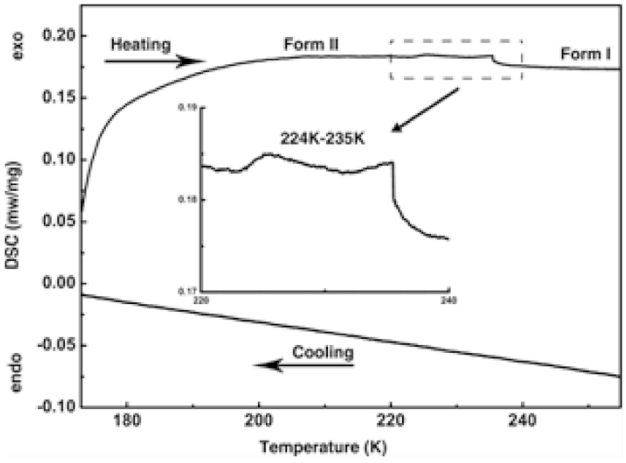

Fig. 13 DSC curve of the CuQ_2–TCNQ cocrystal. Reproduced with permission from [89]. Copyright © 2013 American Chemical Society

3.3 Exciton Dynamics Studies of Cocrystals

The optoelectronic performance of an organic material is closely related to the dynamics of excitons in that material, including their generation, dissociation, diffusion, and recombination. Frenkel excitons, which are strongly localized on individual molecules, are formed in most organic materials. In donor–acceptor systems, however, charge-transfer states are formed by electron–hole coupling between donor and acceptor molecules. Therefore, research into exciton behavior in donor–acceptor systems has attracted much attention, but such research is a challenge in materials science as well as nanotechnology due to the microsecond and ultrafast processes involved, meaning that characterization requires highly advanced equipment and techniques. Time-resolved techniques such as femtosecond laser-induced transient absorption measurements and time-resolved fluorescence spectra [74, 90] are most commonly employed to study ultrafast processes. Studies of cocrystals using such advanced techniques are scarce, as the research field of cocrystals is relatively new. However, these methods have been applied to donor–acceptor mixed solutions and film blends, which show similar mechanisms to cocrystals, meaning that those studies could aid the design of future cocrystal studies utilizing these advanced techniques.

For instance, in a mixed solution of C_{60}Im and ZnNc [91, 92], the fluorescence lifetime of ZnNc was found to be shortened and the decay–time curve was biexponential. The shallower exponential was similar to the decay–time curve of the free donor, while the steeper exponential decay was attributed to the complex. The transient absorption spectrum at 10 ps showed bands attributable to the S_1–S_n transitions of ^{1}ZnNc* and $^1C_{60}$* in the 400–1200 nm region. At 200 ps, there were two new absorption bands at 710 and 985 nm, which were assigned to $ZnNc^+$. A band from C_{60}^- was expected to appear at 1000 nm, where it would have been buried by the absorption band of $ZnNc^+$ at 985 nm. Therefore, it is clear that a charge-separated (CS) state of the complex was formed. Moreover, Fig. 14 shows that the CS process is so fast that it happens within about 100 ps, in accordance with the decay of ^{1}ZnNc*. At

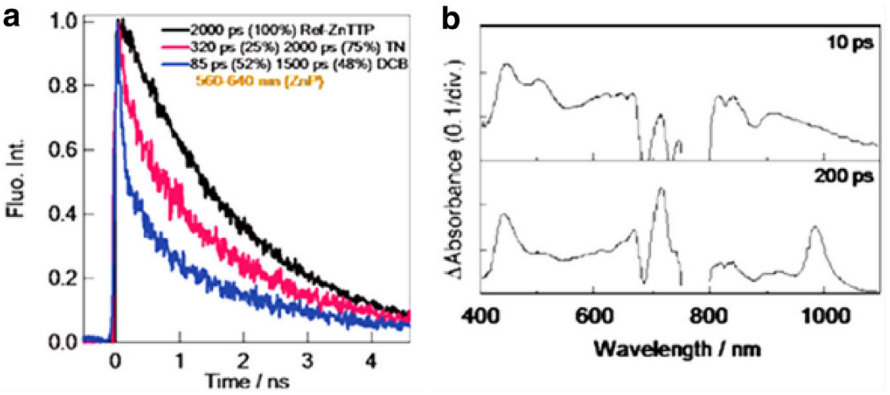

Fig. 14 **a** Fluorescence decay curves of ZnNc in C_{60}Im → ZnNc. **b** Picosecond transient absorption spectra for the C_{60}Im → ZnNc complex. Reproduced with permission from [91, 92]

100–150 ps, the $ZnNc^+$ absorption intensity reaches a maximum, after which it decays due to the charge recombination (CR) process. Since quenching can account for the CS from the singlet excited state of ZnNc to coordinated fullerene, the rate constant and quantum yield of CS can be evaluated as follows:

$$k_{CS}^{singlet} = (1/\tau_f)_{sample} - (1/\tau_f)_{ref}$$
$$\Phi_{CS}^{singlet} = [(1/\tau_f)_{sample} - (1/\tau_f)_{ref}]/(1/\tau_f)_{sample}$$

The measured values of $k_{CS}^{singlet}$ and $\Phi_{CS}^{singlet}$ were found to be 109–1010 s^{-1} and 0.5–0.9, respectively, indicating that efficient CS takes place in the complex.

Although there have been some important achievements in the field of exciton dynamics in recent years, research in this area is still full of challenges, and current techniques limit the development of this field. Therefore, to study exciton processes in depth, more time-resolved as well as spatially resolved techniques and methods need to be developed. In 2012, Tsutsumi and Hasegawa succeeded in applying a laser-beam-induced current (LBIC) technique to the analysis of photocarrier generation and diffusion characteristics in charge-transfer complexes [93]. The setup used for that study is shown in Fig. 15a. The photocurrent was detected by a current preamplifier linked to a lock-in amplifier. The laser beam was finely focused on the crystal surface. The photocurrent was measured as a function of the distance between the illumination position and the semiconductor/electrode interface. Moreover, the profile for the spatial decay of the photocurrent made it possible to study the diffusion of excitons and photocarriers. The authors investigated a series of mixed-stacking charge-transfer cocrystals; the LBIC profiles are shown in Fig. 15b. The results showed that cocrystals with larger CT gap energies (>0.7 eV) exhibited longer diffusion lengths (>10 μm), while those with smaller CT gap energies exhibited smaller diffusion lengths (<2 μm) due to the suppression of photocarrier diffusion. These results were explained by the Marcus theory: carrier recombination was promoted when the gap energy was small or comparable to the molecular reorganization energy, thus leading to a short diffusion length.

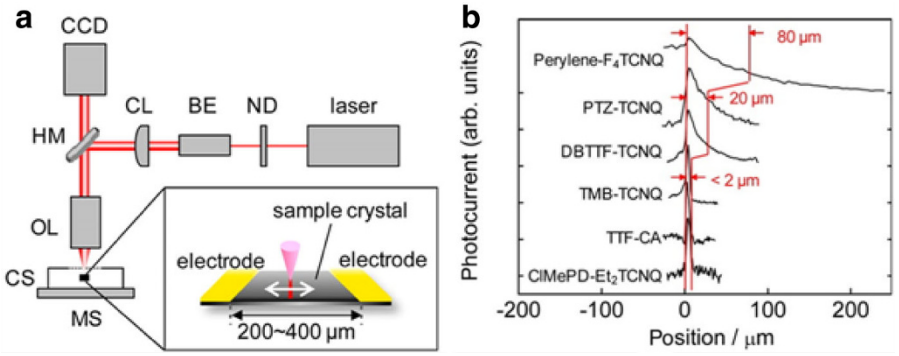

Fig. 15 **a** Instrumental setup for the laser-beam-induced current (LBIC) technique. **b** LBIC curves for six different charge-transfer cocrystals. Reproduced with permission from [93]. Copyright © 2012 American Chemical Society

4 Applications of Cocrystals

Since the discovery in 1973 that TTF–TCNQ cocrystals are as conductive as metals, the field of cocrystal engineering has grown and demonstrated great potential applicability in various areas. For instance, Gotoh and Kubodera reported exceptionally large third-order optical nonlinearity of a CT complex in 1989 [94]. In 2000, abnormal magnetic properties were observed in an ionic cocrystal [95], and in 2004, scientists discovered an cocrystal that had a liquid phase [96]. Below, we provide a brief introduction to optoelectronics, given that cocrystals exhibit fantastic optoelectronic properties such as ambipolar transport, ferroelectricity, and white light emission that are only rarely displayed by single-component materials.

4.1 Electronics

4.1.1 Ambipolar Charge Transport

Ambipolar charge transport has been a challenge in the field of organic electronics for decades. However, cocrystals that are combinations of both p-type and n-type materials demonstrate good ambipolar charge-transport properties. Since the first report of an ambipolar charge-transport cocrystal in 2004, such cocrystals have attracted a great deal of attention, and research on them remains popular. Herein, we provide an introduction to cocrystals based on DPTTA.

DPTTA, an electron donor with a hole mobility of 0.25 $cm^2\ V^{-1}\ s^{-1}$, can form complexes with various acceptors, including TCNQ, C_{60}, C_{70} and DTTCNQ, through simple drop casting, as shown in Fig. 16. Organic field-effect transistors (OFET) of these cocrystals were fabricated by an organic ribbon mask method

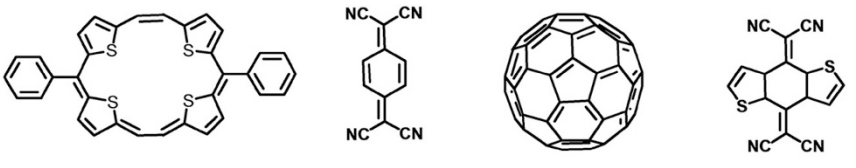

	Driving force	$\mu_e/cm^2V^{-1}S^{-1}$	$\mu_h/cm^2V^{-1}S^{-1}$
DPTTA-TCNQ	π-π	0.03	0.04
DPTTA-C_{60}	π-π; vdW force	0.01	0.3
DPTTA-C_{70}	π-π; vdW force	0.05	0.07
DPTTA-DTTCNQ	π-π; N···H-C; S···H-C	0.24	0.77

Fig. 16 Chemical structures of DPTTA, TCNQ, C_{60}, and DTTCNQ, and the mobilities of cocrystals based on them

[97, 98]. Surprisingly, all of the cocrystals presented good ambipolar charge-transport properties.

As confirmed by its UV spectrum, there is no CT interaction in the cocrystal DPTTA–TCNQ [75] in the ground state; the π–π interaction drives the formation of the cocrystal. The face-to-face stacking present in the cocrystal means that there is no continuous separate stacking in it. Lateral interactions were seen between the DPTTA or TCNQ molecules in adjacent columns, resulting in transport channels for holes or electrons. The transfer curves for the cocrystal showed that the electron and hole mobilities were 0.03 and 0.04 $cm^2\ V^{-1}\ s^{-1}$, respectively.

When DPTTA complexes with fullerenes (C_{60} and C_{70}) [38], the driving force changes to π–π interactions, polar electrostatic interactions, and van der Waals (vdW) forces. In the two resulting crystals, the stacking of DPTTA and fullerene molecules in an alternating fashion leads to a linear column structure, and the efficient π–π interactions between donor and acceptor molecules serve as electron and hole transport channels, respectively. The mobilities of C_{60}-DPTTA nanosheets were found to be $\mu_e = 0.01\ cm^2\ V^{-1}\ s^{-1}$ and $\mu_h = 0.3\ cm^2\ V^{-1}\ s^{-1}$, respectively, while C_{70}-DPTTA nanosheets displayed balanced ambipolar transport properties, and their mobilities were $\mu_e = 0.05\ cm^2\ V^{-1}\ s^{-1}$ and $\mu_h = 0.07\ cm^2\ V^{-1}\ s^{-1}$.

Since acceptors with good n-type mobilities are relatively rare, DTTCNQ was synthesized, which can complex with DPTTA [81]. The resulting cocrystal has a stoichiometry of 1:1, with donor and acceptor molecules stacking alternately along the *c* axis. Therefore, π–π interactions among the DPTTA and DTTCNQ molecules are expected to provide a charge-transport path in this cocrystal. The electron and hole mobilities of the cocrystal DPTTA–DTTCNQ were calculated as 0.24 and 0.77 $cm^2\ V^{-1}\ s^{-1}$, which are much higher than those of cocrystals containing TCNQ and fullerenes.

4.1.2 Photoresponse

Despite their ambipolar charge-transport characteristics, cocrystals also have high potential applicability in photoresponse devices, which are also important components in organic optoelectronics and for increasing energy efficiency [99]. A novel organic charge-transfer cocrystal composed of a pyrene derivative (PyTs) and a viologen derivative (BuV) with a mixed-stacking structure (see Fig. 17) was found to have switchable photoconductivity [76]. Under a light power of 100 mW/mm^2, the photocurrent from this cocrystal reached 2.3 nA at a bias voltage of 30 V. Photoswitching curves for the cocrystal showed that it responded rapidly to light and had a high on/off ratio of 30. The switchable photoconductivity of this cocrystal may be due to its mixed-stacking structure, which promotes efficient transport of photogenerated carriers.

4.1.3 Ferroelectricity

Ferroelectricity is a property of materials that show electric polarization which can be influenced by an external electric field. This property has a wide range of

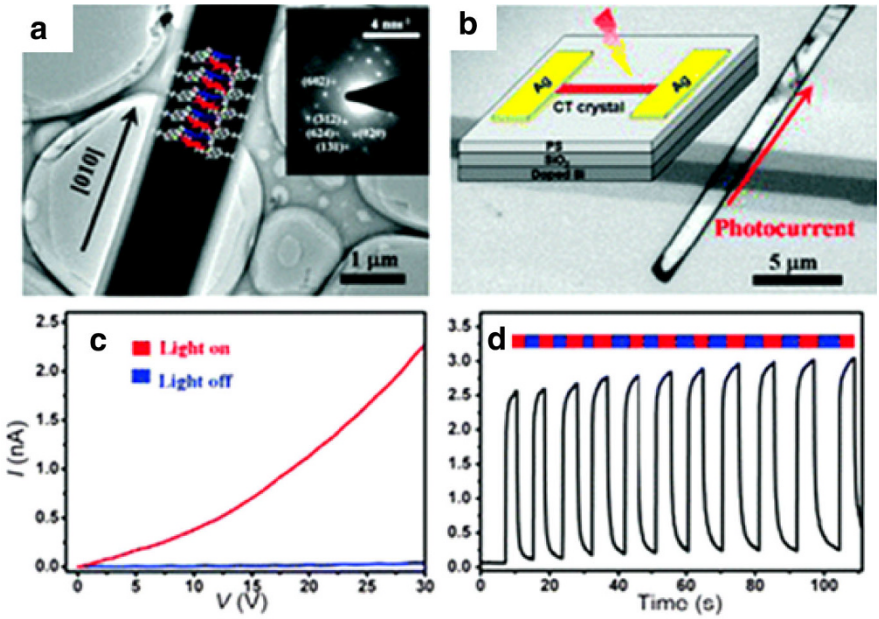

Fig. 17 **a** TEM image of the PyTs–BuV cocrystal. **b** Optical image of a cocrystal device. **c** Photoconductive *I*–*V* curves of the device. **d** Photoconductive on/off characteristics. Reproduced with permission from [76]

potential applications in nonvolatile computer memories, sensors, and optics [100]. Historically, organic ferroelectric materials have been limited to polymers and a few compounds with low molecular masses. However, more recently, it was found that the cocrystallization of two or more components can yield organic materials with promising near-room-temperature ferroelectric properties [101, 102]. Such cocrystals can be separated into two types: charge-transfer complexes and donor–acceptor compounds based on intermolecular hydrogen bonds.

As ferroelectricity results from one of the most representative phase transitions in solids, a ferroelectric charge-transfer complex is a typical displacive type of ferroelectric material in that the ferroelectricity results from the displacement of oppositely charged species, as shown in Fig. 18b. The most systematically well-studied ferroelectric CT complex is the cocrystal TTF–CA [103]. This cocrystal shows a temperature-induced neutral–ionic (NI) phase transition. The C=O stretching frequency of chloranil changes from 1685 cm^{-1} at 300 K to 1525 cm^{-1} at 15 K, indicating a shift from neutral to ionic due to molecular overlap along the stack.

As reported in 2005 [104], Phz–H_2*x*a (*x* = b, c) cocrystals display ferroelectricity near room temperature. Due to strong hydrogen bonding, the dielectric constant of the cocrystal exceeds 100 even at room temperature. The mechanism for the production of ferroelectricity may be the displacement of hydrogen atoms. As shown in Fig. 18c, the hydrogen of H_2*x*a in the ferroelectric phase shifts 0.2–0.3 Å towards the central position of the O–H···N bond compared to its position in the

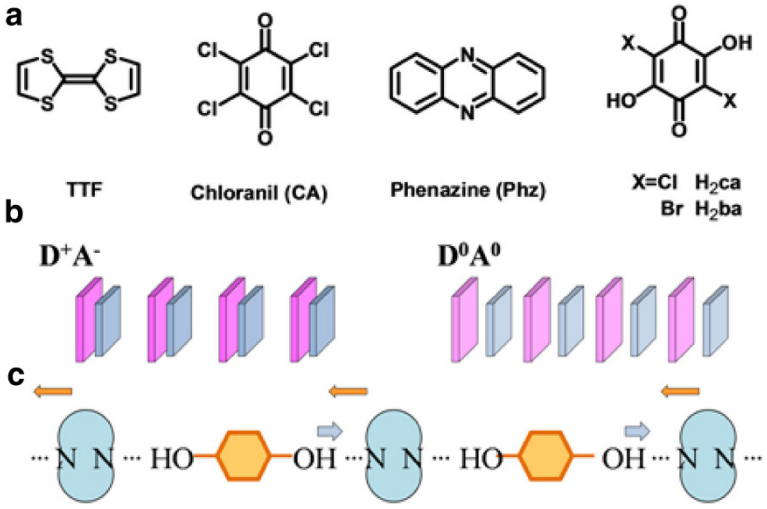

Fig. 18 **a** Chemical structures of TTF, CA, Phz, H_2ca, and H_2ba. **b** Schematic diagram of the ionic and neutral phases of TTF–CA. **c** Schematic diagram of the displacement of the H atoms (*blue arrows*) and molecules (*orange arrows*) in the ferroelectric phase

paraelectric phase. The hydrogen bond strengthens as the O···N distance decreases, resulting in molecular displacement.

4.2 Photoproperties

4.2.1 White Light Emission

White light emission (WLE), as we all know, has many potential applications in the field of organic optoelectronics, for example in organic solid-state lighting sources, optical detectors, optical waveguides, and light-emitting diodes [105].

In order to obtain white light emission, we generally combine two or more light emitters: a high-energy (e.g., blue) emitter and a low-energy (e.g., green or yellow) emitter [106]. However, there is usually Förster resonance energy transfer between these emitters due to the overlap between the emission spectrum of the high-energy emitter and the absorption spectrum of the low-energy emitter, leading to emission only from the low-energy emitter. That said, Liao and Lee have reported a white-light-emitting material obtained through doping [65], as shown in Fig. 19. Naphthalene–TCNB exhibits strong blue emission, whereas pyrene–TCNB exhibits only weak orange emission, but there is strong FRET from excited naphthalene–TCNB to pyrene–TCNB. When pyrene is doped into naphthalene–TCNB, the complex exhibits light ranging from blue to white to orange, depending on the dopant concentration (0.015% pyrene results in white light emission).

Doping is not the only way to produce a white light emitter. The cocrystal Bpe–F_4DIB, based on halogen bonding, also emits white light [107]. This cocrystal has a mixed-stacking structure with no charge transfer, and the PL lifetimes of the

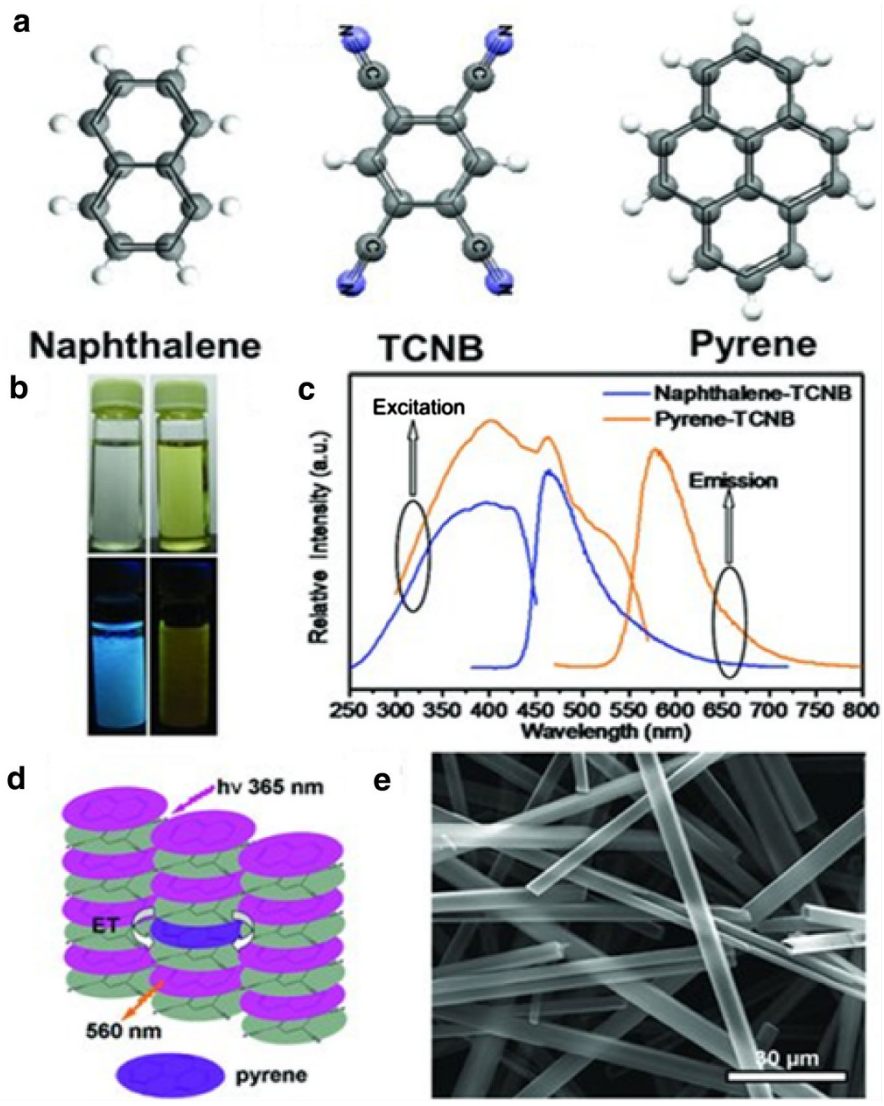

Fig. 19 Self-assembly of naphthalene, TCNB, and pyrene into mixed CT microtubes that emit white light. Reproduced with permission from [65]

cocrystal and the Bpe are almost the same, indicating the incorporation of F_4DIB into the cocrystal, which may facilitate white light emission.

4.2.2 Nonlinear Optics

Organic nonlinear optical (NLO) materials have a range of practical uses in electro-optical applications, especially in fast electro-optical modulation. While first-order

nonlinear optical materials require chromophores with extended π-conjugation and large hyperpolarizabilities, achieving second-order macroscopic nonlinearity requires the appropriate arrangement of chromophores in a crystalline solid, thus necessitating high-quality crystals that exhibit non-centrosymmetric packing. Since most organic chromophores crystallize centrosymmetrically, organic nonlinear materials are rather more difficult to realize than polymer materials. Moreover, most optimized NLO chromophores present poor crystallinity, limiting the growth of high-quality crystals.

A cocrystal reported in 1996 [108] displayed strong second-harmonic generation (SHG) signals. The dye merocyanine is one of the best NLO chromophores, with high hyperpolarizability and good photostability and thermal stability. It has two resonance structures, a quinonoid form (Mq) and a zwitterionic form (Mz), as shown in Fig. 20; the structure adopted by the dye strongly depends on its dielectric environment. However, this compound and its derivatives have poor crystallinity, making it difficult to grow crystals of good quality. When this dye is hydrogen bonded with another chromophore, 2,4-dihydroxybenzaldehyde (DB, introduced via crystal engineering), the resulting M2–DB cocrystal not only shows ideal chromophoric alignment and good optical quality (as checked with polarized light microscopy), but it also constructively reinforces the first-order hyperpolarizability, making it an interesting novel electro-optic crystal.

In 1997, cocrystals based on merocyanine were observed to exhibit strong SHG signals, as shown in [109], making them potentially very useful for second-order nonlinear optical applications. The SHG signal of the cocrystal M2–DA (DA = 2,4-dihydroxyacetophone) was even three orders of magnitude higher than that of the urea standard with a non-centrosymmetric structure. As the presence of hydrogen bonding leads to a polar chain in this cocrystal, the chains stack such that their long axes are parallel, resulting in a large macroscopic nonlinear response. These results point to a promising future for organic nonlinear optics.

4.2.3 Phosphorescence

Room-temperature phosphorescence has a great many potential applications in, for example, organic light-emitting devices, biosensors, and bioimaging technology [110]. Organic phosphorescent materials are usually categorized into organometallics and inorganics; pure organic phosphorescent materials are very rare.

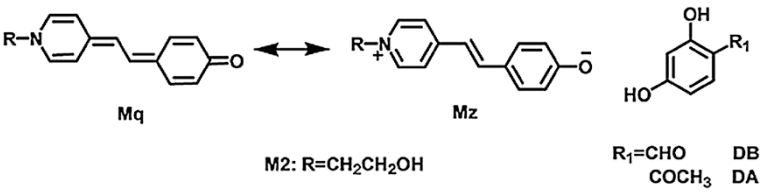

Fig. 20 The two resonance structures of the dye merocyanine, and chemical structures of M2, DA, and DB

By introducing intermolecular halogen bonding through the cocrystallization of Br6A and Br6, a material that exhibits green phosphorescence with high quantum yields of 55% can be obtained [111]. Figure 21 shows the design principle for this cocrystal, which can be summarized as three factors: aromatic carbonyls, the heavy atom effect, and the halogen bond. Triplet-producing aromatic aldehydes enhance the spin–orbit coupling at the carbonyl oxygen, which allows for the generation of a triplet state through intersystem crossing, and the triplet-promoting bromine results in the heavy atom effect as well as the halogen bond, which promotes singlet–triplet conversion and delocalizes electrons from the oxygen partially onto the bromine. In the solution phase, the halogen bond is absent, and there is no triplet emission because it is not efficient enough to prevent fluorescence. In the crystalline phase, hydrogen bonding couples the bromine and aldehyde, promoting phosphorescence. High-quality 2,5-dihexyloxy-4-bromobenzaldehyde (Br6A) crystals can emit phosphorescence, albeit with a low quantum yield of 2.9% due to self-quenching. However, the cocrystal Br6–Br6A with halogen bonding exhibits similar phosphorescence to Br6A but with a much higher quantum yield, indicating that cocrystal

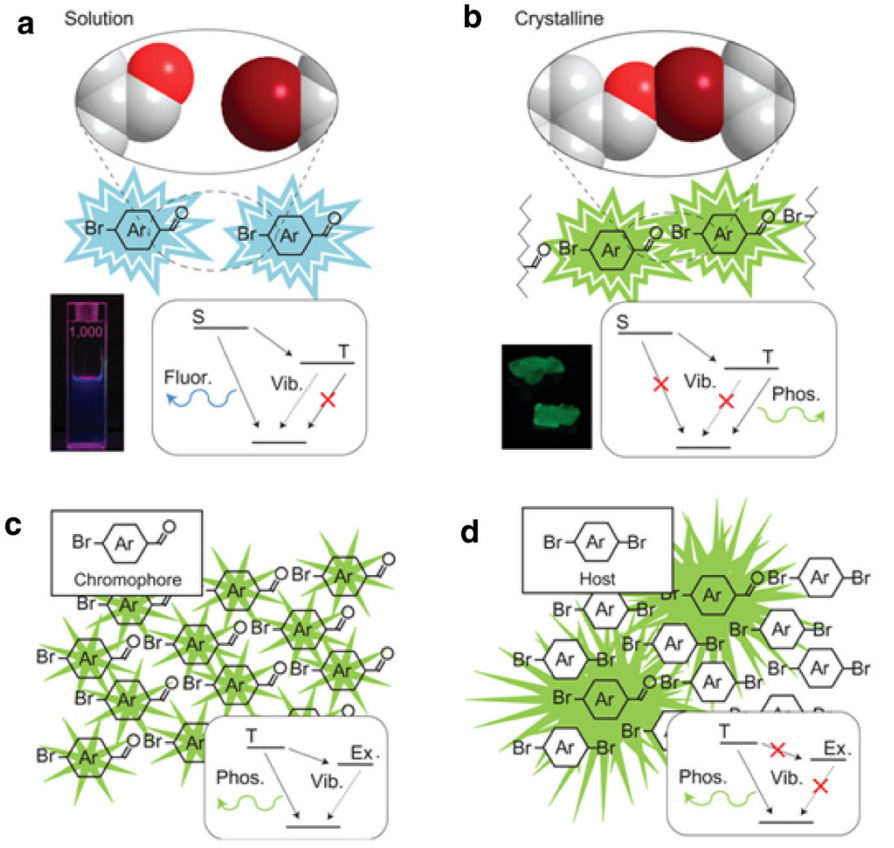

Fig. 21 Design principle for a cocrystal that presents room-temperature phosphorescence. Reproduced with permission from [111]

formation reduces the self-quenching of Br6A. According to the design principle defined above, the authors synthesized a series of cocrystals that phosphoresce different colors by varying the electron density and the triplet level. As shown in Fig. 22, the cocrystals BrC6A–BrC6, Np6A–Np6, and BrS6A–BrS6 emit blue, yellow, and orange phosphorescence, respectively. However, when iodine was used instead of bromine, no phosphorescence was observed. This may be due to the large size of the iodine atom, which blocks access to the aldehyde.

However, it is possible for cocrystals containing iodine to produce phosphorescence. In 2012, three such cocrystals were reported: fluorine–1,4-DITFB, dibenzofuran–1,4-DITFB, and dibenzothiophene–1,4-DITFB, which were synthesized through halogen bonding [112]. 1,4-DITFB was introduced into the cocrystal system for two main reasons: the strong intermolecular interaction with fluorine and its heterocyclic analogues, and the heavy atom effect, which promotes phosphorescence by improving spin-orbital coupling. It may also act as a dilution agent to prevent luminescence from quenching caused by aggregation.

4.3 Highly Luminescent Materials with Ambipolar Charge Transport Properties

Highly luminescent organic materials with ambipolar charge transport properties are required for optoelectronic integrated devices. However, it is proving very difficult to produce such materials based on single components. Cocrystal engineering may, however, be an efficient way to achieve this goal. For instance, the cocrystal composed of 4M-DSB and CN-TFPA (Fig. 23) exhibits quasi-1D ambipolar charge-transport properties ($\mu_h = 6.7 \times 10^{-3}$ cm^2 V^{-1} s^{-1} and $\mu_e = 6.7 \times 10^{-2}$ cm^2 V^{-1} s^{-1}) along with efficient red luminescence ($\Phi_{PL} = 31\%$). The donor and acceptor both efficiently produce luminescence in the visible, leading to the optical properties of the cocrystal. The components also have similar structures, including (different) small-volume substituents (CH_3 and CF_3, respectively), leading to the dense mixed stacking observed for this cocrystal. Moreover, the presence of

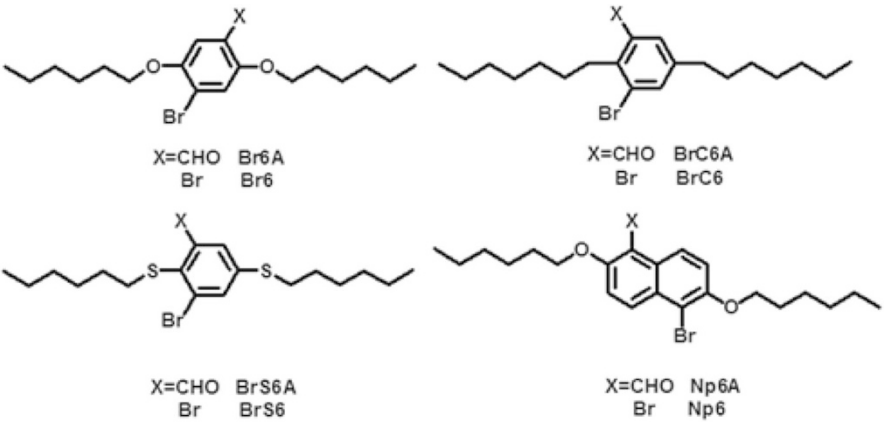

Fig. 22 Chemical structures of Br6A, Br6, BrC6A, BrC6, BrS6A, BrS6, Np6A, and Np6

alternating π-stacking and H-bonding maximizes the MO offset. The remarkable properties of this cocrystal open the door to the production of materials with ambipolar charge transport and highly efficient luminescence, which has important implications for next-generation optoelectronic applications [113].

5 Outlook

Organic cocrystals which combine donor with acceptor molecules usually exhibit attractive properties that are difficult to find in single-component materials, including ambipolar charge transport, ferroelectricity, and phosphorescence. However, while cocrystals are attractive materials, this research area is still in its infancy and remains full of challenges [114]. In this section, we attempt to predict future directions in cocrystal engineering.

Although there have been some important achievements in the field of cocrystallization recently [69, 115, 116], the basic mechanism for cocrystallization is still unclear. It is well known that the donor and acceptor molecules in a cocrystal interact with each other, but cocrystallization only occurs between some donor–acceptor combinations. Successful cocrystal design requires an understanding of not only the intermolecular interactions between the donor and acceptor molecules but also the crystal growth process for multicomponent materials [116]. It is believed that strong intermolecular interactions, similar solubilities of the donor and acceptor molecules, and a planar structure facilitate cocrystallization. However, there do not appear to be any stringent rules for determining which types of donors and acceptors will self-assemble into a cocrystal. Moreover, cocrystallization depends on the appropriate selection of not only the donor and acceptor but also the synthetic method, such as synthesis in solution [66, 117] or the vapor phase [7, 59], and so on [68]. Therefore, a guiding theory for cocrystal design is urgently required.

Another research direction is to obtain a deeper understanding of the charge-transfer interactions and exciton dynamics in organic cocrystals. Since the optoelectronic properties of cocrystals are closely related to their charge-transfer behavior, more in-depth studies of the dynamics of excitons in cocrystals should be performed.

For instance, spectroscopic and ESR studies as well as theoretical calculations were carried out to study the charge-transfer behavior of the cocrystal Bpe–TCNB (BTCs) [80]. Compared to the absorption spectra of its individual components, the cocrystal presented a new redshifted absorption peak at 363 nm linked to charge-transfer transitions. Moreover, ESR measurements pointed to a weak but sharp resonance signal with a calculated g factor close to that of a free electron, revealing the existence of unpaired electrons. There was also a new shifted peak in the PL spectrum of the BTCs, located at 420 nm. In addition, the decay–time profiles of the BTCs were monoexponential, demonstrating that the fluorescence of the cocrystals originates from one excited state and that there was no competing radiative deactivation process. Combining these results with those from theoretical calculations yielded some new insights into the evolution of CT excitons, as shown in Fig. 24. When the molecules are excited, optical transitions occur from the CT_0 state to CT_n states, followed by relaxation to the lowest of those states, CT_1, and

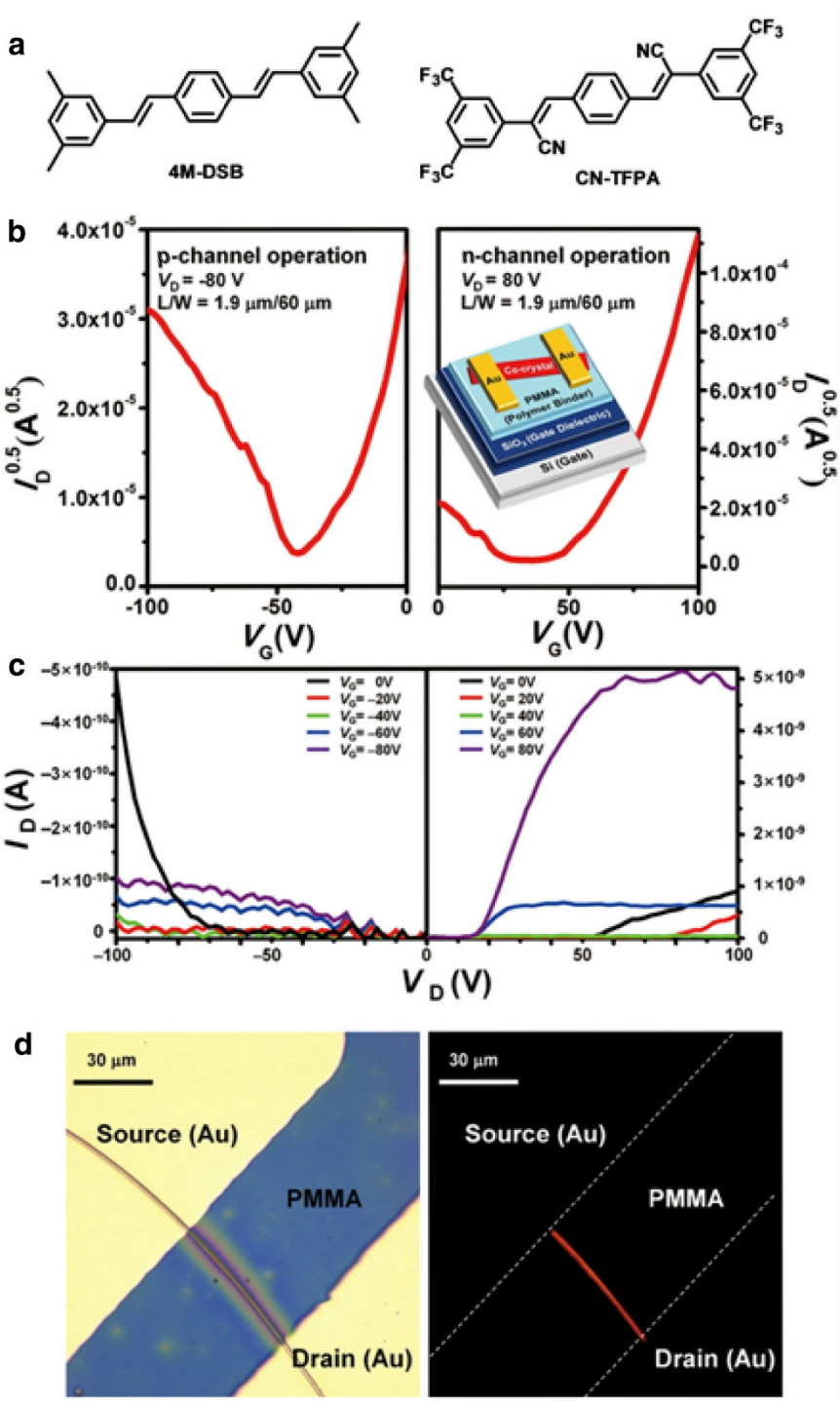
a
4M-DSB
CN-TFPA
b
p-channel operation
V_D = -80 V
L/W = 1.9 μm/60 μm
n-channel operation
V_D = 80 V
L/W = 1.9 μm/60 μm
Au
Co-crystal
PMMA (Polymer Binder)
SiO_2 (Gate Dielectric)
Si (Gate)
$I_D^{0.5}(A^{0.5})$
V_G(V)
c
V_G= 0V
V_G= −20V
V_G= −40V
V_G= −60V
V_G= −80V
V_G= 20V
V_G= 40V
V_G= 60V
V_G= 80V
I_D(A)
V_D(V)
d
30 μm
Source (Au)
PMMA
Drain (Au)

◀**Fig. 23** Properties of the cocrystal of 4M-DSB and CN-TFPA. Reproduced with permission from [113]. Copyright © 2013 American Chemical Society

fluorescence. The CT_1 excitons are generated, delocalized, and recombined in the cocrystal, and are responsible for the PL.

Therefore, further study of the exciton dynamics and related molecular dynamics in cocrystals should be carried out using advanced time-resolved spectroscopic techniques. Although charge-transfer behavior in donor–acceptor mixed solutions can be investigated using these time-resolved techniques, which could advance our understanding of the mechanisms for the characteristics of cocrystals, such research in solids is limited by the techniques and equipment currently available.

Other studies should focus on the relationship between cocrystal structure and properties and explore cocrystals with new physicochemical properties. For instance, two similar halogen-bonded cocrystals, Bpe–IFB and Bpe–F_4DIB, were

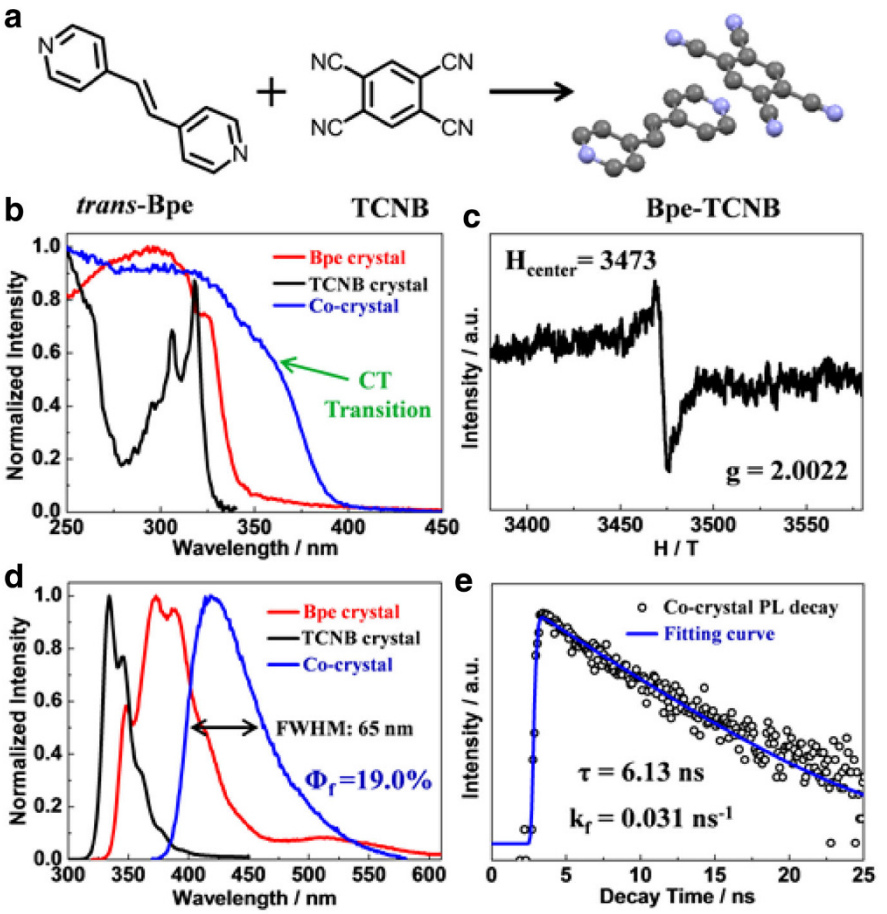

Fig. 24 The nature of the cocrystal Bpe–TCNB. Reproduced with permission from [80]

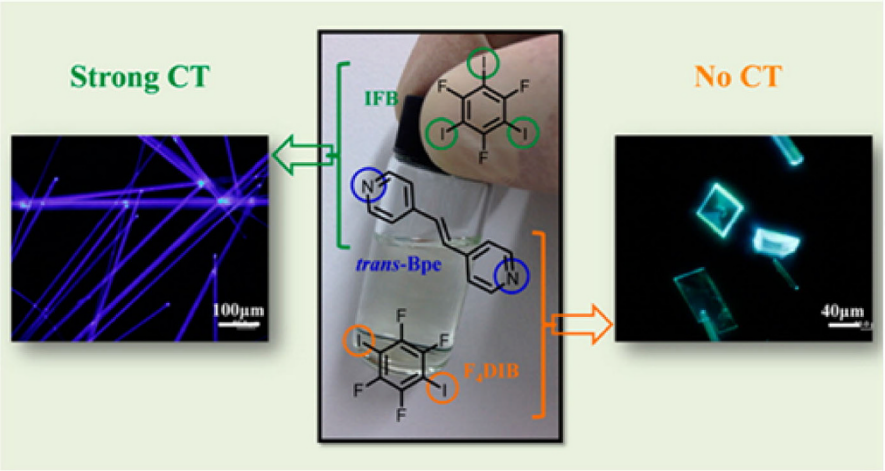

Fig. 25 Comparison of the cocrystals Bpe–IFB and Bpe–F_4DIB. Reproduced with permission from [107]. Copyright © 2015 American Chemical Society

comprehensively investigated and compared in order to explore their structure–property relationships (Fig. 25) [107]. While Bpe–IFB is wire-like and exhibits segregated stacking, Bpe–F_4DIB is block-like and shows mixed stacking. Due to its strong charge-transfer interactions, Bpe–IFB is a quasi-one-dimensional semiconductor that produces strong violet-blue photoluminescence. In comparison, due to its lack of CT interactions, Bpe–F_4DIB acts as an insulator and exhibits white light emission along with 2D optical waveguide properties. It was demonstrated that the charge-transfer interactions that occur in cocrystals are closely related to their molecular packing and can be controlled by crystal engineering, meaning that such engineering can be employed to tailor the optoelectronic properties of an organic cocrystal.

6 Conclusion

Cocrystal engineering has been studied for decades due to the great potential of cocrystals in physicochemical applications relating to various areas, such as ferroelectronics, white-light emission, and nonlinear optics. In this paper, we have provided a brief introduction to the general characteristics of organic cocrystals as well as their characterization and applications. We have also discussed the challenges that lay ahead for the field of cocrystal engineering: the basic mechanisms for cocrystal growth and the structure–property relationships of cocrystals remain unclear, which presents a significant barrier to the development of new attractive cocrystal materials. Therefore, more in-depth studies need to be carried out in this field of research. Since cocrystal engineering provides a new strategy for designing multifunctional materials, it will attract increasing attention in the near future due to its tremendous development potential.

Acknowledgements W. Hu and H. Dong acknowledge the National Natural Science Foundation of China (91,222,203, 91233205, and 91433115), the Ministry of Science and Technology of China (2013CB933403, 2013CB933504), the Strategic Priority Research Program of the Chinese Academy of Sciences (XDB12030300), the Beijing NOVA Program (Z131101000413038), and the Beijing Local College Innovation Team Improve Plan (IDHT20140512).

References

1. Dong H, Wang C, Hu W (2010) Chem Commun 46(29):5211–5222
2. Dong H, Fu X, Liu J, Wang Z, Hu W (2013) Adv Mater 25(43):6158–6182
3. Zhang C, Chen P, Hu W (2015) Chem Soc Rev 44(8):2087–2107
4. Wang C, Dong H, Hu W, Liu Y, Zhu D (2012) Chem Rev 112(4):2208–2267
5. Wakahara T, D'Angelo P, Miyazawa KI, Nemoto Y, Ito O, Tanigaki N, Bradley DDC, Anthopoulos TD (2012) J Am Chem Soc 134(17):7204–7206
6. Wu H, Wang F, Xiao Y, Pan G (2013) J Mater Chem C 1(12):2286–2289
7. Black H, Perepichka D (2014) Angew Chem Int Ed 53(8):2138–2142
8. Rupasinghe T, Hutchins K, Bandaranayake B, Ghorai S, Karunatilake C, Bucar D, Swenson D, Arnold M, MacGillivray L, Tivanski A (2015) J Am Chem Soc 137(40):12768–12771
9. Zhao Y, Fu H, Peng A, Ma Y, Liao Q, Yao J (2010) Acc Chem Res 43(3):409–418
10. Yan D, Delori A, Lloyd GO, Friscic T, Day GM, Jones W, Lu J, Wei M, Evans DG, Duan X (2011) Angew Chem Int Ed 50(52):12483–12486
11. Lei YL, Liao LS, Lee ST (2013) J Am Chem Soc 135(10):3744–3747
12. Xiao J, Yin Z, Li H, Zhang Q, Boey F, Zhang H, Zhang Q (2010) J Am Chem Soc 132(20):6926–6928
13. Wöhler F (1844) Justus Liebigs Annalen der Chemie 51(2):145–163
14. Ferraris J, Walatka V, Perlstei JH, Cowan DO (1973) J Am Chem Soc 95(3):948–949
15. Odom SA, Caruso MM, Finke AD, Prokup AM, Ritchey JA, Leonard JH, White SR, Sottos NR, Moore JS (2010) Adv Funct Mater 20(11):1721–1727
16. Hasegawa T, Mattenberger K, Takeya J, Batlogg B (2004) Phys Rev B 69(24):245115
17. Tayi AS, Kaeser A, Matsumoto M, Aida T, Stupp SI (2015) Nature Chem 7(4):281–294
18. Collet E, Lemee-Cailleau MH, Buron-Le Cointe M, Cailleau H, Wulff M, Luty T, Koshihara SY, Meyer M, Toupet L, Rabiller P, Techert S (2003) Science 300(5619):612–615
19. Wuest JD (2012) Nature Chem 4(2):74–75
20. Davey R, Garside J (2001) From molecules to crystallizers: an introduction to crystallization. Oxford Chemistry Primers. Oxford University Press, New York
21. Herbstein FH (2003) Acta Crystallogr Sect B 59:303–304
22. Dunitz JD (2003) CrystEngComm 5:506
23. Desiraju GR (2003) CrystEngComm 5:466–467
24. Aakeroy CB, Salmon DJ (2005) CrystEngComm 7:439–448
25. Bond AD (2007) CrystEngComm 9(9):833–834
26. Stahly GP (2009) Cryst Growth Des 9(10):4212–4229
27. Aitipamula S, Banerjee R, Bansal AK, Biradha K, Cheney ML, Choudhury AR, Desiraju GR, Dikundwar AG, Dubey R, Duggirala N, Ghogale PP, Ghosh S, Goswami PK, Goud NR, Jetti RRKR, Karpinski P, Kaushik P, Kumar D, Kumar V, Moulton B, Mukherjee A, Mukherjee G, Myerson AS, Puri V, Ramanan A, Rajamannar T, Reddy CM, Rodriguez-Hornedo N, Rogers RD, Row TNG, Sanphui P, Shan N, Shete G, Singh A, Sun CC, Swift JA, Thaimattam R, Thakur TS, Thaper RK, Thomas SP, Tothadi S, Vangala VR, Variankaval N, Vishweshwar P, Weyna DR, Zaworotko MJ (2012) Cryst Growth Des 12(5):2147–2152
28. Zhu W, Zhen Y, Dong H, Fu H, Hu W (2014) Prog Chem 26(8):1292–1306
29. Zhu W, Yi Y, Zhen Y, Hu W (2015) Small 11:2150–2156
30. Dillon RJ, Bardeen CJ (2012) J Phys Chem A 116(21):5145–5150
31. Lee TH, Li JH, Huang WS, Hu B, Huang JCA, Guo TF, Wen TC (2011) Appl Phys Lett 99:073307
32. Epstein AJ, Etemad S, Garito AF, Heeger AJ (1972) Phys Rev B 5(3):952–977
33. Butler MA, Wudl F, Soos ZG (1975) Phys Rev B 12(11):4708–4719
34. Hobi M, Zurcher S, Gramlich V, Burckhardt U, Mensing C, Spahr M, Togni A (1996) Organometallics 15(25):5342–5346

35. Krishnan A, Pal SK, Nandakumar P, Samuelson AG, Das PK (2001) Chem Phys 265(3):313–322
36. Claessens CG, Stoddart JF (1997) J Phys Org Chem 10(5):254–272
37. Perez EM, Martin N (2015) Chem Soc Rev 44(18):6425–6433
38. Zhang J, Tan J, Ma Z, Xu W, Zhao G, Geng H, Di CA, Hu W, Shuai Z, Singh K, Zhu D (2013) J Am Chem Soc 135(2):558–561
39. Etter MC (1991) J Phys Chem 95(12):4601–4610
40. Bosshard C, Pan F, Wong MS, Manetta S, Spreiter R, Cai CZ, Gunter P, Gramlich V (1999) Chem Phys 245(1–3):377–394
41. Harris KDM, Stainton NM, Callan AM, Howie RA (1993) J Mater Chem 3(9):947–952
42. Fourmigue M (2008) Struct Bond 126:181–207
43. Theobald JA, Oxtoby NS, Phillips MA, Champness NR, Beton PH (2003) Nature 424(6952):1029–1031
44. Cavallo G, Metrangolo P, Milani R, Pilati T, Priimagi A, Resnati G, Terraneo G (2016) Chem Rev 116(4):2478–2601
45. Catalano L, Cavallo G, Metrangolo P, Resnati G, Terraneo G (2016) Top Curr Chem 373:289–309. doi:10.1007/128_2015_666
46. Zheng Q-N, Liu X-H, Chen T, Yan H-J, Cook T, Wang D, Stang PJ, Wan L-J (2015) J Am Chem Soc 137(19):6128–6131
47. Goetz KP, Vermeulen D, Payne ME, Kloc C, McNeil LE, Jurchescu OD (2014) J Mater Chem C 2(17):3065–3076
48. Jiang H, Yang X, Cui Z, Liu Y, Li H, Hu W (2009) Appl Phys Lett 94(12):123308
49. Kobayashi H, Nakayama J (1981) Bull Chem Soc Jpn 54(8):2408–2411
50. Konarev DV, Lyubovskaya RN, Drichko NV, Yudanova EI, Shul'ga YM, Litvinov AL, Semkin VN, Tarasov BP (2000) J Mater Chem 10(4):803–818
51. Olmstead MM, de Bettencourt-Dias A, Lee HM, Pham D, Balch AL (2003) Dalton Trans 16:3227–3232
52. Reinheimer EW, Zhao H, Dunbar KR (2010) J Chem Crystallogr 40(6):514–519
53. Menard E, Podzorov V, Hur SH, Gaur A, Gershenson ME, Rogers JA (2004) Adv Mater 16(23–24):2097–2101
54. Iwata S, Tanaka J, Nagakura S (1966) J Am Chem Soc 88(5):894–902
55. El-Khouly ME, Ito O, Smith PM, D'Souza F (2004) J Photochem Photobio C 5(1):79–104
56. Kawase T, Kurata H (2006) Chem Rev 106(12):5250–5273
57. Buurma AJC, Jurchescu OD, Shokaryev I, Baas J, Meetsma A, de Wijs GA, de Groot RA, Palstra TTM (2007) J Phys Chem C 111(8):3486–3489
58. Emge TJ, Wiygul FM, Chappell JS, Bloch AN, Ferraris JP, Cowan DO, Kistenmacher TJ (1982) Mol Cryst Liq Cryst 87(1–2):137–161
59. Yoshida Y, Kumagai Y, Mizuno M, Isomura K, Nakamura Y, Kishida H, Saito G (2015) Cryst Growth Des 15(11):5513–5518
60. Zhu L, Yi Y, Li Y, Kim E-G, Coropceanu V, Bredas J-L (2012) J Am Chem Soc 134(4):2340–2347
61. Torrance JB (1979) Acc Chem Res 12(3):79–86
62. Torrance JB (1985) Mol Cryst Liq Cryst 126(1):55–67
63. Torrance JB, Vazquez JE, Mayerle JJ, Lee VY (1981) Phys Rev Lett 46(4):253–257
64. Shokaryev I, Buurma AJC, Jurchescu OD, Uijttewaal MA, de Wijs GA, Palstra TTM, de Groot RA (2008) J Phys Chem A 112(11):2497–2502
65. Lei YL, Jin Y, Zhou DY, Gu W, Shi XB, Liao LS, Lee ST (2012) Adv Mater 24(39):5345–5351
66. Liu C, Minari T, Lu X, Kumatani A, Takimiya K, Tsukagoshi K (2011) Adv Mater 23(4):523–526
67. Mahns B, Kataeva O, Islamov D, Hampel S, Steckel F, Hess C, Knupfer M, Buechner B, Himcinschi C, Hahn T, Renger R, Kortus J (2014) Cryst Growth Des 14(3):1338–1346
68. Braga D, Maini L, Grepioni F (2013) Chem Soc Rev 42(18):7638–7648
69. Friscic T, Jones W (2009) Cryst Growth Des 9(3):1621–1637
70. Thordarson P (2011) Chem Soc Rev 40(3):1305–1323
71. Grimm B, Santos J, Illescas BM, Munoz A, Guldi DM, Martin N (2010) J Am Chem Soc 132(49):17387–17389
72. Li Y, Wang W, Leow WR, Zhu B, Meng F, Zheng L, Zhu J, Chen X (2014) Small 10(14):2776–2781 **(2740)**
73. Molina-Ontoria A, Fernandez G, Wielopolski M, Atienza C, Sanchez L, Gouloumis A, Clark T, Martin N, Guldi DM (2009) J Am Chem Soc 131(34):12218–12229

74. Aoki T, Sakai H, Ohkubo K, Sakanoue T, Takenobu T, Fukuzumi S, Hasobe T (2015) Chem Sci 6(2):1498–1509
75. Zhang J, Geng H, Virk TS, Zhao Y, Tan J, Di C-a XuW, Singh K, Hu W, Shuai Z, Liu Y, Zhu D (2012) Adv Mater 24(19):2603–2607
76. Yu W, Wang XY, Li J, Li ZT, Yan YK, Wang W, Pei J (2013) Chem Commun 49(1):54–56
77. Wang J, Wang D, Miller EK, Moses D, Bazan GC, Heeger AJ (2000) Macromolecules 33(14):5153–5158
78. Matte HSSR, Subrahmanyam KS, Rao KV, George SJ, Rao CNR (2011) Chem Phys Lett 506(4–6):260–264
79. Vogt FG, Clawson JS, Strohmeier M, Edwards AJ, Pham TN, Watson SA (2009) Cryst Growth Des 9(2):921–937
80. Zhu W, Zheng R, Fu X, Fu H, Shi Q, Zhen Y, Dong H, Hu W (2015) Angew Chem Int Ed 54(23):6785–6789
81. Qin Y, Zhang J, Zheng X, Geng H, Zhao G, Xu W, Hu W, Shuai Z, Zhu D (2014) Adv Mater 26(24):4093–4099
82. Coulon C, Clerac R (2004) Chem Rev 104(11):5655–5687
83. Assour JM (1965) J Chem Phys 43(7):2477–2489
84. Moriyama H, Kobayashi H, Kobayashi A, Watanabe T (1993) J Am Chem Soc 115(3):1185–1187
85. Umland TC, Allie S, Kuhlmann T, Coppens P (1988) J Phys Chem 92(22):6456–6460
86. Kistenmacher TJ, Emge TJ, Bloch AN, Cowan DO (1982) Acta Crystallogr Sect B 38(APR):1193–1199
87. Flandrois S, Chasseau D (1977) Acta Crystallogr Sect B 33(SEP15):2744–2750
88. Goetz KP, Fonari A, Vermeulen D, Hu P, Jiang H, Diemer PJ, Ward JW, Payne ME, Day CS, Kloc C, Coropceanu V, McNeil LE, Jurchescu OD (2014) Nat Commun 5:5642
89. Liu G, Liu J, Liu Y, Tao X (2014) J Am Chem Soc 136(2):590–593
90. Ichida M, Nakamura A, Shinohara H, Saitoh Y (1998) Chem Phys Lett 289(5–6):579–585
91. El-Khouly ME, Rogers LM, Zandler ME, Suresh G, Fujitsuka M, Ito O, D'Souza F (2003) ChemPhysChem 4(5):474–481
92. D'Souza F, Ito O (2009) Chem Commun 33:4913–4928
93. Tsutsumi J, Matsui H, Yamada T, Kumai R, Hasegawa T (2012) J Phys Chem C 116(45):23957–23964
94. Gotoh T, Kondoh T, Egawa K, Kubodera K (1989) J Opt Soc Am B Opt Phys 6(4):703–706
95. Hasegawa T, Mochida T, Kondo R, Kagoshima S, Iwasa Y, Akutagawa T, Nakamura T, Saito G (2000) Phys Rev B 62(15):10059–10066
96. Nguyen HL, Horton PN, Hursthouse MB, Legon AC, Bruce DW (2004) J Am Chem Soc 126(1):16–17
97. Tang Q, Li H, Liu Y, Hu W (2006) J Am Chem Soc 128(45):14634–14639
98. Tang Q, Li L, Song Y, Liu Y, Li H, Xu W, Liu Y, Hu W, Zhu D (2007) Adv Mater 19(18):2624–2628
99. Dong H, Zhu H, Meng Q, Gong X, Hu W (2012) Chem Soc Rev 41(5):1754–1808
100. Horiuchi S, Tokura Y (2008) Nat Mater 7(5):357–366
101. Kunkel DA, Hooper J, Bradley B, Schlueter L, Rasmussen T, Costa P, Beniwal S, Ducharme S, Zurek E, Enders A (2016) J Phys Chem Lett 7(3):435–440
102. Kumai R, Horiuchi S, Sagayama H, Arima T-h, Watanabe M, Noda Y, Tokura Y (2007) J Am Chem Soc 129(43):12920–12921
103. Torrance JB, Girlando A, Mayerle JJ, Crowley JI, Lee VY, Batail P, LaPlaca SJ (1981) Phys Rev Lett 47(24):1747–1750
104. Horiuchi S, Ishii F, Kumai R, Okimoto Y, Tachibana H, Nagaosa N, Tokura Y (2005) Nat Mater 4(2):163–166
105. Reineke S, Lindner F, Schwartz G, Seidler N, Walzer K, Luessem B, Leo K (2009) Nature 459(7244):234–238
106. Thompson J, Blyth RIR, Mazzeo M, Anni M, Gigli G, Cingolani R (2001) Appl Phys Lett 79(5):560
107. Zhu W, Zheng R, Zhen Y, Yu Z, Dong H, Fu H, Shi Q, Hu W (2015) J Am Chem Soc 137(34):11038–11046
108. Pan F, Wong MS, Gramlich V, Bosshard C, Gunter P (1996) J Am Chem Soc 118(26):6315–6316
109. Bosshard C, Wong MS, Pan F, Gunter P, Gramlich V (1997) Adv Mater 9(7):554–557
110. Gong Y, Chen G, Peng Q, Yuan WZ, Xie Y, Li S, Zhang Y, Tang BZ (2015) Adv Mater 27(40):6195–6201

111. Bolton O, Lee K, Kim HJ, Lin KY, Kim J (2011) Nature Chem 3(3):205–210
112. Gao HY, Zhao XR, Wang H, Pang X, Jin WJ (2012) Cryst Growth Des 12(9):4377–4387
113. Park SK, Varghese S, Kim JH, Yoon SJ, Kwon OK, An BK, Gierschner J, Park SY (2013) J Am Chem Soc 135(12):4757–4764
114. Zhu W, Dong H, Zhen Y, Hu W (2015) Sci China Mater 58(11):854–859
115. Gagniere E, Mangin D, Puel F, Rivoire A, Monnier O, Garcia E, Klein JR (2009) J Cryst Growth 311(9):2689–2695
116. Blagden N, Berry DJ, Parkin A, Javed H, Ibrahim A, Gavan PT, De Matos LL, Seaton CC (2008) New J Chem 32(10):1659
117. Wakahara T, Sathish M, Miyazawa KI, Hu C, Tateyama Y, Nemoto Y, Sasaki T, Ito O (2009) J Am Chem Soc 131(29):9940–9944